



Journal of Turbomachinery

Published Quarterly by ASME

VOLUME 131 • NUMBER 3 • JULY 2009

RESEARCH PAPERS

- 031001 Evaluation of Alternatives for Two-Dimensional Linear Cascade Facilities**
Paul M. Kodzwa, Jr., Amanda Vicharelli, Gorazd Medic, Christopher J. Elkins, John K. Eaton, Gregory M. Laskowski, and Paul A. Durbin
- 031002 Numerical Investigations of Localized Vibrations of Mistuned Blade Integrated Disks (Blisks)**
T. Klauke, A. Kühhorn, B. Beirow, and M. Golze
- 031003 Time-Accurate Predictions for a Fully Cooled High-Pressure Turbine Stage—Part I: Comparison of Predictions With Data**
S. A. Southworth, M. G. Dunn, C. W. Haldeman, J.-P. Chen, G. Heitland, and J. Liu
- 031004 Time-Accurate Predictions for a Fully Cooled High-Pressure Turbine Stage—Part II: Methodology for Quantifications of Prediction Quality**
C. W. Haldeman, M. G. Dunn, S. A. Southworth, J.-P. Chen, G. Heitland, and J. Liu
- 031005 Effect of Inlet Flow Angle on Gas Turbine Blade Tip Film Cooling**
Zhihong Gao, Diganta Narzary, Shantanu Mhetras, and Je-Chin Han
- 031006 A Parametric Study of the Blade Row Interaction in a High Pressure Turbine Stage**
G. Persico, P. Gaetani, and C. Osnaghi
- 031007 Reduced-Order Model of a Bladed Rotor With Geometric Mistuning**
Alok Sinha
- 031008 An Approach for Inclusion of a Nonlocal Transition Model in a Parallel Unstructured Computational Fluid Dynamics Code**
Dragan Kožulović and B. Leigh Lapworth
- 031009 Developments in Hot-Streak Simulators for Turbine Testing**
Thomas Povey and Imran Qureshi
- 031010 A Comparison of the Flow Structures and Losses Within Vaned and Vaneless Stators for Radial Turbines**
A. T. Simpson, S. W. T. Spence, and J. K. Watterson
- 031011 Effects of Compressor Tip Injection on Aircraft Engine Performance and Stability**
Wolfgang Horn, Klaus-Jürgen Schmidt, and Stephan Staudacher
- 031012 Spike and Modal Stall Inception in an Advanced Turbocharger Centrifugal Compressor**
Z. S. Spakovszky and C. H. Roduner
- 031013 Validation of MISES Two-Dimensional Boundary Layer Code for High-Pressure Turbine Aerodynamic Design**
Philip L. Andrew and Harika S. Kahveci
- 031014 Surface Shear Stress and Pressure Measurements in a Turbine Cascade**
Brian M. Holley and Lee S. Langston
- 031015 Numerical Investigation on Unsteady Effects of Hot Streak on Flow and Heat Transfer in a Turbine Stage**
Bai-Tao An, Jian-Jun Liu, and Hong-De Jiang

(Contents continued on inside back cover)

This journal is printed on acid-free paper, which exceeds the ANSI Z39.48-1992 specification for permanence of paper and library materials. ©™
♻️ 85% recycled content, including 10% post-consumer fibers.

Editor, **DAVID C. WISLER** (2013)
Assistant to the Editor: **ELIZABETH WISLER**
Associate Editors
Gas Turbine (Review Chairs)
K. BRUN (2009)
T. SATTELMAYER (2009)
Aeromechanics
M. MONTGOMERY (2009)
A. SINHA (2009)
Boundary Layers and Turbulence
G. WALKER (2009)
Compressor Aero
ZOLTAN S. SPAKOVSKY (2011)
Computational Fluid Dynamics
J. ADAMCZYK (2009)
M. CASEY (2009)
Experimental Methods
W.-F. NG (2009)
Heat Transfer
R. BUNKER (2009)
J.-C. HAN (2009)
Radial Turbomachinery
R. VAN DEN BRAEMBUSSCHE (2009)
Turbomachinery Aero
S. GALLIMORE (2009)
D. PRASAD (2009)
A. R. WADIA (2009)

PUBLICATIONS COMMITTEE
Chair, **BAHRAM RAVANI**

OFFICERS OF THE ASME
President, **AMOS E. HOLT**
Executive Director, **THOMAS G. LOUGHLIN**
Treasurer, **T. PESTORIUS**

PUBLISHING STAFF
Managing Director, Publishing
PHILIP DI VIETRO
Manager, Journals
COLIN MCATEER
Production Coordinator
JUDITH SIERANT

Transactions of the ASME, Journal of Turbomachinery (ISSN 0889-504X) is published quarterly (Jan., Apr., July, Oct.) by The American Society of Mechanical Engineers, Three Park Avenue, New York, NY 10016. Periodicals postage paid at New York, NY and additional mailing offices.
POSTMASTER: Send address changes to Transactions of the ASME, Journal of Turbomachinery, c/o THE AMERICAN SOCIETY OF MECHANICAL ENGINEERS, 22 Law Drive, Box 2300, Fairfield, NJ 07007-2300.
CHANGES OF ADDRESS must be received at Society headquarters seven weeks before they are to be effective. Please send old label and new address.

STATEMENT from By-Laws. The Society shall not be responsible for statements or opinions advanced in papers or ... printed in its publications (B7.1, Par. 3).

COPYRIGHT © 2009 by the American Society of Mechanical Engineers. For authorization to photocopy material for internal or personal use under those circumstances not falling within the fair use provisions of the Copyright Act, contact the Copyright Clearance Center (CCC), 222 Rosewood Drive, Danvers, MA 01923, tel: 978-750-8400, www.copyright.com. Request for special permission or bulk copying should be addressed to Reprints/Permission Department. Canadian Goods & Services Tax Registration #126148048

- 031016 **Extended Models for Transitional Rough Wall Boundary Layers With Heat Transfer—Part I: Model Formulations**
M. Stripf, A. Schulz, H.-J. Bauer, and S. Wittig
- 031017 **Extended Models for Transitional Rough Wall Boundary Layers With Heat Transfer—Part II: Model Validation and Benchmarking**
M. Stripf, A. Schulz, H.-J. Bauer, and S. Wittig
- 031018 **On the Coupling of Designer Experience and Modularity in the Aerothermal Design of Turbomachinery**
Jerome P. Jarrett, Tiziano Ghisu, and Geoffrey T. Parks
- 031019 **On the Role of the Deterministic and Circumferential Stresses in Throughflow Calculations**
J.-F. Simon, J. P. Thomas, and O. Léonard

2007 IGTI SCHOLAR LECTURE

- 031101 **Some Aerodynamic Problems of Aircraft Engines: Fifty Years After -The 2007 IGTI Scholar Lecture-**
Edward M. Greitzer

The ASME Journal of Turbomachinery is abstracted and indexed in the following:

Aluminum Industry Abstracts, Aquatic Science and Fisheries Abstracts, Ceramics Abstracts, Chemical Abstracts, Civil Engineering Abstracts, Compendex (The electronic equivalent of Engineering Index), Corrosion Abstracts, Current Contents, Ei EncompassLit, Electronics & Communications Abstracts, Energy Information Abstracts, Engineered Materials Abstracts, Engineering Index, Environmental Science and Pollution Management, Excerpta Medica, Fluidex, Fuel and Energy Abstracts, INSPEC, Index to Scientific Reviews, Materials Science Citation Index, Mechanical & Transportation Engineering Abstracts, Mechanical Engineering Abstracts, METADEX (The electronic equivalent of Metals Abstracts and Alloys Index), Metals Abstracts, Oceanic Abstracts, Pollution Abstracts, Referativnyi Zhurnal, Shock & Vibration Digest, Steels Alert

Paul M. Kodzwa, Jr.

Amanda Vicharelli

Gorazd Medic

Christopher J. Elkins

John K. Eaton¹

e-mail: eatonj@stanford.edu

Department of Mechanical Engineering,
Flow Physics and Computation Division,
Stanford University,
Stanford, CA 94305

Gregory M. Laskowski

Energy and Propulsion Technology Laboratories,
General Electric Global Research Center,
Niskayuna, NY 12309

Paul A. Durbin

Department of Aerospace Engineering,
Iowa State University,
Ames, IA 50011

Evaluation of Alternatives for Two-Dimensional Linear Cascade Facilities

This paper presents two low-cost alternatives for turbine blade surface heat transfer and fluid dynamics measurements. These models embody careful compromises between typical academic and full-scale turbomachinery experiments and represent a comprehensive strategy to develop experiments that can directly test shortcomings in current turbomachinery simulation tools. A full contextual history of the wide range of approaches to simulate turbine flow conditions is presented, along with a discussion of their deficiencies. Both models are simplifications of a linear cascade: the current standard for simulating two-dimensional turbine blade geometries. A single passage model is presented as a curved duct consisting of two half-blade geometries, carefully designed inlet and exit walls and inlet suction. This facility was determined to be best suited for heat transfer measurements where minimal surface conduction losses are necessary to allow accurate numerical model replication. A double passage model is defined as a single blade with two precisely designed outer walls, which is most appropriate for flow measurements. The design procedures necessary to achieve a desired flow condition are discussed.

[DOI: 10.1115/1.2985073]

1 Introduction

Large-scale efforts to compare simulations to experiments, as performed by Garg [1] and Haldeman and Dunn [2], demonstrate that many of the characteristic state-of-the-art modeling applications routinely fail when applied to modern turbine blade geometries. However, Dunn [3] pointed out that it is unclear if such failures are due to specific modeling issues, or deficiencies in the experimental measurements. There are several approaches presented in the open literature to experimentally simulate the flow field around a given gas turbine engine rotor or stator blade geometry. Turbomachinery testing facilities can, in general, be divided into two main subsets: nonrotating cascades (linear and annular) and rotating facilities. The first simplification from an actual turbine is a steady state annular rotating cascade, as demonstrated by Atassi et al. [4]. This approach is primarily used for compressor geometries as implemented by Schulz and Gallus [5] and Wisler et al. [6]. Blair [7] obtained highly resolved maps of the heat transfer coefficient without film cooling using an incompressible, steady, ambient temperature, large-scale turbine rotor passage.

Transient rotating annular cascades driven by either a large tank in blowdown mode (as illustrated by Abhari and Epstein [8]), a shock-tube (as pioneered by Dunn and Stoddard [9], Dunn [10], Dunn and Chupp [11], and Dunn et al. [12]), or an isentropic light piston (as demonstrated by Chana and Jones [13]) offer cost advantages when compared to steady state facilities as these have reduced flow requirements due to their ephemeral run times. Such tests often have a duration of a few hundred milliseconds requiring the use of complex transient measurement techniques to extract heat transfer and pressure data on test engine components. This approach only allows for low spatial resolution measurements of surface heat flux and pressure [3]. The heat transfer sensors in these studies, thin-film heat flux gauges, provide a high

frequency response that allows time-accurate measurements of unsteady convective heat transfer rates. These sensors use a quasi-1D conduction model to calculate the surface heat flux. Dunn [14] and Epstein et al. [15] presented typical analyses used to extract time-resolved heat flux data from these gauges. This approach presents several problems that can make the measurements difficult to interpret and model. Mukerji et al. [16] demonstrated that such sensors can corrupt the heat transfer measurement by as much as 30%, by changing the thermal boundary condition on the blade, if the sensor substrate has a significantly lower thermal diffusivity than the surrounding material. The substrate causes a local temperature rise over the gauge, producing a wall temperature step. This has been termed as the "heat island effect" by Dunn et al. [17]. Corrections for this problem have been proposed by Moffat et al. [18]. Furthermore, Diller [19] argued that the flow conditions in blade passages are highly sensitive to local perturbations: i.e., a poorly installed gauge can cause physical disruptions of the boundary layer, affecting the measurements by as much as 75% [20]. Such concerns effectively limit their usefulness to modeling efforts. Furthermore, the harsh conditions in these experiments cause these sensors to have a relatively high mortality rate. This behavior can be traced to the high inlet temperatures of these experiments that are on the order of 500 K and mechanical stresses due to rotation rates as fast as 10,000 rpm. Another issue with these experiments is the necessary lead time to develop the experimental apparatus. Typically, there is at least a 3–4 year evolution from "drawing board" to data collection [21]. These facts do not obviate the usefulness of rotating facilities, as they can match all relevant nondimensional parameters. However, it suggests that to obtain higher measurement fidelity and use measurement techniques that can be precisely replicated numerically (constant heat flux or isothermal surfaces) it is practical to simplify the flow field, especially if the blade midspan behavior is of primary interest. However, it is important to note that the primary trade-off of such an approach is the inability to match all relevant nondimensional parameters and lack of rotation. Never-

¹Corresponding author.

Manuscript received December 9, 2006; final manuscript received July 26, 2008; published online April 2, 2009. Review conducted by Roger L. Davis.

theless, as the objective of such experiments is to improve numerical modeling efforts, such compromises are often acceptable.

A further simplification of the flow field is a nonrotating annular cascade, which consists either of a full annulus or a 60 deg sector, based on flow requirements. Martinez-Botas et al. [22] presented uncooled heat transfer results in an annular cascade driven by an isentropic light piston. Thermochromic liquid crystal paint was used to obtain spatially resolved measurements in this experiment. However, the time and expense required to build such a facility give them no real advantage over linear cascades.

Linear cascades are considered an acceptable compromise to provide well-resolved data and well-defined conditions for both design and modeling improvement purposes. Baughn [23] and Guenette et al. [24] suggested that the flow around the center airfoil of a two-dimensional linear cascade presents nearly identical flow characteristics as that found along the midspan position of a blade in a rotating annular cascade. These facilities provide tremendous flexibility in investigating a variety of conditions, including reducing endwall losses by axisymmetric endwall contouring [25]; endwall and blade heat transfer [26,27]; incidence effects on film cooling performance [28]; and film cooling-generated aerodynamics losses [29]. They are amenable to optical fluid mechanics and heat transfer measurement techniques such as laser-Doppler anemometry (LDA) [30], infrared thermography [31], and thermochromic liquid crystals [32]. Additionally, linear cascades can be run in steady state or transient modes, the latter being more cost effective due to reduced flow requirements. A popular fashion of performing transient linear cascade tests is to use an isentropic light piston with ceramic test blades, as illustrated by Camci and Arts [28] and Sieverding et al. [33]. It is important to point out that depending on the choice of measurement technique the ability of a given flow facility to achieve various nondimensional numbers is often constrained. For example, thermochromic liquid crystals, which change temperature over a narrow temperature range (at most 10–15 °C), limit the possible temperature range for a given facility. However, this measurement technique allows high-resolution temperature maps that can be directly compared against numerical simulations. The number of blades has been found to be important in ensuring that the desired flow conditions are achieved. To obtain a periodic flow field around the center measurement blade in a typical linear cascade, several “dummy” blades are required. As the typical mass flow rate through a passage in between two blades is approximately 1 kg/s, the requirement for so many passages places a substantial flow requirement for the facility. In the case of Giel et al. [34], the required flow rate was 26 kg/s at steady state conditions.

To further reduce the cost of performing heat transfer measurements on real turbine blade geometries, the restriction on the number of blades can be relaxed. However, this makes achieving a periodic flow condition more difficult. Abuaf et al. [35] proved this point with a transonic four-passage cascade that was used to collect heat transfer measurements. An examination of the mass flow rates through each passage revealed that the flow in this cascade was not periodic. Goldstein and Spores [36], Radomsky and Thole [37], and Priddy and Bayley [38] presented a further simplification, termed a double passage cascade. These models comprise of a single blade bounded by two shaped outer walls. Yet another simplification is a single passage model. This model consists of a single passage bounded by two walls, which are shaped by the blade geometry under examination. Blair [39] first utilized a single passage model to perform endwall heat transfer and film cooling measurements. Bailey [40], Chung and Simon [41], and Chung et al. [42] extended this approach to study airfoil aerodynamics. Buck and Prakash [43] combined a single passage model with a mass transfer analogy technique to perform film cooling measurements. It is important to note that both double and single passage models have been actively used with entirely sup-

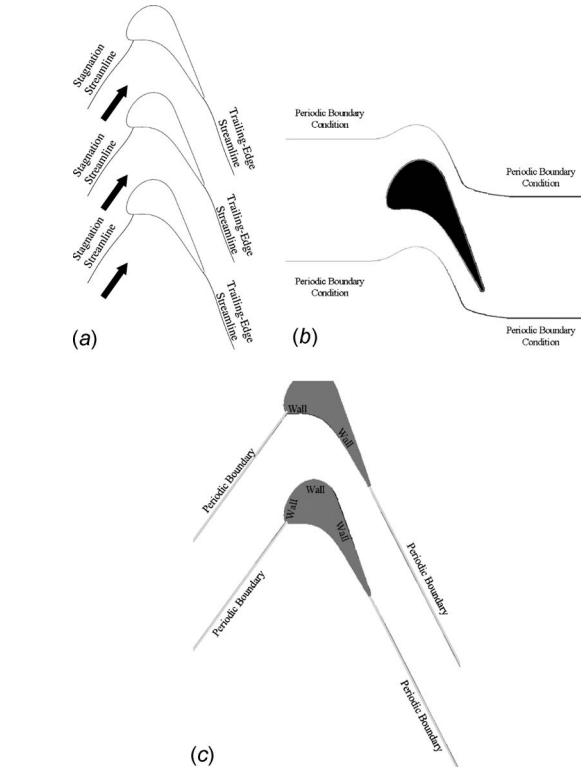


Fig. 1 (a) Three arbitrary blades from an idealized 2D infinite cascade with representative computational domains. (b) Single arbitrary blade with periodic boundary conditions at midpitch. (c) Blade passage with inlet and outlet periodic boundary conditions.

sonic flows. Thus, it was unclear how to extend these techniques to more modern blade geometries with significantly increased turning angle and supersonic flow conditions.

This paper discusses recent efforts to design double and single passage models to achieve periodic flow conditions for a transonic, highly cambered blade geometry. Such experimental facilities have the advantage of providing highly resolved fluid mechanics and heat transfer measurements at steady state conditions without massive flow supply requirements. Consequently, these models are considerably cheaper and provide the same data as a full linear cascade. Our objective is to use these facilities with well-defined flow and thermal boundary conditions to improve the numerical modeling of such flows. It is important to point out, however, that these models are intended for use for a specific inlet flow angle and pressure ratio. Consequently, it is unclear how useful these models are for significantly off-design conditions.

2 Overview of Passage Design Concepts

There are two well-accepted computational domains for nonrotating two-dimensional turbine blade geometries. Both these approaches simulate an infinite row of blades, as shown in Fig. 1(a). Incoming and departing streamlines have been included in this figure for discussion purposes. One approach is a single blade with periodic boundary conditions at midpitch, as shown in Fig. 1(b). The other uses two blade surfaces, the pressure surface of the upper blade and the suction surface of the lower blade with periodic boundaries leading up to and departing from these surfaces, as shown in Fig. 1(c). A variation of this approach uses one full blade and two blade surfaces, as demonstrated in Fig. 2.

The single and double passage experimental techniques mimic these approaches although the inlet and exit periodic boundary condition surfaces in Fig. 1(c) and Fig. 2 are replaced with walls. The ultimate design objective is to establish a flow field that

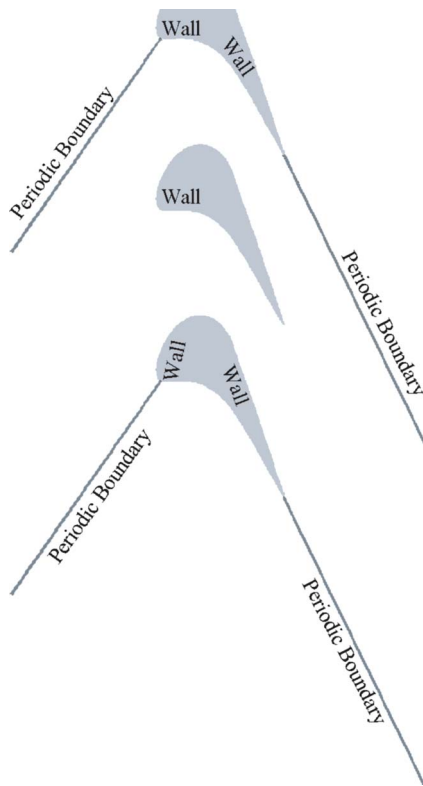


Fig. 2 Blade passage with inlet and outlet periodic boundary conditions

matches a two-dimensional infinite cascade flow condition. Kodzwa and Eaton [44] demonstrated that the single passage model is ideal for steady state heat transfer measurements with two well-insulated blade surfaces, access for optical surface heat transfer measurements, and reduced flow requirements. Conversely, the double passage model of Laskowski [45] is ideal for optical flow measurements as demonstrated by Vicharelli and Eaton [46]. The double passage approach was not deemed optimal for heat transfer measurements as the thermal losses within the instrumented center blade were determined to be unacceptable. Both approaches are useful for one operating condition and new walls are necessary for different run conditions. The aerodynamic design procedure incorporated 2D and 3D full-geometry simulations. The essence of the procedure is indicated as follows.

1. Perform infinite cascade simulation on two-dimensional blade geometry at the conditions of interest.
2. Obtain calculated streamlines from simulation to develop initial guesses for the shape of passage walls and suction rates, if appropriate. Additionally, obtain the surface pressure distribution, skin friction, and various flow field parameters around airfoil for comparative purposes.
3. Perform a numerical optimization on these shapes and suction rates to achieve an infinite cascade flow field.
4. Verify the design with experimental data.
5. Iterate between steps 3 and 4, if necessary.

Note that our approach assumes that computational fluid dynamics (CFD) can accurately predict the target pressure distribution for a given airfoil. Previous studies have indeed indicated that such an assumption is reasonable for transonic and subsonic airfoils with fully attached boundary layers [1,47]. Nevertheless, it is important to state that this assumption requires additional validation with varying airfoil geometries to establish its limitations. An immediate example would be airfoils with potential boundary layer separation. The Reynolds-averaged Navier–Stokes (RANS) equations

Table 1 Flow conditions for experimental blade geometry

Parameter	Test condition
Chord length, c_{blade} (mm)	36.1
Leading edge diameter (mm)	≈ 6
Airfoil pitch spacing (mm)	39.8
$\gamma_{\text{inlet}} = c_p / c_v$	1.4
Inlet angle	29.2 deg
Exit angle	-68.6 deg
$P_{0,\text{inlet}} / P_{\text{exit}}$	2.57
$P_{0,\text{inlet}}$ (Pa)	2.60×10^5
$T_{0,\text{inlet}}$ (K)	300
Approximate inlet Mach number	≈ 0.34
Reynolds number, $Re_c = \rho \bar{u}_{\text{inlet}} c_{\text{blade}} / \mu$	6.62×10^5

for a compressible turbulent flow were solved using a commercial CFD package, STAR-CD [48]. In all the simulations for the aerodynamics design, a two-layer, two-equation $k-\epsilon$ turbulence model was implemented. Table 1 summarizes the expected flow conditions for the given blade geometry at typical test conditions (from Buck [49]). The models are designed around an advanced first stage rotor blade geometry. This airfoil is highly cambered and operates at transonic conditions, with meanflow Mach numbers as high as 1.5. This geometry was used by Haldeman et al. [50] in full rotating aerodynamic and heat transfer tests. The model scale (1.3) was selected based on instrumentation concerns and flow supply limitations. The experiment was designed to run at ambient conditions with the model back pressure assumed to be at atmospheric pressure.

Figures 3 and 4 show a schematic of experimental single and double passage models with their salient features identified. The presented single passage model was designed to be placed on top of a plenum with flow passing upwards either from a plenum through a bellmouth (in the case of the single passage) or from a carefully designed nozzle (in the case of the double passage). The inlet duct length was chosen to be long enough such that there would be adequate clearance between the exhaust flow and the inlet and also to provide probe access to an inlet measurement station. The downstream duct length was chosen to be long enough such that the exhaust manifold shape would have minimal effect on the flow in the test region.

3 Infinite Cascade

Infinite cascade simulations were conducted to develop a baseline and provide target data to complete the passage model designs. Details on these viscous and inviscid simulations and methodology can be found in Refs. [44,45]. The following summarizes the results of these analyses. Figure 5 displays the calculated pressure distribution using these approaches, presented as the isentropic Mach number, M_{is} , versus the surface coordinate, s_c / c_{blade} . This parameter is a reformulation of the pressure distribution, using the inlet stagnation pressure to compute a Mach number as follows:

$$M_{\text{is}} = \sqrt{\frac{2}{\gamma - 1} \left(\left(\frac{P_{0,\text{inlet}}}{P} \right)^{(\gamma-1)/\gamma} - 1 \right)} \quad (1)$$

The negative surface distance positions shown in this figure correspond to locations on the pressure side of the airfoil, while the positive surface positions correspond to the suction surface. Figure 6 provides a visual description of these surface coordinate positions, along with a definition of the axial location along the blade. Table 2 presents the computed stagnation point locations using inviscid calculations and various turbulence models. Of interest is the sensitivity of the standard $k-\epsilon$ turbulence model to changes in the inlet turbulence condition. This sensitivity was removed when the modeling equations were modified to limit the production of turbulent kinetic energy, as proposed by Chen and

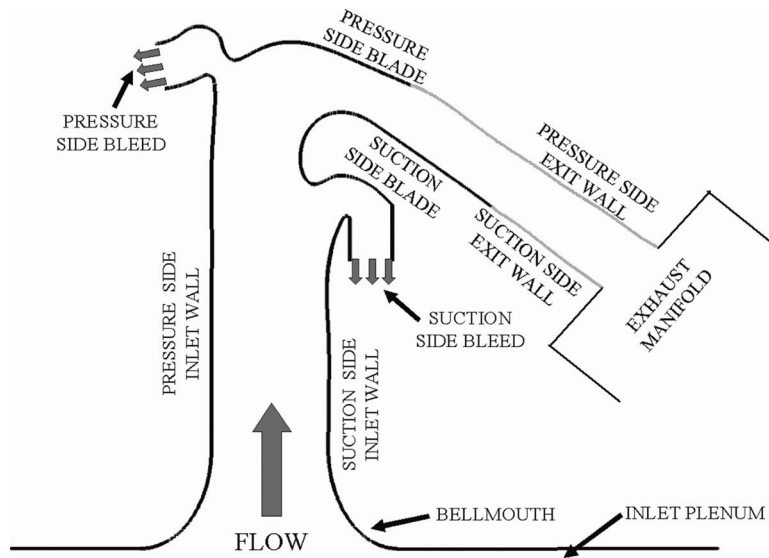


Fig. 3 Experimental single passage model

Kim [51]. Figure 7(a) shows Mach number contours for the two-dimensional RANS calculation using this model. To design the shape of the inlet and outlet walls and the amount of suction, streamlines were extracted from this simulation. Figure 7(b) presents the streamlines in the initial orientation of the blade geometry, and the streamlines after the domain was rotated for implementation in the presented experimental facilities.

4 Single Passage Model

A heuristic-based numerical simulation approach was developed to design the inlet and exit wall shapes. Full details can be found in Ref. [44]. The design procedure involved the following steps.

1. Correctly position the stagnation point on the suction and pressure side surfaces by adjusting the shape of the inlet walls using streamlines from the RANS infinite cascade calculation to achieve satisfactory agreement with respect to the location of the stagnation point on the two measurement surfaces.
2. To decouple this from any effect from the shape of the exit

passage, enforce periodic boundary conditions, instead of wall boundary conditions along the trailing edge surfaces of the domain.

3. Correctly position and set up the shock structure on the aft side of the airfoil geometry by shaping the exit duct walls again using streamlines from the RANS simulation produced from step 1.

4.1 Flow Model. The computational grid for the single passage was generated in a multiblock fashion utilizing an in-house structured iterative elliptic grid generator developed by Wu [52]. This approach ensures grid line orthogonality on all the boundaries of the domain. Three H -grid blocks were used in constructing the domain; two blocks were used for each bleed section and one for the main passage. The cell heights near the walls were stretched to achieve y^+ values ranging from 0.14 to 3.7. We performed a grid refinement study to determine the smallest possible grid size that could be run while maintaining satisfactory accuracy in M_{is} ; this resulted in a mesh size of approximately 60,000 cells for the majority of results presented here. The largest two-dimensional grid during the design process contained approximately 150,000 cells. This study revealed that the oblique shock structure observed along the suction surface primary flow feature was highly sensitive to grid resolution. A stagnation boundary condition was specified at the inlet and constant pressure boundary conditions were implemented on the bleed exit boundaries.

4.2 Inlet Wall Design. To design the inlet walls, the exit surfaces were replaced with periodic boundary conditions that extended one-chord length (c_{blade}) in the axial direction downstream of the trailing edges of the airfoils. This approach equated the values of all flow variables along the boundaries. The ideal inlet wall shapes would generate a streamline one-displacement-thickness (δ_1) away from the surface that would correspond to a streamline in the infinite cascade flow field. For this to occur, the boundary layer must remain attached to the bleed to function correctly. Thence, the chosen wall shape must have streamwise pressure gradients that ensure attached thin boundary layers. This goal was achieved by taking successive streamlines from the infinite cascade simulation and performing a two-dimensional RANS calculation to determine the predicted M_{is} distribution. The streamlines were chosen consistent with the desired direction of movement for the predicted stagnation point. The bellmouth was redesigned using ovals with dimensions consistent with the chosen inlet streamlines.

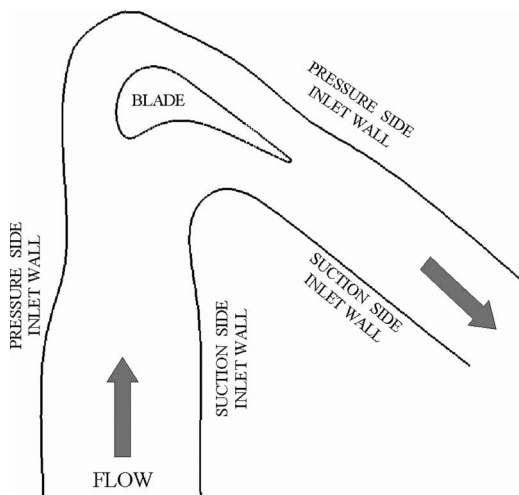


Fig. 4 Experimental double passage

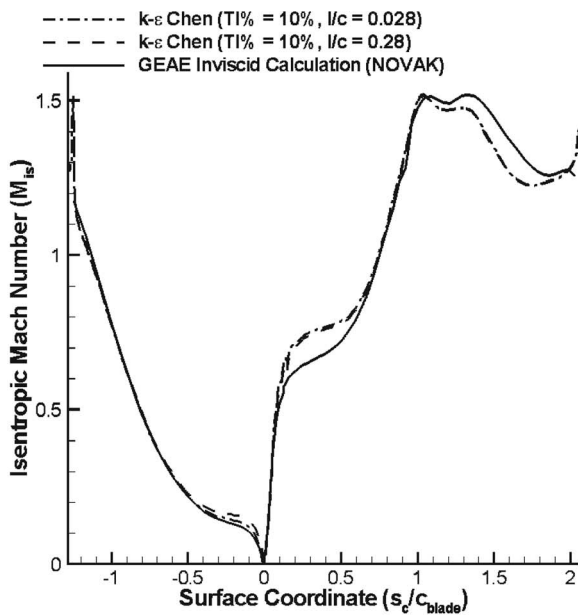
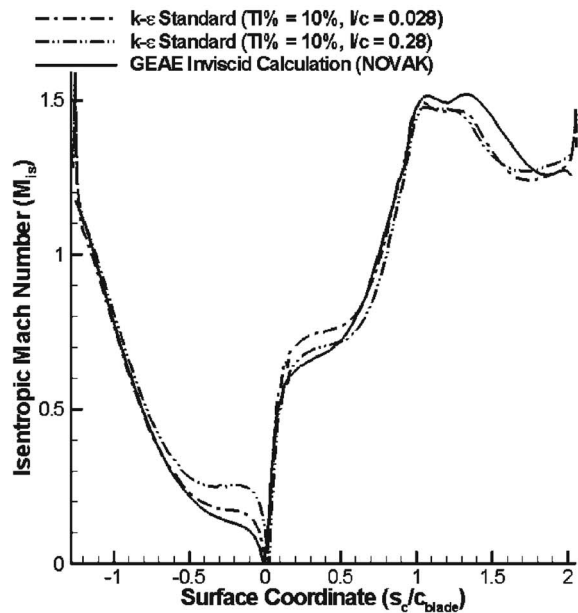


Fig. 5 Computed isentropic Mach number distributions for experimental turbine blade geometry using Chen variant of the $k-\epsilon$ turbulence model (Refs. [53,55])

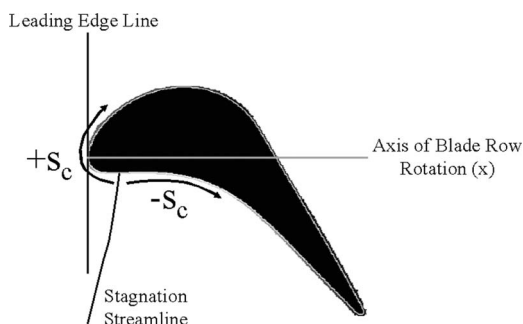


Fig. 6 Definition of axial location

Table 2 Comparison of computed stagnation point locations using various turbulence models and conditions for infinite two-dimensional cascade

Turbulence model	$M_{is}=0(x/c_{blade})$
$k-\epsilon$ standard (TI% = 10% , $l/c_{blade}=0.028$)	2.28×10^{-3}
$k-\epsilon$ standard (TI% = 10% , $l/c_{blade}=0.028$)	1.37×10^{-3}
$k-\epsilon$ Chen (TI% = 10% , $l/c_{blade}=0.028$)	2.76×10^{-3}
$k-\epsilon$ Chen (TI% = 10% , $l/c_{blade}=0.028$)	2.28×10^{-3}
Inviscid calculation (NOVAK)	2.76×10^{-3}

Table 3 compares the agreement between the stagnation point locations on both surfaces using the previously described approach, an alternative approach developed by Buck and Prakash [43] and the infinite cascade. Figure 8 presents predicted M_{is} distributions for designs using the Buck and Prakash technique and the design practice discussed here. An examination of these distributions verified that the bleed conditions have a negligible ef-

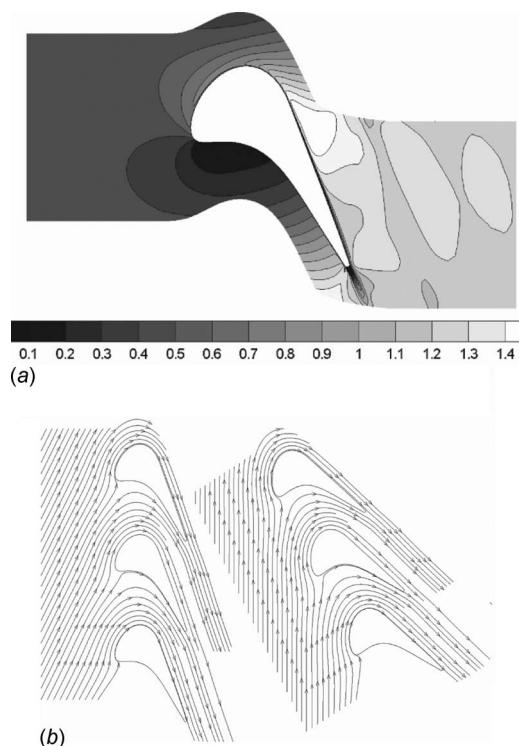


Fig. 7 (a) Mach number contours for 2D infinite cascade viscous simulation and (b) streamlines from infinite cascade simulation as calculated and rotated by inlet angle for implementation in passage models

Table 3 Comparison of computed stagnation point axial locations for new design versus infinite cascade and Buck and Prakash [43] design

Turbulence model	$M_{is}=0(x/c_{blade})$
$k-\epsilon$ Chen (TI% = 10% , $l/c_{blade}=0.28$)	2.28×10^{-3}
Suction side blade, $k-\epsilon$ Chen (TI% = 10% , $l/c_{blade}=0.28$)	2.64×10^{-3}
Pressure side blade, $k-\epsilon$ Chen (TI% = 10% , $l/c_{blade}=0.28$)	2.64×10^{-3}
Suction side blade [43], $k-\epsilon$ Chen (TI% = 10% , $l/c_{blade}=0.28$)	1.24×10^{-3}
Pressure side blade [43], $k-\epsilon$ Chen (TI% = 10% , $l/c_{blade}=0.28$)	3.71×10^{-3}

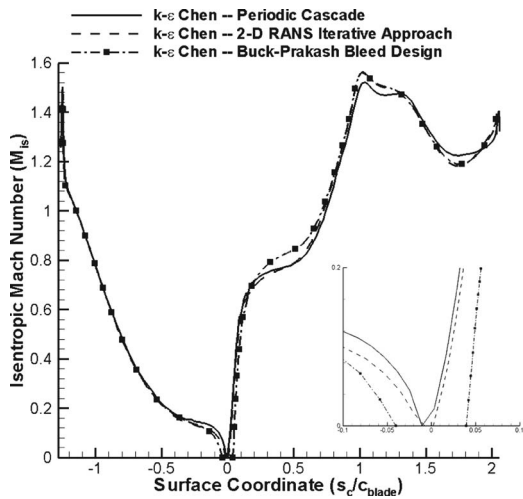


Fig. 8 Comparison of M_{is} distributions for Buck and Prakash [43] and new single passage design approaches demonstrating the effect of bleed geometry

fect on the downstream shock structure. The computed skin friction coefficients along the bleed walls indicated that these walls would produce no separation.

4.3 Exit Wall Design (Tailboards). The results presented by Kodzwa and Eaton [44] demonstrated the necessity of curved exit walls in achieving the desired shock structure. By extension from the design process for the inlet walls, the desired exit wall designs should be those that produce streamlines a δ_1 away from the wall that closely follow those of an infinite cascade flow field. Furthermore, considering that the displacement thicknesses of the boundary layers on the exit walls are strongly coupled to the shock structure, it is virtually impossible to determine a priori the optimal wall shape. Thus some form of iterative scheme must be used to design the exit walls.

Figure 9 evinces the similarities in the shock structure between the infinite cascade flow field and one with periodic tailboards and properly designed bleeds. The maximum error between the flow fields was estimated to be approximately 8%. The error was defined using the following equation:

$$\epsilon_{M_{IC}} = \left| \frac{M_{IC}}{M_{2DRANS}} - 1 \right| \quad (2)$$

where M_{IC} is the computed Mach number from the infinite cascade simulation and M_{2DRANS} is the computed Mach number from

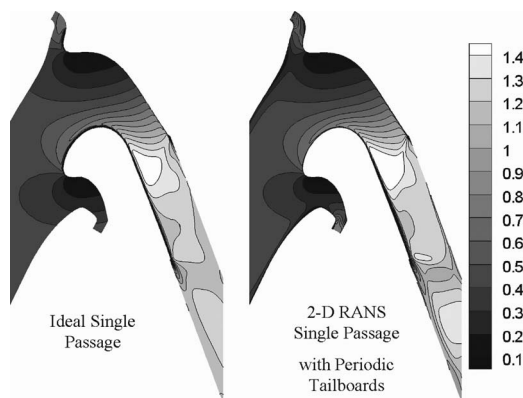


Fig. 9 Comparison of Mach number for ideal single passage model and single passage model with periodic tailboards

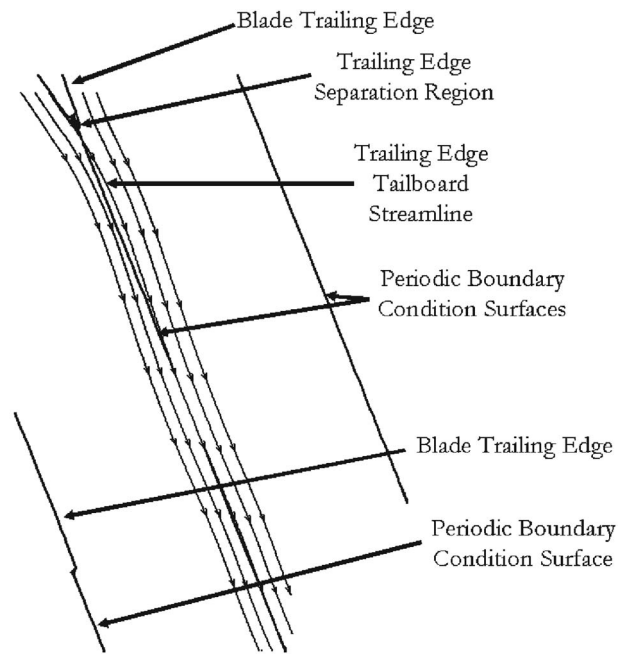


Fig. 10 Computed trailing edge streamlines from single passage calculation with periodic exit boundaries. These are used to design the tailboards.

the single passage simulation.

Figure 10 displays computed trailing edge streamlines from the single passage computation with periodic exit boundaries. The design procedure for the exit wall is based on the postulate that the ideal wall shape consists of the closest streamline to the trailing edge, rotated to account for the growing boundary layer along the wall. The pivot point for this rotation was assumed to be at the trailing edge of each blade, as shown in Fig. 11. Based on previous results, it was conjectured that it was only necessary to adjust the pressure surface exit wall. Hence, this wall was rotated counterclockwise by a defined angle, ϕ_{ps} . A rotation angle for the suction surface exit wall was also defined (ϕ_{ss}). However, this was found to be unnecessary by exploratory simulations.

Figure 12 presents the evolution of the single passage M_{is} dis-

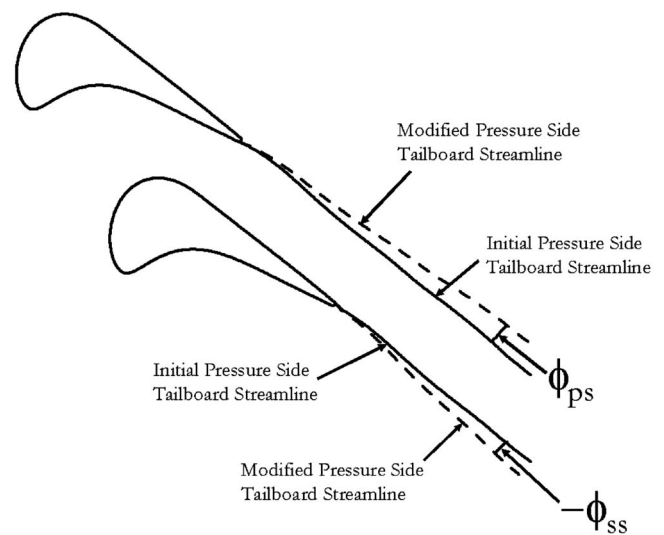


Fig. 11 Definition of rotation angles for pressure and suction side blade surfaces. Complete blades are shown in this figure for ease of identification.

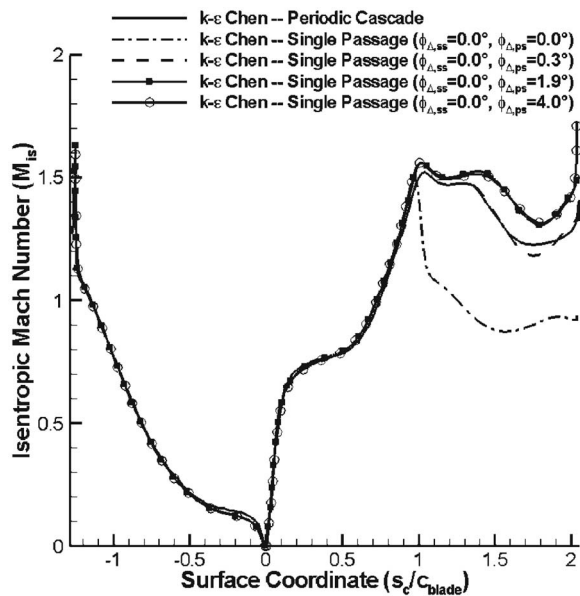


Fig. 12 Comparison of M_{is} distributions for various pressure tailboard angles

tribution with increasing angle of rotation for the pressure side wall. When $\phi_{ps} \approx 0$ deg, the interference of the boundary layer with the mainstream flow causes a strong initial shock to form, evidenced by the dramatic drop in the suction side M_{is} distribution. As ϕ_{ps} increases, the M_{is} distribution along the suction side blade wall approaches that of the infinite cascade simulation. The difference between these two results is minimized at a particular angle; in these simulations it was at $\phi_{ps} = 0.3$ deg. Beyond this value, the oblique shocks continue to weaken, resulting in even faster flow over the suction side wall. These results also indicate that beyond an angle of approximately $\phi_{ps} \approx 1.90$ deg, there is a limited change in the surface pressure distribution. In all cases, there was no noticeable effect on the location of the stagnation points due to the changing of the exit wall geometry.

The initial build for the single passage used a tailboard angle of $\phi_{ps} = 0.3$ deg. This angle was predicted to give the best M_{is} agreement. The computed flow field “error” for this geometry ($\epsilon_{M_{IC}} = |M_{IC}/M_{2DRANS} - 1|$) demonstrated that high quality agreement with the infinite cascade M_{is} distribution ensures a flow field that closely matches that found in an infinite cascade. This result is important as it suggests that precisely matching the desired M_{is} distribution guarantees a match to the flow field conditions. Kodzwa and Eaton [44] experimentally determined, however, that such a model produced a strong normal shock in the passage. After successive experimental iterations, the implemented tailboard angle was $\phi_{ps} = 1.90$ deg; this produced a pressure distribution that closely followed the infinite cascade simulation, which differed significantly from the prediction. This angle choice was heuristically described as a “safety margin” to account for the three-dimensional effects that resulted from thicker tailboard boundary layers than those predicted by the two-dimensional RANS design process or uncertainty in the manufacturing process. As the flow field is very sensitive to this angle, instead of using adjustable tailboards, we chose to machine this part out of a solid piece of Ren Shape.

4.4 Experimental Validation. To evaluate the flow conditions in the blade passage, two airfoil surfaces with closely spaced pressure taps were installed in a model constructed out of a low-thermal conductivity material (Ren Shape 450, a high-density polyurethane material) to minimize thermal losses as much as possible. The taps consisted of cross-drilled holes; the tap on the

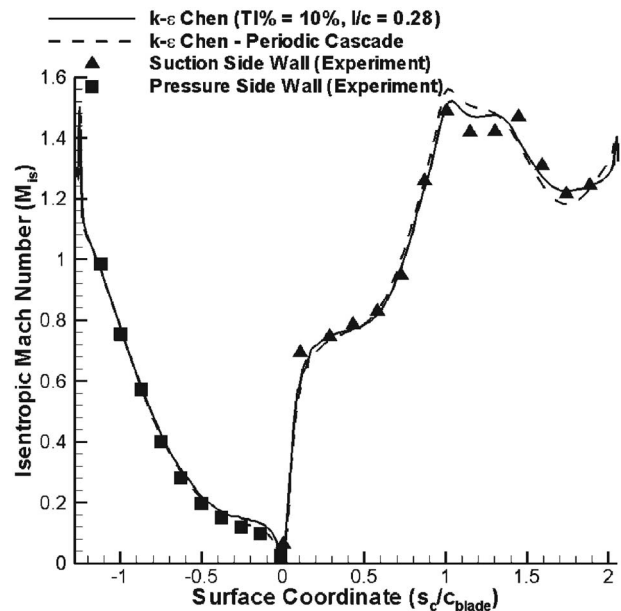


Fig. 13 Measurements of M_{is} for low turbulence condition for a single passage model

surface was a 0.62 mm diameter hole, drilled perpendicular to the local surface tangent and the cross-drilled port was a 1.6 mm diameter hole. A 1.59 mm diameter copper tube with an internal diameter of 0.88 mm was glued into the port. 1.59 mm diameter Tygon tubes were push-fit over the ends of the copper tubes and connected to a Scanivalve (Scanivalve Corporation #SSS-48C Mk III).

Figure 13 presents the measured M_{is} distribution without a turbulence grid installed. For comparison, the desired pressure distribution for the given airfoil geometry and the computed M_{is} distribution for the periodic single passage is included. The uncertainty of M_{is} was computed to be ± 0.046 ($P = 0.95$). These results show close agreement with the desired pressure distribution for the given airfoil geometry. The sole location where there is a significant difference between prediction and experiment is at $s_c/c_{blade} \approx 1.0$. Grid refinement studies suggested that this difference was due to (i) inadequate grid resolution around the shock and (ii) our chosen numerical algorithm. However, it is important to note that this agreement is equivalent to that illustrated by Medic and Durbin for the transonic rotor airfoil used by Camci and Arts [28] ($\pm 10\%$). Thus we considered the agreement here to be acceptable.

Table 4 compares the mass flow rates for the two design results to their measured counterparts from the as-built model, as reported by Kodzwa and Eaton [44]. The estimated uncertainties for the mainstream and bleed mass flow rates were 1% and 6%, respectively. The substantial difference between the measured and predicted mass flow rates could be due to three-dimensional effects or deficiencies in our numerical models; however, further study would be necessary to confirm the exact cause.

Kodzwa and Eaton reported experimental film effectiveness and

Table 4 Comparison of computed and experimentally measured (Kodzwa and Eaton [44]) bleed mass flow rates

Parameter	Design	Measured
Suction side bleed (\dot{m}_{ssb} , kg/s)	8.93×10^{-2}	8.2×10^{-2}
Pressure side bleed (\dot{m}_{psb} , kg/s)	9.29×10^{-2}	7.2×10^{-2}
Mainstream mass flow rate (\dot{m} , kg/s)	0.616	0.670

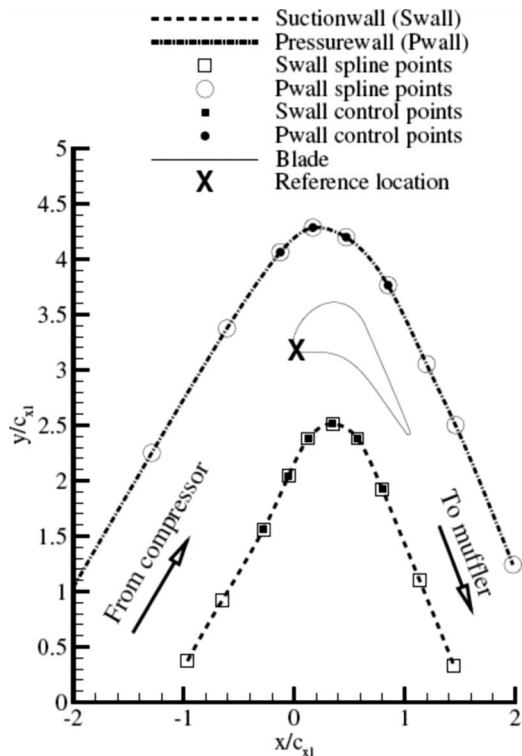


Fig. 14 Flow model for a double passage model design (from Laskowski et al. [53])

heat transfer measurement data collected using this model. It is important to state that these experiments were conducted at near ambient conditions; consequently these data are not directly applicable to engine design. However, we believe that they are best suited for comparison to numerical models due to their well-defined thermal and flow boundary conditions.

5 Double Passage Model

In the double passage model, as no bleeds are present, it is necessary to design the outer walls to account for boundary growth from inlet to exit. The primary benefit of the double passage approach is that the difficulties associated with bleeds and exit walls are circumvented. The general procedure is as follows.

1. Select the outer wall streamlines from the infinite cascade simulation that generate minimal separation and a computed pressure distribution that is close to the infinite cascade solution.
2. Using an optimization procedure, refine these wall shapes to account for boundary layer growth along the wall.

5.1 Flow Model. Figure 14 presents the computational domain used to develop this model. The maximum value of y^+ for the nearest grid point to the blade was 0.9. The same inflow and outflow conditions as those used in the single passage model simulations were used. In order to keep the number of grid cells to a minimum, a two-layer $k-\epsilon$ model was specified at the blade surface and wall functions were used for the passage walls. The results were monitored to ensure that the cell nearest to the wall was well within the viscous sublayer around the blade, and within the log-layer along the passage walls. Grid refinement studies showed that at least 70,000 cells were required for the simulations.

5.2 Outer Wall Design. Laskowski et al. [53] presents a detailed implementation of this approach for the previously described blade geometry. An inverse procedure is utilized to deter-

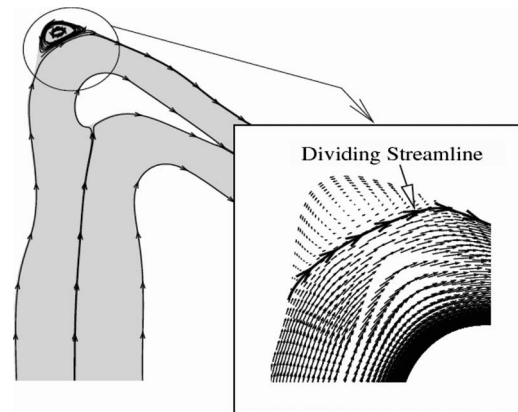


Fig. 15 Separation zone along the pressure side wall of double passage (from Laskowski et al. [53])

mine the wall shape that will give the same surface pressure and skin friction on the blade surface as that of the infinite cascade result. The essence of this approach is the computation of a cost function based on the blade surface pressure distribution and skin friction. The ultimate objective is to develop outer wall shapes such that streamlines a δ_1 away from the wall closely follow those of an infinite cascade flow field. However, a critical issue is the selection of the initial wall shapes. The streamlines selected by Laskowski et al. [53] were approximated from the predicted stagnation streamlines from the infinite cascade simulation. Subsequent calculations using these outer walls resulted in pressure gradients along the upper wall large enough to produce a separation zone (as shown in Figure 15). Consequently, a penalty function was added to the cost function to ensure that the flow remained attached along both the passage walls. Alternative choices for streamlines for the initial set of outer walls were not explored to determine if this could be avoided. Figure 16(a) presents the final wall shapes for the double passage. The suction surface wall was found to require little modification from the initial guess, as the pressure gradients along this wall are favorable. This feature encouraged the development of thin boundary layers that minimally affected the flow field. Figure 16(b) compares the computed Mach number contours for the infinite cascade and the double passage model, demonstrating the flow field agreement between the numerically designed double passage and the infinite cascade condition.

5.3 Experimental Validation. To experimentally measure the flow conditions in the double passage, an instrumented airfoil with 17 pressure taps was installed in the model. The walls were fabricated from Plexiglas to allow the transmission of laser light for high-accuracy particle-image velocimetry (PIV) and LDA. This procedure allowed for measurement of the mean flow field and various turbulence correlations.

The taps consisted of cross-drilled holes. The tap on the surface was a 0.58 mm diameter hole, drilled perpendicular to the local surface tangent. These were connected to the Scanivalve. Figure 17 compares the measured and predicted M_{15} distributions for the model against the infinite cascade simulation. This figure demonstrates that the numerical optimization procedure indeed developed a model that met the desired distribution. The measured mass flow rate through the system was 0.63 kg/s, which is slightly lower than the single passage.

However, even after considerable numerical design effort, PIV measurements by Vicharelli and Eaton [46] indicated that the separation zone along the pressure side wall persisted in the completed model and affected the measured turbulence flow field. This result was observed in spite of the fact that the mean flow measurements around the blade were in relatively good agreement with their computed counterparts. This observation demonstrates

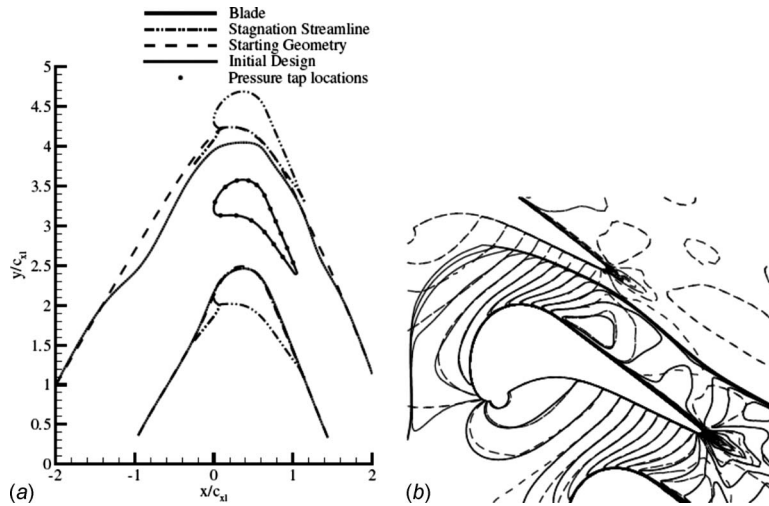


Fig. 16 (a) Final wall shapes for the double passage model and (b) comparison between the computed double passage design and infinite cascade Mach number contours (from Laskowski et al. [53])

that future facilities should specifically target elimination of this issue. We are currently in the process of performing high-resolution, boundary layer LDA measurements for comparison against numerical predictions. These data may be used to establish various boundary layer thickness parameters around the airfoil.

6 3-D Simulation Results

The models were developed using two-dimensional flow computations. Nevertheless, in the actual experimental facility, the flow is inherently three dimensional, in part due to the presence of flat endwalls that enclose the model. Researchers such as Langston [54] and Chung and Simon [41] have demonstrated that the boundary layers that develop along the endwalls cause highly complex three-dimensional flow features in between cascade blades. With this in mind, the aspect ratio of the model was chosen to be $AS=1.276$, where AS is defined as:

$$AS = \frac{H_{\text{model}}}{AP} \quad (3)$$

AP is the blade pitch spacing and H_{model} is the passage height. This value was based on recommended practice as reported by Buck [49] and flow supply limitations. Ideally, this aspect ratio is large enough such that the three-dimensional effects are limited to the near-endwall regions. This design approach would result in a

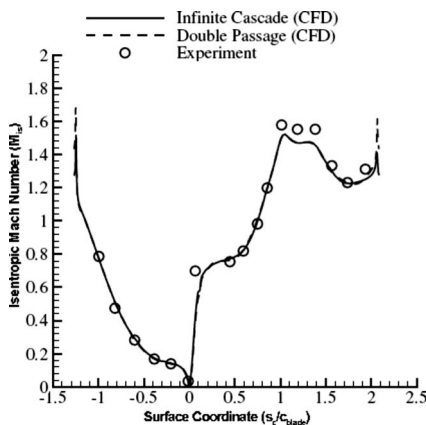


Fig. 17 Measurements of M_{is} for low turbulence condition for the double passage model (from Laskowski et al. [53])

highly two-dimensional flow field over a wide-band encompassing the midspan region of the blade. Three-dimensional RANS simulations of the single and double passages were used to verify this assumption; further details can be found in Ref. [44,45]. Results from the single passage model calculations are only presented here, in the interests of brevity. However, the double passage model simulations exhibit practically identical characteristics.

The calculation domain included one-half of the channel width with a symmetry boundary condition at the channel centerline. A hyperbolic tangent grid stretching was used to resolve the endwall boundary layers. The computational grid contained approximately 2.6×10^6 cells, with y^+ values ranging from $1.3 \times 10^{-4} \leq y^+ \leq 3.0$.

The computed three-dimensional M_{is} distribution at midspan of the model ($Z' = z/H_{\text{model}} = 0.0$) was found to closely agree with the two-dimensional simulation. This result demonstrated that the two-dimensional calculation is a good representation of the mid-span flow conditions. Figure 18 compares the M_{is} distribution at

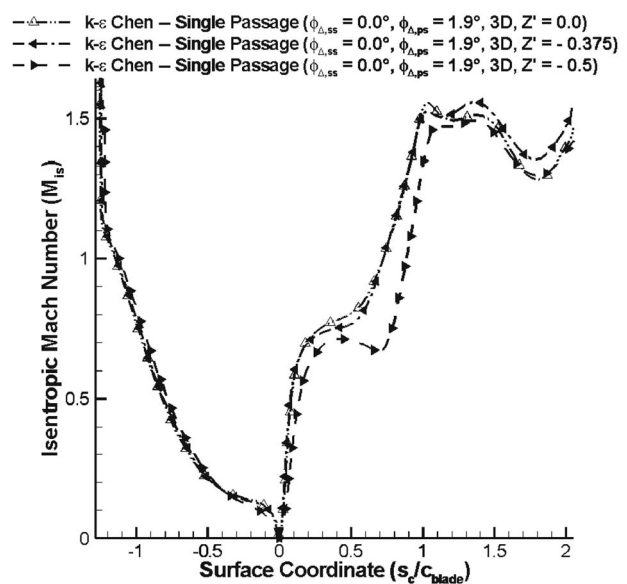


Fig. 18 Comparison of M_{is} distributions at $Z' = 0.0$ (centerline), $Z' = -0.375$, and $Z' = -0.5$ (endwall)

the endwall ($Z' = -0.5$), at the centerline ($Z' = 0.0$), and at an exemplary intermediate location ($Z' = -0.375$). The effect of three-dimensionality is primarily observed on the suction side wall. This behavior was subsequently attributed to vortical structures that form from the endwall boundary layers. An examination of predicted M_{ij} distributions at various locations evinced that the three-dimensional nature of the flow is limited to region $-0.25 \leq Z' \leq -0.5$. It should be stated that these results are specific to this geometry and flow conditions; hence, it is difficult to extend these results to other facilities.

7 Conclusions

Two alternative approaches for achieving well-documented flow at conditions of interest to gas turbine designers have been presented. The design procedure and philosophies for transonic single and double passage models have been introduced and developed. Single passage models are advocated as a means of obtaining highly resolved heat transfer measurements with minimal surface conduction losses, whereas double passage models have been presented as a manner to obtain high-resolution fluid dynamics measurements around turbine airfoil geometries. Both approaches have been developed to produce a two-dimensional flow field that is identical to that in a two-dimensional infinite cascade. Pressure measurements from facilities built using these design procedures were used to verify this assertion. These facilities offer tremendous savings over linear cascades, as only one or two passages are utilized. This approach allows the use of steady state heat transfer measurement techniques that are more amenable to comparisons with numerical simulations. We have performed surface heat transfer and PIV measurements using both models. We are also in the process of performing detailed boundary layer measurements around the center blade in our double passage experiment. It should be stated that the mass flow requirements of these two facilities were approximately identical. This result is due to the fact that the single passage model has boundary layer bleeds to limit viscous effects. Thus the cost of running and manufacturing both facilities is practically identical. It is important to point out that these models are designed for a specific inlet flow angle and pressure ratio; it is unclear how useful this approach would be for significantly off-design conditions. Furthermore, we have only validated these design philosophies for a transonic rotor blade geometry with fully attached boundary layers. Consequently, an important question that future efforts must answer is the utility of these models with significantly different airfoil geometries.

Acknowledgment

This research is sponsored by GE Aircraft Engines, through their University Strategic Alliance Program and by AFOSR Contract No. F49620-02-1-0284 monitored by T. Beutner. P.M.K. received support from the National Science Foundation via a three year graduate fellowship. The authors would like to express their sincere gratitude to D. Mukerji (at Stanford) and F. Buck (at GEAE) for their assistance and advice. Additionally, the authors would like to thank X. Wu and C. McNeil for their support in developing and executing the computational models. J. Hammer, L. Johal, and S. Sutton are gratefully acknowledged for their high level of expertise in manufacturing various parts in the experiments necessary to conduct this research.

Nomenclature

AS	= aspect ratio (mm)
AP	= blade pitch spacing (mm)
c_{blade}	= blade chord length (mm)
c_v	= specific heat with constant volume
ϵ	= error
H_{model}	= model height (mm)
ℓ	= integral length scale (mm)
\dot{m}	= mass flow rate (kg/s)

c_p	= specific heat with constant pressure
M	= Mach number
P	= static pressure (Pa)
P_0	= stagnation (total) pressure (Pa)
T	= static temperature (K)
T_0	= stagnation (total) temperature (K)
TI%	= turbulence intensity
\bar{u}_{inlet}	= area-averaged inlet velocity
s_c	= distance relative to stagnation point along airfoil surface (mm)
x	= axial distance relative to airfoil leading edge (mm)
y^+	= dimensionless wall normal distance
z	= spanwise surface coordinate relative to the centerline of the passage (mm)
Z'	= dimensionless spanwise surface coordinate relative to the centerline of the passage
δ_1	= displacement boundary layer thickness (mm)
ϕ	= rotation angle (degrees)
γ	= ratio of specific heats (c_p/c_v)
ρ	= density (kg/m^3)
μ	= kinematic viscosity ($\text{Pa}\cdot\text{s}$)

Large subscripts/superscripts

2DRANS	= refers to two-dimensional RANS simulation
\prime	= refers to dimensionless distance
+	= refers to dimensionless distance
blade	= refers to blade dimensions
c	= refers to blade surface
IC	= refers to infinite cascade simulation
is	= refers to isentropic condition
model	= model
p	= referring to constant pressure
plenum	= plenum condition
0	= stagnation (total) condition
rec	= recovery condition
v	= refers to constant volume
ss	= refers to suction surface
ps	= refers to pressure surface

References

- [1] Garg, V., 1999, "Heat Transfer on a Film-Cooled Rotating Blade Using Different Turbulence Models," *Int. J. Heat Mass Transfer*, **42**, pp. 789–802.
- [2] Haldeman, C., and Dunn, M., 2004, "Heat-Transfer Measurements and Predictions for the Vane and Blade of a Rotating High-Pressure Turbine Stage," *ASME J. Turbomach.*, **126**(1), pp. 101–109.
- [3] Dunn, M., 2001, "Convective Heat Transfer and Aerodynamics in Axial Flow Turbines," *ASME J. Turbomach.*, **123**(4), pp. 637–686.
- [4] Atassi, H., Ali, A., Atassi, O., and Vinogradov, I., 2004, "Scattering of Incident Disturbances by an Annular Cascade in a Swirling Flow," *J. Fluid Mech.*, **499**, pp. 111–138.
- [5] Schulz, H., and Gallus, H., 1988, "Experimental Investigation of the Three-Dimensional Flow in an Annular Cascade," *ASME J. Turbomach.*, **110**(4), pp. 467–478.
- [6] Wisler, D., Bauer, R., and Okiishi, T., 1987, "Secondary Flow Turbulent Diffusion and Mixing in an Axial Flow Compressor," *ASME J. Turbomach.*, **109**(4), pp. 455–482.
- [7] Blair, M., 1994, "An Experimental Study of Heat Transfer in a Large-Scale Turbine Rotor Passage," *ASME J. Turbomach.*, **116**(1), pp. 1–13.
- [8] Abhari, R., and Epstein, A., 1994, "An Experimental Study of Film Cooling in a Rotating Transonic Turbine," *ASME J. Turbomach.*, **116**(1), pp. 63–70.
- [9] Dunn, M., and Stoddard, F., 1979, "Measurement of Heat-Transfer Rate to a Gas Turbine Stator," *ASME J. Eng. Power*, **101**(2), pp. 275–280.
- [10] Dunn, M., 1986, "Heat-Flux Measurements for the Rotor of a Full-Stage Turbine: Part I—Time Averaged Results," *ASME J. Turbomach.*, **108**(3), pp. 90–97.
- [11] Dunn, M., and Chupp, R., 1988, "Time-Averaged Heat-Flux Distributions and Comparisons With Prediction for the Teledyne 702 HP Turbine Stage," *ASME J. Turbomach.*, **110**(1), pp. 51–56.
- [12] Dunn, M., Kim, J., Civinskas, K. C., and Boyle, R. J., 1994, "Time-Averaged Heat Transfer and Pressure Measurements and Comparison With Prediction for a Two-Stage Turbine," *ASME J. Turbomach.*, **116**(1), pp. 14–22.
- [13] Chana, K. S., and Jones, T. V., 2003, "An Investigation on Turbine Tip and Shroud Heat Transfer," *ASME J. Turbomach.*, **125**(3), pp. 513–520.
- [14] Dunn, M., 1986, "Heat-Flux Measurements for the Rotor of a Full-Stage Tur-

- bine: Part I—Time Averaged Results,” *ASME J. Turbomach.*, **108**(3), pp. 90–97.
- [15] Epstein, A., Guenette, G., Norton, R., and Yuzhang, C., 1986, “High-Frequency Response Heat Flux Gauge,” *Rev. Sci. Instrum.*, **57**(4), pp. 639–649.
- [16] Mukerji, D., Eaton, J. K., Moffat, R. J., and Elkins, C. J., 1999, “A 2-D Numerical Study of the Heat-Island Effect for Button-Type Heat Flux Gages,” *Proceedings of the 5th ASME/ISME Joint Thermal Engineering Conference*, San Diego, CA, March 15–19, Paper No. AJTE99/6186.
- [17] Dunn, M., Kim, J., and Rae, W., 1997, “Investigation of the Heat Island Effect for Heat-Flux Measurements in Short Duration Facilities,” *ASME J. Turbomach.*, **119**(4), pp. 753–760.
- [18] Moffat, R. J., Eaton, J. K., and Mukerji, D., 2000, “General Method for Calculating the Heat Island Correction and Uncertainties for Button Gauges,” *Meas. Sci. Technol.*, **11**(7), pp. 920–932.
- [19] Diller, T., 1993, “Advances in Heat Flux Measurements,” *Adv. Heat Transfer*, **23**, pp. 279–368.
- [20] Peabody, H. L., and Diller, T. E., 1998, “Evaluation of an Insert Heat Flux Gage in a Transonic Turbine Cascade,” *Proceedings of the ASME Heat Transfer Division 5*, Anaheim, CA, Nov. 15–20, Vols. 361–365, pp. 625–630.
- [21] Dunn, M., 2000, private communication.
- [22] Martinez-Botas, R., Lock, G., and Jones, T., 1995, “Heat Transfer Measurements in an Annular Cascade of Transonic Gas Turbine Blades Using the Transient Liquid Crystal Technique,” *ASME J. Turbomach.*, **117**(3), pp. 425–431.
- [23] Baughn, J., 1995, “Liquid Crystal Methods for Studying Turbulent Heat Transfer,” *Int. J. Heat Fluid Flow*, **16**(5), pp. 365–375.
- [24] Guenette, G., Epstein, A., Giles, M., Haines, R., and Norton, R., 1989, “Fully Scaled Transonic Turbine Rotor Heat Transfer Measurements,” *ASME J. Turbomach.*, **102**, pp. 1–7.
- [25] Armstrong, W., 1955, “The Secondary Flow in a Cascade of Turbine Blades,” ARC Report and Memorandum.
- [26] Giel, P., Thurman, D., Van Fossen, G., Hippensteele, S., and Boyle, R., 1996, “Endwall Heat Transfer Measurements in a Transonic Turbine Cascade,” ASME Paper No. 96-GT-180.
- [27] Giel, P., Van Fossen, G., Boyle, R., Thurmann, D., and Civinskas, K., 1999, “Blade Heat Transfer Measurements and Predictions in a Transonic Turbine Cascade,” ASME Paper No. 99-GT-125.
- [28] Camci, C., and Arts, T., 1991, “Effect of Incidence on Wall Heating Rates and Aerodynamics on a Film-Cooled Transonic Test Blade,” *ASME J. Turbomach.*, **113**(3), pp. 493–501.
- [29] Yamamoto, A., Kondo, Y., and Murao, R., 1991, “Cooling-Air Injection Into Secondary Flow and Loss Fields Within a Linear Turbine Cascade,” *ASME J. Turbomach.*, **113**(2), pp. 375–383.
- [30] Hobson, G., Caruso, T. M., and Carlson, J. R., 2003, “Three-Component LDV Measurements in the Wake of a Compressor Cascade With Flow Separation,” *Proceedings of the ASME International Gas Turbine Institute*, Atlanta, GA, June 16–19, 6(A), pp. 91–103.
- [31] Gottlich, E., Lang, H., Sanz, W., and Woisetschlager, J., 2002, “Experimental Investigation of an Innovative Cooling System (ICS) for High Temperature Transonic Turbine Stages,” *Proceedings of the ASME International Gas Turbine Institute*, Amsterdam, The Netherlands, June 3–6, 5(A), pp. 159–167.
- [32] Drost, U., and Bölcs, A., 1999, “Investigation of Detailed Film Cooling Effectiveness and Heat Transfer Distribution on a Gas Turbine Airfoil,” *ASME J. Turbomach.*, **121**(2), pp. 233–242.
- [33] Sieverding, C. H., Arts, T., Denos, R., and Martelli, F., 1996, “Investigation of the Flow Field Downstream of a Turbine Trailing Edge Cooled Nozzle Guide Vane,” *ASME J. Turbomach.*, **118**(2), pp. 291–300.
- [34] Giel, P., Boyle, R., and Bunker, R., 2004, “Measurements and Predictions of Heat Transfer on Rotor Blades in a Transonic Turbine Cascade,” *ASME J. Turbomach.*, **126**(1), pp. 110–121.
- [35] Abuaf, N., Bunker, D., and Lee, C., 1997, “Heat Transfer and Film Cooling Effectiveness in a Linear Airfoil Cascade,” *ASME J. Turbomach.*, **119**(2), pp. 302–309.
- [36] Goldstein, R., and Spores, R., 1988, “Turbulent Transport on the Endwall in the Region Between Adjacent Turbine Blades,” *ASME J. Heat Transfer*, **110**(4), pp. 862–869.
- [37] Radomsky, R., and Thole, K., 2000, “Flowfield Measurements for a Highly Turbulent Flow in a Stator Vane Passage,” *ASME J. Turbomach.*, **122**(2), pp. 255–262.
- [38] Priddy, W., and Bayley, F., 1988, “Turbulence Measurements in Turbine Blade Passages and Implications for Heat Transfer,” *ASME J. Turbomach.*, **110**(1), pp. 73–79.
- [39] Blair, M., 1974, “Experimental Study of Heat Transfer and Film Cooling on Large-Scale Turbine Endwalls,” *ASME J. Heat Transfer*, **96**(4), pp. 524–529.
- [40] Bailey, D., 1980, “Study of Mean and Turbulent-Velocity Fields in a Large-Scale Turbine-Vane Passage,” *ASME J. Eng. Power*, **102**(1), pp. 88–97.
- [41] Chung, J., and Simon, T., 1991, “Three-Dimensional Flow Near the Blade/Endwall Junction of a Gas Turbine: Application of a Boundary Layer Fence,” ASME Paper No. 90-WA/HT4-4.
- [42] Chung, J., Simon, T., and Buddhavarapu, J., 1991, “Three-Dimensional Flow Near the Blade/Endwall Junction of a Gas Turbine: Visualization in a Large-Scale Cascade Simulator,” ASME Paper No. 91-GT-45.
- [43] Buck, F., and Prakash, C., 1995, “Design and Evaluation of a Single Passage Test Model to Obtain Turbine Airfoil Film Cooling Effectiveness Data,” ASME Paper No. 95-GT-19.
- [44] Kodzwa, P., and Eaton, J., 2005, “Measurements of Film Cooling Performance in a Transonic Single Passage Model,” Technical Report No. TF 93, Stanford University, Stanford CA, available at <http://www.stanford.edu/group/fpc/Publications/TF.html>.
- [45] Laskowski, G., 2004, “Inverse Design of a Turbine Cascade Passage and DNS of a Stationary and Rotating Serpentine Passage,” Ph.D. thesis, Stanford University, Stanford.
- [46] Vicharelli, A., and Eaton, J., 2006, “Turbulence Measurements in a Transonic Two-Passage Turbine Cascade,” *Exp. Fluids*, **40**(6), pp. 897–917.
- [47] Medic, G., and Durbin, P., 2002, “Toward Improved Prediction of Heat Transfer on Turbine Blades,” *ASME J. Turbomach.*, **124**(1), pp. 187–192.
- [48] CD Adapco Group, 2001, *STAR-CD Version 3.15, Methodology, Computational Dynamics*, Melville, NY.
- [49] Buck, F., 2000, private communication.
- [50] Haldeman, C., Dunn, M., Barter, J., Green, B., and Bergholz, R., 2005, “Aerodynamic and Heat-Flux Measurements With Predictions on a Modern One and One-Half State High Pressure Transonic Turbine,” *ASME J. Turbomach.*, **127**(3), pp. 522–531.
- [51] Chen, Y., and Kim, S., 1987, “Computation of Turbulent Flows Using an Extended $k-\epsilon$ Turbulence Closure Model,” NASA Report No. CR179204.
- [52] Wu, X., 2000, private communication.
- [53] Laskowski, G., Vicharelli, A., Medic, G., Elkins, C., Eaton, J., and Durbin, P., 2005, “Inverse Design of and Experimental Measurements in a Double Passage Transonic Cascade Model,” *ASME J. Turbomach.*, **127**(3), pp. 619–625.
- [54] Langston, L., 1980, “Crossflows in a Turbine Cascade Passage,” *ASME J. Eng. Power*, **102**(4), pp. 866–874.
- [55] Athans, R., 2000, private communication.

T. Klauke
Chair of Structural Mechanics and Vehicle
Vibrational Technology
e-mail: thomas.klauke@tu-cottbus.de

A. Kühhorn

B. Beirow

M. Golze

BTU Cottbus,
Siemens-Halske-Ring 14,
03046 Cottbus, Germany

Numerical Investigations of Localized Vibrations of Mistuned Blade Integrated Disks (Blisks)

Blade-to-blade variations of bladed disk assemblies result in local zoning of vibration modes as well as amplitude magnifications, which primarily reduces the high cycle fatigue life of aeroengines. Criteria were introduced to determine the level of these mode localization effects depending on various parameters of a real high pressure compressor blisk rotor. The investigations show that blade vibration modes with lower interblade coupling, e.g., torsion modes or modes with high numbers of nodal diameter lines, have a significantly higher sensitivity to blade mistuning, which can be characterized by the higher percentage of blades on the total blisk strain energy. [DOI: 10.1115/1.2985074]

Keywords: blisk, mistuning, mode localization, blade vibration

1 Introduction

The vibration behavior of conventional bladed disk assemblies was investigated in detail a long time ago (for example, Refs. [1–5]).

Due to the manufacturing process (milling, polishing, friction welding, etc.) and material inhomogeneities of the alloy, blade-to-blade variations in bladed structures such as compressor rotors occur. This so-called mistuning results in a lot of negative effects that have been studied for more than thirty years. Ewins [6,7] showed that these blade-to-blade deviations occur in higher blade displacement amplitudes in combination with a splitting of double modes. Whitehead [8,9] derived a maximum amplitude magnification factor, which predicts the maximum forced vibration response of blades due to mistuning.

Wei and Pierre [10,11] considered that the mistuned case represents perturbations of the tuned system using the perturbation technique. They concluded that the vibration behavior depends on the ratio of absolute amount of mistuning strength and the coupling between the blades through the disk. In addition, Griffin and Hoosac [12] as well as Bladh et al. [13,14] determined the influence of interblade coupling on localized blade modes.

Kielb and Kaza [15], Wildheim [16], Wilson [17], and Yingfeng et al. [18] measured unsteady blade loads arising from the fluctuating forces due to the passing of wakes through the blade rows. The aerodynamic coupling of the blades was included in the calculation approach by Pierre and Murthy [19]. Schrape et al. [20,21] investigated the effects of in- and also antiphase-blade-motion of tuned and mistuned blisks on aerodynamic damping.

All of the previous characteristics of mistuned bladed disks have to be regarded also during the design and test-phase of future aeroengine rotors. At this integrated bladed disks (blisks¹) become more important aiming at more environmental-friendly, more efficient, and more powerful aeroengines [22,23]. The deletion of the heavy blade-disk connection results in reduced masses, higher maximum rotational velocities, and improved pressure ratios (increased efficiency factors). In this connection also, a number of disadvantages occur such as very low structural damping and higher sensitivity with regard to mistuning [24]. Thus especially the mode localization has to be kept in mind during the rig test vibration monitoring because only a few blades will be instrumented with strain gauges (s/g). Due to the demand for an ac-

ceptable signal-to-noise ratio, only blades with high amplitudes are suitable for s/g instrumentation. That implies that an optimal choice of suitable blades is indispensable to avoid critical misinterpretations during measurement-result-analysis.

Up to now, the ability to predict the sensitivity of different blisk designs and blade vibration modes to mode localization and the knowledge of how to design less mistuning sensitive blisks is still missing [25]. To achieve a better understanding of these contexts, free and forced vibration behaviors of updated full finite element (FE) models of the first rotor stage from the Engine 3E² high pressure compressor (HPC) is analyzed using different evaluation factors.

2 Natural Vibrations of Tuned Blisks

Integrated bladed disks have a multitude of different eigenmodes, which can be characterized by the number of diametric and concentric nodal lines.³

In general, the eigenmodes of a tuned blisk can be divided into three categories using the blade's contribution to the total blisk strain energy: disk-dominated, blade-dominated, and "coupled" vibrations (Fig. 1).

2.1 Disk-Dominated Vibrations. The disk dominates the vibration mode of the total blisk (see Fig. 2). The blades can be idealized as covibrating rigid bodies, which contain only a small part of the total blisk strain energy (see Fig. 1, left side).

Due to the existence of nodal diameters (ND), a cyclic symmetry mode (CSM) appears. The maximum number of nodal diameters depends on the blade number N .

$$CSM_{\max} = \frac{N}{2} \quad \text{for even } N \quad (1)$$

$$CSM_{\max} = \frac{N-1}{2} \quad \text{for odd } N \quad (2)$$

The solution of the eigenvalue equations always generates double eigenvalues except for two cases,^{4,5} which result in two orthogo-

¹Or integrated bladed rotor (IBR).

Manuscript received January 29, 2007; final manuscript received August 15, 2008; published online April 2, 2009. Review conducted by Matthew Montgomery.

²German research program aiming at new HPC technologies. 3E=efficiency, economy, and environment.

³Diametric nodal lines: nodal diameters (ND), concentric nodal lines: nodes circles.

⁴In case of the CSM 0, only a single eigenvalue occurs.

⁵If the number of blades is even, the CSM_{\max} has a single eigenvalue only.

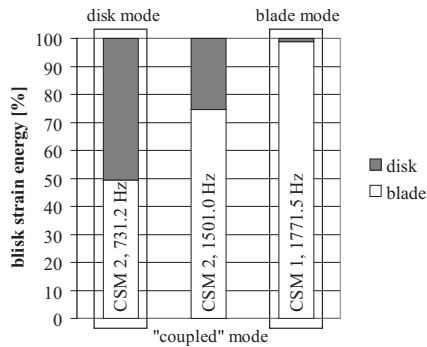


Fig. 1 Vibration mode characterization using the blade's contribution to the total blisk strain energy (mean value of double eigenmodes)

nal eigenvectors.

Caused by the homogeneous mass and stiffness distribution, the eigenmodes of the blisk have no spatial orientation with respect to the blisk.

2.2 Blade-Dominated Vibrations. Neglecting the three-dimensional geometry of modern compressor blades as a first assumption, the blades can be considered as a plain plate.

Generally, the fundamental eigenmodes with the lowest eigenfrequencies of a cantilever plate are the first flap and the first torsion mode, respectively. Depending on the aspect ratio of the plates, modes with higher eigenfrequencies will follow, e.g., higher flap or torsion modes and also other complex blade modes such as edgewise modes, tramline modes, etc. (see Fig. 3).

Analogous to the disk-dominated modes, nodal diameters also appear in blade-dominated modes. There are 0 to CSM_{max} characteristic nodal diameters per fundamental blade mode (see Figs. 4 and 5). The maximum number of blade vibration modes can be determined to N .⁶

2.3 Coupled Vibrations. The so-called coupled vibration modes represent a combination of disk-dominated and blade-dominated modes. Caused by the physical connection between the disk and the blades, all vibration modes are coupled, so the nota-

⁶If $CSM = CSM_{max}$, all blades oscillate in counter phase to each other.

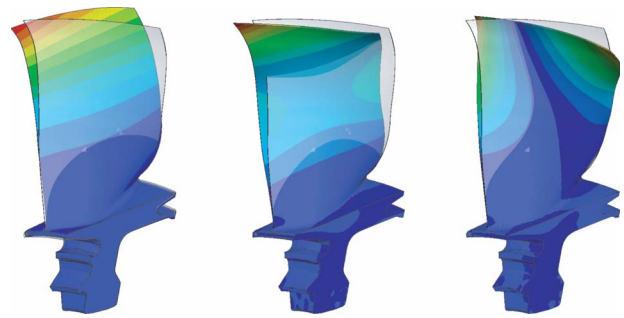


Fig. 3 Fundamental blade vibration modes (first flap mode (left), second flap mode (middle), first torsion mode (right)), fixed sector model, magnitude of displacements

tion is not indisputable.⁷

In technical terminology, this term is used for vibration modes, where both disk and blades store a similar high quantity of the total blisk strain energy (see Fig. 1, middle).

This classification of blisk modes supports an improved rating of high cycle fatigue (HCF)-sensitive vibration modes, because generally only blade modes result in critical blade strain levels. Thus a benefit results from strain gauge calibration, where only s/g response signals of blade modes have to be referred to blade displacement amplitudes. If the adjacent disk and/or coupled modes with dominating disk displacements and negligible blade displacements are included, misinterpretations of vibration-monitoring-system results are probable.

2.4 Coupling Diagram. The coupling diagram offers the possibility to illustrate the complex vibration behavior of a blisk. The eigenfrequencies are printed depending on the number of nodal diameters (see Fig. 4).

Looking at all modes of one fundamental blade mode family, one can recognize that, in general, the eigenfrequencies increase up to the frequency of the clamped blade with an ascending number of nodal diameters⁸ (see Fig. 5).

The reason for that is the stiffer reaction of the disk with as-

⁷If the disk displacement can be disabled (which means a complete decoupling of blades and disk), the blade alone frequency (also called as single blade frequency) can be determined for an infinite stiff clamping, respectively.

⁸Blisk vibration modes with a low number of nodal diameters are often exceptional cases in cases of free boundary conditions.

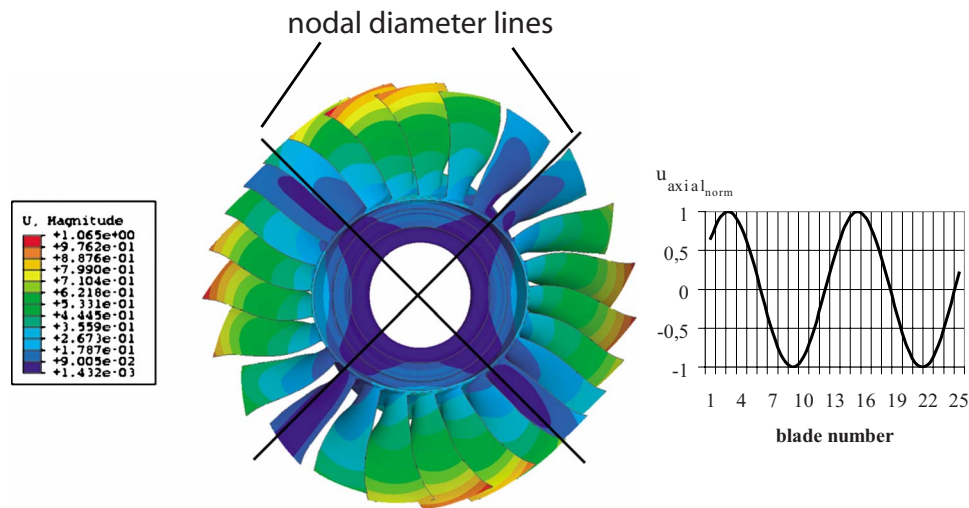


Fig. 2 Disk-dominated vibration mode (CSM 2, 731.2 Hz; displacement magnitude (left), normalized axial displacements at all blade tips (right), Engine 3E HPC Rotor 1)

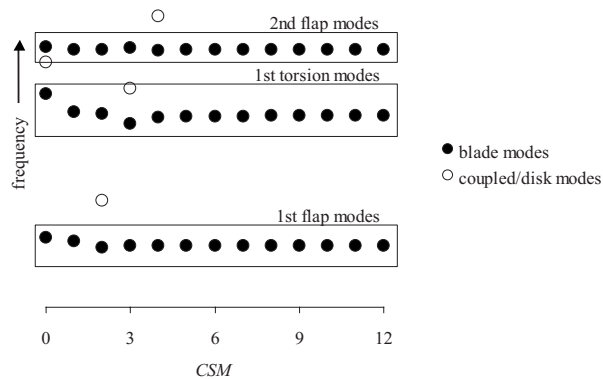


Fig. 4 Coupling diagram of Engine 3E HPC Stage 1, illustration of the first three blade modes, free boundary conditions

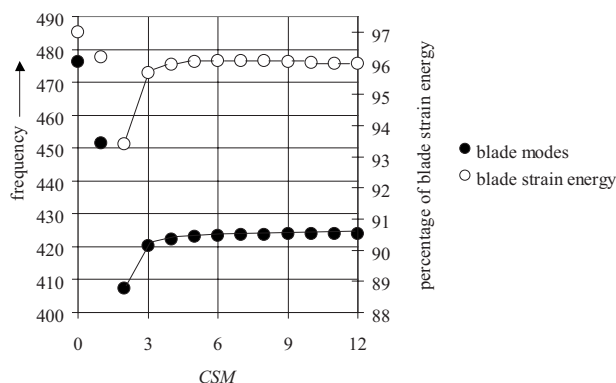


Fig. 5 Enlarged section of the coupling diagram compared to the blade's contributions to the total blisk strain energy, first torsion modes, free boundary conditions

ending number of nodal diameters (see also Refs. [2,5]).

In general blade vibration modes govern the maximum operational lifetime of compressor rotors caused by the high strain levels of the blades, so the focus of the following chapters is located on these. In this context, the disk and coupled modes will be neglected in all further investigations.

Kenyon [26] pointed out that high amplitude magnifications of so-called veering regions do not necessarily indicate maximum blade amplitudes higher than those possible for isolated mode families. The appearing higher magnification factors are a result of the reduced tuned response of veering regions.

3 Forced Vibrations of Tuned Blisks

According to the requirement of correlation of vibration mode shape and excitation mode shape, a k th CSM can only be excited by a k th engine order (EO), respectively, k th-aliasing EO, in case of a tuned system.

In a real aeroengine, the number of generated wakes, which determines the EO mainly depends on the number of the upstream and downstream located guide vanes as well as the number of blades⁹ of the adjacent compressor stages and their multiples.

If the wakes, which produce a local pressure gradient, are passed by the blades during rotation, the blades will be excited with the number of wakes (see also Ref. [18]). The number of existing wakes determines the value of the engine order. The displacement amplitudes of each blade and all displacement components i are similar and appear with a delay of the interblade phase angle φ_{CSM} :

⁹In case of multishaft aeroengine with different rpm.

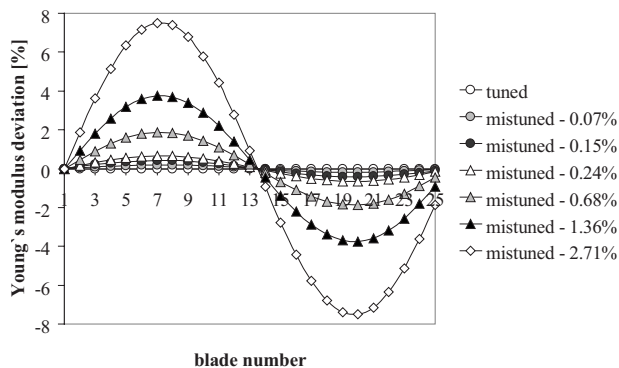


Fig. 6 Different artificial sinusoidal mistuning distributions caused by blade Young's modulus modification of Engine 3E HPC Rotor 1

$$\varphi_{CSM} = \frac{2\pi CSM}{N}, \quad CSM = 0 \text{ to } CSM_{max} \quad (3)$$

It is valid:

$$\hat{U}_i = \hat{U}_{i1} = \hat{U}_{iN} \quad (4)$$

4 Natural Vibrations of Mistuned Blisks

4.1 Modeling of Blade Mistuning. The modeling of the individual blade mistuning using a full FE-model can be realized by changing the material properties: Due to the decrease and increase in the individual blade's Young modulus E_i , the blade eigenfrequencies can be modified without changing the blade geometry (*material dependent mistuning*).

At this, Young's modulus of the disk is constant. It is valid:

$$f_i \sim \sqrt{E_i} \quad (5)$$

The change in blade eigenfrequencies is proportional to the change in the square root of the blade's Young moduli (see Fig. 6). Due to easier adaptability in contrast to alternative mesh morphing method (*geometry dependent mistuning*), this procedure is chosen for all further investigations.

In contrast to the measured mistuning distributions (Fig. 7), which differ from blade mode to blade mode and can be characterized by a Weibull-distribution, different artificial sinusoidal blade mistuning deviations are used to get better clearness comparing different blade modes and mistuning levels with each other. Here, the number of full sine waves around the blisk circumference was chosen to be 1, 4, and CSM_{max} (12) with standard de-

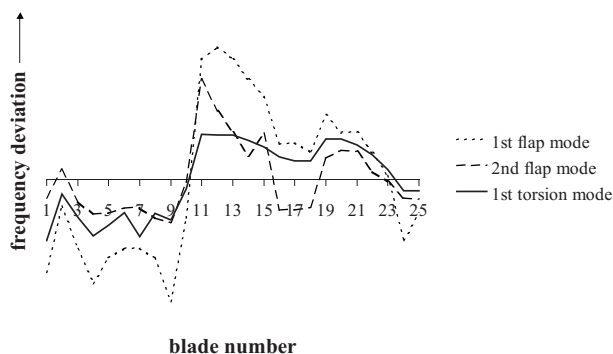


Fig. 7 Measured blade eigenfrequency deviations of Engine 3E HPC Rotor 1, (···) first flap mode, (---) second flap mode, (—) first torsion mode

viations of 0.07%, 0.15%, 0.24%, 0.68%, 1.36%, and 2.71%. Generally, the mistuning of a blade-disk-assembly results in several fundamental effects.

4.2 Splitting of Double Modes. The pairwise appearing eigenvalues of the system are split into two closely adjacent eigenvalues caused by the missing symmetry, see, for example, Ref. [27].

For the case described below, a stronger mode splitting can be observed with higher eigenfrequencies. The associated double eigenmodes (so-called double modes) with different eigenfrequencies have a fixed orientation on the blisk. By increasing the mistuning of the system, the distance between the adjacent eigenfrequencies increases.

4.3 Mode Localization. The local concentration of higher blade displacement amplitudes — the so-called mode localization — also indicates modified vibration behavior of mistuned blisks.

The vibration modes are characterized by regions of high and low displacement amplitudes. The worst case is the fully localized mode characterized by only one oscillating blade (Fig. 8). Thus a clear assignment of the single vibration modes to a CSM becomes more difficult. The displaced nodal diameters of the CSM are transformed into modified cyclic symmetry modes (MCSM), in case of slight mistuning. With increased mistuning, warped nodal diameter lines also vanish. The formerly pure sinusoidal vibration modes of the tuned system are transformed into a superposition of many single sinusoidal vibration modes, where the percentages of the several harmonic vibrations may be different (see Fig. 11).

5 Forced Vibrations of Mistuned Blisks

A completely symmetric manufactured tuned blisk without any imperfections is not possible at the current state of the art. Thus a mistuned excited blisk can be regarded as the regular case during operation of an aeroengine.

5.1 Forced-Response Analyses. Induced by the huge number of Fourier coefficients of the modified vibration modes, many resonance peaks can be observed in the frequency response function (FRF) of the individual blades during the excitation by a k th engine order. Each peak correlates with a vibration mode, which has a k th harmonic in its Fourier decomposition. The maximum amplitude level of the FRF depends on the percentage of the k th harmonic on all Fourier coefficients (see Fig. 9).

5.2 Amplitude Magnification. As an additional effect of the vibration behavior of mistuned blisks local magnifications and minifications of the blade displacements appear compared to the tuned ideal blisk (for example, Refs. [8,9]), which are essential for high cycle fatigue during excitation. At this, the maximum blade displacement magnification factor differs from blade-to-blade. It is defined as

$$\frac{U_{mt\ i}}{U_{tn\ i}} \quad (6)$$

The magnification of an amplitude can reach a value >2 , depending on the mistuning level, the blisk geometry, the corresponding total mode damping, and the exciting EO (see also Refs. [10,11,28,29]). In addition, Srinivasan [30] and Slater et al. [25] published compendiums of mistuning effects.

Recapitulating the maximum blade amplitude magnification and the splitting of the double modes play major roles for high cycle vibration fatigue and resonance excitability, whereas mode localization has to be kept in mind for rotor instrumentation and strain gauge measurement result analysis.

6 Concept of the Mode Fill Factor

The variation of the vibration modes of the blisk depends on many parameters. In order to get a clear statement of the magnitude of these mode variations, a discrete Fourier transform (DFT)

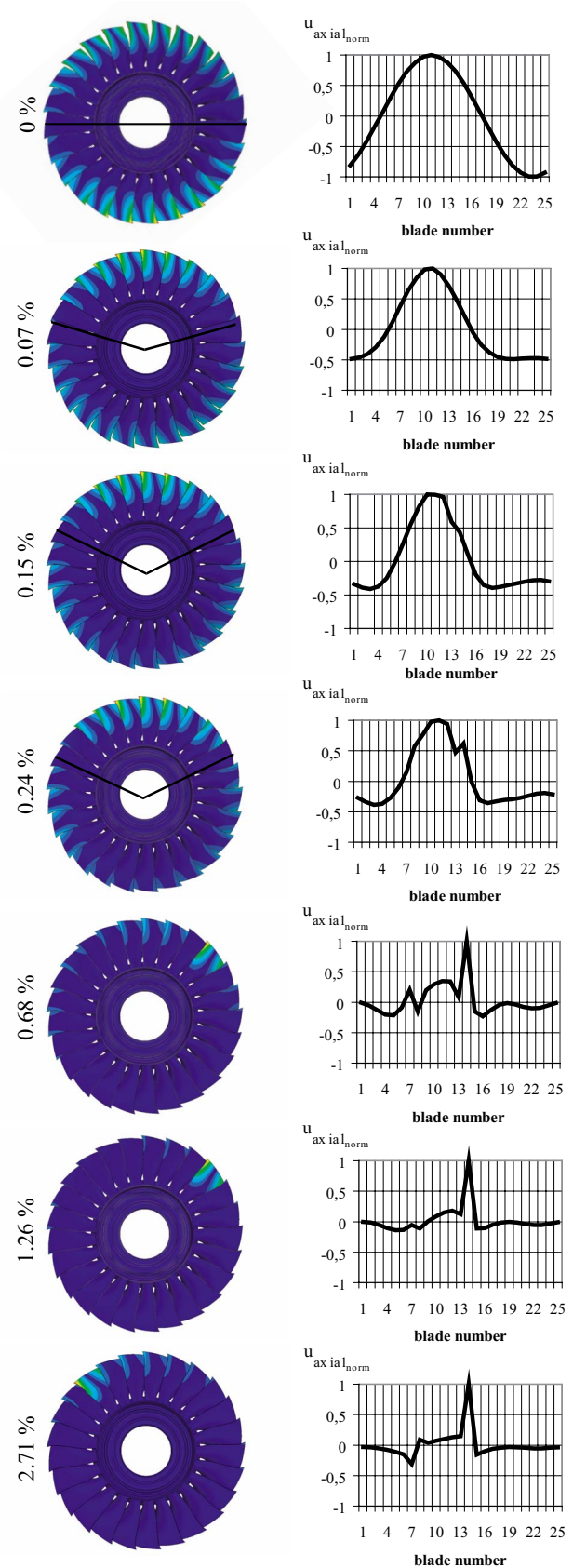


Fig. 8 Influence of different blade mistuning levels on vibration modes (first torsion modes, (M)CSMs 1; left: displacement amplitudes; right: normalized axial displacements at each leading edge blade tip)

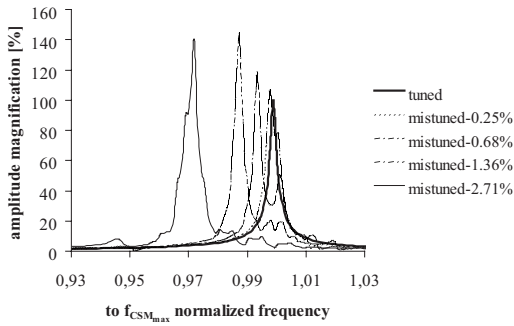


Fig. 9 FRFs of blade No. 6 for different mistuning levels, EO 1, first torsion mode, magnitude amplification of axial displacements at leading edge blade tip, $D=1.0\%$ ($Q=500$)

can be used as basis to evaluate the mistuning modes such as done before by Castanier and Pierre [31] and Kenyon et al. [32]. Similar to these publications, the mistuned mode is represented as a superposition of tuned modes, where the coefficients of the single tuned modes in the modal summation characterize the level of mode distortion. Again the criterion introduced below describes the deviations of the vibration modes of a mistuned system compared to the tuned one independent from the blade number.

6.1 Tuned Systems. Except CSM 0, which has similar displacements for all blades at the same time t , 1 to CSM_{max} sine waves appear for all of the vibration modes of the tuned system around the circumference of the blisk. By using a Fourier decomposition of the circumferential blade displacements, the vibration mode can be split into harmonic parts and a constant part, which describes the zero offset.

In case of the tuned system, only one of the Fourier coefficients DFT_i is unequal to zero. With the exception of CSM 0, a pure sinusoidal vibration mode appears without disturbing sidebands. The Fourier coefficient corresponds to the number of the CSM of the corresponding vibration mode (Fig. 10). The ratio of the sum of all Fourier coefficients to the maximum Fourier coefficient ξ_{tuned} is defined as

$$\xi_{tuned} = \left(\frac{\sum_{i=0}^{CSM_{max}} DFT_i}{DFT_{max}} \right)_{tuned} = \frac{DFT_{max}}{DFT_{max}} = 1 \quad (7)$$

In case of the tuned system, the mean value of all Fourier coefficients

$$\overline{DFT} = \frac{1}{CSM_{max} + 1} \sum_{i=0}^{CSM_{max}} DFT_i \quad (8)$$

can be determined as

$$\overline{DFT}_{tuned} = \frac{DFT_{max}}{CSM_{max} + 1} \quad (9)$$

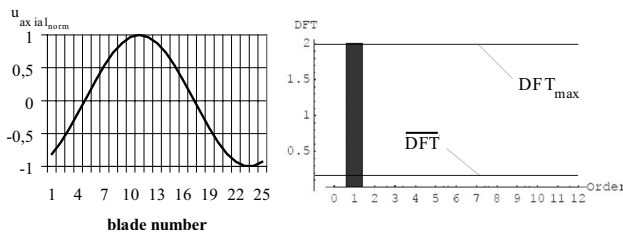


Fig. 10 Left: normalized axial blade displacements at all leading edge blade tips of CSM 1 (tuned system, torsion mode); right: Fourier decomposition of the vibration mode

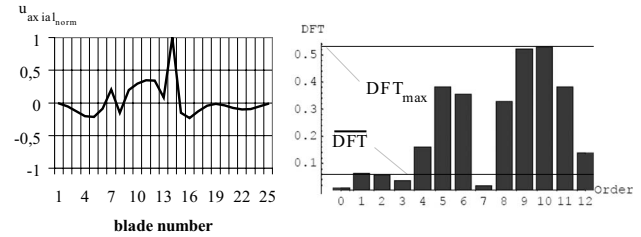


Fig. 11 Left: normalized axial blade displacements at all leading edge blade tips (torsion mode, mistuned system); right: Fourier decomposition of the vibration mode $\sigma_{mistuning}=0.68\%$

6.2 Mistuned Systems. If the blade eigenfrequencies differ from each other, locally limited and variable blade displacements appear around the blisk's circumference. These effects result in additional Fourier coefficients. Due to the deviations in the vibration modes compared to the tuned systems, the sum of all Fourier coefficients is increased (Fig. 11).

The maximum ratio of the sum of all Fourier coefficients to the maximum Fourier coefficient $\xi_{mistuned}$ occurs, if all Fourier coefficients have identical values. At this $\xi_{mistuned}$ will reach its maximum because of $DFT = DFT_{max} = DFT_i$. According to Eq. (7) the maximum is

$$\xi_{mistuned,max} = \left(\frac{\sum_{i=0}^{CSM_{max}} DFT_i}{DFT_{max}} \right)_{mistuned,max} = CSM_{max} + 1 \quad (10)$$

Hence, $\xi_{mistuned,max}$ just depends on the number of blades N or the maximum number of cyclic symmetry modes $CSM_{max} + 1$, respectively.

6.3 Definition of the Mode Fill Factor. To compare the magnitudes of mode filling of different blade modes or different blisks designs with each other, the transformation of the blade-number-dependent ratio ξ to the mode fill factor using

$$\text{mode fill factor} = \frac{100}{CSM_{max}} (\xi - 1) (\%) \quad (11)$$

is helpful. This factor specifies the number of harmonics that are included in the vibration mode in a range between 0% (pure sinusoidal vibration mode,¹⁰ $\xi=1$, no sidebands) up to 100% (all Fourier coefficients are equal, $\xi=CSM_{max}+1$). In other words, how strong is the deviation of this mode with regard to a pure sinusoidal vibration mode and how many EOs are able to excite this (M)CSM? Using this additional information helps the aeroengine designer to evaluate critical areas in the campbell diagram of mistuned bladed disks.

7 Concept of the Localization Factor

The single use of the amplification factor gives no information about the number of high displacement blades during forced response analysis of a mistuned blisk. Hence, it is possible that a number of blades reach high magnification factors or only one single blade reaches a higher displacement level, which is important in terms of an optimum blade selection for strain gauge instrumentation of rotor stages and vibration results analysis¹¹

In addition to the magnification factor, which determines the maximum displacement magnification of all blades regarding the tuned system, a localization factor (LF) shows how many blades will achieve this high magnification levels. Although Ewins [7] and others observed vibration localization phenomena, Hodges [33] showed first that it is a kind of Anderson [34] localization,

¹⁰In case of $1 < CSM < CSM_{max}$.

¹¹Due to many restrictions, the maximum number of strain gauges on blades per rotor is limited to ~6–9. Thus only blades with high blade amplitudes are suitable to achieve a sufficient signal-to-noise ratio during vibration monitoring.

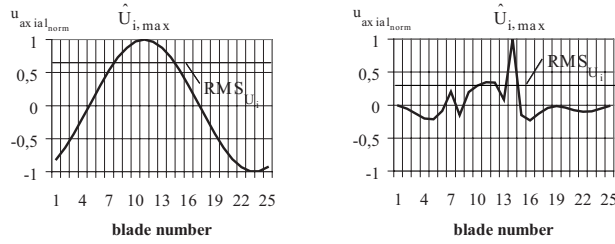


Fig. 12 Normalized axial blade displacements at all leading edge blade tips of CSM 1 (left) and MCSM 1 (right), first torsion modes

which is characterized by increasing mode localization levels in case of increased disorder of substructures. In many localization studies, the Lyapunov exponent is used to define mode localization (see also Ref. [35]). In contrast to these classical definitions, a method is introduced below, which transforms the complex vibration behavior of a huge number of blades into one illustrative indicator to ensure an efficient and fast evaluation of the localization sensitivity of different blisk designs or blade modes. A further approach can be found in Ref. [36].

7.1 Tuned Systems. Regarding the blade circumferential displacements at the time t , one gets a number of blades N discrete representation of the corresponding vibration mode. With the exception of CSM 0, where all blades have identical displacement at the same time t , all of the other vibration modes are characterized by discrete sine waves around the circumference depending on the CSM.

A special feature of the undisturbed sine waves is the constant ratio of the maximum blade displacement amplitude $\hat{U}_{i,\max}$ to the root mean square (RMS) of all blade displacement values. Hence,

$$\text{RMS}_{U_{i,\text{tuned}}} = \sqrt{\frac{1}{N} \sum_{j=1}^N U_{ij}^2} \quad (12)$$

is independent of the number of sine waves around the circumference (see Fig. 12, left side), which constitutes the basis of the following calculations.

The ratio of the maximum blade displacement amplitude to the root mean square of all blade displacements ζ_{tuned} is

$$\zeta_{\text{tuned}} = \frac{\hat{U}_{i,\max}}{\text{RMS}_{U_{i,\text{tuned}}}} = \frac{\hat{U}_{i,\max}}{\hat{U}_{i,\max} \times 1/\sqrt{2}} = \sqrt{2} \quad (13)$$

for $1 \leq \text{CSM} \leq \text{CSM}_{\max}$ (odd N) or $1 \leq \text{CSM} < \text{CSM}_{\max}$ (even N).

In case of the umbrella mode with $\hat{U}_{i1} = \hat{U}_{iN} = \hat{U}_{i,\max}$ or CSM_{\max} ($N = \text{even}$) with $\text{RMS}_{U_{i,\text{tuned}}} = \hat{U}_{i,\max}$ it follows

$$\zeta_{\text{tuned}} = \frac{\hat{U}_{i,\max}}{\text{RMS}_{U_{i,\text{tuned}}}} = \frac{\hat{U}_{i,\max}}{\hat{U}_{i,\max} \times 1} = 1 \quad (14)$$

7.2 Mistuned Systems. If the blade eigenfrequencies differ from each other, a noncyclic-symmetric, unevenly blisk vibration mode (MCSM) appears represented by various blade displacement magnitudes around the circumference of the mistuned blisk. Due to the deviations of the eigenmode of the mistuned system compared to the tuned one, the root mean square of the blade displacements decreases (see Fig. 12, right side).

The maximum mode localization that is characterized by only one oscillating blade results in the minimum root mean square value.

$$\text{RMS}_{U_{i,\text{mistuned},\min}} = \sqrt{\frac{1}{N} U_{i,\max}^2} = \sqrt{\frac{1}{N}} U_{i,\max} \quad (15)$$

Thus the maximum ratio of the maximum blade displacement amplitudes to the root mean square of all blade displacements $\zeta_{\text{mistuned},\max}$ is defined as

$$\zeta_{\text{mistuned},\max} = \frac{\hat{U}_{i,\max}}{\text{RMS}_{U_{i,\text{mistuned},\min}}} = \frac{\hat{U}_{i,\max}}{\sqrt{\frac{1}{N} \hat{U}_{i,\max}^2}} = \sqrt{N} \quad (16)$$

for $0 \leq (\text{M})\text{CSM} \leq \text{CSM}_{\max}$

and just depending on the number of blades N .

7.3 Definition of the Localization Factor. Analogous to the mode fill factor presented before a transformation of ζ into the blade number independent LF is necessary for the comparability of the mode localization level of different blisk designs with different blade numbers. This factor describes the local limitation of the vibration mode in a defined range of 0% (no mode localization, pure sinusoidal vibration mode, $\zeta_{1 \leq \text{CSM} \leq \text{CSM}_{\max}, N = \text{even}} = \sqrt{2}$ and $\zeta_{\text{CSM} \neq 0, N = \text{odd}} = \sqrt{2}$, respectively, $\zeta_{\text{CSM} = 0} = 1$ or $\zeta_{\text{CSM}_{\max}, N = \text{even}} = 1$) up to 100% (maximum mode localization, only one blade oscillating, $\zeta = \sqrt{N}$).

Consequently, the localization factor is defined as

$$\text{LF} = \frac{100}{\sqrt{N} - \sqrt{2}} (\zeta - \sqrt{2}) \quad (\%)$$

if $1 \leq (\text{M})\text{CSM} \leq (\text{M})\text{CSM}_{\max}$ (odd N)
or $1 \leq (\text{M})\text{CSM} < (\text{M})\text{CSM}_{\max}$ (even N)

and

$$\text{LF} = \frac{100}{\sqrt{N} - 1} (\zeta - 1) \quad (\%)$$

if $(\text{M})\text{CSM} = 0$
or $(\text{M})\text{CSM} = (\text{M})\text{CSM}_{\max}$ (even N)

respectively.

8 Localization Phenomena of a Real High Pressure Compressor Blisk

The evaluation criteria of mode filling and mode localization are exemplarily computed for blisk rotor 1 of the Engine 3E HPC. Again the measured blade mistuning distributions are substituted by different artificial sinusoidal blade mistuning distributions with different mistuning levels to ensure the comparability of different blade modes.

8.1 Natural Vibrations

8.1.1 Influence of Mistuning Level and Blade Mode. According to Eq. (17) or Eq. (18), respectively, localization factors of blisk with different mistuning levels were calculated (see Figs. 13 and 14).

Starting from the tuned system without any mode localization, a continuous increase in the localization factors can be observed with increasing blade mistuning for all of the three fundamental blade modes as well as the disk and coupled modes (see Fig. 14). At this, it has to be mentioned that in case of lower MCSM (1–4) significantly lower localization factors occur in contrast to higher MCSMs. Furthermore the bandwidth of eigenfrequencies increases (double mode splitting) with increasing mistuning levels — the eigenfrequencies of the various vibration modes are bearing off from each other (see Fig. 13), so the bandwidth of possible blade mode resonances enlarges, which has to be regarded during the aeroengine development to avoid critical resonances in

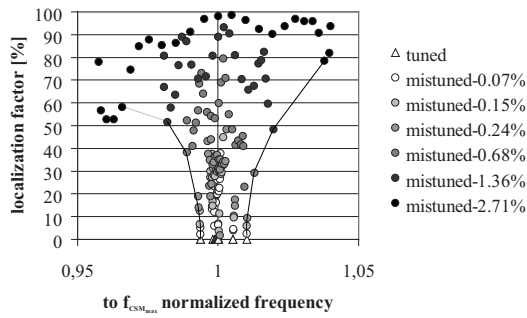


Fig. 13 Localization factors of natural vibrations depending on the blade mistuning standard deviation of first torsion modes 1-sine-wave mistuning distribution around blisk circumference

operation.

It can also be recognized that disk-dominated and coupled modes are less sensitive to mode localization due to their lower blade percentage on the total blisk strain energy (see Figs. 14 and 19). In contrast to the medium localization factors of mistuned flap modes, the mode localization of torsion modes is significantly more pronounced caused by the lower coupling between the individual blades (see Figs. 13 and 19).

Complemental Fig. 15 shows the context between localization factor and the level of mistuning. As one can recognize, the curve shapes of the localization factors are very sensitive regarding blade mistuning for small mistuning levels ($0\% < \sigma_{\text{mistuning}}$

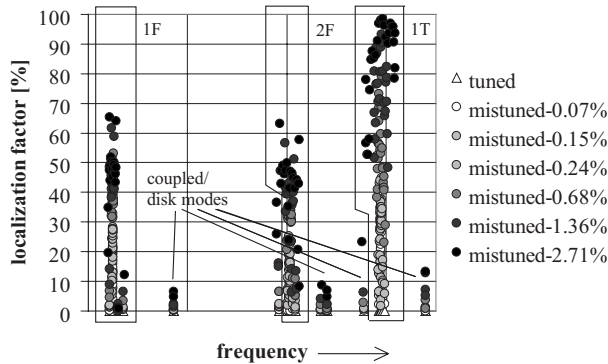


Fig. 14 Localization factors of natural vibrations depending on the blade mistuning standard deviation (first three blade modes) 1-sine-wave mistuning distribution around blisk circumference

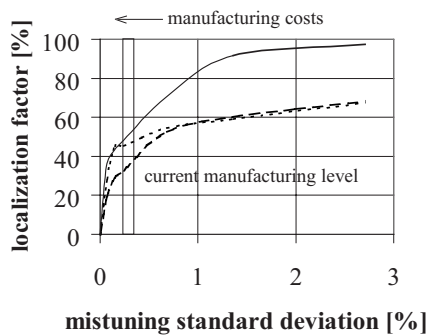


Fig. 15 Maximum localization factors of the first three blade modes depending on the blade mistuning standard deviation; (···) first flap mode, (---) second flap mode, (—) first torsion mode, average of three artificial sine-wave blade mistuning distributions

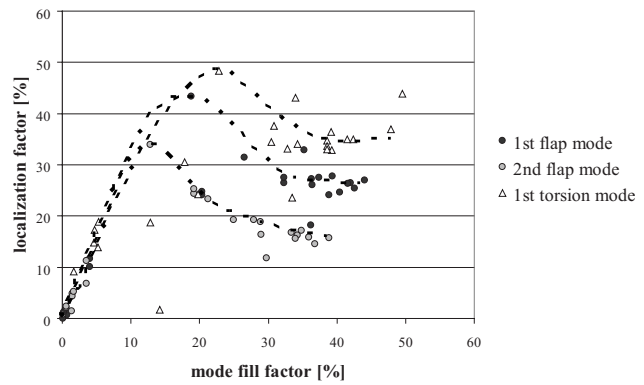


Fig. 16 Localization factor versus mode fill factor of natural vibrations, 1-sine-wave mistuning distribution around blisk circumference, $\sigma_{\text{mistuning}}=0.24\%$

$\leq 0.2\%$). A nearly linear relation between mistuning standard deviation and localization factor occurs. With increasing mistuning standard deviations, local maxima and minima can appear ($0.2\% < \sigma_{\text{mistuning}} \leq 0.4\%$) followed by a continuously increase in the localization factors ($\sigma_{\text{mistuning}} < 0.4\%$) upto 67.5% (first flap mode), 68.3% (second flap mode) and 97.5% (first torsion mode).

Caused by the inevitability of manufacturing tolerances as well as material inhomogeneities, it makes no good economic sense to reduce the mistuning level as low as needed for a significant decrease in mode localization effects ($\sigma_{\text{mistuning}} < 0.1\%$). Thus a reliable and robust prediction of the maximum mode localization, the corresponding blades, and the maximum amplitude magnification is not only the prerequisite for dimensioning of aeroengine compressors but also for the optimum selection of blades to be instrumented with strain gauge, in particular, in case of low-damped blisk rotors.

Using the mode fill factor computation for all three fundamental vibration modes according to Eq. (10), an increase in mode filling can be observed for increasing blade mistuning levels too. Just like the maximum localization factors, the maximum mode fill factors appear at the first torsion modes (87.8% at $\sigma_{\text{mistuning}} = 2.71\%$). In contrast to the torsion mode, both of the flap mode families result in lower mode fill factors (first flap mode: 58.9%, second flap mode: 55.1%, resp.).

The relevant difference between both factors is pointed out using Fig. 16. High mode fill factors are not accompanied by the high localization factors in any case: Vibrational modes with moderate mode fill factors (which means modes with a moderate number of harmonics in their Fourier decomposition) are more sensitive to mode localization than modes with a high number of harmonics. This characteristic is much more pronounced in the case of slightly mistuned blisks than for strong blade mistuning (Fig. 17).

With an increased mistuning level, the percentage of blades on the total blisk strain energy decreases due to lower number of mode-participating blades. Hence, in case of the high localized torsion modes the mean value of blade percentage decreases from 98.8% to 98.4% (see Fig. 18, in addition: first flap mode: 95.9% \rightarrow 93.9%, second flap mode: 89.1% \rightarrow 83.5%).

The highest mode localization appears for the highest cyclic symmetry mode MCSM 12 independently from the mistuning level (see Fig. 19).

Again the mean level of mode localization of all three fundamental blade modes corresponds with the blade percentage on the total blisk strain energy (Fig. 19). Hence, in conformity with Slater et al. [25] and Kenyon et al. [37] who concluded that strong internal coupling prevent mode localization in mistuned systems, one can agree to their statement that internal coupling is always mode dependent. In addition to this, Crawley [38] showed that the

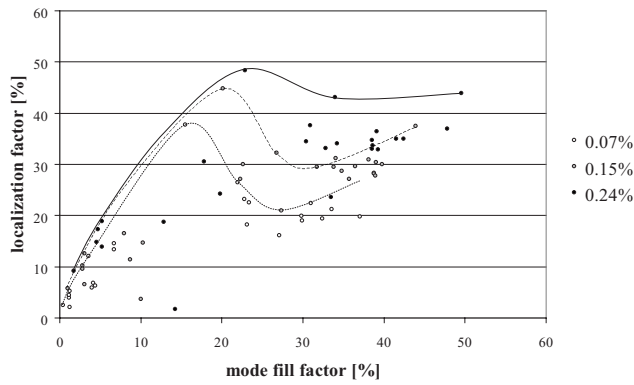


Fig. 17 Localization factor versus mode fill factor of the first torsion mode depending on the mistuning level, 1-sine-wave mistuning distribution around blisk circumference

interblade coupling also depends on the stagger angle of the blades. Complementary coherences between the energy input via coupling and stress amplifications were also derived by Lim et al. [39].

8.1.2 Effect of Disk Stiffness. Because of the known influence of disk stiffness on interblade coupling (see Refs. [14,40]), aeroengine manufacturers are interested in reducing mode localization as well as blade amplitude magnification using modified

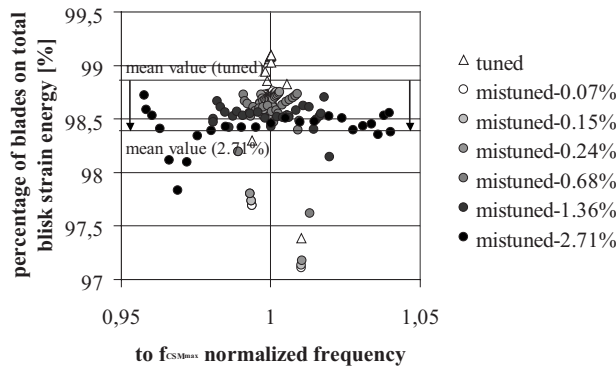


Fig. 18 Percentage of blades on total blisk strain energy of natural vibrations depending on the blade mistuning standard deviation of first torsion mode, 1-sine-wave mistuning distribution around blisk circumference

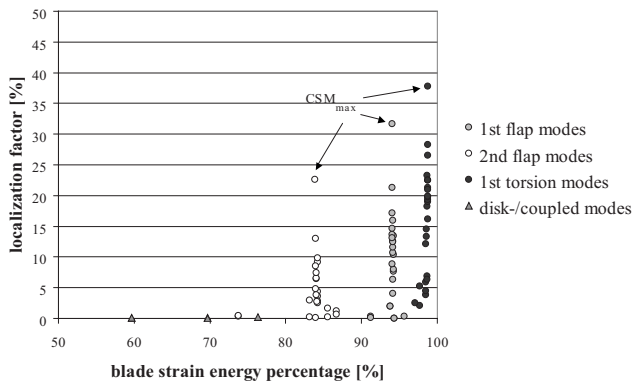


Fig. 19 Localization factor versus percentage of blades on total blisk strain energy of natural vibrations depending on the mistuning level, 1-sine-wave mistuning distribution around blisk circumference, $\sigma_{\text{mistuning}}=0.24\%$

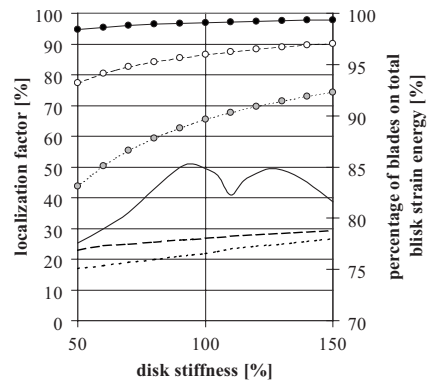


Fig. 20 Percentage of blades on total blisk strain energy compared to the resulting averaged localization factor of natural vibrations depending on the disk stiffness; (\cdots , white dotted) first flap mode, (\cdots , grey dotted) second flap mode, (\cdots , black dotted) first torsion mode, average of three artificial sine-wave mistuning distributions

hub sections to extend service life.

To verify suitable disk stiffness ratios, the Young's modulus of the disk section was modified by $\pm 50\%$ of the original value in the first step. As presented in Figs. 20 and 21, the percentage of blades on the total blisk strain energy steadily increases with higher disk stiffness caused by the stiffer embedding of the blades on the disk.

As a result, the eigenfrequencies of the blade modes as well as the eigenfrequencies of the disk and coupled modes increase. In addition to this, an increasing mode localization can be observed due to the decreased interblade coupling.

In contrast to the first and second blade flap modes with steadily increasing mode localization, in the case of the first blade torsion modes local maxima (at 95% and 125% of the original disk stiffness) and minima (at 70% and 115% of the original disk stiffness) occur.

Aiming at a minimization of the mode localization effects, the modification of the disk stiffness has to take all of the relevant blade modes into consideration. Within the realms of constructive possibilities and without consideration of the local maxima and minima, this indicates a reduction in disk stiffness to increase the interblade coupling and to decrease the structural blade-to-blade isolation.

8.2 Forced Vibrations. The focus of the following chapter is set on forced response analyses to cover the aerodynamic forces, which excite compressor rotors during both, operation and rig test

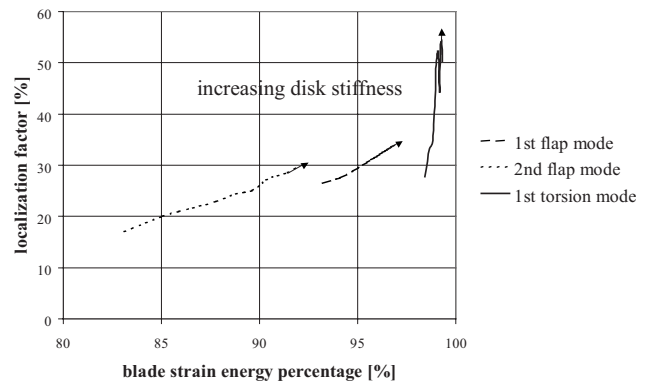


Fig. 21 Localization factor versus percentage of blades on total blisk strain energy depending on the disk stiffness; (\cdots) first flap mode, (\cdots) second flap mode, (\cdots) first torsion mode, average of three artificial sine-wave mistuning distributions

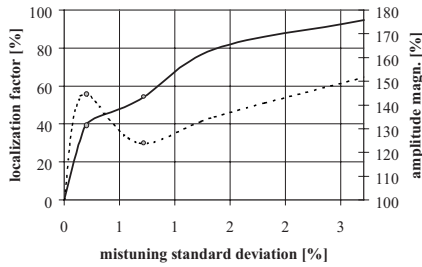


Fig. 22 Maximum localization factor (—) of first torsion modes versus maximum amplitude magnification factor (---) depending on the mistuning level, forced response analysis, $D=0.1\%$ ($Q=500$), EO CSM_{max}, 1 sine-wave mistuning distribution

runs depending on the operating point. At this aerodynamical damping¹² including fluid-structure-interactions¹³ and structural damping¹⁴ will limit the resulting blade amplitudes. As a first assumption, a modal damping value of $D=0.1\%$ ($Q=500$) was selected as basis for the following analyses. Engine orders 1, 4 and CSM_{max} (12) were chosen for the illustration of various forced responses.

8.2.1 Influence of Mistuning Level and Blade Mode. The curve shapes of the localization factor of the forced response results are similar to the curve shapes of the former determined eigenmodes (see first torsion mode results in Fig. 15 for example). Again, the localization factors and mode fill factors of the torsion modes are higher than the corresponding values of the first and second flap modes at identical mistuning levels. As maximum localization factors 83.0% for first torsion mode, 70.3% for first flap mode and 61.4% for second flap mode are found. The selected average modal damping value of $D=0.1\%$ reduces the clarity of the local maxima and minima compared to the eigenmode analysis (see also paragraph “Effect of Modal Damping”). To achieve a better understanding, the corresponding maximum blade amplitude magnifications for EO CSM_{max} of the first torsion modes are added in Fig. 22 for illustration.

It can be recognized that for slightly mistuned systems mode localizations steadily increase with higher mistuning levels. In general a local maximum of blade amplitude magnification appears at small or moderate mistuning levels. The reason for this special behavior is the better transfer of vibration energy between adjacent blades through the disk in case of nearly similar blade eigenfrequencies.

If the eigenfrequencies of the blades are more differing, the interblade energy transfer is decreasing, which is characterized by lower amplitude magnifications whereas the mode localization is steadily increasing.

Overall due to the lower interblade-coupling and the resulting higher structural isolation, forced torsion modes are more sensitive regarding blade mistuning than flap modes.

8.2.2 Effect of Modal Damping. During the flight cycle, the present aerodynamic damping changes depending on the current aeroengine operating point. This damping amount strongly affects the forced response behavior not only of tuned blisks but also of mistuned blisks. Figure 23 below exemplarily presents the correlation between amplitude magnification and localization factor in the case of EO depending on the modal damping value.

Contrary to the structural interblade coupling through the disk a highly compressed fluid between the in-phase and counterphase

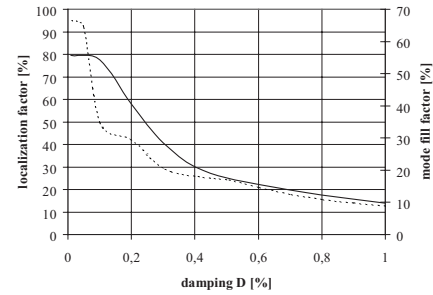


Fig. 23 Maximum localization factor (—) and amplitude magnification (---) depending on the damping value, forced response analysis for EO 1, $\sigma_{\text{mistuning}}=0.68\%$, 1 sine-wave mistuning, first torsion mode

oscillating blades extend the coupling with an aerodynamic component as well as the total damping value. Thus both mode localization and amplitude magnification decrease at higher damping levels so high modal damping is advantageous regarding blade mistuning effects. This means operational conditions with high aerodynamic damping result in lower localized blade mode shapes than conditions with low aerodynamic damping.

8.2.3 Effect of Disk Stiffness. Analogous to the previous chapter, the disk stiffness will be changed again around $\pm 50\%$, which corresponds to a more stiffer or more softer design of the disk, respectively.

For a better understanding of the disk-stiffness-variation effects, one has to be distinguished between the tuned and the mistuned case.

For that purpose the blade displacement amplitudes of the tuned blisk were computed first for EO/CSM 1, 4 and CSM_{max} depending on the disk stiffness. As exemplarily shown in Fig. 24 the maximum blade displacements decrease with increasing disk stiffness as a result of the more stiffer clamping of the blades on the disk. Because of the lower percentage of disk on the total blisk strain energy (see also Fig. 5) this effect is less pronounced for high CSMs than for low CSMs. Hence, in general it is valid that the stiffer the disk, the lower the blade displacement magnitudes at identical excitation gets.

In contrast to this, another effect occurs in the case of mistuned system: A softer disk section increases the interblade coupling through the disk, which results in higher mode localization. As presented in Fig. 25, the localization of the two flap modes slightly increases with increasing disk stiffness. Thus a smaller number of blades has to absorb a larger percentage of the total excitation energy, which results in modified blade amplitude magnifications (see Fig. 26). This stiffening effect is more pronounced for the second flap modes than for the first flap modes.

As presented in the previous chapter, in case of forced torsion

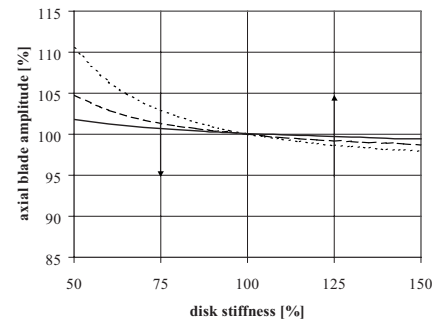


Fig. 24 Maximum axial blade amplitude depending on the disk stiffness, first torsion mode, tuned system, $D=0.1\%$ ($Q=500$), (···) EO/CSM 1, (---) EO/CSM 4, (—) EO/CSM 12 (CSM_{max})

¹²Caused by the airflow around the blades.

¹³In-phase and counter-phase-blade-vibrations of tuned and mistuned bladed disks result in additional aerodynamic forces and aerodynamic damping due to the compression of the flow between the vibrating blades.

¹⁴In case of blisks, only the material damping occurs because of the missing blade-disk-connection.

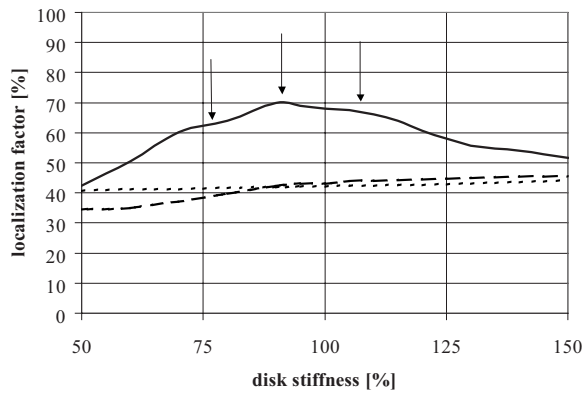


Fig. 25 Maximum localization factor depending on the disk stiffness, mistuned system ($\sigma_{\text{mistuning}}=0.68\%$), $D=0.1\%$ ($Q=500$), (···) first flap mode, (---) second flap mode, (—) first torsion mode, averaged values of EO 1, EO 4, EO 12 (CSM_{max}) excitation and three artificial sinusoidal mistuning distributions

modes local maxima and minima occur depending on the disk stiffness. It has to be mentioned that the positions of all of these local extreme values of the localization factor are not similar to the eigenmode analysis in all cases. Hence, high localization factors occur at $\sim 70\%$, $\sim 90\%$, and $\sim 110\%$ of original disk stiffness. In contrast to this, low values of mode localization occur below 60% and above 125% of original disk stiffness. Also at the curve of amplitude magnification of the first torsion modes local maxima and minima at the same disk stiffness levels occur although these extreme values are more distinctive than for the localization factors.

Again both flap modes are less affected by disk stiffness variations compared to the torsion mode. The amplitude magnifications of the first flap mode second are only slightly decreasing with increasing disk stiffness while the amplitude magnifications of the second flap mode are increasing with a stiffer disk.

Summarizing all of the former results regarding the three fundamental blade modes of the Engine 3E HPC rotor 1, one can conclude that a more softer disk section ($\leq 60\%$) is advantageous regarding mode localization as well as amplitude magnifications compared to the original design. At this point, it has to be reiterated that the disk stiffness modification is only useful inside the bounds of all other criteria (maximum permissible blade deformation, HCF, etc.) and also a softer disk results in a slight increase in blade displacements amplitudes of all blades (\rightarrow blade tip rubbing at outer compressor casing).

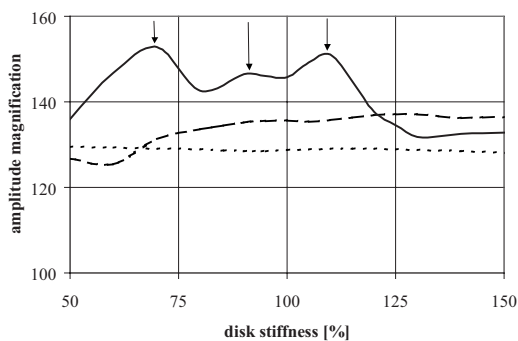


Fig. 26 Maximum amplitude magnification depending on the disk stiffness, mistuned system ($\sigma_{\text{mistuning}}=0.68\%$), $D=0.1\%$ ($Q=500$), (···) first flap mode, (---) second flap mode, (—) first torsion mode, averaged values of EO 1, EO 4, EO 12 (CSM_{max}) excitation and three artificial sinusoidal mistuning distributions

9 Conclusions and Summary

Due to the very low structural damping, the appearing vibration modes of blade integrated disks (blisks) are very sensitive to individual blade mistuning. In contrast to the tuned design model characterized by similar blade amplitudes for all blades, a more or less local zoning of the vibration modes occurs — the so-called mode localization. At this, it can be confirmed that many of the fundamental aspects of this study are in agreement with earlier work (for example, Refs. [25,30,41,42]).

Supplementing for a clear and objective comparison of various blisk designs, blade modes and excitation parameters criteria of evaluation (*mode fill factor* and *localization factor*) have been introduced. A front HPC blisk rotor of the German Engine 3E research program has been used for the comparison of the vibration behavior of different modes, damping values, and disk stiffness ratios.

The determined localization factors show that in general torsion modes of mistuned blisks have a more pronounced local zoning of vibration modes than flap modes. These higher sensitivity, regarding blade mistuning, results from a stronger structural isolation of the adjacent individual blades due to their lower interblade coupling, which can be characterized using, for example, the percentage of blades on the total blisk strain energy.

The same effect is valid for noncyclic-symmetric blade modes that arose from tuned cyclic symmetry modes caused by blade mistuning. Modes with lower numbers of (warped) nodal diameter lines are less sensitive regarding mistuning than blade modes that arise from tuned modes with larger numbers of nodal diameter lines. Again the different interblade coupling between these blade modes is the cause of this effect.

In case of the two investigated fundamental flap modes blisks with stiffer hub sections result in higher mode localization than blisks with a softer disk design compared to the initial disk design. In contrast, additional local maxima and minima occur in the case of the torsion modes. Generally a decline in mode localization can be observed if disk stiffness is decreased due to design modifications. Depending on the blisk geometry, a slight increase in all absolute blade displacement amplitudes occurs caused by the softer fixation of the blades on the disk.

In general high amplitude magnifications of forced vibrations appear at moderate mistuning levels for slightly damped systems, whereas the localization of blade modes steadily increases with higher blade mistuning.

An understanding of these correlations is a step toward improvement of future blisk design (sensitivity to mode localization, design and/or modification of hub section, e.g., bladed integrated ring (bling)), the reduction of mistuning caused effects for future aeroengines and the improvement of strain gauge instrumentation of mistuned bladed integrated disks (see also Refs. [43] for further information).

Acknowledgment

The work presented in this paper has been supported by Rolls Royce Deutschland GmbH & Co KG. The authors thank for this commitment. The investigations are part of the DeSK blisk validation program (FKZ: 80121978), which is funded by the state of Brandenburg and the European Fund for Regional Development (efreinfo@mw.brandenburg.de).

Nomenclature

- CSM_{max} = highest cyclic symmetry mode
- D = dimensionless damping value
- $\overline{\text{DFT}}$ = coefficient of Fourier transformation
- $\overline{\text{DFT}}$ = mean value of all Fourier coefficients
- E = Young's modulus (N/mm^2)
- f = frequency (Hz)
- f_n = eigenfrequency of blade n (Hz)
- \bar{f} = mean value of all blade eigenfrequencies (Hz)

i = component of displacement vector, blade number resp.
 N = number of blades of a blisk
 Q = quality factor, $Q=1/2D$
 s/g = strain gauge
 t = time (s)
 U = displacement vector
 ζ = maximum blade displacement/root mean square
 ξ = sum of all DFT coefficients/max. DFT coefficient
 φ_{CSM} = blade phase angle (rad)
 ω = eigenfrequency, $\omega=2\pi f$

References

- [1] Campbell, W., 1924, "The Protection Of Steam Turbine Disk Wheels From Axial Vibration," presented at the Spring Meeting, Cleveland, OH, May 26–29, ASME, Vol. 46(19-20), pp. 31–160.
- [2] Malkin, I., 1942, "On A Generalization of Kirchhoff's Theory Of Transversal Plate Vibration Problem Of Steam Turbine Disks," J. Franklin Inst., **234**, pp. 355–370 and pp. 431–452.
- [3] Armstrong, E. K., 1955, "An Investigation Into the Coupling Between Turbine Disc and Blade Vibration," Ph.D. thesis, University of Cambridge, Cambridge.
- [4] Kirkhope, J., and Wilson, G. J., 1971, "Analysis of Coupled Blade Disk Assemblies in Axial Flow Turbine and Fans," AIAA Paper No. 71-375, pp. 1–11.
- [5] Soares, C. A. M., Petyt, M., and Salama, A. M., 1976, "Finite Element Analysis of Bladed Disks," *Proceedings of the Winter Annual Meeting*, ASME, pp. 73–92.
- [6] Ewins, D. J., 1969, "The Effects Of Detuning Upon the Forced Vibrations of Bladed Disks," J. Sound Vib., **9**(1), pp. 65–79.
- [7] Ewins, D. J., 1973, "Vibration Characteristics of Bladed Disc Assemblies," J. Mech. Eng. Sci., **15**, pp. 165–186.
- [8] Whitehead, D. S., 1966, "Effect of Mistuning on the Vibration of Turbomachine Blades Induced by Wakes," J. Mech. Eng. Sci., **8**(1), pp. 15–21.
- [9] Whitehead, D. S., 1998, "The Maximum Factor by Which Forced Vibration of Blades can Increase Due to Mistuning," ASME J. Eng. Gas Turbines Power, **120**, pp. 115–119.
- [10] Wei, S. T., and Pierre, C., 1987, "Localization Phenomena in Mistuned Assemblies With Cyclic Symmetry, Part I: Free Vibrations," Department of Mechanical Engineering and Applied Mechanics, University of Michigan, Ann Arbor, MI.
- [11] Wei, S. T., and Pierre, C., 1987, "Localization Phenomena in Mistuned Assemblies With Cyclic Symmetry, Part II: Forced Vibrations," Department of Mechanical Engineering and Applied Mechanics, University of Michigan, Ann Arbor, MI.
- [12] Griffin, J. H., and Hoosac, T. M., 1984, "Model Development and Statistical Investigation of Turbine Blade Mistuning," Trans. ASME, J. Vib., Acoust., Stress, Reliab. Des., **106**(2), pp. 204–210.
- [13] Bladh, R., Pierre, C., Castanier, M. P., and Kruse, M. J., 2002, "Dynamic Response Predictions for a Mistuned Industrial Turbomachinery Rotor Using Reduced-Order Modeling," ASME J. Eng. Gas Turbines Power, **124**(2), pp. 311–324.
- [14] Bladh, R., Pierre, C., and Castanier, M. P., 2003, "Effect of Multistage Coupling Disk Flexibility on Mistuned Bladed Disk Dynamics," ASME J. Eng. Gas Turbines Power, **125**, pp. 121–130.
- [15] Kielb, R. E., and Kaza, K. R. V., 1984, "Effects of Structural Coupling on Mistuned Cascade Flutter and Response," ASME J. Eng. Gas Turbines Power, **106**, pp. 17–24.
- [16] Wildheim, J., 1979, "Excitation of Rotationally Periodic Structures," ASME J. Appl. Mech., **46**, pp. 878–882.
- [17] Wilson, A., and Utengen, T., 1993, "Turbine Blade Dynamics and Blade-Vane Interaction in a Radial Inflow Turbine," Ulstein Turbine A/S, Kongsberg, Norway.
- [18] Yingfeng, W., Jun, H., and Yong, Z., 2005, "Effect of Upstream Rotor on the Aerodynamic Force of Downstream Stator Blades," Najing University of Aeronautics and Astronautics, ISABE-2005-1268.
- [19] Pierre, C., and Murthy, D., 1994, "Localization of Aeroelastic Modes in Mistuned High-energy Turbines," J. Propul. Power, **10**, pp. 318–328.
- [20] Schrape, S., Kühhorn, A., and Golze, M., 2006, "Simulation of Fluid Damped Structural Vibrations," *Proceedings of the Seventh MpCCI User Forum*, Schloss Birlinghoven, Sankt Augustin, Germany, Feb. 21–22, ISSN 1860-6296.
- [21] Schrape, S., Kühhorn, A., and Golze, M., 2006, "FSI of a Simplified Aero Engine Compressor Cascade Configuration," Proc. Appl. Math. Mech., **6**, pp. 457–458.
- [22] Steffens, K., 2000, "Next Engine Generation: Materials, Surface Technology, Manufacturing Processes, What Comes After 2000?," SurTec Conference, Cannes, France.
- [23] Steffens, K., 2001, "Advanced Compressor Technology—Key Success Factor for Competitiveness in Modern Aero Engines," 15th International Symposium on Air Breathing Engines, ISABE, Bagalore, India.
- [24] Beirrow, B., Kühhorn, A., Golze, M., Klauke, T., and Parchem, R., 2005, "Experimental and Numerical Investigations of High Pressure Compressor Blades Vibration Behavior Considering Mistuning," *10th International NAFEMS World Congress*, Malta, ISBN 1 174 376 03 4.
- [25] Slater, J. C., Minkiewicz, G. R., and Blair, A. J., 1999, "Forced Response of Bladed Disk Assemblies—A Survey," Shock Vib. Dig., **31**(1), pp. 17–24.
- [26] Kenyon, J. A., 2004, "Maximum Mistuned Bladed Disk Forced Response With Frequency Veering," 40th AIAA/ASME/SAE/ASEE Joint Propulsion Conference and Exhibit, Fort Lauderdale, AIAA 2004-3753.
- [27] Kellerer, R., and Stetter, H., 1992, "Double Mode Behavior of Bladed Disk Assemblies in the Resonance Frequency Range, Visualized by Means of Holographic Interferometry," ASME Paper No. 92-GT-438.
- [28] Mück, B., 2004, "Flutter and Forced Response Prediction in Compressor Blade Design," *Proceedings of the 11th Blade Mechanics Seminar*, ABB Turbo Systems Ltd., Thermal Machinery Laboratory, Baden/Switzerland.
- [29] Pianka, C., 2004, "Considering Mistuning Effects on Blisks in the Specification of Engine Vibration Surveys," *Proceedings of the 11th Blade Mechanics Seminar*, ABB Turbo Systems Ltd., Thermal Machinery Laboratory, Baden/Switzerland.
- [30] Srinivasan, A. V., 1997, "Flutter and Resonant Vibration Characteristics of Engine Blades," ASME J. Eng. Gas Turbines Power, **119**(4), pp. 742–775.
- [31] Castanier, M. P., and Pierre, C., 2002, "Using Intentional Mistuning in the Design of Turbomachinery Rotors," AIAA J., **40**(10), pp. 2077–2086.
- [32] Kenyon, J. A., Griffin, J., and Feiner, D., 2003, "Maximum Bladed Disk Forced Response From Distortion of a Structural Mode," ASME J. Turbomach., **125**(2), pp. 352–363.
- [33] Hodges, C. H., 1982, "Confinement of Vibration by Structural Irregularity," J. Sound Vib., **82**(3), pp. 411–424.
- [34] Anderson, P. W., 1958, "Absence of Diffusion in Certain Random Lattices," Phys. Rev., **109**(5), pp. 1492–1505.
- [35] Bendiksen, O. O., 2000, "Localization Phenomena in Structural Dynamics," Chaos, Solitons Fractals, **11**, pp. 1621–1660.
- [36] Kahl, G., 2002, "Aeroelastic Effect of Mistuning and Coupling in Turbomachinery Bladings," Ph.D. thesis, Ecole Polytechnique Federale De Lausanne, Lausanne.
- [37] Kenyon, J. A., Cross, C. J., and Minkiewicz, G. R., 2000, "Mechanical Coupling Effects on Turbomachine Mistuned Response," J. Propul. Power, **16**(6), pp. 1149–1154.
- [38] Crawley, E. F., and Mokodam, D. R., 1984, "Stagger Angle Dependence of Inertial and Elastic Coupling in Bladed Disks," ASME J. Vib., Acoust., Stress, Reliab. Des., **106**, pp. 181–188.
- [39] Lim, S.-H., Castanier, M. P., and Pierre, C., 2004, "Predicting Mistuned Blade Amplitude Bounds and Stress Increases from Energy Formulations," *Proceedings of the Ninth National Turbine Engine High Cycle Fatigue Conference*, Pinehurst, NC.
- [40] Baik, S., Pierre, C., and Castanier, M. P., 2004, "Mistuning Sensitivity Prediction of Bladed Disks Using Eigenvalue Curve Veerings," *Proceedings of the Ninth National Turbine Engine HCF Conference*, Pinehurst, NC.
- [41] Myhre, M., 2003, "Numerical Investigations of the Sensitivity of Forced Response Characteristics of Bladed Disks to Mistuning," Licentiate thesis, Royal Institute of Technology, Stockholm, Sweden.
- [42] Castanier, M. P., and Pierre, C., 2006, "Modeling and Analysis of Mistuned Bladed Disk Vibration: Status and Emerging Directions," J. Propul. Power, **22**(2), pp. 384–396.
- [43] Klauke, T., Kühhorn, A., and Beirrow, B., 2005, "Experimental and Numerical Investigations of Blade Mistuning and Strain Gauge Application Effects in Aero Engine Development," *Proceedings of the 12th Blade Mechanics Seminar*, ABB Turbo Systems Ltd., Thermal Machinery Laboratory, Baden/Switzerland.

Time-Accurate Predictions for a Fully Cooled High-Pressure Turbine Stage—Part I: Comparison of Predictions With Data

S. A. Southworth

M. G. Dunn

C. W. Haldeman

J.-P. Chen

The Ohio State University,
Enarson Hall,
154 W 12th Avenue,
Columbus, OH 43210

G. Heitland

J. Liu

Honeywell Aerospace,
Phoenix, AZ 85072

The aerodynamics of a fully cooled axial single stage high-pressure turbine operating at design corrected conditions of corrected speed, flow function, and stage pressure ratio has been investigated. This paper focuses on flow field predictions obtained from the viewpoint of a turbine designer using the computational fluid dynamics (CFD) codes Numeca's FINE/TURBO and the code TURBO. The predictions were all performed with only knowledge of the stage operating conditions, but without knowledge of the surface pressure measurements. Predictions were obtained with and without distributed cooling flow simulation. The FINE/TURBO model was run in 3-D viscous steady and time-accurate modes; the TURBO model was used to provide only 3-D viscous time-accurate results. Both FINE/TURBO and TURBO utilized phase-lagged boundary conditions to simplify the time-accurate model and to significantly reduce the computing time and resources. The time-accurate surface pressure loadings and steady state predictions are compared to measurements for the blade, vane, and shroud as time-averaged, time series, and power spectrum data. The measurements were obtained using The Ohio State University Gas Turbine Laboratory Turbine Test Facility. The time-average and steady comparisons of measurements and predictions are presented for 50% span on the vane and blade. Comparisons are also presented for several locations along the blade to illustrate local differences in the CFD behavior. The comparisons for the shroud are made across the blade passage at axial blade chord locations corresponding to the pressure transducer locations. The power spectrum decompositions of individual transducers (based on the fast Fourier transform (FFT)) are also included to lend insight into the unsteady nature of the flow. The comparisons show that both computational tools are capable of providing reasonable aerodynamic predictions for the vane, blade, and stationary shroud. The CFD model predictions show the encouraging trend of improved matching to the experimental data with increasing model fidelity from mass averaged to distributed cooling flow inclusion and as the codes change from steady to time-accurate modes.

[DOI: 10.1115/1.2985075]

Nomenclature and Definitions

Wetted distance location. Location along the airfoil contour (x) normalized by the total distance along each surface (S). Measured from -100% to 100% with 0 at the stagnation point, and the negative side is the pressure side of the airfoil.

$$\text{pressure side} = -\frac{x}{S_{\text{pressure side}}} 100 \quad \text{suction side} = \frac{x}{S_{\text{suction side}}} 100$$

Gauge location relative to cooling holes (x/d). Distance of the heat-flux sensors from the immediate upstream cooling hole based on that hole diameter (d).

Normalized Pressure. Local static pressure/vane inlet total pressure.

$$\frac{P_{\text{local}(L)}}{P_{\text{total}}}$$

Normalized pressure fluctuation. Local static pressure/vane inlet total pressure—Time-Average of the local static pressure/vane

inlet total pressure for one blade or vane passage. This is equivalent to the unsteady component of the normalized pressure.

$$\frac{P_{\text{local}(L)}}{P_{\text{total}}} - \frac{P_{\text{local}(L)}}{P_{\text{total}}}$$

Percent deviation from data. (Value of the prediction – Data)*100/Data at any given location

$$\frac{(\text{prediction} - \text{data}) 100}{\text{data}} \Bigg|_{\text{location}=x}$$

1 Introduction

Computational design tools play a vital role in the design of today's turbomachinery. Such tools have a proven value by the capability to provide reasonable predictions of the flow physics for the aerodynamics of the fan, compressor, and turbine stages of modern gas turbine engines. In the specific case of the high-pressure turbine component, some studies have compared the predictions to data obtained using real world engine hardware and operating conditions. The presence of full-stage cooling flows has generally been ignored to simplify the models and measurement programs. In contrast, cooling flows are present in nearly all

Manuscript received April 25, 2007; final manuscript received January 17, 2008; published online April 7, 2009. Review conducted by David Wisler.

modern-day high-pressure turbine designs. This adds a level of complexity to both the computational and experimental work that needs to be addressed in a realistic manner.

For the study described in this paper, actual engine hardware was made available and used in a short-duration facility that has been updated to handle the complex cooling requirements for a full-stage high-pressure turbine operating at design corrected conditions. With such data, the process of updating the computational modeling to include cooling, and thus predicting the unsteady aerodynamics and heat transfer, has become the next logical step in the design and development process.

This paper is presented in two parts. In Part I of this paper, the results obtained with the different CFD design approaches are compared with data. It becomes clear that different methodologies of approximating the cooling flow affect the prediction quality. However, the overall agreement has become good enough that a more quantifiable method needs to be developed to define "the degree of goodness" of the comparison. This will be done in Part II of this paper.

It is important to emphasize that none of the comparisons in either part of this paper are designed to (or should be used to) infer that one of the codes is superior to the other. As discussed in this paper, there are some differences in the codes, particularly in the use of the turbulence models. However the individual differences in the capabilities of the two codes are dwarfed by the differences in how the designer applies the grids, boundary conditions, and general problem setup. Both parts of this paper will show comparisons between the predictions and data for different models. And there are places where there are substantial differences in how the models perform, but that does not imply that the code itself is at fault. As will be discussed in this paper, this is a result of the general modeling conditions being used.

1.1 Scope of Study. This study concentrates on the aerodynamics of a single stage high-pressure turbine (vane row and rotating blade row). The material presented includes detailed comparisons between computational and experimental results. The computational work utilizes a commercial analysis code FINE/TURBO described by Aube and Hirsch [1] operated in both steady and time-accurate modes and with and without distributed injection, as well as a research analysis code NASA MSU TURBO (hereafter referred to as TURBO), operated in the time-accurate mode only. Two TURBO results are provided for comparison because this code has proven its ability to provide accurate predictions, as shown in the work of Green et al. [2] and in the work of Barter et al. [3].

All of the experimental work discussed in this paper was performed at The OSU GTL, and the procedure has been documented previously by Haldeman and co-workers [4,5]. The measurements were obtained using a fully cooled full-scale high-pressure turbine stage. The initial measurements were performed at a low Reynolds number condition to check out the various systems of the facility since this condition represents one of the more difficult operating conditions.

The present work builds on the previous FINE/TURBO uncooled predictions shown in Ref. [5] by including different models of the cooling flow and by comparing the unsteady results with the research code TURBO predictions. The comparison of the CFD predictions will focus on the steady and the time-average of the time-accurate surface pressure for the vanes and blades, as well as for the stationary shroud. The corresponding heat transfer predictions are left to a future study.

This study provides insight into the quality of a commercial CFD tool FINE TURBO when operated in several different modeling modes. Comparing the results from these different operations shows the differences between a time-accurate prediction and a steady prediction, as well as the ability of the codes to capture the flow behavior in highly unsteady areas. This work presents results in three fundamentally different flow regimes in the turbine stage: the vane, the blade, and the tip/shroud region. These parts of the

machine have different flow characteristics and offer more insight into the codes and each modeling approaches predictive capabilities and the importance of the initial computational grid than could be deduced by examining only one area.

Previous computational work was performed during the initial phase of this research by Garg [6] using the same engine hardware as was modeled in this work, but his work concentrated on the heat transfer for the blade. Garg did not include the film cooling of the vane and how the upstream vane cooling flow might influence the blade results. The primary goal of the current computational work was to provide a full set of aerodynamic predictions generated from the perspective of the turbine designer by adding the cooling flow as either a lumped mass (LM) (the measured cooling flow from both the vane and rotor is added at the inlet/exit interface) or by adding the coolant flow as distributed source terms (located at each cooling hole).

1.2 Review of Past Work. The subject of film cooling is by no means a new area of research. Many film cooling studies have been performed, typically using flat plate and cascade facilities. The issue with flat plate and cascade data is that the test conditions are far away from those of actual turbine operating conditions [7]. Even those film cooling studies that have been performed in more realistic environments have not involved cooling flows in a way that is comparable to the cooling seen in actual engine hardware. The previous studies, however, did provide the foundation of knowledge necessary to implement actual engine conditions in a current full-scale rotating rig [1,2].

The CFD capabilities are at a point where several codes have demonstrated the ability to predict pressure loadings and some can handle heat transfer as well, such as UNSFLO-2D that was developed by Giles [8,9], Guenette et al. [10], and Abhari and Giles [11] and the vane blade interaction (VBI) code developed by Delaney et al. [12–14]. The codes generally exclude full film cooling flow models, although Abhari [15] did incorporate an early version of his macromodel into UNSFLO-2D. Although UNSFLO-2D and the VBI code proved to be capable of doing time-accurate heat transfer and aerodynamic predictions, it is important to remember that these codes were 2D, and thus should not be used in the shroud area, a location of high interest. Work done by Green et al. [2], verified that TURBO is capable of predicting pressure loadings for a 3D uncooled high-pressure turbine stage, while the work of Molter et al. [16] expanded on Green's work and looked at the same geometry using the steady state version of the commercial analysis code STAR-CD. Busby et al. [17], Venable et al. [18], and Barter et al. [3] also showed comparisons of several different research codes to the Allison VBI data set, but their work utilized an uncooled turbine stage.

There are many other examples of research that have also helped develop the experimental and computational techniques needed for this type of full-scale rotating experiment. Hoyningen-Huene and Jung [19] discussed techniques that were used to improve the overall efficiency of unsteady calculations when using periodic boundary conditions. Mildner and Gallus [20] provided an analytical framework for dealing with added coolant flow. Denos and co-workers [21,22] have more recently focused on measuring the efficiency of a cooled turbine stage, but their measurement focused primarily on the wake propagation from the vane through the rotor using measurements taken after the rotor, as opposed to detailed measurements on the blade rows. The Massachusetts Institute of Technology (MIT) blowdown rig has also been used to look at efficiency measurements of uncooled and cooled turbine stages as shown by Keogh and co-workers [23,24]

The cooling model development that has occurred typically follows one of two techniques. One group has used the idea of fully solving the entire flow field within each cooling hole, within the supply plenums and the external flow over the airfoil. Leylek and Zerkel [25] have reported on results with this technique. The other technique being pursued is that used by Abhari [15], Bernsdorf et al. [26], and Burchet et al. [27], which uses a macromodel ap-

proach that expands on past injection models. The injection method accounts for the penetration and spreading of the coolant jet, as well as the entrainment of the boundary layer fluid by the coolant.

The results provided herein provide some validation of the primary computational code used for this work (FINE/TURBO). There are relatively few references to the code FINE/TURBO and even fewer references in open literature to the code being used to perform unsteady predictions. One unsteady analysis performed by Aube and Hirsch [1] showed the comparison of FINE/TURBO predictions to data. There did not appear to be a large amount of data available in that work, so the predictive capabilities of FINE/TURBO were seen, but not fully verified. Other works using FINE/TURBO examine predictions using steady analyses, as in Ref. [28], or look at the modeling capabilities of FINE/TURBO across the rotor/stator interface, as in Ref. [29], or examine the unsteady calculation of a film-cooled turbine stage as in Ref. [30]. However, in all of these references, the experimental data that were available were very limited and were not for a fully cooled high-pressure turbine stage as are the data shown in this work. The limited work involving FINE/TURBO does not give one a good sense of the accuracy of the predictions obtained using this code. Therefore, the current study has the opportunity to test the code since data were available at many locations within the turbine stage.

There is an abundance of literature available on the topic of film cooling but in the existing literature the work is mostly specific to simplified flow geometries with uncooled modeling of the hardware. The first step in advancing the CFD modeling to include cooling modeling is to compare the uncooled predictions to cooled data and to fully determine the effect cooling has on the predicted pressure loading. The results for the next step of using a fully cooled unsteady model were obtained using source term modeling for the cooling and are included. The results of the lumped mass addition and the distributed source computational modeling work will help push code developers toward better cooling modeling and advance the understanding of such film cooling problems.

2 Experimental Investigation

The experimental results are representative of a low Reynolds number experimental condition of a multiphased measurement program currently underway at the OSU GTL. The experimental results provided a unique data set for a fully cooled single stage real world turbine operating at design corrected conditions.

2.1 Experimental Facility. The shock-tunnel facility at the OSU GTL was used for the experimental work. The facility uses a large shock tube operated in blowdown mode to provide a short duration of heated and pressurized air directed through the turbine stage. The shock tube, expansion nozzle, large dump tank, and turbine rig housing the stage comprised the experimental facility used for the previous uncooled experiments in this facility. The major differences between the previous measurement programs utilizing this facility and the one described here are that for the cooling experiments, the shock tube is operated in blowdown mode. A large cooling facility (LCF) was added to provide the cooling gas to the vanes and blades, a combustor emulator was added to provide the heat addition to the main stream flow, and the capability to include a turbulence grid was added. The operation of this facility was extensively documented by Haldeman et al. [4] and will not be discussed in detail here.

2.2 Turbine Rig. A single stage high-pressure turbine manufactured by Honeywell Engines is the research vehicle for this work. Three independently controlled flow paths provide the cooling flow to the vanes and blades, as seen in Fig. 1. In the case of the vane the inner path is the control for the showerhead pressure and suction surface cooling holes while the outer path provides cooling gas to the trailing edge. For this set of experiments, the

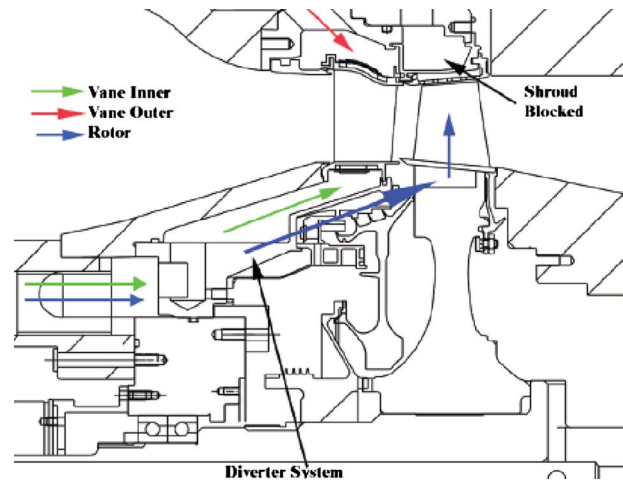


Fig. 1 Turbine cooling paths

shroud cooling holes were blocked as indicated.

The rig uses 12 vane doublets (24 vanes total) and 38 blades. Photographs of the vane and blade cooling hole geometry are given in Haldeman et al. [4]. The vane has 12 rows of film holes and a row of trailing edge slots while the blade has 8 rows of holes spread out along the surface in a 3D pattern. The main operating conditions for the experimental data and the predictions reported in this paper are shown in Table 1.

2.3 Instrumentation. The majority of the instrumentation for this rig consists of Kulite XCQ-062-100A pressure transducers (typical frequency response is in excess of 100 kHz) and double-sided Kapton heat-flux gauges. The Kulite pressure transducers are calibrated through the entire data system prior to and after each day of running. Small effects due to the g -loading and temperature shift are accounted for by comparing pressures at the rotational speed and at a temperature with a nonrotating (non-Kulite) pressure standard. The discussion of this paper is confined to the aerodynamics of the stage so only the pressure measurements are described, but heat transfer results are given in Haldeman et al. [31]. The vane is instrumented externally at 50% span (16 surface pressure transducers) while the blade is instrumented at 50% span with 17 pressure transducers and at 90% span with 14 pressure transducers, but only the midspan results are included herein. There are also internally mounted pressure transducers located at approximately 50% span to provide the pressure within the various cooling cavities. Of the 38 blades, 22 have been instrumented to some extent.

2.4 Data Reduction. The data are acquired in a time-resolved manner at a sampling frequency of 100 kHz (approximately 14 times the blade passing frequency) with the appropriate anti-aliasing filters and basic numerical processing done over the data window to obtain the information used for this analysis. There are

Table 1 Operating conditions for the turbine rig

Property	Rig operating point
Total pressure ratio	3.672 ± 0.085
Corrected speed (rpm)	9719
T_{core}/T_{metal}	1.39
$T_{cooling}/T_{metal}$	0.883
Mass flow ratio (vane inner to vane outer)	1.816
Mass flow ratio (vane inner to rotor)	1.057
Reynolds number (Re)	1.760×10^7

many ways to characterize the time-accurate data so both power spectrums and envelope magnitudes are presented. Analysis that focuses only on the fundamental frequency and its corresponding amplitude provided by power spectrums can lead to an underprediction of the overall unsteadiness because many of the higher order harmonics contribute to the shape of the unsteadiness. Therefore, often envelope magnitudes are used to provide a single number estimate of the unsteady effects.

An uncertainty analysis was also done on the data, and demonstrated that the uncertainty in the pressure measurement was generally within the confines of the symbol. Range bars are provided in the data, but for the pressure data presented here the range bars show the magnitude of unsteady envelopes, and thus represent the periodic behavior of the flow and are not traditional “uncertainties.” More information on these techniques and the uncertainty analysis can be found in Refs. [31,32].

3 Computational Investigation

The two codes of interest for this investigation are Numeca's FINE/TURBO and the NASA/MSU code TURBO. The commercially available CFD code FINE/TURBO was used to generate the grid, a steady solution, and a time-accurate solution for the case matching the experimental operating conditions. This same experimental condition was analyzed using the code TURBO. TURBO has proven its ability to provide accurate predictions as mentioned previously. FINE/TURBO has not been used for as many published works, especially not in a time-accurate analysis for a high-pressure turbine stage. Because the predictions obtained herein were done from a designer's perspective (assuming that the designer did not have access to experimental results), no attempt was made to alter the selected turbulence models or grid structure to make the predictions compare better with the data.

3.1 FINE/Turbo. Numeca's FINE/TURBO code is a Reynolds averaged Navier–Stokes (RANS) based code capable of making steady or time-accurate calculations. This code is specialized for turbomachinery and is capable of handling 2D and 3D flows for complex geometries. The preprocessor, solver, and postprocessor are bundled into a single system, which can complete the simulation from grid generation to postprocessing/visualization. FINE/TURBO is an explicit solver using a cell center control volume scheme. The code is second order spatial and temporal accurate. A full multigrid strategy can be and was employed for the steady initialization and solution to accelerate the residual convergence. More details on the flow solver can be found in Aube and Hirsch [1].

The CFD analyses first utilized the steady 3D viscous code that solves the RANS equations in Cartesian coordinates. The flow solver is capable of handling flows modeled as either inviscid (Euler) or viscous (laminar or turbulent Navier–Stokes), for this work only the viscous turbulent Navier–Stokes model was used.

The code is also capable of utilizing different turbulence models. Initially the steady analyses used the $k-\epsilon$ extended wall function model. Although this turbulence model was suitable for use in the time-accurate analysis, there were convergence issues with the time-accurate case. The turbulence model was changed to help with the resolution of this problem. The new turbulence model that was used for both the steady and time-accurate analyses was the Spalart–Allmaras model. For this model, the y^+ values should be in the range of $15 < y^+ < 100$. The y^+ values obtained from the steady analysis varied from 0 to 140 with the majority of the values falling within the desired range (15–100). The y^+ values tend to be higher within the tip region, which is where the values over 100 all occur. This is not an issue as the tip clearance flow consists of a thoroughly sheared vortical fluid that undergoes a significant acceleration and is therefore quite different than a standard boundary layer. The steady solution and the time-accurate solution used all of the same parameters to provide a consistent

basis for solution comparison.

The time-accurate calculations used the phase-lagged boundary condition approach. Since the ratio of vanes to blades does not reduce to a simple fraction (such as 1/2 or 2/3) the computational domain cannot be easily scaled so that only one or two passages need to be modeled. Either the domain would have to be left in its entirety or scaled down leaving 12 vanes and 19 blades that still need to be modeled. This would require a very large amount of computing time and resources. The alternative method of phase-lagged boundary conditions means that only one blade and vane passage needs to be included in the computational domain and this significantly reduces the amount of time and computing resources. Overall, the time-accurate calculation still takes quite some time to process, but it is on the order of days rather than months using a single PC based processor.

3.2 TURBO. TURBO, like FINE/TURBO, is also a Reynolds averaged Navier–Stokes based code capable of time-accurate calculations. This code is a cell-centered finite volume scheme solving the 3D viscous governing equations in the rotating Cartesian coordinates [33]. The equations are discretized based on an implicit upwind Newton scheme [34]. In this study three Newton iterations with six Gauss–Seidel subiterations are used to achieve time-accurate solution. The spatial accuracy is three and temporal accuracy is two. The turbulence model is the CMOTT $k-\epsilon$ model with wall functions [35]. The y^+ values of the grids on the vane are on the order of 1, while those on the blade and the tip clearance region are on the order of 20–30. The wall shear stress is computed either with the integration to the wall or with a wall function based on the y^+ value. In this case, the vane is computed with the integration to the wall and the blade with the wall function. More details of this flow solver can be found in Ref. [36].

TURBO has three options for performing a time-accurate analysis for a turbine stage. The first technique is to compute a periodic sector of the wheel to model the exact blade counts of the vane and blade. This technique can also be extended to model the full wheel with TURBO's efficient parallelization capability and is critical for multistage machines that need the complete modeling of the spatial and temporal unsteady effects between blade rows [37].

The second technique is the phase-lagged mode that reduces the unsteady modeling of multistage problems to only one blade passage per blade row. The coupling of the time-dependent behavior of the blade rows (vanes and blades) is done with an assumed unsteady frequency set by the blade counts. The phase-lagged model is that of the direct storage method versus the Fourier-decomposition method of FINE/TURBO and is capable of capturing the nonlinear blade row interactions. This technique is further described in Refs. [36,38].

The third technique is known as the wake blade interaction (WBI). In this approach only a single blade passage is computed. The disturbances from the upstream or downstream are introduced into the computational domain by an inlet or exit time-dependent boundary condition. The blade row interaction is modeled through the use of phase-lagged boundary conditions at periodic boundaries. More details on this technique can be found in Ref. [36].

As Green et al. [2] showed, the phase-lagged and the WBI techniques produce different results in some locations, but in general the trends of the two are very similar. Since the computational resources are higher for the phase-lagged technique, the WBI technique becomes more attractive to the designer. However, for stages where the upstream blade row is affected by the potential field of the downstream blade row, the phase-lagged method is preferred over the WBI method because it accounts for the real-time unsteady effects. In this study the phase-lagged method was used.

Film cooling effect can also be modeled through the discrete body forces that prescribe the mass, momentum, and energy fluxes of the jet out of each cooling hole. However, the body force terms are generated by a standalone preprocessor and are not included in this study.

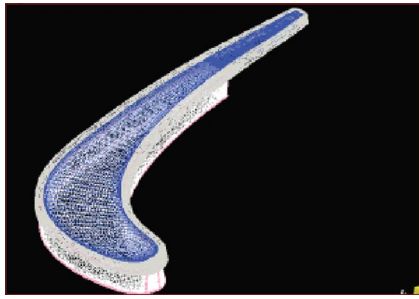


Fig. 2 Blade tip clearance, cap, and cavity blocks

There are both advantages and disadvantages of using FINE/TURBO over TURBO. FINE/TURBO offers an easy approach to incorporate cooling flows as source terms. This cooling option has proved to be a reasonable way to model cooling in calculations such as those presented here. The disadvantage of using FINE/TURBO is that the OSU GTL does not have a source code, but has the source code for TURBO. The importance of access to the source code becomes obvious when one progresses with the incorporation of modeling the film cooling into the heat transfer predictions.

3.3 Computational Modeling. The meshing process for the set of multiblock grids is quite sophisticated. The inlet block is comprised of a pure H-mesh and the vane block of a pure O-mesh using FINE/TURBO's AutoGrid automated meshing tool. The blade block is made of an H-mesh, which was also made in AutoGrid. An external grid process was developed at Honeywell to automatically create the tip clearance, tip cap, and plenum blocks. These blocks consist of either H- or O-meshes and among the three blocks shown in Fig. 2, there are over 165,000 cells in the blade tip and clearance regions alone.

The vane consists of about 241,000 cells and the blade contains over 269,000 cells, the remaining cells (220,000) are in the blade tip region for a total of over 730,000 cells making up the single stage model shown in Fig. 3. A 2D slice through the grid of Fig. 3 is shown in Fig. 4, where it is possible to see a little more of the detail of the grid geometry. The cooling flows and rim leakage flows can be introduced into the model as source terms, and steady and time-accurate computations using cooling were performed.

Originally, the same mesh was to be used by both codes, but because of the use of nonmatching boundary conditions in FINE/TURBO, the same mesh could not be used in TURBO. Four blocks consisting of the vane passage (605,696 cells), the blade passage (524,160 cells), the tip clearance (16,384 cells), and the blade tip gap (5760 cells) were generated for TURBO, all with H-mesh. By comparison, TURBO had about 2.5 times the grid density in the vane, about two times the grid density on the blade, and about one-tenth the resolution in the blade tip area. This is important

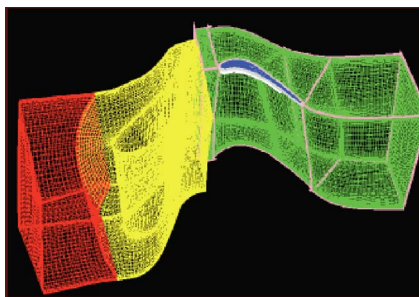


Fig. 3 Entire meshed model including blocks for the inlet, vane, blade, and tip

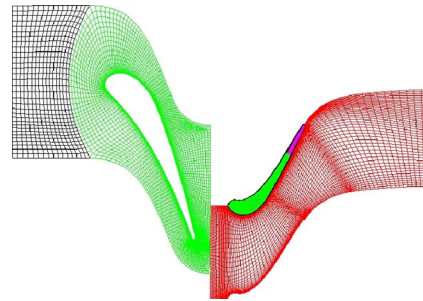


Fig. 4 2D Slice of the grid used for fine/turbo

when comparing the predictions from the two codes because the accuracy of any code is dependent on the density of the grid. For the calculations presented here the grid sizes selected are consistent with the current best practice for aerodynamic performance evaluation.

The inlet boundary conditions were obtained from the data set, which uses a uniform inlet total temperature and total pressure condition. Isothermal boundary conditions were imposed on the wall for FINE/TURBO. Since only pressure measurement is considered in this study the adiabatic wall condition is used for TURBO. Parameters such as the downstream and upstream pressure, rotational speed, stage mass flow, and temperatures were all available for input conditions to the model to match those used for the experiment. In TURBO, the time step is set to advance one rotor pitch with 120 time steps and uses three Newton subiterations for each time step. The simulation is considered converged as the inlet and exit flow rates agree within 0.02% of the mean flow rate. The experimental operating conditions are shown in Table 1. The boundary conditions were not adjusted and just one steady and one time-accurate run were done using FINE/TURBO and a single time-accurate solution for TURBO, therefore the predictions seen in the next section are truly predictions.

3.4 Reduction of the CFD Results. An unsteady analysis provides a very large amount of data to process. For this paper, the primary areas of interest are at those locations where the instrumentation is located. The surface pressures on the vane and blade at the 50% spanwise location were the first parts to be processed. The time-accurate pressure predictions were taken for each time step at the instrumentation locations.

The frequency content was also desired so the fast Fourier transform (FFT) was done on the time-accurate data at a given wetted distance and spanwise location. The magnitudes of the FFTs were examined and provided clear indications of the fundamental passing frequencies, as well as the harmonic content, showing the unsteady nature of the flow through the turbine stage. The turbine inlet total pressure was used to normalize all of the pressure measurements except for the time-averaged vane pressure data, which were normalized by an arbitrary reference pressure.

Time-accurate predictions were also obtained for the stationary shroud. These predictions require more postprocessing to achieve the blade-passing period in the stationary reference frame. Surfaces were created at given axial chord locations corresponding to the pressure transducer locations, and the corresponding surface pressure for each time step was stored over one period of the unsteady solution (one blade passage). Due to the way the grid was created, the area above the blade is not defined as a part of the shroud in the CFD postprocessor, so these predictions need to be carefully analyzed. Thus, the shroud definition includes not just the passage between the blades, but also the location above the blade; both areas were included in the processing of the computational results.

4 Discussion of Results

The results from the experiments and the CFD analyses are compared for different locations within the turbine stage. The pressure loadings on the vane and blade are examined first by looking at the steady and time-averaged predictions as compared to the measurements as a function of wetted distance. Then detailed examinations of the time-resolved measurements (both in the time domain as pressure envelopes and in the frequency domain as power spectra) for each wetted distance location are done to compare the results from the different codes and different approaches for incorporating cooling. A similar procedure will be used for the shroud comparisons. These areas represent different flow physics and thus are good locations to verify code capability.

4.1 Steady and Time-Averaged Results for Vane and Blade. Predictions were obtained using FINE/TURBO operated in both the steady mode (Steady in the figures) and in time-accurate mode (TA in the figures) for both the distributed cooling gas injection (distributed mass DM in the figures) and for the case where the measured stage pressure ratio and physical speed were used as an input condition (lumped mass LM in the figures). The primary reason for running the steady solution is to provide an initial solution to use with the time-accurate mode. Another reason for looking at the steady solution and at the two different ways of incorporating the cooling gas is to see how it compares to the corresponding time-averaged predictions, which provides insight into how the prediction technique and the unsteadiness affects the results. Figure 5 gives the steady and time-averaged predictions on the vane at 50% span along with the data and the time-averaged solution from TURBO. The TURBO solution (lumped mass flow model) was obtained using the measured stage pressure ratio and physical speed as input conditions. TURBO was not run using the distributed injection model.

The predictions are quite similar over most of the pressure side and on the suction side until approximately 50% wetted distance. At this location, the time-averaged and steady predictions begin to diverge, which is not surprising for a turbine with a relatively high stage pressure ratio. Although there are significant differences among the predictions, the distributed mass (DM) and LM steady and time-averaged predictions all agree with the available data in this region. The green squares shown in Fig. 5 represent the vane internal cooling passage pressure measurements.

The overall trend is well established in Fig. 5. In general, all the predictions are compared very well with data except downstream of the 50% wetted distance on the suction surface. This is the uncovered portion after the throat. A Mach number contour from the steady state, mixing plane computation is given in Fig. 6 and indicates the trailing edge shock across the passage impinging on the suction surface at around 50% wetted distance location.

Figure 7 shows the same Mach number contours from the time unsteady results. The potential waves from the downstream rotor

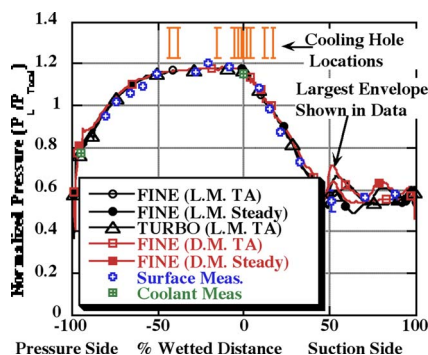


Fig. 5 Predicted static pressure loading, vane at 50% span

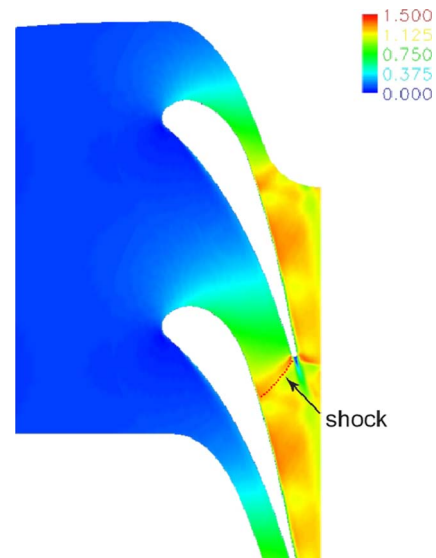


Fig. 6 Mach number contours at 50% span using a steady-state (mixing-plane) analysis

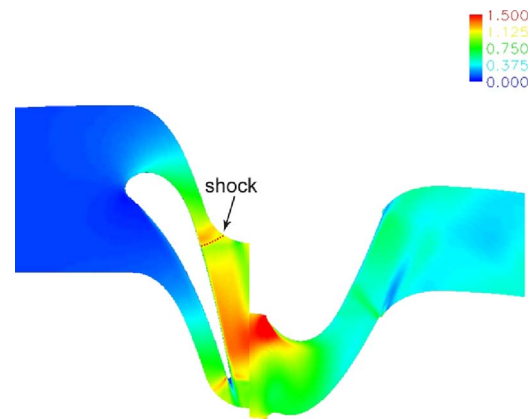


Fig. 7 Mach number contours at 50% span from unsteady results

traveling upstream and hitting the suction side of the vane in the uncovered portion are clearly seen. This phenomenon is not captured by the mixing plane results.

To compare how well individual codes and operation modes are performing, the deviations of the predictions from the data need to be plotted, as shown in Fig. 8 (more discussion about the quantification of comparisons will be done in Part II of this paper).

For Fig. 8, the open symbols are the differences in the time-

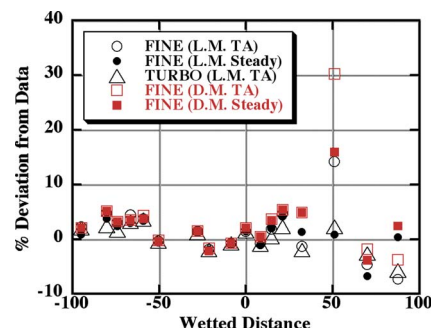


Fig. 8 Vane at 50% span, prediction data

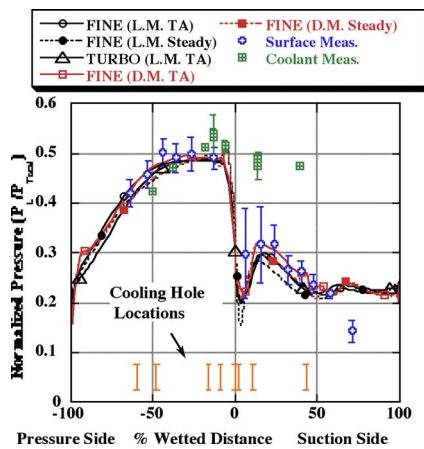


Fig. 9 Predicted static pressure loading, blade at 50% span

average of the time-accurate solution, and the closed symbols are the steady solutions. All of the black symbols represent lumped mass solutions, with the large triangles showing the TURBO solution. In this figure one can see that near the sonic line at 50% wetted distance, one sees the biggest variation among the predictions of the different codes. Examining the absolute deviations of the differences (all positive values), one can see that averaged over all locations, TURBO agrees with the data to about 2% with a maximum variation of about 6%. The FINE modes deviate from the data between about 2% and 3% on average (if the 50% point is removed), but the maximum variation changes from about 7.4% for the lumped mass time-average calculation down to about 5.4% for the distributed mass time steady and the distributed mass time average. The large improvement at the 50% location implies that the finer grid used by TURBO is required near these sonic locations. However, at least on the vane, there is relatively little improvement as one varies the modeling characteristics of the FINE code.

In Fig. 9 the steady and time-averaged predictions for the blade from FINE/TURBO and the time-averaged prediction from TURBO are shown and compared to the experimental data for the 50% span location. Again, the square symbol on this figure represents the measured internal blade pressure. Unlike the vane pressure loading, the FINE/TURBO steady and time-averaged predictions differ over nearly the entire surface of the blade and the inclusion of the distributed cooling flow has a significant effect as well. The steady predictions are below the data and the time-averaged predictions as would be expected because the unsteady effects are not being considered for this highly unsteady portion of the airfoil. When the time-averaged predictions are examined, they compare much better with the data than the steady prediction does, especially for the DM prediction on the pressure side of the airfoil (where a significant portion of the cooling flow is injected). Although the steady predictions do not have the correct magnitude, their trends do follow the data, but a designer would need to be careful in using this steady tool since it significantly underpredicts the experimental results. The TURBO prediction does a reasonable job of predicting the loading on the blade as well. It is very similar to the time-averaged prediction of FINE/TURBO with the most significant difference occurring from approximately 50% to 100% wetted distance on the pressure side. The exception to this is the data point at 71.2% wetted distance on the suction surface. This particular data point will be discussed in more detail later in this paper.

A similar plot to Fig. 8 can be made for the blade and is given in Fig. 10. Figure 10 illustrates that there are two areas where all the codes/methodologies are substantially different from the data: immediately at the leading edge and at the trailing edge of the suction surface. Outside of those areas the differences among the predictions of the various codes is interesting with the FINE results

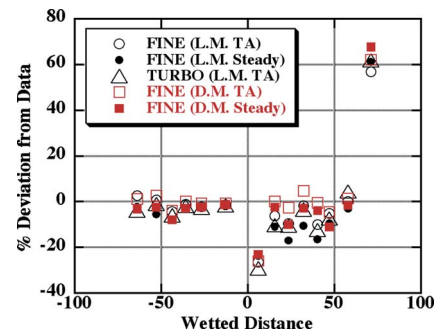


Fig. 10 Blade at 50% span differences, prediction data

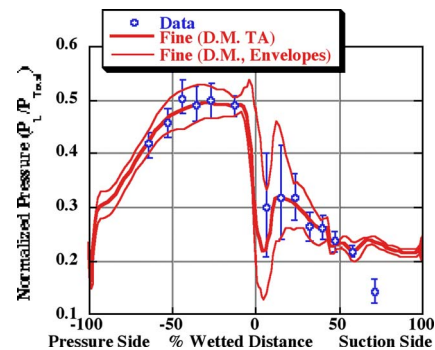


Fig. 11 Computational envelopes, blade at 50% span

varying from an average deviation of about 2% (distributed mass, time averaged) to 7.5% (lumped mass steady) while TURBO has an average variation of about 5.5%. The maximum deviations for this same data range from 5% to 18% for the FINE predictions and about 12% for TURBO.

In Fig. 11, the computational envelope from the FINE distributed mass prediction is shown as a function of wetted distance. The unsteadiness is high near the leading edge area on the suction surface and reduces toward the trailing edge on both the suction and pressure surfaces. Neither of the codes used herein do a particularly good job of predicting the rapid acceleration around the suction side of the airfoil in the vicinity of 0–6% wetted distance. However, the distributed mass methodology does a good job of capturing the time-averaged data and the envelope size for the remainder of the airfoil. A quantification of this comparison between the prediction and data along with that of the other methodologies will be discussed in significantly more detail in Part II of this paper. It can also be seen that the magnitude of the unsteady pressure envelope over a significant portion of the airfoil pressure surface remains relatively constant.

Comparing the results on the vane with the blade one can see that the improved grid resolution of TURBO is only required for the vane near the sonic line location, and that one can achieve very similar results at other locations with the lower fidelity models. On the blade, the real improvements come in the distributed mass time-average models, which do much better than the other models both in an average and in a maximum deviation case.

4.2 Time-Resolved Pressure Data and Frequency Content.

Figures 5 and 9 summarize the comparison between the prediction and data for the time-average values on the vane and blade airfoils, as a percentage of the recorded data. In this section the time-resolved data and predictions that make up the comparison presented in Fig. 9 are compared with the time-accurate predictions for many locations along the airfoil surface at the 50% span-wise location. The total inlet pressure to the vane is used to normalize the local pressure, and what is plotted is this variation from the average value (or the unsteady or periodic component).

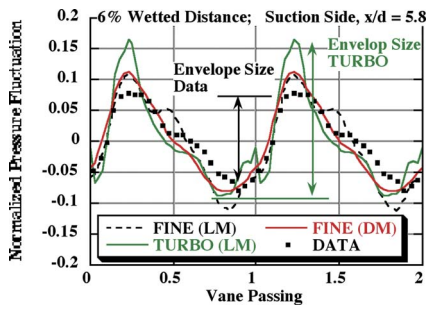


Fig. 12 Blade at 50% span time-resolved pressure data and prediction comparisons at 6% wetted distance

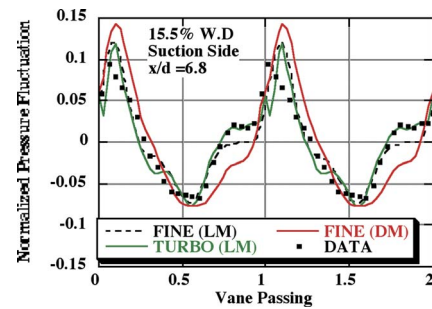


Fig. 14 Blade at 50% span time-resolved pressure data and prediction comparisons at 15.5% wetted distance

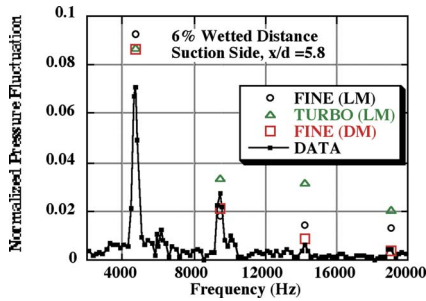


Fig. 13 Frequency content at 6% wetted distance

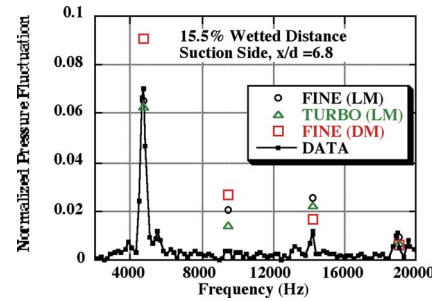


Fig. 15 Frequency content at 15.5% wetted distance

Changes in time-average values are not shown in these plots (for that information, refer to the time-average plots such as in Fig. 9). The plots show the fluctuation in the local pressure as the blades move past the individual vanes. Also included with each pressure plot is the corresponding FFT, which provides the energy content as a function of frequency. These figures are helpful in illustrating that locally the prediction may not be in agreement with the data, but when the prediction is time-averaged the resulting pressure is reasonably close to the measured value. An example of this is given in Fig. 25 for the blade at -35.9% wetted distance where the FFT agreement at the higher harmonics may not be as good as one would like, but the time-averaged data at this position (Fig. 10) are quite close. A more detailed discussion about the quantification of the comparisons will be given in Part II of this paper.

Starting at the leading edge on the suction side of the blade, Figs. 12 and 13 show the 6% wetted distance location normalized pressures. The location of the sensor relative to the immediate upstream cooling hole row is given in the figure as a function of hole diameter (x/d) and care has to be taken since this is real engine hardware and the hole diameters change with cooling row. The relative sizes of the envelopes (discussed more in Sec. 5) are also shown in Fig. 12 for the data and the TURBO prediction only. The DM and LM time-resolved surface pressure predictions from FINE/TURBO correspond very well with the data. Both CFD codes capture the correct trend, but there are some relatively minor local differences in the magnitude of the local pressure and TURBO overpredicts the peak magnitude by about 50%. FINE/TURBO overpredicts the magnitude of the fundamental frequency (slightly less than 5000 Hz) by about 20%, as illustrated in Fig. 13, but for this parameter such comparison is still considered to be good. The FFT of the CFD predictions captures the fundamental frequency location and the harmonic frequencies fairly well. As can be seen, the first harmonic at about 9000 Hz has a significant magnitude. Figure 12 illustrates that the peak magnitude of the pressure waveform is about 0.1, but the magnitude of the fundamental frequency is only about 0.07. This is because the harmonics add to the unsteadiness as well and if all of the magnitudes of the harmonics are summed up, the total magnitude of the FFT becomes much closer to the peak magnitude of the waveform. This shows why

the envelope size is often a better measure of the overall unsteadiness than any specific amplitude from a power spectrum plot.

In Figs. 14 and 15 the time-resolved predictions are compared to data a little farther along the suction side of the blade at 15.5% wetted distance. Once again the predictions capture the trend of the data nicely but still overpredict the peaks. This is again reflected in the FFT. The FFT of the predictions suggests that the first harmonic (at about 9000 Hz) is more significant than the data indicates. Both the data and the prediction show that the second harmonic is the strongest, but with the large overprediction of the first harmonic, the CFD shows that the models are not perfect, but for an initial prediction still do a good job with predicting trends.

At the next location, 23.5% wetted distance, the magnitude of the pressure fluctuation decreases from what it was at the leading edge of the blade as would have been anticipated from other similar studies, e.g., Green et al. [2]. Figs. 16 and 17 show that the CFD is consistent with this trend. The peak magnitude is not being overpredicted at the 23.5% location either. The fundamental and harmonic frequencies still line up with the data and overall the CFD predicts the behavior of the pressure on this portion of the blade.

At the 40.3% wetted distance, FINE/TURBO seems to do the best job as far as the predictions for the suction side are concerned. The trend and magnitude shown in Figs. 18 and 19 are remarkably close to the data. The FFT of the FINE/TURBO predictions is very close to having the same magnitude as the FFT of the data, and the location of the fundamental vane passing frequency and the predicted harmonic frequencies also line up with the measurement. TURBO overpredicts the peak magnitude and this is reflected in both the waveform and the frequency plots. It is important to note that this location on the airfoil is beyond the cooling holes.

At both the 23.5% and 40.3% wetted distance locations (Figs. 17 and 19), the FFTs show that the fundamental vane passing frequency and the first harmonic are of similar magnitude with the first harmonic being larger at some of these locations, indicating that the energy is almost completely split between the fundamental frequency and the first harmonic. This first harmonic is very influential on the way the pressure loading fluctuation looks in the vane passage plots. As this first harmonic grows in magnitude,

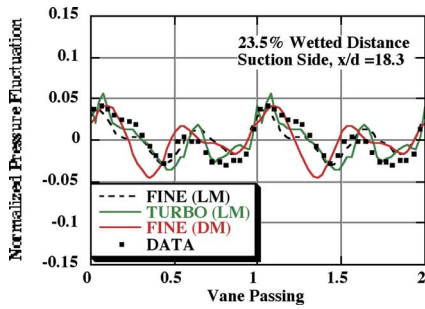


Fig. 16 Blade at 50% span time-resolved pressure data and prediction comparisons at 23.5% wetted distance

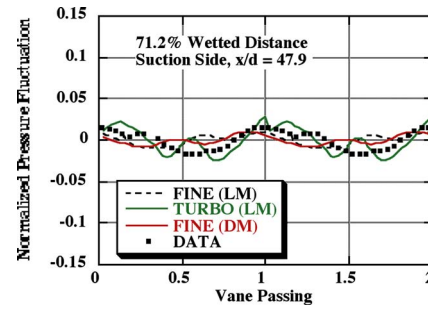


Fig. 20 Blade at 50% span time-resolved pressure data and prediction comparisons at 71.2% wetted distance

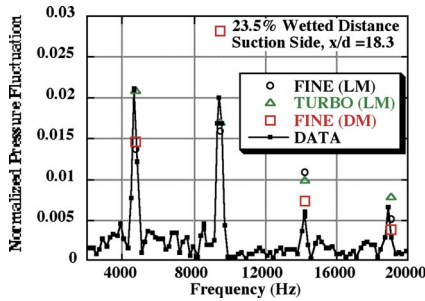


Fig. 17 Frequency content at 23.5% wetted distance

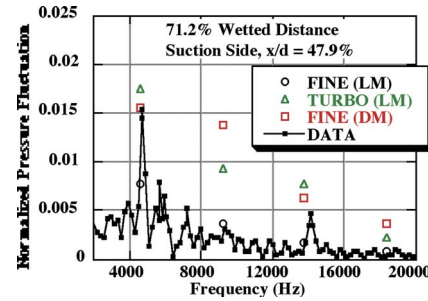


Fig. 21 Frequency content at 71.2% wetted distance

waveforms appear to gain a second peak rather than having one large peak. When the first harmonic amplitude is much smaller than the fundamental, as seen in Figs. 13 and 15, the waveform is more of a well-defined single peak. This is an important observation for a designer to make because the waveform plots show the overall integral effect of the harmonics. This gives the designer a way of deciding how much cooling margin is needed. Because the suction surface does not have cooling holes after about 30% wetted distance, the margin is not of great importance on this side.

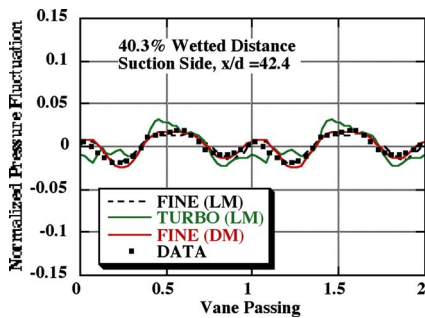


Fig. 18 Blade at 50% span time-resolved pressure data and prediction comparisons at 40.3% wetted distance

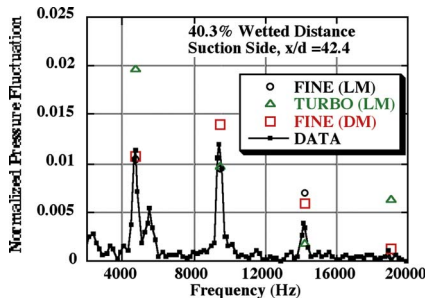


Fig. 19 Frequency content at 40.3% wetted distance

The pressure side has a large number of cooling holes, even past the 30% wetted distance, and therefore the idea of deciding how much cooling margin is needed becomes important. As will be seen on the pressure side, moving from the leading edge to the trailing edge the magnitudes decrease and this indicates that the designer can design for this lower margin toward the trailing edge of the blade, which is useful for higher overall engine efficiencies.

As noted above, the data point at 71.2% wetted distance on the suction surface of the airfoil does not agree with any of the predictions. The comparison of the predictions and the data for both the envelopes (Fig. 20) and the frequency (Fig. 21) show that the shapes begin to differ at these very low levels of pressure fluctuations that occur. It is important to realize that these levels are small. While one can see the difference in the shapes, it is harder to see the differences in the frequency content, with the exception of the FINE (LM) model, which underpredicts at all frequencies. The comparison in these figures as opposed to the time-average data shown in Figs. 9 and 10 suggests that the main difference is not in the unsteady predictions but rather in the time-average values. This might be due to either a bad exit condition (all models used the same conditions) or a bad data point.

Comparisons for the pressure side of the blade are given in the remainder of the figures in this section. Figures 22 and 23 start off near the leading edge of the blade at a wetted distance of -26.8%. The magnitude is significantly smaller than it was on the suction side of the blade near the leading edge. Since the plots are looking at pressure fluctuations, this appears to imply that the unsteady effects do not cause a lot of variation in the pressure on the pressure side. However, the pressure is obviously higher on this side of the blade, as seen in Fig. 9, so the fluctuation is much less noticeable. The small margin on the pressure surface causes the fluctuations in pressure to be hidden, and this is apparent in Fig. 9 by looking at the relatively constant range bars on the data along the pressure surface. The smaller magnitudes do not mean there are not as many mechanisms causing the flow to fluctuate. These magnitudes just indicate that one must be careful in analyzing the unsteady effects on the pressure surface because, as they are normalized, they are not as visible as they are on the suction surface.

For the wetted distance location of -26.8%, both codes under-

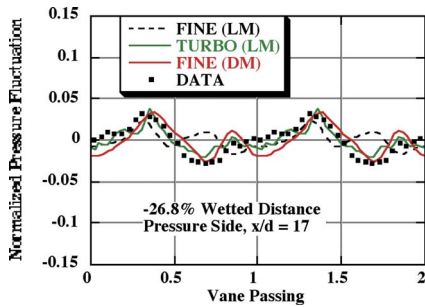


Fig. 22 Blade at 50% span time-resolved pressure data and prediction comparisons at -26.8% wetted distance

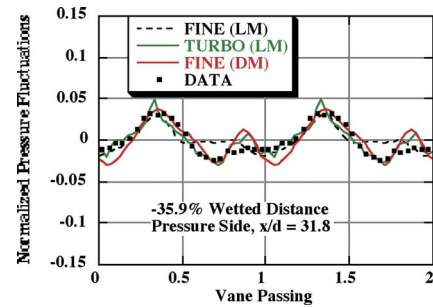


Fig. 24 Blade at 50% span time-resolved pressure data and prediction comparisons at -35.9% wetted distance

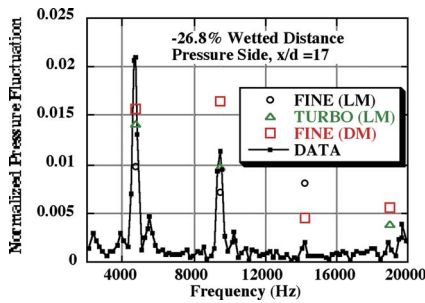


Fig. 23 Frequency content at -26.8% wetted distance

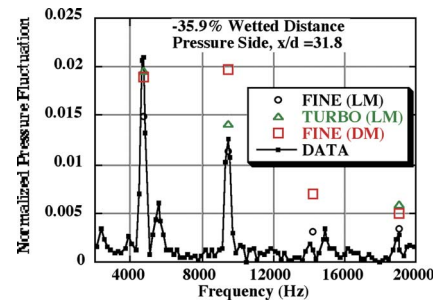


Fig. 25 Frequency content at -35.9% wetted distance

predict the magnitude for most of the vane passage, but the FINE/TURBO DM is the closest in predicting the peak magnitude. The FFT agrees with this and as seen, the predicted magnitude of the fundamental and first harmonic for TURBO and FINE/TURBO LM is lower than the data indicates. The prediction of the second harmonic shows significantly higher amplitude than the data. This helps explain the overprediction of the low peak on the waveform seen in the data. When the data is at its lowest on the waveform, the prediction has a positive peak instead of becoming a negative peak. Since the CFD shows a higher magnitude in the second harmonic, this affects the waveform and causes the positive peak to occur where the valley should be occurring.

As shown in Figs. 24 and 25, the -35.9% wetted distance shows good agreement between the waveforms and the FFTs of the prediction and data. The amplitude is slightly underpredicted by FINE/TURBO and slightly overpredicted by TURBO, but in general both codes come close to the data at this location.

For the wetted distance location of -43.8% , the CFD and data are in good agreement, as shown in Figs. 26 and 27. The shape of the waveform and the magnitude are both captured and the predicted fundamental and harmonic frequencies of the FFT are very similar to those of the data.

Although the -43.8% wetted distance location predictions are in good agreement with the data, the FINE/TURBO prediction seems to deviate the most from the data. This is most likely due to the proximity of this location to cooling holes on the pressure side. The closer to the cooling holes, the more likely it is that pressure fluctuations will be observed.

The last location on the pressure side of the blade is the -52.8% wetted distance and the waveforms and FFTs for this location are shown in Figs. 28 and 29. As was the case for the waveforms on the suction side of the blade, the CFD predicts the shape of the waveform on the pressure side well. In both cases the amplitude of the fundamental frequency is overpredicted. This is reflected in the overprediction of the amplitude on the waveform as well. It is also seen that the amplitude is a little higher at these locations than when it was closer to the leading edge of the blade. It is not a huge difference in amplitude, but it does show that there is slightly more unsteadiness near the trailing edge on the pressure

side than at the leading edge. This is not surprising since there are cooling slots all along the trailing edge of the blade that inject a significant amount of cooled gas relative to the hot flow path gas. When this gas is injected, the flow over the trailing edge of the blade is disturbed. The trailing edge cooling slots have significantly larger injection areas than the individual cooling holes near the leading edge locations and it is likely that this is reflected in the measurement.

In general the time-resolved predictions show a good correla-

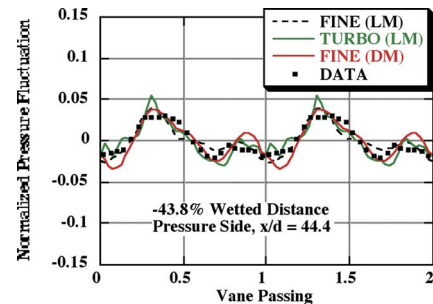


Fig. 26 Blade at 50% span time-resolved pressure data and prediction comparisons at -43.8% wetted distance

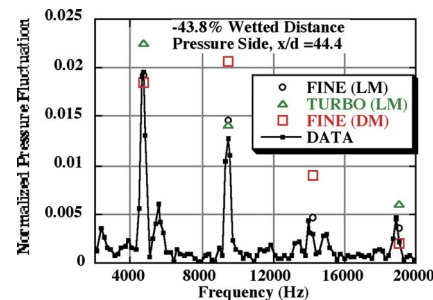


Fig. 27 Frequency content at -43.8% wetted distance

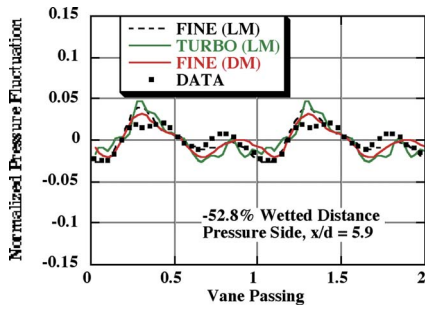


Fig. 28 Blade at 50% span time-resolved pressure data and prediction comparisons at -52.8% wetted distance

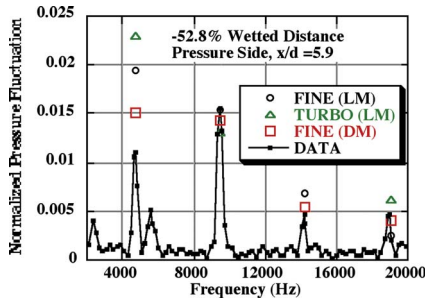


Fig. 29 Frequency content at -52.8% wetted distance

tion with the data, especially for a true prediction without any grid refinement or turbulence model optimization. The unsteady CFD that was performed using a lumped mass for the cooling flow injection appeared to be capable of capturing many of the unsteady behaviors at most locations on the blade and adding distributed cooling addition sites appeared to improve the correlation in some locations, but not always. This analysis gives a great deal of confidence to a designer that given the operating conditions, the aerodynamic behavior within the turbine stage can be predicted fairly well. It is also important to note that even though the grid used in FINE/TURBO was half as dense as that used in TURBO, the predictions from FINE/TURBO were of the same quality as those from TURBO. This is not a reflection of the capability of the individual codes, but rather that the lower grid resolution is adequate for most locations.

4.3 Pressure Predictions for the Shroud. In this section, the steady, time-accurate, and time-averaged pressure results are presented for the stationary shroud. Those performing the predictions were given the measured blade tip/shroud clearance at the running condition. There were six pressure transducers located on the shroud at different axial positions defined as a percentage of the axial blade chord, where 0% is at the blade leading edge and 100% is at the blade trailing edge. The time-resolved results show the pressure fluctuations as the individual moving blades approach and retreat from the pressure transducer.

Figure 30 shows the normalized pressure for the steady and time-averaged CFD predictions for the stationary shroud as compared to the measurements. The vane inlet total pressure is used to normalize the local static pressure measurement. The range bars appearing at each measurement location represent the envelope size due to the unsteady effects. The processing of the steady state prediction deserves a note of explanation. Since the steady case would not be able to pick up multiple readings due to the lack of time dependence, an average over the entire shroud at a particular axial blade chord location was taken. By taking an average for the steady case, a better sense of the predictive capability is obtained for a steady model. If a pressure reading were taken at just one grid point at the given axial location, then that reading does not

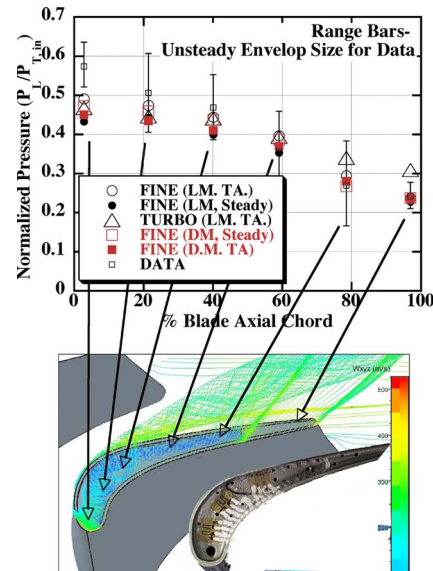


Fig. 30 Time averaged and steady uncooled static pressure loading predictions on the shroud with the stream-tube analysis and picture of blade tip

reflect the true simulation because the shroud pressure fluctuates a great deal over the span of the blade passage, especially when the blade is directly below the specific location of interest.

Figure 30 illustrates the streamline locations in the tip/shroud region calculated using FINE/TURBO, which helps to explain the large fluctuation in the shroud pressure occurring very near the end of the recessed tip region cooling cavity (80% axial chord). The location of the end of the recess is near the location of the pressure transducer in the adjoining stationary shroud as shown in the figure. For added comparison, a photo of the blade tip, scaled to the approximate dimensions of the streamline plot, also helps show that the first instrument location (at about 2% axial chord) is almost directly over the dirt purge hole on the blade tip. Heat-flux sensors installed in the tip cavity are also shown in this photo.

As done in the previous section, the differences between the predictions and the measurements can be illustrated, as in Fig. 31.

The time-averaged and steady predictions differ the most from the data and from each other near the leading edge at the 2.8% axial blade chord location. This region is a rather complicated flow field region, being immediately downstream of the vane outer wall exit and near the leading edge of the blade. Previous detailed studies of Green et al. [2] and Molter et al. [16] illustrate that as the flow goes over the tip of the blade and into the tip cavity, there are significant velocity and pressure fluctuations in this particular region. It is interesting to note that the different modes of code operation tend to group, with the exception of the

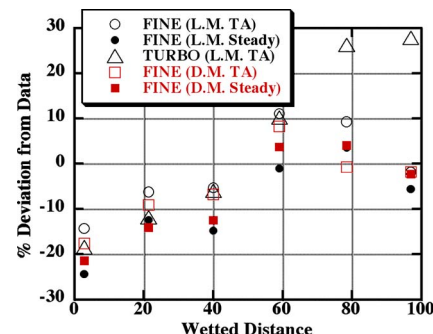


Fig. 31 Blade/shroud predictions and data differences

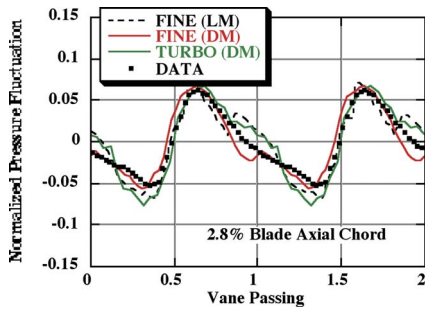


Fig. 32 Unsteady static pressure fluctuation on the shroud (2.8% axial blade chord)

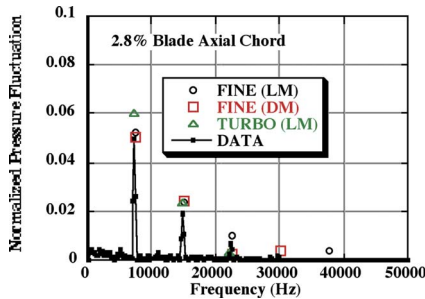


Fig. 33 Shroud frequency content at 2.8% axial blade chord

trailing edge where TURBO is much different. As with the blade, predictions obtained using the time-average modes are closer to the data than those obtained with the steady mode, but that in general, the shroud comparisons are not as good as the blade with averages for the FINE code being between 7.5% and 10.5%, and TURBO being about 17%. The maximum deviations are larger (14–25%). Once again the FINE distributed mass time-averaged mode being in best agreement with the data, most likely the result of the more complete model was used in FINE for this calculation.

Another area of interest is the 78.5% axial blade chord location. The data shows a very large pressure envelope for this location. The envelope size here is about 20% of the vane inlet total pressure, and the time-averaged value is only about 27% of the pressure. Therefore, a variation of almost 100% of the time-averaged value occurs at this location. This is explained by the flow through the tip region. It is at this approximate location that the tip cavity ends. When the cavity steps up at this point, the flow through the tip is forced out of the cavity and this creates a large envelope of velocities and pressures, which is what is reflected in the data at this location, as illustrated by the computational results shown in Fig. 30.

In general, the time-averaged predictions are closer to the data than the steady prediction for both the DM and LM cases. Both FINE/TURBO and TURBO pick up the general trend of the data but FINE/TURBO seems to do a better job with the shroud predictions, especially near the trailing edge of the blade. Both the steady and time-averaged methods predict well the pressure behavior along the shroud, but as was seen on the blade surface, the time-averaged solution provided the best result for a designer.

The figures presented in the remainder of this section are included to document the results that were used to obtain the time-averaged comparison presented in Fig. 30. Figure 32 shows the time-resolved pressure waveform on the shroud at the 2.8% blade axial chord location as compared to the unsteady CFD predictions. The predicted waveforms at this location compare well with the data. The magnitude of the peaks is captured and the overall shape of the predicted waveform is very similar to that of the data. The fact that the magnitude was captured by the CFD is also apparent in the FFT results shown in Fig. 33. The FFT of the CFD picks up

not only the magnitude of the fundamental blade passing frequency at about 7500 Hz, but it captures the magnitude of the harmonics as well.

Figure 34 shows the time-resolved pressure at the 21.4% axial blade chord location. At this location, both codes underpredict the peak magnitude seen in the data, but also overpredict the valley magnitude. Despite the miss on predicting the correct magnitudes, the general shape of the waveform is consistent between the CFD and the data. The frequency domain results shown in Fig. 35 illustrate that the magnitude is underpredicted at the fundamental blade passing frequency, but not by as much as the underprediction seen on the waveform. However, the third and fourth harmonics are also significantly underpredicted, and the combination of the underpredictions at the fundamental and harmonic frequencies is what combines to create the overall underprediction of the waveform.

Figures 36 and 37 show the waveforms and frequency content near midchord at 59.1% blade axial chord. For this location, the CFD captures the shape of the waveform fairly well and reasonably predicts the magnitude. TURBO captures the peak magnitude at 59.1% wetted distance, but has a slightly different shape. The FFT plot reflects this and shows that the magnitudes at the fundamental and the harmonic frequencies are again captured by the CFD.

As mentioned earlier, the data obtained at the 78.5% axial chord location shows a great deal of unsteadiness. The CFD does not have any difficulties in picking up the unsteadiness at this location, as shown in Figs. 38 and 39, although the DM results from FINE/TURBO show a lower magnitude than the data shows but the shape of the waveform correlates fairly well to that of the data. The waveforms of the CFD and data overlap for the most part with more fluctuations occurring in the CFD. The predictions capture the peak pressure at this highly unsteady location on the shroud. The frequency domain comparison presented in Fig. 39 illustrates that the prediction also agrees quite well with the data. The only discrepancies for the LM predictions occur at the second and third harmonics where the CFD picks up a larger magnitude than the data shows. The addition of these components to the

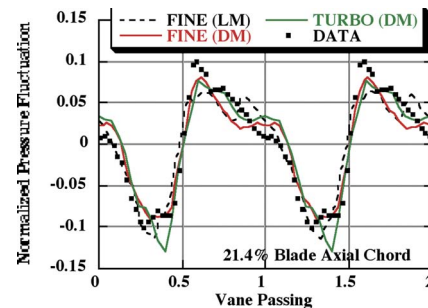


Fig. 34 Unsteady static pressure fluctuation on the shroud (21.4% axial blade chord)

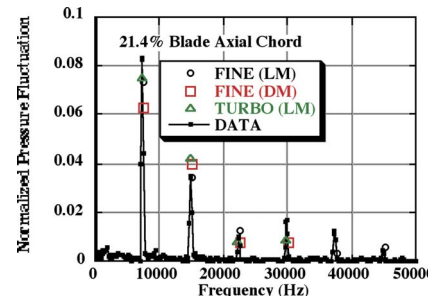


Fig. 35 Shroud frequency content at 21.4% axial blade chord

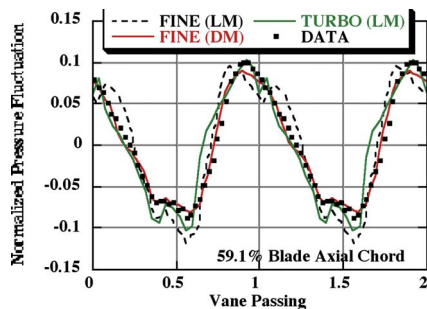


Fig. 36 Unsteady static pressure fluctuation on the shroud (59.1% axial blade chord)

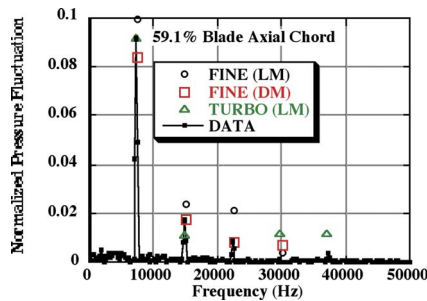


Fig. 37 Shroud frequency content at 59.1% axial blade chord

fundamental behavior is what likely causes some of the extra fluctuation, or unsteadiness, to appear on the waveform.

The shroud region is a good test of the CFD code capability since this region does not represent a simple flow field situation with the flow going over the blade tip and creating vortical structures both in the recessed tip and on the suction side of the blade. Considering that the comparisons of CFD to data just shown were true predictions (as opposed to postpredictions) without any grid refinement or changes made to the computational model after looking at the comparison between prediction and data, the CFD

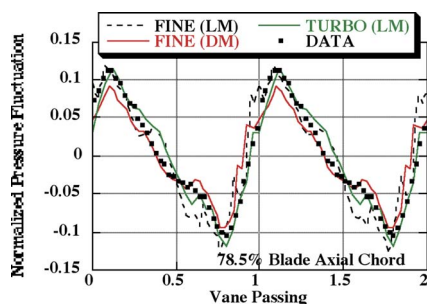


Fig. 38 Unsteady static pressure fluctuation on the shroud (78.5% axial blade chord)

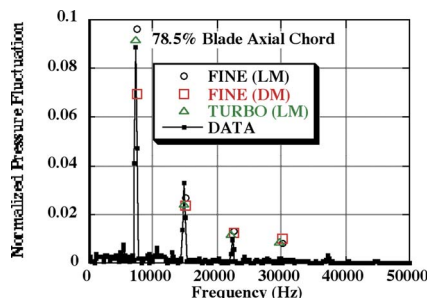


Fig. 39 Shroud frequency content at 78.5% axial blade chord

performed well at nearly all of the axial locations. The leading edge and trailing edge were the areas where the most significant discrepancies were seen, but even at these locations, the results suggest that a designer could have confidence in these predictive tools. The biggest surprise was how good of a job the CFD did in predicting the 78.5% behavior considering that for this blade tip configuration this particular area is likely to be highly unsteady. Overall, the CFD shows that it is capable of making reasonable predictions at any location on the shroud.

5 Summary and Conclusions

The fully cooled data for a rotating full-stage Honeywell high-pressure turbine stage operating at design corrected conditions have been presented and compared to predictions. Both steady and time-accurate computations were performed using FINE/TURBO with distributed mass and lumped mass cooling models. The predictions using TURBO were also time accurate, but only used the lumped mass injection system. Both codes utilized phase-lagged boundary conditions, which have reduced the solution area down to only one passage for both the vane and blade. Predictions were compared to the data on the vane and blade at midspan and at the rotor shroud, since these three areas provide locations where the flow physics differ greatly, and thus they represent a good basis for comparison. The data and predictions were evaluated as time-averaged values, time-resolved data (in terms of blade passing shapes), and in the frequency domain (as harmonic analysis). Part II of this paper examines the overall quality of the comparisons and provides a methodology for creating an overall quantitative number for each prediction method.

Overall, the fact that the two codes and the multiple methodologies agree so well is very encouraging. While the methodologies are different, the solution accuracy is very comparable. A full comparison of which code is better is beyond the scope of this paper, and is really not a useful question, as so many design specific questions go into that evaluation, such as how easy is the system to grid, postprocess, and the type of data the solution produces change from task to task. However, by doing these types of comparisons between codes and their operating mode, one can begin to find places where small local improvements in grid resolution, or changes in grid densities, can improve the overall quality without sacrificing the overall performance. These are the types of trade-offs that are needed as full 3D unsteady predictions are pushed from the research world into the design world.

Acknowledgment

The NASA/DoD URETI for Aeropropulsion and Power at The Ohio State University and NASA Contract No. NCC3-1086 supported the research reported here. The NASA technical monitor for this work is Ms. Kim Pham. The authors would like to acknowledge Costas Vogiatzis of Honeywell Engines for providing the grid used in the FINE/TURBO calculations, as well as Bill Troha, Malak Malak, and Ron Rich of Honeywell Engines for their support during the course of this work. The authors would also like to acknowledge the dedicated staff of the OSU GTL for their effort in preparing the instrumented turbine stage and for helping in completion of the measurements.

References

- [1] Aube, M., and Hirsch, C., 2001 "Numerical Investigation of a 1-1/2 Axial Turbine Stage at Quasi-Steady and Fully Unsteady Conditions," ASME Paper GT 2001-0309.
- [2] Green, B. R., Barter, J. W., Haldeman, C. W., and Dunn, M. G., 2005, "Time-Averaged and Time-Accurate Aero-Dynamics for the Recessed Tip Cavity of a High-Pressure Turbine Blade and the Outer Stationary Shroud: Comparison of Computational and Experimental Results," ASME J. Turbomach., **127**, pp. 736–746.
- [3] Barter, J. W., Vitt, P. H., and Chen, J. P., 2000, "Interaction Effects in a Transonic Turbine Stage," ASME Paper No. 2000-GT-0376.
- [4] Haldeman, C. M., Mathison, R. M., Dunn, M. G., Southworth, S., Harral, J. W., and Heitland, G., 2008, "Aerodynamic and Heat Flux Measurements in a Single Stage Fully Cooled Turbine—Part I: Experimental Approach," ASME

- J. Turbomach., **130**(2), p. 021015.
- [5] Haldeman, C. W., Mathison, R. M., Dunn, M. G., Southworth, S., Harral, J. W., and Heitland, G., 2006, "Aerodynamic and Heat Flux Measurements in a Single Stage Fully Cooled Turbine—Part II: Experimental Results," *ASME J. Turbomach.*, **130**(2), p. 021016.
- [6] Garg, V. J., 1999, "Heat Transfer on a Film-Cooled Rotating Blade," *ASME Paper No. 99-GT-44*.
- [7] Dunn, M. G., 2001, "Convective Heat Transfer and Aerodynamics in Axial Flow Turbines," *ASME J. Turbomach.*, **123**, pp. 637–686.
- [8] Giles, M. B., 1988, "UNSFLO: A Numerical Method for Unsteady Inviscid Flow in Turbomachinery," MIT Gas Turbine Laboratory Report No. 195.
- [9] Giles, M. B., 1988, "Calculation of Unsteady Wake Rotor Interaction," *AIAA J.*, **4**(4), pp. 356–362.
- [10] Guenette, G. R., Epstein, A. H., Giles, M. B., Haimes, R., and Norton, R. J. G., 1988, "Fully Scaled Transonic Turbine Rotor Heat Transfer Measurements," Paper No. 88-GT-171.
- [11] Abhari, R. S., and Giles, M. B., 1997, "A Navier–Stokes Analysis of Airfoils in Oscillating Transonic Cascades for the Prediction of Aerodynamic Damping," *AIAA J.*, **119**, pp. 77–81.
- [12] Rao, K. V., Delaney, R. A., and Dunn, M. G., 1994, "Vane-Blade Interaction in a Transonic Turbine: Part II—Heat Transfer," *AIAA J.*, **10**(3), pp. 312–317.
- [13] Rao, K. V., Delaney, R. A., and Dunn, M. G., 1994, "Vane-Blade Interaction in a Transonic Turbine: Part I—Aerodynamics," *AIAA J.*, **10**(3), pp. 305–311.
- [14] Dunn, M. G., Bennett, W. A., Delaney, R. A., and Rao, K. V., 1992, "Investigation of Unsteady Flow Through a Transonic Turbine Stage: Data/Prediction Comparison for Time-Averaged and Phase-Resolved Pressure Data," *ASME J. Turbomach.*, **114**, pp. 91–99.
- [15] Abhari, R. S., 1996, "Impact of Rotor-Stator Interaction on Turbine Blade Film Cooling," *ASME J. Turbomach.*, **118**, pp. 123–133.
- [16] Molter, S. M., Dunn, M. G., Haldeman, C. W., Bergholz, R. F., and Vitt, P., 2006, "Heat-Flux Measurements and Predictions for the Blade Tip Region of a High-Pressure Turbine," *ASME Turbo Expo, Barcelona, Spain, May 8–11*.
- [17] Busby, J. A., Davis, R. L., Dorney, D. J., Dunn, M. G., Haldeman, C. W., Abhari, R. S., Venable, B. L., and Delaney, R. A., 1999, "Influence of Vane-Blade Spacing on Transonic Turbine Stage Aerodynamics. Part II: Time-Resolved Data and Analysis," *ASME J. Turbomach.*, **121**, pp. 673–682.
- [18] Venable, B. L., Delaney, R. A., Busby, J. A., Davis, R. L., Dorney, D. J., Dunn, M. G., Haldeman, C. W., and Abhari, R. S., 1999, "Influence of Vane-Blade Spacing on Transonic Turbine Stage Aerodynamics. Part I: Time-Averaged Data and Analysis," *ASME J. Turbomach.*, **121**, pp. 663–672.
- [19] Hoyningen-Huene, M. V., and Jung, A. R., 2000, "Comparison of Different Acceleration Techniques and Methods for Periodic Boundary Treatment in Unsteady Turbine Stage Flow Simulation," *ASME J. Turbomach.*, **122**, pp. 234–246.
- [20] Mildner, F., and Gallus, H. E., 1998, "An Analysis Method for Multistage Transonic Turbines With Coolant Mass Flow Addition," *ASME J. Turbomach.*, **120**, pp. 744–752.
- [21] Denos, R., Fidalgo, V. J., and Adami, P., 2006, "Transport of Unsteadiness Across the Rotor of a Transonic Turbine Stage," *ASME Paper No. GT2006-9046*.
- [22] Denos, R., Paniagua, G., Yasa, T., and Fortugno, E., 2006, "Determination of the Efficiency of a Cooled HP Turbine in a Compression Tube Facility," *ASME Paper No. GT2006-90460*.
- [23] Keogh, R. C., Guenette, G. R., and Sommer, T. P., 2000, "Aerodynamic Performance Measurements of a Fully-Scaled Turbine in a Short Duration Facility," *ASME Paper No. 2000-GT-486*.
- [24] Keogh, R. C., Guenette, G. R., Spadaccini, C. M., Sommer, T. P., and Florjancic, S., 2002, "Aerodynamic Performance Measurements of a Film-Cooled Turbine Stage—Experimental Results," *ASME Paper No. GT-2002-30344*.
- [25] Leylek, J. H., and Zerkel, R. D., 1994, "Discrete-Jet Film Cooling: A Comparison of Computational Results With Experiments," *ASME J. Turbomach.*, **116**, pp. 358–386.
- [26] Bernsdorf, S., Rose, M. G., and Abhari, R. S., 2005, "Modeling of Film Cooling—Part I: Experimental Study of Flow Structure," *ASME Paper No. GT2005-68783*.
- [27] Burdet, A., Abhari, R. S., and Rose, M. G., 2005, "Modeling of Film Cooling—Part II: Model for Use in 3D CFD," *ASME Paper No. GT2005-68780*.
- [28] Hildebrandt, T., Ganzert, W., and Fottner, L., 2000, "Systematic Experimental and Numerical Investigation on the Aerothermodynamics of a Film Cooled Turbine Cascade With Variation of the Cooling Hole Shape," *ASME Paper No. GT2000-0298*.
- [29] Vilmin, S., Lorrain, E., Hirsch, C., and Swoboda, M., 2006, "Unsteady Flow Modeling Across the Rotor/Stator Interface Using the Nonlinear Harmonic Method," *ASME Paper No. GT-2006-90210*.
- [30] Hildebrandt, T., and Ettrich, J., 2003, "Unsteady 3D Navier–Stokes Calculation of a Film-Cooled Turbine Stage With Discrete Cooling Holes," *ISUAAT 2003, Durham, NC, Sept. 8–11*.
- [31] Haldeman, C. W., Mathison, R. M., Dunn, M. G., Southworth, S., Harral, J. W., and Heitland, G., 2006, "Aerodynamic and Heat Flux Measurements in a Single Stage Fully Cooled Turbine—Part I: Experimental Approach," *ASME Turbo Expo, Barcelona, Spain, May 8–11*.
- [32] Haldeman, C. W., 2003, "An Experimental Investigation of Clocking Effects on Turbine Aerodynamics Using a Modern 3-D One and One-Half Stage High Pressure Turbine for Code Verification and Flow Model Development," MS thesis, Ohio State University, Columbus, OH.
- [33] Chen, J. P., Grosh, A. R., Sreenivas, K., and Whitfield, D. L., 1997, "Comparison of Computations Using Navier–Stokes Equations in Rotating and Fixed Coordinates for Flow Through Turbomachinery," Paper No. AIAA-97-0878.
- [34] Whitfield, D. L., Janus, J. M., and Simpson, L. B., 1988, "Implicit Finite Volume High Resolution Wave-Split Scheme for Solving the Unsteady Three Dimensional Euler and Navier–Stokes Equations on Stationary or Dynamic Grids," Paper No. MSSU-EIRS-ASE-88-2.
- [35] Shih, T. H., Liou, W. W., Shabbir, A., Yang, Z., and Zhu, J., 1995, "A New k-ε Eddy Viscosity Model for High Reynolds Number Turbulent Flows," *Comput. Fluids*, **24**, pp. 227–237.
- [36] Chen, J. P., Celestina, M. L., and Adamczyk, J. J., 1994, "A New Procedure for Simulating Unsteady Flows Through Turbomachinery Blade Passages," *ASME Paper No. 94-GT-151*.
- [37] Zante, D. E. V., Chen, J. P., Hathaway, M. D., and Chris, R., 2005, "The Influence of Compressor Blade Row Interaction Modeling on Performance Estimates From Time-Accurate, Multi-Stage, Navier–Stokes Simulations," *ASME Turbo Expo 2005: Power for Land, Sea and Air, Reno-Tahoe, NV, June 6–9*.
- [38] Chen, J. P., and Barter, J. W., 1998, "Comparison of Time-Accurate Calculations for the Unsteady Interaction in a Turbomachinery Stage," *AIAA Paper No. 98-3292*.

Time-Accurate Predictions for a Fully Cooled High-Pressure Turbine Stage—Part II: Methodology for Quantifications of Prediction Quality

C. W. Haldeman

M. G. Dunn

S. A. Southworth

J.-P. Chen

The Ohio State University,
Columbus, OH 43210

G. Heitland

J. Liu

Honeywell Aerospace,
Phoenix AZ 85072

The aerodynamics of a fully cooled, axial, single stage high-pressure turbine operating at design corrected conditions of corrected speed, flow function, and stage pressure ratio has been investigated experimentally and computationally and presented in Part I of this paper. In that portion of the paper, flow-field predictions obtained using the computational fluid dynamics codes Numeca's FINETURBO and the code TURBO were obtained using different design methodologies that approximated the fully-cooled turbine stage in different ways. These predictions were compared to measurements obtained using the Ohio State University Gas Turbine Laboratory Turbine Test Facility, in a process that was essentially a design methodology validation study, instead of a computational methodology optimization study. The difference between the two is that the designers were given one chance to use their codes (as a designer would normally do) instead of using the existing data to fine-tune their grids/methodologies by doing grid studies and changes in the turbulence models employed. Part I of this paper showed differing results from the two solvers, which appeared to be mainly dependent on the differences in grid resolution and/or modeling features selected by the code users. Examining these occurrences points to places where the design methodology could be improved, but it became clear that metrics were needed to compare overall performance of each approach. In this part of the paper, three criteria are proposed for measuring overall prediction quality of the unsteady predictions, which include the unsteady envelope size, envelope shape, and power spectrum. These measures capture the main characteristics of the unsteady data and allow designers to use the criteria of most interest to them. In addition, these can be used to track how well predictions improve over time as grid resolutions and modeling techniques change. [DOI: 10.1115/1.2985076]

Introduction

In the not too distant past, time-resolved predictions and measurements from a high-pressure turbine stage operating at the proper corrected conditions were considered to be “in good agreement” if they could be plotted on the same scale on the plot. This of course has not kept many firms from using computational design tools for the design of today's turbomachinery. Many times, these codes were built up internally within the firm integrating much of the local historical empirical database and were only used within a relatively narrow design envelope. As commercial codes became more available, information that validated the code, no matter how simple the experiment, was highly sought after. As discussed by Dunn [1] and in Part I of this paper, the historical progression of predictions has shown that full time-resolution of the flow-field is more complicated to obtain but critical to proper designs than simple steady-state solutions. In addition, heat-transfer predictions are more difficult to obtain than pressure predictions.

As codes have progressed for predicting heat-transfer and aerodynamics, two separate trends have become apparent. The first is the shift to full 3D time-accurate codes. Early successes in the 1980s and 1990s used time-accurate 2D codes such as Delaney's VBI code [2–4] and Giles' UNSFLO-2D [5,6] to predict both the time-resolved pressure and heat-transfer on the turbine stage at the

midspan location throughout the stage. With these successes, computational fluid dynamics (CFD) codes were developed, which handled the 3D nature of turbomachinery, examining in addition to the flow over the airfoils the completely different flow patterns seen near the hub or in the tip region. However, these came at the expense of significantly increased computational requirements. While some researchers [7] have been successful in running multiple blade rows in a full 3D unsteady environment, this was accomplished by running clusters of computers (sometimes numbering in the thousands) for extremely long periods of time (months) to obtain solutions. This of course did not account for the post processing time. This has set up a line of research, which has looked at ways of achieving similar results to these “full-models” but with much less computational time.

The second trend is using any available codes to predict experimental results (instead of tuning the code using the experimental data) and to provide more realistic experiments with more complicated data sets. The data sets presented for a counter-rotating turbine [8,9] and for the full-stage cooling experiments [10,11] are examples of these more complicated turbine experiments.

As researchers have shown the capability of providing time-accurate predictions for complicated turbine geometries or operating conditions, the more recent efforts have focused on transforming this capability into design practices. This has primarily focused on methods for reducing the calculation time, including simplifying the computational models (examples are the lumped-mass method and distributed mass methods of modeling the cooling flow discussed in Part I of this paper). However, it also in-

Manuscript received April 25, 2007; final manuscript received February 15, 2008; published online April 7, 2009. Review conducted by David Wisler.

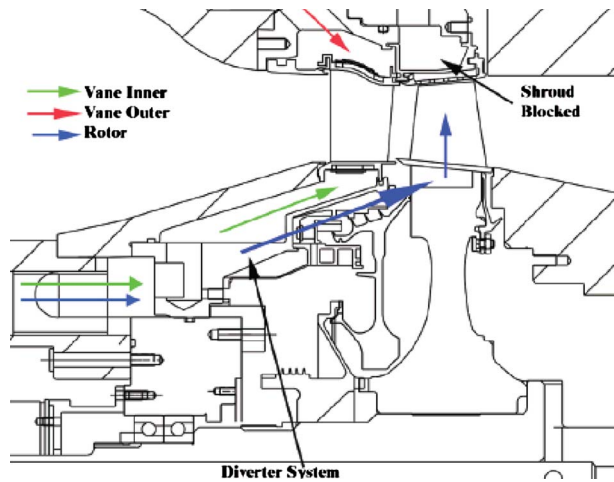


Fig. 1 Turbine cooling paths

cludes the development of other physics based models for incorporation into the overall computational system such as the work of Praisner and Clark [12] relating to separation transition. Also included is the development of computational tools such as phase-lagged boundary conditions to model just one blade passage in each blade row.

However, one area that has not been addressed to date is how much each of these design tools/improvements helps improve the overall quality of the predictions. When researchers discuss the quality of their predictions, they often focus on one area (such as a vane or blade) and use terms such as the “agreement is good,” or “the trend of the prediction and the data are similar.” The authors of this paper have used similar words in the past. At this time however, a more quantitative measure of agreement is needed to objectively measure the quality of the predictions. In this regard, it is important that the prediction is a “true prediction” as is the case in this paper and not an attempt to correlate the data.

A review of the literature in this area has not shown any previous methodology that has been used to accomplish this task with respect to the unsteady predictions in gas turbines, which is the focus of Part II of this paper using the data and predictions from Part I as the inputs to the analysis. However, there has been some work defining the problems of fully verifying and validating CFD codes specifically from the standpoint of knowing that the codes are operational. These tasks have been defined by the AIAA as “validation and verification” and there are two groups of work that have focused on this [13–19]. While the criteria for a reasonable metric in these references are similar to what is proposed in this paper, the goal is not the same. In our case, the goal is to quantify the deviations between the prediction and experimental data, regardless of the source of the discrepancy whether it be code based, inappropriate boundary conditions, or overall simplification, as opposed to the approach advocated by these papers, which is a full validation of the code. Thus this part of the paper is split into two main sections: the first describes the development of the quantification technique, and the second part uses the data from Part I of the paper to evaluate how the different codes have performed. As a reference, the sketch of the experimental rig (Fig. 1) is reproduced from Part I of this paper and readers are referred to that part for more details about the computational methods used and for the details of the experiments.

1 Quantification of Comparison Quality

1.1 Analytical Framework. As shown in Part I, it is often difficult to judge “how good” the predictions are when simply looking at the data and the predictions. Given the improving quality of predictions, it is important to develop some type of quanti-

fiable measure of the prediction accuracy. This is important for two main reasons. First, one needs a way to measure how good a code is doing over all stage locations of interest. As one looks back on the figures of the previous section, there are places where the TURBO predictions appear to be better to the reader, or on the other hand at a different location the FINE (DM) predictions appear to be better. There are still other locations where perhaps the FINE (DM) envelope looks best, but the fundamental frequencies are matched better by TURBO. Secondly, a quantifiable measure of quality is needed because the intent is to take what has been learned from this work and apply it to future work, and a method is needed to determine how much better the predictions have become that is based upon more than appearance. A very good example is given by the vane data presented in Figs. 4 and 5 of Part I where it is clear that higher grid resolution is required at the sonic line (50% wetted distance). The TURBO code runs with a much higher grid resolution in this area than the FINE/TURBO code. The next logical step would be to change the grid in this one area to see if the predictions improve for the FINE/TURBO code. We therefore desire a criterion to quantify how much better this next prediction would be.

The problem of developing workable criteria for comparing predictions and data or just data in a time-accurate frame was discussed in some detail by Haldeman [20], where it was pointed out that the problem reduces to the fact that there are a great many surrogate measures of the time-accurate data. Unlike time-average data, where there is only one measure (the time-average value), time-accurate data can have several different measures. In this paper, the envelopes and the power spectrums are examples of the time-accurate data. However as pointed out in Ref. [20], there are many times where the envelope size (a single number) is better than the power spectrum fundamental amplitude (also a single number) at representing the unsteadiness. However, that conclusion often depends on the information being sought. For those interested only in forcing function issues (such as for high-cycle fatigue) clearly the power spectrum at defined frequencies is of primary interest.

Requirements for the Metric. Several different methodologies were examined. In the evaluation procedure, it became clear that whatever system was adopted had to accomplish several goals.

- (1) It had to be able to produce a single number for the entire model. This is critical since one needs a measure that says Technique X produces an overall prediction quality of Y and thus is better on average than a previous attempt.
- (2) It has to also be able to produce the same type of measure locally.
- (3) The methodology should be able to be applied to various types of measurements.

Any methodology that meets these requirements should be suitable. It is important to realize that Parts I and II are intrinsically connected. The idea is that one can generate comparisons of predictions and data for each instrument location (such as Fig. 5, Part I) and then be able to integrate these positions together to achieve one number. Thus the problem reduces to one of defining the difference between the predictions and the data locally, at each instrument location, and then deciding on a technique to integrate them over the entire rig. This step needs to be fairly independent of measurement resolution, so that occasions where there is much higher or lower measurement resolution do not significantly affect the aggregate number assuming that there is sufficient measurement resolution to capture the flow physics of interest.

Two different methods have been proposed to calculate the difference between the predictions and the data, the difference between them being in how the data are normalized. One method relates the differences to a reference value such as the total inlet conditions, and the second method normalizes by the individual measurement. The methods can be generalized by using the term

(P) for prediction and (D) for data, and these can represent any quantity (e.g., pressure, temperature, heat-flux, Stanton number, etc.), however this paper will concentrate on surface pressures.

Method 1—Relative to a Reference Value (IP). In this case the absolute values of the differences between the predictions and the data at any location (i) will form a calculation that is a percentage of some reference value. For most of the measurements in this paper, this is the total inlet pressure (unless otherwise noted), where P_L is the local pressure, and the “ $\hat{\cdot}$ ” represents a prediction.

$$(|\hat{P} - D|)_i \Rightarrow \left(\left| \frac{\hat{P}_L}{P_{\text{total,inlet}}} - \frac{P_L}{P_{\text{total,inlet}}} \right| \right)_i \Rightarrow \frac{(|\hat{P}_L - P_L|)_i}{P_{\text{total,inlet}}}$$

The absolute values here are important as one compares measurements from one location (i) to another location (j) as will be done in the next step. For instance, one would not want a system that reads a difference of -100% at one location to balance out another location where the error was $+100\%$ to come up with an index that claims a 0% difference or “perfect prediction.” This method also has the benefit of having an outside reference. For instance, the standard calibration accuracy of the pressure transducers in these experiments is about 0.5% of the total inlet pressure [10,11]. This does not mean that pressure signals cannot be resolved to a lower level, but the difference between the predictions and the data at that level could equally be due to transducer calibration accuracy issues as well as prediction accuracies. Thus in this technique differences of 0.5% in this calculation can be easily compared to the experimental calibration level (0.5%), and it is easy to see when one has a significant deviation or not.

Method 2—Relative to Reading (Read). In this method the operation done in Method 1 is now normalized by the data, resulting in a value given in percent of the actual reading, instead of the reference value: the total inlet pressure.

$$\left(\frac{|\hat{P} - D|}{D} \right)_i \Rightarrow \left(\left| \frac{\frac{\hat{P}_L}{P_{\text{total,inlet}}} - \frac{P_L}{P_{\text{total,inlet}}}}{\frac{P_L}{P_{\text{total,inlet}}}} \right| \right)_i \Rightarrow \left(\frac{|\hat{P}_L - P_L|}{P_L} \right)_i$$

This method has the advantage that engineers tend to think of the quality in these terms, but it does have a problem in that it takes the ratio of the difference over the reading, so that small differences at locations where the signal is large will have a small value, whereas the same size difference at a location where the signal is very small will have a much bigger error. This method was used in Figs. 5 and 7 of Part I for making the comparisons on the time-average data.

Both methods have their advantages and disadvantages, and one can see that it will be difficult to make a blanket statement that one method is preferred over the others. When looking back onto the requirements for the methodology, at this step it appears as though both items 2 and 3 are satisfied. Any measure could be either applied locally or integrated and could be used in these formulas.

The step of integrating the results into a single value has more possibilities but does not have to be complicated. Since the definitions use an absolute value, one can simply average the results over all locations and perform statistics on them. They can be aggregated at any level. One could provide a single number for the entire rig or have different single values for the tip region, vane, and blade. A lot depends on what is expected from the design predictions. If one has changed the grid resolution locally on the vane only, then one would get a better representation of the importance of that step by looking at the vane data by itself. One could also provide a more complicated integration model, where each measurement difference is weighted by how much spatial resolution is associated with that measure (essentially dividing up the wetted distance by all the instruments and multiplying the measurement by the area it represents). For this study, the simpler

straight average will be used, as we are creating a base line, but one could envision a system in the future that would require the weighting of the differences by the amount of area they represent.

1.2 Measurements Used. As shown in Part I, there are several different engineering values that can be compared between the predictions and the data. Each provides more insight into the overall flow. Relative to the predictive quality of unsteady flow characteristics, these metrics have been reduced to three comparison criteria as defined below.

The envelope size index (ESI) takes a single value that is the difference between the maximum and minimum pressure during one blade (or vane) passage, (see Fig. 8 of Part I for the definition) and compares the predictions of this range with the measurements. However, it is important to account both for the envelope size, and how important the envelope size is relative to the time-average value. Weighting the size of the envelope and the time-average value of the envelope at each location (i) by the sum of these measures accomplishes this accounting. This is called the envelope size calculation (ESC), which is performed for each gauge location (i).

$$ESC_{M,i} = \left(M_{TA} \left(\frac{TA}{TA + ES} \right) \right)_i + \left(M_{ES} \left(\frac{ES}{TA + ES} \right) \right)_i$$

where TA represents the time-average value (at location i) and ES is the envelope size, also at location i , and M represents the method being used to evaluate the comparison (given above, either relative to the inlet pressure or relative to the reading). Rearranging the terms shows how the time-average and the envelope are connected to influence the final ESC number.

$$ESC_{M,i} = \left(M_{TA} \left(\frac{TA}{TA + ES} \right) \right)_i \left(1 + \left(\frac{M_{ES} \left(\frac{ES}{TA} \right)}{M_{TA} \left(\frac{TA}{TA} \right)} \right) \right)_i$$

This equation is equally valid if one is using Method 1, which compares the predictions and data based on a reference value or Method 2 where the comparisons are based on readings. The only thing different would be the physical values of M . In the above equation, M_{TA} and M_{ES} would have the following definitions based on the methods used.

$$M_{TA} = \left| \frac{\text{time avg} - \text{time avg}}{P_{\text{total inlet}}} - \frac{\text{time avg}}{P_{\text{total inlet}}} \right|, \quad \text{relative to inlet pressure}$$

$$M_{TA} = \left| \frac{\text{time avg} - \text{time avg}}{\text{time avg}} \right|, \quad \text{relative to reading}$$

where once again the “ $\hat{\cdot}$ ” represents the predicted value. It should also be noted that in these cases, since one of the variables that is matched between the predictions and the data is the upstream total inlet pressure, no real difference should exist between them.

$$P_{\text{total inlet}} = P_{\text{total inlet}}$$

In a similar manner, the measurement based on the envelope size would be as follows for the two different systems:

$$M_{ES} = \left| \frac{\text{envelope size} - \text{envelope size}}{\hat{P}_{\text{total inlet}}} - \frac{\text{envelope size}}{P_{\text{total inlet}}} \right|,$$

relative to inlet pressure

$$M_{ES} = \left| \frac{\text{envelope size} - \text{envelope size}}{\text{envelope size}} \right|, \quad \text{relative to reading}$$

One can see that in this formulation, the first term in the ESC calculation reflects the importance of the time-average calculation weighted by how large the envelope size is relative to the time-average value. For locations where the envelope size is small (such as on the vane leading edge), this weighting factor approaches 1, and the second term goes to 0, thus making this a comparison of just the time-average values. For locations where

the envelope sizes are large, we will now weigh the influence of the envelope size prediction by how important the envelope size is relative to the time-average (the ES/TA weighting function). The overall envelope size index (ESI) is obtained by processing the ESCs over all locations. In general, the average value will be reported in this paper, although one could provide more advanced statistics such as the standard deviation, peak-to-peak variation etc., or as mentioned previously a more advanced integration technique.

$$ESI_M = \frac{\sum_{i=1}^n ESC_{M,i}}{n}$$

This measure provides a good overall estimate of the importance of the unsteady envelopes with the current information. However, it is very sensitive to just one measure, the envelope size. As can be seen from the unsteady pressure envelopes on the blade (Figs. 8, 10, 12, and 14 of Part I), the envelope sizes change depending upon the particular location. Thus locations with large envelope sizes will have a different impact on the index than locations with small envelopes. Over or underprediction of the envelope size may be due to grid resolution issues, as opposed to some mistake in the boundary condition or flow physics. As mentioned in Ref. [20] the envelope size is a measure of the integrated effects over all frequencies of the time-resolved data. It nominally contains the same data as the power spectrum but also includes the effects of phase and higher order harmonics. As it is taken in the time domain and not just in the frequency domain, there is much less processing involved.

One can extend the idea of the ESC, which examines the magnitude of the envelope, to another index that evaluates the shape of the envelope. This is accomplished by comparing the time-resolved values (data and prediction) over the entire passage and then averaging them together to get one calculation at a given location. This is called the envelope quality index (EQI). The EQI is similar in concept to the ESI but has a finer temporal resolution (in terms of the comparison as a function of vane or blade passage) and uses this information (which is not present in the ESI) to create an index for each gauge location. In a manner similar to the previous index, we want to weigh each point in the calculation by the importance of that point relative to all the other points. To do this though, both the predictions and the data need to have the same spatial resolution (number of points per passage) so that one makes an accurate comparison, which as in this case, involves interpolating the predictions onto the data time-base thus tending to reduce the extremes.

$$EQC_{M,i} = \left(\sum_{i=0}^K \left(M_i \frac{D_i}{\sum_{j=0}^K D_j} \right) \right)_i$$

Here the method ($P-D$: Method 1, or $(P-D)/D$: Method 2) at any location i is used to evaluate the comparison of the prediction and the data. The calculation is the sum of all the comparisons of the waveform (where l is the index along the waveform and K is the total number of points in the waveform). The weighting function is just the local data point divided by the sum of all the data in the waveform. In this case, the data and the prediction must have the time-average values included in the data (they cannot be just the unsteady component or have a zero mean) since in that case one would not account for the time-average values. As in the envelope size index, the overall index is taken from averaging over all wetted distance locations (i).

$$EQI_M = \frac{\sum_{i=1}^n EQC_{M,i}}{n}$$

Both of these criteria deal specifically with surrogates of the time-dependent data in the time domain, but as mentioned earlier, often looking at the time-dependent data in the frequency domain can provide more unique insight for a specific analysis.

The power spectrum index (PSI) operates in a manner similar to

the EQI, where the calculation of individual locations comes from adding up the effects at each frequency of interest. In this case, the time-average (0 frequency), the fundamental frequency, and three harmonics are used to provide a reasonable estimate of the code's predictive capability in the frequency domain. This particular index does not look at accuracy in frequency or phase prediction, only the amplitude.

$$PSC_{M,i} = \left(M_i \frac{D_i}{\sum_{j=0}^K D_j} \right)$$

Thus the overall index is the average of the calculations at the different locations.

$$PSI_M = \frac{\sum_{i=1}^n PSC_{M,i}}{n}$$

1.3 Code Prediction Quality on Blade. Using the various indices outlined above, the calculations were performed for both methods; however, the results for the method based on readings yield similar trends (although different numerical results) and thus only the plots for the relative to input pressure (IP) method will be shown below. Plotted below are the three calculations: the envelope size calculation, the envelope quality calculation and the power spectrum calculation, all performed at each gauge location along the blade. These have been averaged together to produce the indices (i.e., ESI, EQI, PSI) for each code procedure and summarized in the legend of each plot. Examining all three plots together yields insight into the performance of each code along the blade.

Figures 2–4 provide some interesting insight. First, one can see that the average difference among the methods is not great when compared to the inlet total pressure. Remember that the basic calibration accuracy is approximately 0.5% on this scale, which is remarkably close to many of the differences between the predictions and the data, and the overall differences in the indices between the different codes is of this order. Although one does see on this scale that the FINE (DM) method on average provides more accurate predictions, independent of the index used, but there is relatively little difference between the methods in terms of average values. However when looking at the prediction for 6% wetted distance, one sees that all predictions provide similar quality for the power spectrum and the envelope quality, but they differ mainly on the envelope size. All the codes miss the data at this location substantially when compared to the average agreement (about 8% versus 1%). However, the fact that the FINE (DM) method seems to have an improved measure for the envelope size index as compared to the other two methods would tend to indicate that the main difference between the predictions and the data is not based generally on grid resolution since both FINE (DM) and FINE (LM) have the same grid. As a comparison, the next main deviation occurs at about 70% wetted distance and the predictions are about 8% different than the data for all indices and codes, which tends to support the argument that grid resolution is not the main problem at this location (as FINE and TURBO have different grid resolutions). Rather there is something basic in the flow dynamics that is not being captured by the models. This may be as simple as not capturing the proper boundary condition at the exit of the stage. The fact that the overall conclusion about the quality of the prediction seems to be independent of the evaluation criteria is also reassuring. Going back to Fig. 6 in Part I of the paper, one can see that the locations with the biggest deviations are close to the cooling holes but only on the suction side. This is especially true with the point at 6% wetted distance where the transducer is located about 5.8 cooling hole diameters downstream (Fig. 6, Part I). Most transducers shown in Part I are further away from the cooling holes, the exception being the gauge at -52.8% wetted distance, which has predictions in good agreement with the data but is only about 5.9 diameters away from the upstream row of cooling holes. This implies that the flow physics of the holes for the pressure side and the suction side of the blade is substantially

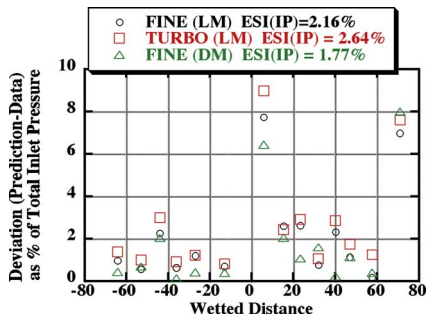


Fig. 2 Blade 50% span, ESC versus wetted distance

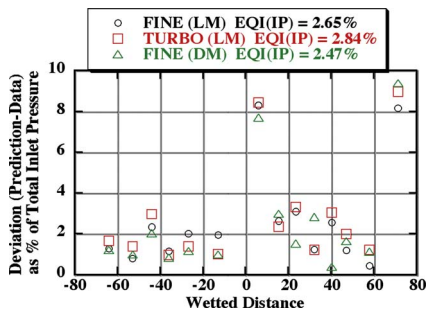


Fig. 3 Blade 50% span, EQC versus wetted distance

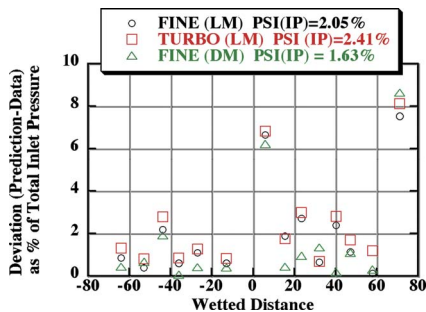


Fig. 4 Blade 50% span, PSC versus wetted distance

different and are influencing the data, since the predictions are not accounting for these differences. This is not surprising, as one would expect the blowing ratio to be much higher for the suction surface.

1.4 Code Prediction Quality on Blade Using the “Relative to Reading” Methodology. The next two figures show the same comparisons for the ESI and ESC but using the methodology that compares the data as a percentage of reading as opposed to as a percentage of the inlet pressure (as shown in Figs. 2 and 3).

The advantages of using both methodologies become clearer when comparing the same index calculated different ways (Fig. 5 with Fig. 2 and Fig. 6 with Fig. 3). While the overall index values are different (roughly 11% of reading versus 2.5% of inlet pressure), the main locations of disagreement are the same (6% and 70% wetted distance). While the plots that represent the variations as a function of inlet pressure can be directly scaled to the overall experimental accuracy, the plots that show the accuracy as a percentage of reading answer the designers’ questions directly: how accurate are my predictions. As was demonstrated with the previous figures 2–4 the differences in each code are not great, and the overall accuracy for the ESI and the EQI are on the order of 10%. In addition, by comparing both methodologies one can tell that the

reason for the large deviation of the two points is not because the reading is small, (from Figs. 2 and 3) but because the deviation is relatively large at these points. The fact that so many of the points have agreements within 5–10% of the measurement suggests that the grid resolution over most of the blade is fine. Improving the prediction quality at these local points, whether it comes from locally increased grid resolution or better modeling of the cooling flow in these areas will be critical to improving the overall accuracy of the predictions. However, given the relative ease of these cooling models, this simplified approach may be acceptable for initial design work given that the accuracy is on the order of 10%.

Code Prediction Quality on Tip Shroud. The same type of analysis can be performed for the tip/shroud predictions and measurement with only the ESI and EQI data being shown, (see Figs. 5 and 6) as the PSI data is similar to these results.

The data in Figs. 7 and 8 are interesting when compared to the blade results of Figs. 2 and 3. One can see that the overall quality of the prediction is less on the shroud than on the blade. In addition, one can see that TURBO, which has a much coarser grid in the blade tip area, generally underperforms more in this area, both in the envelope size and in quality. This is particularly the situation near the leading edge more so than at the trailing edge, suggesting that improved grid resolution is needed only in the leading edge for the FINE models, and an overall improvement in grid resolution is needed in the region for the TURBO predictions. It is also interesting to note that in general the FINE (LM) model behaves the best in the tip shroud area, although the difference between that and the FINE (DM) model is not significant.

If one switches to the percentage of reading methodology (Figs. 9 and 10), one sees that on average the FINE (DM) method is better for predicting the data, generally once again on the order of about 10%. As shown in the data presented as a percentage of the inlet pressure, it is the locations toward the trailing edge of the shroud that have the largest deviations.

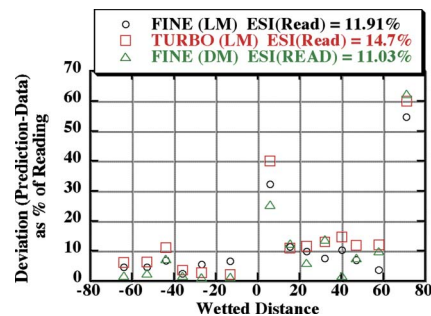


Fig. 5 Blade 50% span, ESI based on reading

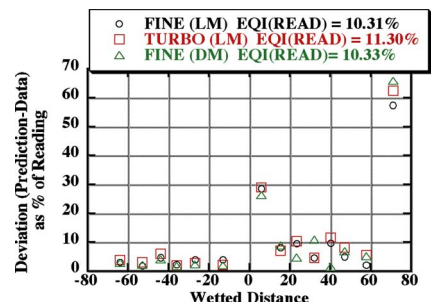


Fig. 6 Blade 50% span, EQI based on reading

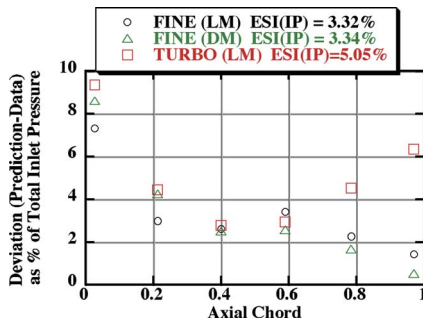


Fig. 7 Tip shroud, ESC as function of axial blade chord

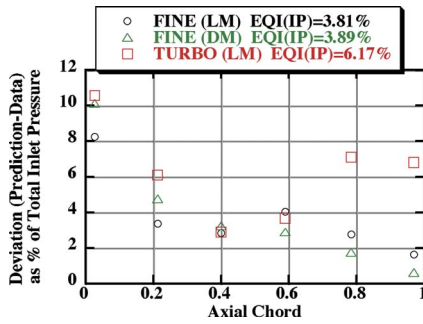


Fig. 8 Tip shroud, EQC as function of axial blade chord

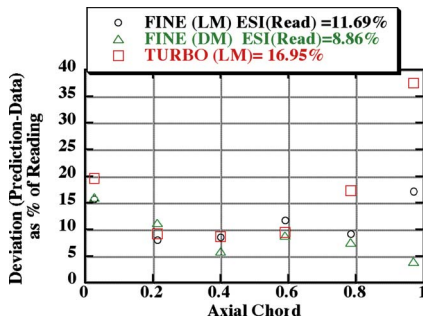


Fig. 9 Shroud ESI based on reading

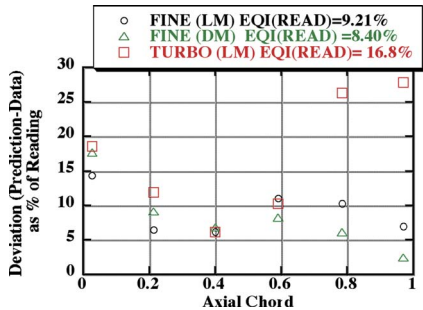


Fig. 10 Tip shroud EQI based on reading

Conclusions

The fully cooled data for a rotating full-stage Honeywell high-pressure turbine stage operating at design corrected conditions has been presented and compared to predictions. Both steady and unsteady computations were performed using FINE/TURBO with distributed mass and lumped-mass cooling models. The predictions using TURBO were also unsteady but only used the lumped-mass injection system. Both codes utilized phase-lagged boundary conditions, which have reduced the solution area down to only one

passage for both the vane and the blade. The predictions were compared to the data on the vane and blade at midspan and at the blade tip/shroud, since these three areas provide locations where the flow physics differ greatly, and thus they represent a good basis for comparison. The data and predictions were evaluated as time-averaged values, time-resolved data (in terms of blade passing shapes), and in the frequency domain (as harmonic analysis).

On the vane it was clear that the time-averaged data did not vary greatly from the predictions along the vane with the exception of the location close to the sonic line (50% wetted distance). At this location, the higher grid resolution of the TURBO code improved the predictions dramatically. However, everywhere else the FINE code is comparable to the TURBO code and is in agreement with the data in a range of 2–6% (depending on the operating mode). While improvements are made with the more refined grids, they are necessary only near the sonic line location on the suction side of the vane. Keeping the grids coarse is a reasonable way to improve overall design time.

For the blade, where unsteadiness is more important, the distributed mass time-accurate predictions dominate over the grid resolution, with the FINE code consistently being in better agreement with the data (about 2% of vane inlet pressure) than TURBO operating in a lumped-mass mode (about 3% of vane inlet pressure).

For the shroud, an area where strong 3D and unsteady effects occur, all codes deviate more from the data than on the blade. However, because of the distribution of the grid TURBO had a coarser grid than FINE in the shroud region, and the effects are apparent with the FINE code accurate to about 3.5% versus the 5% for TURBO. In the shroud area, there was no appreciable difference between the FINE distributed mass mode and the FINE lumped-mass mode. An analysis of the power spectrums show that, on average, they track the envelope sizes in terms of estimating the accuracy of the predictions

Three quantitative criteria have been proposed to measure the accuracy of the predictions, which govern the envelope size, shape, and the comparisons of the power spectrums. These can be evaluated in terms of percentage of inlet pressure or as percentage of reading. While the number changes based on the criteria, the trends remain the same. In addition, these criteria point to locations where increased grid resolution may be required, but it is clear that there are many locations that do not require any increase in grid resolution. These criteria can be used to compare predictions for different geometries and run conditions, which provide a method to quantitatively track how well the predictions are improving.

The pressure results showed that even with a mesh that was between 2–2.5 times less dense than TURBO, FINE/TURBO is capable of making very reasonable aerodynamic predictions in many of the complex flow regions for this turbine stage. As the importance of grid resolution is not critical in all locations, this type of work allows designers to increase grid resolution in those areas that are necessary (such as on the vane at the sonic line) without increasing resolution everywhere which should shorten the overall time required for calculations. By utilizing comparisons performed both as a percentage of reading and as a percentage of inlet pressure, one can answer two distinctly different questions. Using the numbers based on percentage of inlet pressure, one can compare the accuracies directly to experimental accuracies and can evaluate if different methods are significantly different from each other. By using the differences calculated as a percentage of reading, one can answer the very basic question from a design perspective of “how good are the predictions.”

Acknowledgment

The NASA/DoD URETI for Aero propulsion and Power at The Ohio State University and NASA Contract No. NCC3-1086 supported the research reported here. The NASA technical monitor for this work is Ms. Kim Pham. The authors would like to ac-

knowledge Costas Vogiatzis of Honeywell Engines for providing the grid used in the FINE/Turbo calculations, as well as Bill Troha, Malak Malak, and Ron Rich of Honeywell Engines for their support during the course of this work. The authors would also like to acknowledge the dedicated staff of the OSU GTL for their efforts in preparing the instrumented turbine stage and for helping in the completion of the measurements.

Nomenclature

Wetted distance = location along the airfoil contour (x)
 location normalized by the total distance along each surface (S). Measured from -100% to 100% with 0 at the stagnation point, and the negative side is the pressure side of the airfoil:
 pressure side = $-(x/S_{\text{pressure side}}) \times 100$,
 suction side = $(x/S_{\text{suction side}}) \times 100$
 Normalized = local static pressure/vane inlet total pressure: $(P_{\text{Local}(L)}/P_{\text{total}})$

References

- [1] Dunn, M. G., 2001, "Convective Heat Transfer and Aerodynamics in Axial Flow Turbines," *ASME J. Turbomach.*, **113**, pp. 637–686.
- [2] Rao, K. V., Delaney, R. A., and Dunn, M. G., 1994, "Vane-Blade Interaction in a Transonic Turbine: Part II—Heat Transfer," *J. Propul. Power*, **10**(3), pp. 312–317.
- [3] Rao, K. V., Delaney, R. A., and Dunn, M. G., 1994, "Vane-Blade Interaction in a Transonic Turbine: Part I—Aerodynamics," *J. Propul. Power*, **10**(3), pp. 305–311.
- [4] Dunn, M. G., Bennett, W. A., Delaney, R. A., and Rao, K. V., 1992, "Investigation of Unsteady Flow Through a Transonic Turbine Stage: Data/Prediction Comparison for Time-averaged and Phase-Resolved Pressure Data," *ASME J. Turbomach.*, **114**, pp. 91–99.
- [5] Giles, M. B., 1988, "UNSFLO: A Numerical Method for Unsteady Inviscid Flow in Turbomachinery," MIT Gas Turbine Laboratory Report No. 195.
- [6] Guenette, G. R., Epstein, A. H., Giles, M. B., Haimes, R., and Norton, R. J. G., 1988, "Fully Scaled Transonic Turbine Rotor Heat Transfer Measurements," ASME Paper No. 88-GT-171.
- [7] Davis, R. L., Yao, J., Clark, J. P., Stetson, G., Alonso, J. J., Jameson, A., Haldeman, C. W., and Dunn, M. G., 2004, "Unsteady Interaction Between a Transonic Turbine Stage and Downstream Components," *Int. J. Rotating Mach.*, **10**(6), pp. 495–506.
- [8] Haldeman, C. W., Dunn, M. G., Abhari, R. S., Johnson, P. D., and Monteseocca, X. A., 2000, "Experimental and Computational Investigation of the Time-Averaged and Time-Resolved Pressure Loading on a Vaneless Counter-Rotating Turbine," ASME Paper No. 2000-GT-0445.
- [9] Weaver, M. W., Manwaring, S., Abhari, R. S., Dunn, M. G., Salay, M. J., Frey, K. K., and Heidegger, N., 2000, "Forcing Function Measurements and Predictions of a Transonic Vaneless Counter-Rotating Turbine," ASME Paper No. 2000-GT-0375.
- [10] Haldeman, C. W., Mathison, R. M., Dunn, M. G., Southworth, S., Harral, J. W., and Heitland, G., 2008, "Aerodynamic and Heat Flux Measurements in a Single Stage Fully Cooled Turbine—Part I: Experimental Approach," *ASME J. Turbomach.*, **130**(2), p. 021015.
- [11] Haldeman, C. W., Mathison, R. M., Dunn, M. G., Southworth, S., Harral, J. W., and Heitland, G., 2008, "Aerodynamic and Heat Flux Measurements in a Single Stage Fully Cooled Turbine—Part II: Experimental Results," *ASME J. Turbomach.*, **130**(2), p. 021016.
- [12] Praisner, T. J., and Clark, J. P., 2007, "Predicting Transition in Turbomachinery, Part I—A Review and New Model Development," *ASME J. Turbomach.*, **129**(1), pp. 1–13.
- [13] Oberkampf, W. L., and Barone, M. F., 2006, "Measures of Agreement Between Computation and Experiment: Validation Metrics," *J. Comput. Phys.*, **217**(1), pp. 5–36.
- [14] Oberkampf, W. L., and Blottner, F. G., 1998, "Issues In Computational Fluid Dynamics Code Verification and Validation," *AIAA J.*, **36**(5), pp. 687–695.
- [15] Oberkampf, W. L., and Trucano, T. G., 2002, "Verification and Validation in Computational Fluid Dynamics," *Prog. Aerosp. Sci.*, **38**(3), pp. 209–272.
- [16] Roy, C. J., 2005, "Review of Code Solution and Verification Procedures for Computational Simulation," *J. Comput. Phys.*, **205**(1), pp. 131–156.
- [17] Stern, F., Wilson, R., Coleman, H., and Paterson, E., 2001, "Comprehensive Approach to Verification and Validation of CFD Simulations—Part 1: Methodologies and Procedures," *ASME J. Fluids Eng.*, **123**(4), pp. 793–802.
- [18] Stern, F., Wilson, R., Coleman, H., and Paterson, E., 2001, "Comprehensive Approach to Verification and Validation of CFD Simulations—Part 2: Application for RANS Simulation of a Cargo/Container Ship," *ASME J. Fluids Eng.*, **123**(4), pp. 803–810.
- [19] Stern, F., Wilson, R., and Shao, J., 2005, "Quantitative V&V of CFD Simulations and Certification of CFD Codes," *Int. J. Numer. Methods Fluids*, **50**(11), pp. 1335–1355.
- [20] Haldeman, C. W., 2003, "An Experimental Investigation of Clocking Effects on Turbine Aerodynamics Using a Modern 3-D One and One-Half Stage High Pressure Turbine for Code Verification and Flow Model Development," Ph.D. thesis, Department of Aeronautical and Astronautical Engineering, Ohio State University, Columbus, p. 345.

Effect of Inlet Flow Angle on Gas Turbine Blade Tip Film Cooling

Zhihong Gao

Diganta Narzary

Shantanu Mhetras

Je-Chin Han

e-mail: jc-han@tamu.edu

Turbine Heat Transfer Laboratory,
Department of Mechanical Engineering,
Texas A&M University,
College Station, TX 77843-3123

The influence of incidence angle on film-cooling effectiveness is studied for a cutback squealer blade tip. Three incidence angles are investigated -0 deg at design condition and ± 5 deg at off-design conditions. Based on mass transfer analogy, the film-cooling effectiveness is measured with pressure sensitive paint techniques. The film-cooling effectiveness distribution on the pressure side near tip region, squealer cavity floor, and squealer rim tip is presented for the three incidence angles at varying blowing ratios. The average blowing ratio is controlled to be 0.5, 1.0, 1.5, and 2.0. One row of shaped holes is provided along the pressure side just below the tip; two rows of cylindrical film-cooling holes are arranged on the blade tip in such a way that one row is offset to the suction side profile and the other row is along the camber line. The pressure side squealer rim wall is cut near the trailing edge to allow the accumulated coolant in the cavity to escape and cool the tip trailing edge. The internal coolant-supply passages of the squealer tipped blade are modeled similar to those in the GE-E³ rotor blade. Test is done in a five-blade linear cascade in a blow-down facility with a tip gap clearance of 1.5% of the blade span. The Mach number and turbulence intensity level at the cascade inlet were 0.23 and 9.7%, respectively. It is observed that the incidence angle affects the coolant jet direction on the pressure side near tip region and the blade tip. The film-cooling effectiveness distribution is also altered. The peak of laterally averaged effectiveness is shifted upstream or downstream depending on the off-design incidence angle. The film cooling effectiveness inside the tip cavity can increase by 25% with the positive incidence angle. However, in general, the overall area-averaged film-cooling effectiveness is not significantly changed by the incidence angles in the range of study. [DOI: 10.1115/1.2987235]

1 Introduction

Hot gases entering the turbine result in a significant heat load on the turbine components. Large leakage flow occurs in the blade tip region due to high pressure difference between the pressure side and the suction side. This leads to higher heat load on the blade tip. Due to the severe operating environment and difficulty in cooling, blade tips are more susceptible to thermal failure. Bunker [1] generalized the aerodynamics, heat transfer, and durability issues for three kinds of blade tip designs: plane tip, squealer tip, and attached tip shroud. Among these designs, the squealer tip is widely used in modern high temperature, high pressure gas turbine engines. To maintain the blade integrity and avoid the excessive oxidization and erosion, film cooling is commonly used in the high pressure blades.

Experimental investigations in the general area of film cooling on a blade tip are limited with few papers available in open literature. Film cooling on a blade tip was first studied by Kim and Metzger [2] and Kim et al. [3] by using a 2D rectangular tip model to simulate leakage flow between the tip and the shroud. The heat transfer coefficients and film-cooling effectiveness were reported for various film-cooling configurations. Kwak and Han [4,5] studied the local heat transfer and film-cooling effectiveness distribution for plane tip and squealer tip geometries in a GE-E³ five-blade linear cascade. They found that film effectiveness increases but overall heat transfer coefficients decrease when the blowing ratio increases. Their results also showed that the squealer geometry presented higher film-cooling effectiveness and lower heat transfer coefficients compared with the plane tip geometry due to the reduced leakage flow. Ahn et al. [6] presented film-cooling effectiveness distribution on a plane and a squealer

blade tip using the pressure sensitive paint (PSP) technique. One row of cylindrical holes was arranged on the camber line normal to the tip surface and another row of angled holes on the pressure side below the tip. They noted that higher blowing ratios gave higher effectiveness. Results with a plane tip showed clear traces of the coolant path while for a squealer tip, coolant accumulation effects were observed on the cavity floor. Christophel et al. [7,8] studied film cooling and heat transfer using the infrared technique on a plane tip under low speed conditions. They used four different coolant flow rates for two tip gaps. A row of holes was located on the pressure side just below the tip with two more dirt purge holes on the tip itself. They found that a smaller tip gap and a larger coolant flow showed better cooling. They also found that higher blowing ratios resulted in higher augmentations on tip heat transfer but with an overall net heat flux reduction when combined with adiabatic effectiveness measurements. Mhetras et al. [9] studied film-cooling effectiveness on all surfaces of a squealer tipped blade in a linear high flow cascade using the PSP technique. Coolant was ejected through shaped holes on the pressure side near tip region and cylindrical holes on the cavity floor. The shaped holes on the pressure side showed a large coolant spread consequently resulting in good film coverage. The coolant from the tip holes was directed toward the pressure side inner squealer rim wall to provide additional cooling. Furthermore, Mhetras et al. [10] optimized the design of film-cooling holes and cut the pressure side squealer rim wall to allow the accumulated coolant in the cavity to escape and cool the tip trailing edge. Two cavity depths 2.1% and 4.2% of blade height were examined. The cutback squealer rim showed high effectiveness in the trailing edge region of the blade tip as compared with a full squealer. The larger cavity depth offered higher effectiveness on all tip surfaces.

There are many papers available in open literature, which discuss heat transfer coefficients on the blade tip and near tip regions. Several of these papers present results under engine representative mainstream flow conditions. Local heat transfer coefficients on a turbine blade tip model with a recessed cavity (squealer tip) were

Contributed by the International Gas Turbine Institute of ASME for publication in the JOURNAL OF TURBOMACHINERY. Manuscript received July 12, 2007; final manuscript received December 13, 2007; published online April 8, 2009. Review conducted by David Wisler. Paper presented at the ASME Turbo Expo 2007: Land, Sea and Air (GT2007), Montreal, QC, Canada, May 14–17, 2007.

studied by Bunker et al. [11]. The effects of tip gap clearance and freestream turbulence intensity levels were investigated. Azad et al. [12,13] studied heat transfer coefficients for a squealer tip and a plane tip, and concluded that the overall heat transfer coefficients were lower for a squealer tip. Bunker and Bailey [14] studied the effect of squealer cavity depth and oxidation on turbine blade tip heat transfer. Azad et al. [15] and Kwak et al. [16] investigated the heat transfer on several different squealer geometries. They found that a suction side squealer tip gave the lowest heat transfer among all cases studied. Heat transfer coefficient distributions for plane tip, squealer tip, and near tip regions were presented by Kwak and Han [17,18] in two papers. By using a squealer tip, heat transfer was found to decrease on the tip and near tip regions.

Some numerical investigations have also been carried out to study heat transfer and film-cooling effectiveness on a blade tip. The effects of tip clearance and casing recess on heat transfer and stage efficiency for several squealer blade tip geometries were predicted by Ameri et al. [19]. Ameri and Rigby [20] also calculated heat transfer coefficients and film-cooling effectiveness on turbine blade models. The numerical results for heat transfer and flow obtained by Ameri et al. [21] were compared with the experimental results from Bunker et al. [11] for a power generation gas turbine. The effects of different hole locations on film-cooling effectiveness and heat transfer were predicted by Yang et al. [22].

Some experimental investigations have also been performed to study heat transfer on the blade tip under rotating conditions. Heat transfer coefficients on the blade tip and the shroud were measured by Metzger et al. [23] using heat flux sensors in a rotating turbine rig. Dunn and Haldeman [24] measured time averaged heat flux at a recessed blade tip for a full-scale rotating turbine stage at transonic vane exit conditions. Their results showed that the heat transfer coefficient at the mid- and rear portion of the cavity floor was of the same order as the blade leading edge value. A recent study by Rhee and Cho [25,26] investigated the mass transfer characteristics for a flat tip on the tip, shroud, and near tip regions. The incidence angle effect was studied by changing the rotational speed. The incidence angle examined the range from -15 deg to $+7$ deg. Heat transfer on the tip under rotating conditions was found to be about 10% lower than the stationary case due to the reduction of the tip gap leakage flow caused by rotation. With the negative incidence angle, the peak regions were reduced and shifted toward the trailing edge and additional peaks were formed near the leading edge region on the tip. Uniform and high values were observed on the tip with positive incidence angles.

As reviewed, most of the previous studies were focused on blade tip heat transfer. A few papers studied blade tip film cooling. Due to the complex tip geometry and flow patterns around the tip regions, the heat transfer and film-cooling characteristic may behave differently at design and off-design conditions. The heat transfer and film-cooling data on the tip region at off-design conditions are very limited, even for plane tips. The main focus of the present study was to investigate the effect of incidence angle on the blade tip film cooling for a cutback squealer blade tip. Three mainstream inlet angles at design condition (0 deg) and off-design conditions (± 5 deg) were investigated. The test was done under relatively high pressure ratio and freestream Mach number. Using the PSP technique, the film-cooling effectiveness was measured for the squealer cavity floor, the pressure side (PS) near tip region, as well as the narrow squealer rim tip. Because the PSP technique is based on mass transfer analogy, the heat conduction is eliminated in the effectiveness measurement. Reliable data near the film-cooling holes and the thin squealer rim can be obtained.

2 Experimental Setup

The schematic view of the test section and the blow-down loop is shown in Fig. 1. The test section consisted of a five-blade linear cascade with blade tip profiles. The inlet cross section of the test

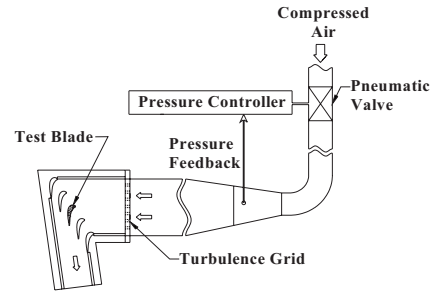


Fig. 1 Schematic of the test section and blow-down facility

section was 31.1 cm (width) \times 12.2 cm (height). A turbulence-generating grid (rectangular bar mesh type) with a porosity of 57% was placed before the inlet. Turbulence intensity was recorded 6 cm upstream of the middle blade (or 20.7 cm downstream of the grid) using a hot-wire probe. Turbulence intensity (Tu) at this location was found to be 9.7% due to the presence of the grid and turbulence length scales were estimated to be 1.5 cm, which was slightly larger than the grid bar size. The bottom and sides on the test section were machined out of 1.27 cm thick polycarbonate sheets whereas a 1.27 cm thick acrylic plate was used for the top for better optical access to the blade tip. The top plate also acted as a shroud for the blades. Flow conditions in adjacent passages of the center blade were ensured to be identical by adjusting the trailing edge tailboards for the cascade. A comprehensive discussion on the flow conditions, including flow periodicity in the cascade and pressure distribution along the blade at design condition (0 deg incidence angle), has been reported by Azad et al. [12,13] and Kwak and Han [4,5]. The blade dimensions and flow conditions are listed in Table 1. During the blow-down test, the cascade inlet air velocity was maintained at 78 m/s for all the three incidence angles, which corresponds to a Mach number of 0.23. The blow-down facility could maintain steady flow in the cascade for about 40 s. Compressed air stored in tanks entered a high flow pneumatic control valve, which could maintain steady flow by receiving downstream pressure feedback. The control valve could maintain a velocity within $\pm 3\%$ of desired value.

A three times scaled model of the GE-E³ blade was used with a blade span of 12.2 cm and an axial chord length of 8.61 cm. Since the blades were placed in a linear cascade, they were machined for a constant cross section for its entire span corresponding to the tip profile of the actual GE-E³ blade. Figure 2 shows the blade profiles, and the inlet and exit angles at design conditions. The blade tip and shroud definitions are also indicated in Fig. 2. The test blade, which was used by Mhetras et al. [10], was made using stereo lithography (SLA). The four guide blades placed in the test section were made of aluminum. To study different mainstream inlet angles, the test blade and its adjacent guide blades were placed on a rotatable circular plate, which served as part of the endwall, as shown in Fig. 3(a). By turning the circular plate, in-

Table 1 Blade geometry and flow conditions

Blade	
Span	12.2 cm
Axial chord length	8.61 cm
Tip clearance	1.5% of span
Flow condition	
Inlet velocity	78 m/s
Mach number at inlet	0.23
Turbulence intensity	9.7%

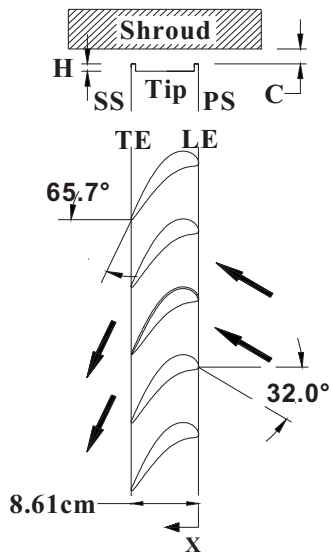


Fig. 2 Definition of the blade tip and shroud

incidence angles at design and off-design conditions were achieved. The incidence angles are indicated in Fig. 3(b). During the test, the lead boards, tail boards, and the two farthest guide blades were kept in the same position as that for a 0 deg incidence angle. This may cause some deviation for the flow angles; however, deviation should be negligible in the small range of angle variation.

Figure 4 shows the film-cooling measurement blade with the internal passage geometry. The passages are numbered from 1 to 6 with passage 1 closest to the leading edge and passage 6 closest to the trailing edge. Coolant was supplied to the test blade through two loops with three serpentine passages with a 3 mm wall thickness in each loop. The design of the passages was based on the E³, stage 1, HPT rotor blade cooling system as discussed by Halila et al. [27]. The leading edge impingement wall in their design was removed to simplify the passage flow analysis. Figure 5 shows the geometry and orientation of the film-cooling holes on the pressure

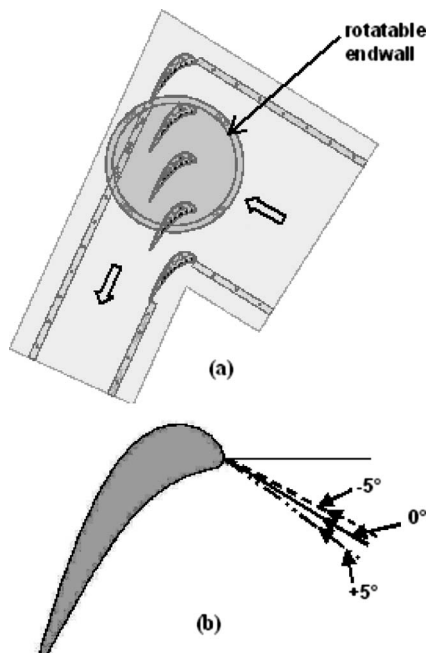


Fig. 3 (a) Test section and (b) flow angles

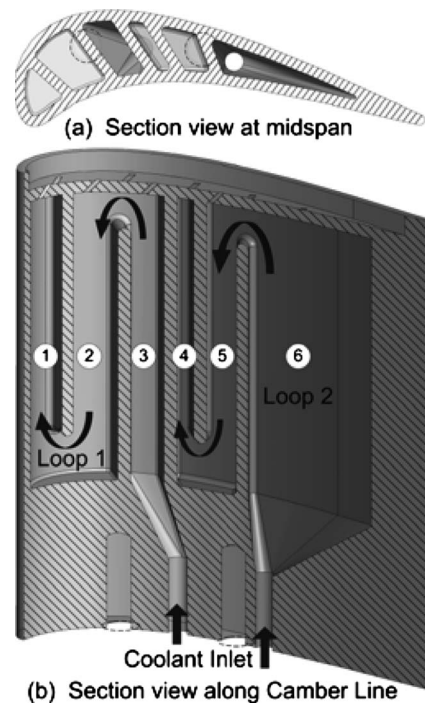


Fig. 4 Internal passage geometry of the test blade

side and on the squealer blade tip. Ten cylindrical tip holes with a diameter of 1.27 mm ($L/d=3.34$) were provided on the tip. Out of these ten holes, four were drilled such that they broke out at 45 deg along the camber line of the blade on the cavity floor. The remaining six holes were drilled at 45 deg along a curve offset to the suction surface of the blade by 5.08 mm and were equally spaced by 18.3 mm. The holes were inclined to the cavity floor in the direction of the bulk fluid flow. The first five tip holes were connected to loop 1 (near leading edge) and the remaining five to loop 2 (near trailing edge). Nine film-cooling holes with a diameter of 1.27 mm were located 9.5 mm below the tip surface. The pressure side holes have a laidback and fan-shaped design expanding by 10 deg in the three directions (10–10–10) with the expansion starting from the middle of the hole length. The hole-to-hole spacing was 8.9 mm. The first three holes near the leading edge were drilled at a radial angle of 45 deg to maximize the coolant spread whereas the remaining six holes were drilled at a compound angle of 45 deg to the blade span and 45 deg with respect to the airfoil pressure surface with $L/d=4$. Figure 6 shows

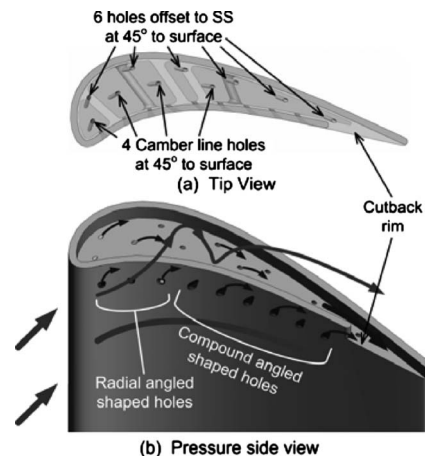


Fig. 5 Orientation of the tip and PS holes

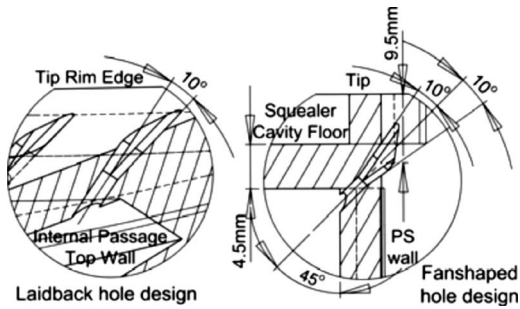


Fig. 6 Detailed geometry of a PS shaped hole

the detailed views of the shaped holes. Coolant to the first four holes was supplied through loop 1 while the remaining five holes were connected to loop 2. The squealer tipped blade with recess of 2.1% of blade span was used in this study. The pressure side rim wall near the trailing edge is cutback by about 25% of the blade chord for the blade to allow accumulated coolant to escape. A detailed description of the film hole configurations can be found in Ref. [10].

This study was performed for a tip gap of 1.5% of blade span (12.2 cm), which was maintained on the middle three blades. Coolant was ejected through tip and pressure side holes. Experiments were performed with four average blowing ratios (M) of 0.5, 1.0, 1.5, and 2.0.

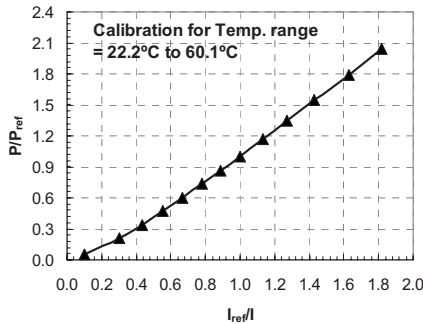


Fig. 7 Calibration curve for PSP

3 Film-Cooling Effectiveness Measurement Theory and Data Analysis

The data for film-cooling effectiveness were obtained by using the PSP technique. PSP is a photoluminescent material that emits light when excited, with the emitted light intensity inversely proportional to the partial pressure of oxygen. This light intensity can be recorded using a charge-coupled device (CCD) camera and be calibrated against the partial pressure of oxygen. The image intensity obtained from PSP by the camera during data acquisition is normalized with a reference image intensity taken under no-flow conditions. Background noise in the optical setup is removed by subtracting the image intensities with the image intensity obtained under no-flow conditions and without excitation. The resulting intensity ratio can be converted to pressure ratio using the predetermined calibration curve and can be expressed as

$$\frac{I_{\text{ref}} - I_{\text{blk}}}{I - I_{\text{blk}}} = f\left(\frac{(P_{\text{O}_2})_{\text{air}}}{(P_{\text{O}_2})_{\text{ref}}}\right) = f(P_{\text{ratio}}) \quad (1)$$

where I denotes the intensity obtained for each pixel and $f(P_{\text{ratio}})$ is the relationship between intensity ratio and pressure ratio obtained after calibrating the PSP.

Calibration for PSP was performed using a vacuum chamber at several known pressures varying from 0 atm to 1.8 atm with intensity recorded for each pressure setting. The calibration curve is shown in Fig. 7. The same optical setup was chosen for calibration as well as for data acquisition during the experiments. PSP is sensitive to temperature with higher temperatures resulting in lower emitted light intensities. Hence, the paint was also calibrated for different temperatures. It was observed that if the emitted light intensity at a certain temperature was normalized with the reference image intensity taken at the same temperature, the temperature sensitivity can be minimized. During testing, it was ensured that temperatures of mainstream air, coolant, and test section were the same while taking reference, air, and nitrogen images to minimize uncertainty. Thermocouples (T -type) located upstream of the test section and in the coolant flow recorded temperatures of air and nitrogen gas. Experiments were conducted in an air-conditioned room (20°C) and temperatures of mainstream air, coolant air, and nitrogen gas were maintained at 20°C. To obtain film-cooling effectiveness, air and nitrogen were used alternately as coolant. Nitrogen, which has nearly the same molecular weight as that of air, displaces the oxygen molecules on the surface causing a change in the emitted light intensity from

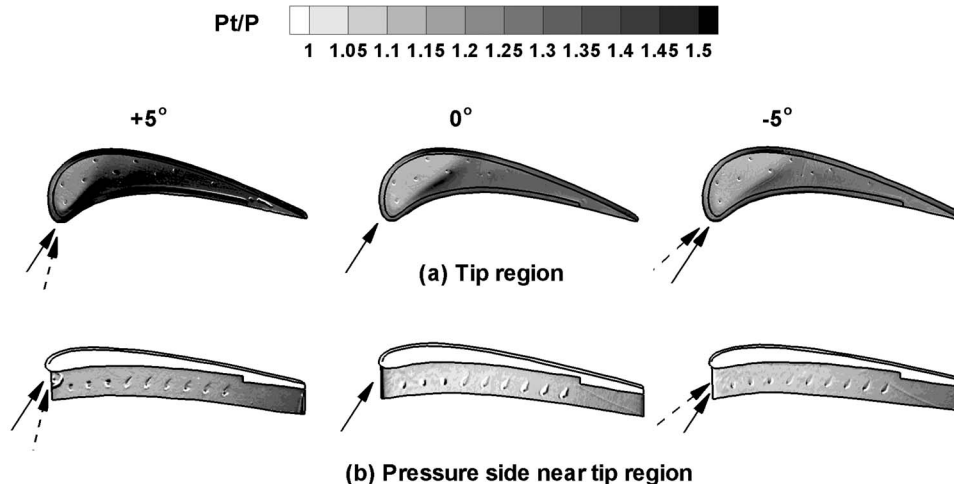


Fig. 8 Pressure ratios for different inlet flow angles without coolant injection

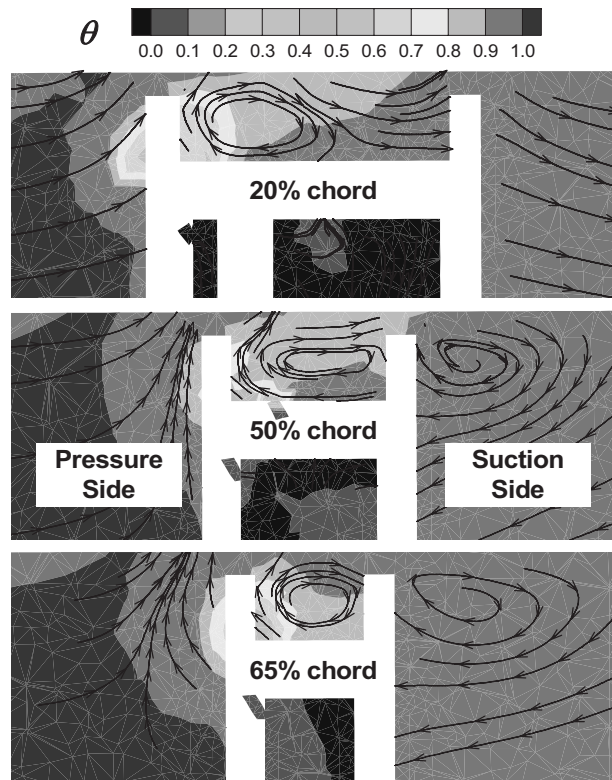


Fig. 9 Stream vectors along with dimensionless temperature contours for three cross sections along the tip [9]

PSP. By noting the difference in partial pressure between the air and nitrogen injection cases, the film-cooling effectiveness can be determined using the following equation:

$$\eta = \frac{C_{\text{mix}} - C_{\text{air}}}{C_{\text{N}_2} - C_{\text{air}}} = \frac{C_{\text{air}} - C_{\text{mix}}}{C_{\text{air}}} = \frac{(P_{\text{O}_2})_{\text{air}} - (P_{\text{O}_2})_{\text{mix}}}{(P_{\text{O}_2})_{\text{air}}} \quad (2)$$

where C_{air} , C_{mix} , and C_{N_2} are the oxygen concentrations of mainstream air, air/nitrogen mixture, and nitrogen on the test surface, respectively. The definition for film effectiveness in Eq. (2) based on mass transfer analogy is of similar form as that for adiabatic film-cooling effectiveness given as follows:

$$\eta = \frac{T_{\text{mix}} - T_m}{T_c - T_m} \quad (3)$$

The accuracy of the PSP technique for measuring film-cooling effectiveness has been compared by Wright et al. [28] on a flat plate with compound angled ejection holes using steady-state infrared (IR) technique and steady-state temperature sensitive paint (TSP) technique. Results were obtained for a range of blowing ratios and showed reasonable agreement with each other with IR, TSP, as well as PSP giving effectiveness results within 15% of each other. Larger uncertainties for heat transfer techniques such as IR and TSP methods were observed due to lateral heat conduction in the flat plate as corrections for heat conduction were not included in the presented results.

The center test blade under investigation was coated with PSP using an air brush. This coated surface was excited using a strobe light fitted with a narrow bandpass interference filter with an optical wavelength of 520 nm. A dual fiber optic guide was used to get a uniform incident light distribution on the test surface. Upon excitation from this green light, the PSP coated surface emitted red light with a wavelength higher than 600 nm. A 12 bit scientific grade CCD camera (Cooke Sensicam QE with CCD temperature maintained at -15°C using a two-stage Peltier cooler) was used to record images and was fitted with a 35 mm lens and a 600 nm longpass filter. The filters were chosen to prevent overlap between the wavelength ranges such that the camera filter blocked the reflected light from the illumination source. Coolant mass flow to each loop was set using two separate rotameters to a flow rate corresponding to the blowing ratio. A pneumatic valve was opened and the pressure controller was set to the desired flow rate for the mainstream air. The images were taken when the mainstream flow was fully developed, i.e., after the initial developing time for flow. The camera and the strobe light were triggered simultaneously using a transistor-transistor logic (TTL) signal from a function generator at 10 Hz. A total of 140 images were captured for each experiment with air and nitrogen injection and the pixel intensity for all images was averaged. The image resolution obtained from the camera was 0.6 mm/pixel. After the images were captured, the pneumatic valve was closed. The duration of a single experiment was about 30 s. A computer program was used to convert these pixel intensities into pressure using the calibration curve and then into film-cooling effectiveness.

Uncertainty calculations were performed based on a confidence level of 95% and are based on the uncertainty analysis method of Coleman and Steele [29]. Lower effectiveness magnitudes have higher uncertainties. For an effectiveness magnitude of 0.3, uncer-

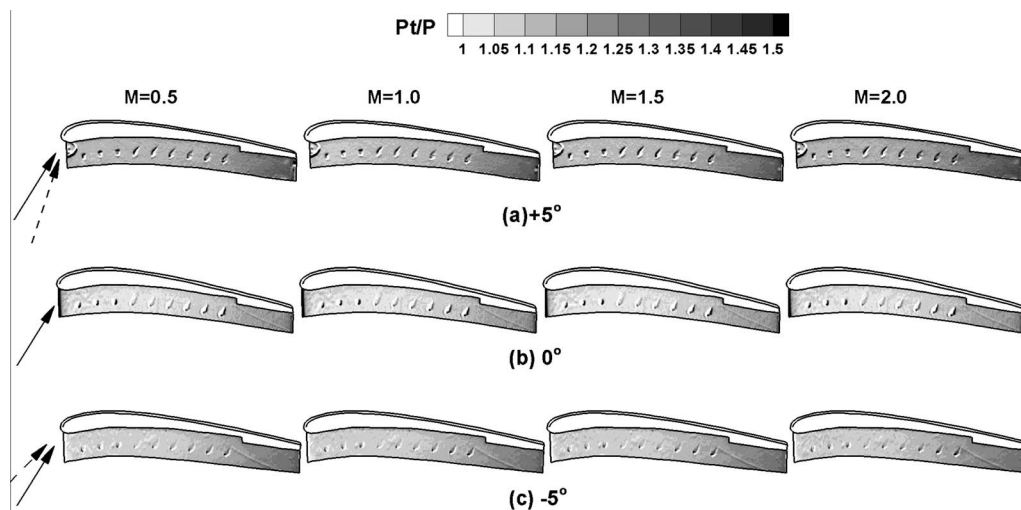


Fig. 10 Pressure ratio at the pressure side near tip region at different incidence angles and blowing ratios

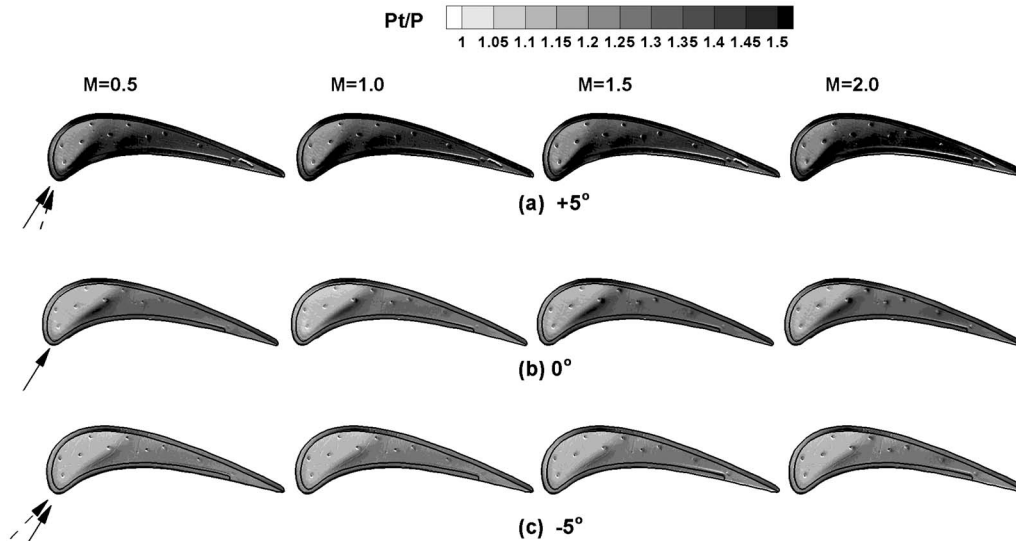


Fig. 11 Pressure ratio at the blade tip at different incidence angles and blowing ratios

tainty was around $\pm 2\%$ while for effectiveness magnitude of 0.07, uncertainty was as high as $\pm 10.3\%$. This uncertainty is the result of uncertainties in calibration (4%) and image capture (1%). The absolute uncertainty for effectiveness varied from 0.01 to 0.02 units. Thus, relative uncertainties for very low effectiveness magnitudes can be very high ($>100\%$ at effectiveness magnitude of 0.01). However, it must be noted that very few data points exist with such high relative uncertainty magnitudes. Uncertainties for the blowing ratios are estimated to be 4%.

4 Pressure Ratio Distributions

Figure 8 shows the pressure ratio (P_t/P) distributions on the blade tip and pressure side near tip region without film cooling for the three incidence angles -0 deg and ± 5 deg. The total pressure P_t was measured with a Pitot tube at the cascade inlet while the local static pressure P was measured with PSP. A higher pressure ratio indicates a higher local velocity adjacent to the surface. On the pressure side near tip region, the flow acceleration is observed from the leading edge to the trailing edge, with the trailing edge possessing the highest velocity. The $+5$ deg inlet angle has the largest pressure ratio on the pressure side among the three angles. Consequently, the highest pressure ratio also appears on the tip for the positive inlet flow. The higher pressure ratio also implies more flow leakage through the tip gap for the positive incidence angle. The pressure ratios for 0 deg and -5 deg are at about the same magnitude.

The pressure side squealer rim acts as a backward facing step to the leakage flow causing the formation of a recirculation zone inside the squealer cavity. The flow recirculation in the cavity has been demonstrated in computational fluid dynamics (CFD) simulation by Mhetras et al. [9]. Figure 9 shows their prediction for a film cooled squealer tip. The streamline along with the dimensionless temperature distribution was presented at three cross sections along the axial chord. Flow separation and reattachment on the tip are observed near the leading edge portion. Toward the trailing edge, the flow is recirculated inside the cavity. The coolant entrained inside the cavity spreads out by the recirculation vortices and cools cavity floor and the squealer inner rim walls. In Fig. 8, flow reattachment on the tip can be observed near the leading edge from the sharp gradient in the pressure ratio distributions. The local velocity on the leading edge region after flow reattachment is relatively low. Higher pressure ratio appears in the mid-to-aft chord regions while this region is completely filled up with the recirculation vortices. This may imply stronger flow recirculation inside the cavity.

The pressure ratio distribution on the pressure side near tip region with coolant ejection is shown in Fig. 10. The pressure ratio does not noticeably vary with the blowing ratios and it is similar to the case without film cooling. This implies that the presence of coolant only slightly affects the local pressure ratio distribution. The pressure ratio for the tip is shown in Fig. 11. Similar to the case for the pressure side near tip regions, the magnitude of the pressure ratio on the tip is about the same as the no coolant ejection case. It can be seen from Figs. 10 and 11 that the inlet flow of $+5$ deg shows the highest pressure ratio. The pressure ratio distribution is influenced by the inlet angle of mainstream flow.

5 Local Blowing Ratios

The average blowing ratio M is defined as $M = \rho_c V_c / \rho_m V_m$, where V_m is the local mainstream velocity near the holes. As the density of the coolant and mainstream is approximately the same, the mass flux ratio is reduced to velocity ratio. V_m was calculated from the inlet total pressure and local static pressure. The inlet total pressure was measured using a Pitot tube, while the local static pressure was obtained from PSP measurement. From the local mainstream velocity and the definition of average blowing ratio, the required coolant mass flow rate in a loop was determined and supplied. The coolant mass flow rate was controlled by two rotameters to the respective loops independently. Hence, the mass flow rate for each loop can be adjusted depending on the averaged blowing ratios (from $M=0.5$ to $M=2.0$). To keep the coolant consumption constant, the coolant mass flow rate for incidence angle ± 5 deg was set same as that for 0 deg. Therefore, the actual average blowing ratio (and the local blowing ratio which will be discussed later) for the case of ± 5 deg is slightly different from that for the case of 0 deg, especially for the case of $+5$ deg whose pressure ratio is higher. Nevertheless, the average blowing ratio based on the case of 0 deg is referred in the discussion of local blowing ratio and film-cooling effectiveness for convenience.

During testing, it was observed that the coolant mass flux could vary from hole to hole. To better explain the results of effectiveness, the local blowing ratios $M_i = \rho_c V_{c,local} / \rho_m V_m$ through each hole have been calculated. The discharge coefficients, C_D , as discussed by Gritsch et al. [30], was expressed as

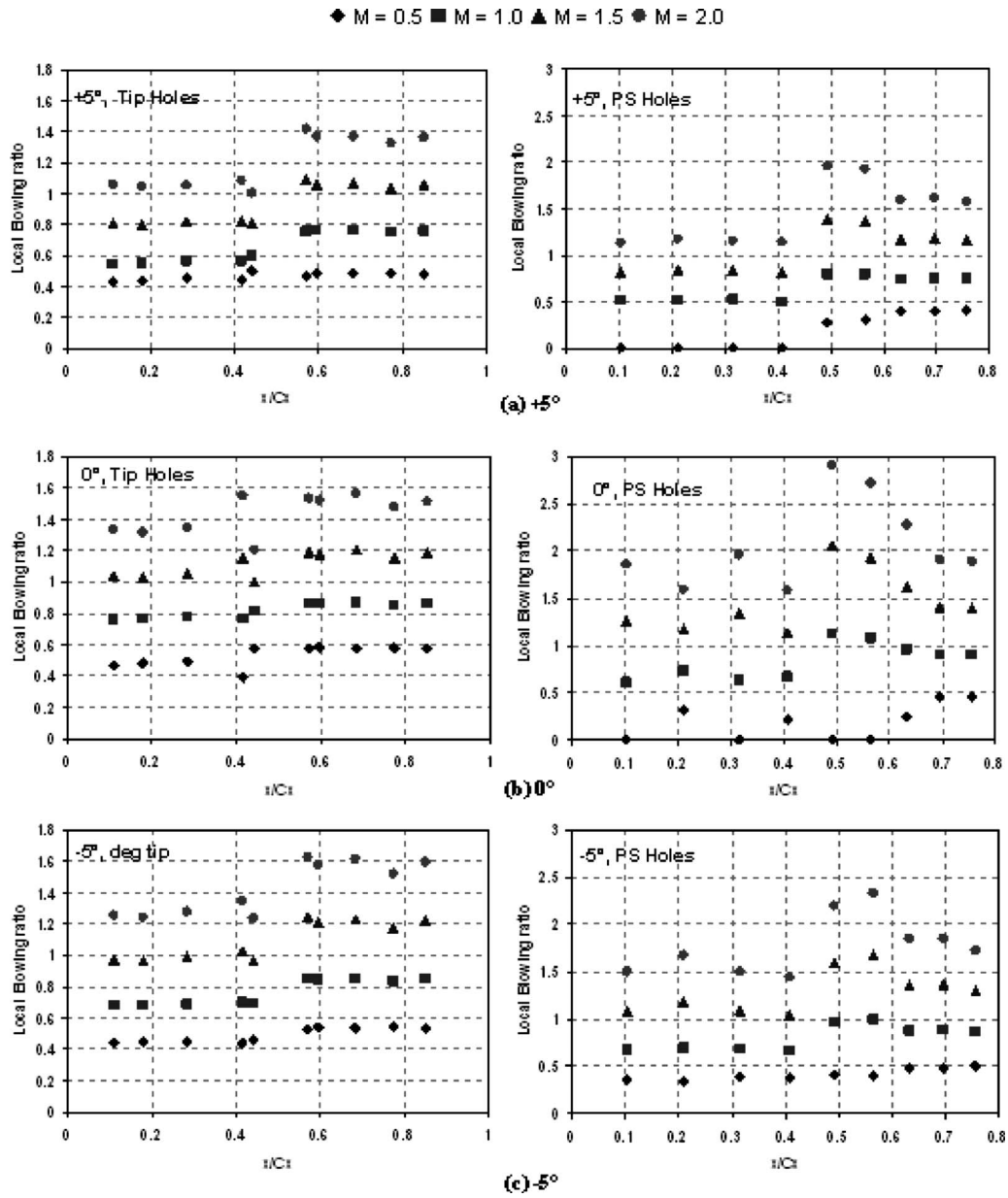


Fig. 12 Local blowing ratio for various incidence angles

$$C_D = \dot{m}_{\text{hole}} \left(\frac{\pi}{4} d^2 \right) \left(P_{t,\text{passage}} \left(\frac{P_{\text{blade}}}{P_{t,\text{passage}}} \right)^{(\gamma+1)/2\gamma} \right) \times \sqrt{\frac{2\gamma}{(\gamma-1)RT_c} \left(\left(\frac{P_{t,\text{passage}}}{P_{\text{blade}}} \right)^{(\gamma-1)/\gamma} - 1 \right)} \quad (4)$$

where P_{blade} is the local static pressure on the blade surface and $P_{t,\text{passage}}$ is the total pressure in the coolant passages. $P_{t,\text{passage}}$ is replaced with the measured static pressure in the coolant passages. The static pressure was measured using 14 static pressure taps on the pressure and suction side inner passage walls located 3.18 mm below the passage top wall. A constant discharge coefficient C_D for all open holes in a loop was assumed for each case (given average blowing ratio and given incidence angle). It should be noted that the constant C_D assumption for all holes in the loop may not be true as C_D depends on not only the geometry but also on the external and internal flow conditions. It was assumed that the deviation in the discharge coefficients from hole to hole is not significant and hence an average value can be assumed without introducing a significant error. By measuring the total mass flow

rate supplied to a coolant loop and the pressures on the blade surface and inside the coolant passages, the discharge coefficient C_D was calculated. The discharge coefficient varies in the range 0.5–0.9 depending on the coolant loop, the average blowing ratio, and the incidence angle. For example, the C_D was 0.67 in loop 1 and 0.71 in loop 2 for $M=1$ at incidence angle $+5^\circ$. Using the calculated discharge coefficient, the coolant mass flow rate and the local blowing ratio for each hole in the loop were determined for a given blowing ratio at a given incidence angle.

Figure 12 shows the local blowing ratios for the tip holes and pressure side holes. For a given incidence angle, the local blowing ratio distributions are low for the first few holes near the leading edge. A bigger high static pressure zone as observed in Fig. 8 may explain this behavior. The local blowing ratio for the PS holes in the second loop gradually decreases (except for $M=0.5$) with increasing chord due to the increase in the mainstream velocity on the pressure side as the flow approaches the throat region. A non-uniform blowing ratio distribution exists between the tip and pressure side holes. The local M_i through the pressure side holes is

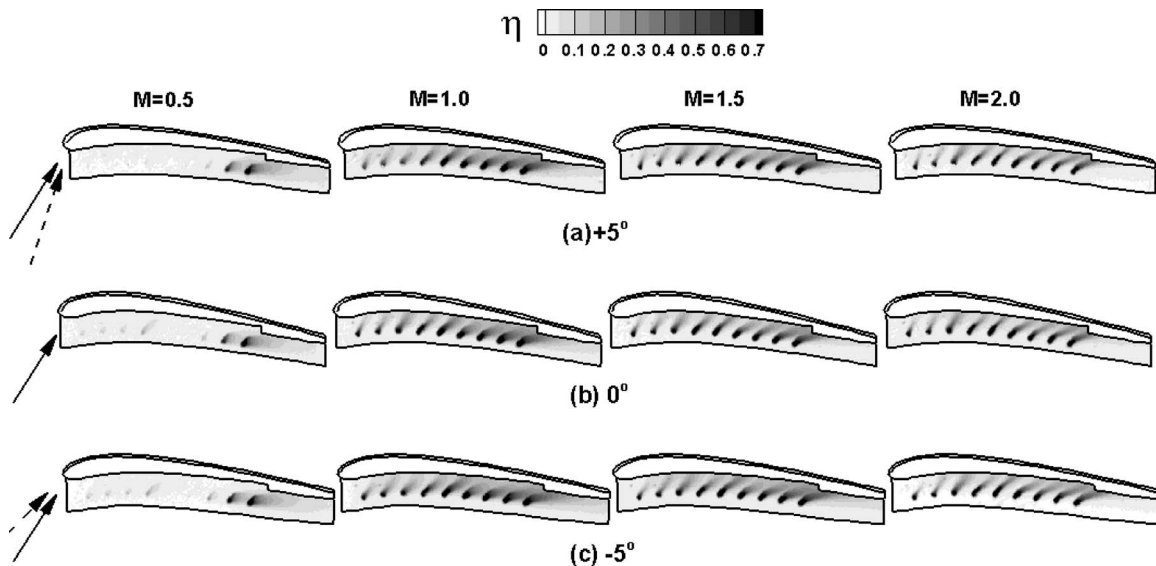


Fig. 13 Film-cooling effectiveness for the near tip pressure side at different incidence angles

higher for higher blowing ratios as compared with tip holes, but at lower blowing ratios, M_i is higher for the tip holes. However, it should be noted that the average mass flow through the tip holes for all blowing ratios is higher than the pressure side holes. In general, the local blowing ratio for the case of incidence angle +5 deg is lower than the other two cases due to its relatively high local velocity. The local blowing ratio distributions for the case of incidence angles 0 deg and -5 deg are similar, particularly for the tip holes.

6 Film-Cooling Effectiveness Results

Figure 13 shows film-cooling effectiveness distribution on the pressure side near tip region. The squealer blade tip with pressure side cutback has a recess of 2.1% of the blade height. The coolant was ejected from both the tip holes and the pressure side holes. The results for the incidence angles -5 deg, 0 deg, and +5 deg are shown in rows while the results for the four blowing ratios of $M=0.5$, 1.0, 1.5, and 2.0 are arranged in a columnwise fashion.

On the pressure side near tip region, blowing ratio of 1.0 gives better effectiveness distribution than $M=1.5$ and $M=2.0$ due to

more coolant spread, although the effectiveness levels are comparable for all three blowing ratios. High film-cooling effectiveness is observed in the region from the midchord to the trailing edge. The compound angled shaped holes provide excellent film coverage. For all the blowing ratios considered, the effectiveness near the leading edge holes is lower due to the higher static pressure near the leading edge of the blade; less coolant ejects through these holes. This is quite apparent at $M=0.5$, where the cooling effectiveness is almost negligible near the upstream holes. More coolant is diverted to the tip holes as observed from the local blowing ratio distributions in Fig. 12. Some mainstream ingestion may also occur for the first three pressure side holes at $M=0.5$. This is more obvious for the case of incidence angle +5 deg as the coolant streak is not observed from the pressure side holes in the first coolant loop. The incidence angle effect on the effectiveness magnitude for the pressure side film cooling is not significant. The effectiveness for the three incidence angles is about the same, except for the slight difference occurring to the four holes in the first coolant loop at a blowing ratio of 1.0. Although the effectiveness level is almost unchanged, the coolant jet direction

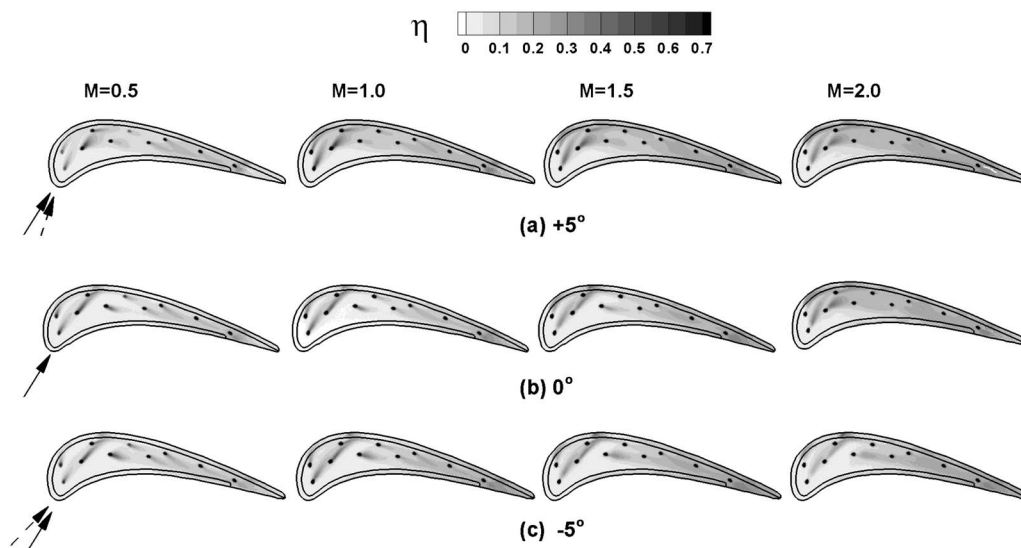


Fig. 14 Film-cooling effectiveness on the blade tip at different incidence angles

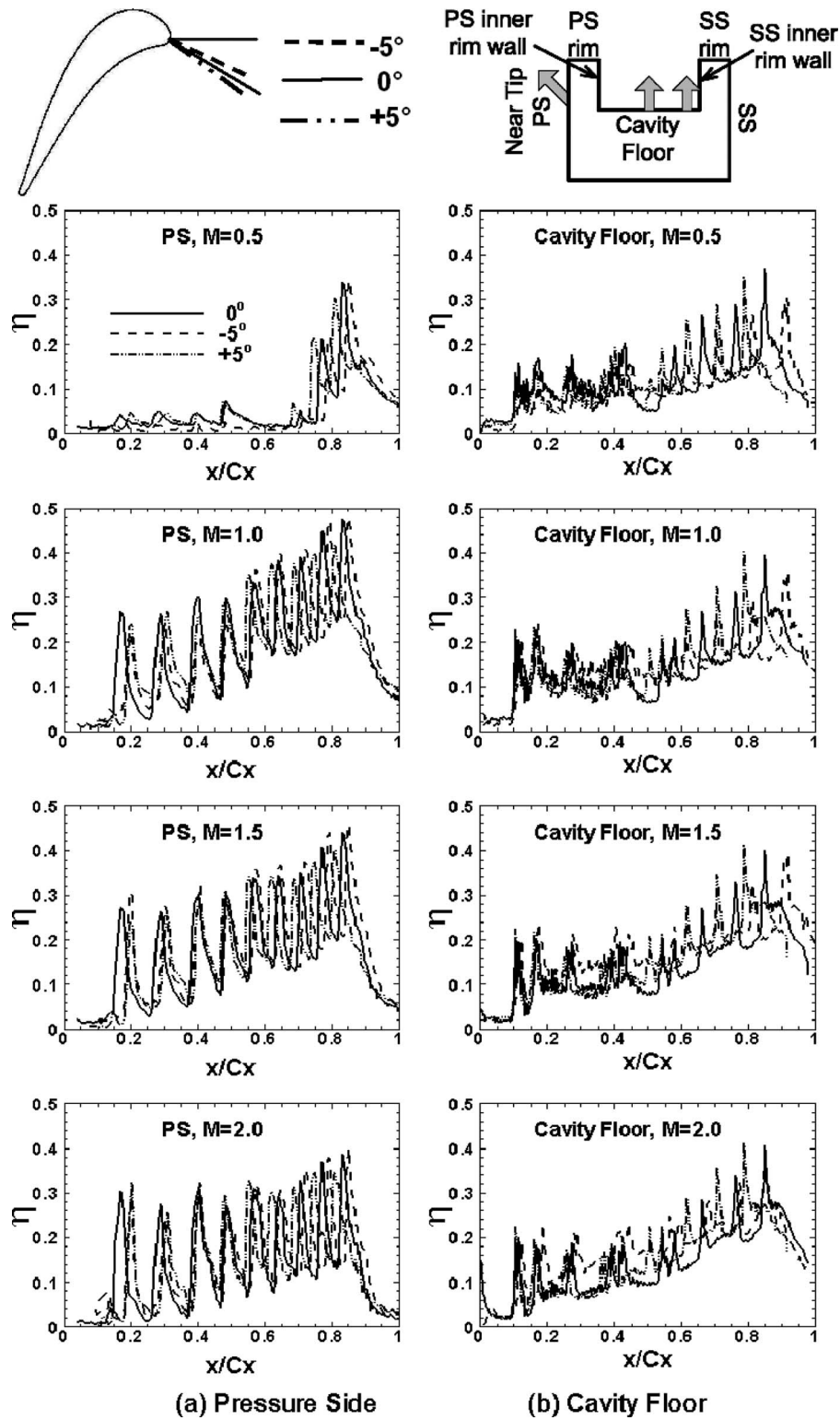


Fig. 15 Laterally averaged film-cooling effectiveness on the pressure side and cavity floor

is altered at different incidence angles. The coolant jets are deflected toward the trailing edge. As the incidence angle varies from +5 deg to 0 deg and -5 deg, the jet deflection is slightly increased. At incident angle -5 deg, the coolant jet is pushed more toward the trailing edge. This is more apparent for the coolant jets from the three radial shaped holes. In the range of this study, the incident angle change seems only slightly altering the

coolant streak on the pressure side film cooling. Larger effect on the pressure side film cooling may be observed when the off-design incidence angle changes more than ± 5 deg.

Figure 14 shows the effectiveness results on squealer rims and cavity floor. On the cavity floor, the film coverage is seen to be improving with the blowing ratio. Increasing the blowing ratio from 1.5 to 2.0, the increase in effectiveness level is not signifi-

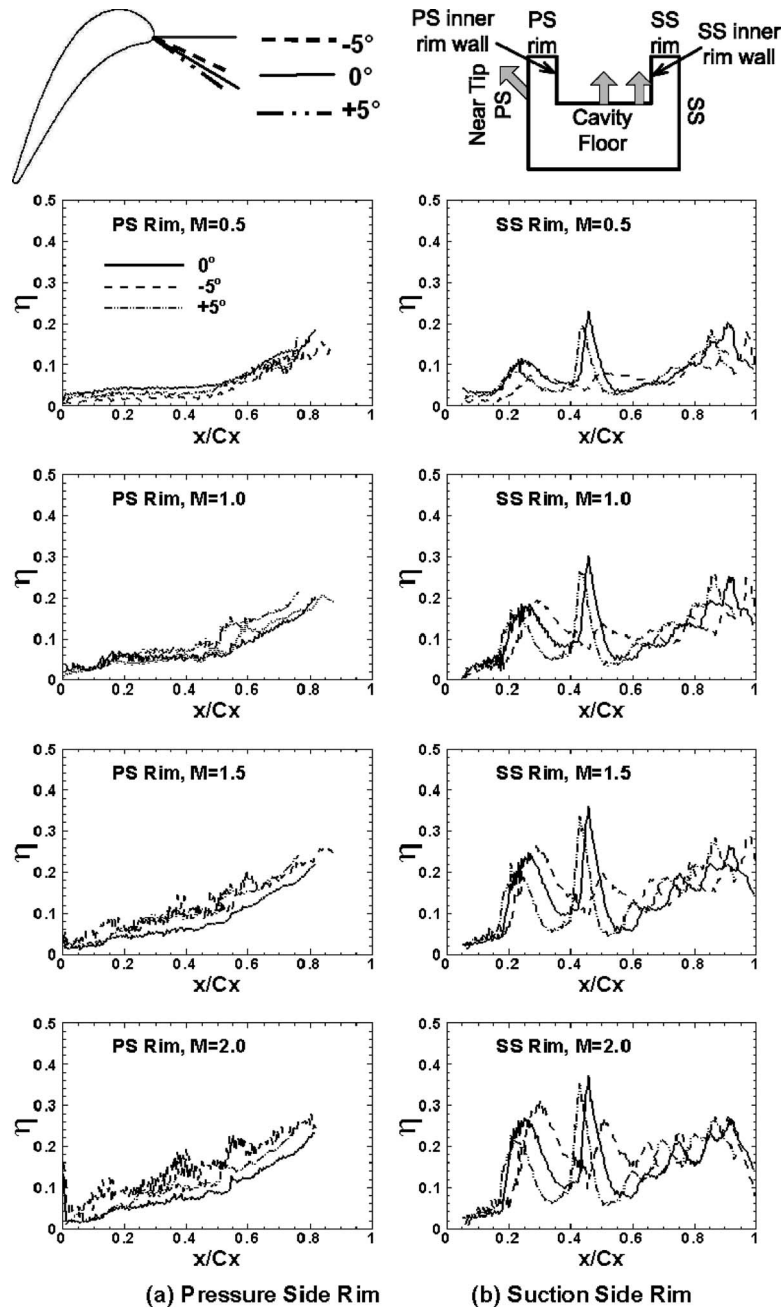


Fig. 16 Laterally averaged film-cooling effectiveness on the pressure side rim and suction side rim

cant. Jet lift off is observed around the holes near the leading edge at a blowing ratio of 2.0 for incidence angles -5° and 0° . Lift off is indicated by a region of low effectiveness immediately downstream of the hole. The local blowing ratio for $+5^\circ$ is relatively low, so the coolant jets stay attached to the tip surface. Due to upstream coolant accumulation, the jet lift off is not observed from midchord to the trailing edge. The incidence angle effect can be detected by observing the coolant flow direction. It can be seen from the CFD prediction in Fig. 9 that, in the squealer cavity, the flow separation and reattachment occur in the leading edge region and flow is recirculated in the midchord to the trailing edge. In the leading edge portion, it is observed in Fig. 14 that the region between the pressure side and the first two/three camber holes (or the third off-camber line hole) is not covered by the coolant. It can be conjectured that the flow separation and reattachment may happen in this region. The leakage flow goes to the

suction side after flow reattachment, so the coolant jets are directed toward the suction side. When the incidence angles change, the flow reattachment location also changes. It seems that the flow reattachment length for $+5^\circ$ is shorter than the other two angles. It takes place between the chamber line and the pressure side. The flow attachment may extend beyond the chamber to the suction side for the angles of 0° and -5° . This results in a relatively larger uncooled area on the cavity floor. Coolant gets accumulated inside the squealer cavity in the region between the midchord and the trailing edge due to flow recirculation in the contracting squealer passage. For the positive incidence angle, the leakage flow is stronger; the flow recirculation inside the cavity is enhanced. The coolant is more entrained and dispersed in the tip cavity to enhance film-cooling effectiveness over the cavity floor. The leakage flow also carries the coolant from the pressure side to

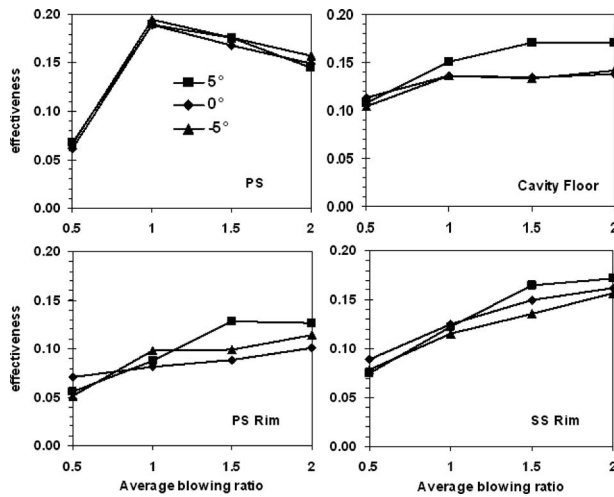


Fig. 17 Area averaged film-cooling effectiveness

the tip region and from the cavity to the suction side at higher blowing ratios; thus, pressure side squealer rim, as well as the suction side rim, is also cooled.

6.1 Averaged Film-Cooling Effectiveness Results. Figures 15 and 16 show the comparison of averaged film-cooling effectiveness obtained from the three incidence angles along the axial chord. The averaged values are obtained by averaging the effectiveness magnitudes at a given x/C_x location. In general, the average effectiveness increases with increasing axial chord distance for all surfaces. Figure 15(a) shows the averaged effectiveness on the pressure side near tip region. The averaged results were obtained by averaging from the base of the hole to the tip. At $M=0.5$, the effectiveness is very low for $x/C_x < 0.7$ for all the incidence angles as there is little coolant jet coming out the holes. For a given blowing ratio, there is no notable difference in effectiveness magnitude among the three angles; while the peak of average effectiveness is shifted after the midchord. The peak tends to shift upstream and downstream at -5 deg and $+5$ deg, respectively, when $x/C_x > 0.5$. The peak shift is not evident when $x/C_x > 0.5$ except for the first jet.

Figure 15(b) shows the averaged effectiveness on the cavity floor. Taking effectiveness at 0 deg as the baseline, the jet shift starts at the fourth peak, which corresponds to the area where the flow reattachment behaves differently for the three angles. The peak tends to shift to the trailing edge at a positive incidence angle and to the leading edge at a negative incidence angle. This trend is obvious for all blowing ratios. The averaged effectiveness increase is observed for a positive incidence angle. The increase in effectiveness for $+5$ deg was found on the contour plot and it will be seen in the area-averaged effectiveness again.

Figure 16(a) shows the averaged effectiveness on the pressure side rim. It can be seen that effectiveness increases along the chord length. Higher blowing ratio gives higher effectiveness. The effectiveness magnitude for the three incidence angles is comparable.

Figure 16(b) shows the averaged effectiveness on the suction side rim. Increasing the blowing ratio, the effectiveness increases as more coolant is carried over to the suction side. The effectiveness peak shifts upstream and downstream for -5 deg and $+5$ deg incidence angles, respectively. This peak shifting implies the change of leakage flow resulting from different incidence angles.

Figure 17 shows the area-averaged film-cooling effectiveness. For pressure side near tip regions, it can be seen that $M=1.0$ gives the highest averaged film-cooling effectiveness. The effect from the incidence angle in the range of study is not significant. For the

cavity floor, the positive incidence angle gives higher average effectiveness at higher blowing ratios. The enhancement is up to 25% at $M=1.5$ for an incidence angle of $+5$ deg. For the pressure side rim and the suction side rim, incidence angle $+5$ deg shows a slightly higher average effectiveness over the other cases when blowing ratio is greater than 1.5. The angle effect on the effectiveness magnitude is more observable on the cavity floor at the $+5$ deg positive incidence angle. On the whole, the overall film-cooling effectiveness for the tip region is small.

7 Conclusions

An experimental study has been performed to investigate the incidence angle effect on blade tip film cooling. Film-cooling effectiveness has been measured for a cutback squealer tip at three incidence angles using pressure sensitive paint. The effectiveness distribution was presented for the cavity floor and the pressure side near tip region. As the PSP technique eliminates the conduction error in effectiveness measurement, reliable effectiveness data were also obtained and presented for the narrow pressure side squealer rim tip and the suction side rim tip.

In general, the incidence angle affects the coolant jet direction on the pressure side near tip region and blade tip. The film-cooling effectiveness distribution is altered. The peak of laterally averaged effectiveness is shifted upstream or downstream depending on the off-design incidence angles. However, the overall area-averaged film-cooling effectiveness is not significantly changed by the incidence angles in the range of study. The coolant jets from the pressure side holes are deflected by the mainstream. As the incidence angle varies from $+5$ deg to 0 deg and -5 deg, the deflection is increased slightly. This causes the peak of laterally averaged effectiveness to shift; however, the area-averaged cooling effectiveness on the pressure side is not affected much by the jet deflection and peak shifting.

The coolant jet spreads more on the cavity floor at the positive incidence angle and results in relatively high and uniform film coverage on the cavity floor. The peak of effectiveness is shifted upstream for negative incidence angle and downstream for positive angle when x/C_x is greater than 0.4. The film-cooling effectiveness in the cavity floor can be increased up to 25% for the positive incidence angle.

In addition to film-cooling effectiveness data, heat transfer coefficients should be measured in order to provide more complete information for blade tip film-cooling performance assessment. The effect of incidence angle on the blade tip film cooling is observed; however, the influence is not strong in the range of study. A study of a larger off-design angle may be required to observe more pronounced incidence angle effect.

Acknowledgment

This work has been funded through the Marcus Easterling Endowment Fund.

Nomenclature

- C = concentration of oxygen
- C_D = discharge coefficient
- C_x = axial chord length of the blade (8.61 cm)
- d = diameter of film-cooling holes
- I = pixel intensity for an image
- L = length of film-cooling hole
- M = average blowing ratio ($=\rho_c V_c / \rho_m V_m$)
- M_i = local blowing ratio ($=\rho_c V_{c,local} / \rho_m V_m$)
- P = local static pressure
- P_t = total pressure
- P_{O_2} = partial pressure of oxygen
- T_c = temperature of coolant at loop inlet
- T_m = temperature of mainstream
- Tu = turbulence intensity level at the cascade inlet
- x = axial distance

V_m = local mainstream velocity at hole location
 V_c = coolant velocity
 η = local film-cooling effectiveness
 ρ_c = density of coolant air
 ρ_m = density of mainstream air
 θ = dimensionless temperature $(= (T - T_c) / (T_m - T_c))$

Subscripts

air = mainstream air with air as coolant
 mix = mainstream air with nitrogen as coolant
 ref = reference image with no mainstream and coolant flow
 blk = image without illumination (black)

References

- [1] Bunker, R., 2006, "Axial Turbine Blade Tips: Function, Design, and Durability," *J. Propul. Power*, **22**(2), pp. 271–285.
- [2] Kim, Y. W., and Metzger, D. E., 1995, "Heat Transfer and Effectiveness on Film Cooled Turbine Blade Tip Model," *ASME J. Turbomach.*, **117**, pp. 12–21.
- [3] Kim, Y. W., Downs, J. P., Soechting, F. O., Abdel-Messeh, W., Steuber, G. D., and Tanrikut, S., 1995, "A Summary of the Cooled Turbine Blade Tip Heat Transfer and Film Effectiveness Investigations Performed by Dr. D. E. Metzger," *ASME J. Turbomach.*, **117**, pp. 1–11.
- [4] Kwak, J. S., and Han, J. C., 2002, "Heat Transfer Coefficient and Film-Cooling Effectiveness on a Gas Turbine Blade Tip," ASME Paper No. GT-2002-30194.
- [5] Kwak, J. S., and Han, J. C., 2002, "Heat Transfer Coefficient and Film-Cooling Effectiveness on the Squealer Tip of a Gas Turbine Blade," ASME Paper No. GT-2002-30555.
- [6] Ahn, J., Mhetras, S. P., and Han, J. C., 2004, "Film-Cooling Effectiveness on a Gas Turbine Blade Tip," ASME Paper No. GT-2004-53249.
- [7] Christophel, J. R., Thole, K. A., and Cunha, F. J., 2004, "Cooling the Tip of a Turbine Blade Using Pressure Side Holes, Part I: Adiabatic Effectiveness Measurements," ASME Paper No. GT-2004-53249.
- [8] Christophel, J. R., Thole, K. A., and Cunha, F. J., 2004, "Cooling the Tip of a Turbine Blade Using Pressure Side Holes, Part II: Heat Transfer Measurements," ASME Paper No. GT-2004-53254.
- [9] Mhetras, S. H., Yang, H., Gao, Z., and Han, J., 2006, "Film-Cooling Effectiveness on Squealer Cavity and Rim Walls of Gas-Turbine Blade Tip," *J. Propul. Power*, **22**(4), pp. 889–899.
- [10] Mhetras, S., Narzary, D., Gao, Z., and Han, J., 2006, "Effect of a Cutback Squealer and Cavity Depth on Film Cooling Effectiveness for a Gas Turbine Blade Tip," AIAA Paper No. 2006-3404.
- [11] Bunker, R. S., Baily, J. C., and Ameri, A. A., 2000, "Heat Transfer and Flow on the First Stage Blade Tip of a Power Generation Gas Turbine: Part I: Experimental Results," *ASME J. Turbomach.*, **122**, pp. 263–271.
- [12] Azad, G. M. S., Han, J. C., Teng, S., and Boyle, R., 2000, "Heat Transfer and Pressure Distributions on a Gas Turbine Blade Tip," *ASME J. Turbomach.*, **122**, pp. 717–724.
- [13] Azad, G. M. S., Han, J. C., and Boyle, R., 2000, "Heat Transfer and Pressure Distributions on the Squealer Tip of a Gas Turbine Blade," *ASME J. Turbomach.*, **122**, pp. 725–732.
- [14] Bunker, R. S., and Baily, J. C., 2001, "Effect of Squealer Cavity Depth and Oxidation on Turbine Blade Tip Heat Transfer," ASME Paper No. 2001-GT-0155.
- [15] Azad, G. M. S., Han, J. C., Bunker, R. S., and Lee, C. P., 2002, "Effect of Squealer Geometry Arrangement on a Gas Turbine Blade Tip Heat Transfer," *ASME J. Heat Transfer*, **124**, pp. 452–459.
- [16] Kwak, J. S., Ahn, J., Han, J. C., Pang Lee, C., Bunker, R. S., Boyle, R., and Gaugler, R., 2002, "Heat Transfer Coefficients on Squealer Tip and Near Tip Regions of a Gas Turbine Blade With Single or Double Squealer," ASME Paper No. GT-2003-38907.
- [17] Kwak, J. S., and Han, J. C., 2003, "Heat Transfer Coefficient on a Gas Turbine Blade Tip and Near Tip Regions," *J. Thermophys. Heat Transfer*, **17**(3), pp. 297–303.
- [18] Kwak, J. S., and Han, J. C., 2003, "Heat Transfer Coefficient on the Squealer Tip and Near Squealer Tip Regions of a Gas Turbine Blade," *ASME J. Heat Transfer*, **125**, pp. 669–677.
- [19] Ameri, A. A., Steinhilber, E., and Rigby, L. D., 1999, "Effects of Tip Clearance and Casing Recess on Heat Transfer and Stage Efficiency in Axial Turbines," *ASME J. Turbomach.*, **121**, pp. 683–693.
- [20] Ameri, A. A., and Rigby, D. L., 1999, "A Numerical Analysis of Heat Transfer and Effectiveness on Film Cooled Turbine Blade Tip Models," NASA Technical Report No. CR-1999-209165.
- [21] Ameri, A. A., and Bunker, R. S., 2000, "Heat Transfer and Flow on the First Stage Blade Tip of a Power Generation Gas Turbine: Part II: Simulation Results," *ASME J. Turbomach.*, **122**, pp. 272–277.
- [22] Yang, H., Chen, H. C., and Han, J. C., 2004, "Numerical Prediction of Film Cooling and Heat Transfer With Different Film Hole Arrangements on the Plane and Squealer Tip of a Gas Turbine Blade," ASME Paper No. 2004-GT-53199.
- [23] Metzger, D. E., Dunn, M. G., and Hah, C., 1991, "Turbine Tip and Shroud Heat Transfer," *ASME J. Turbomach.*, **113**, pp. 502–507.
- [24] Dunn, M. G., and Haldeman, C. W., 2000, "Time-Averaged Heat Flux for a Recessed Tip, Lip, and Platform of a Transonic Turbine Blade," *ASME J. Turbomach.*, **122**, pp. 692–697.
- [25] Rhee, D., and Cho, H., 2006, "Local Heat/Mass Transfer Characteristics on a Rotating Blade With Flat Tip in Low-Speed Annular Cascade, Part I: Near Tip Surface," *ASME J. Turbomach.*, **128**, pp. 96–109.
- [26] Rhee, D., and Cho, H., 2006, "Local Heat/Mass Transfer Characteristics on a Rotating Blade With Flat Tip in Low-Speed Annular Cascade, Part II: Tip and Shroud," *ASME J. Turbomach.*, **128**, pp. 110–119.
- [27] Halila, E. E., Lenahan, D. T., and Thomas, T. T., 1982, "Energy Efficient Engine," General Electric Company, NASA, Report No. CR-167955.
- [28] Wright, L. M., Gao, Z., Varvel, T. A., and Han, J. C., 2005, "Assessment of Steady State PSP, TSP and IR Measurement Techniques for Flat Plate Film Cooling," ASME Paper No. HT-2005-72363.
- [29] Coleman, H. W., and Steele, W. G., 1989, *Experimentation and Uncertainty Analysis for Engineers*, Wiley, New York.
- [30] Gritsch, M., Schulz, A., and Wittig, S., 1997, "Discharge Coefficient Measurements of Film-Cooling Holes With Expanded Exits," ASME Paper No. 97-GT-165.

A Parametric Study of the Blade Row Interaction in a High Pressure Turbine Stage

G. Persico

e-mail: giacomo.persico@polimi.it

P. Gaetani

C. Osnaghi

Dipartimento di Energia,
Politecnico di Milano,
Via la Masa 34,
Milano 20158, Italy

An extensive experimental analysis on the subject of the unsteady periodic flow in a high subsonic high pressure (HP) turbine stage has been carried out at the Laboratorio di Fluidodinamica delle Macchine of the Politecnico di Milano (Italy). In this paper the aerodynamic blade row interaction in HP turbines, enforced by increasing the stator and rotor blade loading and by reducing the stator-rotor axial gap, is studied in detail. The time-averaged three-dimensional flowfield in the stator-rotor gap was investigated by means of a conventional five-hole probe for the nominal (0 deg) and highly positive (+22 deg) stator incidences. The evolution of the viscous flow structures downstream of the stator is presented to characterize the rotor incoming flow. The blade row interaction was evaluated on the basis of unsteady aerodynamic measurements at the rotor exit, performed with a fast-response aerodynamic pressure probe. Results show a strong dependence of the time-averaged and phase-resolved flowfield and of the stage performance on the stator incidence. The structure of the vortex-blade interaction changes significantly as the magnitude of the rotor-inlet vortices increases, and very different residual traces of the stator secondary flows are found downstream of the rotor. On the contrary, the increase in rotor loading enhances the unsteadiness in the rotor secondary flows but has a little effect on the vortex-vortex interaction. For the large axial gap, a reduction of stator-related effects at the rotor exit is encountered when the stator incidence is increased as a result of the different mixing rate within the cascade gap.

[DOI: 10.1115/1.2987236]

1 Introduction

The flow downstream of a subsonic turbine cascade is not uniform in space due to potential effects, wakes, and secondary flows. The relative motion between axially adjacent blade rows makes intrinsically unsteady the interaction of these flow structures with the downstream blade row, resulting in a complex unsteady 3D flowfield downstream of a turbine stage.

In subsonic turbine stages the main aspects of the two-dimensional stator-rotor interaction are related to the cascade potential field and to the blade wake. In the relative frame, the stator wake velocity defect results in a slip velocity component directed toward the suction side of the rotor blade, which activates a migration in the rotor suction side boundary layer and finally in the rotor wake (wake rectification). The bowing, the chopping, and the shearing of the stator wake during its convection inside the rotor channel have been highlighted in both numerical [1] and experimental [2] investigations.

The wake-blade interaction can play only a marginal role if, as usual in HP turbines, low aspect-ratio blades are encountered: In this case the major loss mechanisms are related to the endwall secondary vortices. The vortex-blade interaction is the core of the stator-rotor interaction studies in HP subsonic turbines. Early studies [3] and more recent analyses [4–6] showed that upstream secondary vortices are convected inside the channel and then released at the stage exit, modifying the under-/overtopping of the flow. It is commonly accepted that an incoming vortex tube behaves like a wake inside a rotor channel; the vortex filament is bowed and re-oriented inside the channel degenerating in two counter-rotating legs called pressure side (PS) leg or suction side

(SS) leg depending on their distance from the airfoil sides. The question on the results of the vortex-blade interaction downstream of the rotor has still not been answered satisfactorily as it can be inferred by the different results documented in Refs. [4] and [5]. Since several scenarios can appear downstream of a HP turbine rotor, parametric analyses are now required to shed some light on the combination of the several effects that affect the rotor aerodynamics and on the reasons why some structures prevail over others. To the knowledge of the authors, similar studies are still not available in literature. In recent papers of the present authors [7,8] the unsteady flow downstream of a HP turbine rotor was investigated at nominal conditions and for a very large axial gap (Case 0).

In the present paper a parametric study of the wake-blade and vortex-blade interactions is proposed by the following:

- increasing the stator loading (Case 1) and thus enhancing the rotor-inlet unsteadiness
- increasing both the stator and rotor loading (Case 2)
- increasing the stator loading and the stator-rotor axial gap (Case 3); the axial gap is increased from the nominal one (equal to the 35% of the stator axial chord and roughly equal to the stator throat) to the very high value of 100% of the stator axial chord to minimize the stator flow effects at the rotor inlet

A summary of the different test cases is given in Table 1.

2 Experimental Approach

The test campaign was carried out in the closed loop test rig for axial and centrifugal turbomachines located at the Laboratorio di Fluidodinamica delle Macchine (LFM) of the Politecnico di Milano. Full details on the test rig, on the axial turbine stage, on the measurement technique, and on the data reduction method can be

Contributed by the International Gas Turbine Institute of ASME for publication in the JOURNAL OF TURBOMACHINERY. Manuscript received July 18, 2007; final manuscript received April 4, 2008; published online April 8, 2009. Review conducted by Dilip Prasad. Paper presented at the ASME Turbo Expo 2007: Land, Sea and Air (GT 2007), Montreal, QC, Canada, May 14–17, 2007.

Table 1 Summary of the test cases

Case	rpm	I_s (deg)	x_{gap}/b_s
Nominal	6800	0	0.35
Case 0	6800	0	1.00
Case 1	6800	22	0.35
Case 2	5800	22	0.35
Case 3	6800	22	1.00

found in Ref. [9]. The main geometrical features and operating conditions of the axial HP turbine stage are recalled in Table 2 and a meridional cut is provided in Fig. 1.

The measurement grid downstream of the stator consists of 1920 points at two axial distances of 35% and 60% of the stator axial chord from the stator trailing edge. The measurement grid at the rotor exit (TR) grid, located at 20% of the rotor axial chord downstream of the stage, is composed of 624 points.

The stator incidence was changed by rotating the centripetal inlet guide vane placed upstream of the turbine stage. A rotor blade incidence increase of 15 deg was enforced by reducing the rotational speed from 6800 rpm (nominal) to 5800 rpm.

Table 2 LFM axial flow turbine stage: Main geometrical and operational characteristics

Expansion ratio	1.40					
Flow rate	3.65 kg/s					
Hub diameter	300 mm					
Tip diameter	400 mm					
Axial gaps	0.35 b_s ; 1.00 b_s					
	Vaness Vane lean=12 deg			Blades BPF=2.83 kHz		
Profiles No.	22			25		
Out. Mach No.	0.55			0.2(abs)–0.45(rel)		
Reynolds No.	750,000			600,000 (rel)		
Radial clearance (mm)	0.15			0.75		
Axial chord (b) (mm)	30.6			46.7		
	Hub	MS	Tip	Hub	MS	Tip
Pitch/axial chord	1.39	1.6	1.86	0.80	0.94	1.07
Inlet geom. angle (deg)	72.5	75.2	77.5	56.9	47.6	25.5
Out. geom. angle (deg)					–67.7	

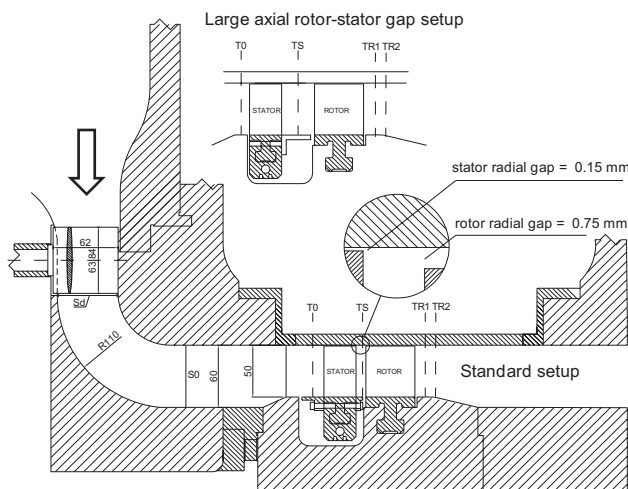


Fig. 1 LFM axial section meridional cut; TS and TR (referred as TR1) are reported

Steady 3D aerodynamic measurements were performed by means of a conventional miniaturized five-hole probe whose accuracy is $\pm 0.5\%$ of the dynamic head for the pressure measurements and ± 0.3 deg for the angle measurements in a wide range of Mach numbers (0.2–1). Steady total temperature measurements were performed upstream and downstream of the stage by means of a thermocouple, whose accuracy is ± 0.25 K.

Unsteady measurements were carried out by means of a cylindrical single-hole fast-response aerodynamic pressure probe, whose diameter is 1.85 mm. The probe is used in a pseudo-three-sensor operational mode to derive the two-dimensional phase-resolved flow. Total and static pressure and flow angle in the blade-to-blade plane (α) are then achieved; the α angle is defined from the axial direction and it is taken positive if directed according to the peripheral velocity. Streamwise vortices can be identified on the basis of the blade-to-blade flow angle by the use of the Rankine vortex model. The probe aerodynamic accuracy is $\pm 0.5\%$ of the dynamic head for the pressure measurements and ± 0.5 deg for α , over a wide Mach number range (0.15–0.6). Full details on the probe development and calibration can be found in Refs. [10] and [11].

The instantaneous pressure signals are acquired at 1 MHz for a period of 1 s to get a good statistical reliability. The raw pressure data are digitally compensated by using the experimental transfer function, phase-locked to the rotor wheel and then phase-averaged to obtain 40 intervals on a single rotor BPP; at this point the flow properties are derived. The relative quantities are calculated from the absolute ones using the time-averaged total temperature. Results are displayed as instantaneous snapshots of the rotor flow in the relative frame at different stator phases; the information included in the snapshots is summarized in the mean rotor flow in the relative frame and in a periodic RMS between the instantaneous and mean snapshots. It is to be noted that this periodic RMS is not a random quantity linked to turbulence. Since in the relative frame the periodic unsteadiness is given by the traces of the stator flowfield downstream of the stage, the periodic RMS estimates the amplitude of the stator-induced periodic fluctuations at the rotor exit. Thus high RMS regions mark the persistence of stator effects and flow structures downstream of the stage.

3 Stator-Exit Absolute Flowfield

Steady measurements between the two rows were performed in several planes located from $x/b_s=0.16$ at the nominal rpm condition both for an incidence of 0 deg and of +22 deg; for the aim of this paper, only the two planes at 35% and 60% of b_s will be briefly discussed while more details can be found in Ref. [7]. Figure 2 provides a general overview of the main flow features for the Nominal Case and Cases 0, 1, and 3, in terms of total pressure loss and streamwise vorticity.

First the nominal configuration (Fig. 2(a)) is discussed. Contours on the loss map clearly evidence the wake, identified by the loss region extending from $\theta/\Delta\theta_s=0.5$ at the hub to $\theta/\Delta\theta_s=0.7$ at the tip; the circumferential distortion of the wake is due to the spanwise gradients of circumferential velocity and to the secondary phenomena next to the endwalls. Three high loss regions (I, II, and III in Fig. 2) are underlined: Regions I and II are related to the secondary flow activity while the third one, showing the highest loss values of the whole measuring plane ($Y=0.42$), is the result of the high dissipation experienced by the flow leaking in the vane tip clearance (see Table 2 and Fig. 1).

The vorticity map, used to identify the stator secondary flows and thus the vortex structures entering the rotor row, shows significant vortical structures only in the hub region, namely, the passage and shed vortices. At the bottom grid border a small core of negative vorticity is probably the trace of the hub corner vortex (CV). Only a weak passage vortex can be acknowledged in the tip region. The relevant asymmetry of the secondary effects on the blade passage is due to the radial pressure gradient acting downstream of the stator, which pulls the low momentum regions to-

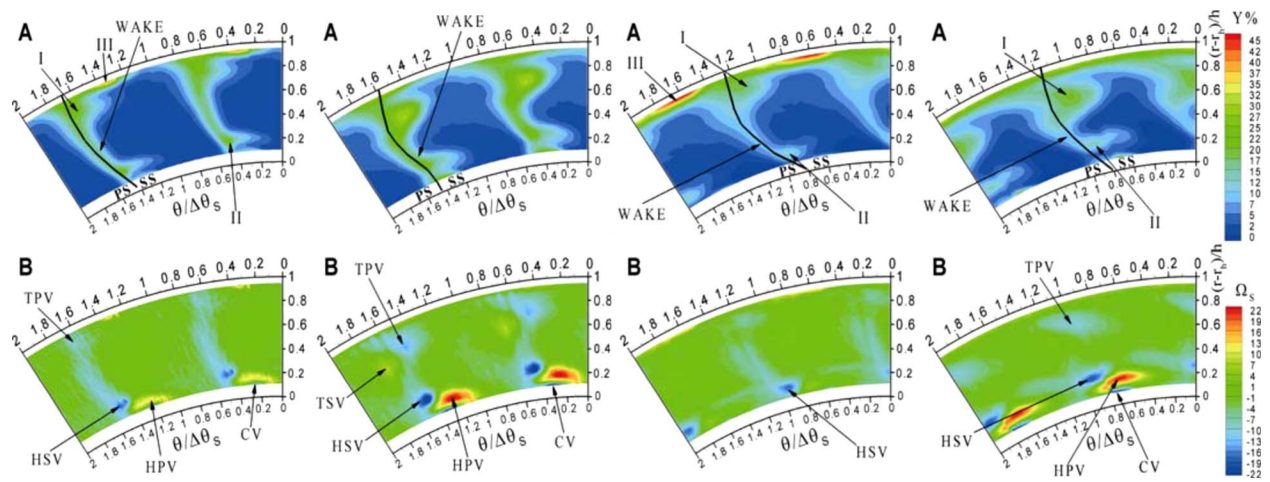


Fig. 2 Steady stator-exit flowfield. Left to right: Nominal Case, Case 1, Case 0, and Case 3. (a) Y and (b) Ω .

ward the hub strengthening the hub loss structures and smearing the tip ones, and to the stator leaned geometry, which activates strong radial flows from the tip to the hub even in the freestream.

The results for high stator incidence are reported in Fig. 2(b). Despite some similarities in the wake shape and in the secondary flow structure, relevant differences arise due to the increase in the stator loading. The wake is much more distorted and the loss cores are wider and more intense due to the action of stronger secondary flows. In particular, it is worth underlining that the effect of the loading is much stronger on the magnitude of the passage vortex, which is doubled with respect to the one measured in the nominal case than on the magnitude of the shed vortex. In leaned blades a contribution to the generation of the shed vorticity is given by the leaned geometry itself [12], while the passage vortex directly depends on the flow turning. As a consequence, in Case 1, two opposite vorticity cores of similar intensity enter the rotor row at the hub, while in the nominal case the hub shed vorticity is significantly stronger.

Moreover increasing the stator loading the tip passage and shed vortices appear as weak but distinct structures, instead of being smeared as found in the nominal case. Also the hub corner vortex is much stronger for the action of a stronger passage vortex. The loss peak related to the stator tip leakage flow is no longer visible for positive stator incidence, as a consequence of the interaction of the leakage flow with the tip passage vortex, which spreads the low momentum fluid in the outer part of the channel.

Since reducing the rpm (Case 2) the stator-exit flowfield does not show significant differences in terms of Y and Ω with respect to Case 1, it is not extensively reported here.

The effect of the streamwise mixing upstream of the rotor is relevant, as visible in the two right frames in Fig. 2 where the stator-exit flowfield for Cases 0 and 3 are reported at $x/b_s=0.6$ (the farthest measuring section). The streamwise evolution bows and diffuses the stator wake, like the tip loss core linked to the secondary flows (almost smeared as visible from the Ω). The huge growth of the casing endwall boundary layer, in comparison with the hub one, is caused by the stator blade leaning that increases the loading and the deflection of the flow in the outer part of the channel [7]. A weaker mixing process is experienced by the hub secondary flows: For Case 0 the shed vortex still remains a well defined structure, and for Case 3 the system of three counter-rotating vortices still exists at $x/b_s=0.6$. The mixing process being not fully developed, a further dissipation could occur between this plane and the rotor leading edge, which is placed at $x/b_s=1.00$.

In Fig. 3 the pitchwise averages of some flow quantities are reported to provide more information on the difference encountered in the various cases. Between the nominal and the first cases the over-/underturning phenomena, the mean deviation angle, and the losses increase, as commonly happens in linear cascade tests with increased blade loading; as a consequence the mass-averaged loss evaluated on the whole plane rises from 5.2% in the nominal case to 7.8% in Case 1. The nonsymmetric profiles around mid-span are due to the annular and leaned stator geometry. As the streamwise mixing develops (Cases 0 and 3), the loss significantly increases at the tip, while the decrease in loss visible below mid-span for both cases is due to the radial inward transport of high

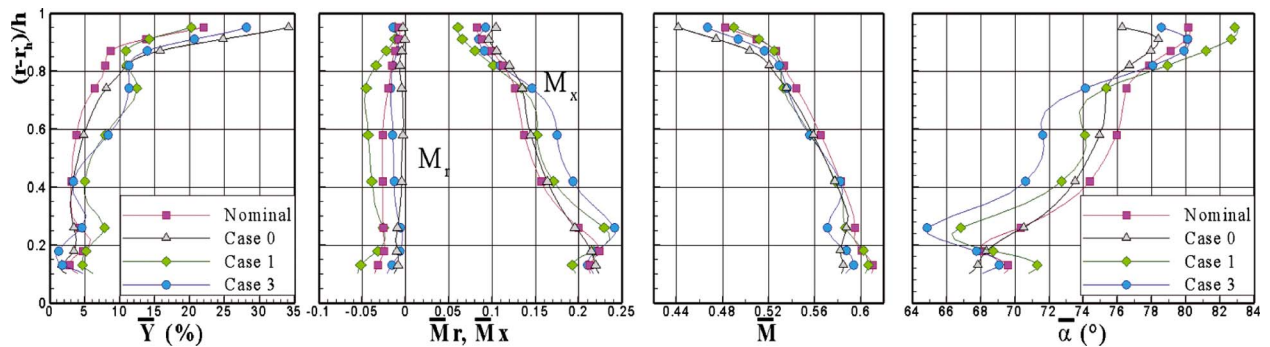


Fig. 3 Radial pitchwise-averaged distributions for the Nominal Case, Case 1, and Case 3. From left to right: total pressure loss (Y), Mach numbers (M_r , M_x , and M), and blade-to-blade flow angle (α).

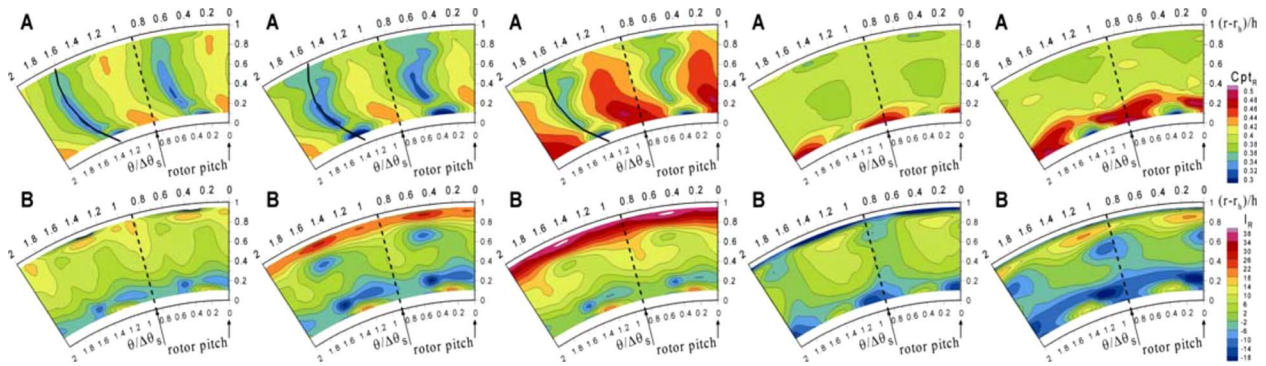


Fig. 4 Rotor-inlet relative flow. Left to right: Nominal Case, Case 1, Case 2, Case 0, and Case 3. (a) Cpt_R and (b) I_R .

energy fluid operated by the radial velocity. Nevertheless, at $x/b_S=0.60$, the overall loss rises up to 6.2% at nominal stator loading (Case 0) and to 8.4% at high stator loading (Case 3).

4 Rotor-Inlet Relative Flowfield

To support the comprehension of the unsteady stage-exit flowfield a complete characterization of the rotor-inlet flow is given by means of the relative total pressure (expressed as Cpt_R) and by the rotor incidence angle (I_R). P_{tR} derives from a complex combination of P_r , P_s , α , and of the peripheral speed; since the direct link from the absolute to the relative total pressure is misleading, the following discussion is crucial to investigate the rotor aerodynamics.

Since the relative quantities are strongly influenced by the rotor rpm, all the cases in Table 1 are reported in Fig. 4; note that all the pitchwise gradients observed in these maps will act as unsteady boundary conditions for the following rotor. The maps of Fig. 4 show quite similar features allowing some general considerations.

First, high pitchwise gradients of Cpt_R are detected as a result of the stator wake (sketched in the Cpt_R maps), which reduces the relative total pressure, and the stator potential field, which locally increases the relative total pressure in the freestream region. The two zones extend spanwise for most of the blade height, but deviate toward the adjacent passage pressure side near the hub, due to the more axial flow direction in this region. A small region of low relative total pressure is also observed at the hub for $\theta/\Delta\theta_S=0.3-0.4$, where the minimum static pressure is found.

The amplitude of the Cpt_R pitchwise fluctuations (i.e., of the inlet total pressure unsteadiness) progressively increases moving from the tip to the hub, a trend enhanced by the increase in stator loading (nominal case/Case 1 and Case 0/Case 3). Above 60% span the increase in stator loading enforces the mixing process downstream of the stator, smearing the wake more than for the nominal case; this is probably due to the leaned shape of the stator blade, which naturally enhances the loading and thus accelerates the mixing in the tip region. At midspan and at the hub, instead, the increase in loading produces an increase in rotor-inlet unsteadiness.

The Cpt_R pitchwise gradients increase along the whole span as the rpm is reduced (Case 1/Case 2, see Ref. [13] for more details on the rpm effect): Increasing the stator and rotor loading the highest Cpt_R inlet unsteadiness is found.

Increasing the stator-rotor axial gap (nominal case/Case 0 and Case 1/Case 3), an almost uniform relative total pressure is found above 40% span, while strong Cpt_R fluctuations are found in the hub region, stronger than that at $x/b_S=0.35$ and higher in the case of increased stator loading.

The rotor incidence angle distribution has a complex shape since secondary vortices, wakes, and the potential field produce local incidence variations. For the nominal case the maximum spanwise gradients (± 15 deg) are encountered above 90% span,

where the stator tip leakage flow affects the flowfield; between 90% and 25% spans the amplitude of the incidence pitchwise fluctuations is almost constant and equal to ± 5 deg, which increases up to ± 10 deg at the hub. Thus the rotor loading in the endwall regions experiences strong unsteady variations as the stator viscous structures are chopped by the rotor leading edge. With increased stator loading (nominal case/Case 1), the rotor incidence experiences higher pitchwise gradients below 80% span. A small constant increase in pitchwise fluctuations (about 2 deg) is detected at and below midspan, while a relevant increase in incidence gradients is found between 60% span and 80% span, mostly due to the stronger tip passage vortex. Very low gradients are found at the tip due to the developed mixing of the stator tip leakage flow upstream of the measuring plane.

A reduction of rpm at high stator loading (Case 1/Case 2) slightly reduces the rotor incidence unsteadiness at all spans (the opposite of what happens for Cpt_R), being still higher than that found in the nominal case.

In Case 0 the rotor incidence angle experiences a strong pitchwise fluctuation of ± 20 deg at the endwall, while at the midpart of the channel (20–80% span) the fluctuation reduces to ± 10 deg. Increasing the stator loading (Case 3), the strengthening of the secondary flows enhances the rotor incidence unsteadiness at the endwalls, while smaller fluctuations (± 5 deg) are found in the midpart of the channel.

The pitchwise-averaged quantities, reported in Fig. 5, show the most important effect of the variation in the operating conditions. The increase in stator incidence induces lower Cpt_R in the endwall regions (mainly at the tip) due to the high loss level, while the reduction in the rotational speed increases the <0.50 with Cpt_R , mainly at the hub. For Cases 0 and 3 the relative velocity further increases at the hub, resulting in the highest Cpt_R values.

The rotor incidence angle undergoes a general reduction as the stator incidence increases, due to the increase in deviation angle, with an exception at the endwalls where the secondary deviation prevails. On the contrary, as the rotor rpm is reduced (Case 2) the incidence angle increases. The mean rotor incidence angle further

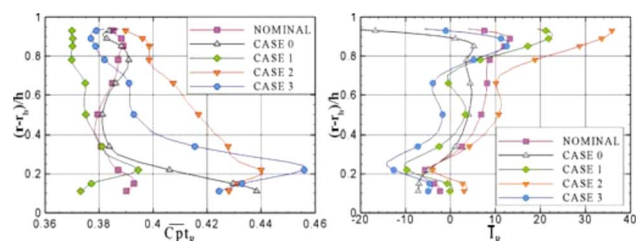


Fig. 5 Pitchwise averaged Cpt_R (left) and I_R (right) at the rotor inlet in the Nominal, 0, 1, 2, and 3 Cases

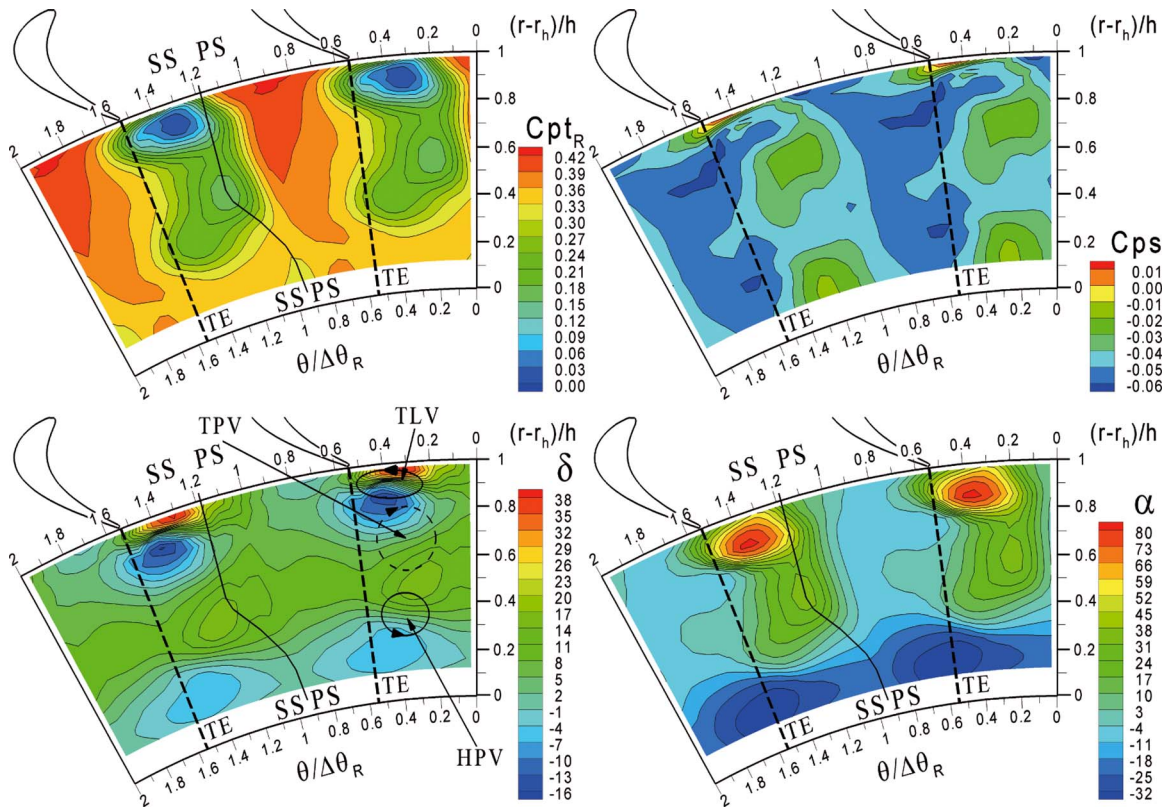


Fig. 6 Mean rotor-exit flow (C_{pt_R} , δ , C_{ps} , and α) in the Nominal Case

reduces as the axial distance increases at high stator loading (Case 3), being 10 deg lower than that found in Case 0 for most of the blade height.

5 Unsteady Flowfield at the Rotor Exit

The flowfield in the relative frame downstream of the stage, derived from the unsteady measurements, is now described with reference to the one at the rotor inlet. It is worth noting that the C_{pt_R} at the rotor outlet can be representative of the losses in the rotor blade row only when compared with the corresponding value at the rotor inlet, and that a rigorous evaluation is only possible along streamlines in the relative frame (the P_{IR} depends also on the peripheral velocity). For the following qualitative discussion these effects are negligible due to the small radial velocity, the small C_{pt_R} radial gradients, and the constant and low blade height to mean diameter ratio.

5.1 Nominal Case

Mean rotor flow. Figure 6 shows the mean rotor-exit flowfield in the relative frame, in terms of C_{pt_R} , δ , C_{ps} , and α .

First, the rotor wake can be clearly identified as the straight region of low C_{pt_R} extended from the tip to the 40% span (sketched as a black solid line). The wake is enlarged in the endwalls by the loss cores linked to the rotor tip leakage vortex (TLV) and by the rotor hub passage vortex (HPV). This interpretation is supported by the deviation angle distribution, which shows two counterclockwise vortical structures centered at 90% and 35% spans, respectively (indicated by solid circles in Fig. 6). The HPV has migrated relatively far from the hub endwall as a consequence of the Coriolis force and of the skewed rotor-inlet boundary layer. The diffused clockwise rotating vortical structure just below the TLV can be identified as a weak tip passage vortex (TPV).

Both the C_{pt_R} freestream level and the wake defect progressively reduce moving from the tip to the hub, resulting in an

almost uniform relative total pressure below 30% span.

The α angle field results as a combination of the relative quantities: Above 40% span the C_{pt_R} gradients dominate, since low relative momentum regions (the TLV and the wake) result in positively deflected flow; in the hub region, where the C_{pt_R} is almost uniform, the δ distribution dominates and the over- and underturning produced by the HPV also appear in the α map.

The static pressure field (C_{ps}) mainly reveals the rotor-exit potential field, being higher on the pressure side and lower on the suction side with respect to the trailing edge (sketched as a dashed line in Fig. 6). Superimposed on this general shape, a core of high C_{ps} exists above 95% span, as a consequence of the lack of expansion in the rotor tip clearance. Low pressure cores are also observed at 90% and 40% of the blade height in the high pressure region, corresponding to the HPV and TLV cores. These vortices appear at $\theta/\Delta\theta_R=0.3$ in the measurement traverse TR as a consequence of the streamwise transport.

Periodic RMS. The description of the stator-rotor interaction is introduced by means of this statistical quantity that marks the flow regions dependent on the stator periodicity.

As reported in Fig. 7, the C_{pt_R} shows a general high level of RMS on the suction side of the rotor wake, according to the wake transport models, with a maximum RMS around 60% span. This is an expected result since, for the nominal case, the stator wake produces a relevant unsteadiness in the inlet C_{pt_R} . The second high RMS region of C_{pt_R} , located below midspan, suggests a strong fluctuation in the HPV and in the hub wake, which is probably not completely mixed out during the whole period. In the tip region, instead, the C_{pt_R} distribution is virtually steady in the relative frame.

The RMS of the deviation angle shows high values in all the three vortex regions identified in the previous paragraph. The rotor HPV unsteadiness has been already observed in the present turbine [8]. The unsteadiness in the rotor TLV is related to the large incidence fluctuations detected at the rotor inlet; note that

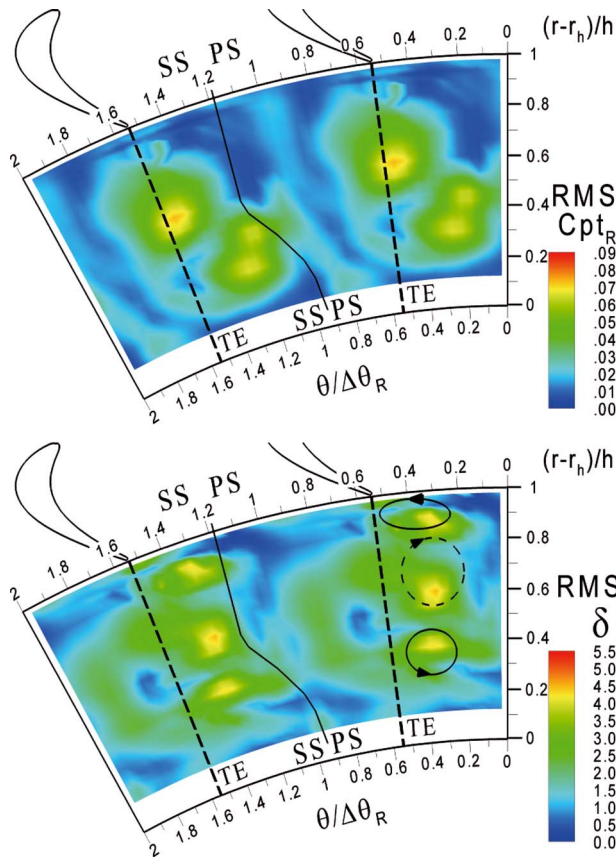


Fig. 7 Periodic RMS (C_{pt_R} and δ) in the Nominal Case

the amplitude of the fluctuations (± 2 deg) is very low with respect to the mean δ gradient and no C_{pt_R} unsteadiness is found in the TLV core. On the contrary the unsteadiness in the rotor TPV is more relevant: This vortex, weak and diffused on a time-averaged scale, does exist for a short portion of the period as discussed in the next paragraph.

Instantaneous flowfield. Four relative-frame snapshots of the relative flowfield downstream of the stage are provided in Fig. 8. The instantaneous flow is synthetically described in the following (see Ref. [13] for more details).

The C_{pt_R} field evidences that the shape and the extension of the wake significantly change during the period. The wake evolves

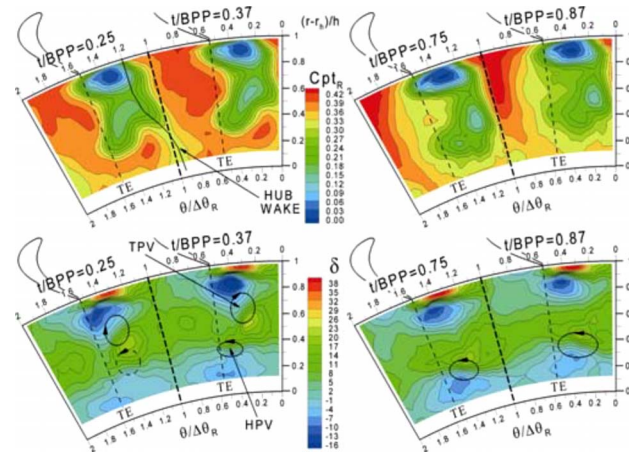


Fig. 8 Instantaneous rotor-exit flowfield in the Nominal Case: C_{pt_R} (top) and δ (bottom)

from a well contoured and almost straight loss region at $t/BPP = 0.37$ to a larger and diffused loss region at the end of the cycle ($t/BPP = 0.75-0.87$), as a consequence of the arrival of the stator wake segment at the measurement plane. The evolution of the rotor deviation angle indicates that the rotor secondary flows are dominated by the stator-rotor interaction, in agreement with the RMS map. The TPV can be clearly identified only at 25% and 37% of the period, as also confirmed by the corresponding presence of relative total pressure losses. The HPV characterizes the flowfield for the most of the period, even if it appears weaker in the first part of the period ($t/BPP = 0.25$). At $t/BPP = 0.37$ the HPV begins to enforce, as shown by a high δ gradient, and in the remaining part of the period the HPV keeps the same magnitude. The C_{pt_R} reflects the HPV dynamics, showing very low losses at the beginning of the period and a well defined loss core linked to that vortex for $t/BPP > 0.25$.

The unsteadiness in the rotor vortices is the result of both the vortex-blade interaction and the fluctuation of the rotor blade loading driven by the stator wake and the potential field. In the tip region the diffused stator vortices at the rotor inlet are too weak to influence the rotor passage vortex, and then it is likely that the fluctuations of rotor TPV magnitude are due to fluctuations in blade loading. Different conclusions can be drawn in the hub region, where a strong HSV and a weak HPV enter the rotor. The dynamics of the rotor HPV can be explained by applying a kinematic vortex transport model to the stator HSV and HPV (see Fig. 12, assuming that the stator HPV is much weaker than the stator HSV). The reduction of the rotor vortex in the first part of the period ($t/BPP = 0.25$) is due to the arrival at the measurement plane of both the PS leg of the stator HSV and the SS leg of the stator HPV, which are counter-rotating with respect to the rotor HPV. The following strengthening of the rotor vortex is caused by its interaction with the corotating SS leg of the stator HSV.

The effect of enforced stator secondary flows on the vortex-blade interaction is studied in Sec. 5.2.

5.2 Effect of Stator Loading: Case 1

Mean rotor flow. The effect of the stator loading (nominal case/ Case 1) on the mean rotor-exit flowfield, reported in Fig. 9, appears at a first glance very weak. The usual spanwise mixing and distortion of the wake and the three vortex cores (TLV, TPV, and HPV) are easily recognized from the C_{pt_R} and δ maps. Despite this, some effects can be highlighted.

While above 40% span the rotor wake is very similar in the two cases, the higher stator loading causes an increase in the wake defect in the hub region where the flow is no longer completely mixed out. This behavior is not linked to the rotor aerodynamics, since the increase in stator loading induces a reduction of rotor incidence, and a smaller velocity defect should occur. Nevertheless the increase in stator loading induces higher unsteadiness in the rotor-inlet flowfield below midspan, and hence, as widely discussed in the following, the observed reduction of relative total pressure downstream of the rotor is the time-averaged trace of the stator viscous structures intermittently released downstream of the stage.

The loss core placed on the suction side of the wake and linked to the HPV (at about 30% span) is less intense and less extended than in the Nominal Case, in agreement with the reduction of rotor incidence. Eventually the tip clearance loss is insensitive to the stator incidence, despite for Case 1 a rotor incidence increase of 10 deg was measured above 80% span. Since the formation process of the TLV mainly occurs in the rear part of the rotor blade, where the effects of incidence on the static pressure field are almost decayed [14], the TLV is weakly sensitive to that.

The freestream deviation angle and its gradients in the tip vortices (TLV and TPV) are almost insensitive to the stator loading. Below 70% span, since the rotor loading reduces as a consequence of the reduction of incidence, the HPV magnitude is significantly weakened with respect to the nominal case: The vortex

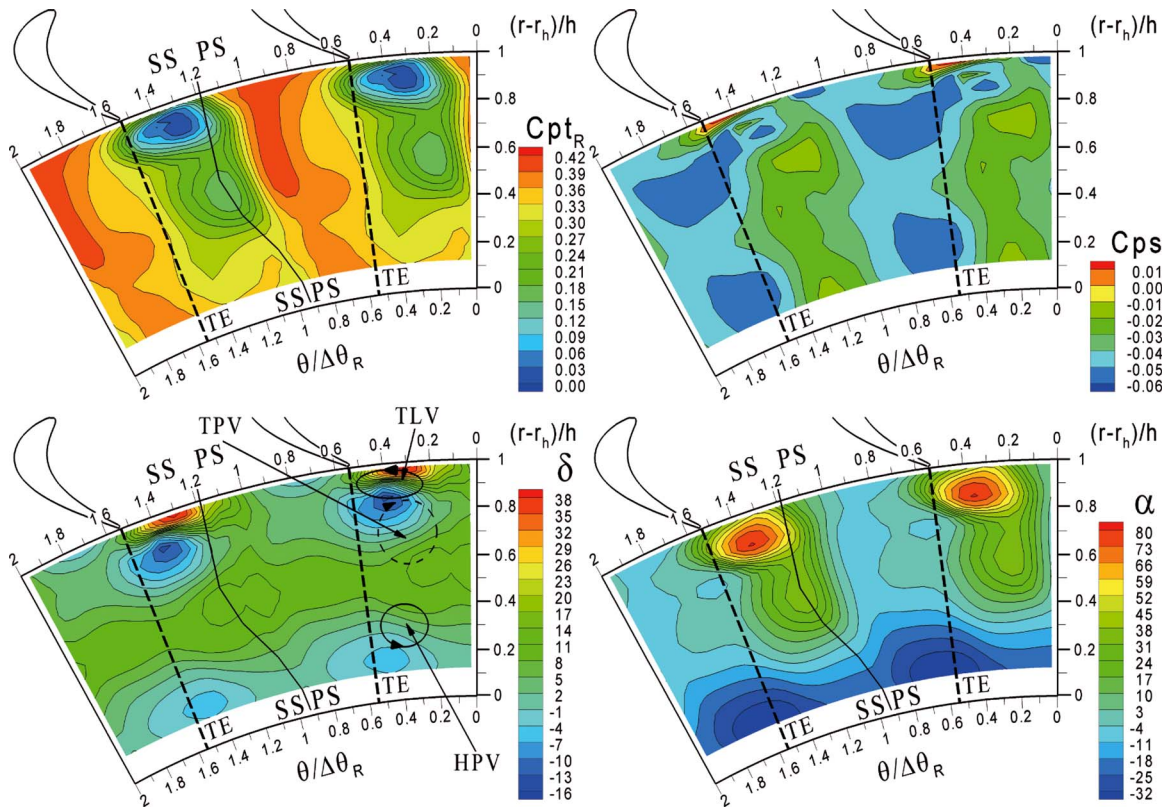


Fig. 9 Mean rotor-exit flow (C_{pt_R} , δ , C_{ps} , and α) for Case 1

is less defined (small δ gradient in the vortex core), it has undergone a smaller radial migration, and its related cross-flow is less intense. As a consequence the HPV does not produce a distinct static pressure perturbation, and below 80% span the C_{ps} map is dominated by the rotor potential field. Actually the hub region is going to experience high stator-rotor interaction processes, and the smeared shape of the mean HPV is the time-averaged trace of a strong fluctuation. Conversely the underturning core at midspan is significantly wider and, with respect to the nominal case, is enlarged toward the pressure side of the rotor wake. The analysis of the instantaneous flowfield is now required to understand the origin and evolution of these structures.

Periodic RMS. The effect of stator loading weak on the mean flow, is very relevant on the stator-rotor interaction: The structure of the deterministic unsteadiness at the rotor exit, reported in Fig. 10, is qualitatively modified by the rotor-inlet unsteadiness.

While the RMS of C_{pt_R} is not dramatically influenced by the stator incidence, showing the common peaks on the suction side of the rotor wake at midspan and in the hub region around the HPV, the strongest effect is found in the RMS of δ . As in the Nominal Case, local peaks of deterministic unsteadiness are detected in the HPV and TPV, while no significant fluctuations are found in the TLV core, being I_R and the rotor inlet C_{pt_R} more uniform at the tip in Case 1. Beside these general features, two new regions of high fluctuations appear. First, a large region of high RMS covers almost the whole rotor pitch between 20% and 40% of the span, a region too large for being only related to the HPV. Even more relevant is the high RMS region visible at midspan on the pressure side of the rotor wake (indicated as P in Fig. 10), where the highest unsteadiness peak is found. This feature did not appear in any of the other configurations tested for the LFM turbine [8,9,13] and represents a novelty that will be widely discussed throughout the analysis of the unsteady interaction process.

Instantaneous flowfield. In Fig. 11 eight snapshots of the rotor-exit relative flowfield are reported.

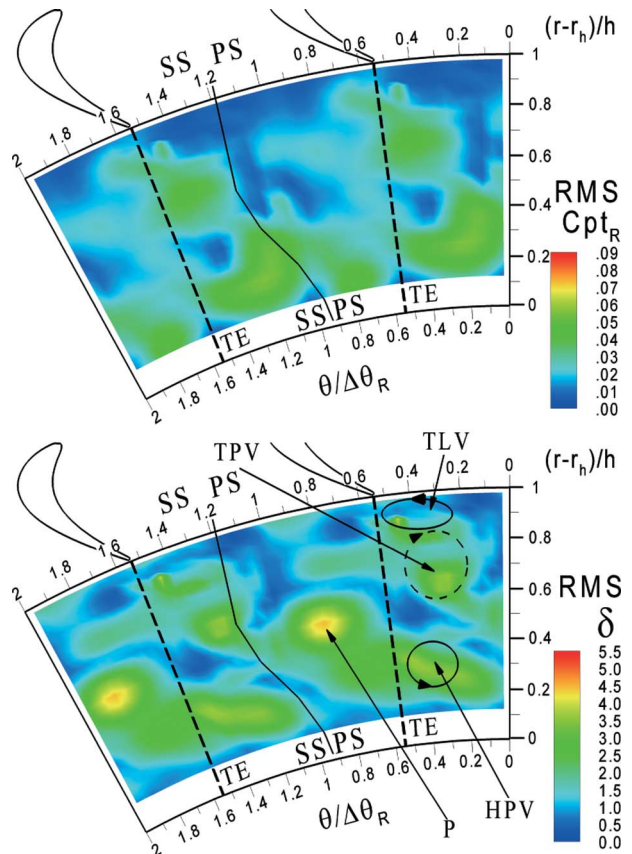


Fig. 10 Periodic RMS (C_{pt_R} and δ) for Case 1

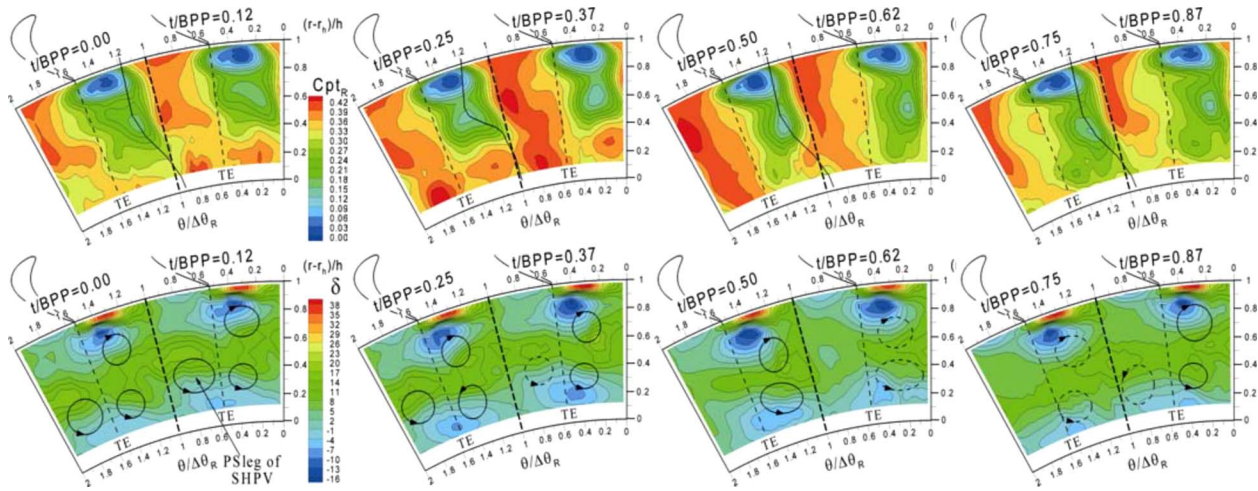


Fig. 11 Instantaneous rotor-exit flowfield for Case 1: C_{pt_R} (top) and δ (bottom)

Concerning the relative total pressure two main phenomena occur. The mean C_{pt_R} level undergoes a fluctuation over the whole period reaching its maximum at $t/BPP=0.37$ where a wide freestream is visible; on the contrary for $0.87 \leq t/BPP \leq 0.00$ the freestream is confined in the outer part of the channel and a wide loss region extends along the whole rotor passage. The second flow feature is concentrated at the hub where, starting from $t/BPP=0.00$, a C_{pt_R} increase is found up to $t/BPP=0.25$ followed by a reduction, though the freestream shows high C_{pt_R} levels. Related to this feature a change in the rotor wake is found between $t/BPP=0.00$ and $t/BPP=0.37$: The wake, located at $\theta/\Delta\theta_R=1$ for $t/BPP=0.00$, reduces its dimension up to $t/BPP=0.5$ while a second loss core arrives at the measuring plane at $\theta/\Delta\theta_R=1.5$ for $t/BPP=0.25$ and strengthens its magnitude up to $t/BPP=0.50$. At $t/BPP=0.87$ the hub loss region extends all over the pitch.

Concerning the deviation angle, the tip region experiences low fluctuation mainly related to the TPV, whose magnitude increases from $0.00 < t/BPP < 0.50$ and reduces in the second half of the period. A strong fluctuation of δ is observed at midspan on the pressure side of the wake ($0.6 < \theta/\Delta\theta_R < 1.0$); the maximum underturning is found at $t/BPP=0.00$, while the minimum is found at $t/BPP=0.50$. In some way an opposite feature is found at the hub where the overturning at the midpassage increases from $t/BPP=0.00$ up to 0.37 followed by a reduction in the final part of the period.

Discussion of the stator-rotor interaction. The dynamics of the rotor wake are fairly similar to that in the nominal case (Fig. 8): Its periodic enlargement is due to the arrival at the measurement plane of the stator wake and loss cores. The wake-wake interaction disappears in the central part of the period ($0.12 < t/BPP < 0.50$) because the original stator wake, chopped by the rotor leading edge, is divided in segments intermittently released downstream of the rotor. Furthermore the spatial enlargement of the rotor wake is more significant in Case 1 and the wake-wake interaction lasts for a higher span of the period. This is because in Case 1 the stator wake is wider than that in the nominal case, and thus the wider segments result in an increase in the interaction time; moreover, since the rotor pitch is smaller than the stator one, an instant exists when the region of low C_{pt_R} covers a large part of the inlet plane, resulting in a wider rotor wake and in a reduction of the C_{pt_R} freestream level at the rotor exit. Due to the circumferential shift of the inlet loss cores related to the wake and to the vortical structures, they appear at different times downstream of the rotor; moreover, the mean axial Mach number is higher at the hub due to the radial equilibrium effect downstream of the stator. By this fact, the hub loss core first reaches the mea-

suring plane at $0.37 < t/BPP < 0.50$, while the general freestream C_{pt_R} reduction starts from $t/BPP=0.62$.

The evolution of the tip vortices is similar to that in the nominal case. Despite the increase in stator loading, no significant vortex-blade interaction processes are activated above midspan. The periodic increase in the rotor TPV is related to the periodic increase in incidence and C_{pt_R} at the rotor inlet and hence to the periodic increase in rotor loading.

The midspan-hub vortical system is, instead, very complex and very different with respect to that in the nominal configuration. Two periodic structures are visible, oscillating in counterphase: Both of them give high RMS and they are located in different positions with respect to the rotor wake.

While the fluctuation of the rotor hub passage vortex is a common feature, the counterclockwise vortex appearing at $t/BPP=0.87$ on the pressure side of the rotor wake is instead a new feature, and it is responsible for the peak observed in the RMS of δ (P in Fig. 10) and for the enlargement of the underturning region at midspan observed in the mean δ distribution (Fig. 9). The pitchwise position of this vortex, adjacent to the wake PS, its radial migration toward midspan, and its sense of rotation, opposite to the stator HPV and equal to the rotor HPV, suggest identifying this structure as the PS leg of the stator hub passage vortex.

The evolution of the hub vortices derives from the combination of two different effects. First the HPV formation mechanism is subjected to the rotor loading fluctuation: The HPV magnitude, in phase with the TPV one, is minimum for $0.50 < t/BPP < 0.75$ and reaches its peak at $t/BPP=0.37$. Superimposed on this trend, the unsteady vortex-vortex interaction influences the secondary field.

A schematic of the flow configuration is reported in Fig. 12, in which the kinematic wake and vortex transport models are applied to the present rotor-inlet flowfield. Let us consider the stator HPV and HSV as two parallel vortex lines; for Helmholtz's vortex theorems, they are transported inside the channel at the local flow velocity, being bowed and stretched, and generating two PS legs and two SS legs (Fig. 12(a)). Given their position on the stator pitch, the HPV enters the rotor channel before the HSV. Hence, the reduction of the rotor HPV for $0.50 \leq t/BPP \leq 0.87$ is probably due to the vortex-vortex interaction with the counter-rotating SS leg of the stator HPV (Fig. 12(b)). It first affects the formation mechanism of the rotor passage vortex inside the channel and then reaches the measuring plane at $t/BPP=0.62$, even if it is not appearing as a distinct vortex core. This is because the incoming vortex is pulled toward the suction side and, being of opposite vorticity, only weakens the more intense rotor passage vortex. The PS leg is detectable as a distinct vorticity core only when located in the freestream far from the rotor HPV, appearing at t/BPP

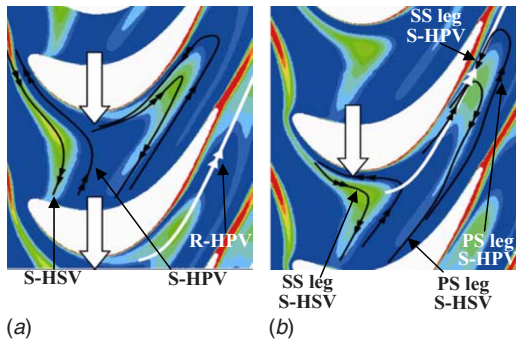


Fig. 12 Kinematic vortex transport model applied to Case 1. (a) Transport of hub stator vortices and (b) vortex-vortex interaction.

$=0.87$ and remaining visible for the half of the period. Similar mechanisms involve, with some delay, the stator HSV, resulting in the increase in rotor HPV at the end of the period, caused by the interaction with the corotating SS leg of the stator HSV.

The comparison of the results obtained in the nominal and first cases clearly shows that the vortex-vortex interaction is highly sensitive to the ratio between the incoming vortices and the ones generated in the rotor. From a quantitative point of view, the doubled stator passage vortex magnitude completely changes the shape of the secondary flows at the rotor exit: The time-averaged rotor passage vortex is weakened (SS leg interaction) but a further stator-related vortex is released at the stage exit in a different position (PS leg interaction). Nevertheless, independently of the sense of rotation of the incoming vortex, only the legs corotating with the dominant vortex structure generated in the rotor actually appear downstream, while the counter-rotating legs cannot be clearly distinguished from the deviation angle. In the authors'

opinion this happens because in HP turbines the magnitude of the rotor secondary flows is in general much greater than that of the stator. The opposite behavior could occur downstream of a second stator (as documented in Ref. [3]) since the inlet vortices are more intense than that generated in the stator.

5.3 Combined Effect of Stator and Rotor Loading: Case 2

Mean rotor flow. The rotor loading is now increased in combination with high stator loading to give more insight into the interaction mechanisms. The effect of the rotor loading on the mean rotor-exit flowfield is reported in Fig. 13.

As the rotor is loaded, the rotor wake enlarges and appears slightly displaced in negative pitchwise direction because of the α angle variation from 0 deg to -20 deg in the freestream.

The influence of the rpm on the rotor secondary flows is mainly related to the rotor incidence spanwise profile, reported in Fig. 5. In Case 2 the incidence increases in radial direction (15 deg higher than that in Case 1 at 80% span). As a consequence, the TPV, weak and smeared in the Nominal Case and in Case 1, becomes a strong and well defined structure for Case 2. In comparison with Case 1, the overturning region placed at 80% span is enlarged, and also the underturning region at midspan, where the two passage vortices interact, is larger. As a consequence, only for high rotor loading the TPV leaves a mean trace of losses, enlarging the suction side of the wake above midspan. The HPV follows the same trend of the TPV, but it is less dependent on the rpm, remaining a well defined structure in all the configurations. Note that in the hub region the spanwise incidence profiles for nominal and second cases are very similar, but the HPV in Case 2 is wider and more diffused than that in the Nominal Case. This is the time-averaged result of a stronger evolution experienced by the HPV in Case 2 with respect to the Nominal Case, as discussed later.

The tip leakage vortex and its related losses appear once again weakly influenced by the rotor incidence angle.

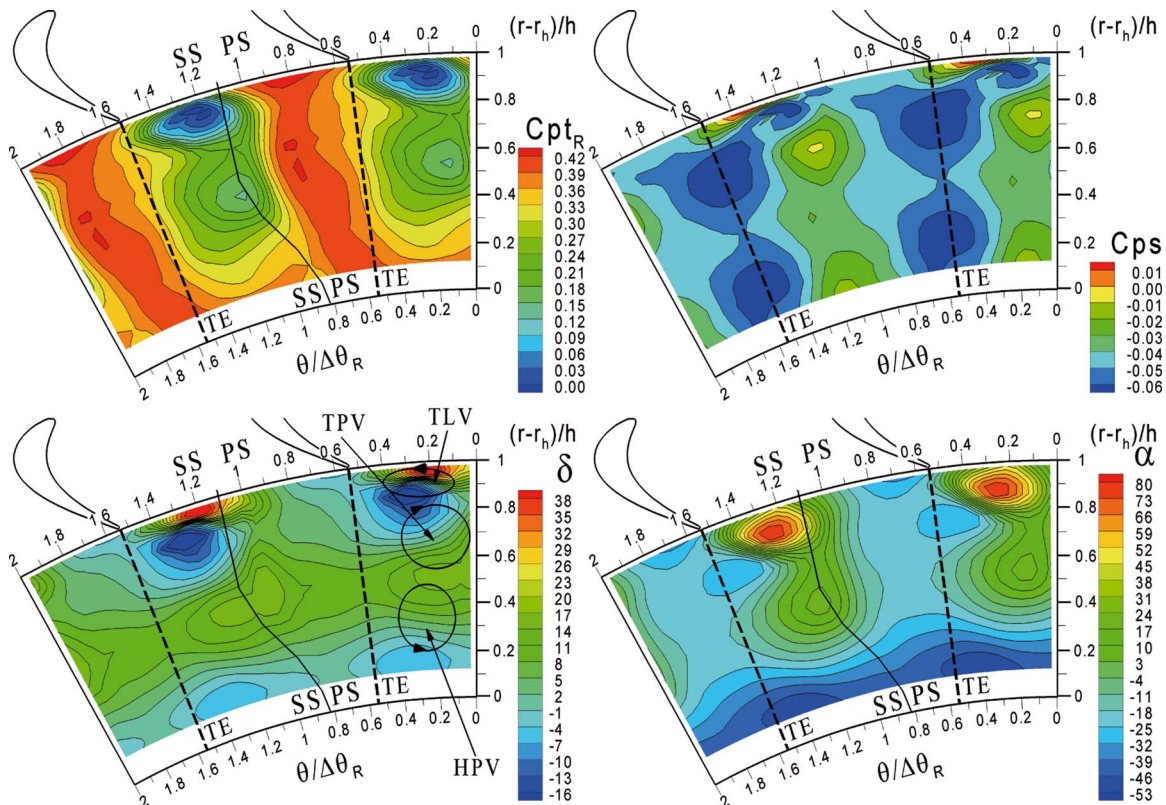


Fig. 13 Mean rotor-exit flow (C_{ptR} , δ , C_{ps} , and α) for Case 2

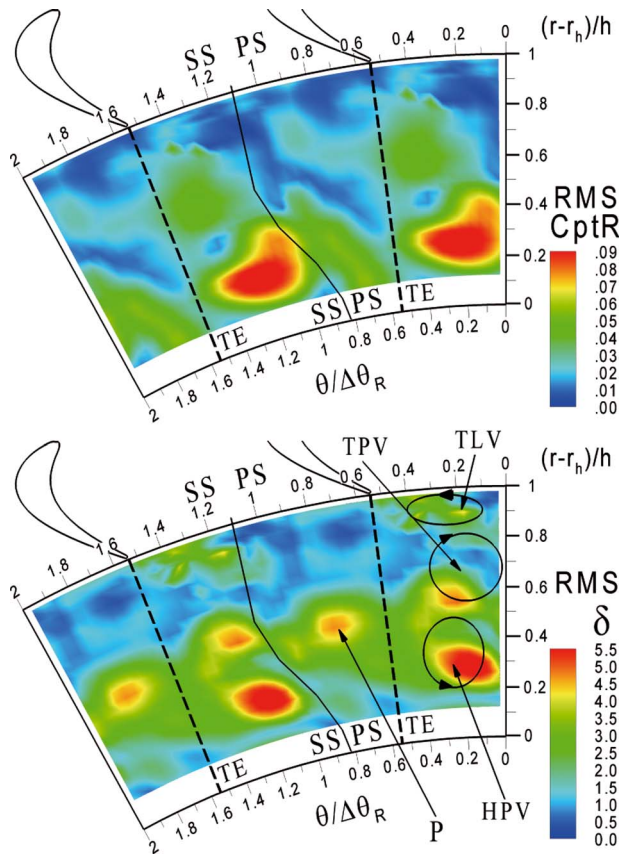


Fig. 14 Periodic RMS (C_{ptR} and δ) for Case 2

The mean static pressure distribution is dominated by the rotor potential field, perturbed by the low pressure vortex cores at the tip and at midspan.

The distribution of the α angle experiences much higher gradients when the rotor loading increases, ranging from 80 deg in the core of the TLV to -50 deg in the HPV overturning leg.

Periodic RMS. The general shape of the RMS maps, reported in Fig. 14, is qualitatively similar to that found for Case 1, but the amplitude of the stator-dependent fluctuations at the rotor exit is strongly increased. The same mechanisms discussed for Case 1 are occurring but the rotor loading has a direct influence on their

amplitude.

The increase in C_{ptR} fluctuation is found especially at the hub, while above midspan no differences are encountered with respect to the other cases. This is in line with what was found at the rotor inlet (see Fig. 3), even if a quantitative comparison between the inlet and outlet unsteadiness could be, in principle, misleading because of the unsteady mechanisms activated in the wake transport process. However, it is worth noting that the amplitude of the unsteadiness upstream and downstream of the rotor is of the same order of magnitude.

The effect of the rpm on the unsteadiness of the rotor secondary flows (δ) is even more relevant. The two RMS peaks corresponding to the rotor passage vortices are significantly enhanced, and also a small fluctuation is visible in the TLV core. On the contrary the RMS peak marked as P in Fig. 13, due to the PS leg of the incoming stator HPV, is almost unaffected by the increase in rotor loading.

Instantaneous flowfield. The snapshots of the relative flowfield measured in Case 2, reported in Fig. 15, are now discussed to investigate the reasons why such high RMS are detected when the rotor loading is increased.

The evolution of the flowfield is not qualitatively different with respect to that found for Case 1. The rotor wake, covering a small region and existing only above 40% span at the beginning of the period ($t/BPP \leq 0.25$), is enlarged at first at the hub ($t/BPP = 0.37$) and progressively all along the span, reaching its maximum extension between $t/BPP = 0.75$ and $t/BPP = 0.87$. The tip leakage vortex, both in terms of losses and δ gradients, is almost constant during the period.

On the contrary the secondary flow features are very different. The TPV periodically changes in magnitude and position, being less intense when the stator wake has completely reached the measurement plane ($t/BPP = 0.50$), and reaching its peak magnitude at $t/BPP = 0.12$. Since for Case 2 the mean rotor incidence is 15 deg higher than that in Case 1 in the outer part of the channel, the TPV remains a strong and well defined structure during the whole period.

The HPV dynamics are, as commonly found, more complex. It partially follows the evolution of the TPV, reaching its minimum and maximum magnitude, respectively, at $t/BPP = 0.50$ and $t/BPP = 0.25$, even if its trend is modified by the action of the incoming vortices that induce a reduction of the HPV magnitude from $t/BPP = 0.50$ to $t/BPP = 0.00$. Moreover, the periodic vortex corotating with the HPV and placed on the pressure side of the channel, identified as the PS leg of the stator HPV in Case 1, is clearly visible for $0.75 \leq t/BPP \leq 0.12$ and reaches its maximum

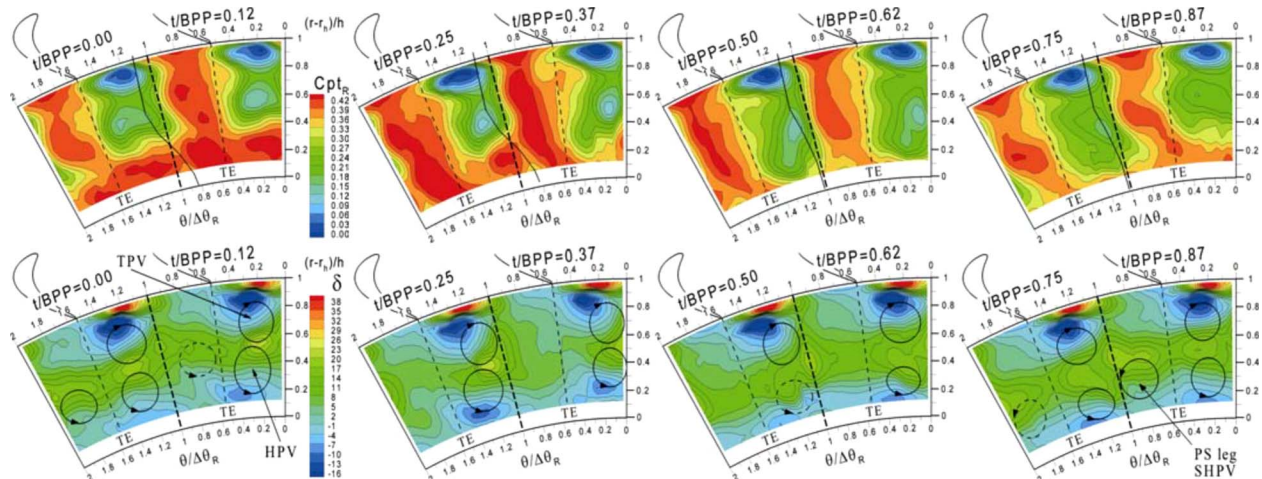


Fig. 15 Instantaneous rotor-exit flowfield for Case 2: C_{ptR} (top) and δ (bottom)

intensity at $t/BPP=0.87$.

Discussion of the stator-rotor interaction. Comparing the rotor-inlet flowfield in the different configurations, a wider and stronger relative wake characterizes Case 2 in comparison with the others; as a consequence, the inlet Cpt_R experiences the maximum unsteadiness in Case 2 especially below midspan, leading to a higher rotor wake unsteadiness. Due to the stator wake leaning, the stator wake segment first appears at the hub ($0.25 < t/BPP < 0.37$), while it reaches the measurement traverse all along the span at $t/BPP=0.50$, being almost merged with the rotor wake. When the stator-exit freestream enters the rotor, the rotor wake disappears at the hub ($t/BPP=0.00$), as commonly found downstream of highly loaded cascades: This suggests that the enlargement of the wake below 40% span visible in the time-mean flowfield is only produced by the wake-blade interaction and would disappear in the presence of a uniform flow at the rotor inlet. Only at $t/BPP=0.12$ a clear rotor-only flowfield is visible. Thus the wake-wake interaction lasts for 75% of the period in Case 2.

The effect of rpm on the vortex-vortex interaction is weak. Nevertheless, some features are discussed. First, since the mean rotor loading is higher, the HPV remains a well defined structure even when its magnitude is minimized ($t/BPP=0.50$). At this instant, the sharp reduction experienced by the rotor HPV at $\theta/\Delta\theta_R=1.2$ is related to the appearance of the counter-rotating SS leg of the stator HPV. This behavior, less evident but visible also in Case 1 at $t/BPP=0.62$, is schematized in Fig. 12(b). Moreover, for Case 2, the trace of the PS leg of the stator HPV also appears, but it remains a well defined structure only for $\frac{1}{4}$ of the BPP, to be compared with the almost $\frac{1}{2}$ of the BPP detected for Case 1. This is because, reducing the rpm, the rotor potential field is strengthened and the stretching of the PS leg is enhanced. As a consequence, the vortex is thinned and, for Kelvin's theorem, its vorticity tends to increase, accelerating the dissipation rate.

The second and most relevant effect of the rpm is mainly quantitative: The reduction of the rpm significantly enhances the unsteadiness in the rotor secondary flows. The present experiments (Case 1/Case 2) show a relevant enforcement of the rotor HPV and TPV in the first part of the period ($0.12 \leq t/BPP \leq 0.25$) and a reduction in the second half of the period. Since the effect of the rpm on the vortex-vortex interaction is weak, a different source of unsteadiness, novel to the knowledge of the authors, does act here. The main change from Case 1 to Case 2 is the dimension and defect of the inlet wake in the relative frame that causes a local, but large, Cpt_R and I_R reduction. The actual flow condition can be modeled in the following quasi-steady way: In the wake flow, the endwall relative total pressure gradient in the boundary layer (and thus the endwall relative vorticity) is much lower with respect to that occurring when the high momentum region of the freestream enters the channel; as a consequence, the rotor passage vortex generated by the stator wake flow is expected to be less intense than the one obtained from the deflection of the freestream flow. This mechanism is further enhanced by the periodic blade loading fluctuation induced by the wake-blade interaction [15], mostly due to the periodic reduction of incidence as the wake sweeps on the blade leading edge. Therefore, the higher is the wake defect, the higher is the fluctuation of rotor loading, and the higher is the oscillation of the rotor secondary flows.

Furthermore the dependence of the passage vortex magnitude on the incidence angle is strongly nonlinear (as visible in turbine cascade data [14]): As a consequence, for a mean positive incidence the passage vortex fluctuations is going to be higher than that found for a mean negative incidence, even for the same inlet unsteadiness.

In Case 2, where both the mean rotor incidence is higher and the inlet relative wake is stronger with respect to Case 1, both the mechanisms discussed above act so to increase the rotor-exit unsteadiness. Comparing Case 2 with the Nominal Case, which have

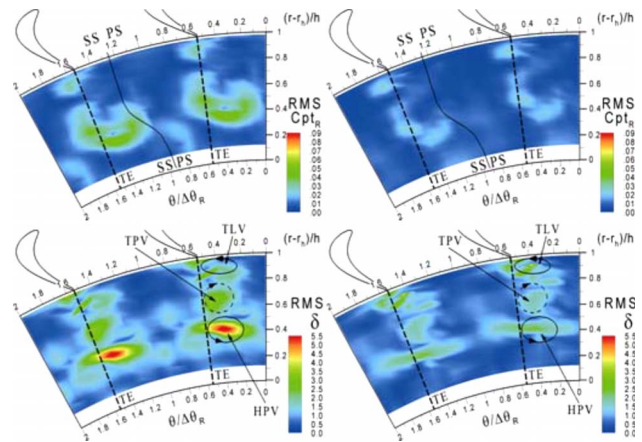


Fig. 16 Periodic RMS comparison between Case 0 (left) and Case 3 (right)

similar values of mean rotor incidence, the much higher passage vortex unsteadiness observed for Case 2 is probably caused only by the higher wake defect.

5.4 Effect of Stator Loading at Large Axial Gap: Case 3.

In Cases 0 and 3 the influence of the stator loading is studied in combination with the increase in the stator-rotor axial gap. For a discussion of the single effect of the axial gap, the reader is referred to Refs. [7] and [8], where the here-defined Nominal Case and Case 0 are compared at $x/b_R=0.45$.

The increase in stator loading at a large axial gap (Case 0/Case 3) has negligible effects on the mean flow.

On the contrary, an interesting result is obtained in terms of stator-rotor interaction. The rotor-inlet flowfield for Case 3 is characterized by a relevant unsteadiness, much stronger than that acting for Case 0 (see Figs. 2–5). Despite this, the rotor-exit unsteadiness, reported in terms of periodic RMS in Fig. 16, shows a clear reduction of the stator-rotor interaction when the stator is loaded, in severe disagreement with what is expected from the analysis of the rotor-inlet flowfield.

A first commentary is required about the mixing process between the farthest measurement plane downstream of the stator ($x/b_S=0.6$) and the rotor leading edge (placed at $x/b_S=1.0$ for large gap). Especially in Case 3, at $x/b_S=0.6$, the flow is far from being mixed out and the interaction between the three counter-rotating vortices is expected to promote a significant diffusion upstream of the rotor, reducing the actual rotor-inlet unsteadiness. However, this is not enough to explain the results of Fig. 16, as confirmed by further tests at an intermediate axial gap. Indeed at $x/b_S=0.5$ (not reported for sake of brevity) a similar reduction of rotor-exit unsteadiness is observed despite the increase in the actual rotor-inlet unsteadiness.

Hence further mixing processes occurring inside the rotor channel are responsible for the reduction of RMS in Case 3. A possible explanation can be given by considering the effect of incidence on the stator-rotor interaction. In Case 3, I_R is negative over 75% of the span, promoting the wake-boundary layer interaction on the rotor suction side, which eventually accelerates the wake rectification process. Moreover the rotor incidence in Case 3 is 10 deg lower than that in Case 0 in the range 20–80% span: This certainly contributes to reduce the RMS in Case 3, since the amplitude of the stator-rotor interaction has been found to be proportional to the rotor incidence (Case 1/Case 2 comparison). Finally, the viscous dissipation rate is higher when two counter-rotating vorticity cores interact with respect to the case where only one vorticity core is present.

As a conclusive remark, when the stator loading is increased for a very large axial gap a virtually steady flowfield in the relative

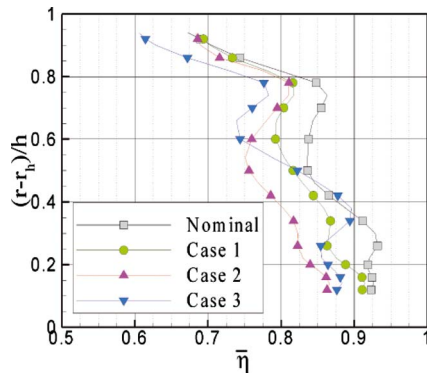


Fig. 17 Radial pitchwise-averaged distributions of stage efficiency

frame is released downstream of the stage. This suggests that, in the presence of a second stator, this configuration would be insensitive to the stator clocking.

6 Stage Efficiency

It is worth concluding the discussion of the stage aerodynamics with an overview of the isentropic stage efficiency. This latter is computed by means of the mass-averaged work at constant radius (estimated from the pitchwise mass-averaged tangential velocities) made nondimensional with respect to the isentropic enthalpy difference from total upstream to static downstream condition, the last being evaluated at constant P_{ref} (Fig. 17). The repeatability of the efficiency estimation is inside $\pm 0.5\%$.

As a general overview, referring also to Figs. 3–5, the tip region experiences the lowest efficiency because of the rotor tip clearance and the high stator losses, these latter being related to the leaned geometry and to the stator tip clearance.

In the hub region the highest efficiency is found and its value depends on the interaction between the stator and rotor structures and on the inlet loss level.

At midspan the efficiency decrease is mainly related to the radial migration of the rotor secondary vortices that causes a strong undertuning and, hence, a positive tangential velocity.

Referring to the stator incidence effect (Nominal Case/Case 1), a negligible difference in the tip region is found, while the strong differences observed below 80% span are mainly due to the higher stator losses for Case 1; the small reduction in the rotor incidence angle, produced by the stator incidence increase, does not balance the increase in the stator losses. Moreover, in the hub region, the stronger vortex-vortex interaction amplifies the reduction of efficiency produced by the stator losses. All these effects cause a significant reduction of overall efficiency, which changes from 84.2% for the nominal case to 81.4% for Case 1.

As the rotor is loaded by a reduction of rpm (Case 1/Case 2), a further decrease of 3.4% in the efficiency is found all along the span. The rotor wake and secondary flow enlargement and the higher flow unsteadiness at the rotor exit (caused by the higher blade loading) support such a result.

Finally the axial gap increase at high stator loading (Case 1/Case 3) causes a reduction in the efficiency mainly above midspan, in agreement with the results presented in Refs. [7,8], resulting in an overall value of 78.3% for Case 3. In the outer part of the channel, the difference depends on the higher inlet loss level caused by the secondary flow mixing and by the casing boundary layer development (enhanced by the blade leaning), which also affect the rotor aerodynamics. Below midspan, the stator secondary flow mixing, the reduction of the inlet loss level, due to the leaned geometry that forces the mass flow toward the hub, and the weaker vortex interaction result in a more complex trend. Between 50% and 25% of the span the increase in efficiency for a

higher axial gap is caused by the combined effect of the reduction of the stator-rotor interaction and of the lower stator-exit losses. Below 25% span the increase in efficiency for Case 1 is due to the stronger cross-flow. It has also to be noted that the increase in stator loading for the large gap, which caused an increase of 2% in the stator loss, weakly affects the stage efficiency, which only decreases by 0.7% in Case 3 with respect to Case 0. The reductions of rotor incidence and of stator-dependent unsteadiness at the rotor exit are therefore connected to a relevant increase in the rotor efficiency.

7 Conclusions

In this paper the stator-rotor interaction in a HP subsonic turbine stage has been investigated, modifying the rotor-inlet unsteadiness with respect to the nominal case. At first the inlet vortices are enforced by increasing the stator loading (Case 1), then the inlet wake and the rotor loading are strengthened by a reduction of the rpm (Case 2), and finally the stator-rotor axial gap is increased for different rotor inlet unsteadiness (Cases 0 and 3).

Results confirm that the inlet vortices are transported inside the rotor channel according to simple kinematic mechanisms resulting in two counter-rotating legs, but the effects of the vortex-vortex interaction downstream of the rotor are found to be very sensitive to the ratio between the stator and rotor vortices. In the nominal case the stator hub shed vortex, stronger than the passage vortex, mostly determines the unsteadiness of the corotating rotor hub passage vortex. When, instead, a stronger stator passage vortex is injected in the rotor channel (Case 1), the rotor secondary flow unsteadiness is mainly caused by the interaction mechanisms between the stator and rotor passage vortices. The common feature observed in the two cases is that only the legs corotating with the rotor passage vortex still appear at the rotor exit, namely, the SS leg of the inlet shed vortex (Nominal Case) and the PS leg of the inlet passage vortex (Case 1): This is related to the much higher intensity of the rotor vortices with respect to the stator ones.

Increasing the width and the defect of the “relative” wake entering the rotor at constant inlet streamwise vorticity (as found in Case 2 with respect to Case 1), the stator-rotor interaction shows weak qualitative changes but results significantly amplified, especially in the rotor passage vortex cores. This behavior, novel to the knowledge of the authors, is probably caused by the periodic reduction of endwall relative total pressure gradient and of blade loading occurring when the inlet wake enters the rotor channel: Thus the wider is the wake, the stronger is the fluctuation activated on the rotor secondary flow formation mechanism.

The analysis of the stator-rotor interaction for a large axial gap (Cases 0 and 3) shows that, when strong counter-rotating vortices are generated by the stator, lower traces of the stator-rotor interaction are found downstream of the stage. This result, linked to the reduction of incidence and to a higher viscous dissipation rate in Case 3, suggests a complex effect of the stator loading on the mixing process acting inside the rotor channel, and brings to a lack of generality when the axial gap is so strongly modified. These data also indicate that an accurate calculation of the turbulent diffusion rate in the secondary flows has a key role in predicting the effects of the stator-rotor interaction in low aspect-ratio turbine stages.

In terms of stage performance, a progressive reduction of efficiency occurs by increasing the blade loading, first because of the increase in stator losses and then because of the strengthening in magnitude and unsteadiness of the rotor secondary flows. If a very large axial gap is used, the efficiency is less sensitive to the stator aerodynamic loading but it is significantly lower than the one at the nominal axial gap.

Nomenclature

- x = axial coordinate
- r = radius
- θ = tangential coordinate

b = axial chord
 h = blade height
 M = Mach number
 $\Delta\theta$ = angular pitch
 BPP, BPF = blade passing period and blade passing frequency
 I = incidence angle
 P_s = static pressure
 P_t = total pressure
 P_{ref} = downstream reference pressure (atmospheric)
 P_{tm} = stator upstream total pressure
 Y = $(P_{\text{tm}} - P_t) / (P_{\text{tm}} - P_s)$: total pressure loss
 C_{ps} = $(P_s - P_{\text{ref}}) / (P_{\text{tm}} - P_{\text{ref}})$: static pressure coefficient
 C_{ptR} = $(P_{tR} - P_{\text{ref}}) / (P_{\text{tm}} - P_{\text{ref}})$: relative total pressure coefficient
 Ω = streamwise vorticity
 α = blade-to-blade absolute flow angle
 δ = rotor deviation angle
 η = isentropic efficiency
 HSV, TSV = hub shed vortex and tip shed vortex

Subscripts

h = hub
 S = stator
 R = rotor, relative
 r = radial
 x = axial

Superscripts

– = pitchwise average

References

[1] Giles, M. B., 1988, "Calculation of Unsteady Wake/Rotor Interaction," J. Pro-

- pul. Power, **4**, pp. 356–362.
- [2] Stieger, R. D., and Hodson, H. P., 2005, "The Unsteady Development of a Turbulent Wake Through a Downstream Low-Pressure Turbine Blade Passage," ASME J. Turbomach., **127**, pp. 388–394.
- [3] Sharma, O. P., Pickett, G. F., and Ni, R. H., 1992, "Assessment of Unsteady Flows in Turbines," ASME J. Turbomach., **114**, pp. 79–90.
- [4] Chaluvadi, V. S. P., Kalfas, A. I., Benieghbal, M. R., Hodson, H. P., and Denton, J. D., 2001, "Blade-Row Interaction in a High-Pressure Turbine," J. Propul. Power, **17**, pp. 892–901.
- [5] Chaluvadi, V. S. P., Kalfas, A. I., Hodson, H. P., Ohyama, H., and Watanabe, E., 2003, "Blade Row Interaction in High-Pressure Steam Turbine," ASME J. Turbomach., **125**, pp. 14–24.
- [6] Pullan, G., and Denton, J. D., 2003, "Numerical Simulation of Vortex-Turbine Blade Interaction," *Proceedings of the Fifth European Conference on Turbomachinery*.
- [7] Gaetani, P., Persico, G., Dossena, V., and Osnaghi, C., 2007, "Investigation of the Flow Field in a HP Turbine Stage for Two Stator-Rotor Axial Gaps, Part I: 3D Time Averaged Flow Field," ASME J. Turbomach., **129**, pp. 572–579.
- [8] Gaetani, P., Persico, G., Dossena, V., and Osnaghi, C., 2007, "Investigation of the Flow Field in a HP Turbine Stage for Two Stator-Rotor Axial Gaps, Part II: Unsteady Flow Field," ASME J. Turbomach., **129**, pp. 580–590.
- [9] Persico, G., 2006, "Unsteady Aerodynamic Stator-Rotor Interaction in High Pressure Turbines," Ph.D. thesis, Politecnico di Milano, Italy.
- [10] Persico, G., Gaetani, P., and Guardone, A., 2005, "Dynamic Calibration of Fast-Response Probes in Low-Pressure Shock Tubes," Meas. Sci. Technol., **16**, pp. 1751–1759.
- [11] Persico, G., Gaetani, P., and Guardone, A., 2005, "Design and Analysis of New Concept Fast-Response Pressure Probes," Meas. Sci. Technol., **16**, pp. 1741–1750.
- [12] Tan, C., Yamamoto, A., Mizuki, S., and Asaga, Y., 2002, "Influence of Blade Curving on Flow Fields of Turbine Stator Cascade," AIAA Paper No. 2002-0378.
- [13] Gaetani, P., Persico, G., and Osnaghi, C., 2007, "Influence of Rotor Loading on the Unsteady Flowfield Downstream of a HP Turbine Stage," *Proceedings of the Seventh European Conference on Turbomachinery*.
- [14] Yamamoto, A., 1988, "Interaction Mechanisms Between Tip Leakage Flow and the Passage Vortex in a Linear Turbine Rotor Cascade," ASME J. Turbomach., **110**, pp. 329–338.
- [15] Lecfort, M. D., 1965, "An Investigation Into the Unsteady Blade Forces in Turbomachines," ASME J. Eng. Power, **87**, pp. 345–354.

Reduced-Order Model of a Bladed Rotor With Geometric Mistuning

Alok Sinha

Department of Mechanical and Nuclear
Engineering,
The Pennsylvania State University,
University Park, PA 16802

This paper deals with the development of an accurate reduced-order model of a bladed disk with geometric mistuning. The method is based on vibratory modes of various tuned systems and proper orthogonal decomposition of coordinate measurement machine data on blade geometries. Results for an academic rotor are presented to establish the validity of the technique. [DOI: 10.1115/1.2987237]

1 Introduction

Mistuning refers to inevitable variations in blades' properties, which arise during the manufacturing process. It has been an active area of research for the past 40 years, e.g., Ref. [1], primarily because it can lead to a significant increase in the maximum vibratory stress in the bladed disk. Other important aspects of mistuning are as follows: the cyclic symmetry is lost, and mistuning parameters are random variables. Both these aspects increase the computational requirements to assess the impact of mistuning. Because of the loss of cyclic symmetry, sector analyses cannot be performed in a standard finite element package such as ANSYS or NASTRAN. Furthermore, because of stochastic aspects of mistuning, Monte Carlo simulation [2] will be required to compute the statistics of the maximum amplitude of blade vibration, particularly the probability that the maximum amplitude will exceed a critical value.

In order to perform Monte Carlo simulation, a reduced-order model was first developed by Yang and Griffin [3] on the basis of the receptance approach. This approach was not found to be accurate near the mode veering region. At about the same time, Castanier et al. [4] developed a reduced-order model on the basis of a component mode synthesis (CMS) approach. This approach has resulted in the REDUCE code, which simulates mistuning only by changes in blades' Young's moduli of elasticity or equivalently specific changes in the stiffness matrix. Next, Yang and Griffin [5] developed a reduced-order model based on the subset of nominal tuned modes (SNMs), which can be obtained from the sector analyses. This method (SNM) has also been called modal domain analysis (MDA). While it has been well known [6] that a mistuned mode can always be expressed as a linear combination of tuned modes, Yang and Griffin [5] were first in applying this concept to develop a reduced-order model of a mistuned bladed disk using tuned modes from the finite element sector analyses. However, they also simulated mistuning only by changes in blades' Young's moduli of elasticity or equivalently the stiffness matrix. Subsequently, Bladh et al. [7] reformulated the CMS method and developed a non-CMS classical modal analysis (CMA) method analogous to the SNM or MDA [5]. In addition, they also developed the secondary modal analysis reduction technique (SMART) for a model already reduced by CMS technique. Again, their mistuning model only considered changes in blades' Young's moduli of elasticity, which represents no change in a blade's mode shape. Later, Lim et al. [8] developed a reduced-order model, CMS_GEO, for geometric mistuning and found that the size of the reduced-order model is quite large. Therefore, Lim et al. [9] developed another reduced-order model via mode-acceleration method with static mode condensation (SMC). Lim et al. [9] also evaluated accu-

cies of various techniques for a rotor with all tuned blades except one with geometric mistuning and found that the accuracy of the CMA was the worst. In general, all techniques except CMS_GEO and SMC were unable to yield accurate results, even for a small change in a blade's mode shape due to mistuning. However, SMC technique requires a large amount of analysis, and Lim et al. [9] did not consider a general case of all blades having geometry mistuning. Petrov et al. [10] proposed to use Woodman-Sherman-Morrison formulas to compute the forced response of a mistuned bladed disk. They did not deal with computation of mistuned frequencies and mode shapes. Furthermore, for a general mistuning case, the matrix that has to be inverted to compute the forced response will be of extremely large dimension; i.e., their method may not be called reduced-order.

This paper deals with the geometric mistuning that refers to variations in geometries of blades, e.g., in an integrally bladed rotor (IBR). Geometries of blades of an IBR are measured by a coordinate measurement machine (CMM). The distinguishing feature of geometric mistuning is that it leads to simultaneous and dependent perturbations in both mass and stiffness matrices. In a previous paper, Sinha et al. [11] showed that vibratory parameters of an individual blade can be extracted from CMM data via proper orthogonal decomposition (POD) analyses. The objective of this paper is to develop a reduced-order model of a bladed disk with geometric mistuning. First, the SNM or MDA was applied to develop the reduced-order model. However, it did not succeed in the presence of simultaneous perturbations in mass and stiffness matrices due to geometric mistuning. This frustrated many researchers because it was difficult to reconcile with the expectation that any mistuned mode must be a linear combination of a subset of tuned modes. After some frustrating moments, the author of this paper realized that the failure of MDA in modeling geometric mistuning is not because any mistuned mode cannot be a linear combination of a subset of tuned modes but because of an insufficient number of tuned modes. As the MDA model with an arbitrarily large number of tuned modes cannot be called reduced-order, the MDA method has been modified in this paper to include tuned modes with blades having geometries perturbed along important POD features [11] as basis functions. The resulting method, modified modal domain approach (MMDA), has yielded a high fidelity reduced-order model. This result is a major breakthrough in the jet engine vibration research. An important aspect of MMDA is that the reduced-order model can be obtained from finite element sector analyses only.

This paper is organized as follows. First, the MMDA algorithm is presented. Next, MMDA results (natural frequencies, mode shapes, and forced response) are presented for an academic rotor with 24 blades and compared with the ANSYS model of the entire bladed disk with geometric mistuning.

2 Reduced-Order Model

2.1 Modal Domain Analysis. A mistuned bladed-disk assembly or a bladed rotor can be described by

Contributed by the International Gas Turbine Institute of ASME for publication in the JOURNAL OF TURBOMACHINERY. Manuscript received July 22, 2007; final manuscript received February 22, 2008; published online April 8, 2009. Review conducted by David Wisler. Paper presented at the ASME Turbo Expo 2007: Land, Sea and Air (GT2007), Montreal, QC, Canada, May 14–17, 2007.

$$M\ddot{\mathbf{x}} + C\dot{\mathbf{x}} + K\mathbf{x} = \mathbf{f}(t) \quad (1)$$

where M , K , and C are mass, stiffness, and damping matrices, respectively. The external excitation vector is represented by \mathbf{f} . Define

$$M = M_t + \delta M \quad (2)$$

and

$$K = K_t + \delta K \quad (3)$$

where M_t and K_t are mass and stiffness matrices of a perfectly tuned system, respectively. Matrices δM and δK are deviations in mass and stiffness matrices due to mistuning.

In the modal domain approach, the following transformation is used:

$$\mathbf{x} = \Phi \mathbf{y} \quad (4)$$

where

$$\Phi = \Phi_1 \quad (5)$$

Furthermore, Φ_1 is an $nt \times r$ matrix containing r modes of a perfectly tuned system, where nt is the total number of degrees of freedom in the finite element model of a full rotor. Substituting Eq. (4) into Eq. (1) and premultiplying by Φ^T , the following reduced-order system is obtained:

$$M_r \ddot{\mathbf{y}} + C_r \dot{\mathbf{y}} + K_r \mathbf{y} = \Phi^T \mathbf{f}(t) \quad (6)$$

where

$$K_r = \Phi^T K \Phi \quad (7)$$

$$M_r = \Phi^T M \Phi \quad (8)$$

$$C_r = \Phi^T C \Phi \quad (9)$$

The natural frequencies and mode shapes of a mistuned system can be obtained by solving the eigenvalue problem corresponding to the reduced-order system:

$$K_r \boldsymbol{\psi} = \omega^2 M_r \boldsymbol{\psi} \quad (10)$$

The reduced-order system is valid when the natural frequencies and mode shapes predicted by Eq. (10) are the same as those predicted by the full-order system:

$$K \phi = \omega^2 M \phi \quad (11)$$

In literature, mistuning is often modeled by considering the variations in Young's modulus of elasticity for each blade. In this case, $\delta M = 0$ and there is no change in a blade's mode shape, and the reduced-order model (6) yields excellent results. However, for the case of geometric mistuning ($\delta M \neq 0$ and $\delta K \neq 0$ with a significant change in a blade's mode shape), results from the reduced-order model (10) do not match with those from the full-order model (11).

2.2 Modified Modal Domain Analysis. The geometry of a blade can be described by

$$\mathbf{w}(\mathbf{p}) = \bar{\mathbf{w}}(\mathbf{p}) + \delta \mathbf{w}(\mathbf{p}) \quad (12)$$

where $\mathbf{w}(\mathbf{p})$ is the coordinate of the blade surface location described by the vector \mathbf{p} . The mean geometry of the blade is denoted by $\bar{\mathbf{w}}(\mathbf{p})$, and $\delta \mathbf{w}(\mathbf{p})$ is the random deviation in the geometry of the blade. Let the covariance matrix of random $\delta \mathbf{w}(\mathbf{p})$ be $C(\mathbf{p}_i, \mathbf{p}_j)$. Using Karhunen–Loeve expansion [12],

$$\delta \mathbf{w}(\mathbf{p}) = \sum_j \xi_j \sqrt{\lambda_j} \mathbf{u}_j \quad (13)$$

where λ_j and \mathbf{u}_j are eigenvalue and eigenvector of the matrix $C(\mathbf{p}_i, \mathbf{p}_j)$, and

$\xi_j =$ random variables with zero mean

and unity standard deviation (14)

In other words,

$$E(\xi_j) = 0, \quad E(\xi_j^2) = 1 \quad (15)$$

and

$$E(\xi_j \xi_p) = 0 \quad \text{when } j \neq p \quad (16)$$

The Karhunen–Loeve expansion [12] is also called POD. It should be noted that the POD expansion (13) is based on the second-order statistics, which is sufficient for a Gaussian distribution. It does not require perturbations in the geometry to be small.

The vector \mathbf{u}_j is also called the j th POD feature. Typically, values of λ_j are almost equal to zero except for few POD features. Hence, considering only np largest values of λ_j , Eq. (13) can be approximated as

$$\delta \mathbf{w}(\mathbf{p}) = \sum_{j=1}^{np} \xi_j \sqrt{\lambda_j} \mathbf{u}_j \quad (17)$$

Now, it is proposed to modify the transformation (4) as follows:

$$\mathbf{x} = \Phi \mathbf{z} \quad (18)$$

where

$$\Phi = [\Phi_1 \quad \Phi_2 \quad \cdots \quad \Phi_{np+1}] \quad (19)$$

Φ_1 : r tuned modes of the system with blades

having the mean geometry (20)

Φ_ℓ : r tuned modes of the system with blades having perturbed

geometry along $(\ell - 1)$ th POD feature, $\ell = 2, \dots, np + 1$ (21)

In this case, the dimension of the reduced-order system will be $r(np + 1)$. The geometry of the blade, which is perturbed along the ℓ th POD feature, is described by

$$\mathbf{w}(\mathbf{p}) = \bar{\mathbf{w}}(\mathbf{p}) + \xi_\ell \sqrt{\lambda_\ell} \mathbf{u}_\ell \quad (22)$$

Hence, the matrix Φ_ℓ is composed of tuned modes of the rotor with all blades having the geometry defined by Eq. (22). The reduced-order system will be again represented by Eqs. (6)–(9).

It should be noted that the equivalent representation of Eq. (19) can also be written as $\Phi_{\text{eq}} = [\Phi_1 \quad (\Phi_2 - \Phi_1) \quad \cdots \quad (\Phi_{np+1} - \Phi_1)]$. Therefore, the use of Φ_ℓ , $\ell = 2, 3, \dots, np + 1$, as basis functions provides information about the effects of the change in geometry along the $(\ell - 1)$ th POD feature with respect to Φ_1 . Qualitatively, $\Phi_\ell - \Phi_1$ is almost orthogonal to Φ_1 ; i.e., effects of geometry change are almost orthogonal to Φ_1 and as a result Φ_1 alone is not able to capture the effects of geometric mistuning.

2.3 Computation of Reduced Order Matrices via Sector Analyses. The computation of reduced-order stiffness and mass matrices (7) and (8) is straightforward whenever the matrices K , M , and Φ , Eq. (19), are known for the full bladed disk. However,

it is a common practice to use the sector analyses for a perfectly tuned system. Therefore, an algorithm has been developed to compute reduced-order matrices K_r and M_r on the basis of only sector analyses; i.e., without requiring any full rotor analyses. From Eqs. (2), (3), (7), and (8),

$$K_r = \Phi^T K_t \Phi + \Phi^T \delta K \Phi \quad (23)$$

$$M_r = \Phi^T M_t \Phi + \Phi^T \delta M \Phi \quad (24)$$

Perturbation matrices δK and δM due to the geometric mistuning of blades have block-diagonal structures:

$$\delta K = \begin{bmatrix} \delta K_1 & 0 & \cdots & 0 \\ 0 & \delta K_2 & \cdots & 0 \\ \vdots & \vdots & \ddots & \vdots \\ 0 & 0 & \cdots & \delta K_n \end{bmatrix} \quad (25)$$

$$\delta M = \begin{bmatrix} \delta M_1 & 0 & \cdots & 0 \\ 0 & \delta M_2 & \cdots & 0 \\ \vdots & \vdots & \ddots & \vdots \\ 0 & 0 & \cdots & \delta M_n \end{bmatrix} \quad (26)$$

Following sector analyses and storage requirements are needed.

- First, a perfectly tuned system with blades having their geometries defined by the average CMM data $\bar{w}(p)$ is considered. ANSYS sector modal analysis is run for each nodal diameter and the following data are stored: (i) modal vector for each nodal diameter and (ii) mass and stiffness matrices for each nodal diameter.
- Next, a blade is constructed with the geometry described by Eq. (22) for each POD feature ℓ between 2 and $np+1$. For each such blade, a tuned bladed disk (a disk with identical blades) is constructed. ANSYS sector modal analysis is run for each nodal diameter, and modal vector for each nodal diameter is stored.
- Lastly, for each actual blade ($j=1, 2, \dots, n$) in a mistuned disk, a tuned bladed disk (a disk with identical blades) is constructed. ANSYS sector analysis is run for only one nodal diameter, and mass and stiffness matrices are stored. Note that there is no need to run the modal analysis here. Subtracting mass and stiffness matrices of the tuned system with "average" blades, δK_j and δM_j in Eqs. (25) and (26) are obtained without any approximations. Matrices on the right hand sides of Eqs. (23) and (24) are symmetric and are expressed as follows:

$$\Phi^T K_t \Phi = \begin{bmatrix} \Phi_1^T K_t \Phi_1 & \Phi_1^T K_t \Phi_2 & \cdots & \Phi_1^T K_t \Phi_{np+1} \\ & \Phi_2^T K_t \Phi_2 & \cdots & \Phi_2^T K_t \Phi_{np+1} \\ & & \ddots & \vdots \\ & & & \Phi_{np+1}^T K_t \Phi_{np+1} \end{bmatrix} \quad (27)$$

$$\Phi^T M_t \Phi = \begin{bmatrix} \Phi_1^T M_t \Phi_1 & \Phi_1^T M_t \Phi_2 & \cdots & \Phi_1^T M_t \Phi_{np+1} \\ & \Phi_2^T M_t \Phi_2 & \cdots & \Phi_2^T M_t \Phi_{np+1} \\ & & \ddots & \vdots \\ & & & \Phi_{np+1}^T M_t \Phi_{np+1} \end{bmatrix} \quad (28)$$

$$\Phi^T \delta K \Phi = \begin{bmatrix} \Phi_1^T \delta K \Phi_1 & \Phi_1^T \delta K \Phi_2 & \cdots & \Phi_1^T \delta K \Phi_{np+1} \\ & \Phi_2^T \delta K \Phi_2 & \cdots & \Phi_2^T \delta K \Phi_{np+1} \\ & & \ddots & \vdots \\ & & & \Phi_{np+1}^T \delta K \Phi_{np+1} \end{bmatrix} \quad (29)$$

$$\Phi^T \delta M \Phi = \begin{bmatrix} \Phi_1^T \delta M \Phi_1 & \Phi_1^T \delta M \Phi_2 & \cdots & \Phi_1^T \delta M \Phi_{np+1} \\ & \Phi_2^T \delta M \Phi_2 & \cdots & \Phi_2^T \delta M \Phi_{np+1} \\ & & \ddots & \vdots \\ & & & \Phi_{np+1}^T \delta M \Phi_{np+1} \end{bmatrix} \quad (30)$$

The computation of $\Phi_i^T K_t \Phi_j$, $\Phi_i^T M_t \Phi_j$, $\Phi_i^T \delta K \Phi_j$, and $\Phi_i^T \delta M \Phi_j$, $i=1, 2, \dots, np+1$, $j=i, i+1, \dots, np+1$, has been achieved by directly using the modal vectors, mass,

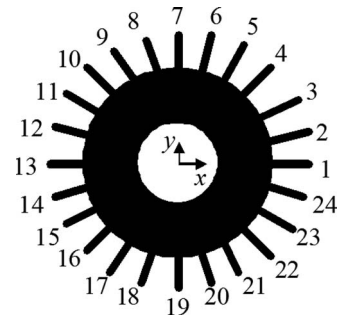


Fig. 1 An academic rotor with 24 blades

and stiffness matrix obtained from ANSYS sector analyses.

3 Numerical Examples

An ANSYS model of an academic rotor (Fig. 1) has been constructed. This model has 24 blades. For each blade, the finite element grid has six circumferential locations, numbered 1–6 in Fig. 2, and nodes are only on the front and back surfaces in the xy plane, with z -coordinates being either $+q$ or $-q$ in., where $2q$ is the thickness of each tuned blade. Therefore, the thickness of the blade is changed at any circumferential location by multiplying the z -coordinate of each node at that circumferential location by the same factor.

To have each blade uniform but of a different thickness, all nodal z -coordinates of a blade are multiplied by

$$1 + \xi_{1i}, \quad i=1, 2, \dots, 24 \quad (31)$$

where ξ_1 is the random variable representing the only POD feature (labeled as No. 1 in Fig. 3) and ξ_{1i} is its value for blade No. i . Based on the multiplying factor (31), a mistuning pattern (No. 1) with mistuned uniform blade thicknesses is created, Table 1.

Another mistuning pattern is created with two POD features. The first POD feature for the change in the thickness is the same as that for the mistuning pattern No. 1, i.e.,

$$\mathbf{u}_1 = [1 \ 1 \ 1 \ 1 \ 1 \ 1]^T \quad (32)$$

whereas the second POD feature, Fig. 3, represents a linear variation in the thickness, i.e.,

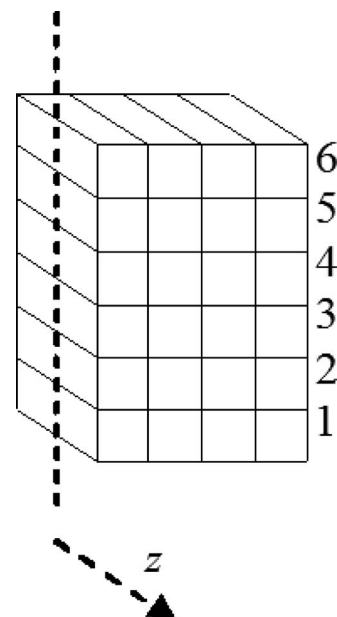


Fig. 2 Discretization of a blade by finite elements

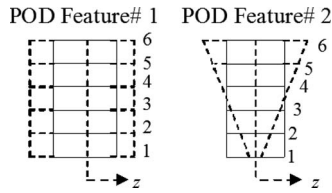


Fig. 3 Blade thickness for each POD feature

Table 1 Random variables for mistuning patterns

Blade No. <i>I</i>	Pattern No. 1 ξ_{1i}	Pattern No. 2 ξ_{1i}	Pattern No. 2 ξ_{2i}
1	0.0051	0.0191	-0.0227
2	0.0263	-0.0202	-0.0150
3	-0.0467	0.0062	0.0126
4	-0.0184	-0.0060	-0.0267
5	-0.0105	-0.0230	-0.0174
6	-0.0485	0.0093	0.0061
7	-0.0528	0.0030	0.0345
8	0.0372	-0.0306	-0.0237
9	0.0004	-0.0184	0.0141
10	-0.0258	-0.0075	-0.0179
11	0.0322	0.0177	-0.0071
12	0.0093	-0.0337	-0.0135
13	-0.0396	-0.0161	0.0283
14	0.05	-0.0130	0.0193
15	0.0116	0.0266	-0.0474
16	0.0492	0.0476	-0.0081
17	0.0455	0.0385	0.0125
18	-0.0274	0.0246	-0.0350
19	-0.0517	0.0088	-0.0047
20	-0.0029	0.0019	-0.0096
21	-0.0132	-0.0405	0.0111
22	-0.0337	-0.0113	-0.0196
23	0.0199	-0.0006	0.0018
24	0.0395	0.0062	-0.0117

$$u_2 = [-1 \quad -0.6 \quad -0.2 \quad 0.2 \quad 0.6 \quad 1]^T \quad (33)$$

Hence, the multiplying factor vector for the thickness change in each blade is represented as

$$u_0 + \xi_{1i}u_1 + \xi_{2i}u_2, \quad i = 1, 2, \dots, 24 \quad (34)$$

where

$$u_0 = u_1 \quad (35)$$

Here, ξ_1 and ξ_2 are two random variables associated with POD feature Nos. 1 and 2, respectively. ξ_{1i} and ξ_{2i} are their values for blade No. i and are presented in Table 1 for the mistuning pattern, labeled as No. 2. It should be noted that both mistuning patterns represent cases of fairly large geometric mistuning, e.g., the standard deviation of the changes in blades' thicknesses for the mistuning pattern No. 1 is 4%.

Natural frequencies and modal vectors are computed from MMDA based on the mode shapes obtained from the full rotor ANSYS analyses for tuned systems. Furthermore, $r=120$ in Eqs. (20) and (21). For mistuning pattern No. 1 with only one POD feature, the Φ matrix is composed of 120 modes (Φ_1) for the tuned system with blades having the mean geometry and 120 modes (Φ_2) for the tuned system with blades having the geometry perturbed along the POD feature. For mistuning pattern No. 2 with two POD features, the Φ matrix is composed of 120 modes (Φ_1) for the tuned system with blades having the mean geometry, 120 modes (Φ_2) for the tuned system with blades having the geometry perturbed along the first POD feature, and 120 modes (Φ_3) for the tuned system with blades having the geometry perturbed along the second POD feature. The matrix Φ_2 is obtained by perturbing the thickness of each blade by 2%, i.e., $\xi_{1i}=0.02$, $i = 1, 2, \dots, 24$, in Eq. (31). The matrix Φ_3 is obtained by perturbing the thickness of each blade according to Eq. (34) with $\xi_{1i}=0$, $\xi_{2i}=0.025$, $i=1, 2, \dots, 24$.

Deviations of MMDA natural frequencies from the tuned system match very well with those from the ANSYS model of the full mistuned rotor, Figs. 4 and 5. The orders of the MMDA models are 240 and 360 for mistuning patterns 1 and 2, respectively.

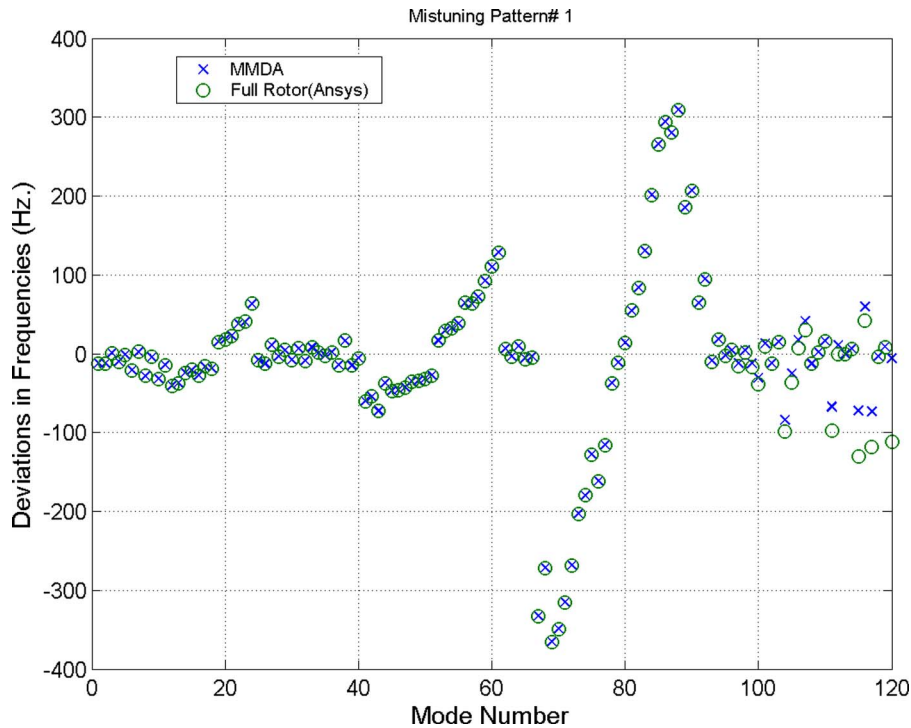


Fig. 4 Mistuned natural frequencies from MMDA (mistuning pattern No. 1)

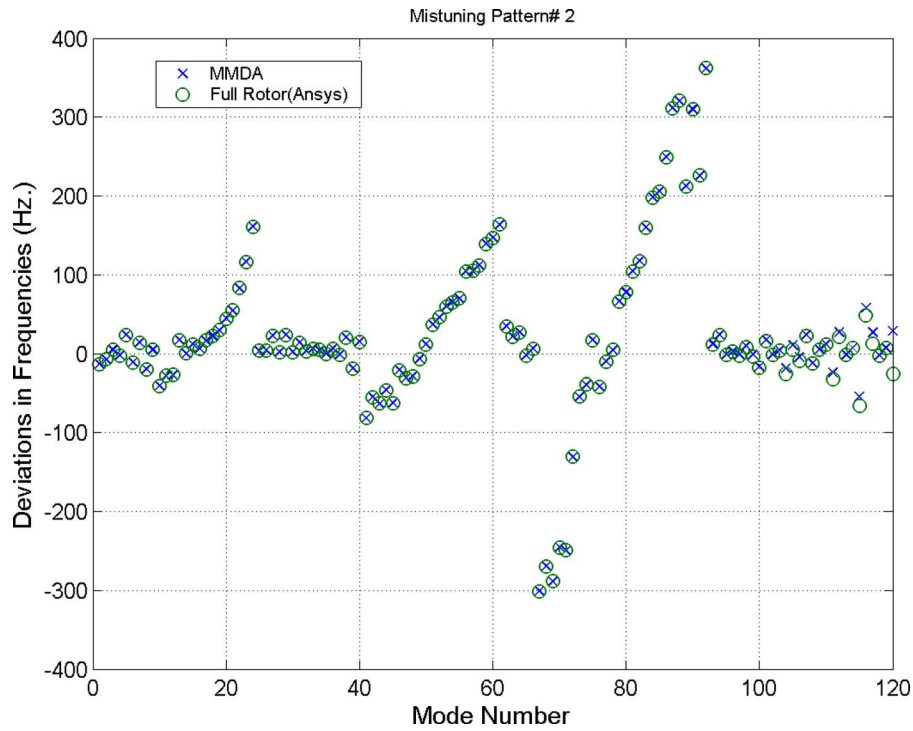


Fig. 5 Mistuned natural frequencies from MMDA (mistuning pattern No. 2)

Some errors can be seen in Figs. 4 and 5 beyond the mode number=100, which is understandable because only sets of 120 modes have been used as basis functions. The important point to note here is that the MMDA solution is almost an “exact” solution for the lower modes, which is further confirmed by comparing mistuned modal vectors obtained from MMDA and ANSYS, Figs. 6 and 7. Each element of a modal vector predicted by MMDA has

been plotted for the full rotor in Fig. 6. It can be seen that the difference between the modal vectors from MMDA and full rotor ANSYS analysis is almost zero, Fig. 7.

Examining tuned frequencies, it has been observed that there are many families of modes; e.g., the first 24 modes represent first bending modes of vibration of blades and very little disk vibration. A reduced-order model is created via MMDA with $r=24$, and

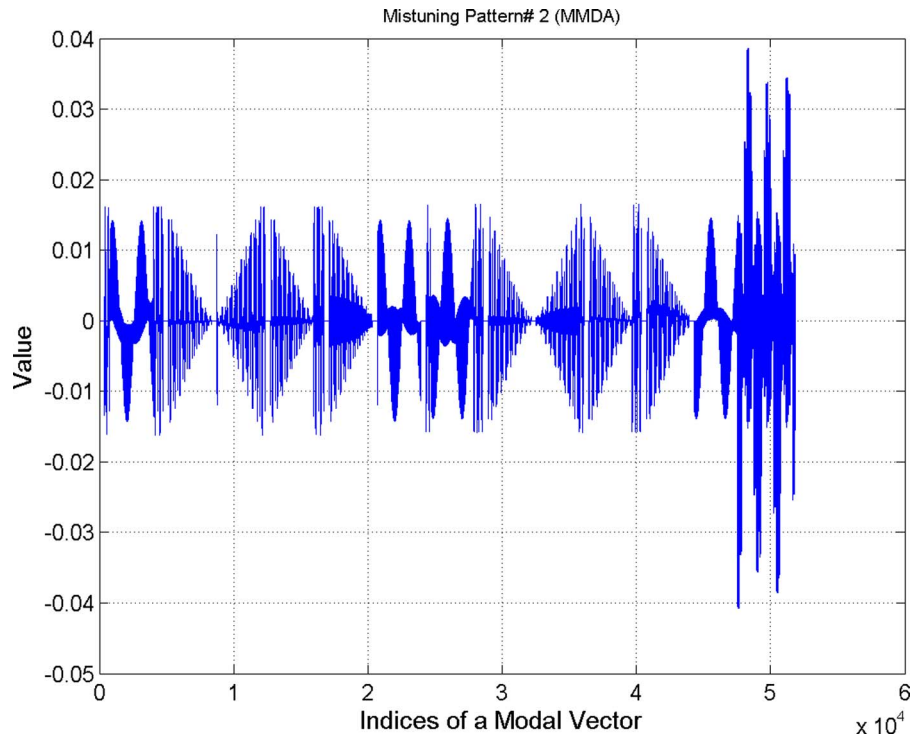


Fig. 6 A mistuned modal vector from MMDA (mistuning pattern No. 2)

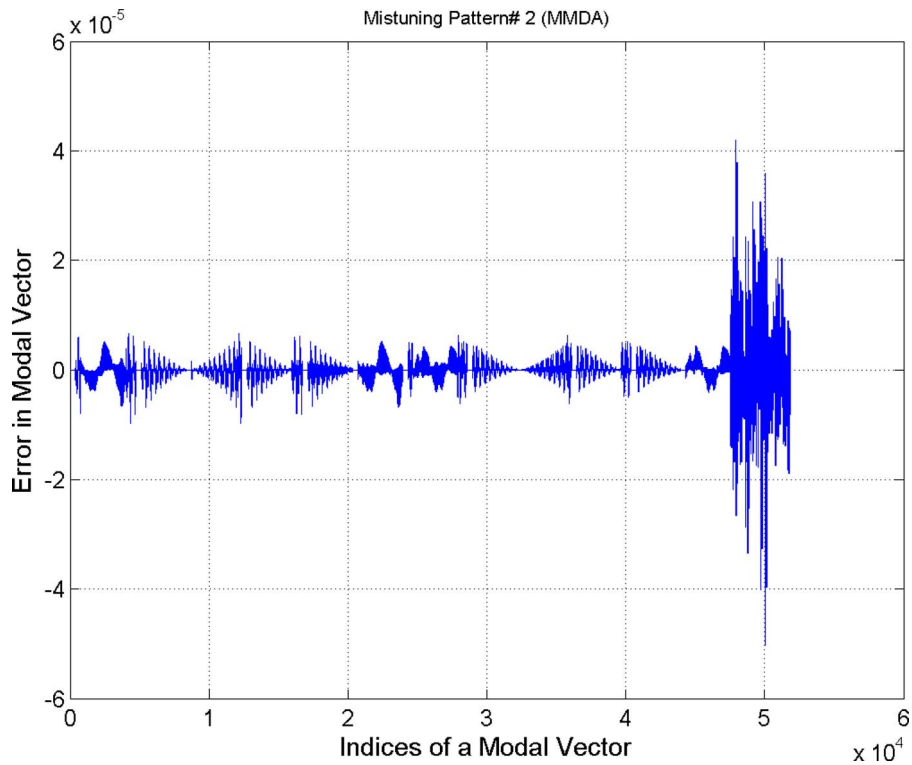


Fig. 7 Difference between modal vectors from MMDA and full rotor ANSYS analysis (mistuning pattern No. 2)

it is found that results are very close to those from MMDA with $r=120$, Fig. 8. This result implies that an accurate reduced-order model can be created by considering modes in the frequency range of interest only.

Next, the forced response from the MMDA model with $r=24$ is

compared with those obtained on the basis of ANSYS mistuned modes, Fig. 9. The modal damping ratio in each case is taken to be 0.001, and the frequency ratio is the excitation frequency divided by the 18th mistuned natural frequency. The forcing function corresponds to the nine nodal diameter excitation. It is again

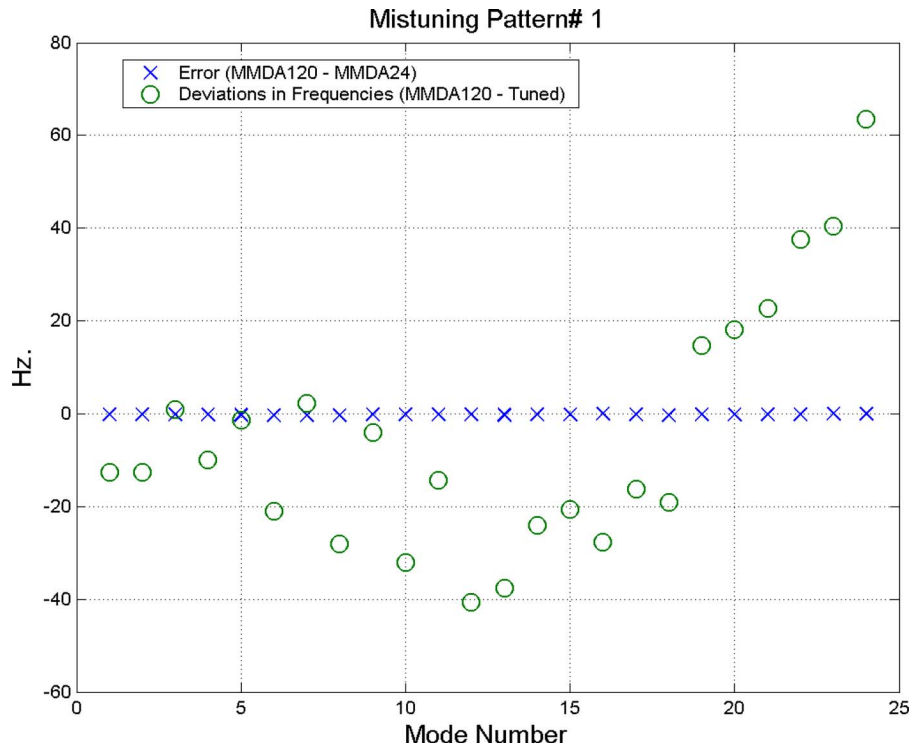


Fig. 8 Comparison between frequencies from MMDA with $r=120$ and $r=24$

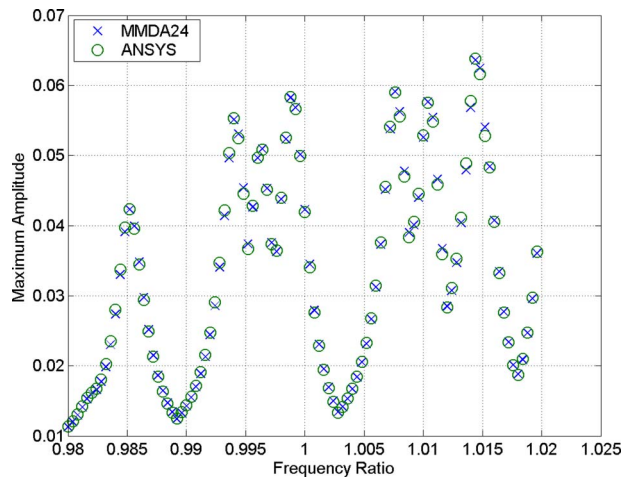


Fig. 9 Steady state response to nine nodal diameter excitation (mistuning pattern No. 1)

seen that the MMDA ($r=24$) leads to almost an exact solution.

Lastly, MMDA results are obtained from sector analyses as outlined in Sec. 2.3. As shown in Fig. 10, these results are indistinguishable from the MMDA with the full rotor ANSYS results. This result confirms the validity of the algorithm based on sector analyses, which has been subsequently used to analyze the vibration characteristics of an integrally bladed rotor (IBR) of an advanced jet engine.

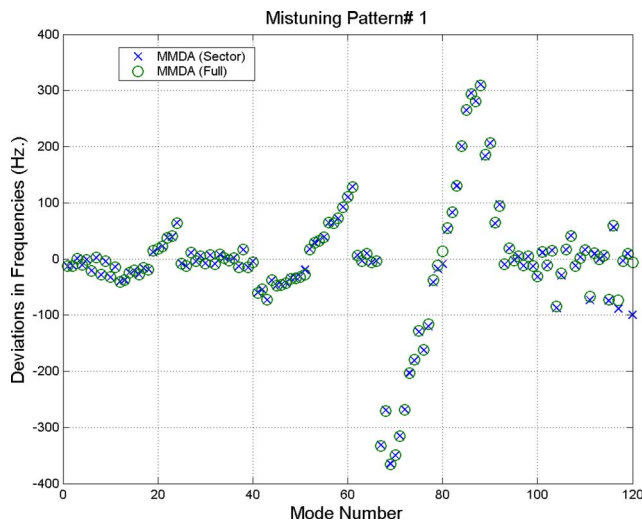


Fig. 10 Comparison between frequencies from MMDA via sector and full rotor ANSYS analyses

4 Conclusions

This paper represents a major breakthrough in the development of an accurate reduced-order model of a bladed disk with geometric mistuning. The algorithm, which has been called MMDA, is based on sector analyses only. It is shown that this method can accurately predict mistuned frequencies, mistuned mode shapes, and forced response of a bladed disk with geometric mistuning, which causes simultaneous and dependent perturbations in both mass and stiffness matrices of blades. Another feature of this method is the use of CMM data on geometries of blades via the POD analysis, which identifies independent and important mistuning parameters. As a result, the MMDA can be applied to any other forms of mistuning, and a generalized mistuning design and analysis code can be developed.

Acknowledgment

Most of the work contained in this paper were performed during the author's sabbatical at Pratt & Whitney, East Hartford, CT. The author wishes to thank Gary Hilbert and Robert Morris for arranging his sabbatical. The author is grateful to Benjamin Hall for helping him with Pratt & Whitney Computing System. The author would also like to thank Gary Hilbert, B. Cassenti, B. Hall, and B. Benedict for useful technical discussions.

References

- [1] Whitehead, D. S., 1966, "Effect of Mistuning on the Vibration of Turbomachine Blades Induced by Wakes," *J. Mech. Eng. Sci.*, **8**, pp. 15–21.
- [2] Sinha, A., 2006, "Statistical Distribution of the Peak Maximum Amplitude of the Forced Response of a Mistuned Bladed Disk: Some Investigations and Applications of Neural Networks," ASME Paper No. GT 2006-90088.
- [3] Yang, M.-T., and Griffin, J. H., 1997, "A Reduced Order Approach for the Vibration of Mistuned Bladed Disk Assemblies," *ASME J. Eng. Gas Turbines Power*, **119**, pp. 161–167.
- [4] Castanier, M. P., Ottarson, G., and Pierre, C., 1997, "A Reduced Order Modeling Technique for Mistuned Bladed Disks," *ASME J. Vib. Acoust.*, **119**(3), pp. 439–447.
- [5] Yang, M.-T., and Griffin, J. H., 2001, "A Reduced Order Model of Mistuning Using a Subset of Nominal System Modes," *ASME J. Eng. Gas Turbines Power*, **123**(4), pp. 893–900.
- [6] Kaza, K. R. V., and Kielb, R. E., 1982, "Effects of Mistuning on Bending-Torsion Flutter and Response of a Cascade in Incompressible Flow," *AIAA J.*, **20**(8), pp. 1120–1127.
- [7] Bladh, R., Castanier, M. P., and Pierre, C., 2001, "Component-Mode-Based Reduced Order Modeling Techniques for Mistuned Bladed Disks, Part I: Theoretical Models, Part II: Application," *ASME J. Eng. Gas Turbines Power*, **123**, pp. 89–108.
- [8] Lim, S.-H., Bladh, R., Castanier, M. P., and Pierre, C., 2003, "A Compact, Generalized Component Mode Mistuning Representation for Modeling Bladed Disk Vibration," *Proceedings of the 44th AIAA/ASME/ASCE/AHS/ASC Structures, Structural Dynamics, and Materials Conference*, Norfolk, VA, Vol. 2, AIAA Paper No. 2003-1545, pp. 1359–1380.
- [9] Lim, S.-H., Castanier, M. P., and Pierre, C., 2004, "Vibration Modeling of Bladed Disks Subjected to Geometric Mistuning and Design Changes," *Proceedings of the 45th AIAA/ASME/ASCE/AHS/ASC Structures, Structural Dynamics, and Materials Conference*, Palm Springs, CA, AIAA Paper No. 2004-1686.
- [10] Petrov, E. P., Sanliturk, K. Y., and Ewins, D. J., 2002, "A New Method for Dynamic Analysis of Mistuned Bladed Disks Based on the Exact Relationship Between Tuned and Mistuned Systems," *ASME J. Eng. Gas Turbines Power*, **124**, pp. 586–597.
- [11] Sinha, A., Hall, B., Cassenti, B., and Hilbert, G., 2008, "Vibratory Parameters of Blades From Coordinate Measurement Machine Data," *ASME J. Turbomach.*, **130**, p. 011013.
- [12] Ghanem, R. G., and Spanos, P. D., 1990, *Stochastic Finite Elements: A Spectral Approach*, Springer-Verlag, New York.

An Approach for Inclusion of a Nonlocal Transition Model in a Parallel Unstructured Computational Fluid Dynamics Code

Dragan Kožulović¹

Institute of Propulsion Technology,
DLR—German Aerospace Center,
Cologne D-51147, Germany
e-mail: dragan.kozulovic@dlr.de

B. Leigh Lapworth

Aerothermal Methods Group,
Rolls-Royce plc.,
Derby DE24 8BJ, UK

The implementation of an integral transition model in a parallel unstructured computational fluid dynamics code is described. In particular, an algorithm for gathering the nonlocal boundary layer values (momentum thickness and shape factor) from parallel distributed computational domains is presented. Transition modeling results are presented for a flat plate and for a low pressure turbine, covering a large variation of Reynolds numbers, Mach numbers, turbulence intensities, and incidence angles. Contrary to fully turbulent simulations, transitional predictions are in very good agreement with measurements. Furthermore, the computational overhead of transitional simulations is only 7% for one multigrid cycle. [DOI: 10.1115/1.2987238]

1 Introduction

Due to the low air density at higher altitudes and to small dimensions of turbomachinery blades, jet engines operate at comparatively low Reynolds numbers at cruise conditions. According to Hourmouziadis [1] and Mayle [2], the lowest Reynolds numbers can be found in the low pressure turbine ($Re < 10^5$), making this component the most sensitive one to efficiency penalties caused by flow separation of laminar boundary layers on highly loaded suction sides of turbine airfoils. This issue is very profound since the efficiency penalty occurs at the *cruise* flight condition. Hence, it is of great importance for the aerodynamic design to accurately predict the loss mechanisms at low Reynolds numbers.

Laminar boundary layers, which are usually encountered at low Reynolds numbers, do not produce as many losses as turbulent boundary layers, but they are more sensitive to flow separation, which in turn can lead to larger overall losses. A quantitative prediction of the overall losses can only be performed by including an appropriate transition model in a computational fluid dynamics (CFD) solver. As will be shown later, fully turbulent simulations fail in accurately predicting losses at low Reynolds numbers. Most of the transition models, which have been developed over the past decades, rely on nonlocal boundary layer information such as shape factor and momentum thickness. Nowadays, these models have reached a certain degree of maturity, making them a valuable and trustworthy part of the aerodynamic design. However, the implementation of nonlocal transition models in modern CFD solvers poses a big problem, since gathering and communicating the nonlocal information over parallel computational processes are nontrivial. This is mainly due to the “arbitrary” decomposition of the computational domain to parallel processes. In this way, a boundary layer can be split to different processes, making integration a very uncomfortable task, see Fig. 1. For this reason, an efficient approach is developed, which com-

bins a nonlocal transition model with a parallel unstructured CFD code. Before proceeding to the algorithm description, the applied solver and transition model are briefly described in Secs. 2 and 3.

2 CFD Solver

HYDRA-CFD is a general purpose flow solver for hybrid unstructured meshes, which uses an efficient edge-based data structure, see Ref. [3]. The flow equations are integrated around median-dual control volumes using a monotone upstream-centered scheme for conservation law (MUSCL) based flux-differencing algorithm. The discrete flow equations are preconditioned using a block Jacobi preconditioner [4] and iterated toward steady state using the five-stage Runge–Kutta scheme of Martinelli [5]. Convergence to steady state is further accelerated through the use of an element-collapsing multigrid algorithm, see Ref. [6]. Nonlinear unsteady calculations are performed using either explicit or implicit dual time-stepping. However, only steady simulations have been conducted in the present work.

3 Transition Modeling

The transition model consists of two modes: natural/bypass mode and separation-induced mode. For both modes, the transition onset and transition development have to be modeled.

The natural/bypass mode is based on the Abu-Ghannam and Shaw [7] criterion and depends on the turbulence intensity Tu and the pressure gradient parameter λ_θ . In this criterion, the transition onset Reynolds number is correlated as follows:

$$Re_{\text{ost}} = \left[1045 \exp\left(-\frac{Tu}{1\%}\right) \right] + f_\lambda + 155 \quad (1)$$

$$f_\lambda = 220 \exp\left(-\frac{Tu}{0.9\%}\right) \cdot \left[\arctan\left(\frac{\lambda_\theta}{0.02} + 0.842\right) - 0.7 \right] \quad (2)$$

$$\lambda_\theta = \min \left[\frac{\theta^2}{\nu} \frac{\partial U_E}{\partial s}, \frac{0.058(H_{12} - 4.0)^2}{H_{12} - 1.0} - 0.068 \right] \quad (3)$$

Furthermore, the transition development is governed by the following intermittency correlation:

¹Present address: Institute of Fluid Mechanics, Technische Universität Braunschweig, Germany.

Contributed by the International Gas Turbine Institute (IGTI) of ASME for publication in the JOURNAL OF TURBOMACHINERY. Manuscript received August 11, 2007; final manuscript received March 14, 2008; published online April 8, 2009. Review conducted by David Wisler. Paper presented at the 2007 ASME Fluids Engineering Division Summer Meeting and Exhibition (FEDSM2007), San Diego, CA, July 30–August 2, 2007.

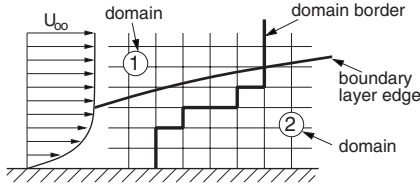


Fig. 1 Splitting of the boundary layer by domain decomposition

$$\gamma_{NB} = 1 - \exp \left[-5 \cdot \left(\frac{\text{Re}_\theta - \text{Re}_{\theta st}}{\text{Re}_{\theta end} - \text{Re}_{\theta st}} \right)^{1.2} \right] \quad (4)$$

$$\text{Re}_{\theta end} = \text{Re}_{\theta st} \cdot \left\{ 1.6 + \left[1.3 \exp \left(-\frac{\text{Tu}}{2\%} \right) \right] \right\} \quad (5)$$

In the current transition model, the momentum thickness Reynolds number Re_θ is essential for the determination of the intermittency γ_{NB} :

$$\gamma_{NB} = 0 \quad \text{for} \quad \text{Re}_\theta < \text{Re}_{\theta st}$$

$$0 < \gamma_{NB} < 1 \quad (\text{Eq. (4)}) \quad \text{for} \quad \text{Re}_{\theta st} < \text{Re}_\theta < \text{Re}_{\theta end}$$

$$\gamma_{NB} = 1 \quad \text{for} \quad \text{Re}_\theta > \text{Re}_{\theta end} \quad (6)$$

where Re_θ is defined as

$$\text{Re}_\theta = \frac{U_E \theta}{\nu_E} \quad (7)$$

As can be seen in Eq. (7), both the boundary layer edge and the integral values of the boundary layer are required by the transition model.

The separation-induced mode is modeled by an increasing intermittency between the separation onset and the reattachment point. This region is characterized by negative wall shear stress τ_w and is denoted as region A in Fig. 2. It is worth to mention that the intermittency γ_S can take values greater than 1 at the rear part of the separation bubble. In this way, the well-known deficiency of the linear eddy viscosity turbulence models for reattaching boundary layers is partly compensated, thus predicting more realistic bubble lengths and velocity profiles in the reattached regions. Following the reattachment point, the intermittency has to be decreased to the turbulent value of $\gamma=1$, as displayed in Fig. 2, region B. The functions for increasing and decreasing separation-induced intermittency γ_S are as follows:

$$\gamma_S = \min \left(\gamma_{up} + 8 \cdot \frac{\Delta s_{up}}{l}, 4 \right) \quad \text{for region A} \quad (\tau_w < 0) \quad (8)$$

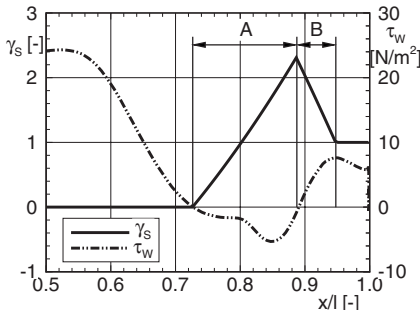


Fig. 2 Intermittency γ of separation-induced transition

$$\gamma_S = \max \left(\gamma_{up} - 10 \cdot \frac{\Delta s_{up}}{l}, 1 \right) \quad \text{for region B (reattached)} \quad (9)$$

In Eqs. (8) and (9), the intermittency from the upstream node γ_{up} and the distance to the upstream node Δs_{up} are necessary in order to determine the intermittency γ_S for the actual node.

After computing the intermittencies for both transition modes, the maximum value is applied:

$$\gamma_P = \max(\gamma_{NB}, \gamma_S) \quad (10)$$

Besides the intermittency γ_P , which is multiplied with the production term of the turbulence model, also the intermittency for the destruction term is needed:

$$\gamma_D = \min[\max(\gamma_P, 0.02), 1.0] \quad (11)$$

Limiting the intermittency γ_D by the lower limit of 0.02 makes sure that the turbulence destruction is also slightly present in laminar boundary layers. In this way, the eddy viscosity from the freestream is gradually eliminated when entering a laminar boundary layer. Furthermore, the upper limit of 1.0 allows additional production of eddy viscosity in regions with $\gamma_P > 1$ (reattaching boundary layers). In the present work, the intermittencies γ_P and γ_D are multiplied with the source terms of the Spalart and Allmaras turbulence model [8]:

$$\begin{aligned} \frac{\partial \tilde{\nu}}{\partial t} + U_j \frac{\partial \tilde{\nu}}{\partial x_j} = & \gamma_P c_{b1} \tilde{S} \tilde{\nu} - \gamma_D c_w f_w \left(\frac{\tilde{\nu}}{d} \right)^2 + \frac{1}{\sigma} \frac{\partial}{\partial x_k} \left[(\nu + \tilde{\nu}) \frac{\partial \tilde{\nu}}{\partial x_k} \right] \\ & + c_{b2} \frac{\partial \tilde{\nu}}{\partial x_k} \frac{\partial \tilde{\nu}}{\partial x_k} \end{aligned} \quad (12)$$

The closure coefficients and further details about the turbulence model can be found in Ref. [8]. Further details about the transition modeling approach are presented in Ref. [9].

4 Concept for Transition Model Implementation

A requirement for the combination of the transition model with the flow solver is the consistency with the parallel paradigm of modern CFD codes. The presented approach coincides with this requirement and is very efficient in terms of computational time (as will be shown later). However, it is not the *only* possible algorithm. Of course, there are many other imaginable approaches, but the presented one appears to be very straightforward, involving only concise extensions to the existing code.

4.1 Approach Description. Although the solver uses several grids for convergence acceleration, the transition modeling has been conducted only at the finest grid. The reason for this is the requirement for a very accurate resolution of the boundary layer ($y^+ \approx 1$), which can only be guaranteed on the finest grid level. Hence, the intermittency is determined only for the finest level and is restricted to the corresponding nodes of the coarser levels.

The implementation of the transition model essentially consists of four steps, which are subsequently described.

4.1.1 Step 1: Generation of Transition Lines. This step is conducted during preprocessing. As can be seen in Fig. 3, the transition lines (index n) are perpendicular to the surface, and they should be long enough to include the complete boundary layer. Transition lines themselves consist of segments (index m), which at both ends coincide with the mesh nodes (index j or k), as displayed in Fig. 3. The relation between the transition lines and the mesh is created by two mappings. The first mapping assigns a relation between segments and nodes, e.g., segment m is connected to nodes j and k . The second mapping sets a relation between the transition lines and segments, e.g., segment m belongs to line n .

In the present work, only the hexahedral meshes (treated as unstructured) have been applied, where both ends of the segment

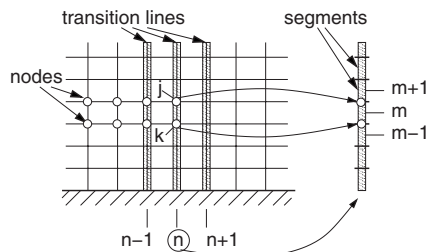


Fig. 3 Transition lines

coincide with the nodes. However, it is also possible to use arbitrary unstructured meshes with a resolution good enough to capture the laminar sublayer ($y^+ \approx 1$). Although the mapping would be more involved in this case, in principle, it is possible to assign the corresponding nodes, from which the segment should receive its information. The current method can also be used on hybrid meshes where there is a structured mesh adjacent to the transitional wall and unstructured mesh elsewhere.

The input routines of the solver should be extended to read in the transition lines, segments, and mappings. Furthermore, the lines and segments can be treated as any other parallel data set in the code, i.e., they can be distributed to different domains and processes. In the present approach, only segments form a distributed data set, whereas the transition lines, which are much smaller in number, are held in the global storage. A numerical array for several float values is allocated for each transition line, in order to accommodate the integral properties.

Gathering the transition line information can be done by feeding the communication routines, which are usually present in the solver, with the mapping data to the corresponding segments. In the subsequent steps, the information will be sent from nodes to segments and from segments to lines. Each time these operations have to take place, the communication routines have to be executed together with the corresponding mappings. Prior to any calculations using the segments, the flow variables at the nodes, which lie on the partition boundary, have to be exchanged. This ensures that segments, which share a common node, use the same value for that node, whether or not they are on the same partition. In the present solver, functions exist, which allow a communication between arbitrary domains and between different data sets (nodes, transition lines, segments, and boundary conditions) if corresponding mappings are present. It is assumed that other parallel unstructured solvers have similar functions.

The importance of the transition lines as fundamental elements of the present concept is stressed by the fact that the transition modeling is conducted for each line separately and independently of each other. All necessary information for the transition model, viz., the integral properties, the values from the boundary layer edge, and the values from the wall, is contained in the numerical array for each transition line.

Considering the choice of the transition lines, certain restrictions have to be taken into account. Since the transition model is based on two-dimensional flows, the transition lines should only be generated for the blade surfaces in the core flow region. In other words, the present transition model is not applicable to the regions of the sidewall influenced by three-dimensional flow, such as secondary and tip leakage flows. Furthermore, the transition lines should not be generated for leading and trailing edges, since the corresponding boundary layers considerably differ from the boundary layers, which are subject of transitional correlations.

4.1.2 Step 2: Find Boundary Layer Edge. Two loops over all segments are needed in order to determine the boundary layer edge. In the first loop, the maximum total pressure defect for each transition line is calculated. Both mappings have to be used in this loop. First, the flow variables are communicated from the nodes to

the segments, in order to determine the total pressure of each segment. Second, the mapping between the segments and the lines is used to assign the maximum total pressure to each line. This assignment is conducted on each partition in parallel and is subsequently synchronized to ensure all processors have the same maximum value. In other words, the total pressure is reduced for the line-global maximum. Similar communication operations have to be executed in the following loops and will not be explicitly mentioned, for the sake of clarity. In the second loop, the segment that exceeds 98% of the total pressure defect and simultaneously has the lowest wall distance is declared as the boundary layer edge.

The maximum total pressure defect is defined as the difference between the maximum total pressure of the transition line (usually located somewhere in the freestream) and the total pressure at the wall. The latter coincides with the static pressure, since the dynamic pressure contribution is equal zero at the wall, due to the no-slip boundary condition. The reason for the application of total pressure instead of other criteria such as velocity is based on the experience of the authors. Judging the pressure defect yields reasonable boundary layer edges even for separated flows or for sloped freestream velocity profiles, which are usually present in the blade-to-blade turbomachinery passages. In contrast, direction-dependent criteria such as velocity would require a sophisticated case distinction in order to handle these flows.

4.1.3 Step 3: Integration of Boundary Layer. Prior to the integration of the boundary layer, an additional loop over all segments has to be conducted. In this loop, the flow variables from the boundary layer edge are assigned to each corresponding transition line. Simultaneously, a weight of 1 is given to the segments inside the boundary layer and a weight of 0 to the segments beyond the boundary layer edge. A special treatment can be conducted with the segment defining the boundary layer edge. Depending on the value of the total pressure defect, a weight somewhere between 0 and 1 can be assigned for the edge segment, in order to achieve a smooth run of integral values between neighboring transition lines. In this way, an improvement of the convergence behavior can be achieved. A simple linear interpolation has been applied in the present work. The integration of the boundary layer is conducted by looping over all segments once again and adding the weighted contribution of each segment to the corresponding transition line. In this loop, the integral properties are accumulated in parallel and are subsequently reduced for the line-global sum, ensuring the same value for all processors. As a result, each transition line should now contain the necessary integral values of the boundary layer.

4.1.4 Step 4: Application of Transition Correlations. The intrinsic transition modeling is performed in this step. For each transition line, the intermittency is determined by comparing the integral values with the correlations. One final loop over all segments has to be conducted, in order to distribute the intermittency to the corresponding mesh nodes.

4.2 Convergence Behavior. The applied multigrid acceleration technique used four grid levels, going from the finest grid to the coarsest and back to the finest grid in the so called "V-cycle." For only one multigrid cycle, the computational overhead of the transitional simulations was about 7%. This value is an averaged value for the conducted simulations of a 2D flat plate and a 2D turbine. It can be expected that the cycle overhead can slightly vary depending on the ratio of the overall mesh nodes to the nodes, which intersect with the transitional lines. If less nodes are involved in the transitional algorithm, the cycle overhead will reduce and vice versa.

In Fig. 4, the root mean square (rms) residual for all five Navier–Stokes equations is presented (the logarithmic value is displayed). It becomes evident that for the calculated turbine flow the transitional simulation achieves very low residuals, which is a sign for a very good convergence. Furthermore, the residual de-

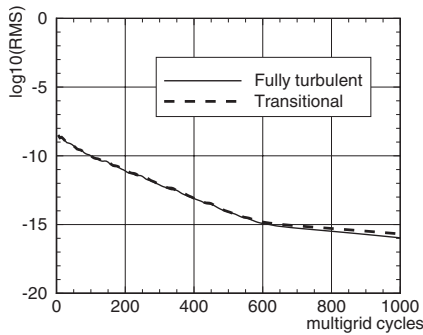


Fig. 4 Root mean square residual from all five Navier–Stokes equations, T106A turbine

velopment over the multigrid cycles and the achieved residual values are comparable to the fully turbulent simulation, which can be considered as a reference computation. The convergence behavior can also be judged by the total pressure at the outflow boundary, which since this depends strongly on the loss within the domain is indicative of the overall convergence rate, see Fig. 5. Figure 5 suggests that the transitional simulation needs about 10% more multigrid cycles as compared with the fully turbulent computation. The reason therefore is the weak coupling of the transition model with the Navier–Stokes equations. First, the intermittency supports the turbulence model in finding the “correct” eddy viscosity (by coupling to the source terms). Second, the eddy viscosity is coupled to the Navier–Stokes equations via diffusion terms and shows larger contributions only in the boundary layers, which make a relatively small region of the complete flow field. In this coupling chain, the information from the transition model needs several additional multigrid cycles to reach the Navier–Stokes equations. On the other hand, this appears to be a general feature when combining a transition model with a Reynolds-averaged Navier–Stokes solver and should not be accounted for as a penalty due to the presented implementation. The above mentioned overhead per one multigrid cycle appears to be a more appropriate assessment value. Nevertheless, the overall computational time is increased by 15–25% when the transition model is applied. The exact value varies depending on the test case, boundary conditions, acceleration techniques, etc.

5 Flat Plate Results

As a first application, the transitional flat plate flow without pressure gradient is presented. The test case is the ERCOFTAC T3 flat plate series, see Ref. [10]. For the investigated configurations, the Mach number was very low, ranging between 0.015 and 0.058. The applied mesh consists of 19,000 nodes, with a boundary layer resolution of 30 nodes and a dimensionless wall distance of wall-adjacent cells of $y^+ \approx 1$.

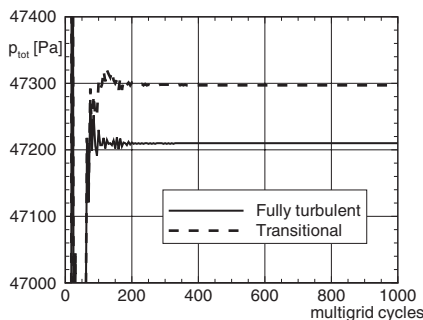


Fig. 5 Circumferentially averaged total pressure at outflow boundary, T106A turbine

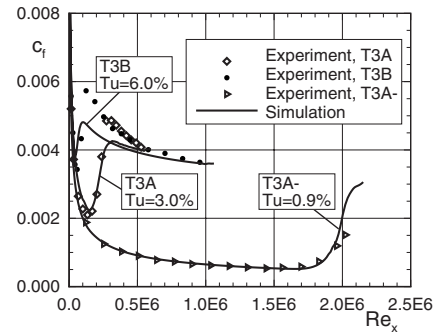


Fig. 6 Skin friction coefficient c_f of T3 flat plate series

Figure 6 shows the skin friction coefficient c_f for three different configurations: T3A, T3B, and T3A-. The varied variables for these configurations are the turbulence intensity (from 0.9% to 6.0%) and the Reynolds number (from 0.6×10^6 to 2.3×10^6). For all three configurations, the transition onset, which is characterized by the increase of the skin friction coefficient, is in a very good agreement with the measurements. Downstream of the transition region, the skin friction is slightly underpredicted. The reason therefore is not contained in the transition modeling, since the predicted intermittency value of $\gamma=1$ indicates a fully turbulent state in this part of the boundary layer.

6 Low Pressure Turbine Cascade T106A

6.1 Test Case Description. Considerable validation of the transition model has been conducted on the turbine cascade T106A, also known as the AGARD test case E/CA-6, see Ref. [11]. A more detailed collection of the measurements can be found in Ref. [12]. Since the measurements yield an axial velocity density ratio of 1 ± 0.005 , the flow can be assumed to be two dimensional. The geometry and the computational mesh of T106A are shown in Fig. 7. The mesh consists of 37,000 nodes and the dimensionless wall distance of wall-adjacent cells is $y^+ \approx 1$. In Fig. 7 also, the inflow angle α_1 and the incidence angle i are sketched. Here, the incidence angle i is defined as the deviation from the design inflow angle of $\alpha_1=37.7$ deg. Furthermore, the regions where the transition lines have been generated are denoted. Except for very small regions at the leading and trailing edges, the transition modeling has been applied to both the pressure and suction sides. The scope of the investigation covers the following variations:

1. Reynolds number Re_{2th} [10^5]: 1.5, 3, 5, 7, 9, 11
2. turbulence intensity Tu (%): 0.5, 4

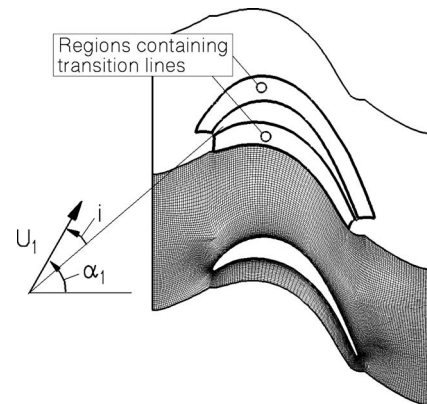


Fig. 7 Geometry and computational domain of the T106A low pressure turbine

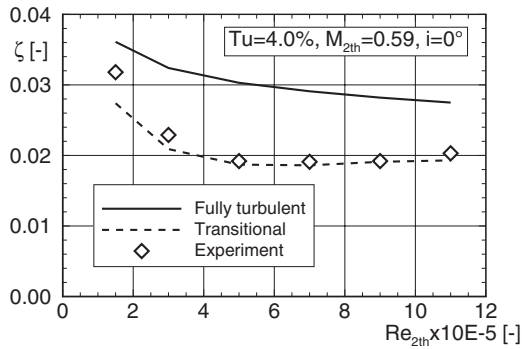


Fig. 8 Influence of Reynolds number Re on the loss coefficient ζ

3. Mach number M_{2th} : 0.3, 0.59 (design), 0.8, 0.9, 0.955
4. inflow angle α_1 (deg): 0, 10, 27.7, 37.7 (design), 47.7, 50

The incidence angle i can be obtained from the inflow angle α_1 by following relation:

$$i = \alpha_1 - 37.7 \text{ deg} \quad (13)$$

In Secs. 6.2–6.5, the influences of the aforementioned variables are discussed separately.

6.2 Influence of Reynolds Number. Figure 8 shows the dependence of the loss coefficient ζ on the Reynolds number Re_{2th} . In particular, there is a considerable increase of losses toward lower Reynolds numbers, which is of great practical importance, since the cruise flight conditions are located at low Reynolds numbers. Figure 8 clearly demonstrates that the fully turbulent simulation is neither able to accurately predict the loss coefficient values nor the loss increase toward the lower Reynolds numbers. In contrast, the transitional simulation yields a much better agreement with the measurements. The improved prediction quality of the transitional simulations is also reflected in the pressure distributions, as can be seen in Fig. 9. The pressure distribution at the lowest Reynolds number indicates a separation bubble at the rear part of the suction side. This separation bubble is also reproduced by the transitional simulation, whereas the fully turbulent computation rather suggests an attached boundary layer. As the Reynolds number increases, the separation bubble becomes smaller and finally disappears for the largest Reynolds number. This trend is also reproduced by the transitional simulations.

The presence of the separation bubble at low Reynolds numbers is also indicated by large values of the shape factor H_{12} , as shown in Fig. 10. For larger Reynolds numbers, the transition model shifts the shape factor from the laminar value of $H_{12}=2.6$ toward the turbulent value of $H_{12}=1.4$, thus preventing a separation.

Following the momentum equation of the boundary layer (see Ref. [13]), there is a direct relation between losses and momentum thickness θ . Hence, the loss producing mechanisms can be studied by the development of the momentum thickness θ , see Fig. 11. For the lowest Reynolds number, the momentum thickness strongly increases at the rear part of the blade, where the separation bubble is located. In other words, the separation bubble is responsible for the large losses at cruise conditions. On the other hand, the separation is not present for the larger Reynolds numbers, which avoids the separation-related loss production. Instead, increased loss production rates can be observed from the positions where the transition to turbulent boundary layers takes place. It is a well-known feature of turbulent boundary layers to produce more losses as compared with laminar ones. As a final observation from the momentum thickness development, the θ values at the trailing edge are compared with the corresponding loss coefficient values ζ from Fig. 8. The greatest trailing edge momentum thickness θ is found for the lowest Reynolds number, which coincides

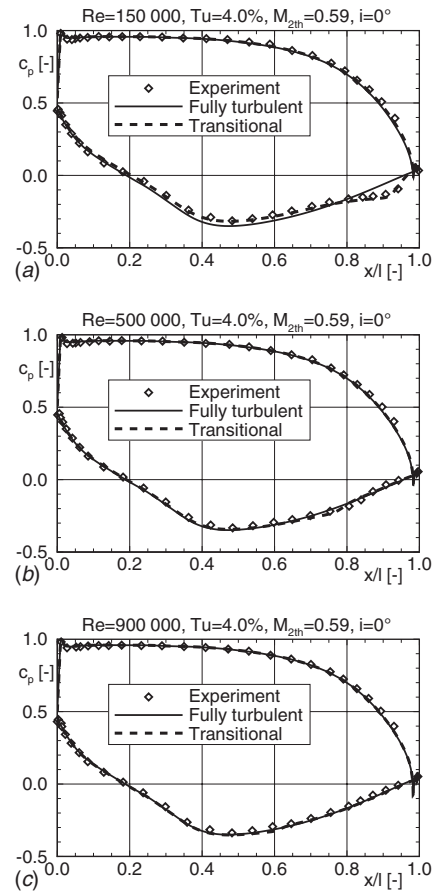


Fig. 9 Pressure distributions at different Reynolds numbers

with the observation for the loss coefficient value ζ . In addition, the momentum thicknesses of the both larger Reynolds numbers are approximately the same, which also coincides with the loss coefficient values. This is not surprising, since the trailing edge momentum thickness can be considered as a very good approximation of overall profile losses (following the boundary layer theory), at least for the trends.

In Figs. 10 and 11, only the suction side is presented, since the pressure side is not sensitive to separation. In addition, the transition model yields a laminar boundary layer at the pressure side (not shown here), which has a less significant contribution to the overall losses and to the blade performance.

The transitional results for different Reynolds numbers yield accurate loss predictions and pressure distributions. Furthermore, the relations between the losses, separation bubbles, pressure dis-

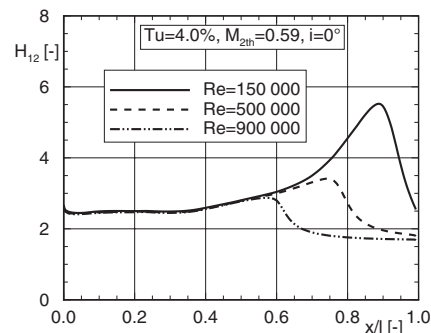


Fig. 10 Shape factor H_{12} of transitional simulations at different Reynolds numbers, suction side

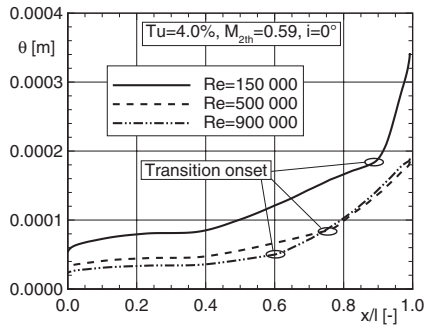


Fig. 11 Momentum thickness θ of transitional simulations at different Reynolds numbers, suction side

tributions, and boundary layer integrals are consistent, demonstrating the transition model's capabilities as a reliable design tool.

6.3 Influence of Turbulence Intensity. Figure 12 shows the loss coefficient values ζ for two different turbulence intensities Tu . Besides the large turbulence intensity of $Tu=4\%$, which is representative for a multistage turbomachinery environment, also a comparatively low value of $Tu=0.5\%$ has been investigated. Apparent loss differences between both turbulence intensities occur only at larger Reynolds numbers, i.e., the losses are lower for lower turbulence intensity. This trend is correctly reproduced by the corresponding transitional simulations.

6.4 Influence of Mach Number. A comparison between the measured and predicted loss coefficients ζ as a function of the Mach number M is given in Fig. 13. Different from the fully turbulent simulation, the transitional simulation is in good agreement with the measurements, in particular, when the loss value at the design Mach number and the steep loss increase at larger

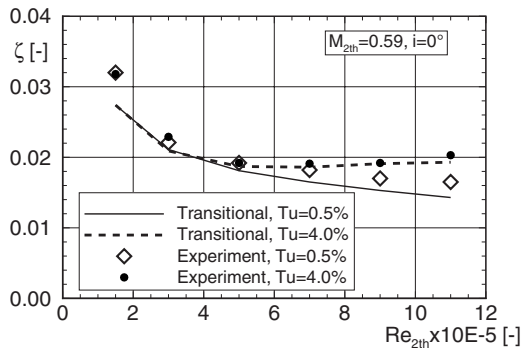


Fig. 12 Influence of turbulence intensity Tu on the loss coefficient ζ

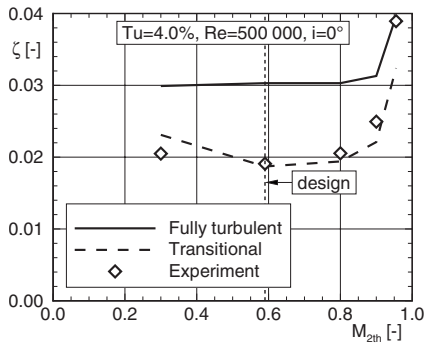


Fig. 13 Influence of Mach number M_{2th} on the loss coefficient ζ

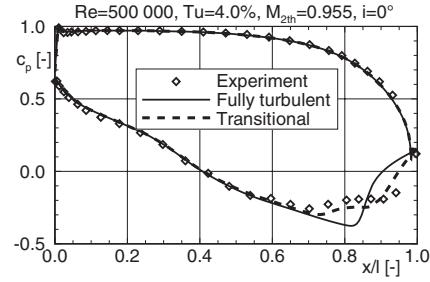


Fig. 14 Pressure distribution at large Mach number

Mach numbers are considered. Toward the lower Mach numbers, the transitional loss value is somewhat overpredicted, but the overall agreement is good.

The improvement of the prediction quality of transitional calculations is visible by the pressure distribution at the largest investigated Mach number, Fig. 14. Especially at the rear part of the suction side, the transitional pressure distribution is in better agreement with the experiment.

6.5 Influence of Inflow Angle. As the final influence factor, the inflow angle is varied. Figure 15 shows the dependence of the loss coefficient ζ on the inflow angle, here expressed in terms of incidence angle i , see Eq. (13). As expected, the lowest losses can be found at the incidence-free configuration ($i=0$), i.e., at the inflow angle the blade was designed for. The losses are increased for both the positive and negative incidences, a trend that is accurately captured by the transition model. Only the transitional prediction at the extremely negative incidence does not fit in this trend. Due to the massive pressure side separation, which starts at the leading edge, the boundary layer does not fit in the transition line, leading to less accurate transition modeling. Once again, the fully turbulent simulation yields considerably wrong results, clearly indicating the need for appropriate transition modeling.

7 Conclusions

An efficient approach for inclusion of a nonlocal transition model into a parallel unstructured multigrid solver has been presented. The concept is based on the so called "transition lines," which are generated in a preprocessing step and use mappings in order to communicate with the nodes of the computational mesh. The implementation of the algorithm is straightforward and only small extensions to the existing code are necessary.

The computational overhead of transitional simulations is approximately 7% for one multigrid cycle and 15–25% for the overall simulation time. Furthermore, the convergence behavior is comparable to the fully turbulent simulations.

To demonstrate the transition model performance, two test cases have been investigated: a flat plate and a low pressure tur-

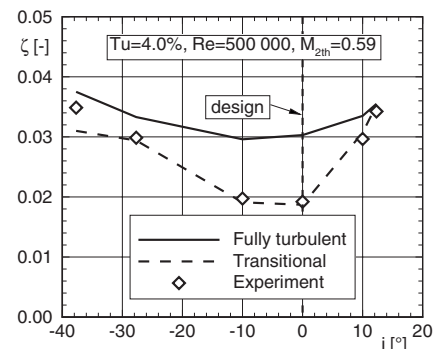


Fig. 15 Influence of incidence angle i on the loss coefficient ζ

bine. The predictions of fully turbulent simulations show large discrepancies at low Reynolds numbers. In contrast, the agreement with the measurements is considerably improved by applying the transition model, stressing a need for appropriate transition modeling for turbomachinery flows at low Reynolds numbers. Furthermore, a broad range of parameters (turbulence intensity, Reynolds number, Mach number, and incidence angle) have been varied, in order to validate the transition model's capability to correctly reproduce their effects at the loss production. Moreover, the predicted losses are consistent to the pressure distributions and boundary layer values.

Acknowledgment

The authors received a lot support from following colleagues: Dr. Peter Stow, Dr. John Coupland, Dr. Frank Haselbach (all from Rolls-Royce Derby), Carsten Clemen (from Rolls-Royce Dahlenburg), Anton Weber (DLR Cologne), Dr. Dirk Nürnberger (DLR Cologne), and Dr. Hong Yang (formerly DLR Cologne). The outstanding support was not only limited to the modeling and programming issues but continued also to the preparation of test cases. Furthermore, the authors would like to thank the colleagues for the fruitful discussions and an exceptionally nice collaboration atmosphere which has established between both groups.

Nomenclature

a	= speed of sound
c_f	= skin friction coefficient, $2\tau_w/(\rho_\infty U_\infty^2)$
c_p	= pressure coefficient, $2(p_w - p_2)/(p_{tot1} - p_2)$
d	= wall distance
H_{12}	= shape factor, δ_1/θ
i	= incidence angle, Eq. (13)
l	= chord length
M	= Mach number, U/a
p	= static pressure
p_{tot}	= total pressure
Re	= Reynolds number, Ul/ν
s	= streamwise direction
t	= time
Tu	= turbulence intensity, %
U	= velocity
u_τ	= friction velocity, $\sqrt{\tau_w/\rho_w}$
x, y, z	= Cartesian coordinates
y^+	= dimensionless wall distance, $u_\tau y/\nu$

Greek Symbols

α	= circumferential angle, Fig. 7
γ	= intermittency
δ	= boundary layer thickness, 98% of total pressure defect
δ_1	= displacement thickness, $\int_0^E (1 - (\rho U/\rho_E U_E)) dy$
λ_θ	= pressure gradient parameter, Eq. (3)
ν	= kinematic viscosity
\tilde{v}	= working variable of the SA turbulence model

ν_T	= eddy viscosity
θ	= momentum thickness, $\int_0^E (\rho U/\rho_E U_E)(1 - (U/U_E)) dy$
ρ	= density
τ_w	= wall shear stress, $\rho\nu(\partial U/\partial y)_w$
ζ	= loss coefficient, $(p_{tot1} - p_{tot2})/(p_{tot1} - p_2)$

Subscripts

D	= destruction
E	= boundary layer edge
end	= end
NB	= natural and bypass transition
P	= production
S	= separation-induced transition
st	= start
T	= turbulent
th	= theoretical
tot	= total
up	= upstream
W	= wall
1	= inflow
2	= outflow
∞	= freestream, inflow

References

- [1] Hourmouziadis, J., 1989, "Aerodynamic Design of Low Pressure Turbines," AGARD Lecture Series, Vol. 167.
- [2] Mayle, R. E., 1991, "The Role of Laminar-Turbulent Transition in Gas Turbine Engines," ASME J. Turbomach., **113**, pp. 509-537.
- [3] Moinier, P., and Giles, M. B., 1998, "Preconditioned Euler and Navier-Stokes Calculations on Unstructured Grids," *Proceedings of the Sixth ICFD Conference on Numerical Methods for Fluid Dynamics*, Oxford, UK.
- [4] Moinier, P., Müller, J.-D., and Giles, M. B., 2002, "Edge-Based Multigrid and Preconditioning for Hybrid Grids," AIAA J., **40**(10), pp. 1954-1960.
- [5] Martinelli, L., 1987, "Calculations of Viscous Flows With a Multigrid Method," Ph.D. thesis, Department of Mechanical and Aerospace Engineering, Princeton University.
- [6] Müller, J.-D., and Giles, M. B., 1998, "Edge-Based Multigrid Schemes for Hybrid Grids," *Proceedings of the Sixth ICFD Conference on Numerical Methods for Fluid Dynamics*, Oxford, UK.
- [7] Abu-Ghannam, B. J., and Shaw, R., 1980, "Natural Transition of Boundary Layers: The Effects of Turbulence, Pressure Gradient and Flow History," J. Mech. Eng. Sci., **22**(5), pp. 213-228.
- [8] Spalart, P. R., and Allmaras, S. R., 1992, "A One-Equation Turbulence Model for Aerodynamic Flows," *La Recherche Aérospatiale (1)*, ONERA, Paris, pp. 5-21, see also AIAA Paper No. 92-439.
- [9] Kožulović, D., Röber, T., and Nürnberger, D., 2007, "Application of a Multi-mode Transition Model to Turbomachinery Flows," *Proceedings of the Seventh European Turbomachinery Conference*, Athens, Greece, pp. 1369-1378.
- [10] Savill, A. M., 1993, "Some Recent Progress in the Turbulence Modelling of By-Pass Transition," *Near Wall Turbulent Flows*, R. M. C. So, C. G. Speziale, and B. E. Launder, eds., Elsevier, Loughton, p. 829, see also <http://cfd.me.umist.ac.uk/ercotac/>
- [11] Hoheisel, H., 1990, "Test Case E/CA-6: Subsonic Turbine Cascade T106," *Test Cases for Computation of Internal Flows in Aero Engine Components*, L. Fottner, ed., SPS, Loughton, Paper No. AGARD-AR-275, pp. 112-123.
- [12] Hoheisel, H., 1981, "Entwicklung neuer Entwurfskonzepte für zwei Turbinengitter, Teil III: Ergebnisse T106," Institutbericht IB 129-81/26, DFLVR, Braunschweig, Germany.
- [13] Schlichting, H., and Gersten, K., 1997, *Grenzschicht-Theorie*, 9th ed., Springer, Berlin.

Developments in Hot-Streak Simulators for Turbine Testing

Thomas Povey

Imran Qureshi

Department of Engineering Science,
University of Oxford,
Parks Road,
Oxford OX1 3PJ, UK

The importance of understanding the impact of hot-streaks, and temperature distortion in general, on the high pressure turbine is widely appreciated, although it is still generally the case that turbines are designed for uniform inlet temperature—often the predicted peak gas temperature. This is because there is an insufficiency of reliable experimental data both from operating combustors and from rotating turbine experiments in which a combustor representative inlet temperature profile has accurately been simulated. There is increasing interest, therefore, in experiments that attempt to address this deficiency. Combustor (hot-streak) simulators have been implemented in six rotating turbine test facilities for the study of the effects on turbine life, heat transfer, aerodynamics, blade forcing, and efficiency. Three methods have been used to simulate the temperature profile: (a) the use of foreign gas to simulate the density gradients that arise due to temperature differences, (b) heat exchanger temperature distortion generators, and (c) cold gas injection temperature distortion generators. Since 2004 three significant new temperature distortion generators have been commissioned, and this points to the current interest in the field. The three new distortion generators are very different in design. The generator designs are reviewed, and the temperature profiles that were measured are compared in the context of the available data from combustors, which are also collected. A universally accepted terminology for referring to and quantifying temperature distortion in turbines has so far not developed, and this has led to a certain amount of confusion regarding definitions and terminology, both of which have proliferated. A simple means of comparing profiles is adopted in the paper and is a possible candidate for future use. New whole-field combustor measurements are presented, and the design of an advanced simulator, which has recently been commissioned to simulate both radial and circumferential temperature nonuniformity profiles in the QinetiQ/Oxford Isentropic Light Piston Turbine Test Facility, is presented. [DOI: 10.1115/1.2987240]

1 Introduction

Turbine inlet temperature distortion (ITD) can cause changes in the flow field in both the high pressure (HP) nozzle and the HP turbine that affect the aerodynamics, heat transfer, loading, life, secondary loss, and, therefore, efficiency.

In the inviscid case where the inlet total pressure distribution is unaltered by ITD, the flow field in the vane is also unaltered; this was first demonstrated on theoretical grounds by Munk and Prim in 1947 [1]. In the thin viscous boundary layers on the HP vane and end wall surfaces, an alteration (distortion from the uniform) of the temperature field alone can alter the secondary flow pattern and therefore influence the heat transfer coefficient and loss. It has been shown experimentally that this effect is generally rather small. The change in local temperature can cause very large changes in heat transfer rate on both the HP vane and end wall, as demonstrated by Povey et al. in 2007 [2], even when the heat transfer coefficient is effectively unaltered: a somewhat obvious, but nonetheless important, result. Where there is a distortion of the inlet total pressure profile, the secondary flow development in the vane can be manifestly altered, as demonstrated both experimentally and theoretically by Thole and Hermanson in 2002 [3]. One would expect a corresponding change in the local heat transfer coefficient and, in the case where the total pressure distortion was accompanied by ITD, a change in local driving gas temperature.

In the HP rotor the effect of ITD is generally more significant. Even in the theoretical case of inviscid flow with uniform HP vane inlet total pressure, in the rotor relative frame ITD causes changes in flow angle, total pressure, total temperature, and Mach number.

These changes cause the well-known temperature segregation effect, which generally causes hot flow to accumulate on the rotor pressure surface and sometimes also a migration of hot flow toward the rotor tip. Secondary flows are therefore induced by ITD, and the associated changes in the heat transfer coefficient and local driving temperature can be significant. The HP rotor designed for a nominally uniform inlet temperature may well prove to be grossly off design when subject to even moderate ITD. The same effects can be observed in the downstream intermediate pressure (IP) or low pressure (LP) vane (Povey et al. [4]) although naturally here the temperature variations will be significantly attenuated.

There are a number of papers and review articles that, together, summarize the experimental investigations to date. For instance, Sharma et al. [5] considered a number of unsteady flow phenomena and an early experimental study of hot-streaks, Dorney et al. [6] reviewed both experiments and computational studies of hot-streak migration, and Povey et al. [2] gave a review of more recent experimental studies. There have been numerous computational studies. The results of these experimental investigations are not reviewed here as the main focus of this work is the simulation of temperature nonuniformity rather than the effects on the turbine.

Despite the significant number of publications that consider the effects of ITD either experimentally or computationally, it is difficult to draw general conclusions that may be applied to turbine design. This is in part because of the complex nature of a flow field in which a number of interrelated phenomena are essentially competing, some of which may be more or less pronounced for a given turbine. There are other factors, however. The scarcity of experimental combustor measurements, especially in the open literature, means that there is no standard test-case profile; indeed, the intensity of simulated profiles differs by almost an order of

Manuscript received September 12, 2007; final manuscript received July 23, 2008; published online April 9, 2009. Review conducted by Ronald S. Bunker.

magnitude between some tests. The difficulty of simulating a temperature profile, even where a clear target exists, means that some experiments have been limited to weak, nonreproducible, or poorly characterized profiles. Especially where a profile is either nonreproducible or poorly characterized, the difficulties of performing heat transfer measurements where the pertinent differences are not predominated by uncertainty are great.

This paper collects some of the experiences gained in the experiments in six rotating facilities in such a way that they can easily be compared. The simulated profiles are discussed in the context of the available combustor measurements. New whole-field combustor measurements at an extreme point in the engine cycle and an advanced combustor simulator capable of accurately and reproducibly simulating the combustor temperature profile are also discussed.

There is growing interest in HP vane and turbine designs that are congruent with current combustor ITD profiles rather than essentially designed for a uniform inlet temperature. Since 2004 three new temperature distortion generators have been commissioned on rotating turbine test facilities, and in the future it would seem likely that combustor simulators will be employed in industrial turbine test facilities. It is hoped that this review and the description of the new advanced combustor simulator will be of use to designers of future combustor simulators.

2 Discussion of Temperature Distortion Factor Definitions

Measurements of temperature at the exit plane of combustors show large radial and circumferential variations in temperature. The flow is, in addition, highly unsteady. The time-mean temperature field measured at the exit plane of a combustor typical of a modern military engine is presented in Fig. 4. Peak temperatures are in excess of 2200 K, while at the hub and casing end walls there are relatively cool regions of flow, with temperatures as low as 1500 K. Circumferential variations (hot-spots) arise because of the discrete nature of fuel and dilution air jets. In addition, combustor lining coolant flow causes a strong radial temperature gradient.

To quantify temperature nonuniformity, temperature distortion (or distribution) factors (TDFs) or so-called pattern and profile Factors (PFs) are used. The former (TDFs) are more common in Europe, while the latter are more common in the U.S. The term “traverse” is also used to describe the temperature field. There are several definitions in current use, many of which are essentially the same. A universally accepted norm has so far not been adopted, and therefore a short discussion is now given.

Combustor flow is highly turbulent, and because hot and cold gas streams are subject to aggressive mixing, typical time-mean combustor exit temperature profiles are generally rather smooth spatially. It may be sufficient in some cases, therefore, to describe an ITD with a single numerical value. A distinction is drawn, however, between the overall TDF (OTDF)—which is synonymous with the pattern factor, which is a measure of the divergence of the hottest gas streak from the mean temperature—and the radial TDF (RTDF)—which is synonymous with the profile factor, which is a measure of the nonuniformity of the circumferentially averaged temperature field. The definitions that are used are as follows:

$$\text{OTDF} = \text{pattern factor} = \frac{T_{4,\max} - \bar{T}_4^{\text{area}}}{\Delta T_{\text{comb}}}$$

$$\text{RTDF} = \text{profile factor} = \frac{\bar{T}_{4,\max}^{\text{circ}} - \bar{T}_4^{\text{area}}}{\Delta T_{\text{comb}}}$$

where

$$\Delta T_{\text{comb}} = \bar{T}_4^{\text{area}} - \bar{T}_3^{\text{area}}$$

where \bar{T}_3^{area} and \bar{T}_4^{area} are the area-mean temperatures at the combustor inlet and exit planes (although sometimes a mass average is taken instead, \bar{T}^{mass}), \bar{T}_4^{circ} is the circumferential mean temperature (expressed as a function of radial height), ΔT_{comb} is the temperature rise across the combustor, and T is the local temperature (a function of span, or area). The subscript “max” identifies that the maximum of the quantity has been taken. Although the above definitions of OTDF, RTDF, and pattern/profile factors are the most commonly accepted (see, for example, Lefebvre [7]) and are the ones generally used by engine manufacturers, there are a number of examples in the literature of alternative definitions: for example, Palaghita and Seitzman [8] used pattern factor $= T_{4,\max} / \bar{T}_4^{\text{area}} - 1$.

Where a description of the form of the profile is required, the local OTDF or pattern factor (LOTDF) and local RTDF or profile factor (LRTDF) forms follow naturally,

$$\text{LOTDF} = \text{local pattern factor} = \frac{T_4 - \bar{T}_4^{\text{area}}}{\Delta T_{\text{comb}}}$$

$$\text{LRTDF} = \text{local profile factor} = \frac{\bar{T}_4^{\text{circ}} - \bar{T}_4^{\text{area}}}{\Delta T_{\text{comb}}}$$

The usefulness of these TDF definitions is not universally understood. In the engine situation, these parameters quantify how completely hot and cold gas streams mix. Although there is no direct analogy in the test-facility situation, it is worth noting that where heat transfer similarity is concerned, as well as both $\bar{T}^{\text{area}}/T_w$ and T_{cool}/T_w (where T_{cool} is the temperature of the cold gas introduced to simulate ITD in the test rig situation), equivalent test-facility (rig) TDFs may be defined,

$$\text{LOTDF}_{\text{rig}} = \frac{T - \bar{T}^{\text{area}}}{\bar{T}^{\text{area}} - T_{\text{cool}}}, \quad \text{LRTDF}_{\text{rig}} = \frac{\bar{T}^{\text{circ}} - \bar{T}^{\text{area}}}{\bar{T}^{\text{area}} - T_{\text{cool}}}$$

Some authors use analogous quantities to $\text{LOTDF}_{\text{rig}}$. For example, Barringer et al. [9] used the local quantity $\theta = \bar{T}^{\text{circ}} / \bar{T}^{\text{area}} - 1$.

It can be shown that if $\text{LOTDF}_{\text{rig}}$ (rig situation) is matched to LOTDF (engine situation), the nondimensional vane inlet temperature profile (T/\bar{T}^{area}) will also be approximately matched. Most importantly, this is so whether or not there is a similarity in mixing processes (between rig and engine) upstream of the vane inlet plane: so the geometry of the simulator used in the rig situation is unimportant. This is clearly seen when the definitions are rearranged to make the nondimensional temperature profile the subject. For the engine,

$$T_4 / \bar{T}_4^{\text{area}} = \text{LOTDF} (1 - \bar{T}_3^{\text{area}} / \bar{T}_4^{\text{area}}) + 1$$

For the rig,

$$T / \bar{T}^{\text{area}} = \text{LOTDF}_{\text{rig}} (1 - T_{\text{cool}} / \bar{T}^{\text{area}}) + 1$$

Where $\bar{T}^{\text{area}}/T_w$ and T_{cool}/T_w are matched between the rig and engine situations (for heat transfer experiments), it follows that $T_{\text{cool}}/\bar{T}^{\text{area}}$ is also matched. In this case, $T_{\text{cool}}/\bar{T}^{\text{area}} \approx \bar{T}_3^{\text{area}}/\bar{T}_4^{\text{area}}$ and the nondimensional temperature profiles are also approximately matched.

2.1 Summary of Definitions and Adopted Convention. Nozzle guide vane (NGV) and rotor blade cooling systems are generally designed for the hottest temperature in the traverse. Where the OTDF (pattern factor) and RTDF (profile factor) definitions are used consistently, they provide a sensible means of comparing temperature nonuniformities for different combustor designs. Where hot-gas migration is important, the local quantities LOTDF/LRTDF allow the exact shape of area/radial profiles to be

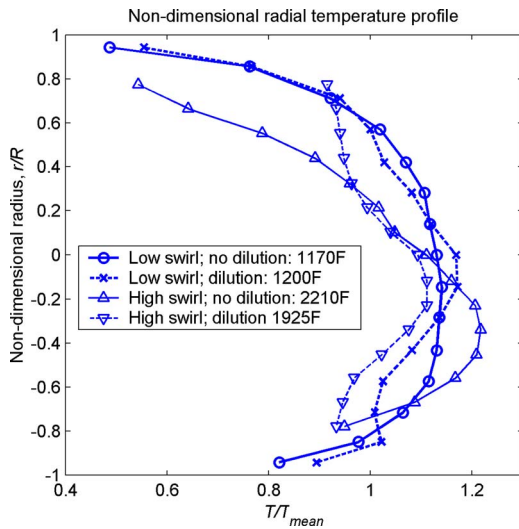


Fig. 1 Measured combustor radial profiles from Goebel et al. [10]

described and provide additional information about the flow exiting the combustor. A resurgence of experimental work to study the effect of temperature nonuniformities has led to the adoption of the analogous rig parameters $LOTDF_{rig}/LRTDF_{rig}$. In the heat transfer experiment, in which \bar{T}^{area}/T_w and T_{cool}/T_w are matched between the rig and engine situations, it has been shown that there is an even more direct parallel between the two definitions such that $LOTDF_{rig} \approx LOTDF$ and, by the same argument, $LRTDF_{rig} \approx LRTDF$.

Although the above definitions can be used to adequately describe all temperature profiles, consistent usage of definitions and terminology is not the norm, and a number of alternative definitions have been presented in the literature. This makes a direct comparison of results from different investigators difficult and is a common source of confusion.

In terms of the forces that affect hot-streak migration, secondary flow formation, and heat transfer, it is sufficient to match the temperature ratio T/\bar{T} (where \bar{T} is either area or mass averaged) between the test facility and engine for similarity to hold. This would appear therefore to be the obvious lingua franca in which all measurements, whether from an engine or an experimental rig, can be described and compared while adding the minimum confusion. Where a radial or circumferential profile is required, the average can be taken in the appropriate direction. This convention has been followed in this paper.

3 Measured Combustor Temperature Profiles

Because of the complex nature of the combustion process (high turbulence and swirl, dilution jets, film cooling, etc.), experiments that aim to study the impact of TDFs on turbine efficiency, heat transfer, and aerodynamics rely on experimentally measured combustor temperature profiles to inform the choice of target inlet profile for temperature profile generators. A review of measured radial and overall combustor temperature profiles is now presented.

3.1 Radial Temperature Profiles. The effect of nozzle swirl and dilution and mixing hole flows on the temperature profile in a small scale combustor was surveyed using a thermocouple probe by Goebel et al. [10]. The authors found that an increase in swirl generally increased the radial nonuniformity, whereas the effect of increased dilution flow was to flatten the profile in the region in which the jets penetrated. The results are shown in Fig. 1, plotted against a nondimensional radius.

Four unattributed temperature profiles (Fig. 2) measured in

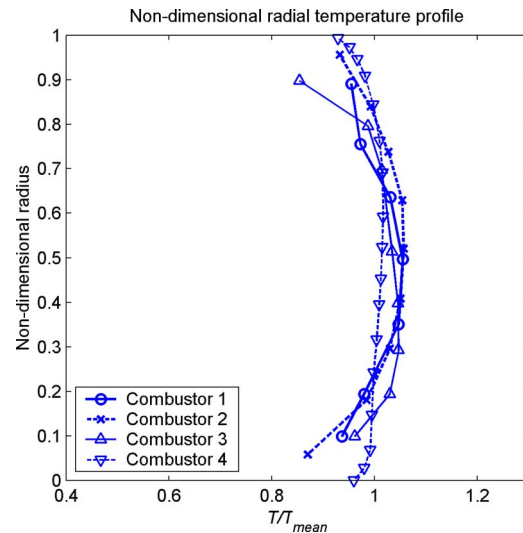


Fig. 2 Measured combustor radial profiles from Barringer et al. [9]

aero-engine combustors (c. 2002) were used by Barringer et al. [9] as the target profiles for a new combustor simulator developed for the Wright Patterson Air Force Base Turbine Research Facility. The profiles are rather flat in comparison to other profiles in the open literature, even in the near wall region, which suggests significant mixing with dilution air.

A combustor radial temperature profile measured by QinetiQ in a combustor typical of a military engine is presented in Fig. 3. The maximum and minimum values of temperature ratio for the radial profile were 1.14 and 0.84, respectively. The corresponding whole-field measurements are presented in Fig. 4. A recent combustor radial temperature profile measured by Rolls-Royce in a modern engine operating at an extreme point in the cycle is also shown in Fig. 3. This was used as the target profile for a new profile simulator for the Isentropic Light Piston Facility at QinetiQ Farnborough. The full combustor area profile is presented in Fig. 6.

3.2 Circumferential Temperature Profiles.

Whole-field combustor measurements performed by QinetiQ (Povey et al. [2])

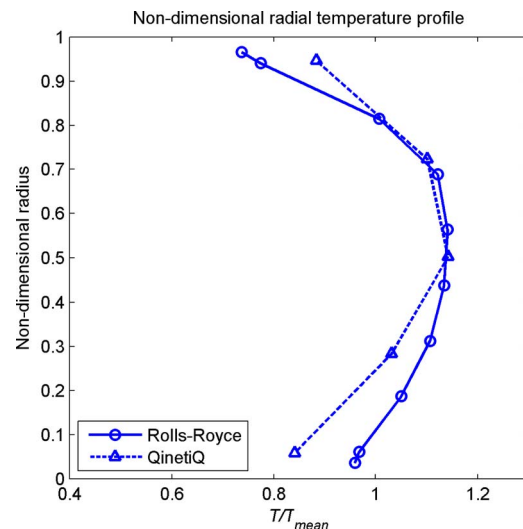


Fig. 3 Combustor exit radial profiles measured in a QinetiQ military engine (Povey et al. [2]) and in a Rolls-Royce engine at an extreme point in the cycle

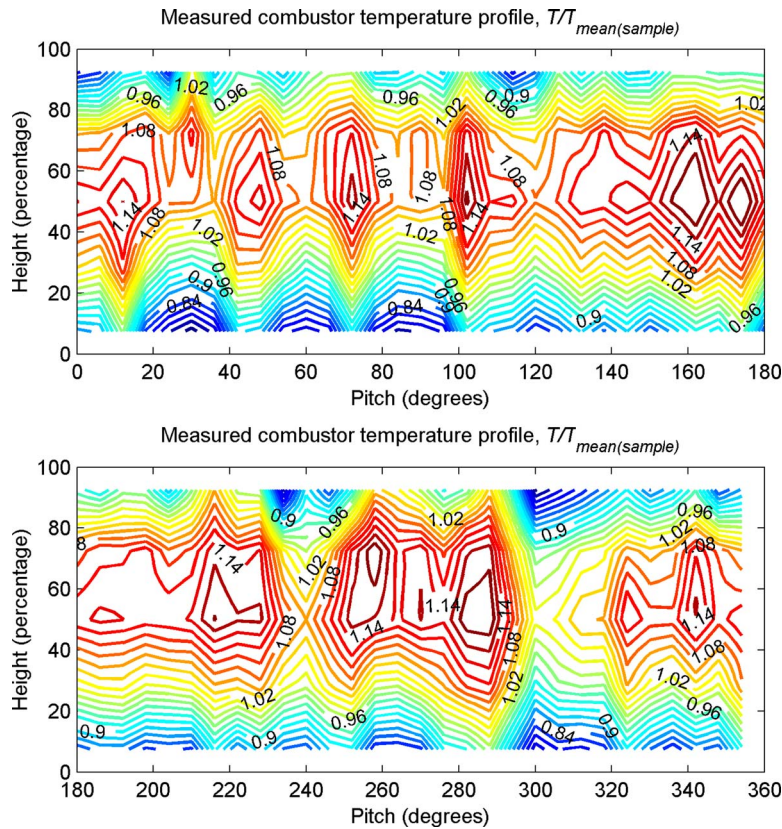


Fig. 4 Measured (QinetiQ) combustor exit temperature profile in a military engine from Povey et al. [2]

at the exit plane of a can-annular combustor typical of a military engine are presented in Fig. 4. The measured nondimensional temperatures were in the range of $0.59 < T/\bar{T} < 1.24$ for a mean temperature of 2072 K. At the hub and casing end walls, there were relatively cool regions of flow caused by the combustor liner coolant flow. Approximately symmetric circumferential variations (hot-streaks) were evident at the fuel injector count, as expected, although asymmetry was introduced with flow from first and second row mixing jets.

Examples of measurements performed by Suzuki et al. [11] in an experimental combustor at the Japanese Defense Agency Technical Research and Development Institute (TRDI) are presented in Fig. 5. The combustor was a 400 mm diameter full-annular reverse-flow arrangement, with 16 air-blast fuel nozzles with corotating double swirlers. Temperature measurements were taken with a radial rake of air-cooled thermocouples rotatable with respect to the axis. The measured nondimensional temperatures were approximately in the range of $0.90 < T/\bar{T} < 1.15$ for a mean temperature of 800 K (a peak temperature of $T/\bar{T}=1.22$ in the region marked Zone A was discounted on the basis that the instrumentation affected the measurement). There was both significant radial and circumferential temperature variations, but individual hot-spots at the burner spacing were not apparent. A large number of experiments were performed at different conditions, and a correlation of the form $RTDF \propto \dot{m}^a p_3^b T_3^c \Delta T^d$ was used to collapse the values of RTDF obtained, although no physical interpretation of the model was given.

New whole-field combustor exit plane measurements performed by Rolls-Royce in a recent engine test for a modern engine operating at an extreme point in the cycle are shown in Fig. 6. This was used as the target profile for a new profile simulator for the Isentropic Light Piston Facility at QinetiQ Farnborough, which is described below. The measured nondimensional tempera-

tures were in the range of $0.68 < T/\bar{T} < 1.21$. In addition to a pronounced radial profile, which was relatively uniform around the annulus, hot-spots were clearly evident at the fuel injector count.

There are very few examples of whole-field temperature measurements published in open literature. It is partly because of the scarcity of data and partly because there is such a wide variation in the inlet temperature profiles between engines that there is little agreement on the magnitude of distortion that might provide a useful test case for studying hot-streak migration in test turbines.

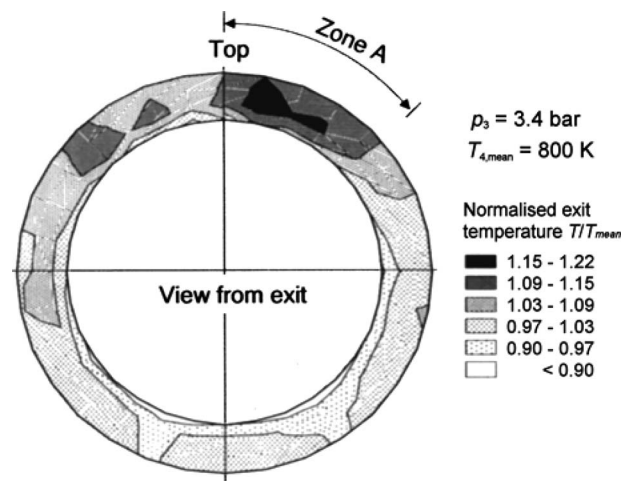


Fig. 5 Measured combustor exit temperature profile in experimental combustor at the Japanese Defense Agency TRDI (adapted from Suzuki et al. [11])

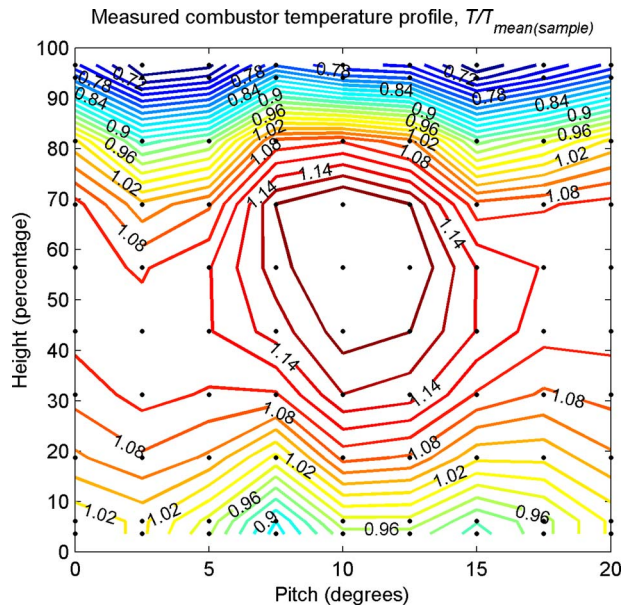


Fig. 6 Combustor exit temperature profile measured (Rolls-Royce) across one burner pitch of a modern engine at an extreme point in the cycle

While it is true that to some extent migration processes are affected by the specific turbine design, for most modern HP turbines, incidence variations and buoyancy forces in the rotor are primarily a function of the inlet distortion to the stage.

The approach taken at the Oxford University and QinetiQ has been to attempt to simulate the magnitude of circumferential and radial temperature distortions present at an extreme point in the cycle (incidence variations and buoyancy forces in the turbine increase as the temperature distortion increases) but with a profile in which the secondary features are removed and at a hot-spot to vane count ratio of 1:1. Although this makes the temperature profile less engine realistic (noninteger hot-streak to vane count ratio in the engine case), it provides a test case in which fundamental processes can more easily be studied and which can be used for CFD validation. For this reason, particular emphasis was placed on achieving low uncertainty in the inlet conditions to the experiment.

4 Temperature Distortion Generators in Experimental Facilities

In the preceding sections, the conventions for presenting TDFs have been discussed, and experimentally measured temperature profiles from combustor experiments have been reviewed. There is a growing interest in the effects of nonuniform inlet temperature on turbine heat transfer, and this is evidenced by the number of programs developed to study these effects. The difficulty associated with adequately and reproducibly simulating temperature distortion in rotating experimental turbine facilities is demonstrated by the significant programs associated with the development and commissioning of combustor simulators.

Experiments with temperature distortion have now been recorded in six different rotating facilities. Three early programs in the 1980s were designed for proof-of-concept investigations. In order of first publication, the facilities were

- (i) 1983: The Warm Core Turbine Test Facility at the NASA Lewis Research Centre, Cleveland, OH
- (ii) 1989: The Large Scale Rotating Rig (LSRR) at the United Technologies Research Centre (UTRC), East Hartford, CT
- (iii) 1989: The Rotating Blow-Down Facility at the Massachusetts Institute of Technology, Cambridge, MA

The more recent programs are designed with the aim to understand the effect of temperature distortion on turbine heat transfer, aerodynamics, and efficiency.

- (iv) 2002: The Isentropic Light Piston Facility (ILPF) at QinetiQ, Farnborough, Hampshire, UK
- (v) 2004: The Turbine Research Facility (TRF) at the Air Force Research Laboratory, Wright-Patterson Air Force Base, Dayton, OH
- (vi) 2004: The Turbine Test Facility Shock-Tunnel at Ohio State University (OSU) Gas Turbine Laboratory

There are essentially two types of temperature distortion simulator: those that use heat exchangers and those that use hot and cold streams of gas, which are introduced and allowed to mix ahead of the NGV inlet plane. Both types have successfully been used to produce radial temperature profiles in test turbines but with varying results in attempting to reproducibly simulate circumferential variation. We will review each facility in turn, with particular focus on the simulator design.

4.1 The Warm Core Turbine Test Facility at the NASA Lewis Research Center (Cleveland, OH).

The NASA Lewis Research Center Warm Core Turbine Test Facility (Whitney et al. [12]) was developed to incorporate a Combustor Exit Radial Temperature Simulator (CERTS) by Schwab et al. [13] (see also Stabe et al. [14]). The facility was designed to test a 0.77 scale model transonic turbine at engine representative conditions. Turbine speed was kept constant using an eddy-current brake, and the inlet air is heated using can combustors. A schematic of the CERTS arrangement is shown in Fig. 7. Relatively cooler air was injected through four infusion slots, which could be independently adjusted and metered. The mean inlet temperature was 672 K with and without the radial temperature profile. The profile achieved is shown in Fig. 8. The maximum and minimum temperature ratios were $T_{\max}/\bar{T}=1.05$ and $T_{\min}/\bar{T}=0.875$.

Tests demonstrated that for the CERTS profile, although the secondary flows were altered by ITD, there was no measurable change in efficiency (corrected for the tip clearance), and the RTDF was essentially mixed out by the rotor.

4.2 The Large Scale Rotating Rig at the United Technologies Research Center (East Hartford, CT).

The LSRR at the United Technologies Research Center is a low speed turbine facility designed to simulate some aspects of turbine flow. It operates at approximately ambient inlet temperature and pressure and nozzle exit Mach number of approximately 0.2. The first temperature distortion generator, described by Butler et al. [15], was designed to introduce a single hot-streak (22 nozzles) upstream of the vanes: power requirements and structural constraints prohibited the introduction of a fully annular profile. The hot-streak was seeded with CO_2 so that a gas concentration probe could be used to investigate hot-streak migration. The hot-streak was a circular top hat shape, with a diameter of approximately one-third of the vane span, located at 40% span. The hot-streak was located so that it passed through the vanes, rather than being incident on the leading edge. A schematic of the arrangement is shown in Fig. 9. The radial profile at a single location through the hot-streak centerline is shown in Fig. 10. The ratio of the maximum to the unheated background temperature was $T_{\max}/\bar{T}=2.0$.

Further experiments conducted in the LSRR were reported by Roback and Dring [16], in which the impact of hot-streaks on the turbine rotor surface temperature was investigated. The arrangement was similar to that used by Butler et al. [15] in that a single circular top-hat-shaped hot-spot was introduced. Temperature ratios in the range of $1.0 \leq T_{\max}/\bar{T} \leq 2.0$ were investigated, but a greater density range $0.5 \leq \rho/\bar{\rho} \leq 1.5$ was possible by using undiluted CO_2 for the streak in some tests. The impact of stator trailing

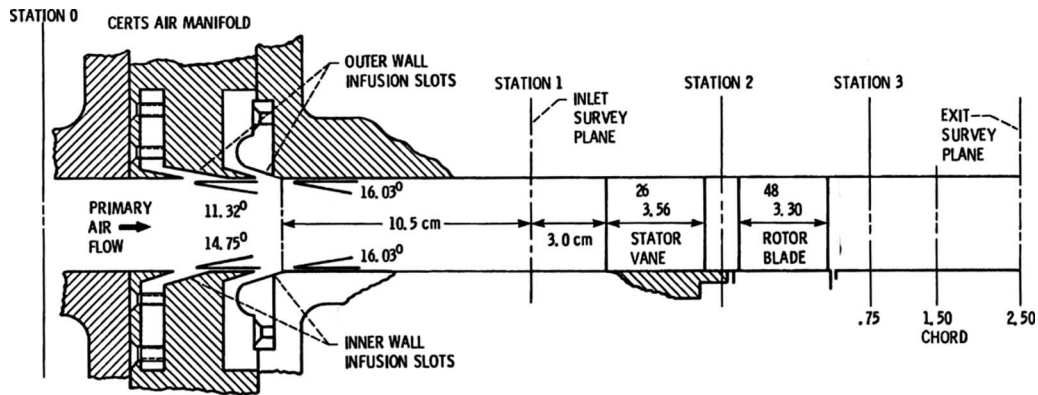


Fig. 7 Flow path through the CERTS inlet to the NASA Lewis Research Center Warm Core Turbine Test Facility (from Stabe et al. [14])

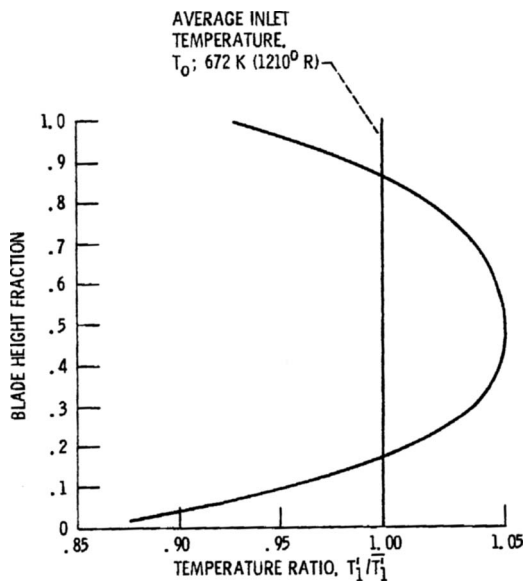


Fig. 8 CERTS inlet radial temperature variation (from Stabe et al. [14])

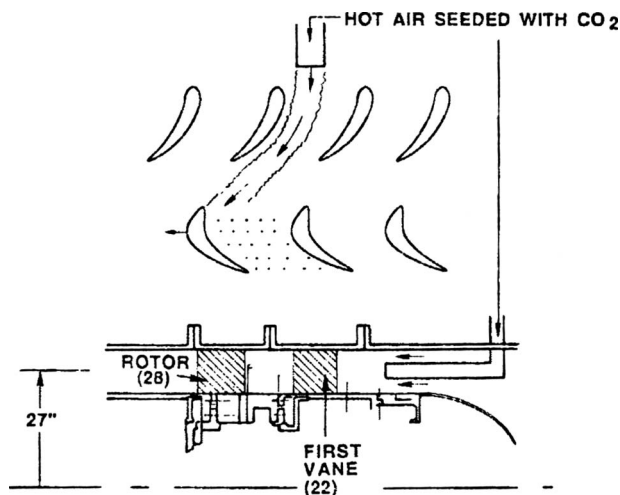


Fig. 9 Schematic of the LSRR single hot-streak generator (from Butler et al. [15])

edge cooling was also investigated. Sharma et al. [5] reported the impact of a single rectangular hot-streak on the rotor surface temperature—the arrangement was similar to that described above.

In the same facility, an axisymmetric radial temperature profile was simulated with a radial trace gas (CO_2) distribution (see Joslyn and Dring [17]). Five concentric injector rings (labeled 1–5 in Fig. 11), each with 144 injectors, were used to introduce the trace gas (CO_2) 12.8 axial chords upstream of the stator. The maximum CO_2 concentration was 1000 ppm above ambient. The flow was unheated, and therefore temperature and density variations were very small. Thus, only the effects of flow redistribution associated secondary flow and total pressure variations could be investigated, as buoyancy and rotor incidence variations were not simulated. The results were reported by Joslyn and Dring [18,19].

4.3 The Rotating Blow-Down Facility at MIT (Cambridge, MA). A passive heat exchanger type temperature distortion generator was developed for the MIT Rotating Blow-Down Facility in 1989 (Haldeman [20]). This was later developed by Shang [21]. The impact of the simulated temperature distortion on the rotor heat load was reported by Shang et al. [22] and Shang and Epstein [23]. The MIT facility is a 0.75 scale transonic blow-down turbine test facility, in which most relevant nondimensional parameters are matched in the 300 ms test time. The ratio of specific heats is matched to engine conditions using an argon/freon-12 foreign gas mixture. For these tests the MIT Blow-Down Facility was configured with the Advanced Core Engine HP turbine stage (designed by Rolls-Royce): this is a 4:1 pressure ratio turbine stage.

The RTDF generator and the four discrete hot-streak (OTDF)

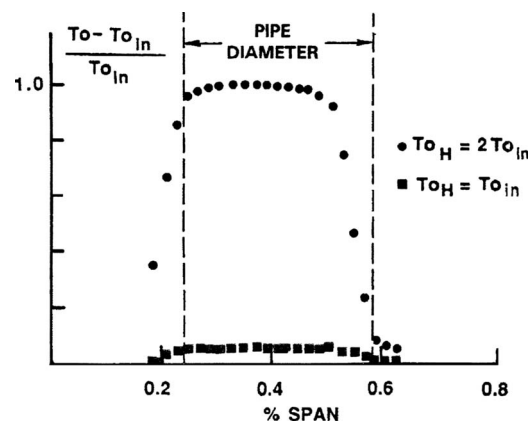


Fig. 10 Temperature profile measured in the LSRR hot-streak generator (from Butler et al. [15])

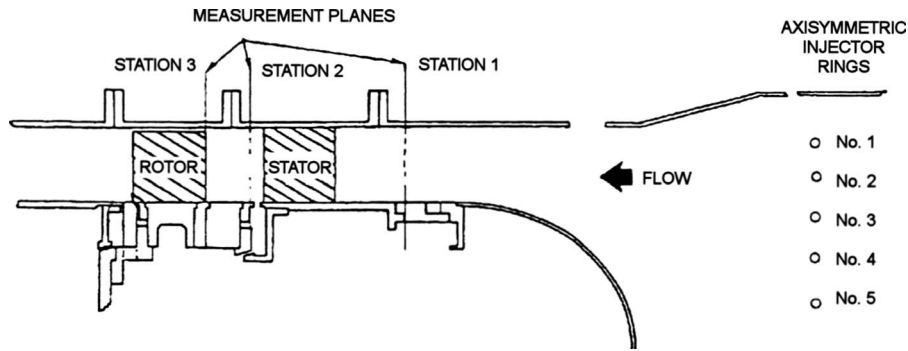


Fig. 11 The LSRR radial temperature profile generator (from Joslyn and Dring [17])

generators are shown in Figs. 12 and 13. The RTDF generator was a stainless steel honeycomb matrix with inner and outer oil jackets and midspan heating elements. The hot-streaks were generated by passing a bypass flow through a tube-bundle heat exchanger before reintroducing the heated flow through an injector. Four injectors were used in one-third of the annulus: the hot-streak to vane count ratio in this sector was 1:3. The RTDF and OTDF generators were approximately 20 and 12 NGV axial chords upstream of the nozzle inlet plane, respectively. The inlet temperature traverse was just downstream of the OTDF injection.

The radial temperature profile measured 12 axial chords upstream of the NGV inlet plane is shown in Fig. 14. The maximum and minimum measured temperatures were approximately $T_{\max} = 525$ K and $T_{\min} = 445$ K. Due to mixing in the inlet duct, a less pronounced profile is to be expected at the NGV inlet plane.

The OTDF profile at the NGV exit plane over the domain of one hot-streak generator is shown in Fig. 15. No measurements were taken at the NGV inlet plane, but temperature redistribution in a NGV passage is driven only by secondary flow development, and the hot-streak intensity at NGV inlet and exit planes would normally be broadly similar. The peak temperature near midspan was $T_{\max} = 530$ K, and the minimum temperature was $T_{\min} = 480$ K.

4.4 The Isentropic Light Piston Facility (ILPF) at QinetiQ (UK). The ILPF at QinetiQ (Farnborough, UK) is a short duration wind tunnel, capable of testing an engine size turbine at the correct nondimensional parameters for fluid mechanics and heat transfer: M , Re , Tu , N/\sqrt{T} , and T_g/T_w are matched to engine conditions. The ILPF has been used to test a HP turbine stage (Hilditch et al. [24]) and a 1.5 turbine stage (Povey et al. [25]). For the experiments described in this paper, only the HP stage was installed. A novel feature of the facility is the aerodynamic turbo-brake (Goodisman et al. [26]), which is on the same shaft as the

turbine and is driven by the turbine exit flow. At the design speed, the turbobrake power is matched with the turbine, and thus constant speed is maintained during a run. Air from a high pressure reservoir drives a piston down a piston tube, isentropically compressing and heating the working gas (air) inside the tube. When the desired pressure is reached, the compressed air is suddenly discharged, by means of a fast acting valve, through the working section. Typically, steady conditions are achieved for 500 ms.

In 2002 an ITD generator designed by Hurrion [27] (see also Chana et al. [28]) was developed for the ILPF. A schematic of the ITD generator is presented in Fig. 16. Hot-streaks, rotatable with respect to the NGV leading edge, were generated by introducing air at ambient temperature into a relatively hot mainstream through annular slots and struts upstream of the HP NGVs. The number of hot-streaks was the same as the HP vane count: 32.

The ILPF has since been used to study the impact of temperature distortion on the IP vane heat transfer (Povey et al. [4]) and on the HP vane heat transfer (Povey et al. [2]). The profiles for which investigations [2,4] were performed were referred to as OTDF1 (hot-streak aligned geometrically with the vane midpassage) and OTDF2 (hot-streak aligned with the vane leading edge). There was no significant difference between the radial temperature profiles (circumferentially averaged), $\bar{T}^{\text{circ}}/\bar{T}^{\text{area}}$, for OTDF1 and OTDF2. The OTDF1 profile is shown in Fig. 17, normalized by the mass averaged temperature. The following was achieved: $T_{\max} = 476$ K and $T_{\min} = 404$ K. The mean temperature, $\bar{T} = 444$ K, was the same for both uniform and nonuniform inlet temperature. Because cool air was injected to create an ITD, a higher main flow temperature was required. This was achieved by increasing the pump-tube compression ratio. The normalized temperature ratios were $T_{\max}/\bar{T}^{\text{mass}} = 1.07$ and $T_{\min}/\bar{T}^{\text{mass}} = 0.91$. The measured radial profiles for OTDF1 and OTDF2 (Fig. 18) were

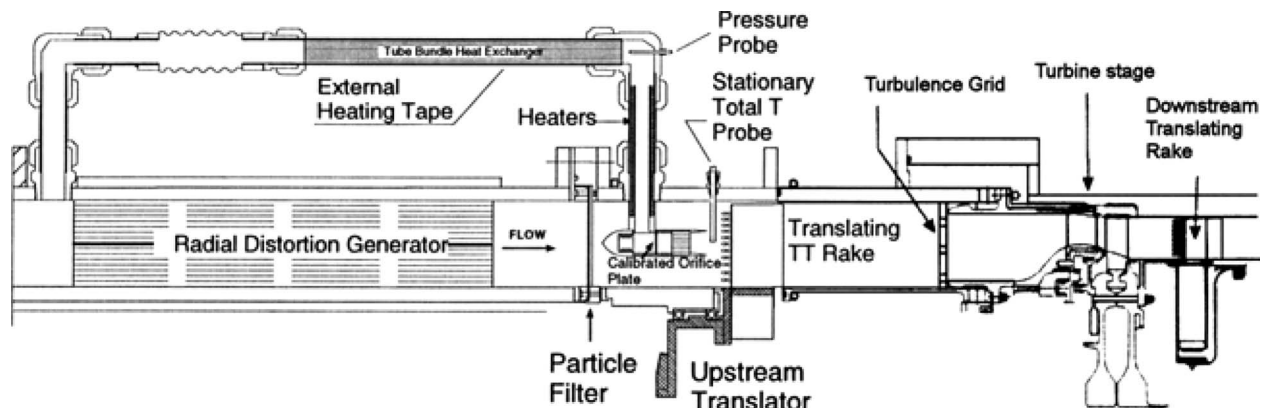


Fig. 12 Schematic of the MIT RTDF and OTDF generators (from Shang et al. [22])

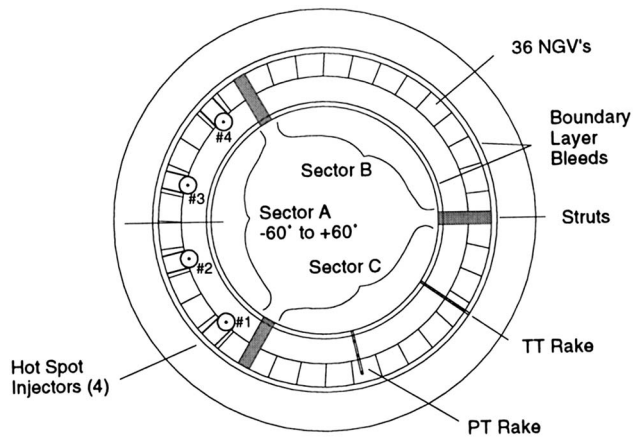


Fig. 13 Cross section of the MIT OTDF generators (from Shang et al. [22])

very similar in both magnitude and form. The maximum and minimum values of $\bar{T}^{circ}/\bar{T}^{area}$ were 1.045 and 0.93, respectively.

4.5 The Turbine Research Facility at the AFRL. An adjustable turbine inlet profile generator was developed (Barringer et al. [29]) for the Turbine Research Facility at the Wright Patterson Air Force Base (Dayton, OH). This was designed to simulate both combustor representative temperature and pressure fields. The evaluation of the temperature profile generator was described by Barringer et al. [9]. The same authors reported the impact on turbine aerodynamics and heat transfer [30]. The Wright Patterson Turbine Research Facility is an engine-scale short duration blow-

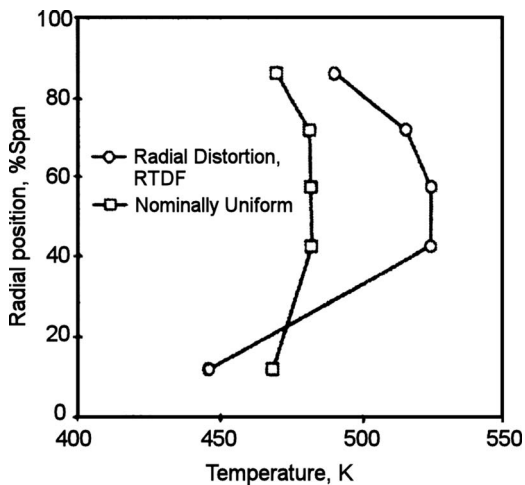


Fig. 14 The MIT RTDF temperature profile (from Shang et al. [22])

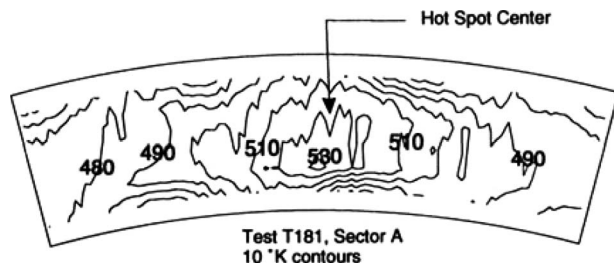


Fig. 15 NGV exit total temperature contours due to hot-streak injection over the domain of one hot-streak or three NGVs (Shang [21])

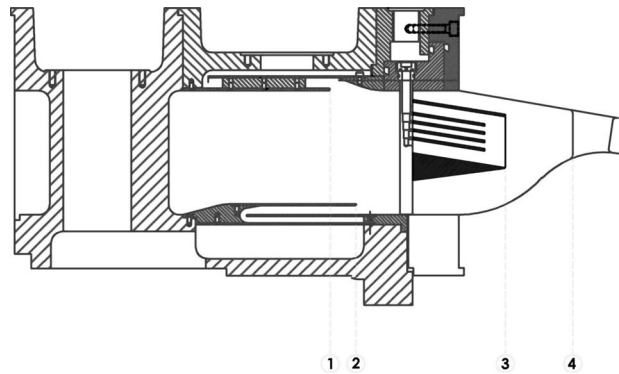


Fig. 16 The OTDF injection system installed on the QinetiQ ILPF in 2002, showing (1) outer annular feed, (2) inner annular feed, (3) radial slot feeds, and (4) NGV inlet plane

down facility [31], in which Re , M , T_g/T_w , N/\sqrt{T} , and C are all modeled. An eddy-current brake is used to maintain constant turbine speed during the 1–5 s run.

The combustor simulator consists of five concentric annular flow paths. The inner and outer annuli contain finned tube heat exchangers, which are used to cool the flow. The cooled stream is injected through primary and secondary dilution holes and film cooling holes, much as in a conventional combustor liner. The primary holes are used to increase the turbulence intensity, while the secondary holes and film cooling holes are used to tailor the temperature profile. A system of five independently rotatable shutter systems allows control of the total pressure of each stream. A schematic of the combustor simulator is shown in Fig. 19.

A parametric study of the combustor simulator was conducted [9], in which the maximum radial temperature variation (averaged over one vane pitch) at the turbine inlet that was measured with this system was $\Delta\theta = (T - T_{av})/T_{av} = 0.10$. The results for a number of tests are shown in Fig. 20. No significant circumferential pattern was distinguishable in the tests, and random fluctuations in $\Delta\theta$ were less than 0.01.

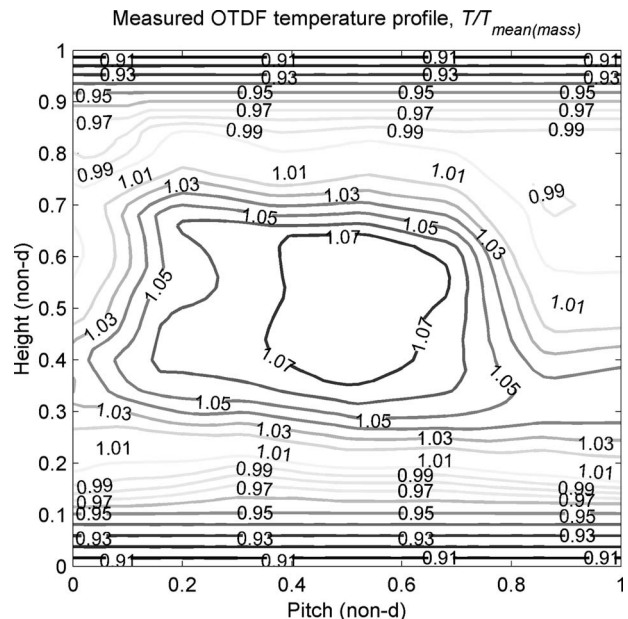


Fig. 17 Measured nondimensional temperature distribution for the OTDF profile (first ITD generator) at the NGV inlet plane

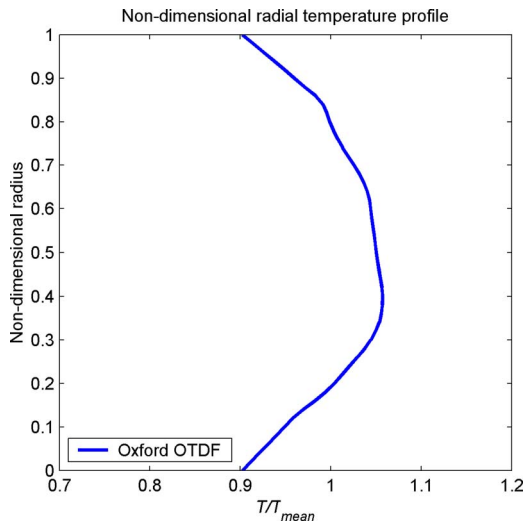


Fig. 18 Measured radial temperature profile for the OTDF profile (first ITD generator) at the NGV inlet plane

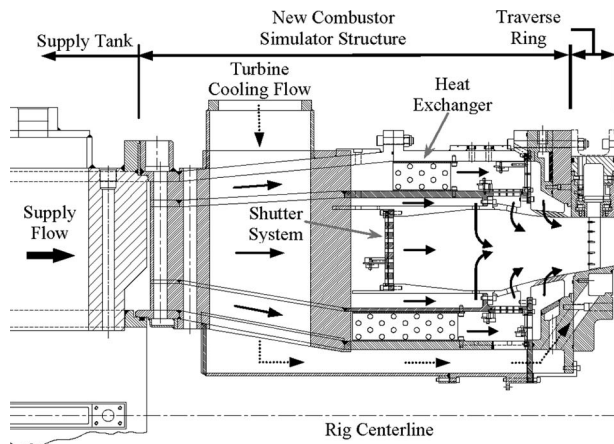


Fig. 19 Schematic of the AFRL combustor simulator (Fig. 6 from Ref. [1])

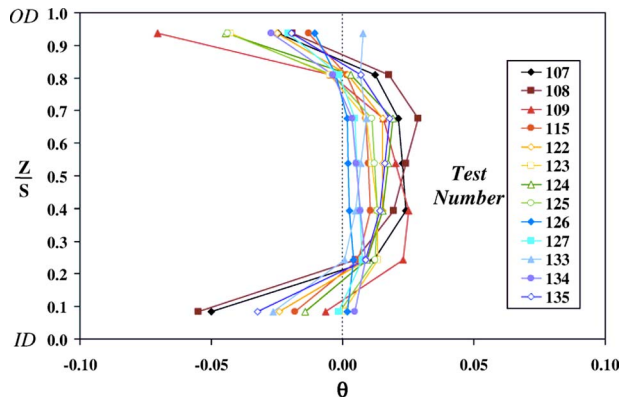


Fig. 20 Temperature profiles measured at the simulator exit plane in the AFRL

4.6 Ohio State University Gas Turbine Laboratory. A combustor-emulator (Fig. 21), which uses passive heat exchangers was recently developed by Haldeman et al. [32] for the Shock-Tunnel Based Turbine Test Facility (TTF) at the Ohio State University Gas Turbine Laboratory (formerly at Calspan). The TTF is a short duration (50 ms run time) tunnel, which employs the shock

heating effect for the main flow path. The time constant for heating of the heat exchanger was of the order of 15 min, while for cooling it was of the order of 1 h.

A typical radial temperature profile measured approximately ten axial chords upstream of the nozzle is shown in Fig. 22. The maximum and minimum measured temperatures were approximately $T_{max}=480$ K and $T_{min}=380$ K. As the profile was measured some way upstream of the vane, a weaker profile would be expected at the nozzle inlet. The circumferential metal temperature profile in the heat exchanger was measured (over 20 axial chords upstream of the NGV inlet) using resistance temperature detectors (RTDs), but no measurements were made near the nozzle inlet plane.

5 Development of an Enhanced Temperature Distortion Generator for the ILPF

In addition to the six experimental programs reviewed above, there is a current program by the Oxford University, QinetiQ, and Rolls-Royce (as part of the Brite-Euram Turbine Aerothermal External Flows II program) to study the impact of both temperature distortion and high inlet swirl on turbine heat transfer, aerodynamics, and efficiency. The development of an enhanced simulator for this program is now discussed.

5.1 Background. The QinetiQ ILPF was recently upgraded to allow turbine aerodynamic performance measurements to be performed with and without combustor representative inlet temperature distortion and swirl. As part of that upgrade, a simulator designed to produce an enhanced overall temperature distortion factor (EOTDF) was developed. The target profile was based on combustor measurements performed by Rolls-Royce at an extreme point in the engine cycle, presented in Figs. 3 and 6.

With the benefit of hindsight, it is the authors' view based on previous studies (see, for example, Povey et al. [2,4]) that one of the greatest difficulties faced in interpreting heat transfer results with temperature distortion arises from uncertainty in form of the inlet profile.

Measured combustor profiles (see Figs. 4, 5, and 6), in addition to the circumferentially averaged RTDF profile and burner-spacing averaged OTDF profiles, have significant random nonuniformities in the temperature profiles and would be unlikely to have a hot-streak to vane count ratio of 1:1. In the experiment, however, simulating such nonuniformities would compound the difficulty of understanding hot-gas migration effects and heat transfer enhancement. Most investigators have taken the view that it is better for the simulated profile to be as regular as possible, so that fundamental trends can be more accurately understood, and for the experiment to serve as a sound test case for CFD validation.

Simulating temperature distortion is inherently difficult, and to date most systems have had shortcomings. One of the shortcomings of the first generation QinetiQ (OTDF1 and OTDF2) generator was pitch-to-pitch asymmetry in the profile. In other profile generators, either a very weak temperature profile or a very poorly defined profile, or both, may, in the view of the authors, present problems in interpreting the effect on the temperature distortion on the turbine stage. Comparative studies of turbine heat transfer and aerodynamics with and without temperature distortion attempt to resolve relatively modest changes in the flow; without a well defined and quantified temperature profile, meaningful comparisons are difficult. It is therefore particularly important to achieve good run-to-run repeatability as both the temperature profile and heat transfer measurements are typically measured over a number of runs.

In situations in which it is desired to perform turbine performance measurements, accurate knowledge of the inlet enthalpy flux is required. As a direct whole-field measurement of inlet flow properties is generally impossible in highly nonuniform flows, the ability to measure the enthalpy flux of hot and cold streams before

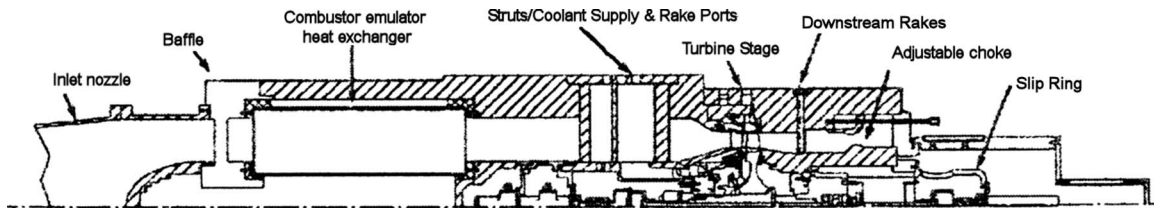


Fig. 21 Schematic of the combustor-emulator in the TTF at the Ohio State University (from Haldeman et al. [32])

mixing would seem to be advantageous. In systems that use heat exchangers for profile generation, the need to rely on the characterization of what may be quite a complex multivariable system would seem to place a lower limit on the uncertainty.

It is in response to these proposed shortcomings that the EOTDF generator was developed for the QinetiQ facility. To summarize, the design's intent was to achieve a strong, well defined, and well characterized profile, with minimal run-to-run variation, using a system in which the inlet enthalpy flux could be evaluated with low overall bias uncertainty and high precision.

5.2 Definition of the Target Temperature Profile. The target temperature EOTDF profile is shown in Fig. 23. The EOTDF profile is based directly on the measured profile shown in Fig. 6, which is at an extreme point in the cycle of a recent engine, but with secondary features removed. There is particular interest in this cycle point because it represents the maximum heat load condition in the engine. The near wall regions (where combustor measurements were not obtained) have also been assigned a nondimensional temperature value by extrapolation at the near wall gradient, so that an analysis of the whole field is possible. Temperatures have been normalized by the mass mean temperature.

To perform an accurate comparison of the impact on turbine aerodynamics, heat transfer, and efficiency, an emphasis was placed in the design on achieving the same mass mean temperature with and without temperature distortion. This was achieved by independently metering the temperature and mass flow of the hot and cold streams before mixing.

A number of relevant parameters are tabulated for reference in Table 1. It is noted that for the EOTDF generator the target value of T_{max}/T_{min} was 1.65, compared with 1.20 for the first generation OTDF generator. This is approximately 3.25 times more intense. Table 1 demonstrates the difficulty in comparing temperature profiles using a single parameter.

5.3 Design of the EOTDF Simulator. The EOTDF simulator design was similar in concept to the first generation OTDF simulator in that the cold gas was introduced into the hot mainstream

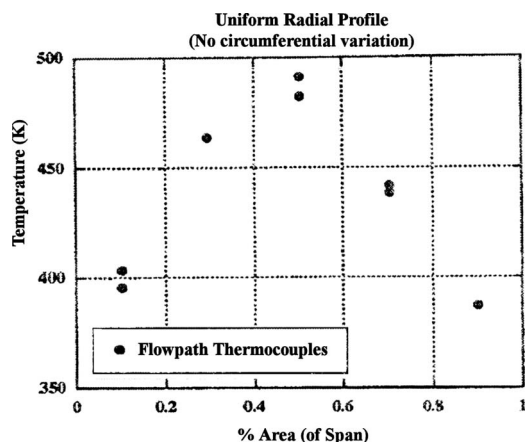


Fig. 22 Typical radial profile measured in the Ohio State University TTF (from Haldeman et al. [32])

using annular slots at the hub and case walls and 32 baffled radial rods (32 vanes, i.e., one hot-spot per vane) to produce circumferential nonuniformities. Otherwise it was very different in design. The differences were driven by the following objectives: (i) the system should be modular so that it could be installed and removed rapidly; (ii) the EOTDF system must produce a very well defined profile, with good periodicity, so that inlet boundary conditions are well known; (iii) the cold gas injection mass flow rate and temperature must be better than 0.7% absolute uncertainty, so that turbine efficiency measurements could be performed with adequate accuracy; (iv) the system must be rotatable, so that clocking could be investigated. These details are summarized in Table 2.

The drawing of the module installed in the facility is shown in Fig. 24. The module was comprised of an annular ring at case (a) and at hub (b), each with an integral annular plenum ((c) and (d)) to ensure circumferentially uniform pressure, interconnected by 32 steel tubes (e), which act both as radial injectors and feeds to the hub plenum. The flow was admitted to the module through eight hoses (f), which were connected via a manifold and upstream sonic venturi flow meter to the cold gas reservoir. To ensure periodicity, the internal Mach numbers in the feed pipes and plena were kept everywhere below 0.1. Two pressure limiters ((g) and (h)) were used at the inlet and outlet of each of the steel tubes to allow independent pressure adjustment of the three cavities and, therefore, profile variation. The system was designed to operate at high internal pressure to keep the module (and tube diameter) small for a given internal Mach number. The flow was admitted to the annular and radial baffles ((l), (m), and (n)) through small holes ((i), (j), and (k)). A sufficient mixing length was allowed to ensure uniform flow at the baffle exit planes. For the radial

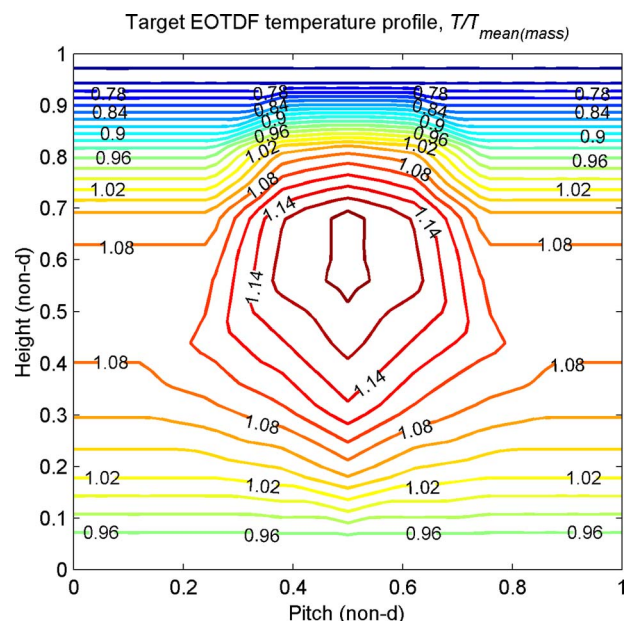


Fig. 23 The target EOTDF temperature profile

Table 1 Comparison of the engine, target, and OTDF temperature profiles

	Whole	Radial	Circumferential	Whole	Radial	Circumferential
	T_{max}/T_{mean} (T_{min}/T_{mean})	T_{max}/T_{mean} (T_{min}/T_{mean})	T_{max}/T_{mean} (T_{min}/T_{mean})			
Engine: $T/T_{mean(sample)}$	1.2115 (0.6834)	1.1413 (0.7375)	1.0458 (0.9650)	1.7727	1.5475	1.0837
Target: $T/T_{mean(mass)}$	1.1873 (0.7205)	1.1243 (0.7205)	1.0618 (0.9956)	1.6479	1.5604	1.0665
OTDF: $T/T_{mean(mass)}$	1.0811 (0.9024)	1.0575 (0.9024)	1.0144 (0.9862)	1.1981	1.1719	1.0286

baffles, an impingement plate (*p*) was incorporated to encourage mixing. Clocking was achieved by simply slackening the blots retaining the downstream plate and by rotating the module holding the rods.

5.4 Commissioning of the EOTDF Simulator. Commissioning of the EOTDF module on the facility was a straightforward process (2 weeks), which required the hot and cold stream valve actuators to be correctly time synched. In the case of uniform temperature, the target mass flow rate was 17.4 kg/s at an inlet total temperature of 444 K (Table 2). In the case of temperature distortion, the hot stream mass flow rate was 11.14 kg/s at a temperature of 530 K, and the cold stream mass flow rate was 6.26 kg/s (combined mass flow rate of 14.4 kg/s) at a temperature of 290 K. A higher hot stream temperature is achieved by operating the piston tube at a higher compression ratio, with the same final total pressure (4.6 bars).

The hot and cold stream mass flow rates for a typical run are

Table 2 Details of the EOTDF injection mass flow rates

Parameter	Nominal	Run-to-run variations for these tests	Bias (%) (to 95% confidence)	Precision (%) (to 95% confidence)
\dot{m}_h	11.14 kg/s	± 1.0	± 1.4	± 0.2
\dot{m}_c	6.26 kg/s	± 1.0	± 0.7	± 0.2
T_h	530 K	± 1.0	± 0.0	± 0.2
T_c	290 K	± 1.0	± 0.0	± 0.2
\dot{m}_{01}	17.40 kg/s	± 1.0	± 1.1	± 0.2
\bar{T}_{01}	444 K	± 1.0	± 1.1	± 0.2
p_{01}	4.6 bars	± 1.0	± 0.1	± 0.1

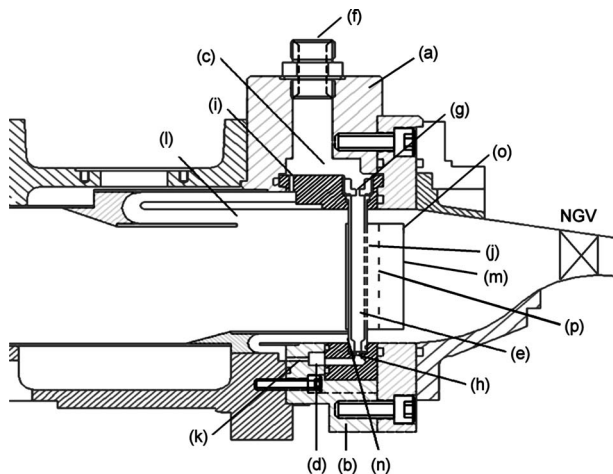


Fig. 24 Cross-section of the second generation combustor simulator

shown in Fig. 25. The flow rates measured at the plane of the meters are denoted by \dot{m}_c and \dot{m}_h . The corrected mass flow rates are denoted by $\dot{m}_{c(corr)}$ and $\dot{m}_{h(corr)}$: these include the unsteady corrections required to account for the change in stored mass in the plena between the meter and the turbine inlet plane. During the 400 ms test window (from approximately 0.7 s to 1.1 s), the unsteady correction terms are small: less than 2% for \dot{m}_c , generally less than 5% for \dot{m}_h , and with a mean of approximately zero. The total mass flow rate is denoted by \dot{m}_{total} . For a typical run, the unsteadiness in \dot{m}_{total} was approximately 2% during the test window and was in phase with the piston oscillations.

The hot and cold stream temperatures (T_h and T_c) for the same run are presented in Fig. 26. During the test window, the variation in T_c was less than 0.3 K (0.1%). The variation in T_h was approximately 10 K (1.9%), with oscillations of up to ± 3 K ($\pm 0.6\%$). The mass mean temperature T_{mean} is shown for the period for which both \dot{m}_c and \dot{m}_h are greater than 0.1 kg/s; outside this range, the mean temperature is poorly defined. The run-to-run repeatability of these conditions was good.

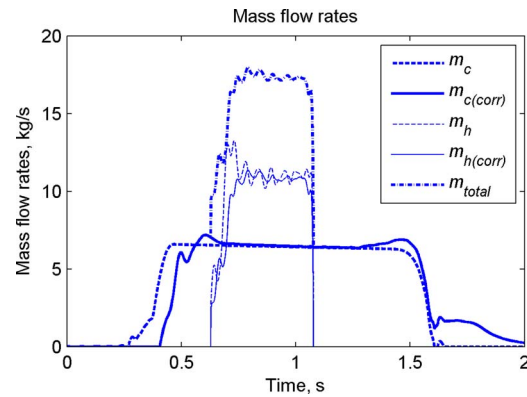


Fig. 25 Hot and cold stream mass flow rates for a typical run

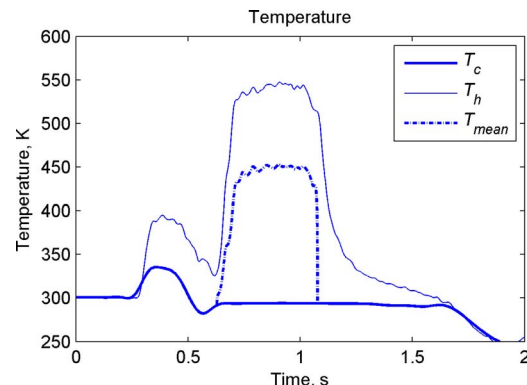


Fig. 26 Hot and cold stream temperatures for a typical run

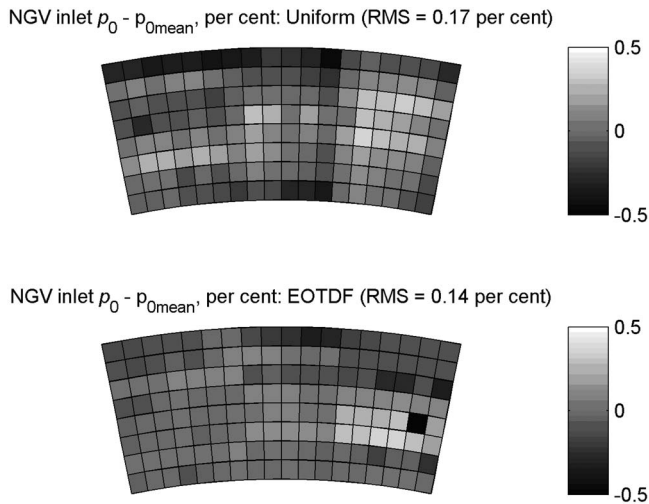


Fig. 27 Measured total pressure profiles for uniform inlet temperature and EOTDF

The uncertainty associated with the hot stream mass flow rate measurement is the same for both uniform inlet temperature and EOTDF: 1.4% bias error and 0.2% precision error to 95% confidence. The cold stream, which is at approximately ambient temperature, is introduced from an independent reservoir through a calibrated sonic venturi nozzle into a manifold ahead of the temperature distortion module. The overall bias error uncertainty associated with the cold stream mass flow rate was 0.7%, of which 0.5% arises from the uncertainty in the discharge coefficient of the nozzle. The precision uncertainty was 0.2%.

The combined bias uncertainty in mass flow rate with and without temperature distortion was therefore 1.37% and 1.13%, respectively, that is, marginally more accurate with temperature distortion. The precision uncertainty was approximately 0.2% in both cases.

The mass averaged temperature was the same for both EOTDF and uniform inlet temperature runs $\bar{T}_{01} = 444 \text{ K} (\pm 1\% \text{ allowed})$. Nondimensional speed based on mean temperature N/\sqrt{T} and turbine stage pressure ratio p_3/p_{01} were the same in both modes of operation.

The inlet total pressure was the same in both cases (4.6 bars). Both the absolute and precision uncertainties in the mean value of the inlet total pressure were better than 0.1–95% confidence. An area survey of the inlet total pressure was also conducted with uniform inlet temperature and EOTDF. Three radially aligned pneumatic total pressure probes, each with tubes at nine radial heights, were used at 19 circumferential locations spanning two NGV pitches at the NGV inlet plane. Thus the pressure survey included 171 measurement points.

The measured inlet total pressure distributions for uniform inlet temperature and EOTDF are shown in Fig. 27, as a percentage departure from the mean value. The profiles were everywhere uniform to within better than $\pm 0.4\%$, and the radial profile was in agreement with the uniform temperature case to within better than 0.2%. The rms values of pressure difference from the mean were 0.17% and 0.14% in the cases of uniform inlet temperature and EOTDF, respectively. It was assumed therefore that any changes in heat transfer should be attributed to the impact of inlet temperature distortion alone rather than of inlet total pressure variation. It should be noted that it is possible to adjust the inlet total pressure profile by varying the area of the injection slots, but in the first experiments a direct comparison to the uniform inlet temperature case was required, for which the total pressure field was uniform.

5.5 Measured EOTDF Temperature Profile. Area traverses

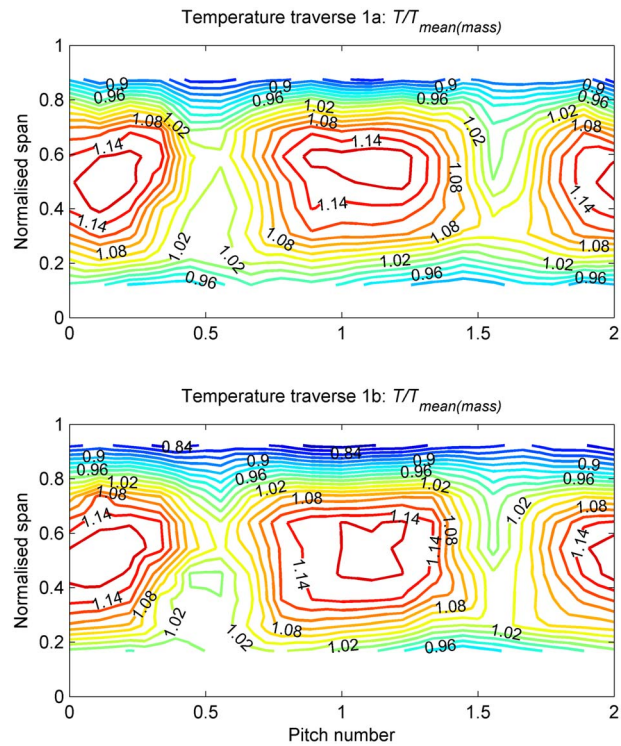


Fig. 28 Measured EOTDF temperature distributions for traverses 1a and 1b

were conducted across two vane pitches at three circumferential locations (1, 2, and 3), distributed approximately equally around the annulus. At each location, two area surveys were conducted (a and b), each composed of 9 radial and 19 circumferential measurement points. Each survey was repeated to gauge measurement repeatability. Between traverses a and b, the probes were moved radially by 3 mm ($\sim 5\%$). Thus a comparison of the profiles was possible before a composite profile was created. Measurements were also conducted at approximately 5% and 97% span, completing a survey of 20 radial and 19 circumferential points (380 in total).

The measured nondimensional temperature distributions for traverses 1a and 1b are shown in Fig. 28. The rms difference between the temperature profiles 1a and 1b was approximately 6.0 K, or 1.4% of the mean temperature (444 K) calculated over two NGV pitches. This gives very high confidence in the run-to-run repeatability of the measurements. Surveys at locations 2 and 3 yielded similar results. Both the radial and circumferential profiles were well defined, very close to the target profile (Fig. 23) in both magnitude and form, and had an excellent pitch-to-pitch symmetry. The uncertainty in the mean inlet temperature, which is measured before mixing the two streams by considering the total enthalpy flux, was an order of magnitude lower than this (approximately 0.113%).

5.6 Comparison to the Target Profile. The measured nondimensional radial temperature profile is compared with the target profile in Fig. 29. Data from traverses 1a and 1b are indicated on the graph, as are the near wall (5% and 97% span) measurements. The quality of the agreement is excellent, both in terms of magnitude and form.

It is worth noting that while the EOTDF simulator was designed in the first instance to accurately simulate a particular engine profile, variations in temperature profile, pressure profile, and clocking are possible, so that the sensitivity of a given turbine to the design profile can be investigated. The temperature profile is adjusted by varying the temperature and mass flow rates of the

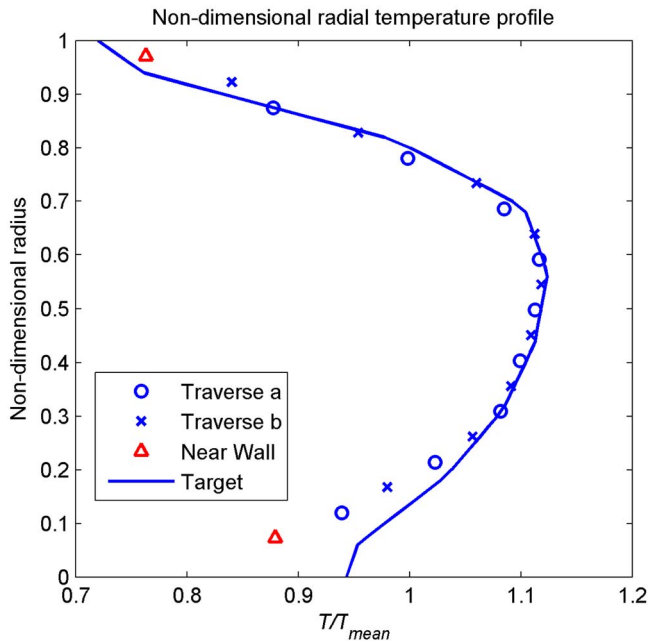


Fig. 29 Measured radial temperature profile

individual slot flows (by varying the limiters sizes). Clocking and pressure profile variation have been discussed. In the following section, the EOTDF temperature profile is compared with the temperature profiles developed in the six facilities previously discussed.

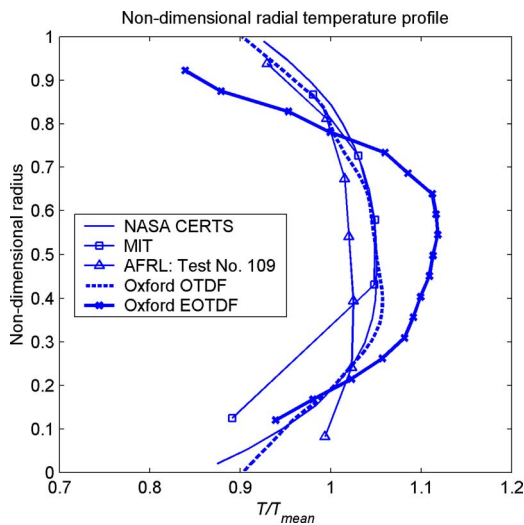


Fig. 30 Comparison of simulated temperature profiles

Table 3 Comparison of radial and circumferential temperature profiles

Parameter	Year of first publication	Circumferential $T_{max} - T_{min} / \bar{T}$	Definition of hot streaks	Hot streak to vane count ratio	Radial $T_{max} - T_{min} / \bar{T}$
NASA	1983	N/A	N/A	N/A	0.176
UTRC (LSRR)	1989	1.0	Top-hat	Single streak	N/A
MIT	1989	~0.10	Rather poor	1:3 (1/3 annulus)	0.158
AFRL	2004	Very weak	Near random	1:1	0.095
OSU	2004	No data yet	No data yet	No data yet	Comparison N/A
QinetiQ/Oxford OTDF	2002	0.06	Well defined	1:1	0.155
QinetiQ/Oxford EOTDF	2008	0.14	Well defined	1:1	0.355

6 Comparison of Simulated Temperature Profiles in Different Facilities

The radial temperature profiles, which were measured at the NGV inlet plane in the NASA, MIT, AFRL, and QinetiQ/Oxford turbine test facilities, are presented in Fig. 30. Measurements taken in the OSU facility were made ten axial chords upstream of the NGV inlet plane, and therefore a direct comparison is not given as the profile would be substantially mixed out at the NGV inlet plane. In the LSRR facility, radial redistribution was studied with preferential seeding of the inlet flow with CO₂ but no temperature difference was simulated.

The profiles are broadly similar in terms of the shape and strength of the radial temperature distortion, with the exception of the QinetiQ/Oxford EOTDF generator, which is more intense and more peaked. The maximum to minimum temperature difference is between 2 and 3.7 times larger than other profiles based on the available data.

The simulated profiles are compared in terms of the circumferential distortion at midspan and the radial distortion in the circumferential mean (Table 3) in terms of the parameter $(T_{max} - T_{min}) / \bar{T}$. The definition of the profile is also qualitatively assessed.

Of the six facilities, five have attempted circumferentially distorted temperature profiles. In the early UTRC LSRR experiment, a single hot-streak was injected directly upstream of the vanes; the definition was perfect, but, as was appreciated at the time, there were considerable limitations with this approach. In the early MIT facility, a poorly defined circumferential profile was obtained in 1/3 of the annulus, with a reasonable circumferential variation $(T_{max} - T_{min}) / \bar{T} \approx 0.1$. The hot-streak to vane count ratio was 1:3, however, which means that the hot-streaks were relatively smoothed out in the circumferential direction. More recently, in the AFRL facility the variation in the circumferential direction was measured to be almost random. No data are yet available from the OSU facility. For both of the OTDF and EOTDF simulators developed by QinetiQ/Oxford, the profiles were very well defined (see Figs. 17 and 28) with an excellent pitch-to-pitch symmetry and with high run-to-run repeatability (rms difference of 0.3% across two NGV pitches). Values of $(T_{max} - T_{min}) / \bar{T}$ of 0.06 and 0.14 were obtained, although it is clear that greater circumferential variations could be simulated if desired.

In terms of the radial profiles, the NASA, MIT, AFRL, OSU, and QinetiQ/Oxford facilities had well defined profiles. The radial variation was in the range of $0.095 < (T_{max} - T_{min}) / \bar{T} < 0.176$, with the exception of the QinetiQ/Oxford EOTDF simulator, which had a peak of intensity $(T_{max} - T_{min}) / \bar{T} = 0.355$.

7 Conclusions

Numerous definitions and terminologies used to describe and quantify temperature distortion in combustors and turbine experiments have developed, yet to date there has been no universal uptake of a single transferable clearly defined quantity that can be

used in both combustor experiments and lower temperature turbine test facilities. This has led to some confusion. The relative merits of the more common definitions have been discussed. On the basis that hot-streak migration, secondary flow formation, and heat transfer are all essentially a function of T/\bar{T} , whether in the test facility or the engine, this simple quantity would appear to be the obvious candidate to universally describe and compare profiles most clearly. Where the shape of the profile is important (which is likely the case in most current investigations), the local quantity T/\bar{T} should be used to describe the whole profile.

Combustor temperature measurements from the open literature have been reviewed and compared with new combustor data measured by Rolls-Royce at an extreme point in the cycle of a modern engine. It is clear that significant differences exist between the measured combustor profiles in open literature. The radial and circumferential variations are strongly dependent on the swirl and dilution flows and also on the point in the engine cycle. The reasons for choosing more clearly defined and, in this sense, less engine representation profiles for fundamental turbine studies have been outlined: essentially the need to have well defined and well characterized inlet conditions, as a platform to understanding fundamental changes in heat transfer and as a test case for CFD validation.

A review of the six combustor simulators developed to date has been undertaken, and in the context of the available combustor measurements, and using the simple quantity T/\bar{T} , the profiles have been compared. The hardware used to simulate temperature distortion is often complex and costly. The three most recent simulators to be commissioned (AFRL, OSU, and QinetiQ/Oxford) were very different in design, and therefore some attention has been given to the details of the designs.

A new EOTDF generator was recently commissioned by Oxford on the QinetiQ ILPF at Farnborough, UK. This simulator is a novel two-stream injection simulator, which is suited to turbine efficiency measurements because of the low uncertainty in the inlet enthalpy flux. With temperature distortion, it is not possible to use the NGV as a flow meter, and downstream meters suffer from the need to perform a large unsteady correction and are sensitive to residual swirl and temperature distortion. The hot and cold streams of the EOTDF generator are independently metered upstream of the turbine stage, giving combined bias uncertainties in mass flow rate with and without temperature distortion of 1.37% and 1.13%, respectively, with a precision uncertainty that was approximately 0.2% in both cases.

The simulated profile using the new Oxford/QinetiQ EOTDF generator has been presented. The temperature distribution has both radial and circumferential variations. It has been shown that both pitch-to-pitch and run-to-run repeatabilities were excellent. The typical rms run-to-run variation across the whole plane was approximately 6.0 K, or 1.4% of the mean temperature (444 K). The uncertainty in the mean inlet temperature, which is measured before mixing the two streams by considering the total enthalpy flux, was an order of magnitude lower than this (approximately 0.113%).

Acknowledgment

The financial support of the partners of the European TATEF II Consortium (Turbine Aerothermal External Flows II) is acknowledged in respect of the experiments performed by Oxford at QinetiQ Farnborough, as is their agreement to allow these data to be published. The contributions of Dr. Frank Haselbach and Andy Smith (Rolls-Royce, Derby, UK) and Kam Chana (QinetiQ, Farnborough, UK) in providing combustor measurements and defining the target profile for the second generation combustor simulator at QinetiQ are appreciated.

Nomenclature

Roman and Greek

C	= capacity
M	= Mach number
\dot{m}	= mass flow rate, kg/s
N/\sqrt{T}	= nondimensional speed
p_{01}	= turbine inlet total pressure, Pa
T_g	= gas temperature, K
T_w	= wall temperature, K
T	= temperature, K
$\bar{T} = T_{\text{mean}}$	= average temperature, K
\bar{T}_{area}	= area-mean temperature, K
\bar{T}^{circ}	= radial temperature profile (circumferential average), K
\bar{T}^{mass}	= mass mean temperature, K
T_{cool}	= coolant temperature, K
Tu	= turbulence intensity
ΔT_{comb}	= temperature rise across combustor, K
ρ	= density, kg/m ³

Subscripts, Superscripts, and Abbreviations

01	= turbine stage inlet plane total
3	= combustor inlet plane
4	= combustor exit plane
c	= cold
(corr)	= corrected
h	= hot
max	= maximum
min	= minimum
rig	= test facility (cf. engine)
Re	= Reynolds number
(total)	= total

References

- [1] Munk, M., and Prim, R. C., 1947, "On the Multiplicity of Steady Gas Flows Having the Same Streamline Pattern," *Proceedings of the National Academy of Sciences*, Vol. 33.
- [2] Povey, T., Chana, K. S., Jones, T. V., and Hurrion, J., 2007, "The Effect of Hot-Streaks on HP Vane Surface and Endwall Heat Transfer: An Experimental and Numerical Study," *ASME J. Turbomach.*, **129**(1), pp. 32–43.
- [3] Hermanson, K. S., and Thole, K. A., 2002, "Effect of Nonuniform Inlet Conditions on Endwall Secondary Flows," *ASME J. Turbomach.*, **124**, pp. 623–631.
- [4] Povey, T., Chana, K. S., and Jones, T. V., 2003, "Heat Transfer Measurements on an Intermediate Pressure Nozzle Guide Vane Tested in a Rotating Annular Turbine Facility, and the Modifying Effects of a Non-Uniform Inlet Temperature Profile," *Proc. Inst. Mech. Eng., Part A* **217** pp. 421–431.
- [5] Sharma, O. P., Pickett, G. F., and Ni, R. H., 1992, "Assessment of Unsteady Flows in Turbomachines," *ASME J. Turbomach.*, **114**, pp. 79–90.
- [6] Dorney, D. J., Gundy-Burlet, K. L., and Sondak, D. L., 1999, "A Survey of Hot-Streak Experiments and Simulations," *Int. J. Turbo Jet Engines*, **16**, pp. 1–15.
- [7] Lefebvre, A. H., 1983, *Gas Turbine Combustion*, Hemisphere, New York.
- [8] Palaghita, T. I., and Seitzman, J. M., 2005, "Pattern Factor Sensing and Control Based on Diode Laser Absorption," *AIAA Paper No. AIAA-2005-3578*.
- [9] Barringer, M. D., Thole, K. A., and Polanka, M. D., 2006, "Experimental Evaluation of an Inlet Profile Generator for High-Pressure Turbine Tests," *ASME Paper No. GT-2006-90401*.
- [10] Goebel, S. G., Abuaf, N., Lovett, J. A., and Lee, C. P., 1993, "Measurements of Combustor Velocity and Turbulence Profiles," *ASME Paper No. 93-GT-228*.
- [11] Suzuki, Y., Satoh, T., Kawano, M., Akikawa, N., and Matsuda, Y., 2003, "Combustion Test Results on an Uncooled Combustor With Ceramic Matrix Composite Liner," *ASME J. Eng. Gas Turbines Power*, **125**, pp. 28–33.
- [12] Whitney, W. J., Stabe, R. G., and Moffitt, T. P., 1980, "Description of the Warm Core Turbine Facility Recently Installed at the NASA Lewis Research Center," *NASA Report No. TM-81562*.
- [13] Schwab, J. R., Stabe, R. G., and Whitney, W. J., 1983, "Analytical and Experimental Study of Flow Through an Axial Turbine Stage With Nonuniform Inlet Radial Temperature Profiles," *NASA Technical Memorandum Report No. 83431*, *AIAA Paper No. 83-1175*.
- [14] Stabe, R. G., Whitney, W. J., and Moffitt, T. P., 1984, "Performance of a High-Work Low Aspect Ratio Turbine Tested With a Realistic Inlet Radial Temperature Profile," *NASA Technical Memorandum Report No. 83655*, *AIAA Paper No. 84-1161*.
- [15] Butler, T. L., Sharma, O. P., Joslyn, H. D., and Dring, R. P., 1989, "Redistri-

- bution of Inlet Temperature Distortion in an Axial Flow Turbine Stage,” *J. Propul. Power*, **5**(1), pp. 64–71.
- [16] Roback, R. J., and Dring, R. P., 1993, “Hot Streaks and Phantom Cooling in a Turbine Rotor Passage, Part I: Separate Effects,” *ASME J. Turbomach.*, **115**(4), pp. 657–666.
- [17] Joslyn, H. D., and Dring, R. P., 1988, “A Trace Gas Technique to Study Mixing in a Turbine Stage,” *ASME J. Turbomach.*, **110**(1), pp. 38–43.
- [18] Joslyn, H. D., and Dring, R. P., 1992, “Three-Dimensional Flow and Temperature Profile Attenuation in an Axial Turbine, Part I: Aerodynamic Measurements,” *ASME J. Turbomach.*, **114**, pp. 61–70.
- [19] Joslyn, H. D., and Dring, R. P., 1992, “Three-Dimensional Flow and Temperature Profile Attenuation in an Axial Turbine, Part II: Profile Attenuation,” *ASME J. Turbomach.*, **114**, pp. 71–78.
- [20] Haldeman, C., 1989, “An Experimental Study of Radial Temperature Profile Effects on Turbine Tip Shroud Heat Transfer,” MS thesis, Aeronautical and Astronautical Engineering, MIT, Cambridge MA.
- [21] Shang, T., 1995, “Influence of Inlet Temperature Distortion on Turbine Heat Transfer,” MS thesis, Department of Aeronautics and Astronautics.
- [22] Shang, T., Guenette, G. R., Epstein, A. H., and Saxer, A. P., 1995, “The Influence of an Inlet Temperature Distortion on Rotor Heat Transfer in a Transonic Turbine,” *AIAA Paper No. 95-3042*.
- [23] Shang, T., and Epstein, A. H., 1996, “Analysis of Hot Streak Effects on Turbine Rotor Heat Load,” *ASME Paper No. 96-GT-118*.
- [24] Hilditch, M. A., Fowler, A., Jones, T. V., Chana, K. S., Oldfield, M. L. G., Ainsworth, R. W., Hogg, S. I., Anderson, S. J., and Smith, G. C., 1994, “Installation of a Turbine Stage in the Pyestock Isentropic Light Piston Facility,” *ASME Paper No. 94-GT-277*.
- [25] Povey, T., Chana, K. S., Jones, T. V., and Oldfield, M. L. G., 2003, “The Design and Performance of a Transonic Flow Deswirling System: An Application of Current CFD Design Techniques Tested Against Model and Full-Scale Experiments,” *Advances of CFD in Fluid Machinery Design*, R. L. Elder, A. Tourlidakis, and M. K. Yates, eds., IMechE Professional Engineering, Bury St. Edmonds, UK, pp. 65–94.
- [26] Goodman, M. I., Oldfield, M. L. G., Kingcombe, R. C., Jones, T. V., Ainsworth, R. W., and Brooks, A. J., 1992, “An Axial Turbobrake,” *ASME J. Turbomach.*, **114**, pp. 419–425.
- [27] Hurriion, J., 2002, “The Effect of an Inlet Temperature Profile on the Heat Transfer to Gas Turbine Blades,” Ph.D. thesis, University of Oxford.
- [28] Chana, K. S., Hurriion, J. R., and Jones, T. V., 2003, “The Design, Development and Testing of a Non-Uniform Inlet Temperature Generator for the Qinetic Transient Turbine Research Facility,” *ASME Paper No. GT-2003-38469*.
- [29] Barringer, M. D., Thole, K. A., and Polanka, M. D., 2004, “Developing a Combustor Simulator for Investigating High Pressure Turbine Aerodynamics and Heat Transfer,” *ASME Paper No. GT-2004-53613*.
- [30] Barringer, M. D., Thole, K. A., and Polanka, M. D., 2006, “Effects of Combustor Exit Profiles on High Pressure Turbine Vane Aerodynamics and Heat Transfer,” *ASME Paper No. GT-2006-90277*.
- [31] Haldeman, C. W., Dunn, M. G., MacArthur, C. D., and Murawski, C. G., 1992, “The USAF Advanced Turbine Aerothermal Research Rig (ATARR),” *NATO AGARD Propulsion and Energetics Panel Conference Proceedings*, Antalya, Turkey, Vol. 527.
- [32] Haldeman, C. W., Mathison, R. M., and Dunn, M. G., 2004, “Design, Construction, and Operation of a Combustor Emulator for Short-Duration High-Pressure Turbine Experiments,” *AIAA Paper No. AIAA-2004-3829*.

A Comparison of the Flow Structures and Losses Within Vaned and Vaneless Stators for Radial Turbines

A. T. Simpson
S. W. T. Spence
J. K. Watterson

School of Mechanical & Aerospace Engineering,
Queen's University Belfast,
Ashby Building,
Stranmillis Road,
Belfast BT9 5AH, UK

This paper details the numerical analysis of different vaned and vaneless radial inflow turbine stators. Selected results are presented from a test program carried out to determine performance differences between the radial turbines with vaned stators and vaneless volutes under the same operating conditions. A commercial computational fluid dynamics code was used to develop numerical models of each of the turbine configurations, which were validated using the experimental results. From the numerical models, areas of loss generation in the different stators were identified and compared, and the stator losses were quantified. Predictions showed the vaneless turbine stators to incur lower losses than the corresponding vaned stator at matching operating conditions, in line with the trends in measured performance. Flow conditions at rotor inlet were studied and validated with internal static pressure measurements so as to judge the levels of circumferential nonuniformity for each stator design. In each case, the vaneless volutes were found to deliver a higher level of uniformity in the rotor inlet pressure field.
[DOI: 10.1115/1.2988493]

Introduction

While radial inflow turbines are employed in a range of applications, by far the most widespread application is in turbochargers for reciprocating engines. Improved design methods for greater performance and efficiency rely on improved knowledge of the internal flow patterns and loss mechanisms throughout the turbine stage. Computational fluid dynamics (CFD) analysis backed up by experimental measurements provides a valuable means of examining and understanding the internal flow in a level of detail that would not be possible by experimental measurements alone. This investigation focuses on the flow structures and losses incurred in the stator of the radial turbine. Radial turbine stators fall into two main categories: a scroll or volute without guide vanes (vaneless volute) and a scroll or housing that incorporates a number of guide vanes preceding the turbine rotor (vaned stator), as illustrated in Fig. 1. While the vaneless volute has traditionally been used in turbocharger applications, increasing demands on engine air handling systems to meet emissions requirements have promoted development of variable geometry turbines (VGTs) to provide increased flexibility and efficiency over the broad flow ranges encountered in turbocharging. These VGT turbochargers employ vaned stators in conjunction with the volute and incorporate some movable element to permit variation of the throat area of the vaned stator.

Excluding the stator vanes brings packaging advantages by reducing the overall size of the turbine housing, which is an important consideration in turbocharging applications. However, where space is less critical, the use of vaned stators has generally been considered to deliver improved efficiency. Bhinder [1] stated that "all factors being equal," the peak efficiency of a radial turbine with a vaneless volute could be 2–3% lower than the equivalent turbine with a vaned stator. The higher level of flow nonuniformity leaving the vaneless stator was cited as the most likely reason for the performance decrement, highlighting that the choice of stator impacts the stage efficiency in two main ways: aerodynamic

losses incurred within the stator and further losses incurred within the rotor as a consequence of flow distortion at stator outlet. Bhinder did not present any experimental data to support this assertion. Previously as part of the Ricardo test program, Palmer carried out static blowing tests on a stator rig, using the same volute design with and without stator vanes [2,3]. Dispensing with the vanes was found to lower the total pressure loss by up to 5%; however, an accompanying increase in nonuniformity was measured in both total pressure and flow angle at discharge. A search of the literature revealed only one previous experimental study directly comparing turbine performance with vaned and vaneless stators, which was reported by Baines and Lavy [4]. The authors observed that the vaned stator delivered improved turbine efficiency across the range of the comparison (up to 15% improvement), although it was observed to have a more sharply peaked efficiency curve, with the efficiency of the vaneless volute holding up better away from the design point. The principal reason for this was determined to be large variations in flow velocity and flow angle around the rotor periphery, leading to changes in rotor incidence and an associated reduction in efficiencies. Static pressure measurements upstream and downstream of the stator vanes showed a significant amount of circumferential variation at vane inlet, despite the housing being designed to supply a uniform low velocity flow to the stator vanes. At outlet from the vaned stator, it was observed that this variation had reduced in magnitude, with the vane row apparently removing much of the flow distortion. There were some factors that may have affected the overall performance comparison; at less than 60%, the efficiencies reported for the vaneless turbine were uncharacteristically low, and despite the design intention, there was some discrepancy in the flow rates between the two turbine stages.

In the available literature, a common reason given for variations in turbine performance with vaned and vaneless stators is the higher level of nonuniformity in the volute discharge flow. Benisek and Spraker [5] carried out flow surveys at the exit of two vaneless volutes having A/r values of 35 mm and 53 mm using laser Doppler velocimetry (LDV). Measured flow properties and directions showed significant nonuniformity at volute discharge, particularly in the tongue region. For the larger volute, incidence

Manuscript received November 30, 2007; final manuscript received March 26, 2008; published online April 9, 2009. Review conducted by Michael Casey.

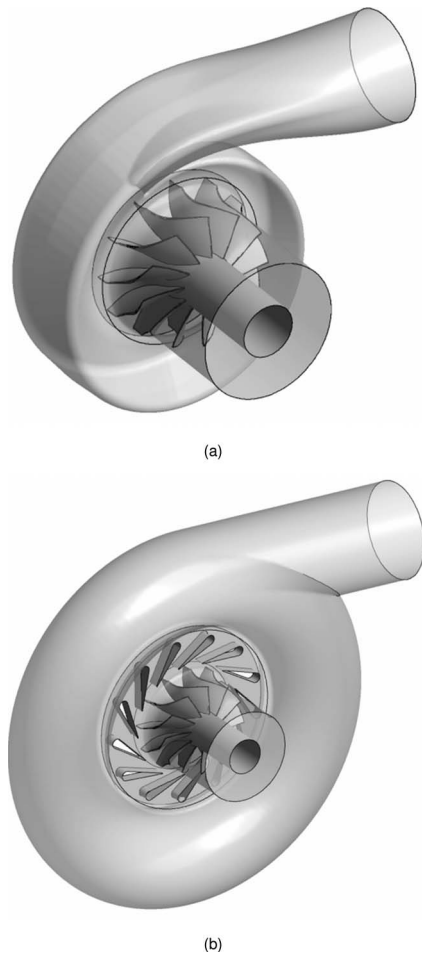


Fig. 1 Vaneless volute (a) and vaned stator (b)

angles varied from -37 deg to -47 deg around the rotor circumference, whereas for the smaller volute, variations from $+14$ deg to -27 deg were measured. The authors surmised that a vaneless volute would normally incur an efficiency penalty of several points compared to a vaned stator of the same flow capacity. In light of this, they expressed surprise that the absence of vanes did not result in a larger efficiency penalty than they found in practice. As part of an experimental investigation of a vaneless volute for use in turbocharger turbines, Hussain and Bhinder [6] presented measurements of total and static pressures and flow angle around the rotor inlet. Stagnation pressure loss was presented along the volute length and rotor periphery, with the authors stating that the loss in the volute was less than 1% of the entry value. Measured flow angle at rotor inlet was found to vary between 71 deg and 80 deg from the radial direction, which showed a significant departure from the design value of 83 deg. The authors stated that resulting variation in incidence angle could have a more significant effect on stage performance than the total pressure losses in the volute.

Scrimshaw and Williams [7] carried out tests on three geometrically similar asymmetric turbine volutes of varying sizes in order to study size effects on performance characteristics. Static pressure and yaw probe measurements were presented at volute discharge for each of the three turbine builds, highlighting the level of nonuniformity in the pressure field and mass flow distribution through which the rotor blades pass. Negative flow angles were observed over the 0 – 20 deg azimuth angle range, indicating flow migration from the rotor into the volute in this region. The authors stated that the high velocity gas entering the volute created an injector type effect, with strong suction conditions over this angle

range. The mixing process in the tongue region was shown to cause high total pressure loss, with a measured peak value of 25% recorded, defined as the total pressure drop normalized by the exit dynamic head. Average stator total pressure loss was observed to increase with decreasing volute size, with percentage losses of 13.5%, 13.8%, and 15% recorded for the 101.65 mm, 67.73 mm, and 50.8 mm turbines, respectively. Similar results were presented by Miller et al. [8], who carried out detailed flow surveys using a five port cobra probe at the inlet of a 110 mm tip diameter turbine housed in a volute with a symmetric cross section. Measured loss coefficients, again defined as the total pressure drop normalized by the exit dynamic head, showed low values in the range of 0.01–0.02 in the 60 deg and 180 deg azimuth angle range, which increased to 0.11 from azimuth angles 180–220 deg. The highest losses were recorded at the tongue, with a loss coefficient value of 0.56 recorded at an azimuth angle of $\theta=0$ deg. The authors compared these measured losses to those obtained by Scrimshaw and Williams [7] and Hussain and Bhinder [6]. Average losses in this case were found to be lower than those measured by Scrimshaw and Williams [7], although the measured distributions showed good agreement considering that Scrimshaw and Williams' measurements were taken in an asymmetrical volute cross section under different operating conditions. The losses measured by Hussain and Bhinder [6] were found to be two to three times smaller. Absolute flow angles around the rotor periphery were found to remain fairly constant at 75 deg, with more radial values of 60–70 deg observed just downstream of the tongue. Scrimshaw and Williams [7] noted the opposite behavior, observing more tangential flow angles near the tongue.

There is a limited amount of measured data relating to the flow characteristics of vaned stators in radial turbines, particularly in comparison to the volume of published work on axial cascades. The fundamental geometrical differences lead to different flow behaviors in radial turbines, arising due to the smaller aspect ratios, reduced turning, and the radial pressure gradient. In 1984, Hashemi et al. [9] carried out a study of the flow in a radial nozzle cascade using both air and water test rigs. Secondary flow patterns in the air cascade were observed using an oil and graphite powder mixture, with the resulting images clearly depicting the formation of horseshoe-type vortices at the leading edge of the vanes. Unlike the classical secondary flow patterns described in published literature for axial cascades, no passage vortex was found. In this case, the radial pressure gradient was found to cause the horseshoe vortices to shift toward the pressure surface of the vanes. The traces showed variation of the vane inlet angle in the circumferential direction, with the resulting vortex patterns observed to vary significantly. At larger incidence, the pressure side vortex curved away from the vane at first and then swept toward the trailing edge, with the authors noting that the vortices appeared larger in magnitude under these conditions.

Eroglu and Tabakoff [10] carried out an investigation to provide detailed experimental measurements of the flow field in a radial turbine guide vane passage using a three component LDV system. The vaned stator investigated contained 18 slightly cambered nozzle vanes each with a chord length of 50 mm. Measurements were taken at three radial locations: upstream of the leading edge, inside the vane passage, and just downstream of the trailing edge. Contour plots at the upstream measurement station showed the flow velocities to be reasonably uniform; however, the contours were not symmetrical between the endwalls due to the influence of the upstream scroll geometry. Just upstream of the throat, the authors noted two low velocity regions: one in the corner between vane suction surface and shroud endwall and another in the same corner closer to the midspan. These low velocity regions suggested the presence of secondary flows transporting low energy boundary layer flow to the suction side corner and also further toward the midspan along the suction surface. At the downstream measurement plane, the authors explained that it was difficult to separate the freestream and wake regions, with contour plots de-

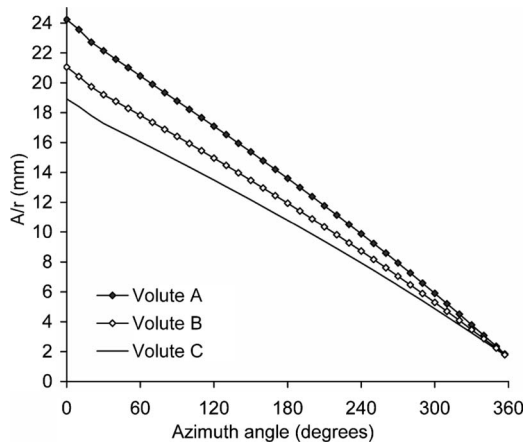


Fig. 2 Variation of A/r ratio with azimuth angle for each vaneless volute

picting a highly disturbed velocity distribution due to the high levels of turbulence and rapid mixing. Based on these results, the authors drew some conclusions on the differences between the secondary flow mechanisms in the axial and radial turbine stators. They stated that the radial pressure gradient tended to encourage secondary flows to move toward the pressure side of the vane; however, the pressure gradient due to the passage geometry has the opposite effect. These two counteracting pressure fields were felt to reduce the strength of the secondary flow structures. Although axial turbines generally have stronger secondary flows due to higher turning, the structures are normally restricted to regions close to the endwalls. In this radial nozzle, the authors found that the secondary flow structures occupied a significantly higher percentage of the total passage area due to the lower aspect ratio.

Putra and Joos [11] carried out an experimental and numerical study of flow through a radial turbine stator vane passage. Reynolds averaged Navier–Stokes (RANS) calculations were carried out using the commercial code Fluent on a single vane passage with a slight camber, with a segment of the upstream asymmetric volute included using a total grid size of 2.2×10^6 nodes. To validate the numerical models, laser-two-focus (L2F) measurements were presented in the midspan and at selected planes inside the guide vane passage and compared to predictions using a Reynolds stress model (RSM) turbulence model and the standard $k-\epsilon$ model. The RSM model showed good agreement with the measured flow angle distribution, whereas the standard $k-\epsilon$ model showed an almost 2D flow pattern. Even with the RSM model implemented, the computed secondary flow vortices were much weaker than those found in axial cascades due to less flow turning in the blade passages. The classic passage vortex observed in axial cascades

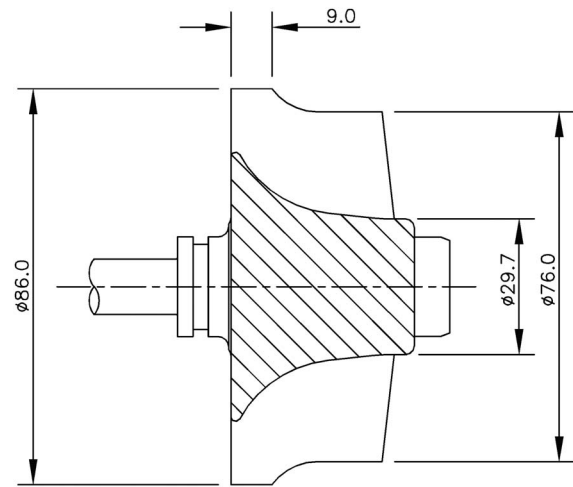


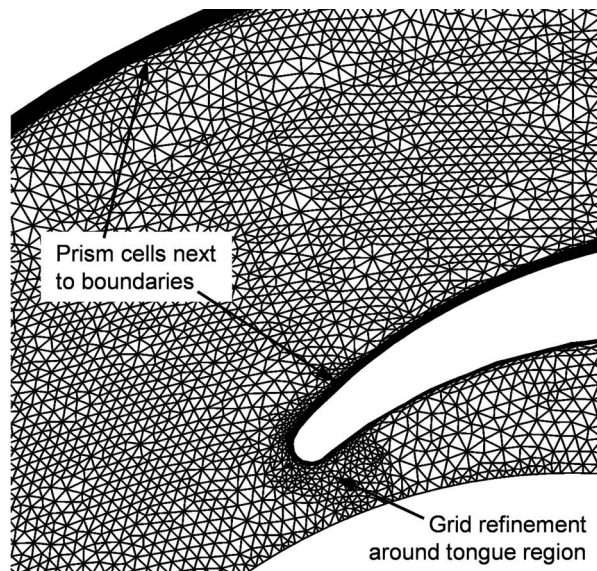
Fig. 3 Meridional view of the turbine rotor

was not found, which is expected as the guide vanes provided a minimal amount of flow turning. An additional vortex was observed, referred to as an “inflow” vortex, which was a product of the asymmetric scroll geometry. The conventional horseshoe vortices were resolved, with the vortex on one endwall observed to be of higher magnitude, which was attributed to the asymmetric scroll geometry. At nozzle exit, the calculated local loss coefficient values were found to exceed 0.54 in the region where the secondary flow structures interacted with the endwall boundary layer.

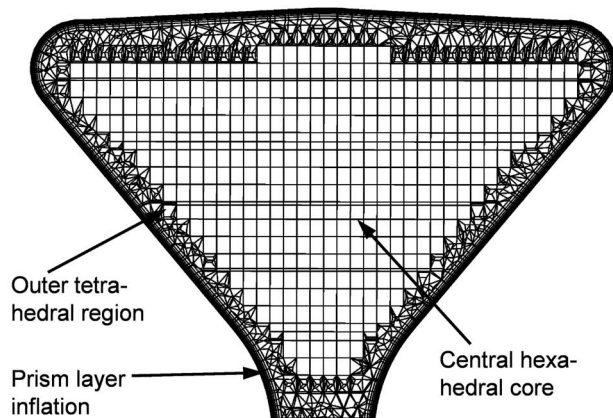
The aim of this investigation is to study the flow patterns and losses through vaned and vaneless turbine stators at matching operating conditions. Although a number of published works have investigated the flow patterns through vaned and vaneless turbine stators, the relative advantages and disadvantages associated with vaned and vaneless turbines are still not well understood in terms of the losses incurred and the flow conditions they deliver to the turbine. An experimental program previously carried out at Queen’s University Belfast, reported by Rosborough [12] and Spence et al. [13], aimed to measure the performance of a radial turbine using the same rotor but with a range of different stator designs. The performance of vaned and vaneless stators was compared over a range of conditions and at particular design points of matching mass flow rate. In each case, higher efficiencies were achievable using a vaneless stator, with efficiency improvements of up to 4.5% measured over the corresponding vaned stator turbine. In addition to stage performance measurements, static pressure measurements were taken at rotor inlet to ascertain the uniformity, or otherwise, of the flow exiting the stator. The present

Table 1 Summary of performance for each turbine configuration

	Turbine A		Turbine B		Turbine C	
	Vaneless volute A	Vaned A	Vaneless volute B	Vaned B	Vaneless volute C	Vaned C
Stage PR	1.80	1.80	2.50	2.50	3.20	3.20
Corrected mass flow (kg/s)	0.243	0.244	0.239	0.237	0.223	0.222
Corrected speed (rev/min)	44922	44912	54902	54871	64892	64889
Specific Speed	0.843	0.844	0.866	0.865	0.932	0.933
U/C	0.668	0.674	0.676	0.675	0.721	0.721
Total-to-total efficiency	0.933	0.896	0.935	0.903	0.945	0.926
Total-to-static efficiency	0.852	0.818	0.844	0.821	0.853	0.836



(a) Outer tetrahedral mesh near volute tongue



(b) Hybrid mesh structure in volute cross-section

Fig. 4 Vaneless volute mesh features

paper reports the results of a detailed numerical study of those experimental turbine configurations using a commercial CFD code (ANSYS CFX), in order to quantify the component losses and gain an understanding of the underlying aerodynamic effects behind the measured performance variations.

Experimental Program

The design and testing of a series of vaned and vaneless stator radial turbines were undertaken by Spence et al. [13]. Three different vaneless volutes were designed based on a free vortex method presented by Chapple et al. [14]. The cross section of the volute flow path was symmetrical, with a reduction in A/r ratio with increasing azimuth angle that was close to linear; the variation of A/r with azimuth angle for one of the vaneless volutes is shown in Fig. 2. The A/r ratio plotted in Fig. 2 is based on the cross-sectional area of the volute including the vaneless space that extends to the tip diameter of the rotor. Three corresponding vaned stators were designed and tested to match the mass flow rate of each vaneless volute at the predefined design point. Three operating conditions, denoted A, B, and C, are compared in Table 1, along with the overall performance measured for each configuration. The turbine speed and mass flow rate shown are corrected to inlet conditions of 288 K and 101,325 Pa. The same 86 mm

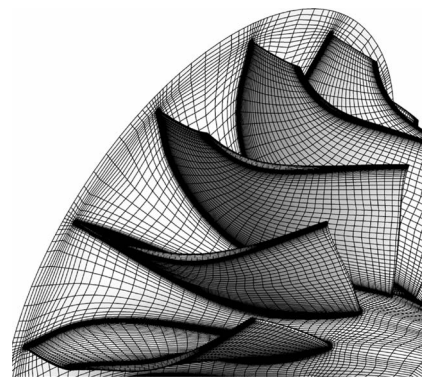


Fig. 5 Rotor grid (full-stage model)

diameter turbine rotor was used for all tests; the rotor geometry is illustrated in Fig. 3. Using the same turbine rotor and maintaining the same mass flow rate at the design points allowed direct comparison of the impact of the vaned and vaneless stators on overall turbine performance. The vaned stators comprised 13 uncambered guide vanes, each having a different throat area to provide the desired mass flow rate. The vaned stators were housed in a large machined torus to distribute the flow to the inlet of the stator vanes.

In addition to overall stage performance measurements, static pressure measurements were taken close to rotor inlet (at a diameter of 87 mm) in each build. There were 24 equispaced circumferential static pressures for each vaneless volute, while only four measurement locations were produced for the vaned stator configurations due to the practical difficulties in accommodating the drillings in the turbine torus. More details of the experimental test configuration and full turbine performance maps are presented in Ref. [13].

Numerical Modeling: Complete Turbine Stage

The objectives of the numerical modeling exercise were to isolate and quantify the stator losses, and to identify important features within the stator flows. In order to accurately reproduce the experimental turbines, full-stage models were generated for each of the six turbine configurations. In this way, the losses incurred in all components of the turbine were accounted for, and the boundary conditions could be inputted directly from the test data and fixed at some point well upstream or downstream of the areas of interest, thus removing the influence of any assumptions associated with specifying velocity profiles at the boundaries.

Full-stage two domain numerical models were constructed for each of the three vaneless turbine configurations, consisting of the full volute and rotor assembly. Each model consisted of approximately 3.6×10^6 nodes in total. For the volutes, the meshes were generated using the ANSYS ICEM CFD meshing software and comprised mostly unstructured tetrahedral elements, with a hexahedral core and prismatic cells in near wall regions so as to achieve better predictions of boundary layer flows. For each of the three volutes, 20 prism layers were used near the walls with an expansion ratio of around 1.2. The mesh was refined in areas of high curvature and in regions where high flow gradients were expected, particularly around the tongue. Figure 4 shows some representative sections of the volute meshes. Surface mesh sizes were prescribed to ensure there was a smooth transition between element sizes throughout the computational domain. Following an extensive grid dependency study, the grid sizes for each of the three volutes were set to be of the order of 1.9×10^6 nodes. A more detailed account of the investigation of different grid sizes for this investigation can be found in Ref. [15]. The rotor grid comprised around 155,000 nodes per blade passage, with a completely structured hexahedral grid in the passages and an O-grid wrapped

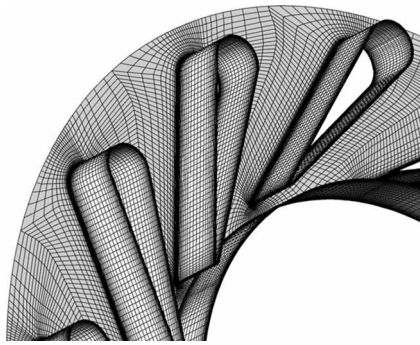


Fig. 6 Nozzle grid (full-stage model)

around the blade to help minimize skew angles at leading and trailing edges. Fifteen uniform cells were used in the clearance gap between the rotor tip and the shroud wall to capture tip leakage flows. When swept around to create the full 360 deg rotor, this equated to a total rotor grid size of 1.8×10^6 nodes, which is shown in Fig. 5. For each of the three vaned turbine configurations, full-stage models were created consisting of three domains and 4.2×10^6 nodes. The same rotor grid was used as that used in the vaneless computations. For the stator vanes, a fully structured hexahedral grid was used containing 150,000 nodes per stator vane passage. A J-grid topology was adopted with an O-grid wrapped around the vane so as to minimize skew angles. Higher grid resolution was set on the hub, shroud, and blade surfaces with an expansion factor of 1.3 so as to model near wall flows as accurately as possible. The grid used in this study is presented in Fig. 6. For the torus delivering the flow to the stator vanes, an unstructured tetrahedral mesh was used with prismatic layers placed near the walls for greater boundary resolution. Grid sizes for the torus were set at 750,000 nodes.

In each case, the $k-\omega$ shear stress transport (SST) turbulence model was adopted, as developed by Menter [16]. This two equation model is based on the eddy viscosity approximation, where the turbulence is assumed to consist of small eddies continuously forming and dissipating, in which the Reynolds stresses are assumed to be proportional to the mean velocity gradients. The SST model has been found to provide improved predictive performance in complex flow fields by comparison with standard $k-\epsilon$ or $k-\omega$ models [17]. Used in conjunction with a scalable wall function approach, the SST model can be applied to arbitrarily fine grids, with the model switching from a standard log-law approximation of the boundary layer profile to a low Reynolds number calculation depending on the local grid resolution. In the case of the full-stage models, the y -plus values attained were not sufficient to resolve all of the details in the boundary layer right down to the laminar sublayer ($50 > y^+ > 100$), and as such each calculation employed a standard wall function approach.

The boundary conditions for the full-stage models at turbine inlet and exit were inputted, from the measured test values, with total pressures and temperatures applied at turbine inlet and an average static pressure boundary applied at exit. This boundary condition combination makes the flow rate an implicit part of the solution and was found to provide the best numerical stability and convergence rates. A frozen rotor interface was used to connect the stationary and rotating domains for each full-stage model. This multiple frame of reference (MFR) approach fixes the relative positions of the stationary and rotating domains throughout the calculation, with the appropriate frame transformation occurring across the interface. Since the solver being used was an implicit coupled solver, arbitrarily large time steps were chosen to aid convergence for the steady state models, using values of the order of $100/\omega$. For each case, the target value for the maximum residuals was set at 5×10^{-4} , which was typically reached after 200–250

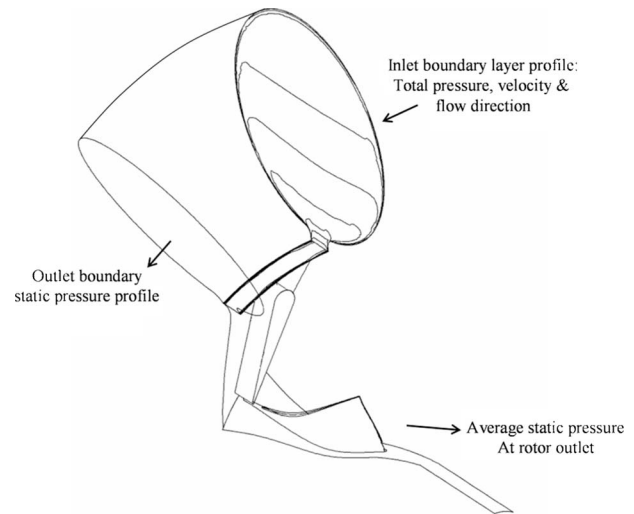


Fig. 7 Refined single passage model

iterations. Using eight compute nodes of a Windows high performance computing (HPC) cluster, run times were around 16 h. In addition to monitoring residuals, convergence was also judged by placing monitor points and expressions at various locations in the flow.

Numerical Modeling: Refined Single Passage Models

As mentioned previously for the full-stage models, the grid resolution attained was not sufficient to resolve the complete boundary layer through to the wall, including the laminar sublayer. So as to investigate the flows and losses in the vaned stator builds in greater detail, refined single passage models were created representing a single stator and rotor blade passage, including a segment of the upstream torus. In this way, the boundary conditions could be inputted from the corresponding full-stage models in the form of total pressure profiles and velocity directions at the torus inlet plane and static pressure profiles at the torus outlet plane. Figure 7 shows the single passage segment of the vaned stator configuration that was modeled. In this way, the flow properties in terms of direction and boundary layer profiles were adequately reproduced at vane inlet, since these were considered to have an appreciable impact on the flow structures in the vane passage. For the single passage models, the Reynolds baseline (BSL) stress turbulence model was implemented, which is based on the transport equations for the Reynolds stresses and dissipation rate. The extra transport equations solved during each coefficient loop combined with the difficulty in creating grids with adequate resolution to properly capture the near wall flow phenomena made the implementation of this model unfeasible for full-stage calculations with the computing resources available for this study. In order to minimize the computational requirement and improve the numerical robustness, fully converged single passage models based on the standard two-equation turbulence models were used to provide initial results to start the calculation with the Reynolds stress turbulence model. It was found that grid sizes of around 1×10^6 nodes were required in both the rotor and stator vane passages in order to obtain y -plus values close to unity and maintain a smooth transition between the different element sizes throughout the computational domain.

Numerical Modeling: Transient Rotor-Stator Modeling

As part of the test program, static pressures were measured at rotor inlet (0.5 mm upstream) for each vaned and vaneless build. For the vaneless builds, 24 equispaced static pressure tapings were drilled around the rotor periphery. For the vaned builds, just four equispaced tapings were drilled, which was due to the dif-

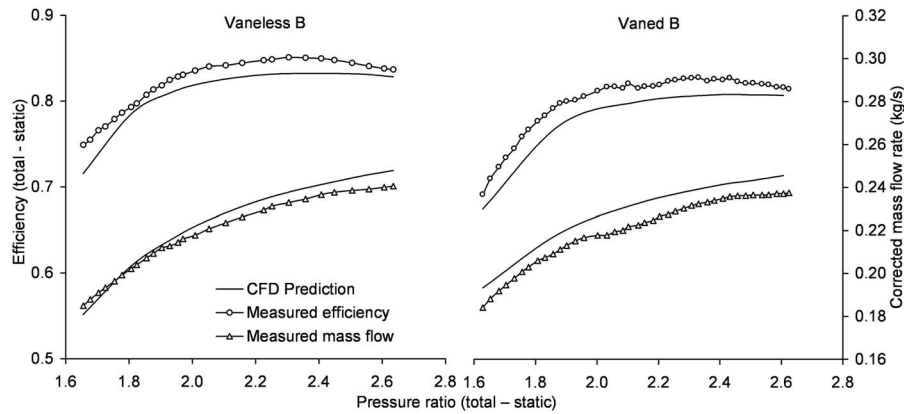


Fig. 8 Comparison of experimental and numerical results for both the vanned and vaneless turbine B configurations at a corrected speed of 55,000 rpm

difficulty in machining static pressure pathways in the vanned housing. Although the experimental pressure measurements available were time averaged steady state values, the flow in this region of the turbine is essentially unsteady due to the interaction of the passing rotor blades. Therefore, it was not possible to study the level of circumferential nonuniformity in the rotor inlet region using a steady state frozen rotor interface, since the resulting flow variation was dominated by the local pressure gradients in the rotor passages. Consequently, transient full-stage CFD models were developed for the vanned and vaneless stator configurations of turbine B, and the resulting time averaged pressure fields were compared to the corresponding time averaged pressure measurements. A sliding mesh interface was used, and physical time step information was supplied based on the rotational speed of the rotor. For each time step, the rotor is rotated by the corresponding angular displacement, with discrete calculations carried out at each position. Such calculations require substantial computational resources, both in terms of solution time, storage space, and manipulation of the resulting quantities of data. For this reason, the node counts for the transient models were reduced to 1.5×10^6 and 2.2×10^6 for the vaneless and vanned stator configurations, respectively. (The previous grid independence studies had shown these grid resolutions to provide reliable predictions of the main flow features.) To start the transient CFD calculation, the model was first run to a converged steady state condition to produce a set of initial results. A time step was chosen to represent one degree of rotor rotation and the transient calculation was performed for the first complete rotor rotation while properties at specified points in the stator were monitored to ensure consistency and confirm that a regular repeating pattern was established. On the second rotor rotation, results were written for selected variables for each one degree step. The total solver times required for the transient calculations, including the initial steady state run, were of the order of 150 h.

Model Validation

Model validation was achieved by comparing the predicted overall turbine performance parameters of flow rate and efficiency with the measured experimental data for the vanned and vaneless turbine B configurations from Ref. [13]. Successive calculations were run at an operating speed of 55,000 rpm (corrected to 288 K at turbine inlet) to produce a constant speed-line across a range of pressure ratios to compare with the performance test speed lines. Figure 8 compares the predicted and experimental performance. The objective of the validation exercise was to ensure that the CFD models were able to predict both the trends and the levels of the measured performance parameters. The trends show excellent agreement in each case, with the CFD models accurately capturing any changes in efficiency and mass flow across the operating

range. It is evident, however, that the absolute efficiency values in each instance are generally underpredicted by the CFD models, while the mass flow rates are overpredicted. The differences are highlighted in Table 2, which shows the global performance figures for each of the full-stage CFD models at the design operating conditions. The absolute flow properties at inlet and outlet that were not set as boundary conditions (i.e., exit total pressure and temperature) are predicted to be within 1% of the experimental data at each point, and the cumulative error in calculating effi-

Table 2 Measured and predicted performance at the comparison point for each turbine configuration

		Vaneless volute	Vanned stator
Stator A	Experimental corrected mass flow (kg/s)	0.243	0.244
	Predicted corrected mass flow (kg/s)	0.248	0.249
	% difference in mass flow	+2.3%	+2.2%
	Experimental efficiency (t-s)	0.852	0.818
	Predicted efficiency (t-s)	0.824	0.788
	% difference in efficiency	-3.6%	-3.6%
	Experimental rotor pressure ratio (s-s)	1.203	1.191
	Predicted rotor pressure ratio (s-s)	1.227	1.189
	% difference in rotor pressure ratio	-1.9%	-0.16%
Stator B	Predicted stator loss coefficient (ζ_{stator})	0.102	0.152
	Predicted turbine specific work (J/kg)	50,363	49,337
	Experimental corrected mass flow (kg/s)	0.239	0.237
	Predicted corrected mass flow (kg/s)	0.241	0.244
	% difference in mass flow	+0.78%	+2.79%
	Experimental efficiency (t-s)	0.844	0.821
	Predicted efficiency (t-s)	0.817	0.809
	% difference in efficiency	-3.2%	-1.5%
	Experimental rotor pressure ratio (s-s)	1.418	1.421
Stator C	Predicted rotor pressure ratio (s-s)	1.393	1.393
	% difference in rotor pressure ratio	-1.8%	-2.0%
	Predicted stator loss coefficient (ζ_{stator})	0.103	0.125
	Predicted turbine specific work (J/kg)	74,845	74,730
	Experimental corrected mass flow (kg/s)	0.223	0.222
	Predicted corrected mass flow (kg/s)	0.225	0.232
	% difference in mass flow	+0.84%	+4.2%
	Experimental efficiency (t-s)	0.853	0.836
	Predicted efficiency (t-s)	0.829	0.819
% difference in efficiency	-2.84%	-2.0%	
Stator C	Experimental rotor pressure ratio (s-s)	1.643	1.721
	Predicted rotor pressure ratio (s-s)	1.656	1.665
	% difference in rotor pressure ratio	-0.82%	-3.2%
	Predicted stator loss coefficient (ζ_{stator})	0.112	0.112
	Predicted turbine specific work (J/kg)	92,591	91,977

ciency using these predicted values leads to efficiency predictions of around 2–4% lower than the experimentally obtained values.

The experimental turbine efficiencies were determined from the measured temperature drop across the turbine, and it could be argued that any heat loss from the turbine stage could lead to artificially high measurements of turbine efficiency. However, the test rig was thoroughly insulated to minimize thermal losses and any such effects would be much more apparent at lower pressure ratios than at higher pressure ratios; a trend that is not borne out by Fig. 8. One possible source of error could be the measurement of static pressure at turbine exit. It is difficult to obtain representative values of static pressure at exit where the flow often has a significant swirl component and where static pressure traverses can be intrusive. The static pressure was measured in the plane of a sudden expansion just downstream of the exducer. The outlet boundary in the CFD model was set at the same point and an average static pressure was applied across the outlet boundary, corresponding to the measured value. The control volume used for the CFD calculations differed from the experimental control volume in that the exit total temperature measurement station was located 400 mm downstream from the exit static pressure measurement and thus further downstream than the CFD outlet boundary. Low exhaust temperatures and the well insulated exhaust duct meant that any heat loss from the exhaust duct would have minimal impact upon the efficiency measurements. Heat transfer was not modeled, and therefore including the additional exhaust duct geometry in the numerical model would have required additional computational effort without making any difference to the predicted temperatures. The differences in measured and computed values of mass flow rate mostly lie within 4%. The greatest difference of 4.2% was observed for the Vaned C build. It is noteworthy that the model generally predicts mass flow more accurately for the vaneless stators than for the vaned ones; however, the opposite is true of the stage efficiency. CFD calculations are generally accepted to be more successful in predicting trends rather than absolute values, and as such it is the ability of the model to successfully capture the trends in the experimental data across the operating range and between different configurations that provide a level of confidence in the results.

The trends in both the experimental and the CFD results show that the greatest difference in efficiencies between the vaned and vaneless stators exists for the A turbine build. This equates to the vaneless turbine A giving an improvement in measured efficiency of 3.4% over the corresponding vaned turbine. The difference in measured efficiencies is reduced to 2.3% for the B turbine builds and to 1.7% for the C builds. This trend is predicted effectively by the results from the CFD calculations, with differences of 3.6%, 0.8%, and 1.0% for the A, B, and C builds, respectively, at the comparison points. Comparing the values of stator loss coefficients, which were obtained from the CFD predictions, the vaned stator shows substantially higher loss levels than the vaneless for turbine A. This agrees with the measured efficiency values. The discrepancy between vaned and vaneless loss levels is less for turbine B, with the vaned configuration still incurring more losses, which agrees with the efficiency trend. Vaneless stator C incurs higher losses than the other volutes, showing a clear trend in increasing losses with a reduction in volute size, as also observed by Scrimshaw and Williams [7]. Also presented in Table 2 is the predicted turbine specific work for each stator configuration, which shows lower specific work for the vaned stators in each instance. This would suggest that the vaned stators produce a more inefficient flow state in the rotor passages, which may further contribute to the lower stage efficiencies for the three vaned builds. This would appear to be the case for stator C, where the vaned build delivers lower efficiencies than the corresponding vaneless build, despite the predicted stator loss coefficients being almost equal.

Comparing these calculated losses to previously published work, those presented here are lower than the measured values

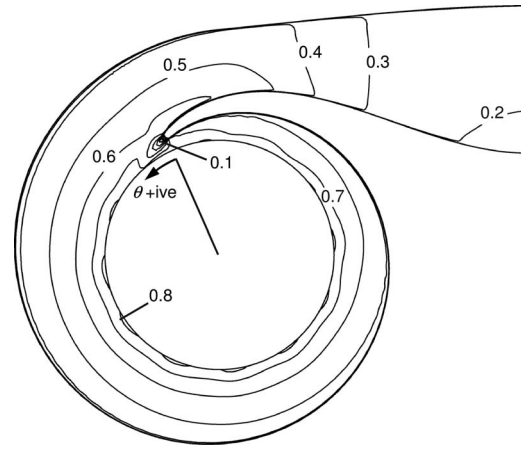


Fig. 9 Mach number distribution in the midspan plane of the vaneless volute

presented by Scrimshaw and Williams [7] by the order of 25%, larger than those presented by Hussain and Bhinder [6] by a factor of 3 and of a similar magnitude to those presented by Miller et al. [8]. In obtaining probe measurements for total pressure, Hussain and Bhinder [6] considered midspan properties only, and the omission of near wall measurements is likely to have led to optimistic total pressure loss values. The loss coefficient values obtained by Miller et al. [8] for a similar axisymmetric trapezoidal section volute to that used here were span averaged values, which included extrapolated near wall values in the calculation and are thus likely to be more representative of the stator losses incurred.

The opposite trend in loss coefficient is shown for the vaned stator configurations to that displayed by the volutes, with loss coefficient reducing from stators A to C. For turbine C, the mass averaged loss coefficient values are practically the same for both the vaned and vaneless turbines; however, the vaned stator still leads to lower efficiencies, albeit by a lower margin than for the A and B builds. This suggests that although the vaned stator incurs similar losses to the corresponding vaneless stator for turbine C, the rotor is still suffering a performance penalty due to the less uniform flow field delivered by the vaned stator, and consequently the vaneless stage is a more efficient overall arrangement.

Results

The function of the stator is to accelerate the flow into the rotor at the required angle and in doing so incur the minimum possible energy loss. In order to obtain a greater understanding of the underlying flow phenomena responsible for the measured efficiency variations, the CFD models were used to study the flow structures and losses throughout the stator passages in detail. The results presented here are for turbine B and show the flow patterns and losses through the vaneless and vaned stator in turn. Although only turbine B is considered in detail, the results are representative of turbines A and C. In the case of the vaned stators, the results from the refined single passage models are also presented.

Vaneless Stator B Results. Figure 9 depicts the Mach number distribution in a midspan plane through the vaneless volute. From this, it can be seen that the flow accelerates uniformly from the inlet duct to the throat region; however, once the passage begins to curve, higher velocities develop on the inside of the bend as the trailing edge of the tongue is approached. The influence of the tongue region is clearly depicted, showing lower momentum flow entering the rotor in this region as a consequence of the wake from the tongue and the mixing of the inlet flow with the flow emerging from under the tongue that has circled the entire rotor. The impact of the wake and mixing from the tongue does not extend any further than an azimuth angle of around 30 deg; be-

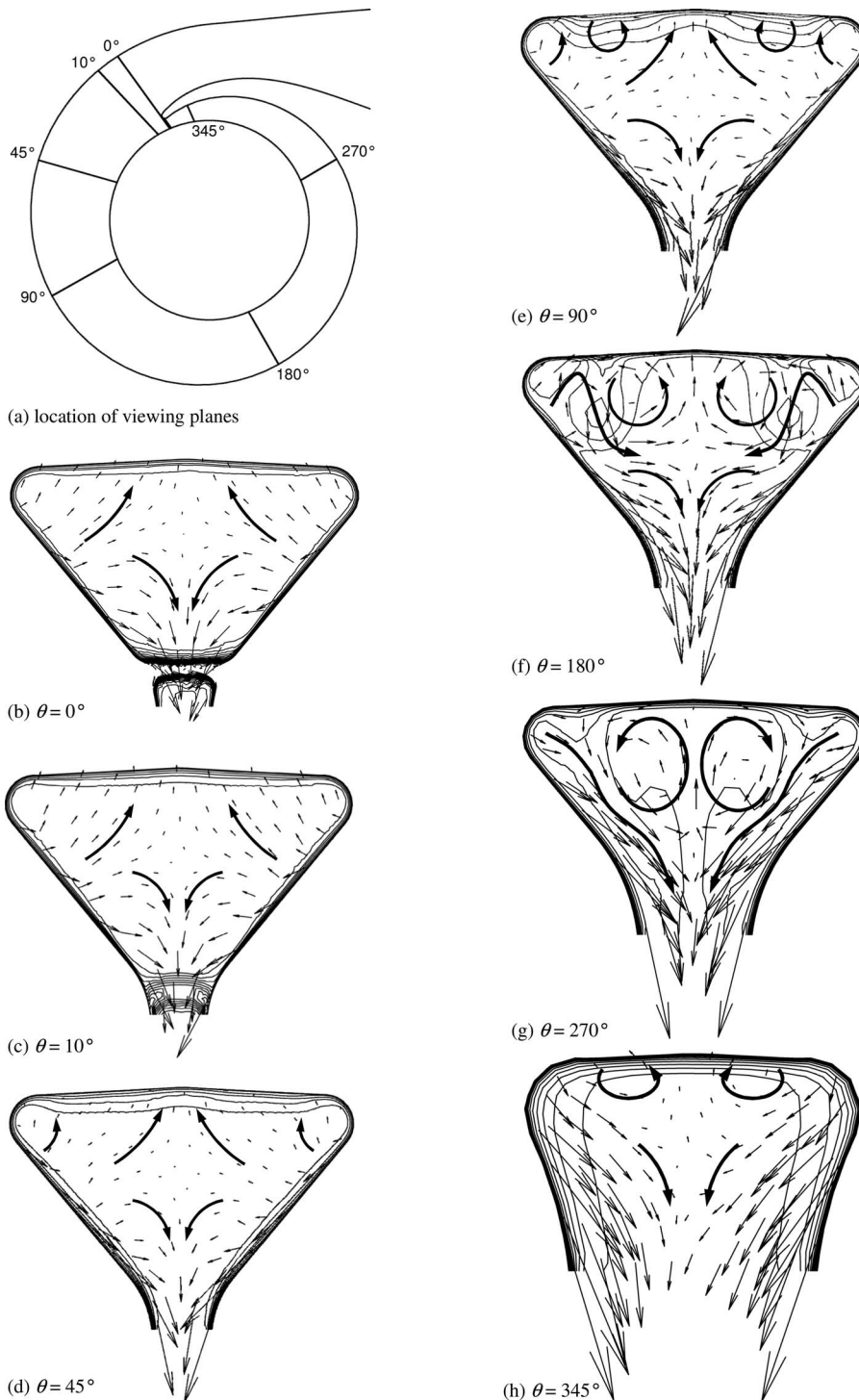
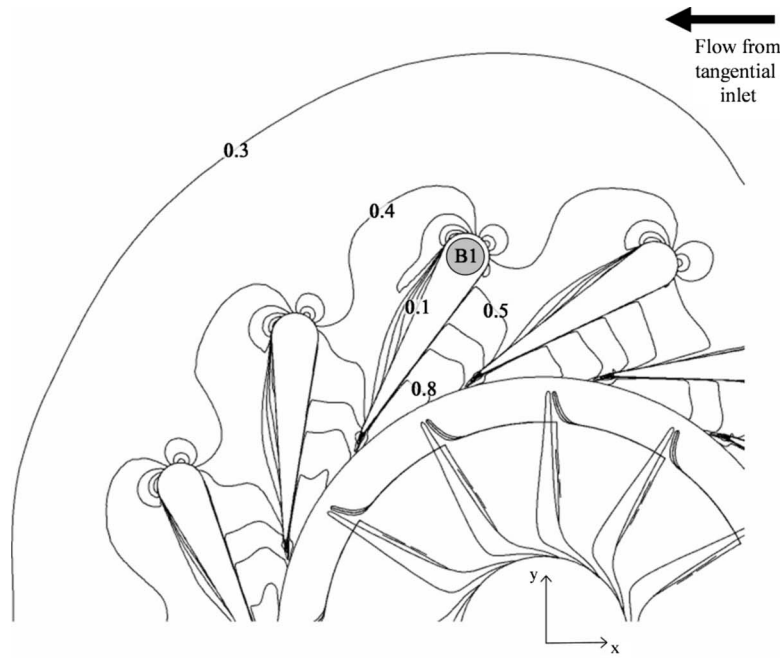


Fig. 10 Total pressure distribution and velocity vectors at various cross-sectional planes in the volute

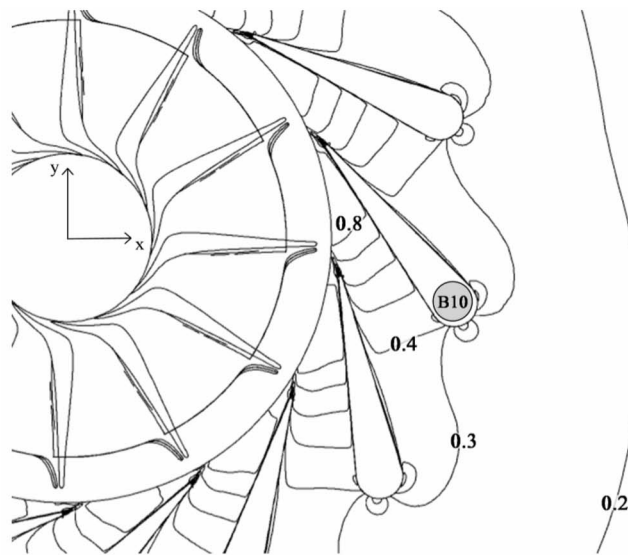
yond this, the volute is seen to deliver excellent uniformity over the remainder of the rotor circumference, delivering flow to rotor inlet at a Mach number of around 0.8. The influence of the blade-to-blade pressure gradients that exist in the rotor is clearly evident on the flow distribution at exit from the volute. Figure 9 also illustrates the growth of a lower momentum boundary layer at the outer wall, but this is only apparent over the first 180 deg of the volute and seems to disappear over the second half of the volute. However, this is only true of the midspan location, and Fig. 10

will show that the lower momentum boundary flow is being displaced away from the central plane into the corners by the strong secondary flow structures that develop further around the volute.

Figure 10 presents a series of plots at various cross-sectional planes in the volute. The location of the seven planes is shown in Fig. 10(a); note that the planes are not purely radial but have been positioned to lie approximately perpendicular to the mainstream flow in order to best depict any secondary flow structures. Each plot shows the total pressure contours with velocity vectors super-



(a) Upper half of stator assembly



(b) Lower half of stator assembly

Fig. 11 Mach number distribution in the midspan plane of the vaned B configuration

imposed. Values have not been included in these plots since the purpose is to show the development of the flow structures, and overall levels of stagnation pressure loss are presented later. The scale of the plots in Figs. 10(b)–10(h) is not consistent, since the cross-sectional area of the volute obviously decreases significantly from Figs. 10(b)–10(h). Figure 10(b) is located just downstream of the trailing edge of the tongue, and the low total pressure wake at the tongue is clearly depicted. Some migration of the flow toward the outer wall of the volute is already apparent at this first plane, which is a consequence of the flow having already turned through a bend from the inlet duct before the tongue is reached. In

the case of this volute, the tongue subtended an arc of 23 deg, although the angle covered by the tongue varies in different designs and it would appear that the larger the tongue angle, the more developed the secondary flow structures would be at this first plane.

Figure 10(c) is only 10 deg further downstream of the tongue trailing edge and while the secondary flow pattern has not changed, it can be seen that the wake from the tongue is mixing into the flow quite quickly. The growth of the boundary layer at the outer wall between the first and second planes is evident from

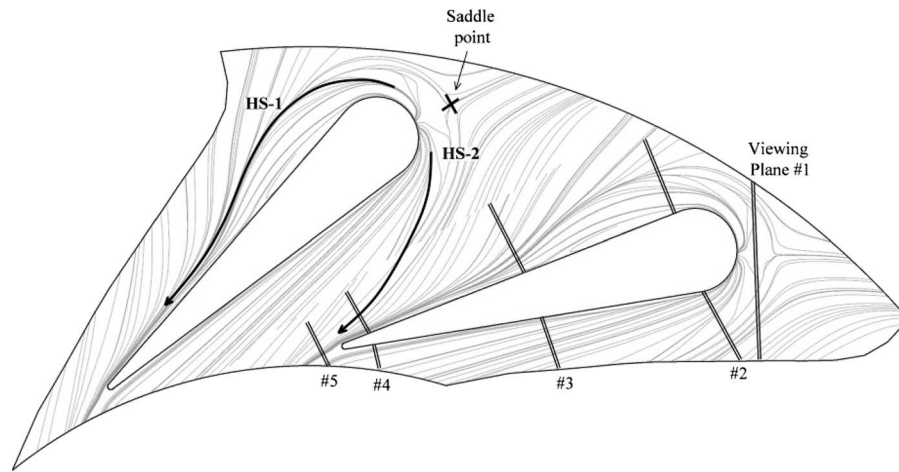


Fig. 12 Hub wall streamlines and viewing plane locations around vane B1

the increased spacing of the total pressure contours. By the 45 deg location in Fig. 10(d), the boundary layer at the outer wall has grown further and small vortical flow structures are beginning to develop in the outer corners of the volute cross section, although no other helical structures are discernable at this point. At the 90 deg plane in Fig. 10(e), two additional secondary vortices are observed to form in the upper region of the volute passage. It can be seen from the pressure contours that these counter-rotating “passage” vortices are transporting low momentum boundary layer fluid away from the midspan location toward the corners.

At 180 deg azimuth angle, the passage vortices have increased in strength and have cleared the boundary layer fluid from the midspan region, which is why boundary layer growth is not apparent over the second half of the volute in Fig. 9. At this stage, the corners of the volute passage are occupied with lower momentum fluid, and the passage vortices are interacting with the smaller corner vortices. However, the strong downward flow into the rotor prevents any significant growth of boundary layer on the sidewalls of the volute. The passage vortices occupy much of the cross section by the 270 deg location in Fig. 10(g), and their presence has transported lower momentum fluid into the center of the passage where it is draining into the rotor. The corner vortices are no longer evident. The passage vortices are still evident just before the tongue trailing edge at 345 deg and they are transported under the tongue to mix with the incoming flow.

The volute geometry was symmetrical and the spanwise pressure gradient that is present at inlet to a radial turbine rotor did not appear to impact the symmetry of the flow structures significantly. For all of the plots in Fig. 10, the left hand side corresponded to the shroud side of the rotor.

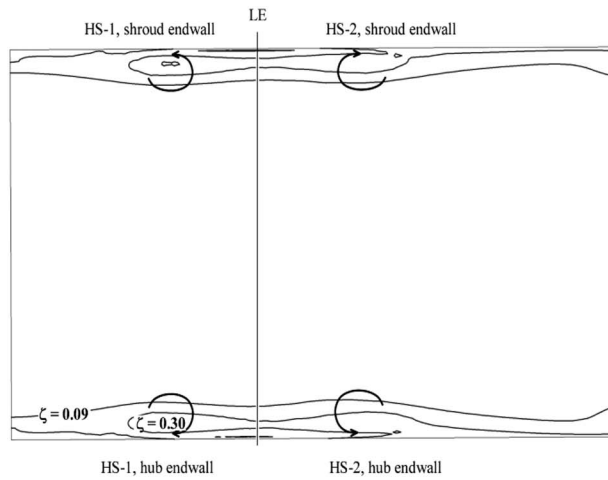
Vaned Stator B Results. The Mach number distribution through the torus and stator vane passages is presented for turbine B in Figs. 11(a) and 11(b). The torus did not deliver a good level of uniformity of flow angle to the inlet of the stator vanes. As indicated in Fig. 11(a), flow in the upper portion of the torus has a significant swirl component due to the tangential inlet position, which leads to flow separation at the leading edge of the vanes immediately downstream of this region. Similar difficulties had been encountered by Baines and Lavy [4]. Further around in the second half of the torus, the vanes experience close to zero inlet incidence, with no significant separation (Fig. 11(b)). Refined single passage model calculations were run for two vanes from different positions in the torus, designated here as vanes B1 and B10, using profile data exported from the full-stage model results. The resulting computed flow patterns are presented in Figs. 12–15.

Figure 12 depicts the streamlines around vane B1 at the hub,

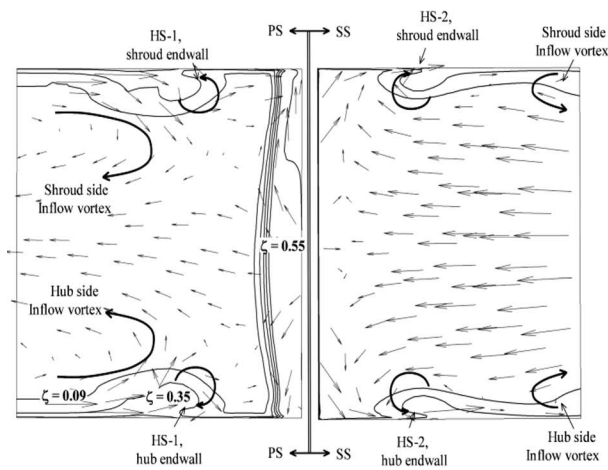
indicating the paths of the pressure and suction side horseshoe vortices, denoted here by HS-1 and HS-2, respectively. Here the dividing streamlines show the pressure side horseshoe vortex moving in an arc from the saddle point upstream of the leading edge around the separated region and then becoming reattached to the vane pressure surface. The suction leg horseshoe vortex is shown to migrate across the passage, eventually passing close to the trailing edge of the adjacent vane. This effect of the radial pressure gradient in shifting the horseshoe vortices toward the adjacent pressure surface has been documented previously by Hashemi et al. [9] and Eroglu [10]. Figure 12 also indicates the location of a set of viewing planes at a series of streamwise locations through the vane passage. The orientation of the planes was set to be perpendicular to the streamlines so as to clearly identify any resolved secondary flow structures, with the resulting flow patterns presented in Fig. 13 in the form of secondary flow vectors and total pressure loss contours.

Figure 13(a) depicts the inlet boundary layer profile developed by the upstream housing geometry, indicating the formation of the pressure and suction side horseshoe vortices at the endwalls, again denoted here by HS-1 and HS-2. Figure 13(b) illustrates the pressure side horseshoe vortex being pushed away from the vane surface due to flow separation, and also indicates two additional vortical structures in the center of the vane passage. Similar “inflow” vortices have been identified previously in numerical studies presented by Putra et al. [11] and are a direct product of the geometry upstream of the stator vane row. In this instance, as the flow entering the torus is turned radially inward by the torus endwalls, two counter-rotating vortices form similar to those shown for the vaneless volute in Fig. 10(g). Figure 13(c) shows these inflow vortices to have a significant effect on the endwall boundary layers. Here, the inflow vortex is seen to interact with both the pressure side horseshoe vortex and the low momentum flow in the separated region, acting to transport low momentum boundary layer fluid into the center of the passage. Figure 13(d) shows the suction side horseshoe vortex, HS-2, to have migrated toward the vane pressure surface. The loss cores associated with HS-2 are seen to remain confined to the endwall, whereas the loss cores associated with HS-1 have been transported into the center of the passage, together with a significant amount of low momentum fluid from the pressure surface boundary layer. At exit, the combined effect of secondary flows and the wake off the trailing edge result in local loss coefficients of 0.8, with values close to unity where the wake and endwall boundary layers interact. The resulting mass averaged loss coefficient for the high incidence vane was calculated as 0.124.

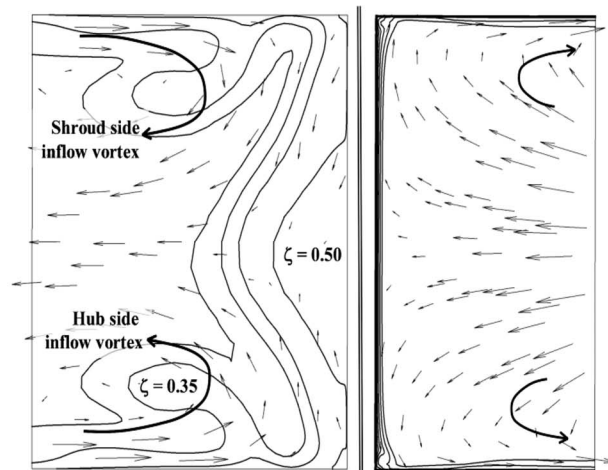
Figure 14 presents vane B10, which experiences a near zero



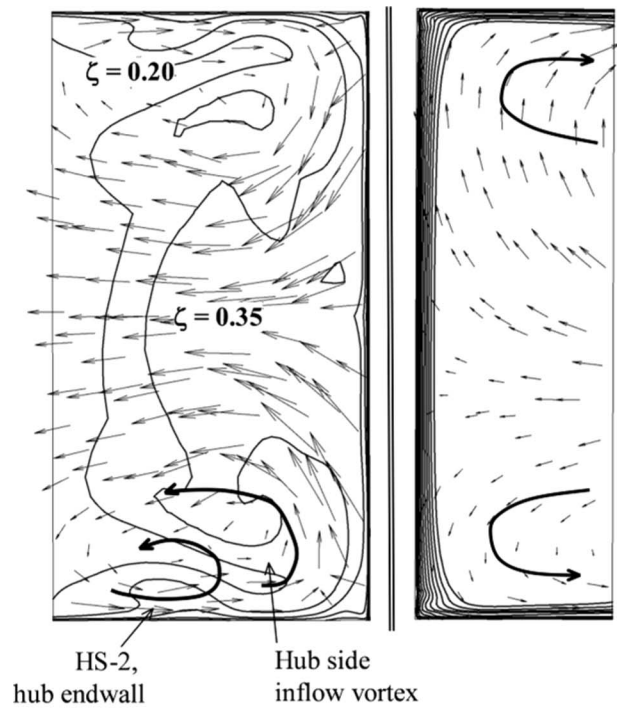
(a) Plane 1



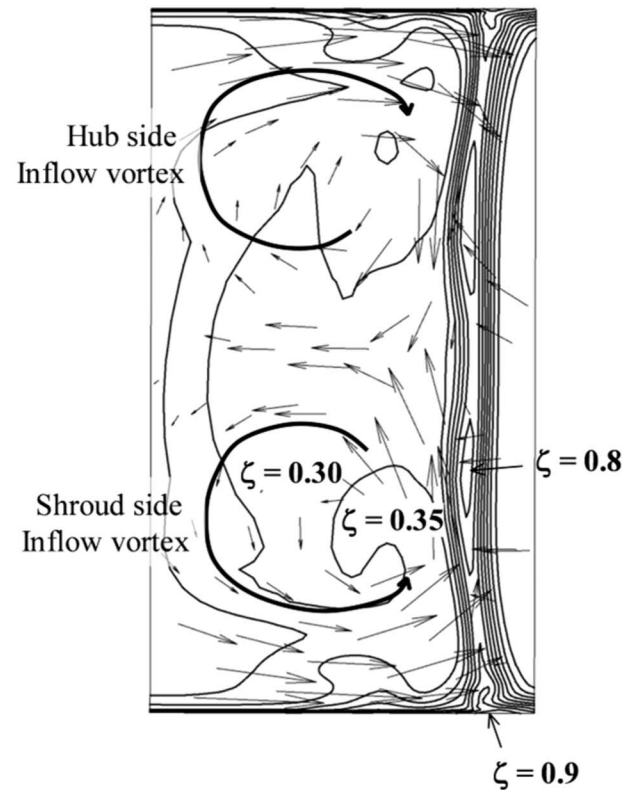
(b) Plane 2



(c) Plane 3



(d) Plane 4



(e) Plane 5

Fig. 13 Secondary flows and total pressure losses at different cross-sectional planes, vane B1

incidence condition. Here, the dividing streamlines indicate the paths followed by the pressure and suction legs of the horseshoe type vortices. The pressure leg of the horseshoe vortex is shown to

remain attached to the vane pressure surface, whereas the suction leg migrates across the passage, following an almost identical path to that shown for vane B1. Figure 15 again presents the secondary

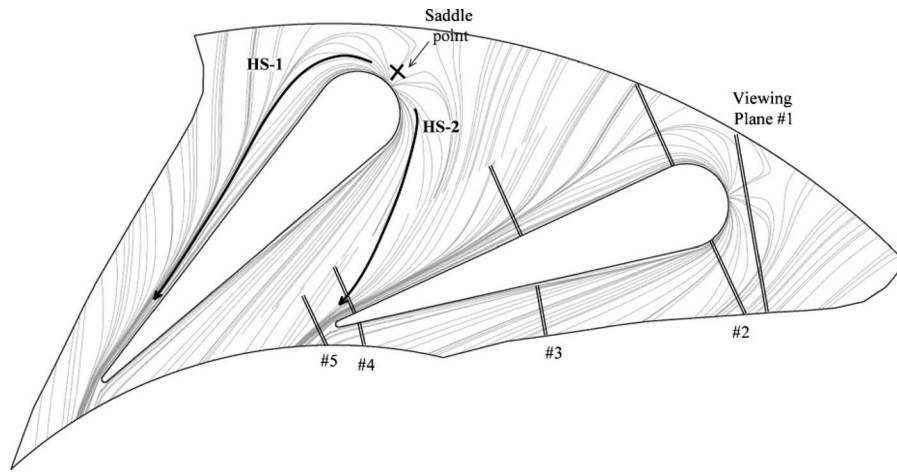


Fig. 14 Hub wall streamlines and viewing plane locations around vane B10

flow vectors and total pressure loss contours on a series of streamwise planes through the passage. At plane 1 in Fig. 15(a), it is indicated that the inlet boundary layer profile shows lower levels of total pressure loss than for the high incidence vane B1, particularly in the regions associated with the horseshoe vortices. Similar distinctions between vanes subjected to high and low inlet incidences were made by Hashemi et al. [9], who also observed vanes subjected to lower inlet incidence displayed weaker secondary flow structures. In this instance, it would seem that the vortices are weaker due to the lower tangential velocities at vane inlet and as a result exhibit a lower level of interaction with the endwall boundary layers. Figure 15(b) again depicts the presence of the two counter-rotating inflow vortices, and in this case the pressure side horseshoe vortices are seen to remain close to the vane surface. At plane 3 in Fig. 15(c), the inflow vortices are again seen to interact with the pressure side horseshoe vortices (HS-1), transporting low momentum fluid away from the endwall. Although there is no noticeable separation present, the inflow vortices are still shown to displace low momentum fluid from the pressure surface boundary layer into the vane passage. Figure 15(d) again shows the loss core associated with the suction side horseshoe vortex now located close to the pressure surface, with further low momentum fluid being displaced from the vane pressure surface boundary layer by the inflow vortices. Comparing the exit states of the two vanes in Figs. 13(e) and 15(e), there is a clear reduction in the overall loss levels in the passage around vane B10, which is a result of the lack of any significant amount of flow separation and weaker secondary flows. These factors serve to lower the mass averaged exit loss value to 0.09, which results in a computed efficiency improvement of 0.7% for this single vane. The full-stage models indicate 4 of the 13 vanes to experience incidence and flow separation, and these results suggest that the expected efficiency improvement with an improved housing design would not be sufficient to bridge the performance gap between the vanned and vaneless turbine builds.

Transient CFD Results for the Vaneless Volute

Figure 16 presents a comparison of the measured and predicted static pressure just upstream of the rotor inlet for the vaneless B configuration. The measured pressure values were obtained from 24 equispaced tappings 0.5 mm upstream of rotor inlet on the shroud side. The predicted values correspond to the same radial position and were taken at 95% span, which was approximately 0.5 mm from the shroud surface. The dashed line shows pressure values from the steady state CFD model; the pressure sampling location was downstream of the interface between the stator and rotor domains, and the resulting pressure values are obviously

dominated by the blade-to-blade pressure gradients in the rotor and do not provide a satisfactory comparison with the measured values.

In order to gain a more useful comparison with the pressure measurements, which were effectively time averaged values, a transient CFD calculation was carried out on the vaneless B turbine. Comparable time averaged results were obtained by extracting values from 360 fixed points around the rotor at each time step, giving a spatial resolution of 1 sample point per degree in the circumferential direction. These data were extracted for a total of 360 time steps, corresponding to one full turn of the rotor and then averaged to give a time averaged solution for the unsteady rotor inlet flow field. As is evident from Fig. 16, the computed results from the transient model are in excellent agreement with the measured data, with the transient CFD model correctly predicting both the trend and the level of the static pressure. The increased pressure just downstream of the tongue is accurately captured, where a low momentum region exists in the flow as the flow that has completed one complete revolution of the scroll interacts with the mainstream flow entering the scroll. The effect that this has on the losses in this region is presented clearly in Fig. 17.

Figure 17 presents the total pressure loss incurred through the vaneless volute in the circumferential direction just upstream of rotor inlet. The pressure loss is presented as a conventional loss coefficient where the loss in total pressure is nondimensionalized by the dynamic pressure based on density and velocity at rotor inlet. In the case of Fig. 17, the values represent average conditions in the spanwise direction. The total pressure loss coefficient averaged around the entire volute is 10%; naturally, the loss level is significantly increased just downstream of the tongue where mixing of incoming flow and the tongue wake occurs, the impact of which extends 45 deg around from the tongue. It is noteworthy that the loss coefficient does not increase over the last quarter of the volute where one might expect that the accumulation of secondary flows and boundary layer fluid would contribute to increased loss. This suggests that the low momentum boundary layer fluid drains progressively into the rotor as it circuits the volute, rather than accumulating to produce a region of higher loss over the later part of the volute.

Figure 17 also includes the absolute flow angle measured from the radial direction. Disturbance in the flow angle due to the influence of the tongue extends over almost 180 deg of the circumference. There is a region downstream of the tongue where the flow is turned to a more radial direction, which coincides with the region of high loss. However, either side of this circumferential area the flow angle is actually more tangential. Similarly Miller et al. [8] observed more radial flow in the volute tongue region, whereas Scrimshaw and Williams [7] found flow to be more tan-

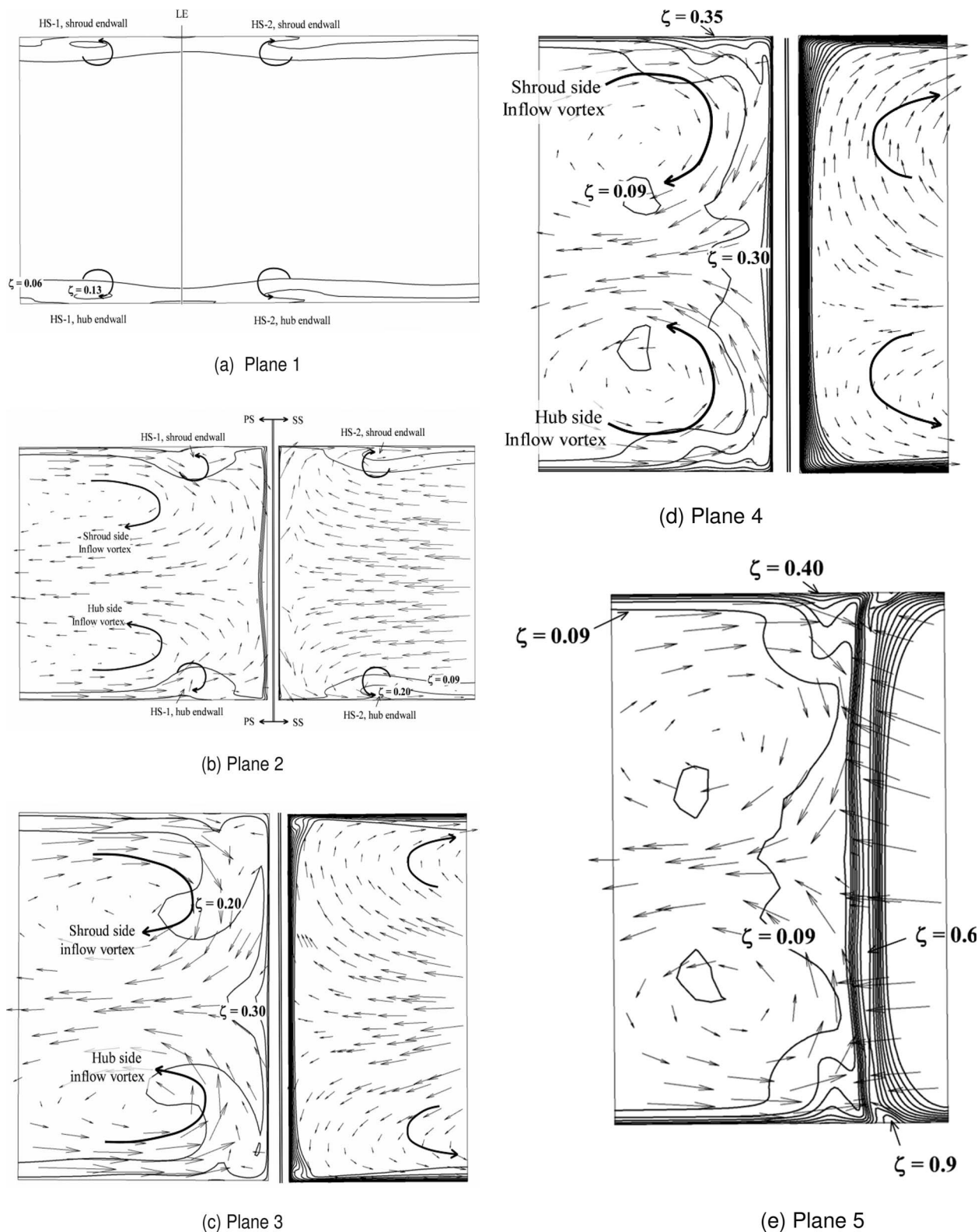


Fig. 15 Secondary flows and total pressure losses at different cross-sectional planes, vane B10

gential downstream of the tongue. There is a 25 deg region of the circumference, where the flow angle is lowest, where the rotor experiences 8% less tangential velocity at inlet than the average over the whole circumference. The effect of this nonuniformity is twofold; not only will efficiency be affected due to losses associated with the circumferential variations in rotor incidence angle

but the process of the rotor blade passing through the wake from the tongue creates a periodic loading cycle, which could excite rotor blade vibrations and promote turbine blade failure due to high cycle fatigue. Away from the tongue region, the flow entering the rotor is relatively uniform, with flow angle variations within ± 1 deg of the design value of 65 deg. Previous investigations

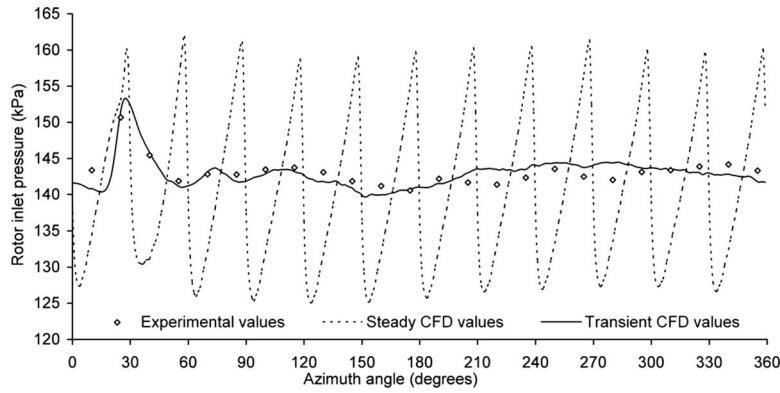


Fig. 16 Comparison of measured and predicted static pressures around rotor inlet

relating to volute discharge conditions have presented significantly higher levels of nonuniformity [5], as well as significant departures from intended design values of rotor inlet flow angle [6]. This suggests that the volute design method used in this instance was effective in minimizing circumferential nonuniformity.

Comparison of Vaned and Vaneless Stator Performance

Figure 18 presents the time averaged rotor inlet pressure for the vaned B turbine configuration, which corresponds to the values presented for the vaneless model in Fig. 16. These were also taken at 1 deg increments from a transient numerical model. The graph shows 13 successive peaks and troughs, which represent the jets

and wakes from the 13 stator vanes. In the case of the vaned turbine tests, static pressure measurement was only provided at four circumferential locations due to the difficulty in machining pathways for internal pressure tapings. In addition, due to the geometry of the vanes in the torus, each static tapping was in a different pitchwise location relative to the vane trailing edges. Although the measured data are not as useful as for the vaneless turbines for the purpose of drawing direct comparisons with the predictions, the predictions still align closely with the experimental results, where they are available. For comparison, Fig. 18 also includes the static pressure variation for the vaneless turbine from Fig. 16. The variation in pressure at rotor inlet is evidently much

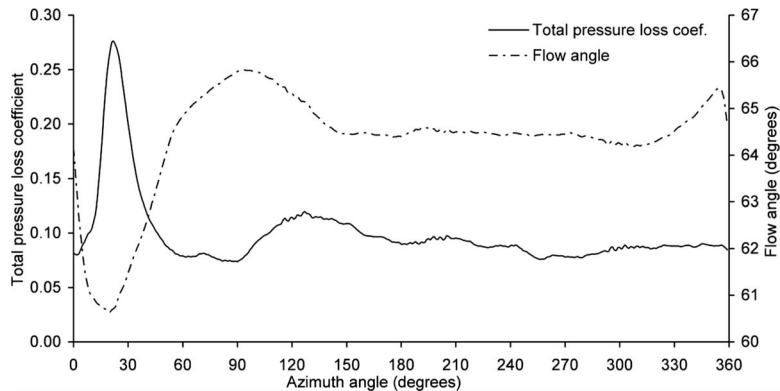


Fig. 17 Circumferential distribution of total pressure loss and flow angle around the rotor inlet of the vaneless B turbine

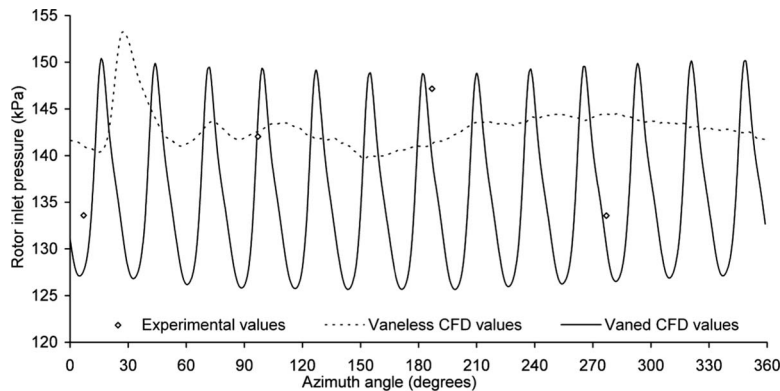


Fig. 18 Comparison of measured and predicted static pressures around rotor inlet on the shroud side of the vaned B turbine

greater for the vaned case, with jets and wakes from the vaned stator passages persisting through the vaneless space prior to the rotor (the radius ratio of the vaneless space for the test turbines was 1.1).

The primary function of the stator is to deliver the desired flow conditions to the rotor uniformly, while incurring the minimum possible energy loss. Plots comparing the total pressure loss coefficient and the variation in flow angle have not been included for the vaned stator, but it is sufficient to summarize their content by saying that the average total pressure loss coefficient varied with vane pitch about an average value of 13.5%, while the flow angle ranged between 62.2 deg and 68.0 deg.

The numerical predictions therefore suggest that the discharge flow field from the vaned stator build contains a higher level of circumferential nonuniformity than that from the corresponding vaneless stator. As discussed previously, this has negative implications for both turbine performance and running life. Previously, it has been considered that high levels of nonuniformity delivered by vaneless volutes contributed to reduced stage efficiencies in relation to vaned stators. As indicated by the results of the steady state models, the additional boundary layer growth on the vane surfaces and the wakes from the trailing edges generally lead to higher overall levels of total pressure loss in the vaned stator, as suggested by the experimentally measured efficiency deficit.

Conclusions

Full-stage CFD calculations have been carried out on a series of vaned and vaneless stator turbine builds, successfully repeating the trends measured during previous turbine performance tests. In general, the vaneless volutes exhibited lower levels of total pressure loss than the corresponding matched vaned stator build and as such yielded improved predicted turbine stage efficiencies.

Detailed secondary flow structures have been successfully captured in both vaned and vaneless stators. For the vaneless volutes, two counter-rotating passage vortices were shown to form at an azimuth angle of approximately 90 deg, and after which followed the outer walls acting to displace low momentum fluid from the passage corners toward the center of the passage. In general, elevated losses associated with secondary flows were shown to be confined to the endwalls.

For the vaned stators, horseshoe vortices were resolved of the type commonly observed in axial turbomachinery, in addition to two counter-rotating inflow vortices resulting from the upstream housing geometry. These secondary flow structures were shown to combine and have a significant influence on the overall loss levels.

Unsteady models successfully captured the variation in static pressure at rotor inlet, indicating the vaneless volute to exhibit higher levels of flow uniformity than the corresponding vaned stator.

The experimental investigations reported in Ref. [13] and the subsequent numerical analysis have shown that an appropriately designed vaneless volute can deliver equivalent or better performance to a vaned stator while providing better levels of flow uniformity at rotor inlet.

Acknowledgment

The authors would like to acknowledge the financial support of EPSRC (Grant Ref. No. GR/M41865), without which this investigation would not have been possible. Thanks are also due to

Holset Engineering Co. Ltd. for ongoing technical and hardware support, and particularly to Nick Sharp for his interest, enthusiasm, and generosity with his time. The authors also acknowledge the help of ANSYS for the use of their CFD software and for technical support.

Nomenclature

- A/r = ratio of the area to the radial location of the centroid of the volute cross-section (mm)
 Δh_{is} = isentropic stage enthalpy drop (J/kg)
 n_s = dimensionless specific speed (rad)
 U/C = Turbine blade speed velocity ratio
 Q_{exit} = volumetric flow rate at rotor exit (m^3/s)
 α = absolute flow angle (deg)
 ω = rotor rotational velocity (rad/s)
 ζ = Stator loss coefficient $(P_{01} - P_{02}) / \frac{1}{2} \rho v_2^2$

References

- [1] Bhinder, F. S., 1969, "Investigation of Flow in the Nozzle-Less Spiral Casing of a Radial Inward-Flow Gas Turbine," *Proc. Inst. Mech. Eng.*, **184**, pp. 66–71.
- [2] Palmer, R. M., 1955, "D.I.G.T. Radial Inflow Turbine—Scroll and Nozzle Performance—Part I," Ricardo Internal Report No. 1365A.
- [3] Palmer, R. M., 1955, "D.I.G.T. Radial Inflow Turbine—Scroll and Nozzle Performance—Part II," Ricardo Internal Report No. 1368.
- [4] Baines, N. C., and Lavy, M., 1990, "Flows in Vaned and Vaneless Stators of Radial Inflow Turbocharger Turbines," Institute of Mechanical Engineers Turbochargers and Turbocharging Conference, Paper No. C405/005, pp. 7–12.
- [5] Benisek, E. F., and Spraker, W. A., 1987, "Laser Velocimeter Measurements at the Rotor Inlet of a Turbocharger Radial Inflow Turbine," *ASME Third International Symposium on Laser Anemometry*, Vol. 55.
- [6] Hussain, M., and Bhinder, F. S., 1984, "Experimental Study of the Performance of a Nozzle-Less Volute Casing for Turbocharger Turbines," SAE Paper No. 840571.
- [7] Scrimshaw, K. H., and Williams, T. J., 1984, "Size Effects in Small Radial Turbines," ASME Paper No. 84-GT-215.
- [8] Miller, E. C., L'Ecuyer, M. R., and Benisek, E. F., 1988, "Flow Field Surveys at the Rotor Inlet of a Radial Inflow Turbine," *ASME J. Turbomach.*, **110**, pp. 552–561.
- [9] Hashemi, S. G. R., Lemak, R. J., and Owczarek, J. A., 1984, "An Investigation of the Flow Characteristics and of Losses in Radial Nozzle Cascades," *Trans. ASME: J. Eng. Gas Turbines Power*, **106**, pp. 502–510.
- [10] Eroglu, H., and Tabakoff, W., 1989, "LDV Measurements and Investigation of Flow Field Through Radial Turbine Guide Vanes," ASME Paper No. 89-GT-162.
- [11] Putra, M. A., and Joos, F., 2006, "Investigation of the Secondary Flow Behaviour in a Radial Turbine Nozzle," ASME Paper No. GT2006-90019.
- [12] Rosborough, R. S. E., 2003, "An Experimental Assessment of Different Vaned and Vaneless Stators for a Radial Inflow Turbine," Ph.D. thesis, School of Mechanical and Manufacturing Engineering, Queen's University of Belfast, Belfast.
- [13] Spence, S. W. T., Rosborough, R. S. E., Artt, D. W., and McCullough, G., 2007, "A Direct Performance Comparison of Vaned and Vaneless Stators for Radial Turbines," *ASME J. Turbomach.*, **129**, pp. 53–61.
- [14] Chapple, P. M., Flynn, P. F., and Mulloy, J. M., 1980, "Aerodynamic Design of Fixed and Variable Geometry Nozzleless Turbine Casings," *Trans. ASME: J. Eng. Gas Turbines Power*, **102**, pp. 141–147.
- [15] Simpson, A. T., 2007, "Aerodynamic Investigation of Different Stator Designs for a Radial Inflow Turbine," Ph.D. thesis, The Queens University of Belfast, Belfast.
- [16] Menter, F. R., 1994, "Two-Equation Eddy-Viscosity Turbulence Models for Engineering Applications," *AIAA J.*, **32**(8), pp. 1598–1605.
- [17] Bardina, J. E., Huang, P. G., and Coakley, T. J., 1997, "Turbulence Modelling Validation," AIAA Paper 97-2121.

Effects of Compressor Tip Injection on Aircraft Engine Performance and Stability

Wolfgang Horn

e-mail: wolfgang.horn@mtu.de

Klaus-Jürgen Schmidt

e-mail: klaus-juergen.schmidt@mtu.de

Department of Engine Performance,
MTU Aero Engines GmbH,
Dachauer Straße 665, 80995 München, Germany

Stephan Staudacher

Institute for Aircraft Propulsion Systems,
University of Stuttgart,
Pfaffenwaldring 6, 70569 Stuttgart, Germany
e-mail: staudacher@ila.uni-stuttgart.de

This analytical study discusses the system aspects of active stability enhancement using mass flow injection in front of the rotor blade tip of a high pressure compressor. Tip injection is modeled as a recirculating bleed in a performance simulation of a commercial turbofan engine. A map correction procedure accounts for the changes in compressor characteristics caused by injection. The correction factors are derived from stage stacking calculations, which include a simple correlation for stability enhancement. The operational characteristic of the actively controlled engine is simulated in steady and transient states. The basic steady-state effect consists of a local change in mass flow and a local increase in gas temperature. This alters the component matching in the engine. The mechanism can be described by the compressor-to-turbine flow ratio and the injection temperature ratio. Both effects reduce the cycle efficiency resulting in an increased turbine temperature and fuel consumption at constant thrust. The negative performance impact becomes negligible if compressor recirculation is only employed at the transient part power and if valves remain closed at the steady-state operation. Detailed calculations show that engine handling requirements and temperature limits will still be met. Tip injection increases the high pressure compressor stability margin substantially during critical maneuvers. The proposed concept in combination with an adequate control logic offers promising benefits at transient operation, leading to an improvement potential for the overall engine performance. [DOI: 10.1115/1.2988159]

1 Introduction

One of the most challenging problems in gas turbine engine operation is the aerodynamic stability of the compression system. Stable operation has to be guaranteed for any aircraft engine throughout its service life. Typically this is achieved by designing the engine with high stability margins to cover any worst case scenario. This required margin limits the overall engine performance and the available component design space.

The concept of an “intelligent engine” first described by Epstein [1] addresses this problem. By the use of additional sensors the propulsion system is able to recognize its current operating condition and capabilities. This awareness enables the engine to react with an adequate action of specially designed actuators whenever necessary [2]. Especially in the compressor this idea could be used to extend the stable operating range beyond current limitations. Paduano and Epstein [3] gave a good overview on this subject.

Tip injection is one of several possible actuation concepts for compressor stability enhancement. A small amount of air is injected through specially shaped holes in the compressor casing into the main flow path in front of a rotating blade. The high momentum jet energizes the unstable flow condition at the rotor tip and thus stabilizes the compression system.

An increasing number of research projects are being conducted to support this observation. Published results, recently summarized by Kefalakis and Papailiou [4], show that compressor stability enhancement is feasible for individual stages and multistage compressors.

Based on the work on component level, a number of projects have evolved that implement active stability control to a complete

engine. Freeman et al. [5] achieved the stabilization of a turbojet by recirculating air around and inside the compressor. With an increase in surge margin of up to $\Delta SM=25\%$, recirculation was found to be more effective than conventional bleed. Nelson et al. [6] controlled the surge of an axialcentrifugal turboshaft engine by injecting external air into the diffuser of the centrifugal compressor. Although the stabilizing effect is not directly comparable to axial compressor tip injection, the measured surge margin benefit along with a thrust increase during active control is remarkable. Leinhos [7] actively controlled stall and surge in a two-spool turbofan engine by injecting external air in front of the low pressure compressor (LPC) and obtained a surge margin increase in $\Delta SM=24\%$. The measurements also indicated an impact on engine performance seen by changes in spool speed and pressure ratio. Additionally, a thrust decrease caused by recirculating the air was observed. Scheidler [8] continued this research and obtained $\Delta SM=32\%$ and a more extended surge margin when injecting external air at a low rotational speed. In his measurements the thrust increased during recirculation with less fuel consumption.

All researchers have observed changes in system behavior due to air injection and recirculation, which highlights the need for a system analysis. A first approach has been published by Kurzke [9], who simulated engine performance with recirculation from the compression system exit to the inlet. He found that recirculation has a negative impact on engine performance and calculated unfavorable results compared with conventional bleed due to the injection temperature.

The objective of this study is to clarify the effects and to assess the benefits and disadvantages of tip injection from a system perspective in order to evaluate the technology's potential for aero engine applications. This will be achieved by a simulation of compressor recirculation in an engine performance model.

2 Engine Configuration

This study assumes a modern commercial turbofan engine, which is equipped with tip injection in the high pressure compres-

Contributed by the International Gas Turbine Institute of ASME for publication in the JOURNAL OF TURBOMACHINERY. Manuscript received December 19, 2007; final manuscript received February 4, 2008; published online April 9, 2009. Review conducted by David Wisler. Paper presented at the ASME Turbo Expo 2007: Land, Sea and Air (GT2007), Montreal, QC, Canada, May 14–17, 2007.

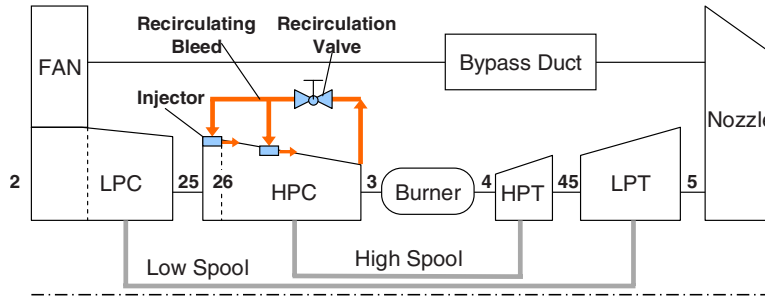


Fig. 1 Simplified engine configuration

sor (HPC). Figure 1 illustrates the basic configuration of the engine. The modeled injectors are fed by compressed air taken from a downstream bleed at the compressor exit. Mass flow will be injected in front of the first and third blade row of the six-stage axial compressor.

The stabilization concept concentrates on the HPC in part-load operation. It will be shown later that recirculation has a negative impact on the overall engine performance, which is not acceptable at high thrust demands. At part power, the transient operating line excursion typically lowers the HPC surge margin during accelerations. The front stages are known to operate near their stability limit at low speeds in a multistage environment. To avoid any part-load problems and to increase the stability margin at spool speeds lower than the design point, tip injection is applied to the front stages. In a complete HPC stabilization concept, additional stability will be provided for the rear stages. The bleed offtake at the exit lowers the compressor operating line and thus off-loads the rear stages during recirculation. Additionally, this position offers enough pressure ratio to inject with high jet velocity over the entire operating range.

The mass flow is injected steadily in the axial direction via several circumferentially distributed injection nozzles, as shown in Fig. 2. The air system was designed to maximize the jet velocity at both injections, while limiting the amount of recirculating air W_{rec} , and to stay within the range of experimental data used. The chosen flow areas distribute the injected mass flow with a constant 1:2 ratio, resulting in $1/3 W_{rec}$ at Rotor 1 and $2/3 W_{rec}$ at Rotor 3. An equal total nozzle area was selected for both injections. This configuration produces similar stage stability enhancements at part speed. A bleed valve controls the amount of recirculating mass flow.

The injection system layout will clearly depend on the individual application. Mass flow rates, as well as injection and bleed

positions, need to be optimized for the specific compressor simultaneously with the aerodynamic design. The optimization will be a function of required and achievable surge margin benefit, overall performance impact, and the control system applied.

3 Performance Synthesis Model

3.1 Effect of Tip Injection on Compressor Characteristic.

Experimental and analytical studies have shown that a compressor stage may be stabilized by tip injection. To understand this effect the three-dimensional flow field above the rotor tip has to be resolved in detail and the mechanism leading to flow instability has to be regarded. Deppe et al. [10] and Chen et al. [11] showed that a high speed jet blown into the tip gap energizes low momentum fluid pockets and moves the tip clearance vortex backward, which correlates well with the spike-initiated stall theory described by Vo et al. [12]. The injected jet reduces the blade incidence and thus unloads the rotor tip. If the injection is modulated, the system dynamics is altered and modal waves as stall precursors are damped out as measured by Weigl et al. [13]. Although this technique might reduce the required injected flow, this performance investigation considers only steady jets.

It becomes obvious that physical processes may be too complex to provide an exact and simple analytical approach. Recent publications show however that dominant parameters are given by the jet velocity and the circumferential coverage. Suder et al. [14] and Strazisar et al. [15] demonstrated that stage stability enhancement is proportional to the mass averaged axial velocity \bar{c}_{ax} , which is defined as follows:

$$\bar{c}_{ax} = \frac{W_{inj} \cdot c_{inj} + W_C \cdot c_{ax,C}}{W_{inj} + W_C}$$

for a plane with the radial extent of the jet at the rotor leading edge, see Fig. 2.

Based on these findings, a simple correlation was developed to provide an estimation of the compressor stability for the performance model. The results obtained for a NASA research compressor are transferred to this study by referring \bar{c}_{ax} to the axial tip velocity at stall $c_{ax, stall, tip}$ without injection, evaluated at the outer annulus. Additionally, test data from the two-stage Larzac low pressure compressor were analyzed for two injection nozzle configurations. The data from Leinhos [7] for the larger nozzle were found to match well with the expected range. The small nozzle used by Scheidler [8] reached a higher surge line improvement for the same injected mass flow but follows a less efficient trend regarding the mass averaged axial velocity. The resulting correlation shown in Fig. 3 is used here to assess the theoretical stage stability improvement (A). However, it is recognized that this approach represents only a rough estimation of the possible stability enhancement.

The impact on the multistage compressor surge line is assessed using a state-of-the-art aerodynamic stage stacking tool. The characteristic of the stage downstream of the injection position is stabilized by moving the stall point to lower flow coefficients ϕ_{stall}

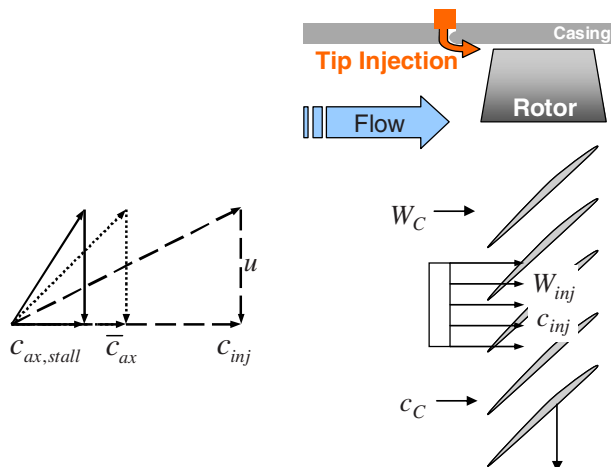


Fig. 2 Schematic representation of tip injection

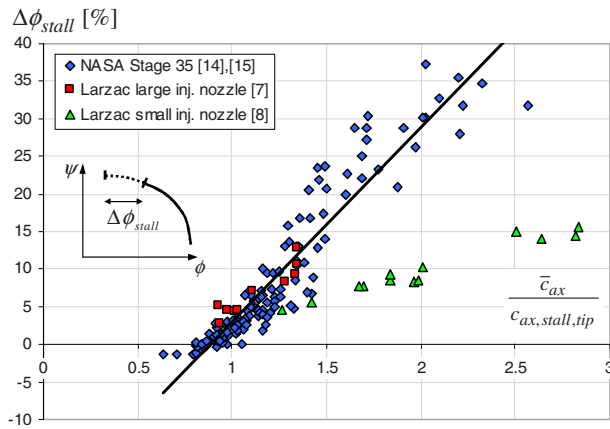


Fig. 3 Correlation for stage stability enhancement by steady tip injection

according to Fig. 3. As the high velocity jet's impact is expected to be beneficial to the downstream stages as well [14], the injection is assumed to generate 50% of the stability enhancement at the subsequent stage (B). Due to the lack of experimental data, this number had to be estimated. The resulting characteristics are stacked, including the injected mass flow, and a new compressor map is obtained.

The stage stacking calculations show that the compressor speed lines move to lower corrected flow W_{25} RST for injection. For the first rotor, only the mass flow and the temperature are changed between Stations 25 and 26. The interstage injection, however, forces the downstream stages to operate at higher mass flows while upstream stages are throttled. As a result, it is possible to actively redistribute the stage loading by the rematching effect of injection, an opposite effect that interstage bleed has. The compressor surge line can thus be raised by independently controlling the throttling of stages or blocks, as observed by Strazisar [15] in a multistage application. The true benefit of injection results from the surge line increase in the critical stage. The stage stacking calculations show that the critical position moves and the new stability limit will be dominated by the stage with the lowest stability enhancement, which in this example is Stages 2 and 4. Hence, the assumption for subsequent stages made above is the determining factor for the surge line potential.

The rear stages are enhanced by a different technology to provide a complete HPC stabilization concept. This will be required to obtain an improved surge margin throughout the operating envelope. With a focus on tip injection the calculations in this study are performed without the rear stages inducing stall (C). Depending on the specific compressor design the calculated surge margin potential will be limited by the rear stages approaching their stability limit, which is especially true at higher speeds. Alternatively, tip injection in front of Stage 5 could be envisaged. Furthermore, it should be noted that for uncritical rotor tips any stall at the hub could limit the stability during injection [16].

The different stability enhancement assumptions A, B, and C are modified in Table 1 to quantify their effect on the surge margin. The results underline that a high stability potential requires not only a high stage sensitivity to tip injection but also a thorough aerodynamic compressor design. With respect to the uncertainties described, more aerodynamic research has to be conducted to ensure the stability increase in modern multistage compressors by tip injection.

In the engine simulation the changes of the compressor characteristics were implemented like secondary map effects [17] by correction factors on the corrected flow, specific work, efficiency, and surge line. The correction was derived by a comparison of compressor maps for different injection mass flow rates. The relative recirculating mass flow W_{rec}/W_{25} and the corrected HP

Table 1 Surge margin increase for different stability enhancement assumptions at 4% recirculating flow and 80% corrected speed

Modified assumption		ΔSM (%)
Modeled surge line		19.6
1/3 stage stability enhancement	(A)	13.5
Full benefit at subsequent stages	(B)	25.1
No benefit at subsequent stages	(B)	9.3
Stalling rear stages	(C)	16.1

spool speed were chosen as the nondimensional governing parameters for map modification due to tip injection. As the bleed offtake position is located downstream of the compressor, it does not affect the compressor map.

3.2 Performance Model Extension. The existing modular performance synthesis model of a commercial turbofan was extended to allow the performance assessment of the compressor tip injection. Compressor recirculation is implemented in the engine model by an additional bleed offtake downstream of the compressor and two mass flow injections into the compressor. The amount of recirculating air is controlled by the orifice area setting of the recirculation valve.

The continuity and energy equations in the compressor module were adapted to include the injection. Hence, the calculation of the compressor takes into account the mass flow and temperature of the injected air with the individual injection position.

In contradiction to the dynamic model of Vo and Paduano [18] the engine simulation does not assume an ideal mixing upstream of the rotor. The injected momentum is thus neglected, due to the fact that the jet dissipates in a complex flow field at the blade tip. The error of this approach was estimated by solving the momentum equation between the injection position and the first rotor leading edge. The maximum total inlet pressure was found to be about 1% lower than that for ideal mixing.

For the transient investigations only the rotor inertia is considered as an additional effect to allow for a clear discussion of the changes in engine behavior. Secondary effects, such as heat transfer, transient clearance changes, and local density changes, should be taken into account for the performance optimization of an actual engine. Transient filling effects may play a role at smaller time scales. Freeman et al. [5] and Leinhos [7] observed local effects in the order of some milliseconds when the injection is activated.

For the calculation of engine transients the performance model switches to a state-space formulation. The simulation environment of MATLAB/SIMULINK was used to integrate the transient thermodynamic model, the electronic engine control unit, and the transfer function models of sensors and actuators to a fully functional engine model, as shown in Fig. 4 and as described by Bolívar et al. [19], for a military engine. The recirculation bleed valve was modeled in the actuator block similar to a conventional compressor bleed valve. A first order transfer function and an additional lag simulate its dynamic response.

4 Effects on Steady-State Performance

In a first step, only the injection in front of Rotor 1 is activated, which has the advantage that no interstage effects occur. In this configuration air is bled off at the HPC exit and the inlet mass flow and inlet temperature is modified by the re-injected air. Two basic parameters can be defined to describe the recirculation.

For the compressor-to-turbine flow ratio,

$$\alpha = \frac{W_{26}}{W_4} = \frac{1}{1 - \frac{W_{rec}}{W_{26}}} \cdot \frac{1}{1 + \frac{W_f}{W_3}}$$

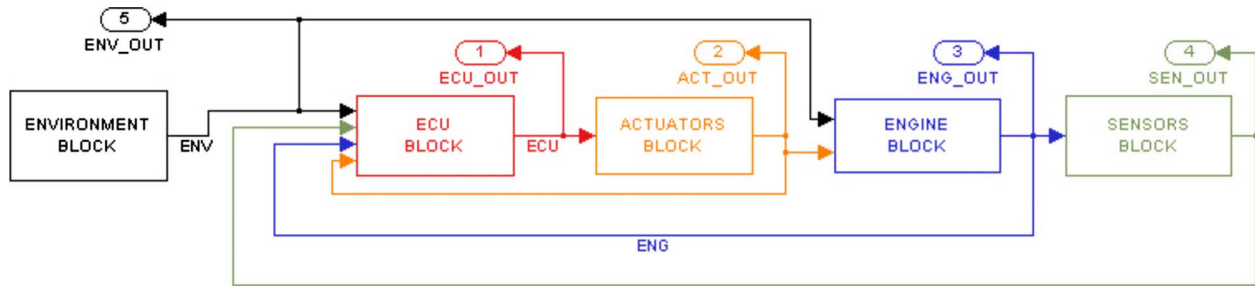


Fig. 4 Performance model embedded in a control simulation environment

and for the injection temperature ratio,

$$\vartheta = \frac{T_{26}}{T_{25}}$$

The mass flow parameter at the compressor inlet station 26 downstream of the injection can be written as:

$$\begin{aligned} \frac{W_{26}\sqrt{T_{26}}}{P_{26}} &= \frac{W_4\sqrt{T_4}}{P_4} \cdot \sqrt{\frac{T_{26}}{T_4}} \cdot \frac{W_{26}}{W_4} \cdot \frac{P_4}{P_3} \cdot \frac{P_3}{P_{26}} \\ &= K \cdot \alpha \cdot \sqrt{\vartheta} \cdot \sqrt{\frac{T_{25}}{T_4}} \cdot \frac{P_3}{P_{26}} \end{aligned} \quad (1)$$

where K is a constant as the variation of turbine capacity and burner pressure losses can be neglected. For the sake of clarity this theoretical approach does not consider any changes in the secondary air system.

Additionally, the operating point is determined by the power balance of the core spool. The compressor pressure ratio can be expressed as:

$$\left(\frac{P_3}{P_{26}}\right)^{c_{pC}/R} = \eta_{isC} \cdot \eta_{isT} \cdot \frac{c_{pT}}{c_{pC}} \cdot \frac{1}{\alpha \cdot \vartheta} \cdot \frac{T_4}{T_{25}} \cdot \left[1 - \left(\frac{P_4}{P_{45}}\right)^{-c_{pC}/R}\right] + 1 \quad (2)$$

For a turbine operating between choked nozzles ($P_4/P_{45} = \text{const}$) Eqs. (1) and (2) lead to the fact that the compressor operating line is a function of α but not of ϑ .

The recirculation can be split into an injection of external air ($\vartheta > 1$) and an overboard bleed ($\alpha > 1$). Figure 5 illustrates the shift in operating point in the compressor map for these different configurations at a constant turbine inlet temperature T_4 . The operating point is given by the intersection between lines of constant $(1/\alpha\sqrt{\vartheta})\sqrt{T_4/T_{25}}$ according to Eq. (1) and the operating line corresponding to the specific exit bleed flow. During external injection, the operating point moves along the same operating line due

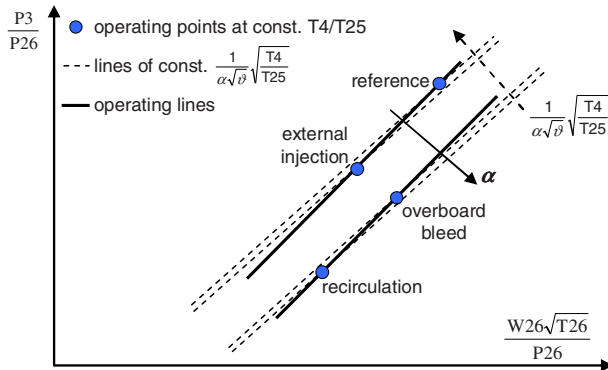


Fig. 5 Schematic influence of recirculation on the compressor operating point

to the changing compressor inlet temperature and speed parameter. Overboard bleed dethrottles the compressor instead and lowers the operating line. Compressor recirculation is a combination of the injection and the bleed effect.

Equation (2) shows further that the turbine must deliver more work to maintain the engine operating point during recirculation. If the additional work is not provided by an increase in fuel flow and thus turbine temperature, recirculation will lead to a reduction in thrust.

Detailed performance synthesis calculations reproduce well the basic phenomena described above. Again, recirculation is compared with an injection fed by an external source at the HPC inlet (injection only) and an overboard bleed at the HPC exit (bleed only). Figure 6 shows that recirculation lowers the HPC operating line mainly due to the bleed effect. As map corrections are applied to the simulation the changes need to be assessed at reference conditions. Injection causes a slight shift due to secondary map effects and a nonchoked turbine nozzle at a low power setting.

Upstream of the injection position, both mass flow and temperature are lower, resulting in a lower flow function than downstream of the injection. As a consequence, the compressor's upstream stages and the upstream components are throttled by the injection. In the case of the analyzed turbofan, HPC recirculation throttles the LPC and consequently raises the LPC operating line. Contrary to the HPC operating line the LPC operation is influenced by both the injection mass flow and the injection temperature by increasing the exit flow parameter. Furthermore, it can be seen in Fig. 7 that the effect of HPC overboard bleed on the LPC is negligible. The booster bleed located between the LPC and HPC lowers the operating line considerably, though, and provides additional stability at the part power for the investigated engine.

The recirculating bleed flow in the high pressure compressor influences the overall engine performance significantly. The effect of the higher mass flow on the compression side (α), which is the

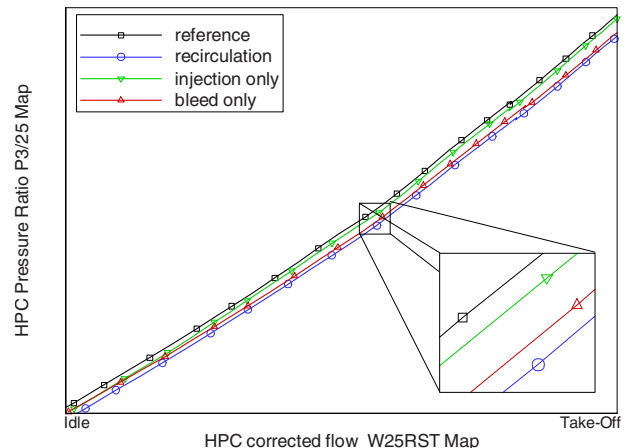


Fig. 6 HPC operating lines at reference condition

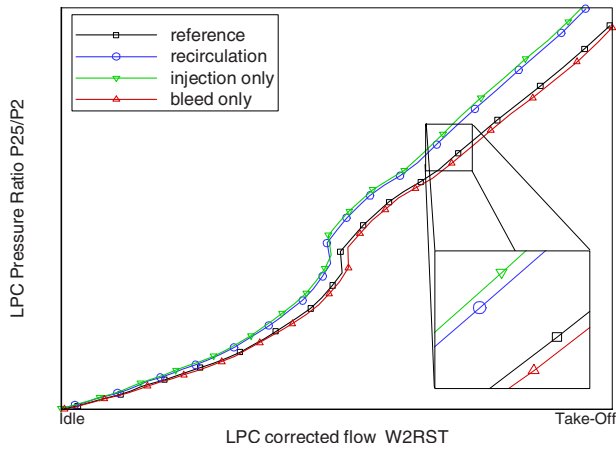


Fig. 7 Effect of HPC recirculation on LPC operating line

main contributor, and the higher compressor inlet temperature (ϑ) lead to a reduction in thrust. The engine thrust shortfall can be compensated by increasing the amount of injected fuel, which also increases turbine inlet temperature $T4$. Obviously there will be hard limits given by turbine durability. The performance degradation in terms of thrust, specific fuel consumption (SFC), and turbine temperature is shown in Fig. 8 for different amounts of recirculating bleed.

Alternatively described, a part of the system's energy is spent for recirculation and cannot be used for thrust generation. The recirculating mass flow has to be compressed but does not contribute to turbine work. Additionally, injection raises compressor inlet temperature, which drives the thermodynamic cycle to higher temperatures.

In Fig. 9, the amount (α) and the temperature (ϑ) of the injected mass flow are independently varied starting from the reference engine without recirculation. Obviously the injection temperature has a minor effect on fuel consumption. The amount of recirculating air causes the cycle to become less efficient.

It is important to note that recirculating bleed changes the relation between the thrust and typical rating parameters, such as the engine pressure ratio (EPR) and the corrected fan speed NLRST. At constant thrust, compressor recirculation causes EPR to rise and NLRST to drop. Both effects are related to a higher temperature level in the core and the shift in component operating lines. Although the changes are small, they potentially have to be taken into account in the rating structures. These considerations show that a thorough analysis is required before practical application.

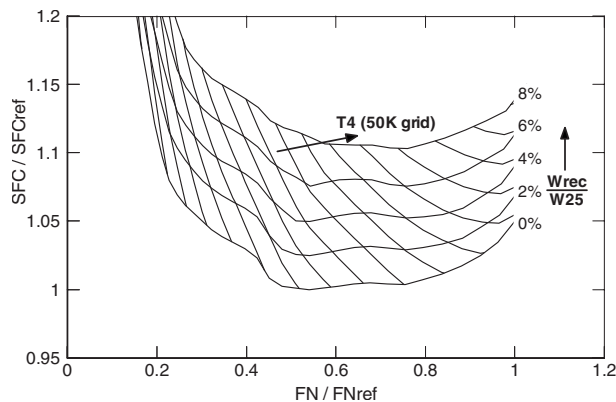


Fig. 8 Impact of recirculation on performance parameters at sea level

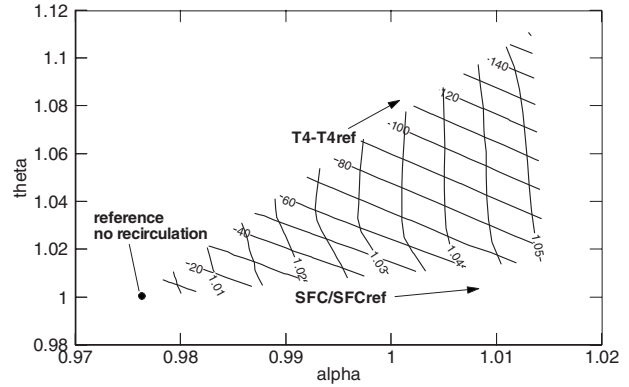


Fig. 9 Influence of the recirculating mass flow at different injection temperatures on performance parameters

Despite the negative impact on the performance, recirculation aims at an improvement in compressor stability. As a fixed injector throat area is used, the stabilization depends on the amount of injected mass and the properties of the flow. Figure 10 shows that more than 46% in surge margin may be gained for the chosen configuration at idle setting, while the benefit is around 12% at high power for stalling front stages. The assumptions required to derive the stability enhancement in Sec. 3.1 should be noted.

The dashed line indicates the choking limit of the injectors. As an operation above this limit is not desired, the lines at higher HPC flow parameters are only extrapolated. The absolute choking flow W_{rec} rises with the speed parameter. The injectors can pass less relative flow W_{rec}/W_{25} at high power because of the higher HPC inlet flow W_{25} . The total pressure in the recirculation duct is throttled by the recirculation valve. The dimensions of the injectors and the valve constitute the governing parameters and may be optimized to achieve the desired level of surge margin benefit.

Most aero engines are already equipped with HPC handling bleed valves to improve the starting behavior and the compressor stability at critical conditions. As the conventional handling bleed is connected to the bypass flow, the energy of the compressed air is not completely lost. Hence, handling bleed has less impact on the overall performance than recirculation.

For a comparison of the two stability measures, an HPC inter-stage bleed was simulated for the same engine. The bleed lowers the operating line and causes an HPC rematching effect. As a beneficial impact on the surge line itself is limited to subidle speeds for this compressor, no surge line effect was considered here. The simulation leads to the result that handling bleed causes

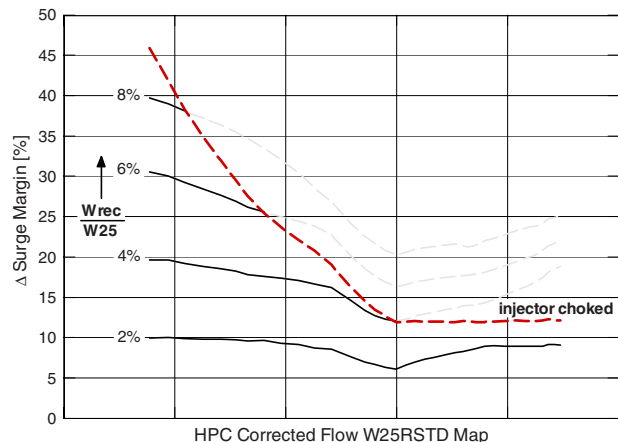


Fig. 10 Impact of the recirculating bleed on HPC surge margin

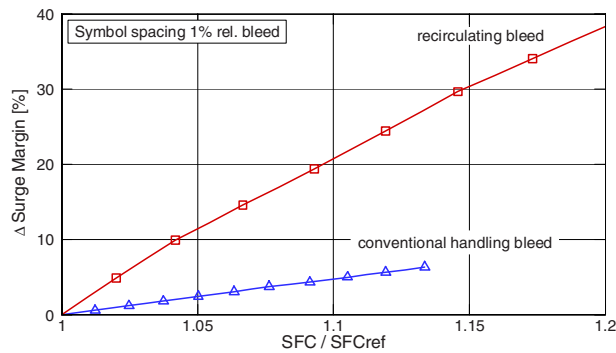


Fig. 11 Comparison between HPC handling bleed and the recirculating bleed at low power

less increase in specific fuel consumption for given bleed flow rates, as shown in Fig. 11. A similar trend can be drawn for the turbine temperature.

However, the achievable level of stability increase is lower than that obtained by recirculating bleed. Regarding the system behavior simulated in this study, recirculation offers a higher potential and works more effectively to obtain a required stability margin. This finding is driven by the fact that both measures are able to lower the operating point of a compressor stage but tip injection additionally raises the stage stability limit. If this stability enhancement cannot be achieved, the surge margin benefits of both options would be similar and HPC handling bleed would be preferable as it has less impact on engine performance.

5 Effects on Transient Performance

5.1 Control Considerations. During engine transients, the power balance of the HP spool corresponding to Eq. (2) will become dependent on the compressor-to-turbine flow ratio α and the injection temperature ratio ϑ when compressor recirculation is activated. As shown in Fig. 12, less excess power will be available for acceleration for the same turbine inlet temperature. Thus any acceleration maneuver will take longer with recirculation. For decelerations the power difference between the compressor and turbine will be larger and maneuvers will take place faster.

However, most of the engine handling and thrust response times are prescribed by the certification authorities and the airframe manufacturer. The transients are typically controlled as a function of the HP acceleration rate (NHDOT). If the controller follows the same transient schedule as that of without recirculation, the duration of the maneuver should not be influenced, but the resulting fuel flow and turbine inlet temperature T_4 will change.

The negative impact of recirculating bleed on engine performance and the higher surge margin potential at low power settings lead to the concept that the recirculation valves should be closed during steady-state and high power operation. Injection should

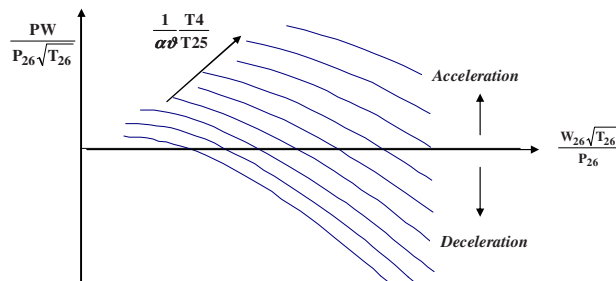


Fig. 12 Parametric representation of the transient excess power

only be employed as a reactive measure to enhance the compressor stability for a short time period. An intelligent control scheme is required to minimize steady-state losses while maintaining the full benefit for stability.

These considerations lead to the following requirements for an effective recirculation logic.

- Recirculation has to be activated fast enough at any point with a low HPC surge margin to reliably enhance the compressor stability.
- Recirculation valves have to be closed during steady-state operation to avoid an increase in mission fuel burn.
- Recirculation valves have to be closed before turbine temperatures exceed a critical limit.
- The recirculating flow should be limited to the necessary amount for HPC stabilization to protect the LPC from stall.

To study the transient effects of compressor recirculation a simple surge anticipation logic was implemented in the control system simulation [20]. The controller opens the recirculation valve to a predefined flow area upon detection of an acceleration. The valve remains open until a limiting corrected HP spool speed is reached. As a result, the logic activates recirculation only during accelerations and compressor part speed.

5.2 Transient Simulations. For further discussion the simulation of a critical engine transient in the flight envelope was carried out. The engine was accelerated from ground idle at sea level static condition to maximum take-off thrust by a throttle slam maneuver. The working line excursion caused by the inertia of the rotating mass reduces the temporary surge margin substantially, especially at the beginning of the acceleration. More severe maneuvers exist in the flight envelope and have to be covered by a stability assessment, but will not be discussed any further in this paper. The engine behavior was simulated for three different cases with the following recirculating bleed settings:

1. conventionally, with the recirculation switched off
2. recirculated, with maximum recirculating mass flow
3. and stability controlled, with the recirculating flow controlled by the surge anticipation logic

All three maneuvers have identical starting and ending thrust settings defined by the power lever angle (PLA). At the steady-state starting point a NLRST schedule controls the engine, which represents a simplification of the actual idle rating. During transient operation a NHDOT schedule takes over. Figure 13 shows the resulting curves of selected engine parameters. The thrust response is nearly identical, if the recirculation valve is opened only during the transient. The case with maximum recirculating flow differs from the other two cases because the bleed valve is already open at idle and stays open at maximum thrust. Therefore the transient starts from a higher idle high spool speed (NH), which results in a decreased acceleration time for the same control schedule.

The curves of the turbine temperature prove the advantage of using the injection control scheme. In the case of a permanently opened recirculation valve, the turbine temperature exceeds the level of the conventional engine considerably at idle and high power. Here, the benefit of additional stability might be compensated by a higher turbine temperature to be cleared.

If tip injection is controlled, temperature level, fuel flow, and spool speed remain unchanged at the steady-state condition. During transient operation, the bleed valve opens and meters the flow according to the additional surge margin requirement of the compressor. This only happens at low and midpower, where the tip-injection flow recovers the front stage surge margin of the HP compressor. The valve will be closed before reaching maximum power, thus avoiding any undesired temperature overshoot.

Figure 14 clearly demonstrates the benefit of the HP compressor recirculation, which consists of a substantial increase in surge

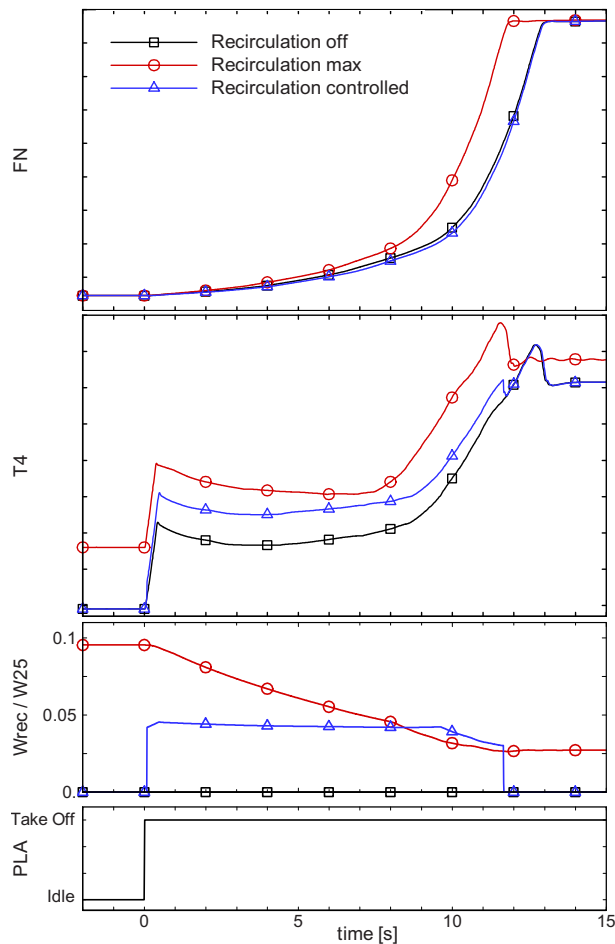


Fig. 13 Acceleration from idle to take-off rating at sea level for different recirculation settings

margin. During acceleration, the gap between the operating and surge line in the HP compressor map closes down due to the operating line excursion. As the recirculation valve opens, tip injection increases the surge line significantly. The stability control is able to recover the temporary compressor stability deficit during the maneuver completely with the surge margin improvement illustrated in the lower diagram of Fig. 14.

In the given example the increase in stability is ruled by the constant valve setting used in the simulation. More surge margin can be gained at low power if the valves are fully opened, but choking injectors and critical rear stages limit the potential at high power. The amount of recirculating flow can be reduced by an optimization of the injection velocity, taking into account the surge margin requirement at low and high power.

The steady-state analysis revealed a rising LPC operating line when the mass flow recirculates in the HP compressor (see Fig. 7). During transients, the same effect can be seen in Fig. 15. However, engine accelerations will produce LPC operating line excursions below the steady-state level, while decelerations cause the LPC operating line to rise. As a consequence, HPC recirculation can be employed without causing LPC stability problems during accelerations. At the beginning of the acceleration, the LPC operating line tends to have an initial excursion due to the HPC characteristic. At this point, recirculation causes a critical effect of about 0.5% LPC surge margin loss. This could be optimized by an adaptation of the LPC bleed valve schedule, which is already employed for low power operation. Special care has to be taken for retrim maneuvers as described by Peitsch et al. [21].

When the engine is decelerated, the transient excursion will rise

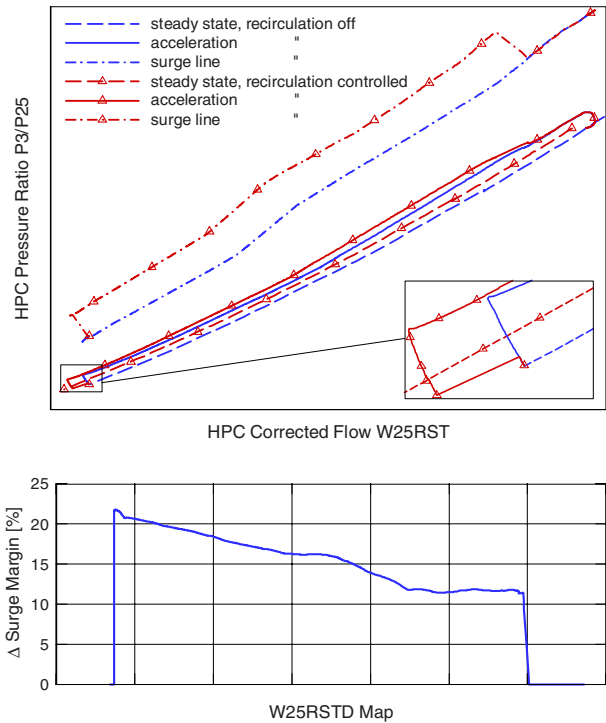


Fig. 14 Operating lines and the surge margin benefit for an acceleration from the idle to take-off rating

above the steady-state LPC operating line with a corresponding negative impact on the LPC surge margin. For those conditions, recirculation is not required due to a lower HPC operating line and thus not advisable. Tip injection could however be beneficial to the LPC itself during decelerations.

6 Potential for Engine Applications

Enhanced surge margin itself does not offer any benefit for a well designed engine. Overall engine performance can be improved if the additional stability is exploited either by enhanced engine dynamics or by an optimized design.

One possibility consists in applying the technology to improve engine operability. Aircraft equipped with active stability control can fly more severe maneuvers or profit from faster thrust response in critical situations.

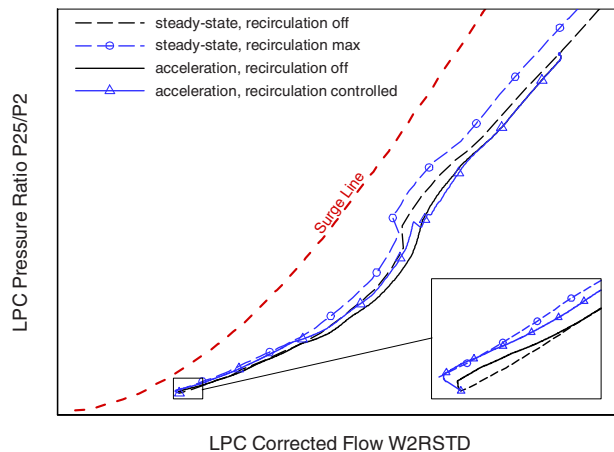


Fig. 15 Steady state LPC operating lines and acceleration from the idle to take-off rating

Another strategy reduces the aircraft's fuel consumption by taking advantage of the larger available design space of the HP compressor. If tip injection is applied to the front stages it may be possible to increase compressor efficiency by an optimized aerodynamic design with higher loadings. Furthermore, lower compressor weight, as well as improved reliability, can be achieved by the replacement of variable stator vanes with active stability enhancement. If tip injection is combined with a stabilization of the rear stages, it is possible to exploit the gained stability by a lift of the operating line. This approach offers a higher overall pressure ratio resulting in lower SFC. Alternatively, a given design pressure ratio can be realized with fewer stages or a decreased airfoil count with a corresponding weight benefit. Concept studies indicate that the specific fuel consumption of a commercial aircraft can be improved if the engine is designed directly with active stability measures.

Tip injection can also be applied to the low pressure compressor to provide either higher stability or lower design requirements. The technology represents an interesting option as a countermeasure to inlet distortion, which is especially true for military engines due to long intakes, extreme aircraft pitch and yaw angles, and missile firing.

7 Conclusion

Tip injection was modeled as a recirculating mass flow in the high pressure compressor of a turbofan engine. A map correction accounts for the aerodynamic stabilization effect, which was derived from stage stacking calculations based on an empirical correlation for stability enhancement. Steady-state and transient engine operation with recirculating bleed was simulated by an adapted performance model.

Compressor recirculation lowers the HPC operating line and increases the HPC inlet temperature while the LPC operating line is raised. These basic effects can be described by the recirculating mass flow and the injection temperature. Overall performance is negatively affected, as fuel flow and turbine temperature have to be increased to achieve the same level of thrust. On the other hand, tip injection is able to raise the surge line considerably, especially at low power settings.

The negative impact of recirculating bleed on engine performance and the higher surge margin potential at low power settings lead to the concept that the recirculation valves should be closed during steady-state and high power operation. Injection should only be employed as a reactive measure to enhance compressor stability for a short time period.

Transient simulations including the engine control system show that the technology indeed offers a large potential in combination with an adequate control logic, without disadvantages in engine performance. The stability control should consider thrust requirement and turbine temperature overshoot, as well as changes in LPC surge margin, which emphasizes the need for a system assessment.

However, a better database is required to support the stability enhancement potential of the tip injection technology. Further development of the control logic, being open-loop or closed-loop, will clear the path to an implementation of active stability enhancement in future gas turbines.

Acknowledgment

This publication has emerged from MTU Aero Engines research activities, which were supported by the German Federal Ministry of Economics and Technology. The authors wish to thank their colleagues for inspiring discussions and MTU Aero Engines for the permission to publish this paper.

Nomenclature

α = compressor-to-turbine flow ratio W_{26}/W_4
 ϑ = injection temperature ratio T_{26}/T_{25}

ϕ = flow coefficient $\phi = c_{ax}/u$ (including W_{inj})
 $\Delta\phi_{stall}$ = shift in the stalling flow coefficient $\Delta\phi_{stall} = \phi_{stall,ref} - \phi_{stall,inj} / \phi_{stall,ref}$
 c = velocity
 \bar{c}_{ax} = mass averaged axial velocity
EPR = engine pressure ratio, $EPR = P_5/P_2$
NLRST = low spool corr. speed, $NLRST = NL/\sqrt{T_2/T_{std}}$
 P = total pressure
PW = power
SM = surge margin at const. flow,
 $SM = \Pi_{SL} - \Pi_{OL} / \Pi_{OL}$
 ΔSM = surge margin gain, $\Delta SM = SM_{rec} - SM_{ref}$
 T = total temperature
 u = circumferential velocity
 W = mass flow
 W_{25} RST = corrected mass flow at Station 25

Subscripts

Ax = axial
C = compressor
f = fuel
inj = injected
OL = operating line
rec = recirculating
ref = reference engine without recirculation
SL = surge line
T = turbine

References

- [1] Epstein, A. H., 1986, "Smart Engine Components: A Micro in Every Blade?," *Aerosp. Am.*, **24**(1), pp. 60–64.
- [2] Jaw, L. C., Mink, G., and Kallappa, P., 2003, "Intelligent Engine Technology Study," ISABE Paper No. ISABE-2003-1186.
- [3] Paduano, J. D., and Epstein, A. H., 2000, "Compressor Stability and Control: Review and Practical Implications," *Proceedings of the RTO AVT Symposium 51 on Active Control Technology for Enhanced Performance Operational Capabilities of Military Aircraft, Land Vehicles and Sea Vehicles*, Braunschweig, Germany.
- [4] Kefalakis, M., and Papailiou, K. D., 2006, "Active Flow Control for Increasing the Surge Margin of an Axial Flow Compressor," *ASME Paper No. GT2006-90113*.
- [5] Freeman, C., Wilson, A. G., Day, I. J., and Swinbanks, M. A., 1998, "Experiments in Active Control of Stall on an Aeroengine Gas Turbine," *ASME J. Turbomach.*, **120**, pp. 637–647.
- [6] Nelson, E. B., Paduano, J. D., and Epstein, A. H., 2000, "Active Stabilization of Surge in an Axicentrifugal Turboshift Engine," *ASME J. Turbomach.*, **122**, pp. 485–493.
- [7] Leinhos, D. C., 2003, "Aktive Stabilisierung der Verdichterströmung in einem Zweikreis-Turbostrahltriebwerk," Ph.D. thesis, University of Armed Forces Munich, Germany.
- [8] Scheidler, G. S., 2005, "Untersuchung der Systemaspekte Stabilitätsverbessernder Maßnahmen in Gasturbinen," Ph.D. thesis, University of Armed Forces Munich, Germany.
- [9] Kurzke, J., 2006, "Effects of Inlet Flow Distortion on the Performance of Aircraft Gas Turbines," *ASME Paper No. GT2006-90419*.
- [10] Deppe, A., Saathoff, H., and Stark, U., 2005, "Spike-Type Stall Inception in Axial Flow Compressors," *Proceedings of the Sixth Conference on Turbomachinery, Fluid Dynamics and Thermodynamics*, Lille, France.
- [11] Chen, J., Webster, R. S., Skoch, G. J., Herrick, G. P., and Hathaway, M. D., 2005, "Technology for Stabilizing the Compression System of a US Army Helicopter Gas Turbine Engine: Validation of Unsteady Simulations," *Proceedings of the American Helicopter Society 61st Annual Forum*, Grapevine.
- [12] Vo, H. D., Tan, C. S., and Greitzer, E. M., 2005, "Criteria for Spike Initiated Rotating Stall," *ASME Paper No. GT2005-68374*.
- [13] Weigl, H. J., Paduano, J. D., Fréchette, A. G., Epstein, A. H., Greitzer, E. M., Bright, M. M., and Strazisar, A. J., 1998, "Active Stabilization of Rotating Stall in a Transonic Single Stage Axial Compressor," *ASME J. Turbomach.*, **120**, pp. 625–636.
- [14] Suder, K. L., Hathaway, M. D., Thorp, S. A., Strazisar, A. J., and Bright, M. M., 2001, "Compressor Stability Enhancement Using Discrete Tip Injection," *ASME J. Turbomach.*, **123**, pp. 14–23.
- [15] Strazisar, A. J., Bright, M. M., Thorp, S. A., Culley, D. E., and Suder, K. L., 2004, "Compressor Stall Control Through Endwall Recirculation," *ASME Paper No. GT2004-54295*.
- [16] Lei, V.-M., Spakovszky, Z. S., and Greitzer, E. M., 2006, "A Criterion for Axial Compressor Hub-Corner Stall," *ASME Paper No. GT2006-91332*.
- [17] Kurzke, J., 1992, "Calculation of Installation Effects Within Performance Computer Programs," Paper No. AGARD-LS-183.

- [18] Vo, H. D., and Paduano, J. D., 1998, "Experimental Development of a Jet Injection Model for Rotating Stall Control," ASME Paper No. 98-GT-308.
- [19] Bolívar, M., Jiménez, A., Pérez, C., Breuer, T., Riegler, C., and Salchow, K., 2003, "Advanced Propulsion System Simulation Model for a Modern Fighter Aircraft Training Aid," *Proceedings of the AIAA Modeling and Simulation Technologies Conference*, Paper No. AIAA-2003-5374.
- [20] Kopetsch, T., 2006, "Untersuchung des Betriebsverhaltens eines zivilen Turbofantriebwerks mit geregelter Umblasung im Verdichter," MS thesis, Technical University Berlin, Germany.
- [21] Peitsch, D., Fiola, R., Brodmuehler, R., and Nielsen, A., 1999, "Validation of the Booster Bleed Valve Control Logic in the New BR715 Jet Engine," ASME Paper No. 99-GT-60.

Spike and Modal Stall Inception in an Advanced Turbocharger Centrifugal Compressor¹

Z. S. Spakovszky

Gas Turbine Laboratory,
Massachusetts Institute of Technology,
Cambridge, MA 02139

C. H. Roduner

ABB Turbo Systems Ltd., Baden 5400,
Switzerland

In turbocharger applications, bleed air near the impeller exit is often used for secondary flow systems to seal bearing compartments and to balance the thrust load on the bearings. There is experimental evidence that the performance and operability of highly-loaded centrifugal compressor designs can be sensitive to the amount of bleed air. To investigate the underlying mechanisms and to assess the impact of bleed air on the compressor dynamic behavior, a research program was carried out on a preproduction, 5.0 pressure ratio, high-speed centrifugal compressor stage of advanced design. The investigations showed that bleed air can significantly reduce the stable flow range. Compressor rig experiments, using an array of unsteady pressure sensors and a bleed valve to simulate a typical turbocharger environment, suggest that the path into compression system instability is altered by the bleed flow. Without the bleed flow, the prestall behavior is dominated by short-wavelength disturbances, or so called "spikes," in the vaneless space between the impeller and the vaned diffuser. Introducing bleed flow at the impeller exit reduces endwall blockage in the vaneless space and destabilizes the highly-loaded vaned diffuser. The impact is a 50% reduction in stable operating range. The altered diffuser characteristic reduces the compression system damping responsible for long-wavelength modal prestall behavior. A four-lobed backward traveling rotating stall wave is experimentally measured in agreement with calculations obtained from a previously developed dynamic compressor model. In addition, a self-contained endwall blockage control strategy was employed, successfully recovering 75% of the loss in surge-margin due to the bleed flow and yielding a one point increase in adiabatic compressor efficiency. [DOI: 10.1115/1.2988166]

1 Introduction and Background

Besides meeting the pressure ratio requirements of the application, one of the major challenges in turbocharger compressor design is to achieve both a broad compressor map and high efficiency levels throughout the entire operating envelope. Over many years, the design trend has been toward highly-loaded advanced compressor designs, as, for example, reported by Rodgers [1]. Impeller designs with increased backsweep can yield improved stability limits but, for the same pressure ratio, require higher rotor speeds and thus enhanced materials. Given the competitive market and cost requirements, more and more high-strength titanium alloys are replaced with aluminum alloys due to their five to eight times lower machining cost. This poses a major design challenge for highly-loaded compressors with enhanced performance and operability goals.

The phenomena limiting the stable operation of centrifugal compression systems are rotating stall and surge. Although the manifestation of the full scale instabilities are similar to the ones observed in axial machines, the path into instability and prestall behavior in centrifugal compressors is less well understood. The pioneering work of Emmons et al. [2] showed that rotating stall can occur prior to surge in centrifugal compressors. Since then, extensive studies, both experimental and theoretical, have been conducted on this topic by a large number of researchers. A summary and detailed discussion can be found in Refs. [3] and [4].

A major challenge in developing a generalized description or theory for rotating stall and surge inception is that the overall

compression system, the compressor geometry, and the impeller speed cover a very large range. However, there is evidence that a number of compressors with vaned diffusers seem to exhibit long-wavelength perturbations prior to the onset of full scale instability. For example, Lawless and Fleeter [5] and Oakes et al. [6] investigated the rotating stall acoustic signature in low- and high-speed compressor experiments with the assumption that rotating stall can be represented as a weak linear disturbance, which grows into a finite stall cell. The results suggest that the compression systems exhibited an extensive repertoire of excited spatial modes. A compression system stability model for centrifugal compressors was developed by Spakovszky [7], capable of dissecting the dynamic behavior of the impeller and the vaned diffuser subcomponents. The theory predicted backward traveling modal prestall waves, which were subsequently measured in a high-speed experiment, confirming the existence of long-wavelength perturbations prior to full scale instability.

The present paper focuses on the stall inception in a preproduction turbocharger centrifugal compressor of pressure ratio 5, representative of high flow capacity advanced designs with highly-loaded vaned diffusers. The work demonstrates that, depending on the amount of endwall blockage in the vaneless space, either short-wavelength or long-wavelength precursors occur before surge is initiated, similar to the description by Camp and Day [8] for axial compressors. The detailed analysis and experimental assessment constitute the scope of the paper and are discussed in depth.

Nature of the issues. The interaction of leakage and bleed flows with the main gas path flow can have a strong impact on compressor performance and dynamic behavior. In turbocharger applications, one such example is the bleed air through an annular slot on the hub side between the impeller and the vaned diffuser. This secondary air is used to seal bearing compartments and to balance the thrust load on the bearings. There is experimental evidence

¹Winner of the "Best Paper Award" Turbomachinery Committee.

Contributed by the International Gas Turbine Institute of ASME for publication in the JOURNAL OF TURBOMACHINERY. Manuscript received December 21, 2007; final manuscript received March 22, 2008; published online April 10, 2009. Review conducted by David Wisler. Paper presented at the ASME Turbo Expo 2007: Land, Sea and Air (GT2007), Montreal, QC, Canada, May 14–17, 2007.

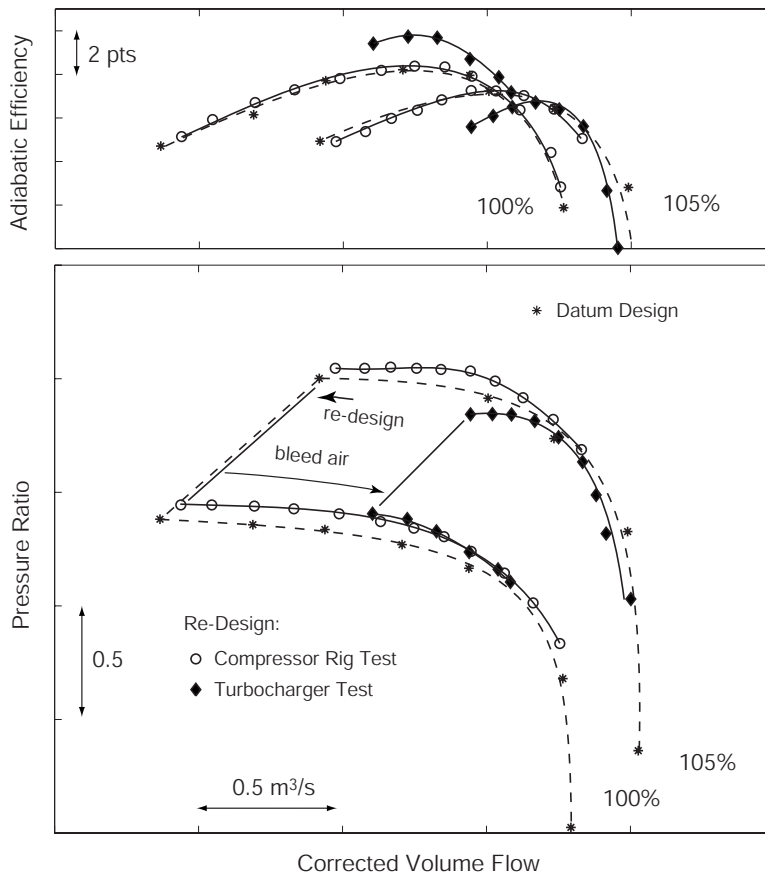


Fig. 1 Measured high-speed performance of data and redesigned compressor configurations

that the stability and performance of highly-loaded centrifugal compressor designs can be strongly affected by the presence of bleed air as captured in Fig. 1. The measured high-speed performance of an advanced compressor is marked by the stars and dashed lines. In a redesign effort with the aim to improve part speed efficiency at some expected loss in stable flow range at high-speed, the impeller exit blade span was increased by shifting the shroud contour without changing the impeller exit metal angle. The diffuser throat area was kept the same to preserve flow capacity but, in order to match the vane diffuser to the impeller exit flow, the diffuser vane setting angle was set to shallower inlet flow angles. The redesigned compressor, from now on denoted as the base line compressor, was first assessed in a centrifugal compressor test rig and achieved the efficiency goal at part speed. However, the stable flow range was unexpectedly maintained at high-speed without deteriorating efficiency and choke mass flow, as indicated by the open circles in Fig. 1. To further validate this design, a turbocharger test was conducted using the same compressor hardware. The solid diamonds show a nearly 50% loss in stable flow range at high-speed² and a significant reduction in pressure ratio at 105% corrected speed. The only difference between the two test environments is that in the turbocharger test bleed air for secondary flow systems was present between the impeller and the vane diffuser. The bleed air mass flow was about 0.5% of the compressor mass flow. The adiabatic compressor efficiency is increased by 1 to 2 points at 100% corrected speed due to the removal of high-entropy air from the hub endwall via the bleed air. At higher speed, the efficiency is deteriorated, in concert with the reduced pressure ratio. This suggests that flow

²The surge line at part speed was unaltered between the compressor rig test and the turbocharger experiment and is thus not shown.

separation occurs in the vaneless space and diffuser inlet region, and it will be discussed in detail later.

Scope of the paper. The two main goals of this paper are to (1) investigate the effects of bleed flow on compressor performance and stability, and (2) improve the performance and operability by means of a simple self-contained control scheme viable in turbocharger environments. In the light of these goals, three hypotheses are addressed. The first hypothesis is that hub leakage flow near the exit of the impeller can destabilize the vaneless and semi-vaneless spaces through changes in the endwall blockage and loading redistribution of the diffuser components. The second hypothesis is that the path into instability is governed by spikes or modes depending on whether the slope of the semi-vaneless space characteristic becomes zero before the peak of the overall diffuser characteristic is reached. The third hypothesis is that controlling the endwall blockage in the vaneless space via a self-contained scheme can extend the stable flow range *and* improve the efficiency of the compressor including the blockage control scheme.

The technical approach combines first principle based plausibility arguments with detailed experiments in an advanced turbocharger centrifugal compressor and a previously developed centrifugal compressor stability model for long-wavelength pre-stall modes. A self-contained endwall blockage control scheme is implemented in the same compressor and is experimentally tested.

2 Experimental Setup

A series of experiments were designed to investigate the pre-stall behavior and the effect of endwall blockage on compressor stability and performance. All experiments were conducted in the SUMA closed loop centrifugal compressor test facility at ABB Turbo Systems in Baden, Switzerland. The mass flow through the compressor is measured by an orifice plate downstream of the

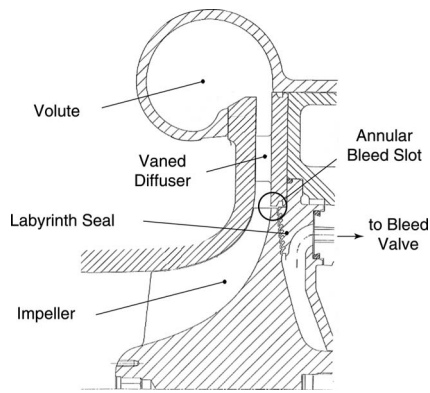


Fig. 2 Schematic of compressor cross section indicating location of bleed flow near impeller exit

compressor test section and a precooler. After passing through the main cooler, the compressor mass flow is regulated by a butterfly-type throttle valve system and is passed through a flow straightener before returning to the compressor. To simulate the bleed flow used to seal the bearing compartment and to provide axial thrust compensation in the actual turbocharger environment, an exhaust valve was installed to the bleed flow through a labyrinth seal near the exit of the impeller at the hub side, as sketched in Fig. 2. The bleed flow was throttled to inlet conditions such that the pressure differential between the impeller inlet and exit, which governs the leakage flow, was independent of inlet conditions.³ This achieved bleed mass flow rates comparable to the ones observed in a typical turbocharger environment.

The test compressor was a pre-production, 5.0 pressure ratio, high-speed centrifugal compressor stage of advanced design. The impeller contained nine main blades and nine splitter blades with backsweep, and the vaned diffuser consisted of 16 aerodynamically profiled vanes.

Steady-state compressor performance measurements such as static pressures at various locations on the shroud side, mass flow, stagnation pressure, and temperature ratios were recorded. The measurement uncertainties are estimated to be about 1% in mass flow, 0.4 points in efficiency, and a few pascals in pressure. To dissect the performance of the diffuser subcomponents, one diffuser channel was instrumented with static pressure taps distributed in the vaneless space, the semi-vaneless space, the diffuser passage, and near the volute. These static pressure taps were mounted on the diffuser hub endwall and are shown in Fig. 3.

A total number of 15 high-response Kistler pressure transducers of type 6052B1 were used to record the instantaneous casing static pressure at selected locations during continuous throttle ramps into surge. A circumferentially distributed array of 11 transducers was installed in the vaneless space as depicted in Fig. 3. Eight transducers were equally spaced and the remaining three were located in between. In addition, single transducers were mounted at the impeller inlet, on the shroud side at the diffuser throat, near the exit of the diffuser passage, and in the volute. Kistler signal conditioners and amplifiers were used to signal condition and filter the transducer signals. For all transducers, the low-pass filter frequencies were set to 10 kHz. Unsteady pressure transducer data were acquired at a sampling frequency of 3 kHz using an in-house high-speed data acquisition system.

3 Steady-State Vaned Diffuser Performance Measurements

To investigate the mechanisms behind the loss in performance and stability when bleed flow is present, extensive measurements of the compressor performance were conducted.

³The closed loop test facility is usually operated at subatmospheric inlet conditions.

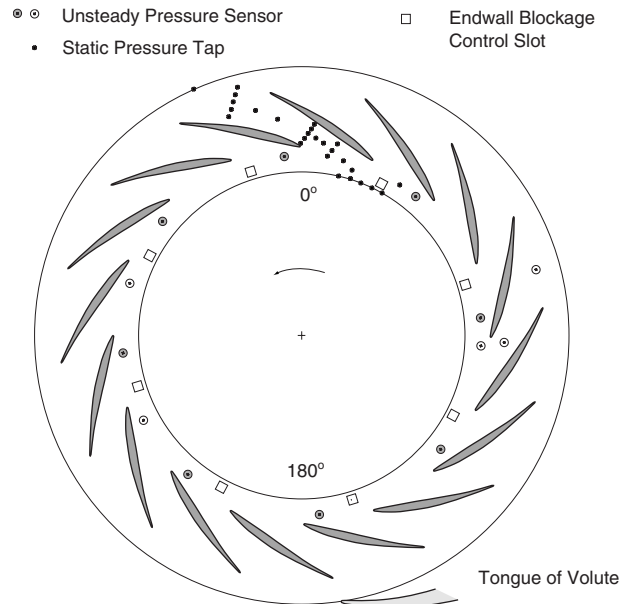


Fig. 3 Steady and unsteady diffuser instrumentation

Subcomponent performance at 100% corrected speed. Figure 4 depicts the measured static pressure rise characteristic of the vaned diffuser subcomponents at 100% corrected speed. The impeller characteristic is unaltered with bleed flow and is thus not shown. The static pressure rise in the vaneless space (circles), the semi-vaneless space (diamonds), and the diffuser passage (squares) were determined using area averaged data acquired from static pressure taps in the diffuser shown in Fig. 3. The baseline characteristics are marked by solid symbols whereas the measurements with bleed flow at the impeller exit are marked by open symbols. The measurements indicate that the diffusion of the flow through the vaneless space is increased with bleed flow (dashed arrow) altering the slope of the characteristic of the semi-vaneless space (solid arrow). The slope changes from negative to zero, suggesting that the diffuser inlet region becomes dynamically unstable⁴ when bleed air is present. Note that the slope of the pressure rise characteristic in the diffuser channel is unaltered and dynamically unstable, independent of the bleed flow at the impeller exit. The implication is that the semi-vaneless space seems to be the weakest element of the compression system governing the dynamic stability limit of the machine.

The reason for the enhanced diffusion in the vaneless space is suggested to be due to the reduced endwall blockage when flow leakage at the impeller exit occurs. This is in concert with diffuser measurements reported by Reneau et al. [9] and interacting boundary layer calculations in diffusers by Greitzer et al. [10]: A 50% reduction in inlet displacement thickness yields a 6% increase in static pressure rise. In comparison to the measurements in Fig. 4, this is about half the increase in static pressure rise in the vaneless space due to the presence of endwall flow leakage.

To qualitatively illustrate the effect of endwall boundary layer blockage on diffuser pressure rise, the low velocity region can be modeled as an inviscid deficit flow with a uniform velocity profile. The situation is depicted in Fig. 5 on the left and can be viewed as the interaction of a viscous flow (the boundary layer giving rise to blockage near the endwall) with an inviscid flow (the core flow in the diffuser generating the pressure rise). Conservation of momentum for steady one-dimensional inviscid flow can be written as

⁴The slope of the static pressure rise characteristic is proportional to the damping of the natural flow oscillations of the compression system, which can grow into full scale instability, rotating stall, and surge.

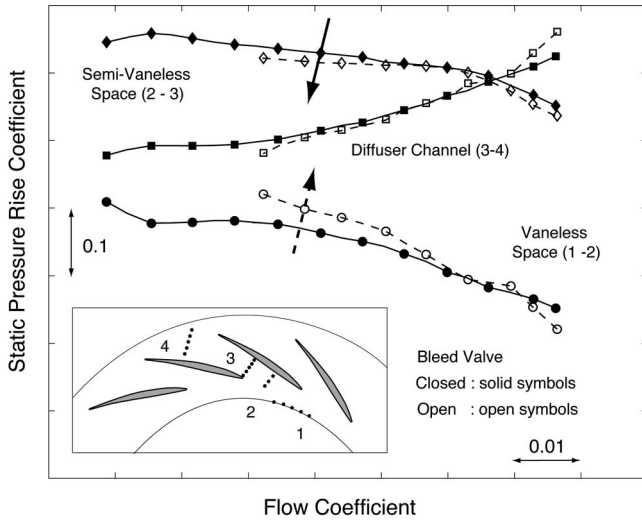


Fig. 4 Static pressure rise characteristics of vanned diffuser subcomponents at 100% corrected speed

$$\frac{du}{u} = -\frac{dp}{\rho u^2} \quad (1)$$

Together with the conservation of mass for incompressible flow along a stream-tube,

$$\frac{du}{u} = -\frac{dA}{A} \quad (2)$$

changes in velocity and stream-tube area can be assessed for fluid particles passing through the diffuser. Since stream-tubes near the endwall and in the core-stream experience the same static pressure rise through the diffuser dp , the relative deceleration in velocity du/u is larger near the endwall due to the lower velocity magnitude as compared with the core-stream. From continuity, the low velocity region grows, decreasing the diffuser pressure rise compared with the situation of uniform flow. With endwall leakage flow, shown on the right in Fig. 5, the relative deceleration in the endwall stream is reduced increasing the overall diffuser pressure rise.

Subcomponent performance at 105% corrected speed. The measurements at 105% corrected speed in Fig. 6 indicate that the flow in the vaneless and the semi-vaneless spaces severely separates when air is bled at the impeller exit. Lower levels of endwall blockage enhance the diffusion in the vaneless space; as a consequence of conservation of angular momentum, the reduced radial velocity component increases the swirl angle (defined from the radial direction). Since swirling boundary layers exhibit different

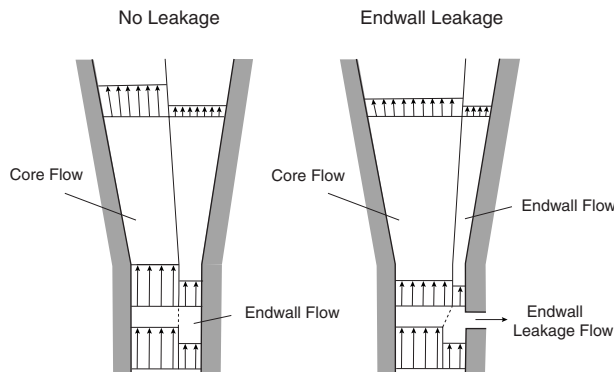


Fig. 5 Qualitative description of change in diffuser static pressure rise due to endwall leakage flow

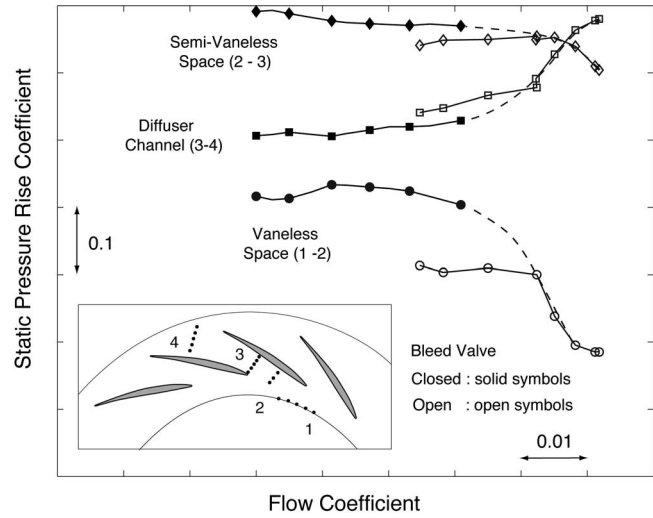


Fig. 6 Static pressure rise characteristics of vanned diffuser subcomponents at 105% corrected speed

features compared with two-dimensional motion, high levels of swirl can yield inward flow (reversed radial velocity) and separation [10].

The swirling flow in the vaneless space is sketched in Fig. 7. Two streamlines are shown, one for a fluid particle in the freestream core flow and the other for a fluid particle in the boundary layer. The vortex lines in the boundary layer are convected with a local velocity proportional to the freestream velocity. As angular momentum in the freestream is conserved, the tangential velocity decreases with the radius, and the vortex lines are tipped in the tangential direction as the fluid moves radially outward. This generates a cross-flow with a tendency for inward flow (reversed radial velocity). For high swirl angles, the streamlines are close to tangential, and the boundary layer fluid is likely to flow inward, eventually leading to flow separation.

In summary, the dissection of the diffuser performance shows that at 100% corrected speed the pressure rise in the vaneless space is significantly affected by the leakage flow at the impeller exit. As a consequence, the semi-vaneless space is destabilized and becomes the weakest element in the compression system. At 105% corrected rotor speed, both the vaneless and semi-vaneless spaces are severely stalled with flow leakage at the impeller exit. It is suggested that, as the mass flow is throttled along the speed-line, the swirl angles increase to a level where the cross-flow reverses the radial velocity and separation occurs. Further work is required to explain the detailed link between the flow in the cavity and the change in endwall blockage when bleed flow is present.

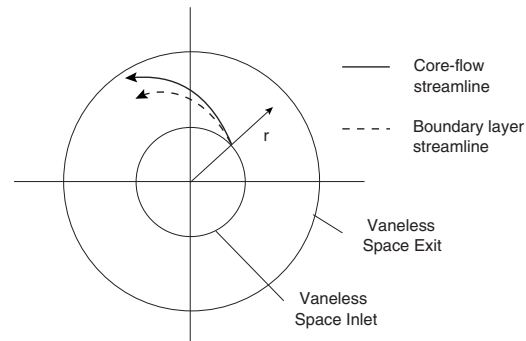


Fig. 7 Streamlines of swirling flow in vaneless space (adopted from Ref. [10])

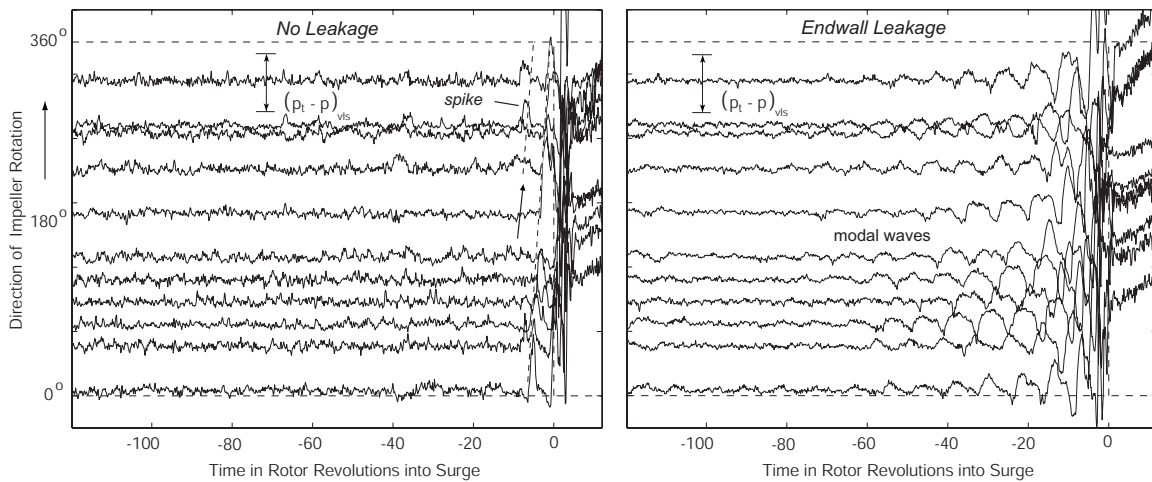


Fig. 8 Unsteady pressure traces in the vaneless space at 100% corrected speed: no leakage (left) and endwall leakage (right)

4 Measured Compressor Dynamic Behavior

Using the circumferential pressure transducer array located in the vaneless space (see Fig. 3), unsteady pressure measurements were conducted during slow throttle ramps into surge at constant corrected speed. For each corrected speed and inlet condition, several stall ramps were conducted to ensure repeatability of the observed phenomena. Experiments were conducted at 100% and 105% corrected speed.

Unsteady pressure measurements at 100% corrected speed. Figure 8 on the left depicts the pressure traces acquired from 11 pressure transducers in the vaneless space with the bleed valve closed. The unsteady pressure signals are nondimensionalized by the vaneless space inlet dynamic pressure. The measurements show no dynamic activity until a few rotor revolutions prior to surge, when a short-wavelength perturbation, or a so-called spike [8], seem to emerge. The spike travels around the circumference at about 20% of rotor frequency in the direction of impeller rotation (the period is about 5 rotor revolutions), grows in amplitude and triggers full scale instability. The corresponding surge point is marked by the solid symbols at the lowest flow coefficient in Fig. 4.

Subsequently, the bleed valve was opened and the same experiment was repeated. The results are plotted in Fig. 8 on the right. The compressor surges at much higher flow coefficients, as indi-

cated by the open symbols in Fig. 4. In this case, long-wavelength prestall waves are observed about 80 rotor revolutions prior to the onset of full scale instability. The amplitude of the perturbations is about a third of the vaneless space inlet dynamic head. The prestall waves grow exponentially and lead to surge. A traveling wave energy analysis [11] was employed on various data sets with the goal to determine the direction of wave rotation. However, the analysis did not yield a coherent rotation frequency and the sense of rotation could not be identified. This is also evidenced by the time signals of two closely coupled sensors near 270 deg in Fig. 8 where the wave structures are 180 deg out of phase.

Unsteady pressure measurements at 105% corrected speed. Similar experiments were conducted at a rotor speed of 105% corrected design speed. In a first set of measurements, the bleed valve was closed and Fig. 9 depicts the unsteady pressure signals obtained from the circumferential sensor array in the vaneless space. The pressures are again nondimensionalized by the vaneless space inlet dynamic pressure. Note that one more pressure transducer was installed in the vaneless space at a circumferential angle upstream of the tongue of the volute shown in Fig. 3. As seen at 100% corrected speed, a spike again emerges about 10 rotor revolutions before surge.

Experiments were next conducted with the bleed valve open. Figure 9 on the right depicts the unsteady pressure measurements

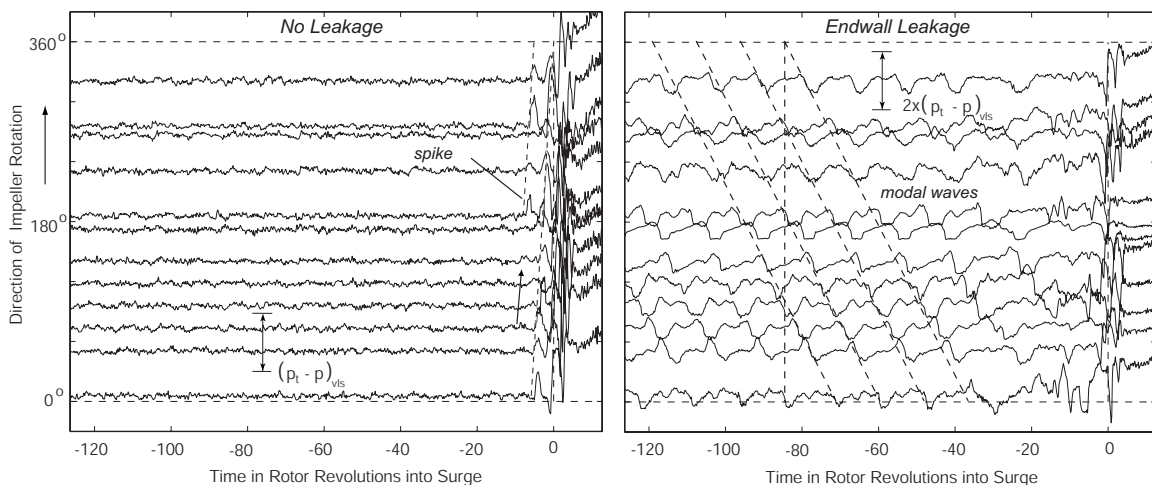


Fig. 9 Unsteady pressure traces in the vaneless space at 105% corrected speed: no leakage (left) and endwall leakage (right)—operating points correspond to the crosses shown in Fig. 10

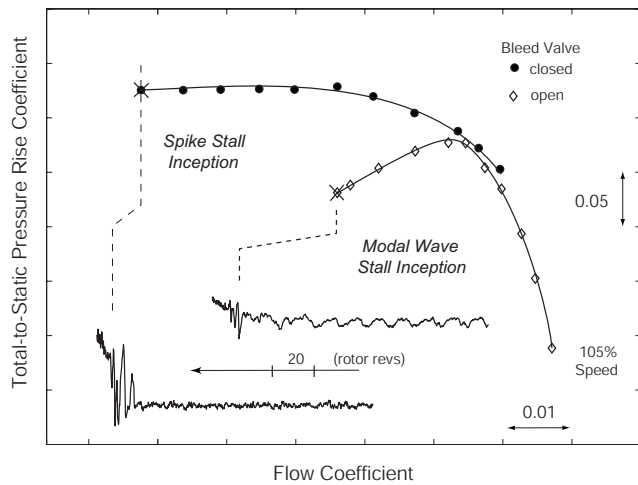


Fig. 10 Two paths into instability: spike and modal stall patterns in centrifugal compressor vaned diffusers

during a slow throttle ramp into surge. The compression system exhibits strong periodic fluctuations with a magnitude of about one vaneless space inlet dynamic pressure. This is about three times larger compared with the perturbations observed at 100% corrected rotor speed (Fig. 8). The amplitude of the fluctuations is large enough such that the nonlinearities of the compressor map are perceived. This is evidenced by the almost rectangular and saw-tooth type shape of the fluctuations. Further analysis of the time signals reveals that the compression system dynamics are dominated by a four-lobed prestall resonance that travels against the direction of impeller rotation, resembling a four-cell backward traveling rotating stall wave. A detailed discussion of the spatial structure of the stall precursors is given in a later section.

5 Spike and Modal Stall Patterns

According to Camp and Day [8], spikes occur in axial-flow compressors when the critical incidence is reached before the slope of the total-to-static-pressure increase characteristic of the stage changes from negative to positive ($\partial\psi/\partial\phi \leq 0$), and modal waves are observed when the peak of the total-to-static pressure increase characteristic ($\partial\psi/\partial\phi = 0$) is reached before critical incidence is exceeded. Although this criterion could not be fully validated here, the measured steady-state diffuser characteristics together with unsteady pressure data suggest a similar behavior for centrifugal compressors.

Figure 10 depicts the static pressure rise characteristic of the vaned diffuser at 105% corrected speed. Without endwall flow leakage, the static pressure rise characteristic plateaus before surge occurs (solid circles). When endwall flow leakage is present, the static pressure rise characteristic peaks and changes slope before the onset of surge (open diamonds). As discussed above, bleeding low momentum endwall flow enhances the diffusion in the vaneless space and destabilizes the semi-vaneless space. This suggests that, if the slope of the semi-vaneless space characteristic becomes zero before the peak of the overall diffuser static pressure rise characteristic (see also Figs. 4 and 6), modal waves emerge. The impeller characteristic (not shown) is not altered by the presence of the leakage flow and has a negative slope near the surge point.

In conclusion, the pre-production advanced high-speed centrifugal compressor stage investigated in this research exhibits an unsteady flow feature commonly observed in axial compressors. Short-wavelength precursors (spikes), traveling at roughly a quarter of the rotor speed in the direction of the impeller rotation, can emanate between the impeller and the vaned diffuser and lead to surge. The path to instability can change from spikes to modal

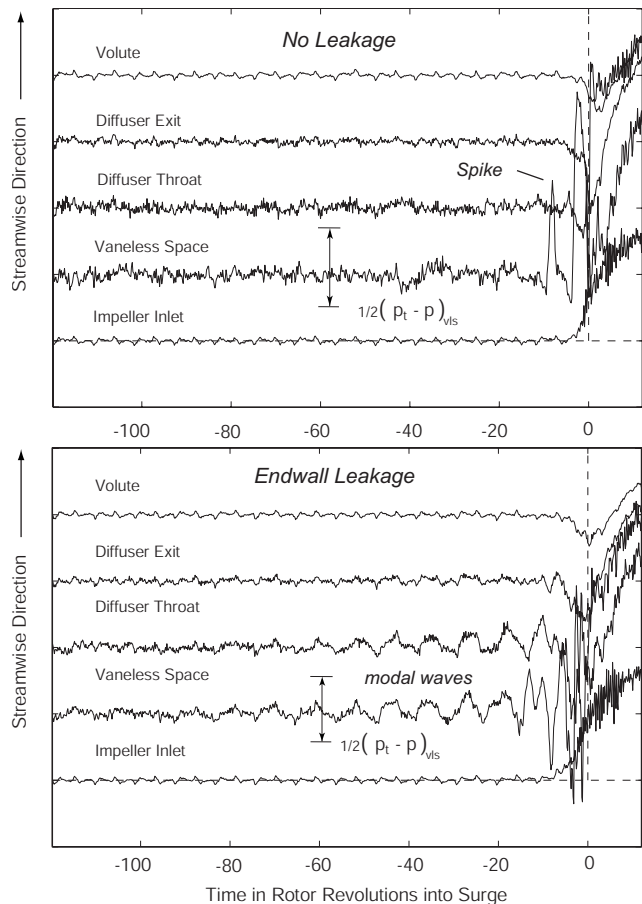


Fig. 11 Streamwise activity of stall precursors at 100% speed: no leakage (top) and endwall leakage (bottom)

waves by altering the matching of the impeller and the vaned diffuser. In the case investigated here, reducing the endwall blockage via flow leakage alters the compressor characteristic and loading distribution in the vaned diffuser and its subcomponents. This has a destabilizing effect on the compression system dynamics and is manifested by the growth of long-wavelength stall precursors. Further work is required to establish a generalized criterion and to fully understand the detailed flow mechanisms responsible for the change in compressor dynamic behavior.

6 Spatial Structure of Stall Precursors

Further analysis of the pressure signals shown in Fig. 9 on the right reveals that the wave fronts of a fourth spatial harmonic prestall wave travel against the direction of the impeller rotation at about -0.08 times rotor frequency (the period is about 12.5 rotor revolutions). The wave fronts of the four-lobed spatial periodicity are marked by the dashed lines. These are negatively sloped with respect to time, indicating backward traveling waves. A traveling wave energy analysis was conducted and confirmed the spatial wave shape and the direction and rate of wave rotation. This modal prestall behavior is markedly different from axial compressors, but similar observations were made in the NASA CC3 transonic centrifugal compressor with prismatic wedge vanes [7]. In the NASA machine, the impeller and the diffuser were much more closely coupled and the four-lobed prestall wave was measured to travel at -0.24 times rotor frequency. The diffuser static pressure rise characteristic of the NASA compressor changes slope from negative to slightly positive when surge is approached, in agreement with the suggested conditions necessary for modal waves as discussed above.

Streamwise activity of stall precursors. Figure 11 depicts unsteady pressure traces obtained from transducers located upstream of the impeller, in the vaneless space, at the diffuser throat, at the exit of the diffuser passage and in the volute during a stall ramp at 100% corrected rotor speed. The short-wavelength stall precursor is most dominant in the vaneless space as seen in the top plot for the case without flow leakage. No activity is observed upstream of the impeller, at the exit of the vaned diffuser and in the volute.⁵ Near the diffuser throat, lower amplitude spike-like features are visible indicating that the spikes are confined to the vaneless space.

With endwall leakage present, the modal waves are most pronounced in the vaneless space and near the diffuser throat. This is in agreement with past observations and measurements in the NASA CC3 high-speed centrifugal compressor [7].

Model assessment of long-wavelength prestall waves. A previously developed unsteady centrifugal compressor model [7] was used to assess the dynamic behavior of the compression system. The model is based on the idea that rotating stall and surge are the mature forms of small amplitude flow perturbations, which are the natural resonances of oscillation in the compression system. These small disturbances grow when background flow conditions are such that their damping becomes negative and the compression system drops into an unstable state, rotating stall, or surge. For each of the compression system components (modules) depicted in Fig. 12 a reduced-order dynamic description of the unsteady flow field is found by making use of the two-dimensional long-wavelength nature of the flow field perturbations. In particular, the following assumptions are made: (1) the amplitude of the unsteady flow perturbations is small, (2) the small amplitude flow perturbations are assumed incompressible,⁶ (3) Reynolds number effects are ignored, and (4) the effects of viscosity and heat transfer outside the blade rows are neglected. To examine the behavior of unsteady small amplitude perturbations to a known steady-state flow field, for each system component the set of governing equations is linearized and solved analytically. Each of the flow field quantities is decomposed into a steady component (the steady-state flow field solution obtained from a mean flow calculation) and an unsteady small amplitude perturbation. For example, the static pressure can be written as

$$p(r, \theta, t) = \bar{p}(r) + \sum_{n=0}^{\infty} \text{Re}\{\tilde{p}_n(r, t) \cdot e^{jn\theta}\} \quad (3)$$

where the unsteady perturbations are decomposed into their circumferential spatial harmonics n . In this description, $\tilde{p}_n(r, t)$ is the n th harmonic spatial Fourier coefficient. With this, the closed solutions for the flow field perturbations are then cast into a form suitable to be linked to other components. Imposing boundary conditions at the inlet and the exit of the compression system, an eigenvalue problem can be formulated and is then solved. Each complex eigenvalue $s = \sigma_n - j\omega_n$ corresponds to a prestall wave of sinusoidal shape. The subscript n denotes that the wave has n lobes on the circumference (Eq. (3)). The wave rotates around the annulus at a rotation rate ω_n , the imaginary part of the eigenvalue. The real part of the eigenvalue σ_n is the growth rate and indicates whether the wave amplitude grows in time and the resonance is unstable (positive growth rate), or decays in time and the resonance is thus stable (negative growth rate). A more detailed description of the unsteady centrifugal compressor model can be found in Ref. [7].

It is important to point out that the model is not appropriate for short length scale spike-type precursors and that it is only used here to assess the long-wavelength prestall waves. The hypothesis

⁵The very low amplitude systematic and periodic oscillation is due to electronic noise.

⁶Although incompressible flow is assumed in the dynamic model, the necessary mean flow calculation used as input to the model is compressible.

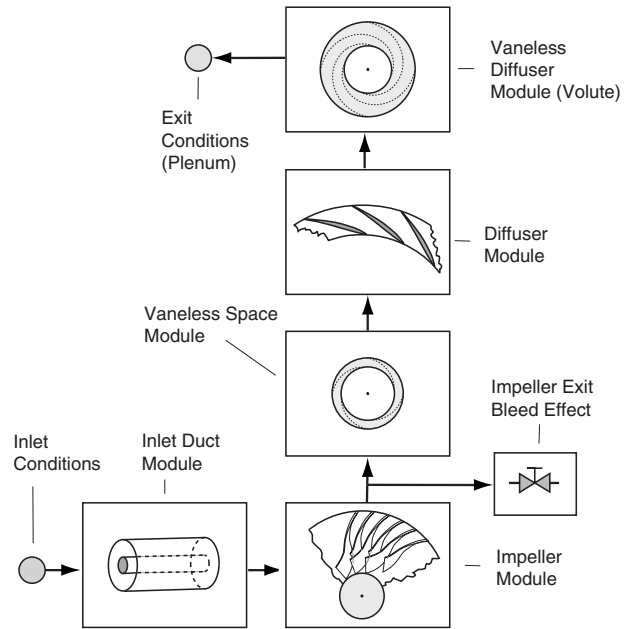


Fig. 12 Unsteady centrifugal compressor model including the effects of endwall flow leakage

is that four-lobed modal waves ($n=4$) emerge when leakage flow is present and that the waves are damped out when the bleed valve is closed, indicating that in reality other mechanisms (in this case spikes) are at play and govern the stability limit.

A compressible mean flow calculation was conducted including the effects of endwall bleed flow in the vaneless space. From this analysis the steady-state impeller and diffuser performance characteristics were extracted and compared against the measurements. Figure 13 depicts the overall total-to-static pressure rise characteristic of the compressor. The no leakage case is marked by the solid line and the case with endwall leakage is marked by the dashed line. The crosses and circles denote experimental data and the solid and dashed lines are obtained from the mean-line calculation. The unsteady centrifugal compressor model was run at two different operating conditions marked by the diamonds. Prestall modes up to a harmonic number of $n=5$ were computed although periodic oscillations of the fifth and higher harmonic waves were

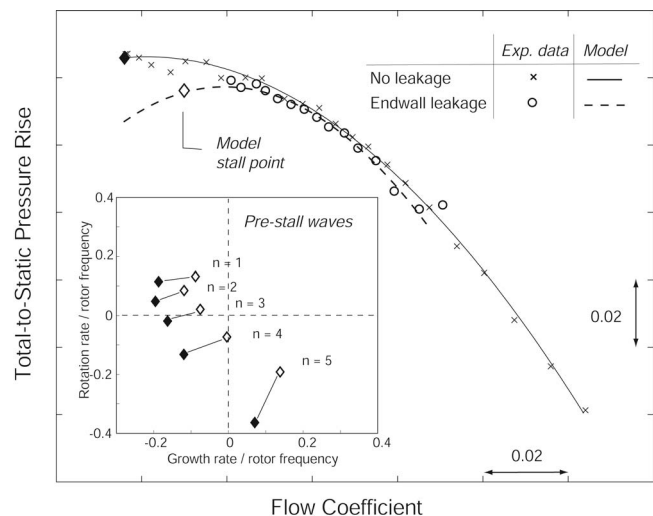


Fig. 13 Calculated long-wavelength perturbations: backward traveling four-lobed wave sets stability limit

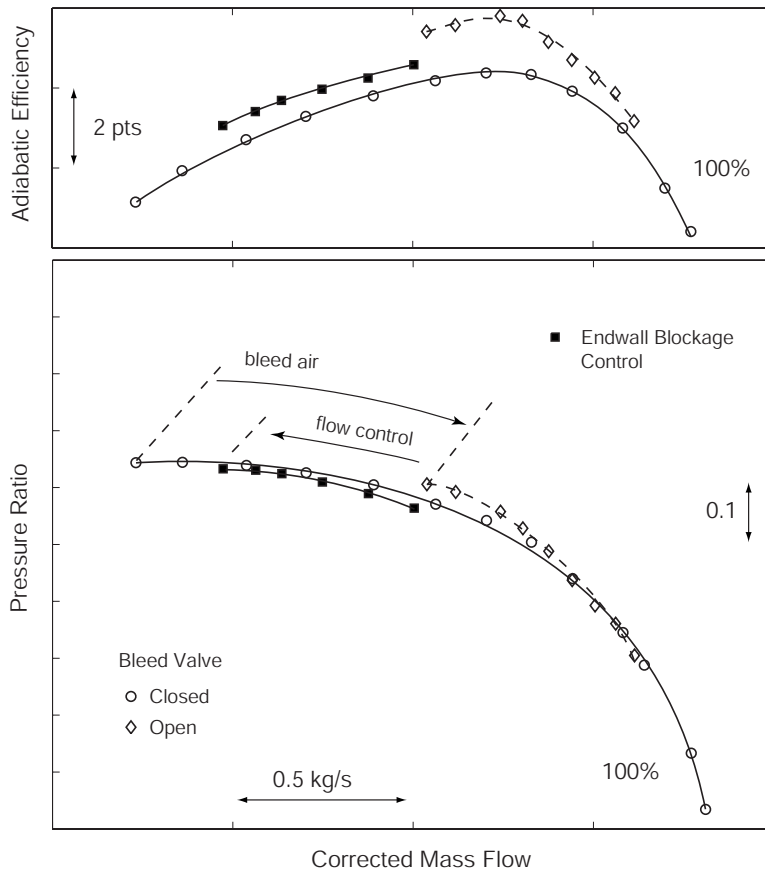


Fig. 14 Effect of self-regulated endwall blockage control on centrifugal compressor performance and stability

not observed in the experiment.⁷ This is similar to the observations made in the NASA CC3 high-speed centrifugal compressor and reported in Ref. [7].

The open diamond indicates the model stall point at which the fourth spatial harmonic mode is neutrally stable (zero growth rate), shown in the inset. Note that the calculated rotation rate of the four-lobed wave is about -0.08 times the rotor frequency, consistent with the experimental measurements plotted in Fig. 9 on the right. The unsteady compressor model was also run without flow leakage at the impeller exit for the lowest measured flow coefficient indicated by the solid black diamond. The calculations show that the fourth spatial harmonic prestall wave yields a negative growth rate and is thus damped out. Modal waves are absent in the unsteady pressure measurements of Fig. 9 on the left, in agreement with the calculations.

7 Endwall Blockage Control

A large number of surge control schemes in centrifugal compressors can be found in the literature, and an extensive review can be found in Ref. [12]. A more recent method reported by Skoch [13] involved injection of air through the diffuser hub surface. The experimental work showed that the compressor flow range did not improve and generally deteriorated as injection rate was increased. However, some flow range improvement was achieved at zero injection due to installation effects of the injector openings.

⁷This suggests that the spatial flow field resolution of the model is limited to the fourth harmonic, indicating that, for the semi-actuator disk assumption to hold, the circumferential length scale of the flow nonuniformity must cover at least two blade pitches within half a wavelength.

The research described in the present paper suggests that endwall blockage in the vaneless space of highly-loaded centrifugal compressors can strongly influence the performance and the stability of the compression system. Based on this, a simple self-regulating endwall blockage control scheme was designed and implemented in the test compressor. The goal was to improve both the stable operating range and the efficiency of the compressor including the endwall blockage control scheme.

A small amount of air, about 0.5% of the compressor mass flow at highly-loaded compressor operating conditions, was recirculated from the volute to the vaneless space and was injected through eight quadratic slots from the compressor shroud, as shown in Fig. 3. The projected slot length was 5.5% of the impeller exit radius and the injection angle was 30 deg. The recirculated air was first fed to a toroidal collector.⁸ Each of the eight injection slots was connected to the collector via supply tubes. The flow rate through the slots was individually controlled by needle shutoff valves. The leakage Mach number through the control slots was a small fraction of the core flow Mach number in the vaneless space generating a controlled amount of endwall blockage. The injection Mach number was set by the flow resistance in the needle shutoff valve.

The working hypothesis is that at highly-loaded conditions near surge, the pressure rise from vaneless space to volute drives a low momentum leakage flow through the slots on the shroud side into the vaneless space. As illustrated in Fig. 5 on the left, the increased blockage reduces the diffusion in the vaneless space. This in turn enhances the dynamic stability of the compression system

⁸The ducting and collector systems were designed using an acoustic flow model to avoid potential resonance phenomena.

and potentially extends the stable operating range. At lower loading levels, the injected flow is reduced such that the recirculation air is self-regulated (the valves need not be adjusted). Given that at all operating conditions leakage flow on the hub side through the labyrinth seal is present, the net endwall blockage in the vaneless space is reduced near design conditions potentially improving compressor efficiency.

Self-contained endwall blockage control results. Experiments were conducted in the same compressor in the modified SUMA centrifugal compressor test facility at ABB Turbo Systems. All of the eight needle valves were set to the same flow resistance such that the total injection flow was about 0.5% of the compressor design mass flow. This is about equal the amount of the endwall leakage flow through the labyrinth seal. Figure 14 shows the measured compressor performance at 100% corrected speed. The self-regulating endwall blockage control scheme yields a 75% recovery of the surge-margin loss due to bleed flow at impeller exit. The overall compressor adiabatic efficiency is improved by about one point compared with the base line case with the bleed valve closed. Although the same amount of mass flow is bled as is injected, the improvement in efficiency with endwall blockage control is less than that with bleed flow only. This is due to the higher temperature and entropy of the recirculated air as compared with the bleed air.

8 Summary and Conclusions

A research program was carried out on a pre-production, 5.0 pressure ratio, high-speed centrifugal compressor stage of advanced design. The investigations showed that bleed air can significantly reduce the stable flow range. Compressor rig experiments, using an array of unsteady pressure sensors and a bleed valve to simulate a typical turbocharger environment, suggest that the path into compression system instability is altered by the bleed flow. Without bleed flow, the prestall behavior is dominated by short-wavelength disturbances, or so called spikes, in the vaneless space between the impeller and the vaned diffuser. Introducing bleed flow at the impeller exit reduces endwall blockage in the vaneless space and destabilizes the highly-loaded vaned diffuser. The impact is a 50% reduction in stable operating range. The altered diffuser characteristic reduces the compression system damping responsible for long-wavelength modal prestall behavior. A four-lobed backward traveling rotating stall wave is experimentally measured, in agreement with calculations obtained from a previously developed dynamic compressor model. It is conjectured that the path into instability is governed by spikes or modes

depending on whether the slope of the semi-vaneless space characteristic becomes zero before the peak of the overall diffuser static pressure increase characteristic is reached. Further work is required to establish a generalized criterion and to fully understand the detailed flow mechanisms responsible for the change in compressor dynamic behavior. Finally, a self-contained endwall blockage control strategy was employed successfully recovering 75% of the loss in surge-margin due to bleed flow and yielding a one point increase in adiabatic compressor efficiency.

Acknowledgment

The authors are greatly indebted to H. Küpfer, P. Hoffmann, and Dr. G. Fitzky for their help in compressor testing; Dr. M. Jung and Dr. A. Weickgenannt for setting up the high-response sensor system; R. Senn for his invaluable help in making the endwall blockage control design a reality; and, H.-P. Michel for getting the hardware ready for testing. The pressure transducers used in the experiments were provided by Kistler Instrumente AG. The support and the technical assistance by J. von Berg and T. Walter are gratefully acknowledged.

References

- [1] Rodgers, C., 2003, "High Specific Speed, High Inducer Tip Mach Number, Centrifugal Compressor," ASME Paper No. GT2003-38949.
- [2] Emmons, H., Pearson, C., and Grant, H., 1955, "Compressor Surge and Stall Propagation," *Trans. ASME*, **77**, pp. 455–469.
- [3] Cumpsty, N., 2004, *Compressor Aerodynamics*, Krieger, Malabar, FL.
- [4] Japikse, D., 1996, *Centrifugal Compressor Design and Performance*, Concepts ETI, Wilder, VT.
- [5] Lawless, P., and Fleeter, S., 1993, "Rotating Stall Acoustic Signature in a Low-Speed Centrifugal Compressor, Part II: Vaned Diffuser," ASME Paper No. 93-GT-254.
- [6] Oakes, W., Lawless, P., and Fleeter, S., 1999, "Instability Pathology of a High Speed Centrifugal Compressor," ASME Paper No. 99-GT-415.
- [7] Spakovszky, Z., 2004, "Backward Traveling Rotating Stall Waves in Centrifugal Compressors," *ASME J. Turbomach.*, **126**, pp. 1–12.
- [8] Camp, T., and Day, I., 1998, "A Study of Spike and Modal Stall Behavior in a Low-Speed Axial Compressor," *ASME J. Turbomach.*, **120**, pp. 393–401.
- [9] Reneau, L., Johnston, J., and Kline, S., 1967, "Performance and Design of Straight, Two-Dimensional Diffusers," *ASME J. Basic Eng.*, **89**, pp. 141–150.
- [10] Greitzer, E., Tan, C., and Graf, M., 2005, *Internal Flow: Concepts and Applications*, Cambridge University Press, Cambridge, England.
- [11] Tryfonidis, M., Etchevers, O., Paduano, J., Epstein, A., and Hendricks, G., 1995, "Pre-Stall Behavior of Several High-Speed Compressors," *ASME J. Turbomach.*, **117**, pp. 62–80.
- [12] Botros, K., and Henderson, J., 1994, "Developments in Centrifugal Compressor Surge Control: A Technology Assessment," *ASME J. Turbomach.*, **116**, pp. 240–249.
- [13] Skoch, G., 2005, "Experimental Investigation of Diffuser Hub Injection to Improve Centrifugal Compressor Stability," *ASME J. Turbomach.*, **127**, pp. 107–117.

Validation of MISES Two-Dimensional Boundary Layer Code for High-Pressure Turbine Aerodynamic Design

Philip L. Andrew
Harika S. Kahveci

GE Energy,
Greenville, SC 29615

Avoiding aerodynamic separation and excessive shock losses in gas turbine turbomachinery components can reduce fuel usage and thus reduce operating cost. In order to achieve this, blading designs should be made robust to a wide range of operating conditions. Consequently, a design tool is needed—one that can be executed quickly for each of many operating conditions and on each of several design sections, which will accurately capture loss, turning, and loading. This paper presents the validation of a boundary layer code, MISES, versus experimental data from a 2D linear cascade approximating the performance of a moderately loaded mid-pitch section from a modern aircraft high-pressure turbine. The validation versus measured loading, turning, and total pressure loss is presented for a range of exit Mach numbers from ≈ 0.5 to 1.2 and across a range of incidence from -10 deg to $+14.5$ deg relative to design incidence.

[DOI: 10.1115/1.2988165]

Keywords: MISES, boundary layer method, 2D cascade, validation, transonic, off-design, HPT, incidence, loss, CFD

1 Introduction

Customers who purchase gas turbines for power generation, propulsion, and mechanical drive applications are impacted by operating costs from three principal sources: fuel burn, operation and maintenance, and initial or product cost. The amount of fuel consumed is a direct function of component efficiency. Initial costs are minimized by increased component loadings via fewer stages and by fewer blades per stage.

These economic forces provide the impetus for aerodynamic design tools that can accurately predict the performance of highly loaded turbomachinery components over a wide range of operating conditions. Further, the requirement for ever-increasing levels of engineering productivity dictates that these tools be computationally fast such that many design iterations of numerous design sections can be evaluated over a wide range of operating conditions. This paper seeks to determine the reliability of a popular 2D boundary method for the prediction of airfoil loading, exit flow angle, and total pressure loss across a wide range of incidences and exit Mach numbers corresponding to a typical gas turbine operation in customer service.

MISES, a blade-to-blade boundary layer solver developed by Drela and Youngren [1], has been used extensively in turbomachinery design. Validation studies in the open literature comparing MISES predictions to experimental data have been infrequent but have generally shown MISES to be a reliable predictor of turbomachinery performance. One such study was that of Schreiber et al. [2], which investigated the transition location on a compressor cascade of controlled-diffusion airfoils for different turbulence levels and Reynolds numbers. Prior investigations had confirmed the ability of the transition model within MISES, known as the Abu-Ghannam and Shaw correlation [3], to provide accurate predictions of transition for low turbulence levels ($<2\%$). The study

of Schreiber et al. [2] showed that the transition location moves upstream on compressor blades for higher turbulence levels and Reynolds numbers. Although an uncertainty of 5% chord in the location of transition was reported, the position of laminar separation and reattachment was found to be quite accurate.

In addition, Sieverding et al. [4] developed a design system for the blade sections of axial compressors, wherein they utilized MISES as the flow solver, in addition to a parametric geometry definition method and an optimization technique. They reported longer convergence times for high Mach number cases, consistent with the experience of the present authors. Detailed comparisons of measured versus predicted loss, turning, and loading were not provided.

Sondergaard et al. [5] applied MISES in an increased blade pitch study of a low-pressure turbine, noting instances wherein MISES did not predict non-reattaching separation and did predict reattachments that were not observed experimentally.

Garzon and Darmofol [6,7] used MISES for examining the sensitivity of compressor airfoil performance to geometric uncertainty, noting the execution speed of MISES as particularly suitable to such studies.

Parvizinia et al. [8] investigated the aerodynamic performance of a low-pressure steam turbine supersonic tip section profile via a cascade experiment and numerical calculations using MISES. Comparisons of flow turning, loss, and loading distribution were provided. These authors noted a lack of accurate modeling of the thickened and separated boundary layer at an extreme off-design condition but a good agreement at the design point. They concluded that MISES is an appropriate tool for computing the flow field within a steam turbine flow passage.

Bons et al. [9] recently applied MISES in the design of low-pressure turbine blading of a Zweifel coefficient of 1.34, where a 17% increase in loading over an industry-standard airfoil was demonstrated using integrated flow control. The transition model was modified for this study. Praisner and Clark [10] argued that the Abu Ghannam and Shaw [3] model used in MISES to predict boundary layer transition is inappropriate for turbomachinery design and that the alternative e^n formulation available within MISES

Contributed by the International Gas Turbine Institute of ASME for publication in the JOURNAL OF TURBOMACHINERY. Manuscript received April 5, 2008; final manuscript received April 21, 2008; published online April 10, 2009. Review conducted by David Wisler. Paper presented at the ASME Turbo Expo 2007: Land, Sea and Air (GT2007), Montreal, QC, Canada, May 14–17, 2007.

is also not relevant since bypass mechanisms dominate transition in a turbomachinery environment.

As an alternative to the standard transition models available within MISES, the transition model of Praisner and Clark [10] was implemented for the first time outside of a RANS-based design system into the inviscid flow solver of Dorney and Davis [11] in order to predict transition onset locations. Pointwise trips were then applied within MISES to force transition at the onset locations; this process was successful in predicting transition, separation, and reattachment locations.

2 The 2D Flow Solver, MISES

MISES, the acronym for Multiple Blade Interacting Streamtube Euler Solver, is a blade-to-blade method developed by Drela and Youngren of MIT [1] for cascade viscous flow analysis, which has been used successfully to optimize compressor and turbine airfoils. In it, the integral boundary layer equations for boundary layer and wake development are solved for by a coupled inviscid/viscous interaction scheme. This interactive package consists of a series of tools for grid generation and initialization, flow analysis, plotting, and interpretation of results.

The code applies the Kutta condition on a blunt trailing edge rather than modeling the trailing edge flow physics in detail. Inviscid analysis is carried out using the Euler equations, whereas the boundary layer equations are used in addition to the Euler equations for viscous flow analysis. The Newton–Raphson technique is used to solve the resulting nonlinear system of equations, and the Abu-Ghannam and Shaw [3] model is used for the prediction of boundary layer transition. No material changes to the original simulation approach have been implemented for the present study.

An inherent disadvantage of this modeling approach is that the Kutta model underpredicts losses arising in the wake region, and, relatedly, it does not predict base pressure at the trailing edge. MISES also suffers from convergence challenges for some transonic and supersonic cases.

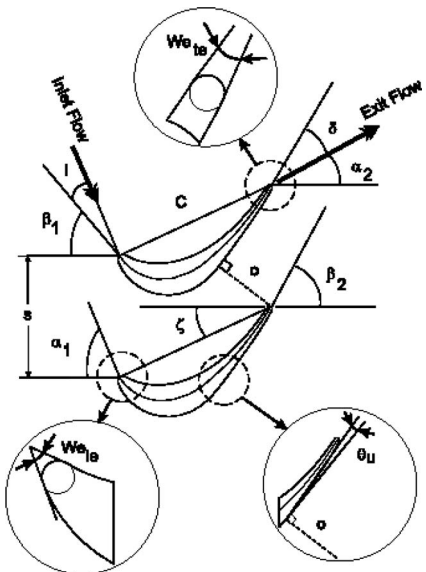
In general, however, MISES is a valuable design tool that enables the rapid evaluation and optimization of section geometries across a wide range of operating conditions. It is also easily integrated into an existing design system. The balance of this paper is provided to quantify the accuracy of those predictions of total pressure loss, turning, and aerodynamic loading in a high-pressure turbine cascade flow.

3 Validation Procedure

Experimental turbine linear cascade data obtained by Jouini, Sjolander, and Moustapha [12] and a more recent study by Coriveau and Sjolander [13] were used in this validation study. The front-loaded midspan section of a high-pressure aircraft turbine blade, designated as HS1A, was the baseline geometry corresponding to the majority of the validation comparisons presented here. A second blade geometry was also modeled in order to evaluate the sensitivity of MISES predictions to slight changes in airfoil geometry. This second blade geometry, designated as HS1B, differed relative to HS1A in terms of leading edge profile shape and in terms of design incidence. The other related studies of these authors are listed as Refs. [14–17]. Blade geometry is provided in Ref. [12]. The cascade parameters can be found in Table 1.

Blade loading, loss, axial velocity density ratio (AVDR), and turning experimental data were provided in Refs. [12,13] for the following discrete values of incidence: -10.0 deg, 0.0 deg, $+4.5$ deg, $+10.0$ deg, and $+14.5$ deg. These incidences are relative to a design incidence of -4.5 deg for geometry HS1A. The experimental Reynolds number varied from 4×10^5 to 1×10^6 , whereas the exit Mach number varied from 0.5 to 1.2.

Table 1 Blade geometric parameters for HS1A and HS1B [12]



Cascade parameters	HS1A	HS1B
Chord length, C	40.0 mm	40.0 mm
Axial chord, Cx	36.98	36.98
Blade span, H	61.0 mm	61.0 mm
Blade spacing, s	29.14	29.14
Trailing edge thickness, t	1.25 mm	1.25 mm
Aspect ratio, H/C	1.525	1.525
Leading metal angle, β_1	50.5 deg	61.0 deg
Trailing metal angle, β_2	59.0 deg	59.0 deg
Leading edge wedge angle, We_{le}	38.0 deg	38.0 deg
Trailing edge wedge angle, We_{te}	6.0 deg	6.0 deg
Maximum thickness-to-chord ratio	0.196	0.182
Design incidence i_{des}	-4.5 deg	-15.0 deg
Stagger angle, ζ	25.1 deg	24.7 deg
Throat opening, o	15.3 mm	15.3 mm
Unguided turning, θ_u	11.5 deg	11.5 deg

Boundary conditions for MISES cases were set to match the experimental cascade pressure ratio, Reynolds number, and incidence. Each MISES run was achieved in a time range varying from a few seconds to a couple minutes. The results of experiments performed on the two blade geometries HS1A and HS1B made it possible to evaluate the sensitivity of MISES in detecting small changes in the blade shape. In addition, the utilization of the second set of data [13] helped us to understand how well MISES captures the effect of Reynolds number on performance.

3.1 Grid Topology. The offset I -type grid was applied at the inlet (designated as t -type in MISES), whereas for the downstream region the periodic H -type grid (f -type) was used (Fig. 1). Grid density is greater for the t -type grid. It is very nearly orthogonal compared with the f -type and also requires more streamlines, which end up in a more accurate solution. However, it takes more time to converge, and convergence is somewhat more problematic. The grid type effect on performance matching will be discussed in the next section in greater detail.

Turbulence intensity was set at 4% for all cases, as measured in the experiment. Abu-Ghannam and Shaw [3] concluded that turbulence level does not affect bypass transition as long as it is above 3%. Both the transition model implemented in the code and the turbulence level are controlled by the MISES parameter “ncrit.” With a positive ncrit value, the amplification factor for the transition model is fixed. A negative ncrit serves to specify the freestream turbulence level. In this study, ncrit is set to -4.0 ,

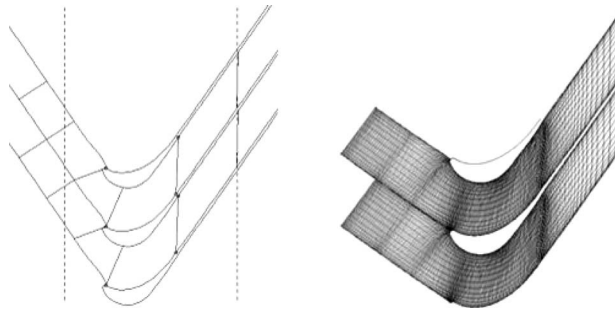


Fig. 1 Grid type selection in MISES

which sets the inlet turbulence intensity to 4.0%.

The measurement plane for experimental traverses of low angle and loss was located 40% of the true chord downstream of the cascade trailing edge, which is about 16 mm or 0.63 in. Loss calculations within MISES were performed at this same location. The MISES version 2.58 makes available to the user the choice of the desired axial location for the loss calculation. In the experiment, the total pressure loss coefficient (w_t) is calculated as

$$W_t = (P_{01} - P_{02}) / (P_{02} - P_2)$$

MISES calculates the loss coefficients ξ_1 and Y_p , which are defined as follows:

$$\xi_1 = (P_{01} - P_{02}) / (P_{01} - P_2)$$

$$W_t \approx Y_p = \xi_1 / (1 - \xi_1)$$

Hence, a comparison of loss predictions with experimental results is based on W_t and Y_p in the discussions to follow.

4 Results and Discussion

4.1 Influence of Grid Type. As shown in Fig. 2, the choice of grid topology was found to have little effect on loading distribution. Here, calculated loading using three types of grid topology is compared with measured loading for the case of design incidence. The experimental uncertainty plotted about each data point was estimated to be about ± 0.02 by Jouini et al. [12]. None of the topologies capture the leading edge loading distribution within the experimental uncertainty, with the largest influence of grid being on the suction surface shock location.

The t - f -type grid provided the best convergence rate for this particular case, as well as for the other cases in general. For this reason, all subsequent validation comparisons are carried out with the t - f -type grid.

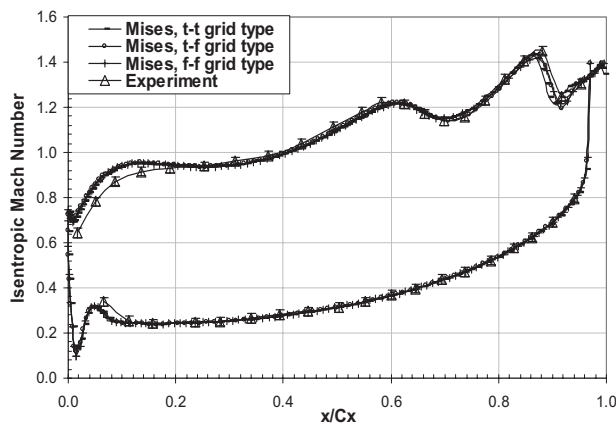


Fig. 2 Blade loading at $M_2=1.14$ and at design incidence ($i_e = 0$ deg) with different type grids

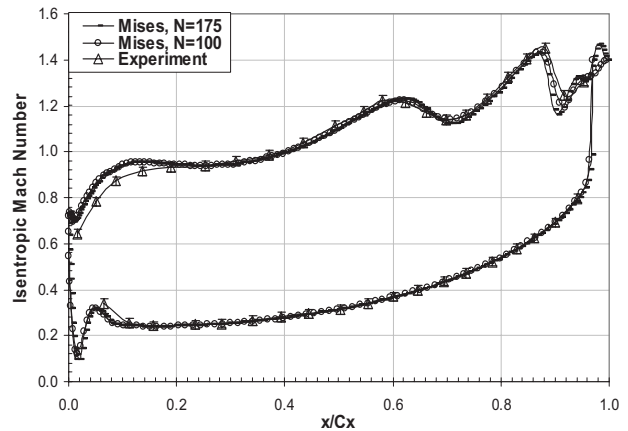


Fig. 3 Blade loading at $M_2=1.14$ and at design incidence ($i_e = 0$ deg) with different node counts

Table 2 Grid properties

Grid type		Number of points	
Inlet	Outlet	Inlet	Outlet
t	f	30	30
Number of streamlines		Number of surface nodes	
20		100	

4.2 Grid Density. Figure 3 contains a comparison of measurement versus prediction for two cases of grid density, namely, 100 and 175 surface nodes. The MISES predictions are shown to be generally within the experimental uncertainty and generally indistinguishable from each other. A grid with 100 nodes was used for subsequent cases of this study, in the interest of improved convergence times. A summary of grid properties used in this study can be found in Table 2.

4.3 Incidence. Figures 4(a)–4(g) characterize the predictive capability of MISES for loading distributions as a function of incidence angle and exit Mach number. Figures 4(a)–4(c) demonstrate the influence of a Mach number sweep from a subsonic level of 0.96 to the near-design level of 1.06 and finally to Mach 1.14, all at the effective incidence of 0 deg.

For the subsonic Mach number case of Fig. 4(a), the loading distribution is captured within the experimental uncertainty of the measurement, except for local areas near the leading edge and near the suction surface shock. At the transonic near-design point case of Fig. 4(b), the suction surface shock capturing is not as accurate as in the subsonic case of Fig. 4(a) or the higher Mach number case of Fig. 4(c).

Figures 4(d) and 4(e) characterize the predictive capabilities of MISES at more extreme incidence levels of +10 deg and +14.5 deg, respectively, at exit Mach numbers fairly close to the design level. MISES does a reasonably good job of predicting loading at these extreme conditions overall, while again exaggerating the loading near the leading edge.

Several of the above figures have indicated a mismatch between measurement and prediction at the leading edge region, which could be associated with uncertainty in the cascade incidence angle of ± 0.5 deg [12]. In order to understand the robustness of MISES to incidence changes, a sensitivity analysis was performed for two nominal incidence levels, one at design incidence and the other at +4.5 deg. Figure 4(f) contains a sweep of loading distributions calculated by MISES for three incidence angles ranging from the experimental value of 0 deg through -2 deg. The largest influence of this incidence change was confined to the leading edge region. The value of the MISES-specified incidence that

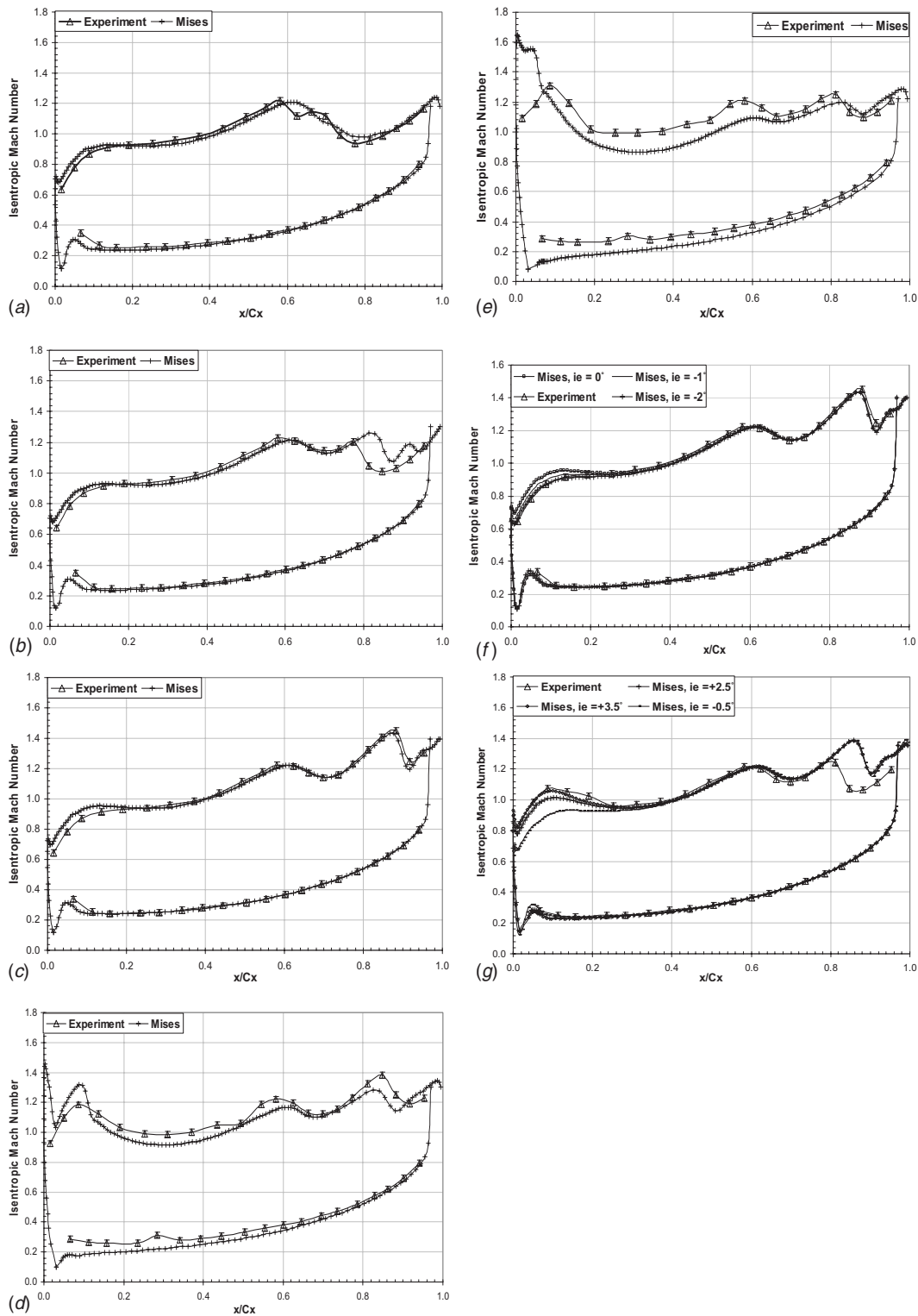


Fig. 4 (a) Blade loading at the design incidence ($i_e=0$ deg) for $M_2=0.96$. (b) Blade loading at the design incidence ($i_e=0$ deg) for $M_2=1.06$. (c) Blade loading at design incidence ($i_e=0$ deg) for $M_2=1.14$. (d) Blade loading around the design exit Mach number ($M_2=1.08$) with an incidence level of +10.0 deg. (e) Blade loading at the design exit Mach number ($M_2=1.05$) with an incidence level of +14.5 deg. (f) Incidence sensitivity study around the design incidence ($i_e=0$ deg, $M_2=1.14$). (g) Incidence sensitivity study around the incidence level of +4.5 deg, $M_2=1.12$.

matched the experimental data most closely can be observed to be -2 deg along both surfaces. Prior to 7% of the chord, there are no experimental data available for comparison.

For the incidence level of +4.5 deg, the best match between

MISES and experimental data is at an incidence of +3.5 deg along the suction side and at -0.5 deg along the pressure side, as shown in Fig. 4(g). Detailed angle clarifications are provided in Tables 3 and 4.

Table 3 Angles for design incidence sensitivity study

α_{MISES} (deg)	$\alpha_{MISES} - \alpha_{expt}$ (deg)	β_1 (leading metal angle) (deg)	i_{des} (deg)	i_e (deg)
46	0	50.5	-4.5	0
45	-1	50.5	-4.5	-1
44	-2	50.5	-4.5	-2

Table 4 Angles for incidence level +4.5 deg sensitivity study

α_{MISES} (deg)	$\alpha_{MISES} - \alpha_{expt}$ (deg)	β_1 (leading metal angle) (deg)	i_{des} (deg)	i_e (deg)
49.5	+3.5	50.5	-4.5	+3.5
48.5	+2.5	50.5	-4.5	+2.5
45.5	-0.5	50.5	-4.5	-0.5

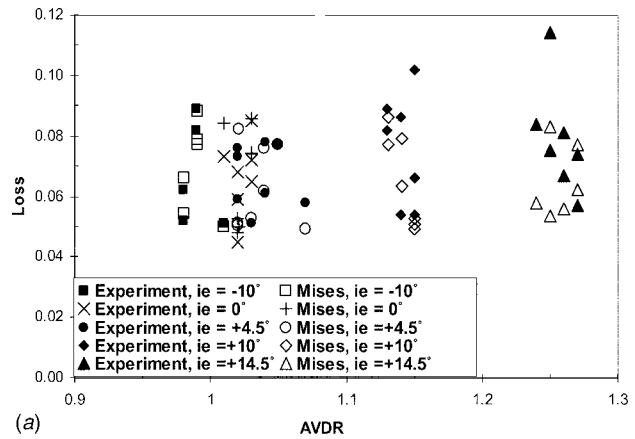
4.4 Axial Velocity Density Ratio (AVDR). The axial velocity density ratio is defined as the ratio of the mass flow rates per unit area at the inlet and the outlet of the cascade [12]. In MISES, this corresponds to the area ratio of the stream tube at the inlet and exit boundary condition planes. In the MISES runs described throughout this study, AVDR was an input parameter generally specified at the experimentally derived values for each case.

Figure 5(a) shows that MISES was generally successful in maintaining the specified (experimental) level of AVDR. The data and predictions are nicely grouped within corresponding AVDR levels. AVDR can be observed to trend higher with elevated levels of incidence. How well the profile losses were predicted will be discussed in detail subsequently.

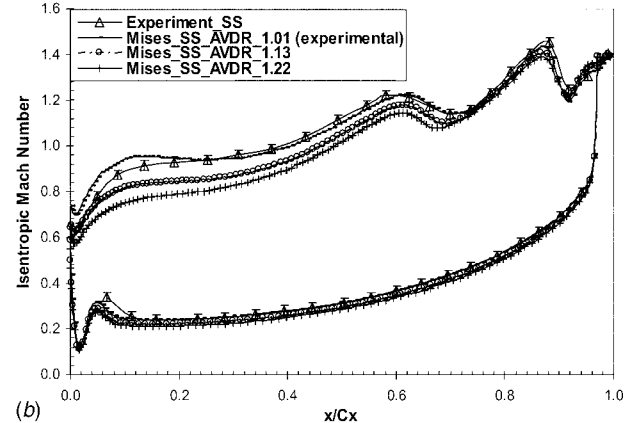
The influence of the specified AVDR on predicted versus measured loading distribution is presented via the sensitivity analysis of Figs. 5(b) and 5(c), wherein the experimental uncertainty in AVDR is plotted as ± 0.02 from Ref. [12]. In these figures, the blade loading is analyzed at two different incidence levels, one at design incidence and one at an off-design incidence of +14.5 deg. Both cases are in the supersonic flow regime, with comparable exit Mach number values. The observation from these comparisons is that the closest match to experimental data occurs in the cases where AVDR was specified in MISES at the experimentally derived level. Further, the influence of AVDR is more significant on the suction surface, as compared with the pressure surface. As can be deduced from Fig. 5(a), AVDR trends higher with higher incidence levels; an analogous trend can be observed from Figs. 5(b) and 5(c). The match with experimental data for a low incidence level is the best, with the lowest AVDR among the given range of AVDR values. Likewise, for a high incidence level, the highest AVDR in the range gives the best match. The lowest and highest AVDRs are the corresponding experimental values for low and high incidences.

4.5 Exit Mach Number, M_2 . As mentioned previously, one of the input parameters to MISES is the boundary condition of the total-to-static pressure. MISES calculates the resulting exit Mach number, which compared well to the experimental value for all cases, as shown in Fig. 6. Here, ΔM_2 is calculated as $(M_2(MISES) - M_2(expt)) / M_2(expt)$. Generally, the error in predictions is within 1%. Further, the exit Mach number calculated by MISES running to the Pt/Ps boundary condition was observed to match the measured exit Mach number within the experimental uncertainty of ± 0.02 , as provided in Ref. [12].

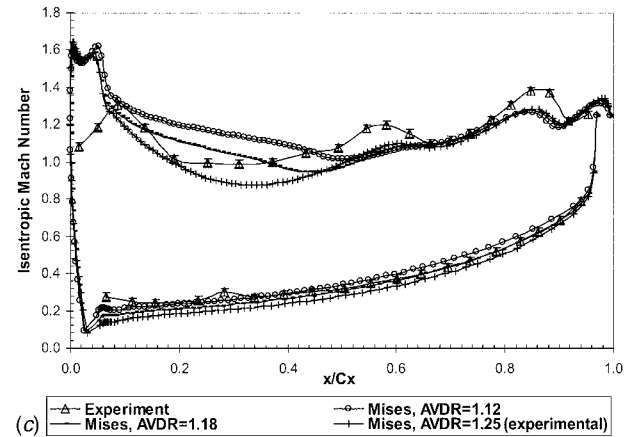
4.6 Exit Angle, α_2 . Figures 7(a)–7(c) contain comparisons of measured exit flow angles to those computed by MISES on a percentage difference basis wherein the experimental uncertainty for flow angles was estimated as ± 0.5 deg in Ref. [12].



(a)



(b)



(c)

Fig. 5 (a) The effect of AVDR on blade performance. (b) Sensitivity to AVDR on blade loading at low incidence level ($i_e = 0$ deg, $M_2 = 1.14$). (c) Sensitivity to AVDR on blade loading at high incidence level ($i_e = +14.5$ deg, $M_2 = 1.10$).

Figure 7(a) shows how the error in angle varies for different incidence cases studied in this paper. Here, $\Delta \alpha_2$ is calculated as $(\alpha_2(MISES) - \alpha_2(expt)) / \alpha_2(expt)$. Generally, the error is within 1% for -10 deg, 0 deg, and +4.5 deg incidence levels. MISES predictions were generally within the experimental uncertainty up to an incidence level of +4.5 deg, beyond which MISES tended to underpredict the exit flow angle by up to 2 deg, particularly for the cases combining the more extreme Mach number and incidence conditions. Additional detail pertaining to these comparisons may be obtained from Tables 5 and 6. The variation in exit angle with Mach number will be discussed next.

Figure 7(b) provides a graphical view of exit flow angle predictions, expressed as a percentage, that vary over a wide range of

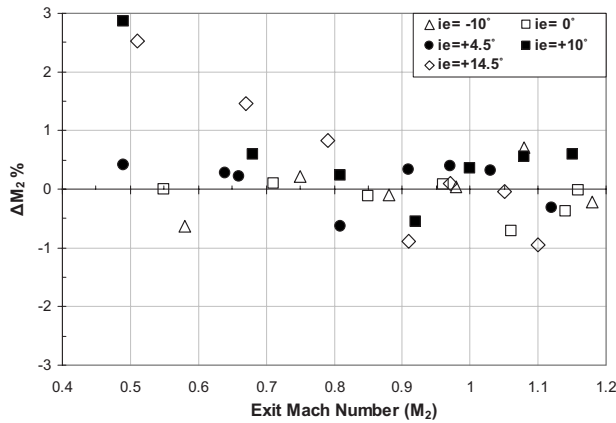


Fig. 6 Error in Mach number predictions

exit Mach numbers for a lower-incidence subset of the data plotted in Fig. 6. These predictions are generally within the experimental uncertainty of ± 0.5 deg for all cases.

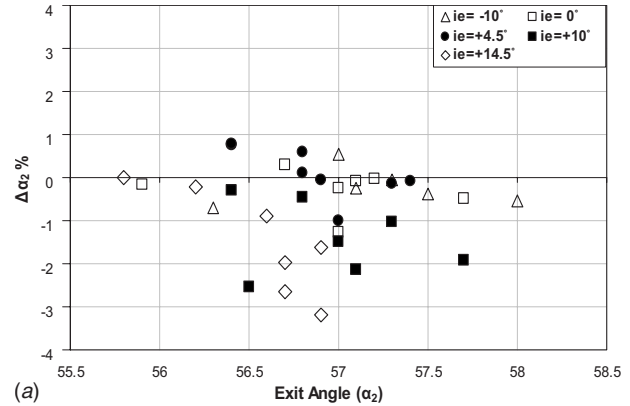
A similar comparison within Fig. 7(c) shows that only the cases combining elevated exit Mach numbers with elevated incidence cause the predicted flow angle to be 1–2 deg less than the measured exit flow angles, which corresponds to upwards of 3% error. This is a difference greater than the experimental uncertainty.

4.7 Profile Losses. Figures 8(a)–8(c) demonstrate the loss ratio of MISES-predicted to calculated profile losses over a wide range of exit Mach numbers and five different incidence levels. The experimental uncertainty for total pressure loss coefficients varied from ± 0.003 to ± 0.005 as a function of the exit Mach number [12]. Figure 8(a) depicts the comparisons for incidences ranging from -10 deg to $+4.5$ deg and including the effective design incidence of 0 deg. The -10 deg incidence case, plotted separately in Fig. 8(b) to compare predicted loss with measured loss, provides the best match, with an agreement generally within the experimental uncertainty. For the remaining incidence cases of Figs. 8(a) and 8(c), there is a tendency to underpredict measured losses at low exit Mach numbers. An analogous trend of increasingly underpredicted loss levels with departure from the design exit Mach number was demonstrated for a supersonic steam turbine cascade tip section by Parvizinia et al. [8].

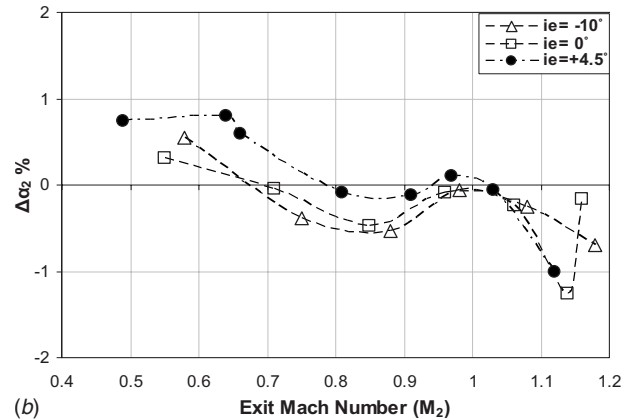
In the high incidence cases of Fig. 8(c), similar trends are captured as for the low incidence cases of Fig. 8(a); at low exit Mach numbers, losses are underpredicted. MISES predictions of loss are generally within experimental uncertainty near the design point Mach Number and incidence.

The overall trends in exit flow angle and loss coefficient versus exit Mach number and incidence presented thus far are found to be in conflict. The discrepancy between experiment and predictions for high exit angles is higher at high exit Mach numbers, and for total loss coefficient it is lower at high exit Mach numbers. However, high incidences have the same effect on both exit angle and loss coefficient: the mismatch is observed to be increasing. Although a good explanation to this phenomenon has not been found yet, the same behavior is observed in the study of Parvizinia et al. [8].

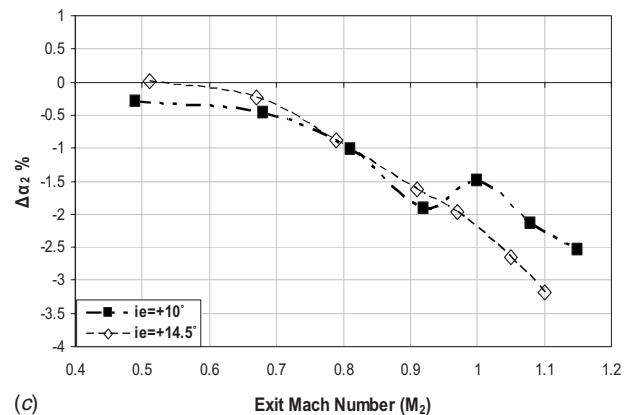
4.8 Influence of Blade Profile. As a final set of comparisons, the sensitivity of MISES to slight changes in blade profile geometry is evaluated. Until this point in the paper, the blade designated as HS1A [12] has been the object of our study. A second blade geometry, designated as HS1B, differs from HS1A mainly in the leading edge region, as shown in overlays of Fig. 9(a). The two geometries also differ in their design incidence, where, as indicated in Table 1, the design incidence (i_{des}) for HS1A is -4.5 deg, and -15 deg for HS1B. The related performance data can be



(a)



(b)



(c)

Fig. 7 (a) Error in exit flow angle predictions. (b) Error trends in exit flow angle predictions at incidence levels of -10 deg, 0 deg, and $+4.5$ deg. (c) Error trends in exit flow angle predictions at high incidence.

found in Table 7.

The effect of the HS1B geometry shows itself immediately in the experimental loading distribution as a laminar separation bubble (LSB) near the leading edge of the pressure surface, as described in Ref. [12]. In contrast to the HS1A calculation at similar incidence and Mach number (Fig. 4(c)), the MISES prediction in this case has a difficult time in replicating the experimental leading edge loading and places the shock location upstream of the measurement. Comparing the MISES predictions for the two geometries in Fig. 9(c) shows that the loading is lessened for the HS1B blade. Note that although the two effective incidences are zero, the absolute incidences differ by 10.5 deg. A discussion of the sensitivity of airfoil performance to leading edge geometry was provided by Garzon and Darmofal [6].

Figure 9(d), in conjunction with Fig. 9(b), comprises two com-

Table 5 Experimental data (* denotes data for $M_2=0.66, 0.81, 0.91,$ and 1.03 averaged for repeating the data in the original study [14])

M_2	HS1A cascade performance data							
	P_2/P_{01}	P_b/P_{01}	q_2/P_{01}	$Re \pm \Delta Re$	Cbp	W_t	α_2	AVDR
HS1A cascade, off-design incidence, $i-i(\text{des})=-10$ deg								
0.58	0.788	0.793	0.184	$52,000 \pm 6800$	0.03	0.062	57	0.98
0.75	0.677	0.668	0.268	$670,000 \pm 12,000$	-0.031	0.051	57.5	1.01
0.88	0.592	0.571	0.321	$780,000 \pm 19,000$	-0.067	0.052	58	0.98
0.98	0.522	0.371	0.35	$870,000 \pm 68,000$	-0.431	0.082	57.3	0.99
1.08	0.458	0.367	0.377	$950,000 \pm 84,000$	-0.242	0.082	57.1	0.99
1.18	0.405	0.312	0.392	$1,020,000 \pm 135,000$	-0.238	0.089	56.3	0.99
HS1A cascade, design incidence, $i-i(\text{des})=0$ deg								
0.55	0.807	-	0.168	$500,000 \pm 5400$	-	0.068	56.7	1.02
0.71	0.704	0.707	0.247	$660,000 \pm 13,000$	0.012	0.059	57.2	1.02
0.85	0.612	-	0.311	$800,000 \pm 20,000$	-	0.045	57.7	1.02
0.96	0.535	0.481	0.346	$880,000 \pm 50,000$	-0.156	0.072	57.1	1.03
1.06	0.479	0.365	0.374	$970,000 \pm 79,000$	-0.304	0.065	57	1.03
1.14	0.429	0.323	0.389	$1,040,000 \pm 97,000$	-0.272	0.073	57	1.01
1.16	0.415	-	0.39	$1,060,000 \pm 126,000$	-	0.085	55.9	1.03
HS1A cascade, off-design incidence, $i-i(\text{des})=+4.5$ deg*								
0.49	0.841	-	0.14	$460,000 \pm 4000$	-	0.073	56.4	1.02
0.64	0.749	-	0.215	$600,000 \pm 8000$	-	0.058	56.4	1.07
0.66	0.736	-	0.224	$630,000 \pm 9000$	-	0.059	56.8	1.02
0.81	0.641	-	0.292	$775,000 \pm 15,000$	-	0.051	57.4	1.03
0.91	0.568	0.563	0.332	$880,000 \pm 27,000$	-0.016	0.061	57.3	1.04
0.97	0.526	-	0.349	$920,000 \pm 66,000$	-	0.077	56.8	1.05
1.03	0.491	0.403	0.366	$975,000 \pm 91,500$	-0.242	0.078	56.9	1.04
1.12	0.44	0.378	0.385	$1,050,000 \pm 90,000$	-0.161	0.076	57	1.02
HS1A cascade, off-design incidence, $i-i(\text{des})=+10$ deg								
0.49	0.834	0.834	0.141	$440,000 \pm 4000$	-0.025	0.102	56.4	1.15
0.68	0.721	0.72	0.233	$620,000 \pm 9700$	-0.033	0.066	56.8	1.15
0.81	0.636	0.636	0.293	$740,000 \pm 15,000$	-0.04	0.054	57.3	1.15
0.92	0.566	0.566	0.335	$840,000 \pm 24,000$	-0.046	0.054	57.7	1.14
1	0.507	0.503	0.356	$920,000 \pm 71,000$	-0.289	0.086	57	1.14
1.08	0.458	0.448	0.377	$1,000,000 \pm 98,000$	-0.15	0.082	57.1	1.13
1.15	0.416	0.405	0.389	$1,070,000 \pm 116,000$	-0.238	0.089	56.5	1.13
HS1A cascade, off-design incidence, $i-i(\text{des})=+14.5$ deg								
0.51	0.822	0.84	0.149	$460,000 \pm 4800$	0.117	0.114	55.8	1.25
0.67	0.722	0.73	0.229	$620,000 \pm 7800$	0.034	0.084	56.2	1.24
0.79	0.645	0.646	0.284	$740,000 \pm 17,000$	0	0.067	56.6	1.26
0.91	0.574	0.569	0.33	$870,000 \pm 24,000$	-0.013	0.057	56.9	1.27
0.97	0.526	0.46	0.348	$940,000 \pm 45,000$	-0.189	0.081	56.7	1.26
1.05	0.478	0.411	0.371	$1,020,000 \pm 83,000$	-0.182	0.074	56.7	1.27
1.1	0.453	0.41	0.38	$1,050,000 \pm 104,000$	-0.113	0.075	56.9	1.25

parisons of measurement versus prediction with the HS1B geometry at design incidence—one with a subsonic exit Mach number and the other with a second supersonic. For both cases MISES has a difficult time replicating the separation at the leading edge pressure surface.

In a separate study not detailed here, the ability of MISES to predict exit flow angle and loss for the HS1B profile operating at design incidence was evaluated. The trends in both flow angle and loss with exit Mach number were found to be similar to those of the HS1A airfoil operating at the higher-incidence angles tested. The comparison at design incidence levels of the two geometries shows that the predictive capacity is generally better for the HS1A flow fields, as one might anticipate from the loading diagrams discussed here.

4.9 Influence of Reynolds Number. A general conclusion deducible from Figs. 8(a)–8(c) is that measured losses significantly exceed predicted losses in cases of low exit Mach numbers (and low exit Reynolds numbers) for all incidences, except the

extreme negative incidence case of -10 deg. Additional design-incidence experimental data from the HS1A cascade presented in Ref. [13] are reproduced here and contrasted with MISES calculations as in Fig. 10(a) in order to further elucidate and isolate the influence of Reynolds number on measured and predicted losses at constant Mach number. For both exit Mach numbers of the figure, the experimental loss may be observed to trend higher with decreasing Reynolds number. This trend is not replicated in the MISES calculations, similar to the discrepancies observed in Figs. 8(a) and 8(c). The related data can be found in Table 8.

Figures 10(b) and 10(c) provide insight into the transition location predicted by MISES for the suction and pressure surfaces, respectively, for both the HS1A and HS1B profiles. The two geometries at design incidence are studied over a range of Reynolds numbers of up to 2,000,000, and at a constant exit Mach number of 1.14 in order to observe how the Reynolds number affects the transition location on the suction side of the blade. The transition onset can be observed to move forward with an increase in Rey-

Table 6 MISES predictions

HS1A MISES data								
M_2	P_2/P_{01}	P_2/P_1	M_1	ξ_1	Y_p	α_2	AVDR	γ
HS1A MISES, off-design incidence, $i-i(\text{des})=-10$ deg								
0.57629	0.788	0.85455	0.34231	0.06211	0.06622	57.315	0.98	1.4
0.75156	0.677	0.7511	0.38808	0.04751	0.04988	57.277	1.01	1.4
0.87919	0.592	0.66753	0.41774	0.05136	0.05415	57.694	0.98	1.4
0.98033	0.522	0.5887	0.41804	0.07291	0.07864	57.265	0.99	1.4
1.08762	0.458	0.51646	0.41783	0.07176	0.07731	56.959	0.99	1.4
1.17738	0.405	0.45671	0.41791	0.08111	0.08827	55.907	0.99	1.4
HS1A MISES, design incidence, $i-i(\text{des})=0$ deg								
0.54995	0.807	0.89362	0.38444	0.04565	0.04784	56.875	1.02	1.4
0.71064	0.704	0.81031	0.45276	0.04749	0.04986	57.177	1.02	1.4
0.84902	0.612	0.71851	0.48431	0.04998	0.05261	57.425	1.02	1.4
0.96072	0.535	0.63013	0.48923	0.06938	0.07455	57.046	1.03	1.4
1.05256	0.479	0.56443	0.48992	0.06871	0.07378	56.863	1.03	1.4
1.13564	0.429	0.50905	0.50048	0.07755	0.08406	56.281	1.01	1.4
1.15977	0.415	0.48906	0.49007	0.07911	0.0859	55.809	1.03	1.4
HS1A MISES, off-design incidence, $i-i(\text{des})=+4.5$ deg								
0.49206	0.841	0.93448	0.39098	0.0478	0.0502	56.82	1.02	1.4
0.64172	0.749	0.86219	0.45294	0.04686	0.04917	56.849	1.07	1.4
0.66142	0.736	0.86612	0.48791	0.0486	0.05108	57.135	1.02	1.4
0.80496	0.641	0.77773	0.53291	0.05004	0.05268	57.347	1.03	1.4
0.91305	0.568	0.69518	0.54509	0.05831	0.06192	57.23	1.04	1.4
0.97386	0.526	0.64292	0.54326	0.07156	0.07708	56.862	1.05	1.4
1.0333	0.49	0.60167	0.54961	0.07073	0.07611	56.867	1.04	1.4
1.11657	0.44	0.54528	0.56218	0.07589	0.08212	56.429	1.02	1.4
HS1A MISES, off-design incidence, $i-i(\text{des})=+10$ deg								
0.50401	0.834	0.93711	0.4115	0.04683	0.04913	56.236	1.15	1.4
0.684	0.721	0.86514	0.51697	0.04812	0.05056	56.538	1.15	1.4
0.81198	0.636	0.78936	0.56421	0.05	0.05264	56.715	1.15	1.4
0.91496	0.566	0.71724	0.59163	0.05949	0.06326	56.597	1.14	1.4
1.00347	0.507	0.64666	0.59995	0.07312	0.07889	56.147	1.14	1.4
1.08587	0.458	0.58755	0.6073	0.07146	0.07696	55.882	1.13	1.4
1.15674	0.416	0.5338	0.6076	0.07939	0.08624	55.072	1.13	1.4
HS1A MISES, off-design incidence, $i-i(\text{des})=+14.5$ deg								
0.52292	0.822	0.94755	0.45523	0.05076	0.05347	55.802	1.25	1.4
0.67982	0.722	0.8961	0.56421	0.05484	0.05802	56.071	1.24	1.4
0.79654	0.645	0.82699	0.6066	0.05306	0.05603	56.1	1.26	1.4
0.90197	0.574	0.74785	0.62658	0.0586	0.06225	55.979	1.27	1.4
0.97102	0.526	0.69532	0.64421	0.07483	0.08088	55.587	1.26	1.4
1.04959	0.478	0.6302	0.64102	0.07155	0.07706	55.199	1.27	1.4
1.08962	0.453	0.60277	0.65206	0.07659	0.08294	55.087	1.25	1.4

nolds number. Figure 10(c) gives a comparison of the two geometries in terms of their transition onset, separation, and reattachment locations along the pressure side. Interestingly, MISES predicts a separation bubble on the pressure surface for both geometries, the extent of the predicted separation being much greater for HS1A. The separation occurs at the transition onset for both geometries, the HS1B transition being somewhat earlier than HS1A. The related MISES study is given in Table 9.

The Reynolds number has only a minor effect on the pressure surface transition, in contrast to its effect on the suction surface. The extent of the pressure surface separation for airfoil HS1B from Fig. 10(c) compares well with the size that might be inferred from Fig. 9(b). Therefore, MISES appears to predict the location of separation well but underpredicts its transverse extent. This can be resolved perhaps by improving the transition model, as in Ref. [9].

4.10 Comparisons to Navier–Stokes Dawes Code. Figure 11, reproduced directly from Ref. [14], compares measurements at design incidence and exit Mach number to calculations using the Navier–Stokes Dawes code [18]. This figure can be contrasted to Fig. 4(b), which compares the same experimental data to MISES computations. The level of measurement versus prediction agreement is comparable between MISES and the Dawes code at the

leading edge. The Dawes code does a better job of capturing the suction surface shock location, and with less oscillation in the solution, as would be expected.

5 Conclusions

Predictions of the boundary layer code, MISES, were compared with measured performance data for a 2D linear cascade from the mid-pitch section of a modern aircraft engine high-pressure turbine.

The influence of incidence, exit Mach number, Reynolds number, and blade geometry on the blade performance was studied. Performance parameters included total pressure loss, Mach number distribution (loading), and flow turning. The influence of grid density, grid topology, and AVDR were also studied. Grid densities greater than the MISES default setting were found to have little influence on the solution fidelity. The selected grid topology also had little impact.

Computed Mach number loading distributions at design incidence match the experiment best at subsonic and supersonic exit Mach numbers, with some inaccuracy in shock location at the design point transonic Mach number of 1.05. A slight mismatch at the leading edge was similar in trend and magnitude to that ob-

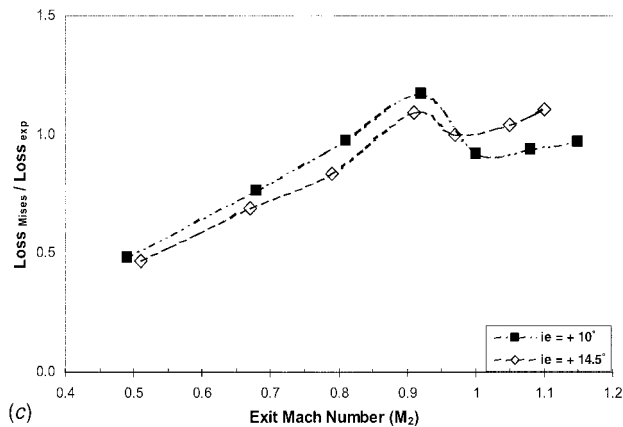
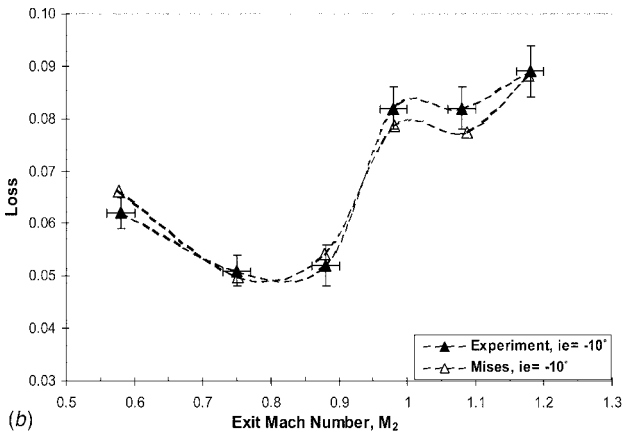
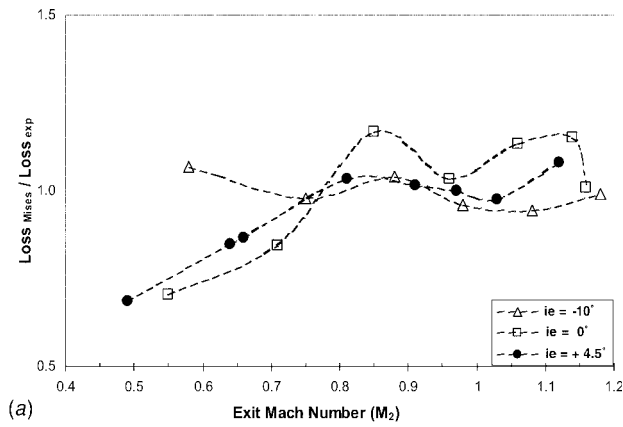


Fig. 8 (a) Loss prediction at incidence levels of -10 deg, 0 deg, and $+4.5$ deg. (b) Loss prediction for the highest negative incidence, -10 deg. (c) Loss prediction at high incidence.

served for calculations with the Navier–Stokes Dawes code. As expected, at incidences other than design, predictions differed from measurements to a greater extent, but not excessively, for fairly extreme levels of off-design incidence. The influence of AVDR was quantified as having a significant influence on loading, underlining the need to integrate MISES into a design quasi-3D system in order to provide this input to MISES accurately. MISES seemed to be insensitive to a slightly different geometry and design incidence, which in combination resulted in a laminar separation bubble on the pressure surface near the leading edge. This suggests the opportunity to improve the prediction of transition and boundary layer development within MISES, perhaps by implementing the modeling of Praisner and Clark [10].

Incidences described herein were derived from cascade passage

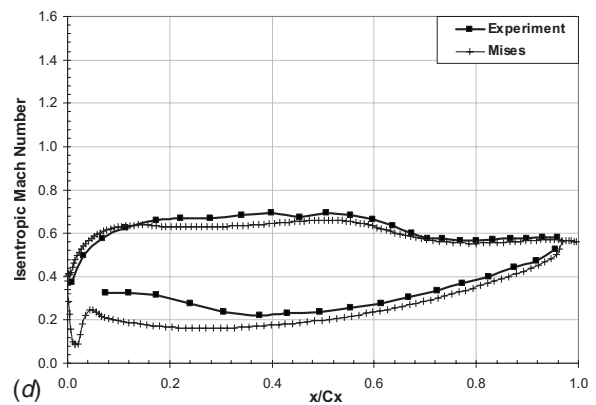
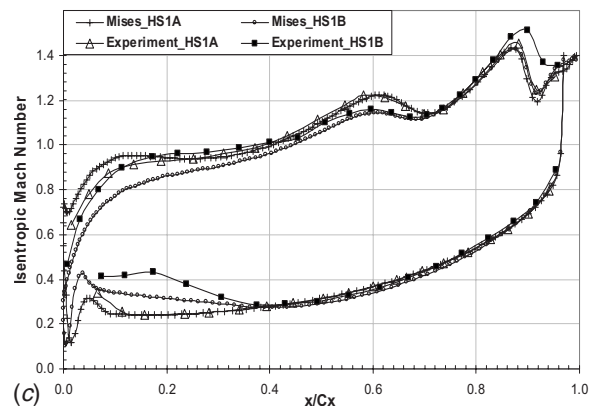
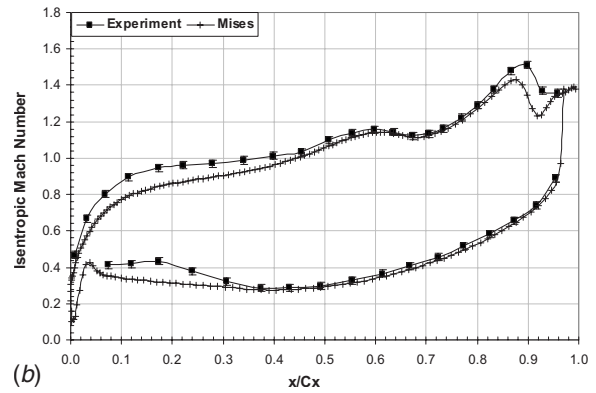
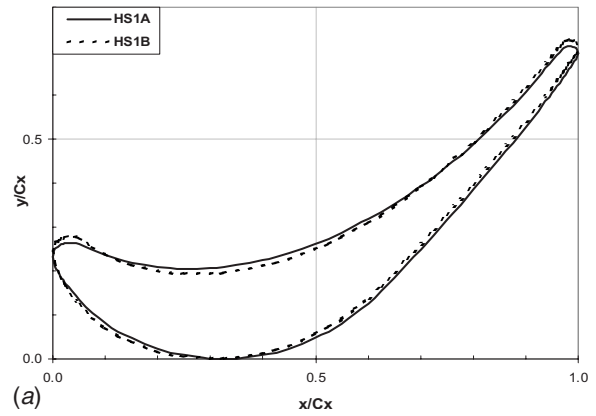
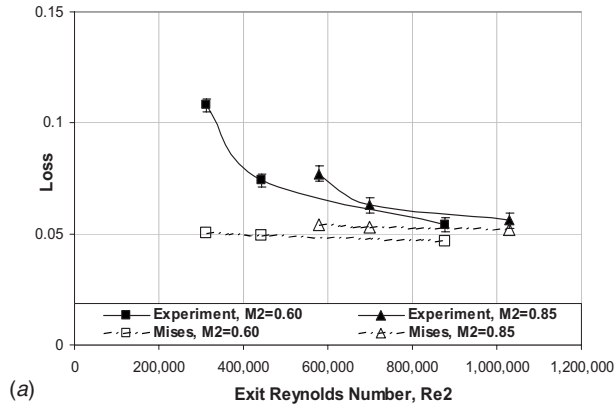


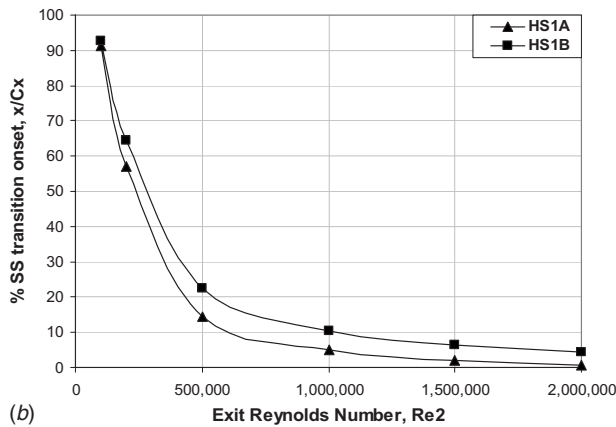
Fig. 9 (a) Comparison of two blade geometries, HS1A and HS1B. (b) HS1B blade loading for design incidence ($i_e = 0$ deg) at $M_2 = 1.14$. (c) Comparison of MISES predictions for HS1A and HS1B at design incidence $i_e = 0$ deg, at $M_2 = 1.14$. (d) HS1B blade loading for design incidence ($i_e = 0$ deg) at $M_2 = 0.50$.

Table 7 HS1B data for $M=0.5$ and $M=1.14$

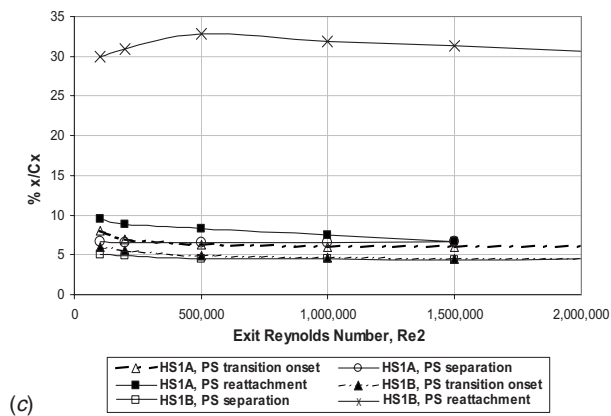
Design incidence, $i-i(\text{des})=0$ deg								
HS1B cascade performance data								
M_2	Ps_2/P_{01}	P_b/P_{01}	q_2/P_{01}	$Re \pm \Delta Re$	Cbp	W_t	α_2	AVDR
0.5	0.831	0.813	0.147	$460,000 \pm 4000$	-0.126	0.081	57.2	1.08
1.14	0.428	0.304	0.386	$1,010,000 \pm 113,000$	-0.321	0.085	57.5	1.06
HS1B MISES data								
M_2	Ps_2/P_{01}	P_2/P_1	M_1	ξ_1	Y_p	α_2	AVDR	γ
0.51004	0.831	0.90089	0.34161	0.04411	0.04615	56.626	1.08	1.4
1.1375	0.428	0.47788	0.4	0.07589	0.08212	55.797	1.06	1.4



(a)



(b)



(c)

Fig. 10 (a) Reynolds number effect on performance at design incidence, $i_e=0$ deg. **(b)** Reynolds number effect on transition onset on suction side at $M_2=1.14$, $i_e=0$ deg. **(c)** Reynolds number effect on transition, separation, and reattachment location on the pressure side at $M_2=1.14$, $i_e=0$ deg.

Table 8 Reynolds number study

HS1A data, $i-i(\text{des})=0$ (deg)	Cascade	MISES
M_2	W_t	Y_p
0.6	311,000	0.05054
0.6	443,000	0.04916
0.6	878,000	0.04687
0.85	578,000	0.05405
0.85	698,000	0.05319
0.85	1,029,000	0.05171

Table 9 Transition study

HS1A data, MISES, at $M=1.14$, $i-i(\text{des})=0$ (deg)				
Re	PS separation	PS reattachment	PS transition	SS transition
100,000	6.6137	9.4725	7.9896	91.2715
200,000	6.475	8.8541	6.9634	56.8987
500,000	6.5978	8.3718	6.2218	14.4386
1,000,000	6.576	7.5118	6.0534	5.1885
1,500,000	6.6519	6.7251	5.993	1.9484
2,000,000	-	-	5.9534	0.6388
HS1B data, MISES, at $M=1.14$, $i-i(\text{des})=0$ (deg)				
100,000	5.0286	29.9597	5.951	92.6507
200,000	4.8424	30.9595	5.5858	64.3013
500,000	4.4974	32.8126	4.8375	22.4057
1,000,000	4.4514	31.9143	4.5989	10.5578
1,500,000	4.4205	31.2968	4.5114	6.5319
2,000,000	4.5235	30.6784	4.4972	4.5023

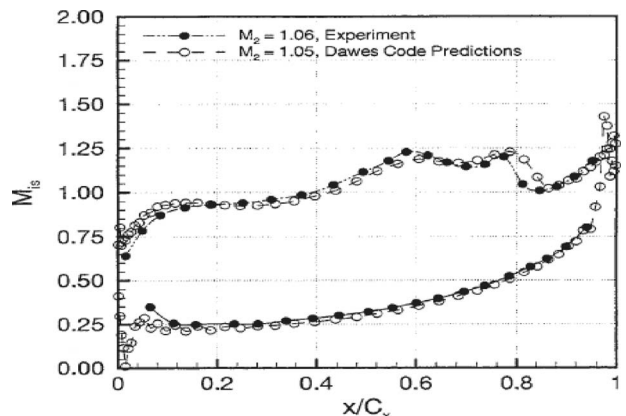


Fig. 11 Dawes code predictions [14]

angles. An improved validation procedure would include the use of a 3D RANS simulation to capture the expected 2–3 deg change in flow angle from the wall to the cascade mid-section, where measurements were obtained. This may resolve the errors in loading described herein near the leading edge with MISES and with the Dawes code [14].

Flow turning was generally predicted by MISES to be within the experimental uncertainty. The combination of a high exit Mach number and a high incidence resulted in the underprediction of the exit flow angle by 1–2 deg.

The total pressure loss was shown to be fairly well captured for the cases studied close to the design exit Mach number. The mismatch in loss increases with low Mach and Reynolds numbers and high incidences.

Acknowledgment

The authors wish to acknowledge with gratitude the permission of the General Electric Company to publish this paper and to thank the reviewers for several helpful suggestions.

Nomenclature

AVDR	= axial velocity density ratio [12]
C_x	= axial chord length
i_{des}	= design incidence
i_e	= effective incidence, $i - i_{des}$
M_2	= exit Mach number
N	= grid surface node count
P_{01}	= inlet total pressure
P_{02}	= exit total pressure
P_2	= exit static pressure
RANS	= Reynolds-averaged Navier–Stokes
Re_2	= exit Reynolds number
W_t	= experimental total pressure loss coefficient, $= (P_{01} - P_{02}) / (P_{02} - P_2)$
Y_p	= MISES loss coefficient, $\xi_1 / (1 - \xi_1)$

Greek Symbols

α	= flow inlet angle, $i + \beta_1$
α_2	= exit angle
β_1	= leading metal angle
ξ_1	= MISES loss coefficient, $(P_{01} - P_{02}) / (P_{01} - P_2)$

References

- [1] Drela, M., and Youngren, H., 1998 “A User’s Guide to MISES 2.53,” MIT Computational Aerospace Sciences Laboratory.
- [2] Schreiber, H., Steinert, W., and Küsters, B., 2000, “Effects of Reynolds Number and Free-Stream Turbulence on Boundary Layer Transition in a Compressor Cascade,” ASME Paper No. 2000-GT-0263.
- [3] Abu-Ghannam, B. J., and Shaw, R., 1980, “Natural Transition of Boundary Layers: The Effects of Turbulence, Pressure Gradient, and Flow History,” *J. Mech. Eng. Sci.*, **22**(5), pp. 213–228.
- [4] Sieverding, F., Ribi, B., Casey, M., and Meyer, M., 2003, “Design of Industrial Axial Compressor Blade Sections for Optimal Range and Performance,” ASME Paper No. GT2003-38036.
- [5] Sondergaard, R., Bons, J. P., and Rivir, R. B., 2002, “Reducing Low-Pressure Turbine Stage Blade Count Using Vortex Generator Jet Separation Control,” IGTI Paper No. GT-2002-30602.
- [6] Garzon, V. E., and Darmofal, D. L., 2004, “On the Aerodynamic Design of Compressor Airfoils for Robustness Under Geometric Uncertainty,” ASME Paper No. GT2004-53581.
- [7] Garzon, V. E., and Darmofal, D. L., 2003, “Impact of Geometric Variability on Axial Compressor Performance,” ASME Paper No. GT2003-38130.
- [8] Parvizinia, M., Berlich, C., Truckenmüller, F., and Stüer, H., 2004, “Numerical and Experimental Investigations Into the Aerodynamic Performance of a Supersonic Turbine Blade Profile,” ASME Paper No. GT2004-53823.
- [9] Bons, J. P., Hansen, L. C., Clark, J. P., Koch, P. J., and Sondergaard, R., 2005, “Designing Low-Pressure Turbine Blades With Integrated Flow Control,” Paper No. GT2005-68962.
- [10] Praisner, T. J., and Clark, J. P., 2004, “Predicting Transition in Turbomachinery, Part I: A Review and New Model Development,” ASME Paper No. GT-2004-54108.
- [11] Dorney, D. J., and Davis, R. L., 1992, “Navier–Stokes Analysis of Turbine Blade Heat Transfer and Performance,” ASME J. Turbomach., **114**, pp. 795–806.
- [12] Jouini, D. B. M., Sjolander, S. A., and Moustapha, S. H., 2002, “Midspan Flow-Field Measurements for Two Tran-Sonic Linear Turbine Cascades at Off-Design Conditions,” ASME J. Turbomach., **124**, pp. 176–186.
- [13] Corriveau, D., and Sjolander, S. A., 2004, “Influence of Loading Distribution on the Performance of Transonic HP Turbine Blades,” ASME J. Turbomach., **126**, pp. 288–296.
- [14] Jouini, D. B. M., 2000, “Experimental Investigation of Two Transonic Linear Turbine Cascades at Off-Design Conditions,” Ph.D. thesis, Carleton University, Ottawa, Canada.
- [15] Jouini, D. B. M., Sjolander, S. A., and Moustapha, S. H., 2001, “Aerodynamic Performance of a Transonic Turbine Cascade at Off-Design Conditions,” ASME J. Turbomach., **123**, pp. 510–518.
- [16] Corriveau, D., and Sjolander, S. A., 2004, “Experimental and Numerical Investigation on the Performance of a Family of Three HP Transonic Turbine Blades,” ASME Paper No. GT2004-53087.
- [17] Corriveau, D., and Sjolander, S. A., 2005, “Aerodynamic Performance of a Family of Three High Pressure Transonic Turbine Blades at Off-Design Incidence,” ASME Paper No. GT2005-68159.
- [18] Dawes, W. N., 1988, “3D Navier–Stokes Solver for Application to all Types of Turbomachinery,” ASME Paper No. 88-GT-70.

Surface Shear Stress and Pressure Measurements in a Turbine Cascade

Brian M. Holley

e-mail: bmmholley@engr.uconn.edu

Lee S. Langston

e-mail: langston@engr.uconn.edu

Department of Mechanical Engineering,
University of Connecticut,
191 Auditorium Road,
U-3139 Storrs, CT 06269

To further the understanding of secondary flow loss, a set of surface measurements is presented for a planar turbine cascade tested at low Mach number (maximum of 0.23) and at an inlet axial chord Reynolds number of 5.9×10^5 . The endwall and airfoil surface measurements are of skin friction, limiting streamline direction, and static pressure. An oil film interferometry measurement technique applied to the endwall and airfoil surfaces (at some 2000 locations) provides an extensive passage surface map of skin friction values and limiting streamline topology. Measurements of pressures on the same passage surfaces are also presented, resulting in a complete picture of endwall and airfoil surface pressure and shear. [DOI: 10.1115/1.2988168]

1 Introduction

In this paper, we present skin friction and surface pressure measurements for subsonic airflow through a plane cascade of turbine airfoils. Skin friction is measured with an oil film interferometry (OFI) measurement technique, as shown in Fig. 1. Light interference patterns from an optically clear oil film are used to indicate the oil film thickness, which in turn is used to infer skin friction on the cascade surface. The cascade is characterized by high turning, low convergence, and low aspect ratio. This experimental study is a continuation of work presented earlier by Holley et al. [1] in which endwall shear measurements made at a smaller number of locations were compared with computational fluid dynamics (CFD) calculations.

Originally, and on the same cascade, endwall static pressure measurements and five-hole and hot-wire probe flow field measurements were carried out by Langston et al. [2]. Then Graziani et al. [3] carried out heat transfer measurements on the airfoil and endwall surfaces of the same cascade under similar flow conditions. The new measurements presented here are also taken at conditions that are similar to the first study. The result is an extensive collection of measurements from the same cascade under similar flow conditions, and this is put forth as a basis for better understanding the complicated flow in this cascade at these conditions.

The secondary flows depicted in Fig. 2 are described by Langston [4], and many other investigators have validated this basic flow picture, as summarized by Sieverding [5] with continuation by Langston [6]. Aerodynamic loss is one of the two primary concerns regarding secondary flows (the other is heat transfer), and Fig. 3 represents the measured mass-averaged total pressure loss as a function of axial distance along the turbine cascade [2]. This severe loss picture is characteristic for high turning, low aspect ratio, and low convergence cascades. According to Sharma and Butler [7], the aerodynamic losses due to the secondary flows can account for 30–50% of the total aerodynamic loss in a blade or stator row. Many investigators have contributed flow field measurements for many experimental configurations, as surveyed by Sieverding [5] and Langston [6]. There are investigations of surface pressure measurements as well [2,8,9]. Despite all these measurements, a widely accepted explanation for secondary flow losses,

where and how they are generated, remains elusive. The purpose of this paper is to offer a comprehensive set of surface measurements that can be used to develop a model for the distribution of loss generation in a particular turbine cascade under a particular set of operating conditions.

2 Description of Experiment

The current surface measurements and the previously acquired measurements were collected from the same large-scale low speed cascade wind tunnel. The cascade consists of four JT9D-34 turbine airfoils scaled to ten times the engine size. The geometry of the cascade is given in Fig. 4 and as follows:

axial chord $b_x=0.281$ m
chord/axial chord 1.1882
pitch/axial chord 0.9555
span/axial chord 0.9888

Periodicity of the cascade is established through adjustment of the tailboards and bleeds so that the flow around airfoils 2 and 3 matches the potential flow solution as indicated by midspan static pressure taps on the airfoils. The static pressure measurements and potential flow solution are shown in Fig. 5. The inlet angle of the cascade is set at 44.7 deg, and the nominal Reynolds number based on axial chord and cascade inlet velocity (about 34 m/s) is set at 5.9×10^5 , which results in a peak Mach number of about 0.23. The boundary layer is described at the upstream location (Fig. 4) with the following scaled by b_x :

boundary layer thickness 0.123
displacement thickness 0.0142
momentum thickness 0.0112
shape factor 1.27

The measured boundary layer thickness is within 5% of that measured by Langston et al. [2]. The measured (OFI) skin friction coefficient at this upstream location is $C_f=3.05 \times 10^{-3}$. The “exact” equation given by White [10] yields $C_f=2.96 \times 10^{-3}$ or $C_f=3.01 \times 10^{-3}$, depending on whether the measured boundary layer thickness or momentum thickness is used in the calculation.

The endwall pressure measurements presented in this work are from the work of Langston et al. [2]. They were collected using the same cascade wind tunnel and airfoils, and under similar test conditions, as reported on here for the endwall and airfoil skin friction measurements. The heat transfer measurements by Graziani et al. [3] were taken at a slightly lower Reynolds number of 5.5×10^5 but with a similar inlet boundary layer profile.

Contributed by the International Gas Turbine Institute of ASME for publication in the JOURNAL OF TURBOMACHINERY. Manuscript received May 8, 2008; final manuscript received July 22, 2008; published online April 10, 2009. Review conducted by David Wisler. Paper presented at the ASME Turbo Expo 2006: Land, Sea and Air (GT2006), Barcelona, Spain, May 8–11, 2006.

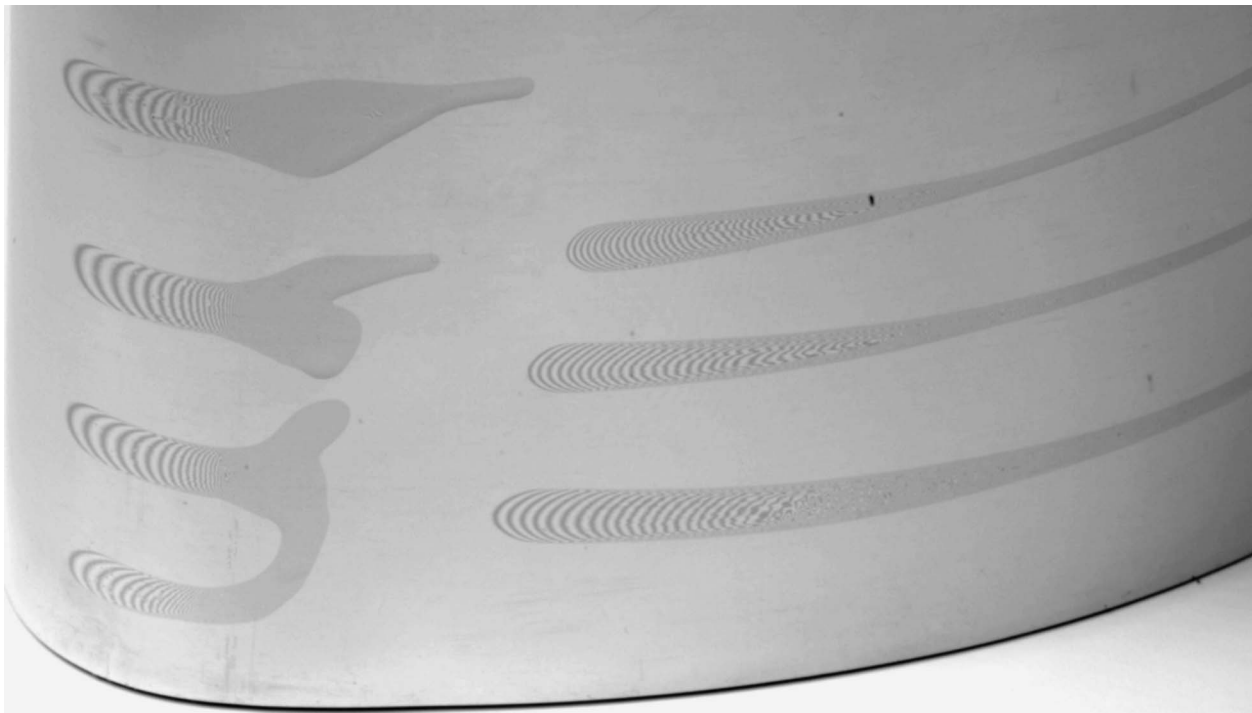


Fig. 1 Photograph of light interference patterns in silicone oil films on the suction side of an airfoil surface

The airfoil pressure measurements are new. The intent is to provide a set of measurements representing more spanwise locations than in the 1977 study [2]. An airfoil was constructed for the specific purpose of taking the new pressure measurements. Acrylic plates were machined to the shape of the airfoil cross section and stacked to form a full airfoil span. One 304 stainless steel plate was machined to the shape of the airfoil cross section and instrumented with 31, 0.50 mm diameter, static pressure taps. The pressure tap locations along the airfoil arc length are duplicates from the original 1977 study [2]. By restacking the assembly, pressure measurements were taken in nine spanwise locations, increments of one-sixteenth span, with the exception of the root location at 0.89% span. The pressure measurements were taken with the instrumented airfoil in the position of airfoil 2 in Fig. 4. The error in static pressure coefficient is within $\pm(0.005)$.

A set of exit plane flow field measurements was made to more thoroughly compare the conditions under which the 1977 [2] and new measurement sets were taken. The exit plane is the first measurement plane downstream of the trailing edge (plane 10, x

$=1.092$) in the 1977 study. A 3.2 mm diameter five-hole pneumatic probe manufactured and calibrated by Aeroprobe Corporation was used over the same measurement grid as was used in the 1977 study. The error in mass flux weighted total pressure loss coefficient obtained with the five-hole probe is evaluated at ± 0.013 .

Skin friction was measured using OFI. An oil film on a surface in a wind tunnel will spread and thin due to the shear acting upon it. Under appropriate conditions, the film thickness will be reduced enough (on the order of the wavelength of light) for it to be measured interferometrically. Knowledge of the film thickness profile in the direction of flow over it provides shear stress information. Good explanations of the technique are provided by Naughton and Sheplak [11], Driver [12], and Davy et al. [13]. The following equation is used to evaluate C_f :

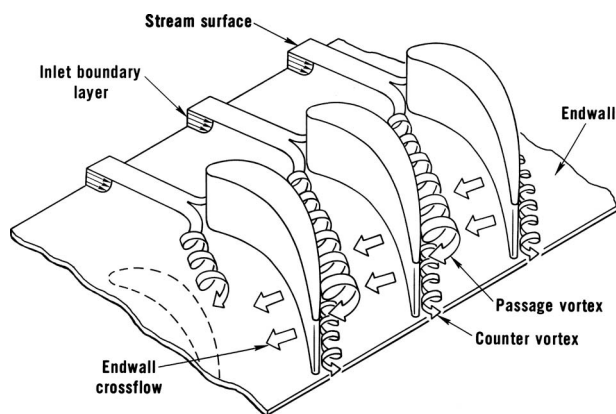


Fig. 2 The three-dimensional separation of a boundary layer entering a planar turbine cascade (from Langston [4])

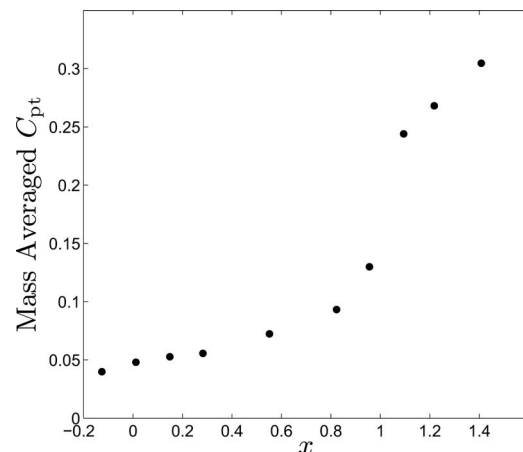


Fig. 3 Development of measured mass-averaged total pressure coefficient through the cascade

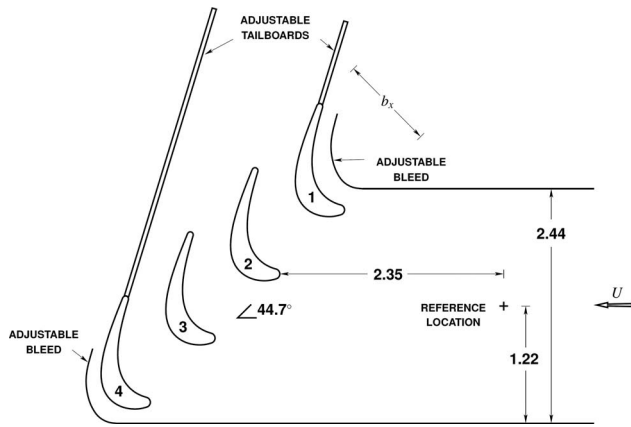


Fig. 4 Schematic of the large-scale plane turbine cascade. Lengths are scaled by axial chord b_x .

$$C_f = \frac{2\ell \sqrt{n_o^2 - n_a^2 \sin^2 \alpha}}{\lambda \int \frac{1}{2} \frac{\rho U^2}{\mu_o} dt} \quad (1)$$

The equation represents three main quantities: (1) the spatial variation in oil thickness, (2) the reference inlet velocity pressure, and (3) the oil viscosity, the latter two being integrated over the wind tunnel run time. The indices of refraction are tabulated properties of air and oil. The oil used is Dow Corning 200 Silicone fluid with nominal viscosities of 100 cS, 200 cS, 500 cS, and 1000 cS. Temperature corrections used for oil viscosity were taken from Naughton and Sheplak [11]. The viscosity of the oils were measured at six temperatures ranging from 15 °C to 40 °C, and the measurements agreed with the correlation within 0.5%. The angle of reflection is dependent on the optical arrangement and is measured. The light wavelength is a property of the source used, which was for this study a low pressure sodium lamp ($\lambda = 589.0, 589.6$ nm). Velocity pressure was measured with a Pitot-static probe at the reference location (midspan), which also served as the location for the reference inlet boundary layer measurement (Fig. 4). Ambient temperature along with the temperature in the cascade entrance section was measured using thermocouples. LABVIEW data acquisition software was used to record the velocity head and temperature quantities throughout a wind tunnel run.

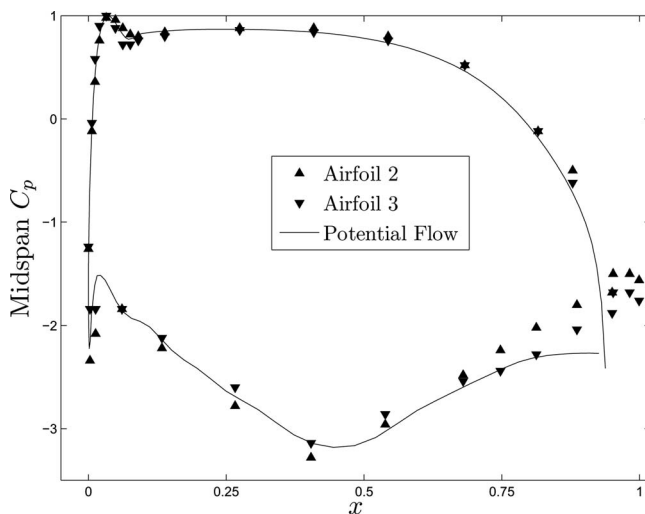


Fig. 5 Midspan static pressure measurements for airfoils 2 and 3 along with the potential flow solution

The collection of interferograms is described as follows. Prior to each run, a rectangular piece of 0.05 mm thick nickel (14 wt % tungsten) foil was adhered to the cascade surface. A series of oil patches was applied to the nickel, and the wind tunnel was brought up to the nominal Reynolds number, where it was maintained within $\pm 2\%$. When fringes were apparent in the oil on the nickel under ambient light, the wind tunnel was shut down, and the nickel was removed to be photographed under the monochromatic light source. The fringes in Fig. 1 indicate contours of equithickness in the oil. The thickness of the oil is on the order of a wavelength of light. The fringe spacing varies due to the varying shear stress τ_s along the surface. Regions of higher shear yield larger fringe spacing.

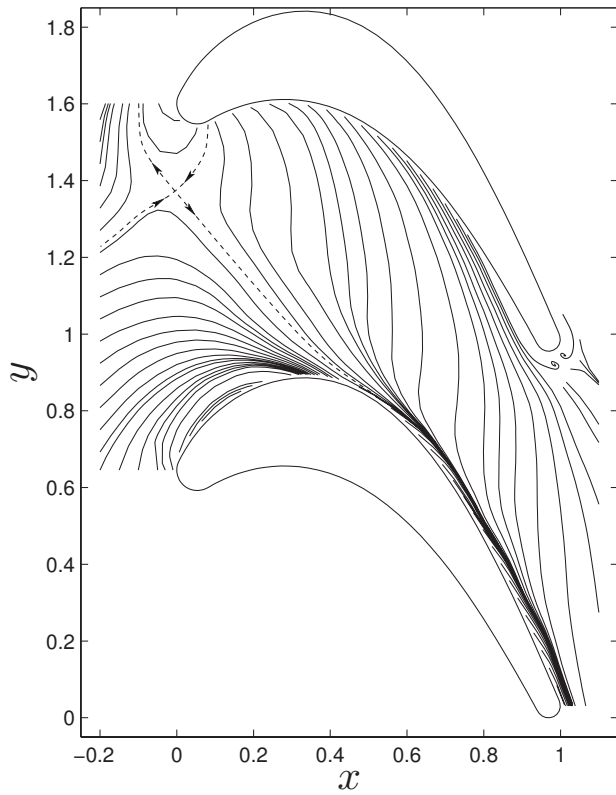
The interferograms were analyzed to evaluate surface skin friction coefficient and limiting streamline direction. IMAGEJ [14], a JAVA based imaging software provided by National Institutes of Health (NIH), was used to analyze the interferograms. By inspection of the fringe pattern and flow of the oil film, the direction of limiting streamlines can be read. Each skin friction measurement is evaluated from a pixel intensity profile of an interferogram along the direction of a limiting streamline. The authors wrote a short JAVA program to work with IMAGEJ and perform a nonlinear fit of a sine function to each intensity profile. The period of the sine function provides the fringe spacing, and the measurement location is taken to be the midpoint along the intensity profile. The spatial, pressure, and temperature measurements were analyzed using MATLAB, a numerical computation software. The analyzed measurements yielded skin friction coefficients and shear directions. An uncertainty analysis pertaining to Eq. (1) and its particular application in this paper was performed, and the skin friction coefficient measurements are expected to have an experimental uncertainty of $\pm 5\%$ (others have quoted $\pm 4\%$ [11]). The main contributions to error are in ℓ and temperature, which affects μ_o .

The skin friction results presented in this work are different from those presented earlier [15]. The largest difference is due to an error in a data analysis program, which led to a $+9$ – 10% error in the measurements. This error was corrected, and the measurement acquisition and analysis procedures were validated with analytical and CFD results from a separate experiment of flow over a cylinder. Measurements on a portion of the airfoil suction surface and on the endwall surface downstream of the throat were affected by the protuberance formed by the edge of the 50 μm thick nickel foil. More details of this are given by Holley and Langston [16].

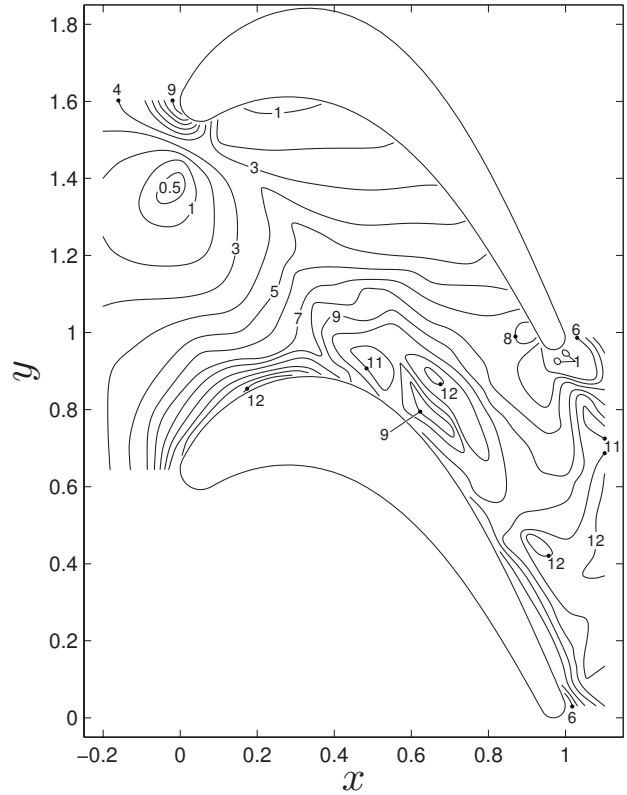
3 Results

Skin friction coefficient and limiting streamline direction were measured on the airfoil and endwall at over 2000 locations. At each location, the oil thickness was on the order of a wavelength of sodium light, 589 nm. The measurement locations were not uniformly distributed. A concentration of measurements was taken, for example, on the pressure side of the airfoil toward the leading edge for a more detailed representation of a three dimensional recirculation bubble. The measurements were mapped to grids for the endwall and airfoil using Delaunay triangulation and linear interpolation. The grid size for the airfoil is 848 nodes, with higher grid density near the leading edge. The grid size for the endwall is 456.

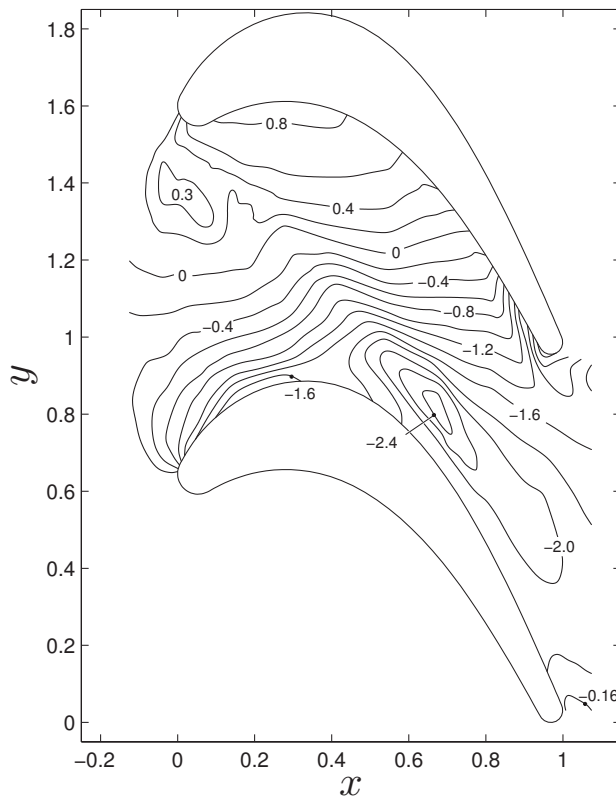
Surface measurements of limiting streamline direction, C_f , C_p , and St are represented in Figs. 6 and 7 for the endwall and airfoil, respectively. The limiting streamlines and C_f contours in Figs. 6 and 7 are based on about 2000 OFI measurements, a small number of which were reported in Ref. [1]. The endwall C_p measurements are taken from Ref. [2]. The Stanton number measurements are taken from Graziani et al. [3] (at $Re = 5.5 \times 10^5$, slightly lower than the present study at 5.9×10^5). All lengths in Figs. 6 and 7 are scaled by axial chord b_x . Consequently, the airfoil extends over $0 \leq x \leq 1$ on the abscissa in the endwall plots of Fig. 6. In Fig. 7, the airfoil outer surface is unwrapped, and the abscissa is



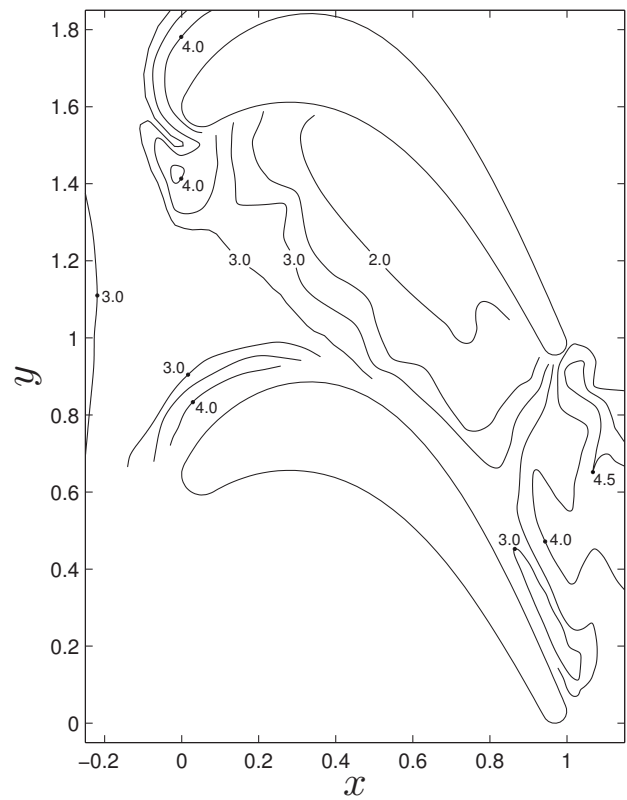
a. Limiting Stream Lines



b. $C_f \times 10^3$



c. C_p



d. $St \times 10^3$ ($Re = 5.5 \times 10^5$)

Fig. 6 Endwall measurements: (a) limiting streamlines, (b) skin friction coefficient, (c) static pressure coefficient [2], and (d) Stanton number [3]

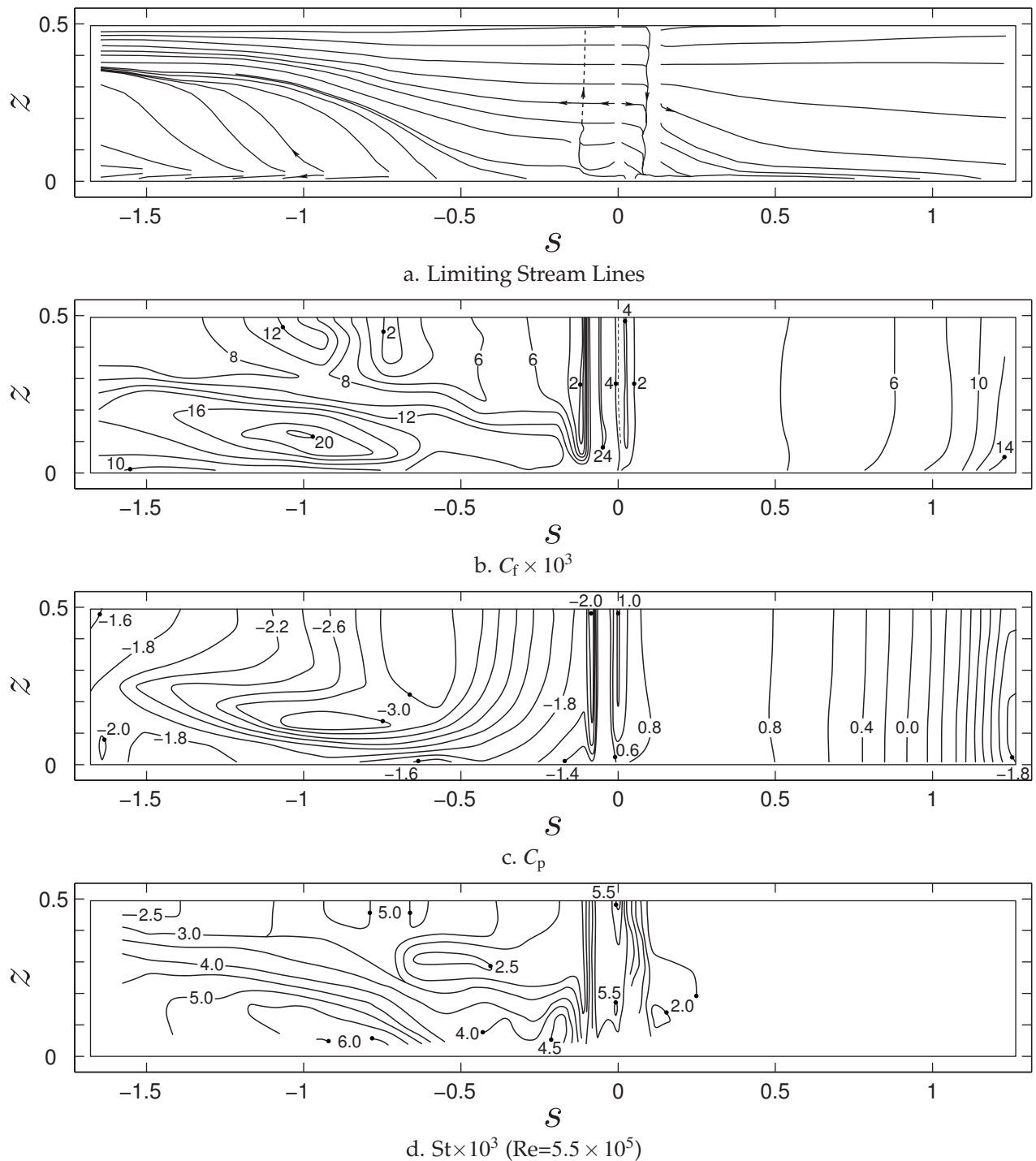


Fig. 7 Airfoil measurements: (a) limiting streamlines, (b) skin friction coefficient, (c) static pressure coefficient, and (d) Stanton number [3]

airfoil arc length, with $s=0$ defined at the primary attachment line for incidence angle of 44.7 deg. The positive values extend to the pressure side and the negative values extend to the suction side. On the ordinate, $z=0$ is at the endwall and $z=0.4944 \approx 0.5$ is at the midspan.

The limiting streamlines indicate the airfoil and endwall cross-flow in this cascade along with other features of the flow, such as the saddle point and the pressure side recirculation bubble. Coincidence of limiting streamlines and curves tangent to wall shear stress vectors is shown by Howarth [17]:

$$\lim_{z \rightarrow 0^+} \frac{u}{v} = \frac{\frac{\partial v}{\partial z}}{\frac{\partial u}{\partial z}} \bigg|_{z=0} = \frac{\tau_{s,y}}{\tau_{s,x}} \quad (2)$$

The limiting streamline direction measurements were made very closely to the cascade surface (10^{-6} m), and a very detailed picture can be formed with a high spatial density of measurement locations. Limiting streamlines were evaluated previously using

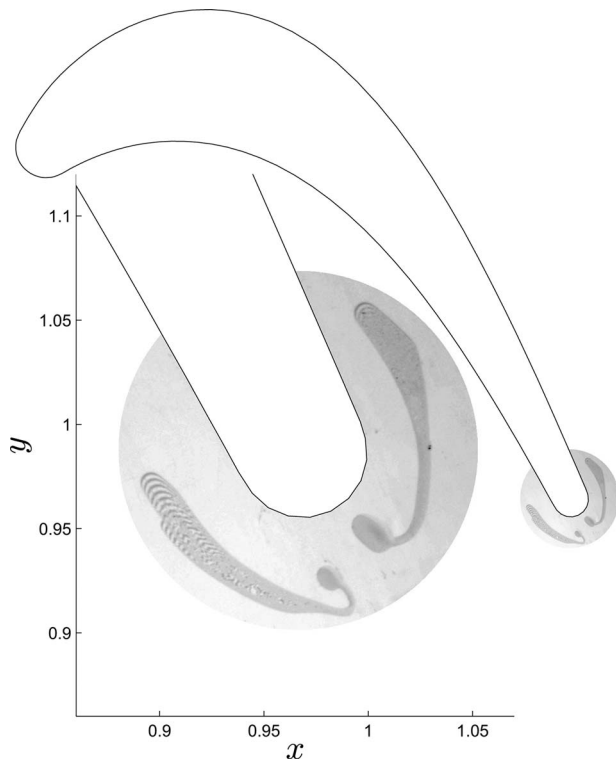


Fig. 8 Cat's eyes on the endwall around the trailing edge of the airfoil, qualitatively resolved with the OFI technique

ink droplets [2]. The ink droplets were injected on the cascade surface during wind tunnel operation. The droplets are driven not only by shear drag but also by pressure drag, which could bring the accuracy of the results into question. There is also influence from surface tension and gravity. The qualitative agreement between the results from the oil drop method and the more accurate OFI method, however, is good.

Endwall features are shown in detail with the OFI, pressure, and heat transfer measurements. In Fig. 6, the limiting streamlines extend into and out of the saddle point, which coincides with minimum skin friction and local maxima in pressure and heat transfer. A small region of $C_f > 0.012$ is located adjacent to the suction side of the airfoil near $x=0.2$, and this region of high shear and heat transfer is consistent with the measurements of Harrison [8]. In the throat region, the skin friction increases from the pressure to the suction side of the passage along a favorable pressure gradient, but the skin friction drops as the flow proceeds to an adverse pressure gradient. The passage vortex separation line extends from the saddle point to the suction side of the passage. A corner vortex is resolved with the measurements aft of $x=0.5$ along the suction side of the passage. In the region of uncovered turning, the measurements exhibit similar increased and somewhat scrambled skin friction, and heat transfer contours in the presence of an adverse pressure gradient and transition to turbulence.

Another feature referred to as the "cat's eyes" is shown on the endwall in the wake of the airfoil trailing edge. More details of the cat's eyes are shown in Fig. 8, where two oil films with interferometric fringes flow toward two vortical separation points. While the wind tunnel is in operation, the oil under the two separation points beads up as if to be drawn from the endwall surface by the low pressure centers of the two vortices, toward the midspan of the trailing edge.

Now we turn our focus to the airfoil, Fig. 7. In Fig. 7(a), the leading edge attachment line defines the arc length origin at $s=0$, with a minimum in skin friction and maxima in both pressure (Fig. 7(c)) and heat transfer (Fig. 7(d)). On the pressure side of the

Table 1 Airfoil loading calculated two ways

Source	F_x	F_y	$ F $
Potential flow	1.62	2.90	3.32
1977: Inlet and exit planes	1.70	2.70	3.19
1977: Airfoil 2 C_p	1.61	2.70	3.14
New: Inlet and exit planes	1.49	2.67	3.06
New: Airfoil 2 C_p	1.49	2.72	3.10
Airfoils 2 and 3 C_f	0.01	-0.01	
Endwall C_f	0.01	-0.00	

attachment line is a separation bubble that runs from midspan toward the endwall. The line meandering spanwise toward the endwall is the separation line. The streamlines begin again just downstream of the attachment line. On the suction side of the leading edge attachment line, skin friction abruptly increases while pressure and heat transfer drop. More details of the leading edge stagnation region are presented in another study [16]. In Fig. 7(c) continuing further along the suction side past $s=0.1$, the pressure rises, and the OFI technique resolves a very narrow separation bubble that runs from near the endwall toward midspan. In Fig. 7(b), further along the suction side past $s=-0.5$ and near midspan, the skin friction drops off as the boundary layer diffuses. The local minimum in time averaged skin friction, together with the peaks in heat transfer, is consistent with unsteady reattachment. Near $s=-1.0$, a local maximum in skin friction occurs adjacent to a minimum in pressure, but the maximum heat transfer lies nearer to the endwall and location of attachment.

The new exit plane ($x=1.092$) flow field measurements allow a more thorough comparison of the conditions under which the new and the 1977 [2] measurements were acquired. The exit plane mass-averaged total pressure loss coefficient is $C_{pt}=0.255$ for the new measurements, which is within 2% of the value of $C_{pt}=0.250$ reported in 1977.

With the measurements made for this study and the 1977 study, there is a unique opportunity to calculate the airfoil loading, axial (x) and tangential (y), using both the surface measurements and flow field measurements.

Consider a control volume for the cascade in the shape of a curvilinear duct of rectangular cross section, similar to the domain of a CFD simulation for the cascade (e.g., Ref. [18]). The cross section extends the span of the cascade and one pitch in the tangential direction, and it contains one airfoil. The control volume is closed by a yz plane at the reference location and the exit plane. The following equates the airfoil loading with quantities integrated over the surface of the control volume:

$$\vec{F} = - \int_{cs} (C_f \vec{t} + C_p \vec{n} + 2\vec{u}\vec{u} \cdot \vec{n}) dA \quad (3)$$

With an inlet static pressure coefficient of zero, and neglecting skin friction for now, the airfoil loading can be calculated with only the inlet velocity profile and the exit plane measurements of velocity and static pressure. The momentum contributions from the top and bottom of the control volume negate one another due to periodicity, and pressures on the endwalls negate one another due to symmetry.

Now consider an alternative control volume containing only an airfoil. The loading can be calculated from the static pressures and skin friction alone, with no velocity crossing the airfoil surface. The following equates the airfoil loading with quantities integrated over the airfoil surface:

$$\vec{F} = \int_{cs} (C_f \vec{t} - C_p \vec{n}) dA \quad (4)$$

Table 1 summarizes the axial and tangential components, and magnitude, of the resultant force on the airfoil calculated from

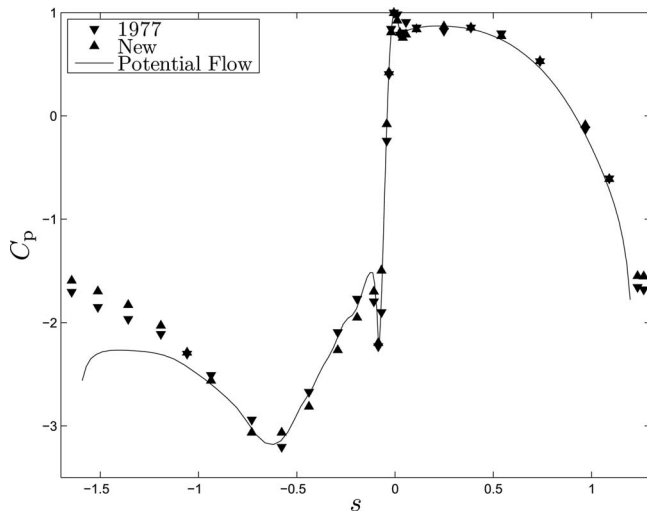


Fig. 9 New and 1977 midspan static pressure measurements for airfoil 2 along with the potential flow solution

different sets of measurements, per Eqs. (3) and (4). The results from the potential flow solution are given first, as the loading for an ideal cascade. Next in the table are the loadings calculated from the 1977 exit plane flow field measurements and airfoil pressure measurements. The following entries in the table are the loadings calculated from the new flow field measurements and the new airfoil pressure measurements. The last two rows in the table are the contributions of skin friction to airfoil loading. There is some disparity (5.6%) between the axial loading calculated from the 1977 flow field and the surface pressure measurements, which could be due to the availability of only four spanwise locations of airfoil surface pressure measurements. The difference in axial loading from 1977 to now indicates that the cascade is slightly more foreloaded under the new conditions. Figure 9 represents the 1977 and new midspan static pressure measurements of airfoil 2. The distribution of the measurements on the suction side of airfoil 2 indicates that the airfoil in 1977 is slightly aftloaded of the potential flow solution and that the airfoil with the new settings is slightly foreloaded of the potential flow solution. Despite the differences in axial loading, the tangential loading values based on the measurements are all within 2%, and the loading magnitudes are all within 5%.

As the values of Table 1 for surface frictions F_x and F_y show that their neglect in the calculation of \vec{F} in Eqs. (3) and (4) is justified. Skin friction, as could be expected from its order of magnitude in Figs. 6 and 7, contributes little to the loading.

4 Discussion

The measurements presented in this study provide information, additional to just loss figures, for comparison with a CFD simulation. Skin friction can be seen as the primary cause of loss in the cascade (without skin friction there would be no loss). If a CFD simulation is to accurately represent the physics of loss generation, and not just the loss value, it would need to yield skin friction profiles similar to those measured. Flow over a large portion of the endwall is best described as laminar, as reported by Harrison [8]. Excessive loss transport predictions are likely in those portions of the endwall if a fully turbulent CFD model is used, leading to erroneously high loss predictions. The shear distributions may be useful for identifying improvements to a CFD turbulence model. Airfoil loading is another parameter to match. Although axial loading was shown to vary with cascade settings, tangential loading, more importantly, varied little as did measured loss.

The consideration of flow topology, skin friction, and surface pressure give insight to the physics behind heat transfer. Turbine designers, lacking information about skin friction or heat transfer, have resorted to Reynolds analogy to infer one from the other. High skin friction coincides with high heat transfer on some parts of the cascade surface, such as on the endwall just forward of the top of the airfoil. In general, however, Reynolds analogy does not hold. In particular, high heat transfer occurs at the leading edge stagnation line where there is zero skin friction. The saddle point also has locally high heat transfer and pressure in combination with low skin friction. Further investigation may show whether the high heat transfer at saddle point is due to it being a location of high mixing (unsteady attachment) or strong attachment. Mixing is evidently in effect on suction side of the airfoil near mid-span, one-half axial chord from the leading edge. There, the heat transfer is high, but the skin friction, which is time averaged, is low. Being able to distinguish different flow patterns can help designers improve heat transfer predictions by applying specific models to specific areas of a turbine stage.

5 Conclusion

Measurements of skin friction coefficient and limiting streamline direction were taken for the airfoil and endwall of a linear turbine cascade. Surface pressure measurements were also taken on the airfoil. These new measurements are presented with previously taken measurements of Stanton number and of endwall static pressure. The inlet boundary layer and cascade periodicity were adjusted to obtain cascade conditions similar to those of the earlier study. Exit plane flow field measurements indicate that the new measurements were taken with cascade settings that reflect figures of loss and tangential loading that are similar to those of the earlier study. The combined measurement set is offered in this paper to help improve understanding of the cascade flow physics, CFD modeling capability, and heat transfer prediction.

Acknowledgment

The work reported here was supported by the National Science Foundation under Grant No. 0412929. We thank NSF and NSF Program Director, Dr. Michael Plesniak, for their sponsorship.

We thank the Aerodynamics Group at Pratt & Whitney, the industrial liaison for the NSF grant, for their advice and critique of this work.

Dr. Minor L. Nice provided help obtaining the 1977 static pressure data.

The nickel-tungsten foil used for the OFI technique was provided by AMETEK Specialty Metal Products, Wallingford, CT.

Nomenclature

- A = area scaled by b_x^2
- b_x = axial chord, m
- C_f = skin friction coefficient, $\tau_s/\frac{1}{2}\rho U^2$
- c_p = specific heat, J/kg K
- C_p = static pressure coefficient, $(P-P_o)/\frac{1}{2}\rho U^2$
- C_{pt} = total pressure coefficient, $(P_{to}-P_t)/\frac{1}{2}\rho U^2$
- cs = control surface
- \vec{F} = airfoil loading scaled by $\frac{1}{2}\rho U^2 b_x^2$, (Eqs. (3) and (4))
- h = convective heat transfer coefficient, W/m² K
- ℓ = interferometric fringe separation, m
- \vec{n} = unit vector normal to surface
- n_a, n_o = indices of refraction of air and oil
- P = pressure, Pa
- Re = Reynolds number, $\rho U b_x/\mu$
- s = airfoil arc length from the leading edge attachment line scaled by b_x
- St = Stanton number, $h/\rho U c_p$
- t = elapsed wind tunnel run time, s

\vec{t} = unit vector tangent to limiting streamline
 \vec{u} = velocity vector scaled by U
 U = cascade inlet velocity, m/s
 u, v = velocities in x and y directions scaled by U
 x = axial coordinate scaled by b_x
 y = tangential coordinate scaled by b_x
 z = coordinate along airfoil span scaled by b_x

Greek Symbols

α = angle of light incidence, rad
 λ = wavelength of light, m
 μ = viscosity, Pa s
 μ_o = oil viscosity, Pa s
 ρ = density, kg/m³
 τ_s = surface shear stress (skin friction) magnitude, Pa

Subscripts

o, t = reference and total
 x, y = x and y directional components

References

- [1] Holley, B. M., Becz, S., and Langston, L. S., 2006, "Measurement and Calculation of Turbine Cascade Endwall Pressure and Shear Stress," *ASME J. Turbomach.*, **128**, pp. 232–239.
- [2] Langston, L. S., Nice, M. L., and Hooper, R. M., 1977, "Three Dimensional Flow Within a Turbine Cascade Passage," *ASME J. Eng. Power*, **99**, pp. 21–28.
- [3] Graziani, R. A., Blair, M. F., Taylor, J. R., and Mayle, R. E., 1980, "An Experimental Study of Endwall and Airfoil Surface Heat Transfer in a Large Scale Turbine Blade Cascade," *ASME J. Eng. Power*, **102**, pp. 257–267.
- [4] Langston, L. S., 1980, "Crossflows in a Turbine Cascade Passage," *ASME J. Eng. Power*, **102**, pp. 866–874.
- [5] Sieverding, C. H., 1985, "Recent Progress in the Understanding of Basic Aspects of Secondary Flows in Turbine Blade Passages," *ASME J. Turbomach.*, **107**, pp. 248–257.
- [6] Langston, L. S., 2001, "Secondary Flows in Axial Turbines: A Review of Heat Transfer in Gas Turbine Systems," *Ann. N.Y. Acad. Sci.*, **934**, pp. 11–26.
- [7] Sharma, O. P., and Butler, T. L., 1987, "Predictions of Endwall Losses and Secondary Flows in Axial Flow Turbine Cascades," *ASME J. Turbomach.*, **109**, pp. 229–236.
- [8] Harrison, S., 1990, "Secondary Loss Generation in a Linear Cascade of High-Turning Turbine Blades," *ASME J. Turbomach.*, **112**, pp. 618–624.
- [9] Harrison, S., 1992, "The Influences of Blade Lean on Turbine Losses," *ASME J. Turbomach.*, **114**, pp. 184–190.
- [10] White, F. M., 1974, *Viscous Fluid Flow*, McGraw-Hill, New York.
- [11] Naughton, J. W., and Sheplak, M., 2002, "Modern Developments in Shear-Stress Measurement," *Prog. Aerosp. Sci.*, **38**, pp. 515–570.
- [12] Driver, D. M., 2003, "Application of Oil-Film Interferometry Skin-Friction Measurement to Large Wind Tunnels," *Exp. Fluids*, **34**, pp. 717–725.
- [13] Davy, C., Alvi, F. S., and Naughton, J. W., 2002, "Surface Flow Measurements of Micro-Supersonic Impinging Jets," *Proceedings of the 22nd AIAA Aerodynamic Measurement Technology and Ground Testing Conference*, St. Louis, MO, Jun. 24–26, AIAA Paper No. 2002-3196.
- [14] Rasband, W. S., 1997–2005, IMAGEJ, U.S. National Institutes of Health, Bethesda Maryland, <http://rsb.info.nih.gov/ij>
- [15] Holley, B. M., and Langston, L. S., 2006, "Surface Shear Stress and Pressure Measurements in a Turbine Cascade," *ASME Paper No. GT2006-90580*.
- [16] Holley, B. M., and Langston, L. S., 2008, "Analytical Modeling of Turbine Cascade Leading Edge Heat Transfer Using Skin Friction and Pressure Measurements," *ASME J. Turbomach.*, **130**, p. 021001.
- [17] Howarth, L., 1959, "Laminar Boundary Layers," *Handbuch der Physik*, S. Flügge, ed., Springer-Verlag, Berlin, Vol. VIII/1, pp. 318–321.
- [18] Dorney, D. J., and Davis, R. L., 1992, "Navier–Stokes Analysis of Turbine Blade Heat Transfer and Performance," *ASME J. Turbomach.*, **114**, pp. 795–806.

Numerical Investigation on Unsteady Effects of Hot Streak on Flow and Heat Transfer in a Turbine Stage

Bai-Tao An

e-mail: anbt@mail.etp.ac.cn

Jian-Jun Liu

e-mail: jjl@mail.etp.ac.cn

Institute of Engineering Thermophysics,
Chinese Academy of Sciences,
Beijing 100190, P.R.C.

Hong-De Jiang

Department of Thermal Engineering,
Tsinghua University,
Beijing 100084, P.R.C.
e-mail: jianghd@tsinghua.edu.cn

This paper presents a detailed flow and heat transfer characteristic analysis on gas turbine first-stage turbine under hot streak inlet conditions. Two kinds of inlet total temperature conditions are specified at the turbine stage inlet. The first is uniform inlet total temperature, and the second is hot streak 2D total temperature contour. The two kinds of inlet conditions have the same mass-averaged total temperature and the same uniform inlet total pressure. The hot streak total temperature contours are obtained according to the exit shape of an annular-can combustor. The ratio of the highest total temperature in the hot streak to the mass-averaged total temperature is about 1.23, and one hot streak corresponds to two vane passages and four blade passages. Six hot streak circumferential positions relative to the Vane 1 leading edge varied from -2% to 81% pitch are computed and analyzed. The results show that hot streak obviously increases the nonuniform degree of vane heat load in comparison with the uniform total temperature inlet condition. The change in hot streak circumferential position leads to the circumferential parameter variation at stator exit and also leads to different transient periodic fluctuating characteristics of heat load and pressure on the rotor blade surface. The hot streak of relative pitch at 65% obtains a similar heat load for the two vanes corresponding to one hot streak and small fluctuation in the averaged heat load on the rotor blade. [DOI: 10.1115/1.2988172]

Keywords: unsteady flow, hot streak, three dimensional numerical simulation, gas turbine

1 Introduction

The inlet temperature field of gas turbine is usually nonuniform or distorted, as the combustor exit flow has both the circumferential and radial temperature gradients. These temperature gradients arise from combustor framework characteristic and combustor surface cooling. Hot streaks have temperature typically twice the freestream temperature in aeroengine. For the heavy duty gas turbine, the ratio of the highest temperature to mass-averaged temperature is slightly low. It is well known that the most important problem in gas turbine is blade or vane reliability under excessive working temperature. The reliability includes two aspects: steady heat reliability such as cooling design of stator vane, and unsteady heat reliability such as thermal fatigue of the rotor blade. Hot streak greatly influences the above two aspects. Therefore, for gas turbine cooling design, especially the first-stage, the effect of hot streak must be considered.

A number of studies have been performed for the hot streak effects on the turbine stage. Jenkins et al. [1] studied the film cooling effects on the dispersion of a simulated hot streak on an experimental cascade. The result showed that film cooling obviously reduces the peak temperature values. Jenkins and Bogard [2] performed experimental studies to discuss the attenuation of a simulated hot streak in the experimental vane cascade, and the major topic focused on the effects of turbulence level and pitch position variations of the hot streak to the peak hot streak temperature at a few axial positions. The studies indicated that the

attenuation rate of hot streak depends on the location of the hot streak relative to the vane due to isolation of the hot streak core by the vane wall. Zhao et al. [3] employed the numerical method to investigate the influence of the hot streak temperature ratio in a high pressure stage of a vaneless counter-rotating turbine. The temperature ratio of a circular shape hot streak varies from 1.0 to 2.4. The results showed that the heat load of the high pressure turbine (HPT) rotor increases with an increase in the hot streak temperature ratio. Ji et al. [4] also performed studies on a counter-rotating turbine using a 3D unsteady Euler solver, and the results showed that the effect of the hot streak on a counter-rotating turbine is nearly the same as a conventional turbine. However, clocking between the hot streak and the vane of the HPT significantly influences on the heat load of the whole HPT stage. Dorney and Gundy-Burlet [5] studied a 1-1/2 stage turbine geometry, in which the position of the hot streak is varied to produce different levels of impingement on the first-stage stator. The results indicated that when the hot streak impinges on the first-stage stator, the pressure surfaces (PSs) of the downstream blade rows reach much higher time-averaged temperature. He et al. [6] carried out computational studies on the effects of hot streak circumferential length-scale in transonic turbine stage. Both aeroforce and aerothermal are considered, and the results showed that the circumferential wavelength of the temperature distortion can significantly change the unsteady forcing as well as the heat transfer to the rotor blades. Dorney et al. [7] performed a numerical investigation of multi-blade count ratio and 3D effects on the hot streak migration in a turbine stage. Three-stator/four-rotor and one-stator/one-rotor were investigated using 2D and 3D numerical methods. Gundy-Burlet and Dorney [8] performed a 3D unsteady simulation to investigate the effects of radial location of the hot streak in

Contributed by the International Gas Turbine Institute of ASME for publication in the JOURNAL OF TURBOMACHINERY. Manuscript received April 9, 2008; final manuscript received April 13, 2008; published online April 20, 2009. Review conducted by David Wisler. Paper presented at the ASME Turbo Expo 2008: Land, Sea and Air (GT2008), Berlin, Germany, June 9–13 2008.

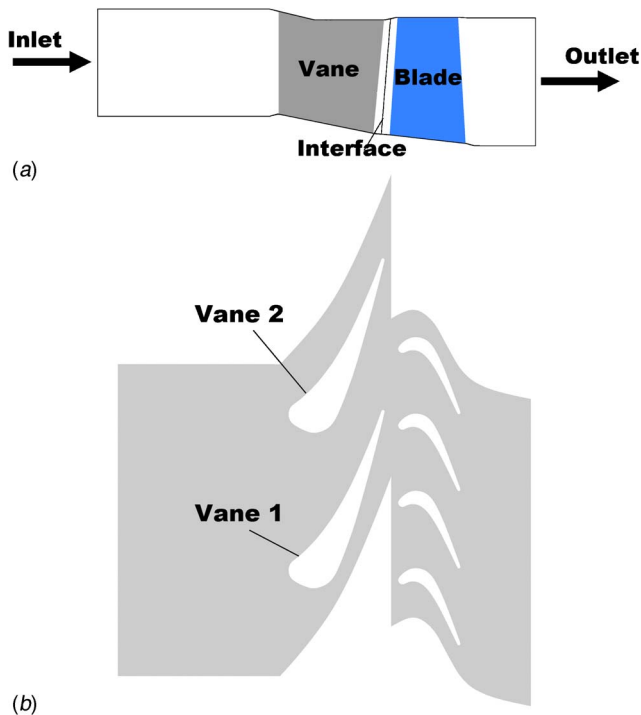


Fig. 1 Model of the first-stage turbine: (a) meridian view, and (b) S1 view ($N=0$)

a 1–1/2 stage turbine, in which the radial location and the clocking position of the hot streak is varied. Shang and Epstein [9] explored the influence of the inlet hot streak temperature distortion on turbine blade heat load in a transonic axial flow turbine stage using a 3D multiblade row unsteady Euler code, and they found that temperature distortion significantly increases both the blade surface heat load nonuniformity and the total blade heat load by as much as 10–30% (mainly on the pressure surface). Zilli et al. [10] discussed the performance of a single stage axial flow HPT, and the analysis demonstrated that the temperature distortion does not have a significant effect on the performance of the HPT apart from a small reduction in efficiency.

From the studies that have been performed for the heat load, more attention is placed on the variation in time-averaged value and few studies paid attention to the transient heat load variation. The emphasis of the present work is on the effects of hot streak on flow and heat transfer characteristics of the first-stage stator and rotor. Six circumferential positions of the hot streak are considered. For the stator, it aims at exploring the hot streak migration in vane passages, exit circumferential parameter variation, and the effects of the hot streak on the vane heat load. For the rotor, it aims at exploring the periodic transient variation characteristics of heat load and aerodynamic force under six hot streak configurations.

2 Geometry of the Turbine Stage

The first-stage turbine model of a heavy duty gas turbine is shown in Fig. 1. The span/chord ratio of the vane and blade is 1.1 and 1.9, respectively. The diameter/height ratio of the vane and blade is 18.6 and 17.8, respectively.

The turbine stage model includes stator domain and rotor domain. The stator-rotor interface is set at 1/2 location between the stator and the rotor domains. There are 20 combustors, 40 vanes, and 82 rotor blades in the full annulus, respectively, in the actual engine. For the transient simulation, the model is simplified to one combustor, two vanes, and four blades to assure that the pitch ratio of the computational domains is 1:1:1, i.e., one hot streak

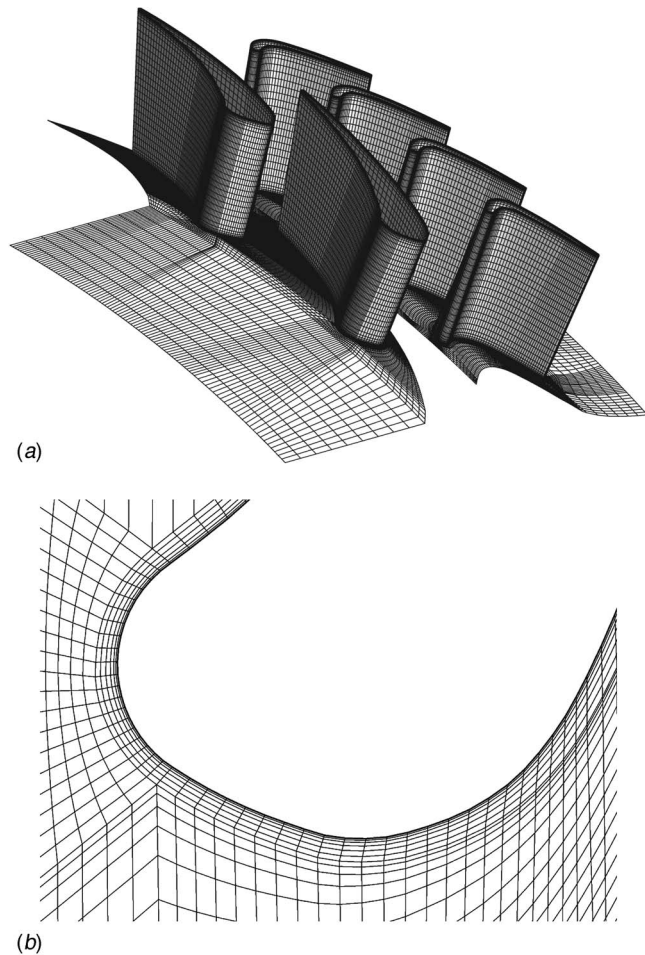


Fig. 2 Computational grid for the present simulations: (a) domain grid, and (b) near wall grid

corresponds to two vane passages and four blade passages. One hot streak periodicity has an 18 deg circumferential angle. The vane number is labeled as Vanes 1 and 2 for analysis. The rotor blade tip clearance is not considered in the present simulations. Forty time steps are set for one-rotor domain period, each time step is 2.5×10^{-5} s.

3 Numerical Method and Validation

The 3D fully implicit coupled Navier–Stokes solver CFX5 is employed to obtain the unsteady time accurate solution. This solver is based on finite-volume method, and the discretization scheme is second-order accurate. In the present simulation, the $k-\omega$ turbulence model and structured grid are employed to solve the 3D unsteady viscous flow. A sliding mesh is adopted at the domain interface. Figure 2(a) shows the grid distribution of the computational domain. There are 0.42 M and 0.4 M grid elements in the stator domain and the rotor domain, respectively, and a total of 0.82 M grid elements in the turbine stage. The grid is dense near the wall for assuring the accuracy of the wall viscous flow and for adapting the requirement of the turbulence model, as shown in Fig. 2(b). Generally, for the $k-\omega$ model, the minimum wall y^+ should be below 1.0. CFX also introduces automatic wall treatment to the $k-\omega$ model to ensure solution robustness. In the present study, the minimal y^+ of the first layer grid is about 0.6.

Steady solution is obtained before transient simulation starts. The steady solution is set as the initial flow for unsteady transient

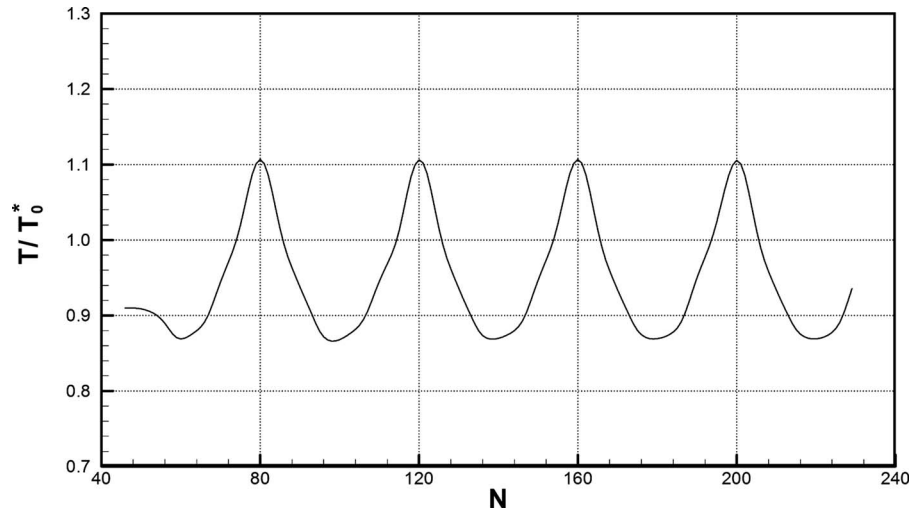


Fig. 3 Temperature periodic variation of the monitor point in rotor domain

simulation. When performing the transient simulations, one monitor point is set in the rotor domain; the monitored parameter is temperature. Multiple periods are computed until the monitored parameter is varied periodically, as shown in Fig. 3.

To validate the accuracy of CFX and the applicability of the $k-\omega$ turbulence model, a steady 3D simulation is performed to compare with the experimental data offered by Hylton et al. [11]. The cascade chosen for comparison is Mark-II. Many experimental conditions have been performed in the experiments of Hylton

et al. [11]. The experimental condition chosen here is No. 5411. Figure 4 shows the computational grid of the Mark-II cascade, the size of the grid elements has two cases for the verification of grid dependence. Case 1 has 0.55 M grid elements, and Case 2 has 0.20 M grid elements. The density of the near wall grid of Case 2 is just like the setting in Fig. 2(b). Case 1 has denser grid in the flow direction and the radial direction especially near the wall than Case 2. In the simulations, the inlet total pressure, inlet total temperature, and exit static pressure are specified according to the test conditions. In addition, the wall temperature is also specified according to the test result. The computed wall heat transfer coefficient is compared with the test result, as shown in Fig. 5.

It can be seen that the wall heat transfer coefficient of the CFX solution agrees well with the experimental result whichever trend and value, except in the region from the leading edge (LE) to $x/C=0.4$ on the suction surface (SS), where the value of the CFX solution is obviously higher than the experimental data. This may be caused by the inaccurate prediction of turbulence transition. In this case, the shear stress transport (SST) turbulence model could be better. However, the SST model needs even fine grid near wall,

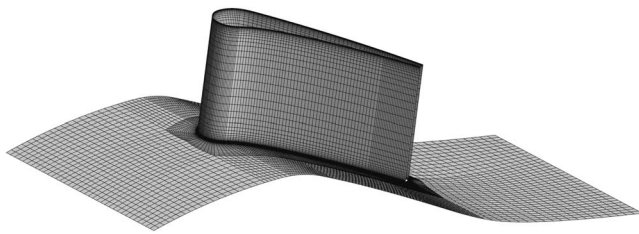


Fig. 4 Computational grid for Mark-II cascade [11]

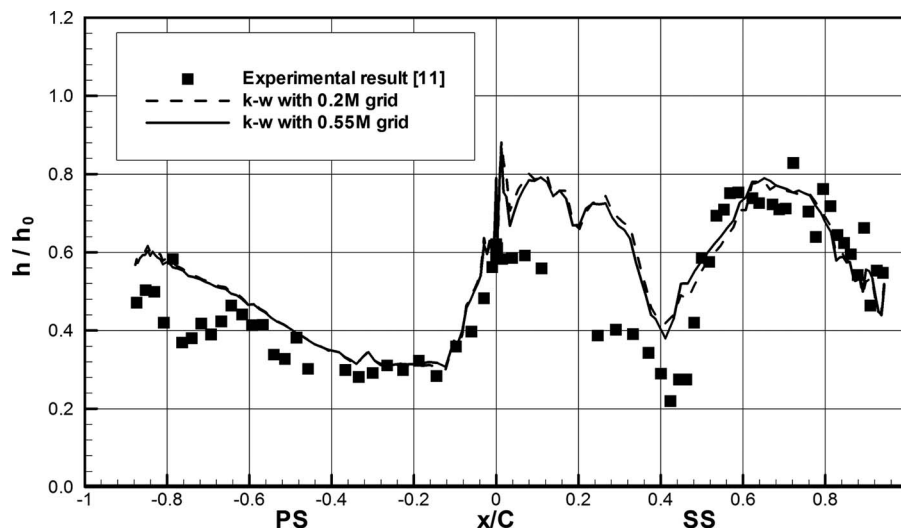


Fig. 5 Wall heat transfer coefficient comparison

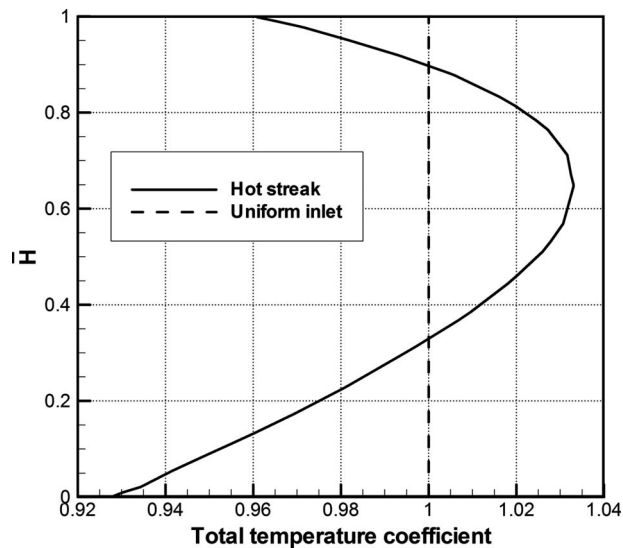


Fig. 6 Circumferential mass-averaged total temperature distribution along radial direction at stage inlet plane

and the computational time will be extremely long for transient simulations. In general, the CFX code with the $k-\omega$ turbulence model can satisfy the need of the present study, at least for qualitative analysis. In addition, the result difference between the fine grid (0.55 M) and the relative coarse grid (0.20 M) is negligible.

4 Boundary Conditions and Schemes

In the present simulation, the uniform total pressure, uniform or nonuniform total temperature, and uniform flow angles are specified at the stage inlet plane, and the averaged static pressure is specified at the stage outlet plane. The inlet turbulence intensity is set to $Tu=10\%$, and the turbulence length-scale is 115 mm. The rotation speed of the rotor blade is 3000 rpm. A constant temperature of about $0.8 T_0^*$ is set to the vane, blade, and end wall referring to the temperature limit of the blade alloy. The wall heat flux q is computed for the analysis of wall heat transfer characteristic, reference wall heat flux q_0 is employed to obtain nondimensional wall heat flux q/q_0 , and q_0 is the average of q over the entire vane and blade under the uniform total temperature inlet condition.

To study the influence of inlet hot streak on flow and heat transfer in the turbine stage, two kinds of inlet total temperature conditions are specified at stage inlet. The first is of uniform distribution of inlet total temperature used mainly for comparison purposes. The second is the 2D contours of the inlet total temperature to simulate the exit temperature field of combustor, which is a hot streak inlet condition. For the hot streak inlet condition, the ratio of the highest total temperature to the mass-averaged total temperature is about 1.23, and the radial position of the highest total temperature locates at about 65% inlet height according to the actual turbine inlet condition. The circumferential mass-averaged total temperature distribution along the radial direction is shown in Fig. 6. The two kinds of total temperature inlet conditions have the same mass-averaged total temperature at the inlet plane.

To study the effects of the circumferential position variations of the hot streak, the hot streak inlet condition has six schemes, as shown in Fig. 7. The circumferential position of the highest total temperature core point changes from the leading edge of Vane 1 to the suction surface of Vane 2, two adjacent schemes of the hot

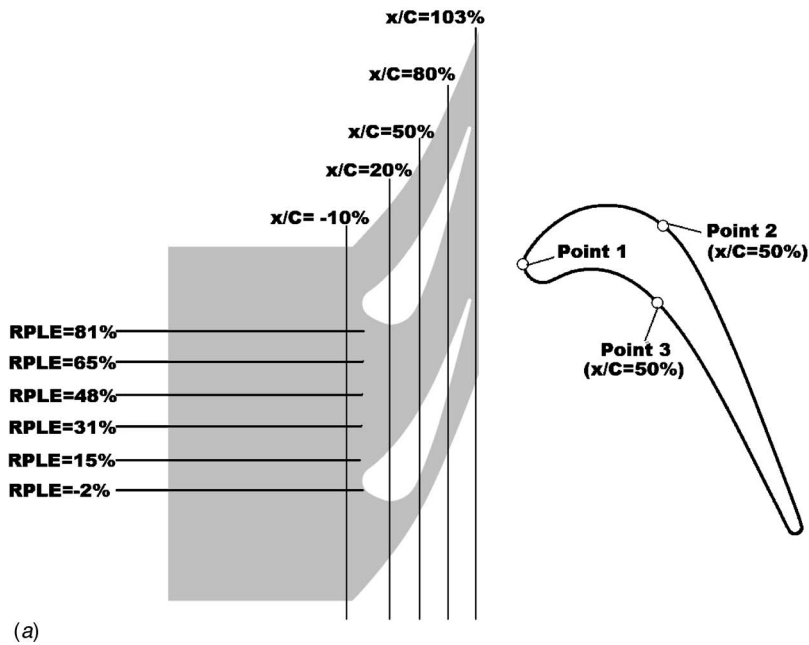
streaks have 1.5 deg circumferential interval, as shown in Fig. 7(a). The white lines in Fig. 7(b) denote the leading edge line of Vane 1, the leading edge line is minimal x position of the vane but not the actual stagnation line. The relative pitch of the hot streaks to the leading edge line of Vane 1 (RPLE) varies at -2% , 15% , 31% , 48% , 65% , and 81% pitch positions.

5 Results and Analysis

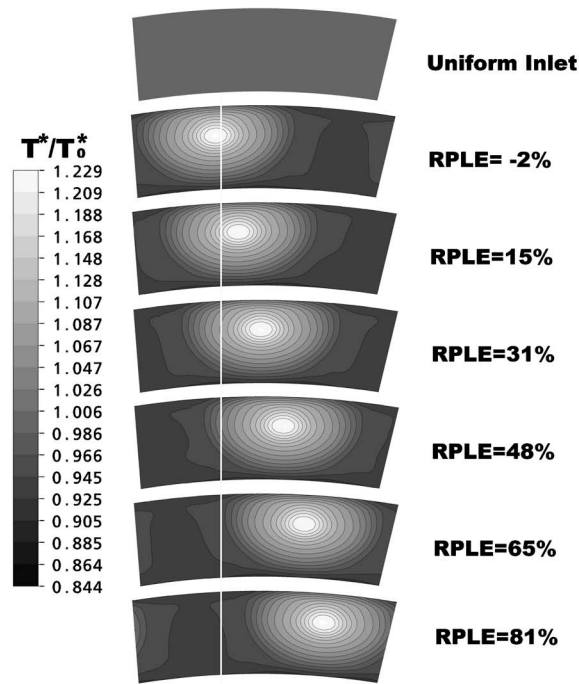
5.1 Hot Streak Development in Stator. The development process of the hot streak in a stator vane passage is very important for flow and heat transfers not only to the vane but also to the rotor blade. Figure 8 shows the relative positions in the blade-to-blade surface between the hot streaks and the Vane 1 leading edge. Six pitch positions of the hot streak can be divided into four cases. In the first case, the hot streak locates at the leading edge of Vane 1 as $RPLE=-2\%$ and 15% . In the second case, the hot streak is close to the Vane 1 pressure surface as $RPLE=31\%$. In the third case, the hot streak locates at the middle passage between Vanes 1 and 2 as $RPLE=48\%$. In the fourth case, the hot streak locates close to the suction surface of Vane 2 as $RPLE=65\%$ and 81% . Because one hot streak period faces two stator vane passages, when the six hot streak positions turn from the passage composed by Vanes 1 and 2 to the next passage, the situation of Vanes 1 and 2 interconvert.

The hot streak migrations in the two stator vane passages for the six relative pitch positions are shown in Fig. 9. The highest temperature region of $RPLE=-2\%$ situates at the leading edge of Vane 1. When entering the vane passages, the ellipsoid high temperature region is divided into two parts by Vane 1. Along with the development downstream, the ellipsoid shape is resumed quickly at the suction side, whereas at the pressure side the high temperature region is pressed to the wall and expands along the radial direction. At vane exit, the two sides of the Vane 1 wake obviously have different temperature shapes. At the suction side, the high temperature region becomes narrow in the radial direction and wide in the circumferential direction, which is caused by the opposite pressure gradient and the extrusion of the 3D separation line on the suction surface. At the pressure side, the high temperature region becomes very narrow in the circumferential direction and extends greatly along the radial direction compared with that of the inlet. The $RPLE=15\%$ has a similar behavior to $RPLE=-2\%$, a little difference is that a larger part of the high temperature core region is situated at the Vane 1 pressure side. This case is similar to the experimental inlet condition in Ref. [1], although the flow conditions are not exactly the same. The temperature reduction in the hot streak at the suction side is faster than the pressure side within the vane passage, i.e., $x/C=20-80\%$. This also agrees with the temperature reduction trend in Ref. [1]. In this case, at vane exit, the high temperature region by the sides of the wake has almost the same size and temperature value due to flow mixing, but the radial location of the peak temperature is different, i.e., the radial location at the suction side is obviously higher than at the pressure side, which is caused by both the 3D viscous flow and the meridional end wall curves of the stator. When the hot streak flows very close to the vane wall, it will be influenced by the wall limiting streamline, see Fig. 10. At the suction side, the 3D separation line caused by the 3D viscous flow exists at the rearward section. For the fluid near the wall, the 3D separation line plays the role similar to constrict the meridional shape. At the pressure side, the wall limiting stream line varies with the meridional end wall curves, whereas the meridional hub curve is diffused, so the radial position difference between suction side and pressure side appears.

The highest temperature region of $RPLE=31\%$ is close to the Vane 1 pressure surface at stator inlet, so it always transports along the pressure surface. At vane exit, it becomes closer to the



(a)



(b)

Fig. 7 Inlet total temperature conditions: (a) the circumferential positions of the inlet hot streak and probing planes and points in stator and rotor domain, and (b) the inlet total temperature contours

pressure surface and has the same pressure-side-behavior with $RPLE = -2\%$ and 15% . The $RPLE = 48\%$ behaves just like $RPLE = 31\%$, although the highest temperature region situates at the middle between Vanes 1 and 2 at stator inlet. The highest temperature region situates close to Vane 1 pressure surface at the vane exit.

The $RPLE = 65\%$ is similar to the $RPLE = 81\%$, i.e., the highest temperature region close to the Vane 2 suction surface at stator inlet. The development of the hot streak has two phases. In the forward section of the vane passage, high temperature region is

elongated along the radial direction corresponding to accelerated flow. In the rearward section of the passage, high temperature region extends along the circumferential direction corresponding to decelerated flow. At vane exit, the temperature contour of the high temperature region almost keeps the same shape as at the inlet.

Figures 11 and 12 are the circumferential and radial temperature distributions at the position across the highest temperature core point at the stator exit plane. The position change in the highest temperature region through the vane passage is very clear.

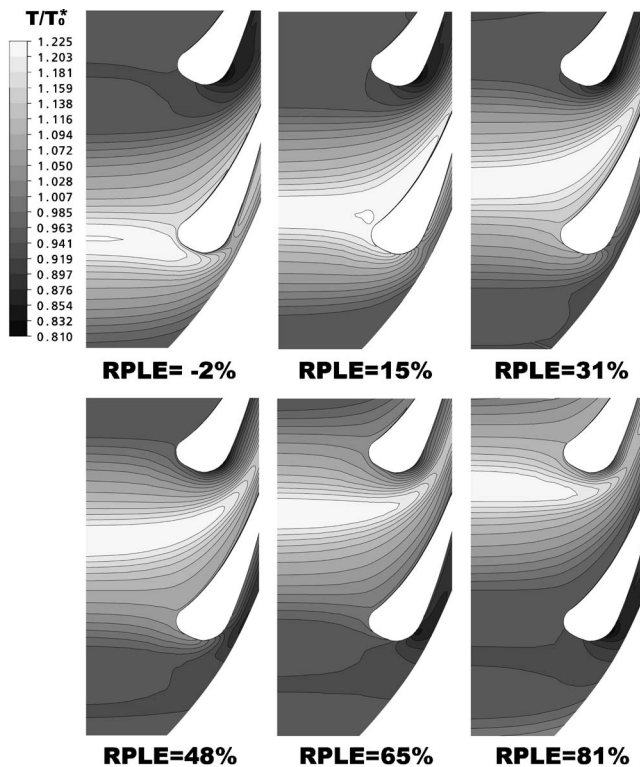


Fig. 8 Temperature contours at 65% vane height

First, Fig. 11 shows that the exit circumferential interval of the highest temperature core point between the adjacent hot streak schemes becomes discord with that of inlet. The circumferential interval is small (<1.5 deg) close to the TE1 pressure side, the circumferential interval becomes large (>1.5 deg) gradually with the hot streak turning from TE1 pressure side to TE2 suction side. It should be noted that the exit circumferential position of the highest temperature core point for the case of RPLE=65% situates at the middle of TE1 and TE2. Second, Fig. 12 shows obviously that the highest temperature core point for RPLE=-2% has the highest radial position than the other hot streak schemes. RPLE=81% behaves just like RPLE=-2%. Although the hot streak RPLE=-2% is classified to the case of impinging on the Vane 1 leading edge, from Fig. 11 we can see that most part of the high temperature region situates at Vane 1 suction side, so this case can also be classified as the hot streak very close to the Vane 1 suction surface (i.e., RPLE=81%). From this point of view, this phenomenon confirms the analysis associated with Fig. 10. The conclusion is that the radial positions of the highest temperature region of the hot streak at stator exit have an increasing trend from the TE1 pressure side to the TE2 suction side. However, the highest location in radial direction cannot exceed the 3D separation line at stator exit. Third, at vane exit, a small peak temperature difference exists among the hot streak schemes. Jenkins and Bogard [2] indicated that the peak hot streak temperature at vane exit was the same for an impinging and nonimpinging hot streak under the steady and adiabatic experimental conditions. The present result has the similar trend. The small peak temperature difference comes from two aspects. One is the heat transfer from the flow to the wall (isothermal wall instead of adiabatic wall). Another is the unsteady rotor-stator interaction of the downstream rotor blades.

In general, after passing the vane passage, the shape, the temperature value, and the radial and circumferential positions of the

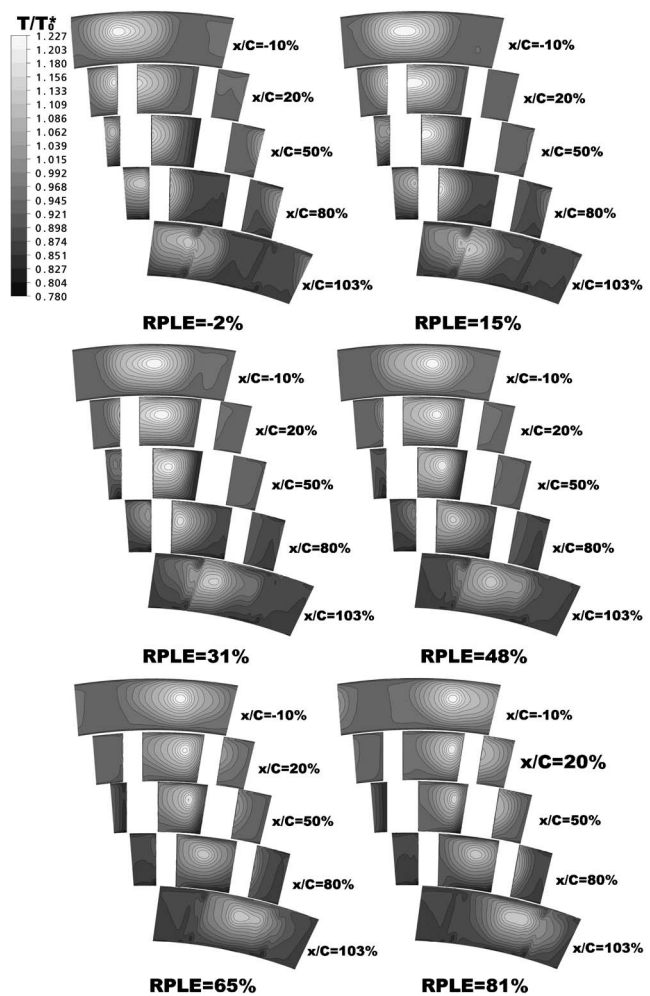


Fig. 9 Hot streak development along flow direction in stator

hot streak will change. The different variations of heat load and aerodynamic parameters of the rotor blade will mainly arise from the above variations.

5.2 Stator Aerodynamic Parameter Variation. Compared with the uniform total temperature inlet condition, hot streak has little effect on vane surface pressure distributions, as shown in Fig. 13. The vane surface pressure distributions of all hot streak schemes agree with that of the uniform total temperature inlet condition at 10% and 65% vane height, only with a little difference at the rearward section of vane suction surface. In a subsonic turbine stage, rotor-stator interaction will lead to vane surface pressure fluctuation periodically, but the pressure fluctuation occurs at the neighborhood of trailing edge and has a small range.

In addition, the inlet hot streak and its circumferential position variations have little effect on the total mass-averaged total pressure, the total temperature, and the flow angle of the whole stator exit compared with that of the uniform total temperature inlet condition, because the two kinds of inlet conditions have the same inlet mass-averaged total temperature and total pressure. However, the hot streak will influence the aerodynamic parameter distribution at stator exit both in the circumferential and radial directions because of the temperature gradients. On account of the rotor blade rotation in the circumferential direction, the pressure and heat load fluctuations of the rotor blade mainly arises from the stator exit circumferential parameter variations. Consequently, the emphasis is put on the circumferential parameter variations caused by the hot streak.

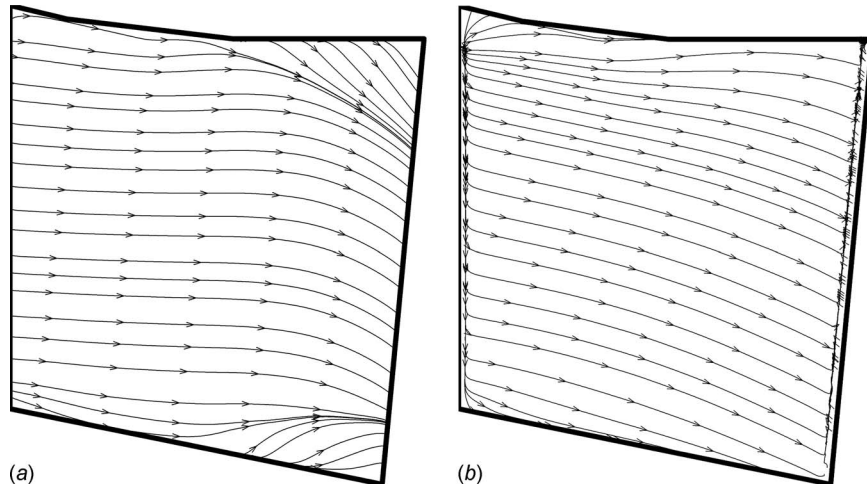


Fig. 10 Wall limiting stream line of the vane under uniform total temperature inlet condition: (a) suction surface, and (b) pressure surface

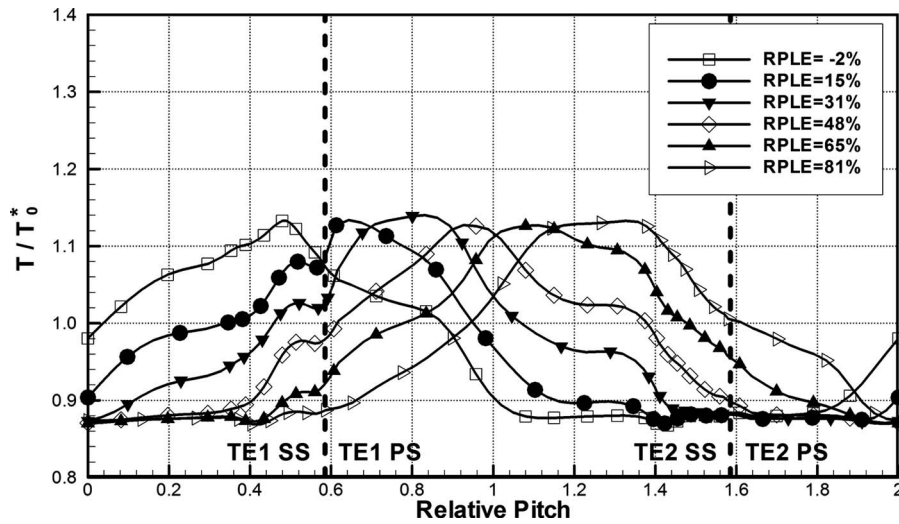


Fig. 11 Exit ($x/C=103\%$) circumferential temperature distribution across the highest temperature point ($N=10$)

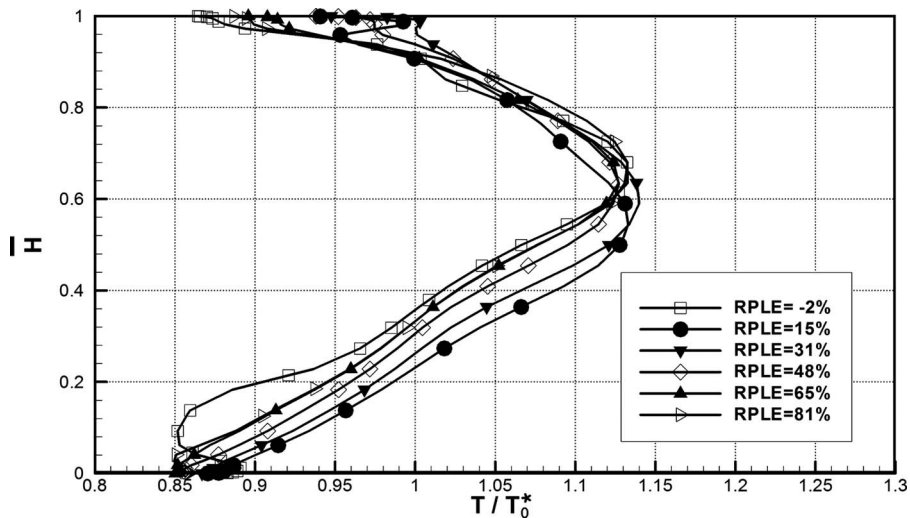


Fig. 12 Exit ($x/C=103\%$) radial temperature distribution across the highest temperature point ($N=10$)

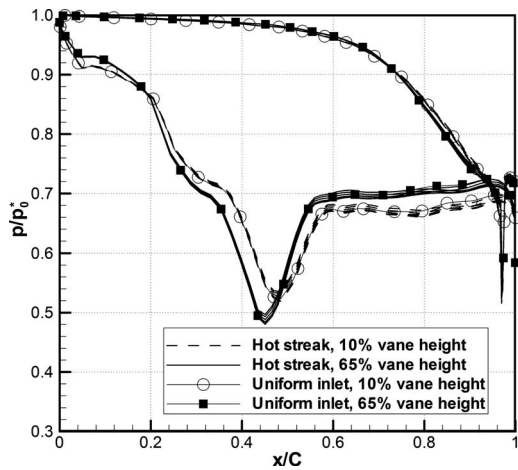


Fig. 13 Surface pressure distributions of Vane 1 ($N=10$)

It is necessary to illuminate the circumferential parameter variations in particular temperature and pressure at stator exit under the uniform total temperature inlet condition, as the base line for comparison. Figure 14 shows that the circumferential static temperature, total temperature, and total pressure at stator exit are obviously nonuniform even under the uniform total temperature inlet condition. The variation in circumferential temperature and pressure comes from the different expansion level when the gases flow through the vane passage, which is the inherent characteristic of the cascade flow, as shown in Figs. 14(a) and 14(b), and comes from the passage vortices as the black arrows indicated in Fig. 14(a). The passage vortices will lead to nonuniform temperature at exit plane, although the size of vortices is small. It is known that the passage vortex is formed by the two branches of the horse vortex due to the interaction of the wall boundary layer and the leading edge. The fluid in the boundary layer usually has low temperature in cooled turbine, so the passage vortices will lead to low temperature region on stator exit plane. Also, the passage vortices will lead to nonuniform total pressure at stator exit plane, as shown in Fig. 14(c). Commonly, the passage vortices are the main sources of stator loss, so the passage vortices will influence the heat transfer of the downstream rotor blade not only by the low temperature but also by the flow characteristic. In addition, the wake should have an influence on the downstream flow and heat transfer. In general, the circumferential variation in temperature and pressure at stator exit under uniform total temperature inlet condition should be consistent for the two vane passages.

Figure 15 shows the circumferential parameter variation at 65% vane height under hot streak and uniform total temperature inlet conditions. Although the highest temperature region is slightly different in the radial direction among the six hot streak schemes, the 65% vane height still is a typical position for trend comparison. Among these parameters, flow angle, Mach number, and total pressure have little difference among the seven schemes; whereas total temperature, static pressure, and velocity have great difference. Total temperature variation combines static temperature and velocity difference, while total pressure difference combines static pressure and velocity difference. Because total pressure difference among the schemes is little, the static pressure difference from one scheme to another comes from the velocity difference. The total temperature variation trend (Fig. 15(e)) is not fully according to the static temperature variation trend (Fig. 11), but also due to the velocity variation (Fig. 15(f)) caused by the hot streak.

The velocity difference at stator exit among the schemes arises from the inlet hot streak. For the present simulation, the outlet averaged static pressure and the inlet uniform total pressure are

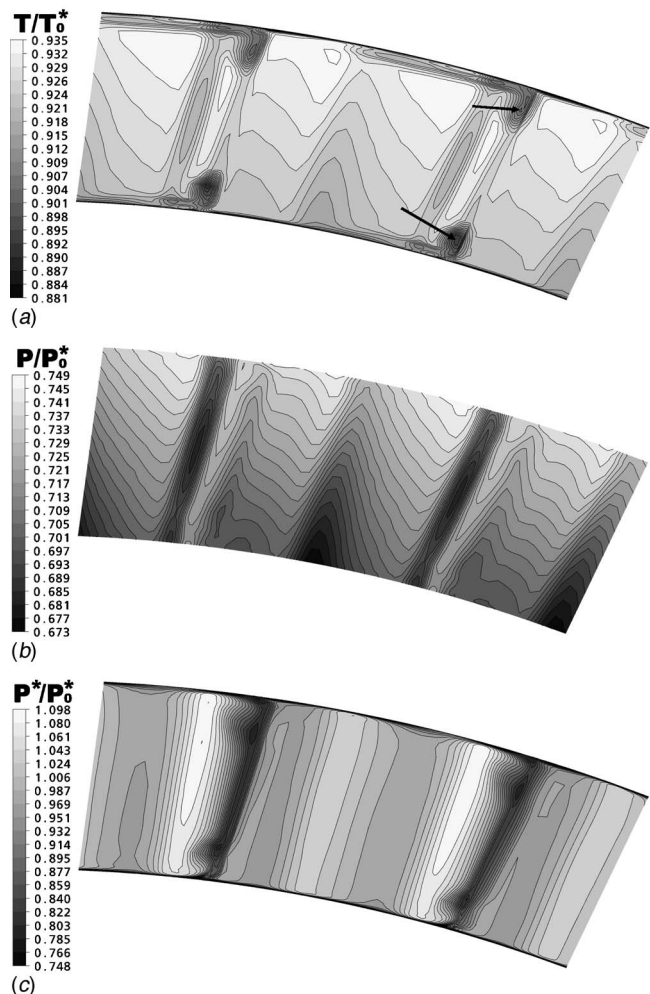


Fig. 14 Stator exit flow field under uniform total temperature inlet condition ($N=0$): (a) static temperature contours, (b) static pressure contours, and (c) total pressure contours

specified. The high total temperature region due to the hot streak at stage inlet has high total enthalpy, which corresponds to the high flow velocity at stator inlet under the same exit pressure. In other words, the circumferential velocity difference among the schemes at stator exit is caused by the relative pitch position variation of the hot streak at stator inlet.

5.3 Rotor Aerodynamic Parameter Variation. The circumferential parameter variation at stator exit is the main factor affecting the aerodynamic parameter variation of the rotor, in particular, the total pressure, total temperature, and velocity. The analysis on the stator indicates that the hot streak influences the circumferential parameter distribution and has little effect on wall pressure distribution because there is only total temperature distortion at the stator inlet. For the rotor, whereas, there are both inlet total temperature distortion and inlet total pressure distortion, as shown in Fig. 16. Thus, the aerodynamic parameter variation in the rotor should be greater than that in the stator.

The analysis on the aerodynamic parameters focuses on the surface pressure transient variation. The surface pressure variation causes the flow change in blade passage. Another aspect, the periodic variation in the surface pressure, results in the transient aerodynamic force of the rotor blade fluctuating periodically, which is remarkable for vibration of the rotor blade.

Figure 17 shows that the surface pressure transient variation

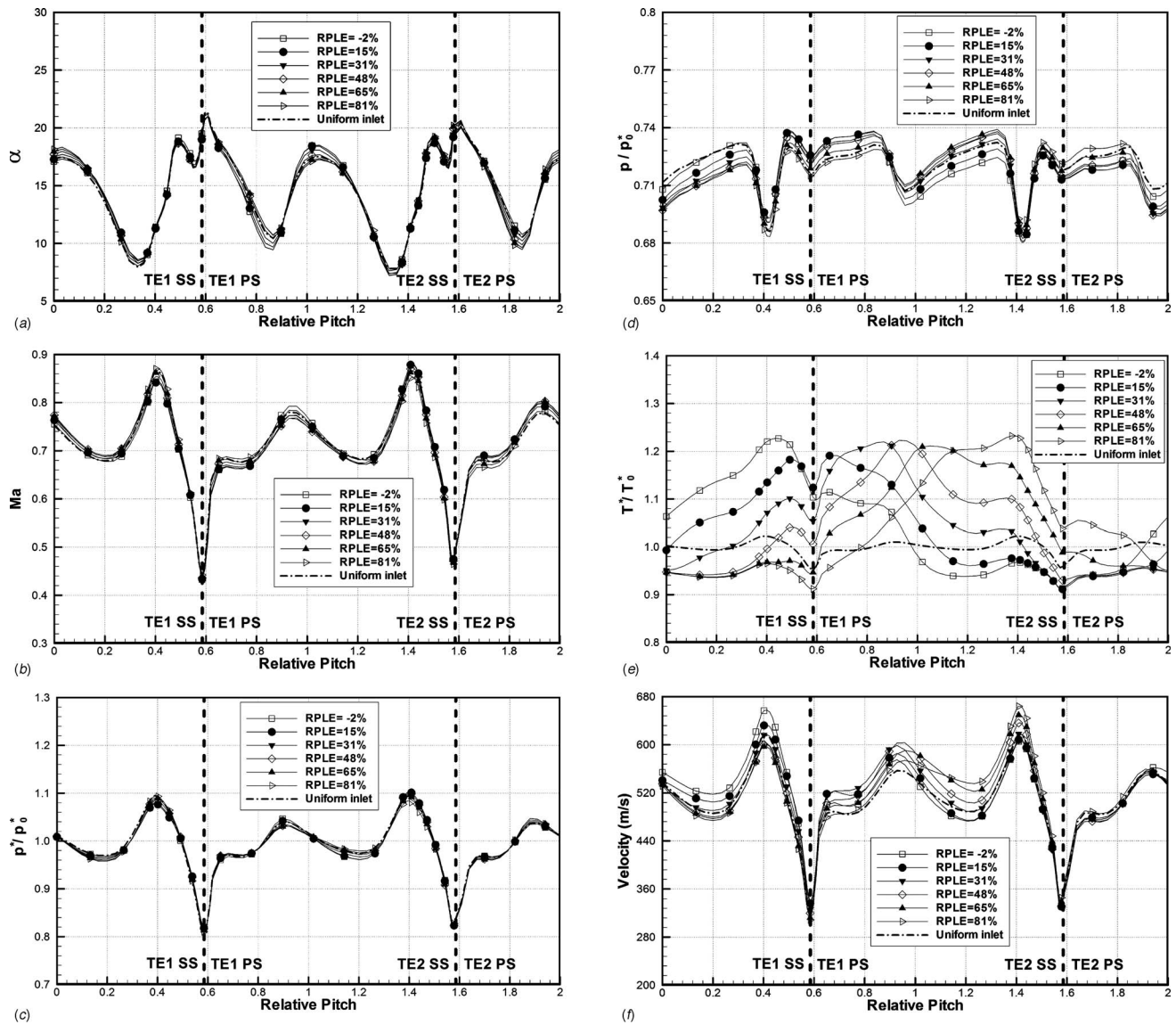


Fig. 15 Exit ($x/C=103\%$) circumferential parameter distribution at 65% vane height ($N=10$): (a) flow angle, (b) Mach number, (c) total pressure, (d) static pressure, (e) total temperature, and (f) velocity

under the hot streak inlet condition is obviously greater than that under the uniform total temperature inlet condition. The transient variation of the surface pressure under uniform total temperature inlet condition comes from the nonuniform circumferential pressure at stator exit, as shown in Fig. 14. Figure 18 gives the surface pressure transient variation within one-rotor domain period at three typical points of 65% blade height. The point positions are shown in Fig. 7(a). At the blade leading edge (Point 1), the fluctuation range of pressure is maximal, the maximal transient pressure difference is about $10\%p_0^*$. The fluctuation range increases by the hot streak but the value is relatively small. At the suction surface (Point 2), the pressure fluctuation range is smaller than the leading edge as a whole, and the effect of the hot streak is relatively greater than the leading edge. Also, the pressure fluctuation on the suction surface is very sensitive to hot streak. When the rotor blade passes the vane exit where the hot streak effect exists (such as $N=6-26$), the fluctuation range increases obviously. At the pressure surface (Point 3), the pressure fluctuation is very small, i.e., only about $2\%p_0^*$ transient pressure difference under

uniform total temperature inlet condition, but the hot streak increases the transient pressure difference to about $4\%p_0^*$.

Because the circumferential parameters are nonuniform in the two vane passages for hot streak inlet condition, the fluctuation periodicity of the surface pressure is altered from 9 deg to 18 deg circumferential interval compared with the uniform total temperature inlet condition.

5.4 Vane Wall Heat Flux Variation. The effect of the hot streak on heat load is more important than on aerodynamic parameters in gas turbine from the viewpoint of reliability. First, hot streaks lead to nonuniform heat load in radial direction whichever for Vane 1 or Vane 2 because of the radial temperature gradient. Second, hot streaks lead to nonuniform heat load for the two vanes in one hot streak period because of the circumferential temperature gradient. The heat load distribution caused by the relative position between the hot streak and the vane is very important for vane cooling design.

Figure 19 shows that at 65% vane height, q/q_0 of Vane 1 de-

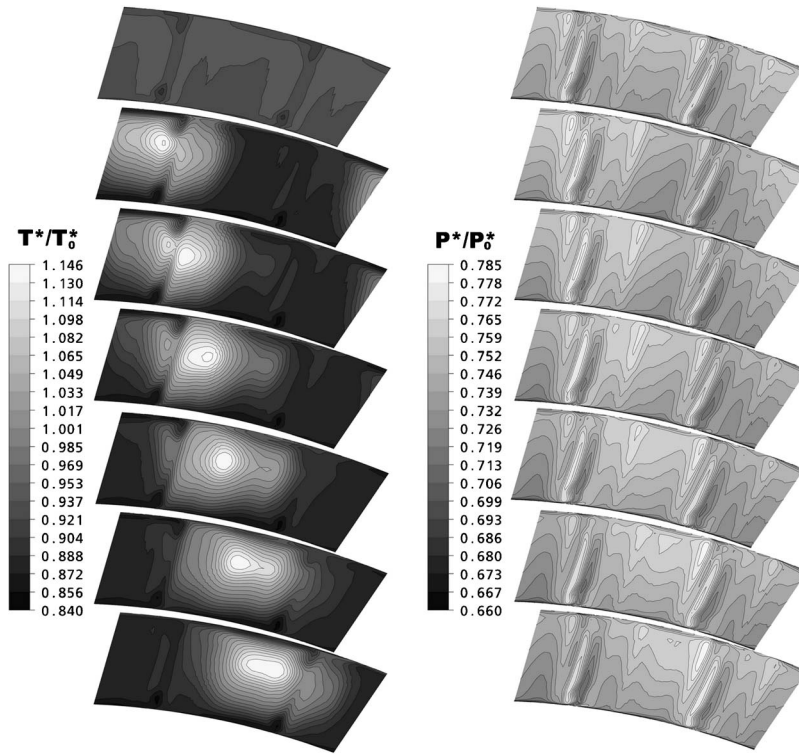


Fig. 16 Total temperature and total pressure contours in rotational frame at rotor inlet for the seven schemes ($N=20$)

creases with the circumferential turning of the hot streak from $RPLE=-2-81\%$. Vane 1 has the maximum q/q_0 when $RPLE=15\%$, at the same time, Vane 2 has the minimum q/q_0 . Hence,

$RPLE=15\%$ causes the maximum heat load nonuniformity between Vanes 1 and 2 in one hot streak period. $RPLE=-2\%$ has a similar behavior compared with $RPLE=15\%$ because the highest total temperature region of hot streak impinges upon the Vane 1 leading edge too. For $RPLE=65\%$, Vane 1 has approximately the same q/q_0 as the uniform total temperature inlet condition. Also, Vanes 1 and 2 have approximate q/q_0 . For $RPLE=81\%$, q/q_0 of Vane 1 is lower than the uniform total temperature inlet condition. Vane 2 has the opposite behavior compared with Vane 1 when the pitch position of the hot streak changed. Figure 20 shows that at the relative low temperature region (10% vane height), q/q_0 is smaller than at 65% vane height for all hot streak schemes. The circumferential position variation of the hot streak has little effect on q/q_0 compared with the relative high temperature region of 65% vane height.

The analysis above indicates that $RPLE=15\%$ causes the maximal circumferential and radial nonuniformities in heat load. $RPLE=65\%$ can obtain almost the same heat load on Vanes 1 and 2, and the minimal nonuniformity in heat load in the radial direction of the vane.

5.5 Blade Wall Heat Flux Variation. Thermal fatigue of the rotor blade is one important aspect for reliability. The thermal fatigue comes from temperature fluctuation on the rotor blade surface. The hot streak is one important factor that can cause the temperature fluctuation on the rotor blade due to its circumferential temperature gradient. Although it is not very clear how much effect can be caused to the blade fatigue life, it is necessary to give the transient fluctuation characteristics of heat load.

The periodic variation of q/q_0 on the rotor blade is mainly caused by the exit circumferential temperature variation of the stator. The wake flow and passage vortices also have some effects too, but the effects are relatively weak. Figure 21 gives q/q_0 comparisons between uniform total temperature inlet condition and hot streak inlet condition (for example, $RPLE=48\%$). It indicates that q/q_0 fluctuates in a small range under uniform total tempera-

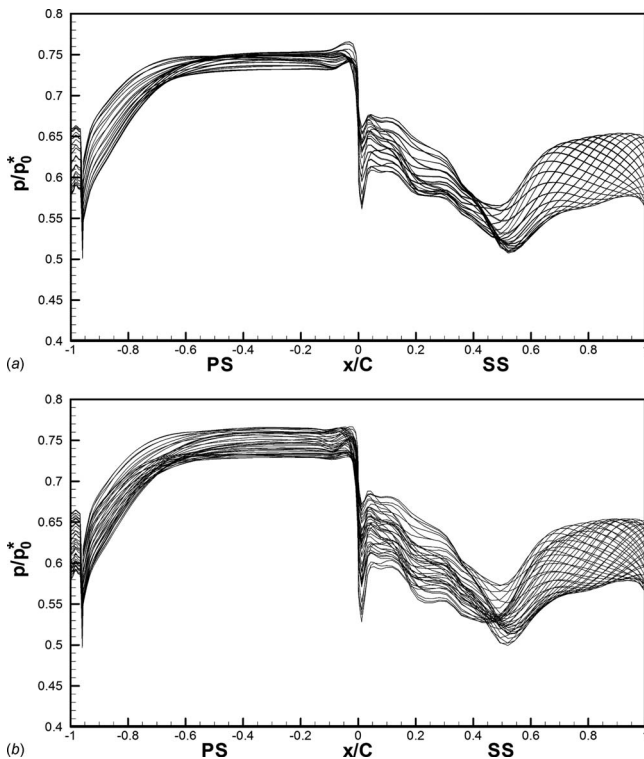


Fig. 17 Surface pressure distributions at 65% blade height ($N=0-39$): (a) uniform total temperature inlet condition, and (b) hot streak inlet condition ($RPLE=48\%$)

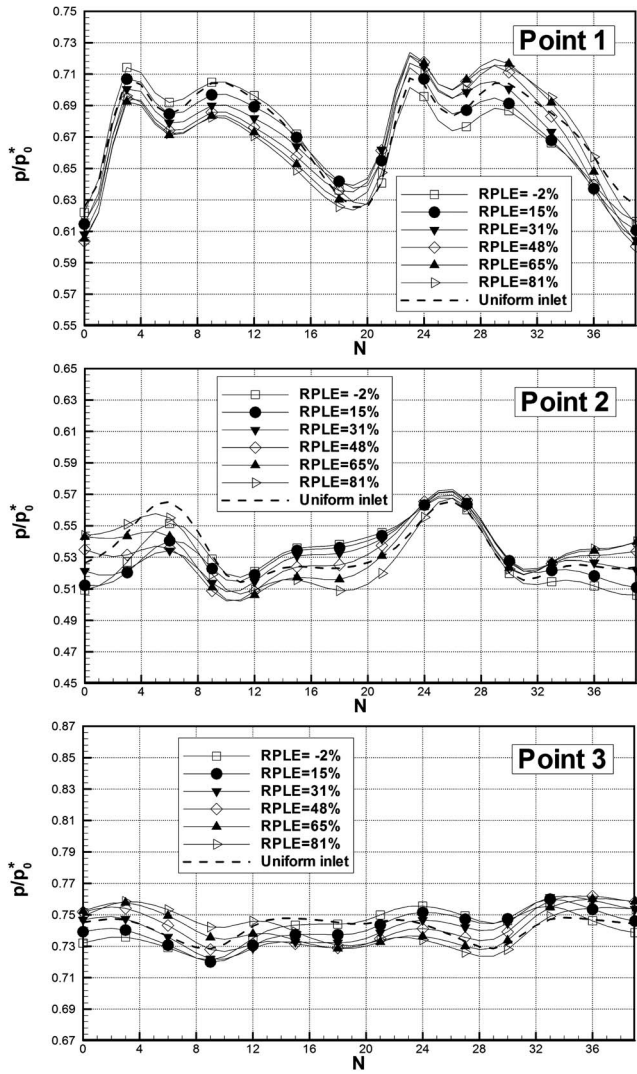


Fig. 18 Transient variation of surface pressure at 65% blade height of three typical points

ture inlet condition, whereas, hot streak inlet condition leads to q/q_0 fluctuating dramatically, in particular, at the blade leading edge, the forward portion of the suction surface, and the rearward portion of the pressure surface. Moreover, the fluctuation range on the suction surface is greater than on the pressure surface. At 65% blade height is greater than at 10% blade height.

The behaviors of the other hot streak schemes are similar to RPLE=48%. This result indicates that hot streaks increase the fluctuation range of wall heat flux and the nonuniform degree of wall heat load.

Figure 22 describes the transient variation process of q/q_0 on the blade suction surface. The process pulls together many factors including temperature field variation caused by hot streak, 3D viscous flow in stator vane passage such as passage vortex and wake flow, and 3D viscous flow in rotor blade passage itself. Hot streak influences heat transfer mainly on the forward section of the blade passage, especially the suction surface, where the influence extends through the whole span. At the rearward section of the rotor blade passage, the 3D separation line on the blade suction surface limits the transports of hot streak. The q/q_0 contours at $N=28-36$ shows the effect of the passage vortices coming from the stator passage, as the black arrows denote. This effect only exists in local regions. In addition, the effect of the hot streak and

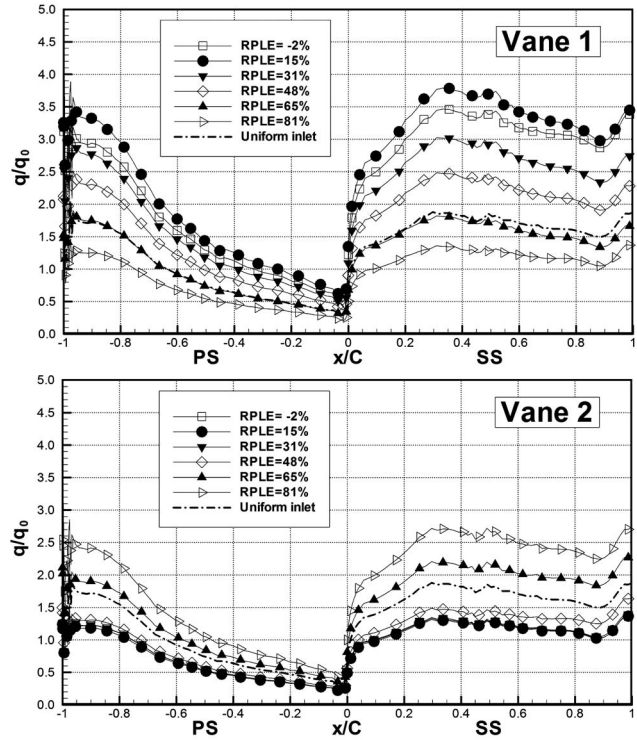


Fig. 19 q/q_0 distributions at 65% vane height ($N=10$)

passage vortices appear at different time steps, which indicates the circumferential position difference between the hot streak and passage vortex at stator exit. The effect of vane wake is not shown distinctly because of the weak effect.

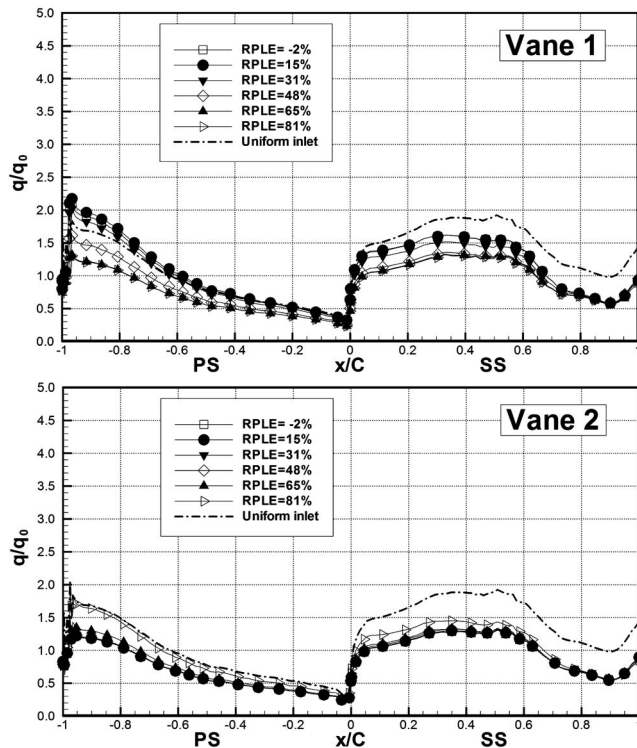


Fig. 20 q/q_0 distributions at 10% vane height ($N=10$)

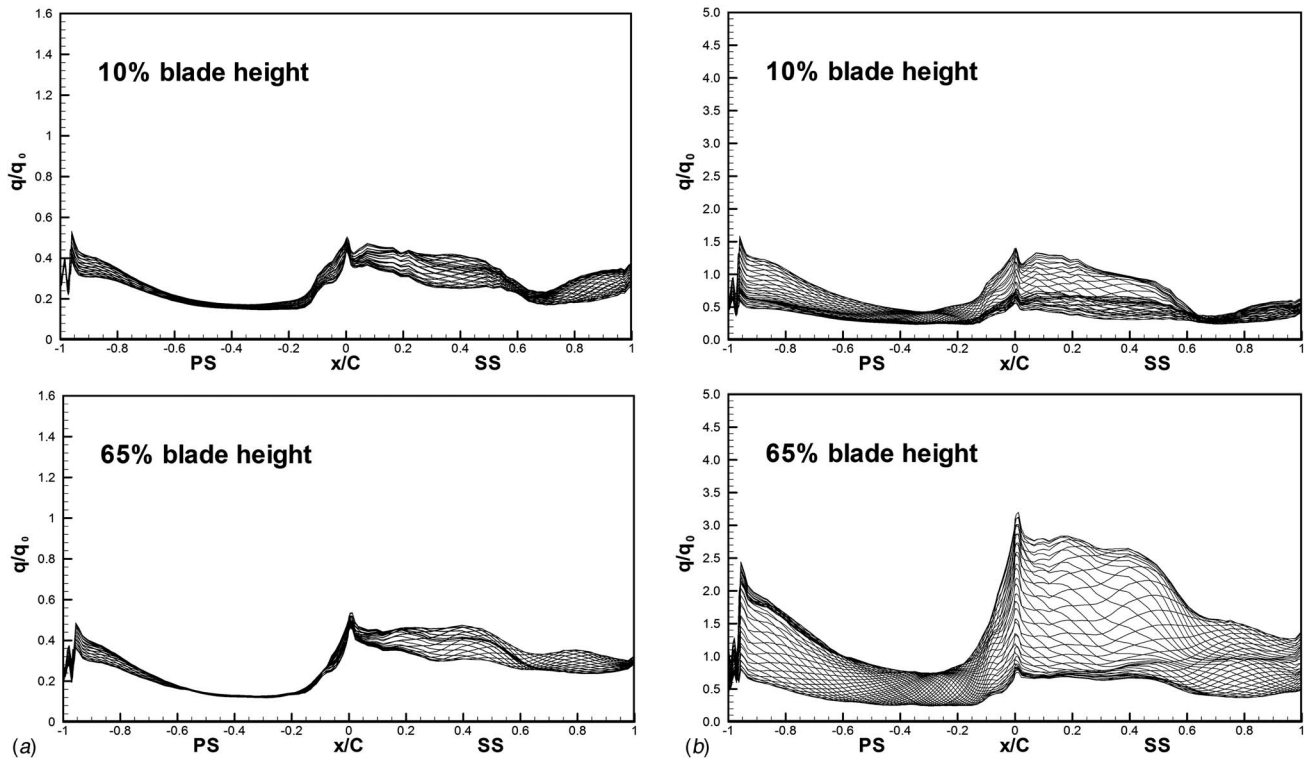


Fig. 21 q/q_0 distributions of rotor blade ($N=0-39$): (a) uniform total temperature inlet condition, and (b) hot streak inlet condition (RPLE=48%)

Figure 23 shows transient temperature contours at 65% blade height. It can be seen that rotor blades experience circumferentially nonuniform temperature field, and for the same blade, there are phase differences between the highest and lowest temperatures among hot streak schemes. For the hot streak flow in blade passages, the typical V-shape temperature distribution agrees with the results in Ref. [7]. Also, the hot streak fluid moves toward the

blade pressure surface distinctly under the similar inlet condition—RPLE=48%. Dorney et al. [7] focused on the time-averaged pressure surface temperature “hot spot.” The present study pays more attention to the transient variation in heat load on both the suction surface and the pressure surface. Figure 24 shows the transient periodic fluctuation of heat flux at three typical points. The point positions are shown in Fig. 7(a). As the pressure

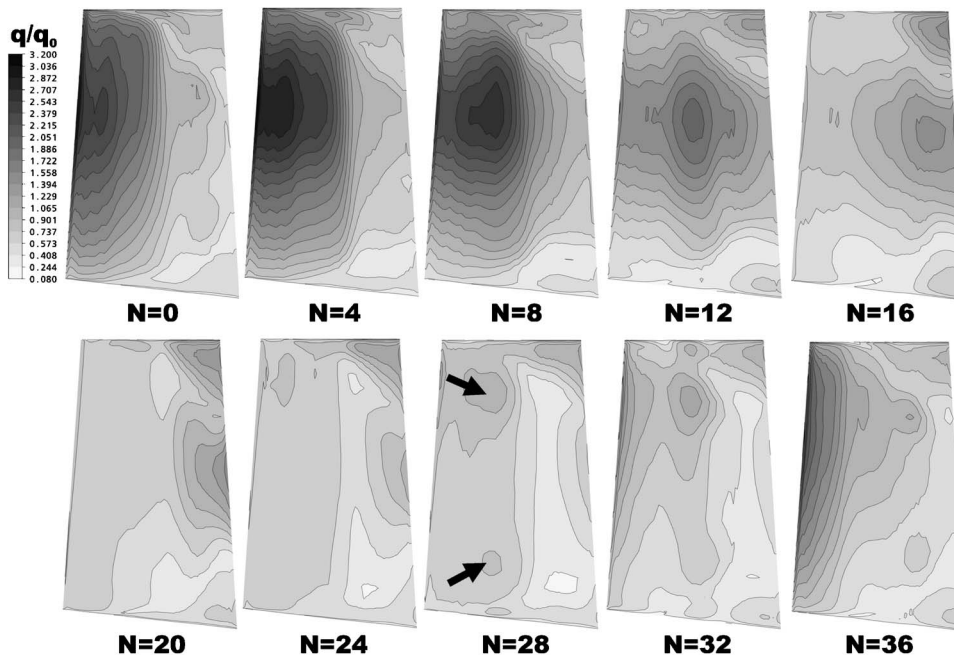


Fig. 22 Transient variation of q/q_0 on blade suction surface (RPLE=48%)

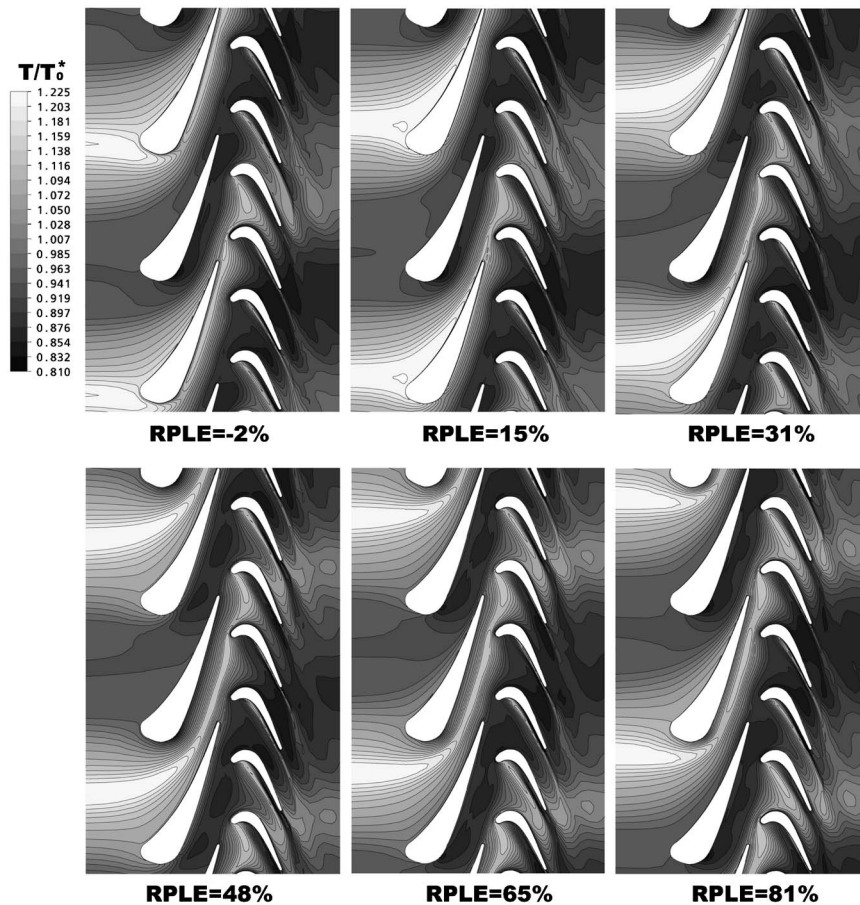


Fig. 23 Transient temperature contours at 65% blade height ($N=15$)

variation trend, the leading edge (Point 1) has the maximal transient q/q_0 difference among the schemes, and the pressure surface (Point 3) has the minimal transient q/q_0 difference. Unlike the pressure fluctuation, two vane passages have one q/q_0 peak value corresponding to one peak hot streak temperature. In addition, the phase difference relates to the vane exit temperature filed directly.

The transient variation of the averaged q/q_0 exhibits the combined unsteady effects of the hot streak, as shown in Fig. 25. This variation can represent the total heat load that the rotor blade endures at each time step. In general, the fluctuation range of the averaged q/q_0 is very small under the uniform total temperature inlet condition, as the dashed line denoted, but hot streak greatly increases the fluctuation range of heat load. The fluctuation range of the averaged q/q_0 on the pressure surface shows the difference about the hot fluid accumulating on the pressure surface when the hot streak circumferential position varies. RPLE=31% has the highest peak averaged q/q_0 , and RPLE=-2% has the smallest peak averaged q/q_0 . This result basically confirms the trend analysis in Ref. [6], i.e., the hot fluid obviously accumulates on the pressure surface when the hot streak locating at the middle of the vane passage inlet, and it is not easily identifiable when the hot streak impinging the vane leading edge. The fluctuation range of the averaged q/q_0 on the suction surface is greater than on the pressure surface for all hot streak schemes. The difference among the hot streak schemes exists in the maximum and minimum values of the averaged q/q_0 and the time of the extreme value appearing, and the value difference is more important. Among all hot streak schemes, RPLE=31% has the highest averaged q/q_0 at the extreme point just like the behavior of the pressure surface, and RPLE=81% has the lowest averaged q/q_0 at the extreme

point. RPLE=65% and RPLE=-2% have a similar behavior to RPLE=81% and the three hot streak inlet conditions have a common point that the highest temperature regions are close to the vane suction surface at stage inlet. Considering the heat load of both the vane and the blade, RPLE=65% has the minimal non-uniform degree of heat load on the vanes, which also results in the small averaged heat load fluctuation on the rotor blade.

6 Conclusions

The circumferential position variations of hot streak at stage inlet lead to the variations in position, shape, and value of high temperature regions at vane exit. After the migrations through the vane passages, the circumferential interval of the highest temperature region becomes wide and the radial position becomes high gradually with the hot streak turning from the TE1 pressure side to the TE2 suction side. At vane exit, if the high temperature region is close to the pressure surface, then it spreads in the radial direction greatly. Also, if the high temperature region is close to the suction surface, then it spreads in the circumferential direction greatly. RPLE=31% has the highest peak temperature.

Compared with uniform total temperature inlet condition, hot streak has little effect on the vane surface pressure and stator exit total mass-averaged parameters regardless of the hot streak circumferential position variation. However, the hot streak has a great effect on the circumferential distributions of the aerodynamic parameters, especially on total temperature, static pressure, and velocity. The velocity variation arises from the stage inlet total temperature distribution, and the relatively high total temperature region results in the relatively high velocity at stage inlet.

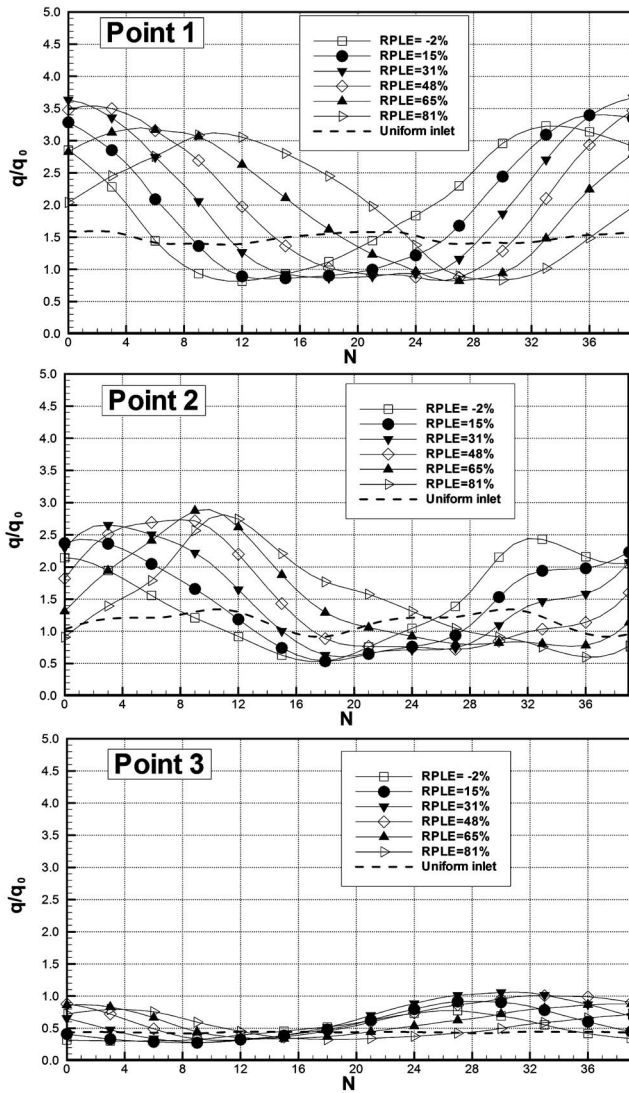


Fig. 24 Transient variation of q/q_0 at 65% blade height of three typical points

Under hot streak inlet conditions, two vanes facing one hot streak have obviously different wall heat load. RPLE=15% has maximal nonuniform level of vane heat load in the circumferential and radial directions due to impinging on the leading edge of Vane 1. RPLE=65% has minimal nonuniform level of vanes heat load, which is close to that of the uniform total temperature inlet condition.

The surface pressure and heat load of rotor blade fluctuates periodically with time even under uniform total temperature inlet condition, but hot streaks increase the fluctuation range greatly, especially the heat load. For the surface pressure, the maximal effect of hot streak occurs on the pressure surface; the fluctuation range increases to about 100%. For the heat load, the effect lies on the relative pitch position of the hot streak. RPLE=31% has the largest range fluctuation of the averaged heat load, and RPLE=81% and 65% have relatively small fluctuation range of the averaged heat load. In addition, the hot streak alters the fluctuation period of the surface pressure and heat load from 9 deg to 18 deg.

In general, the hot streak RPLE=65% obtains similar heat load for the two vanes corresponding to one hot streak; at the same time, it obtains small fluctuations in the averaged heat load on rotor blade.

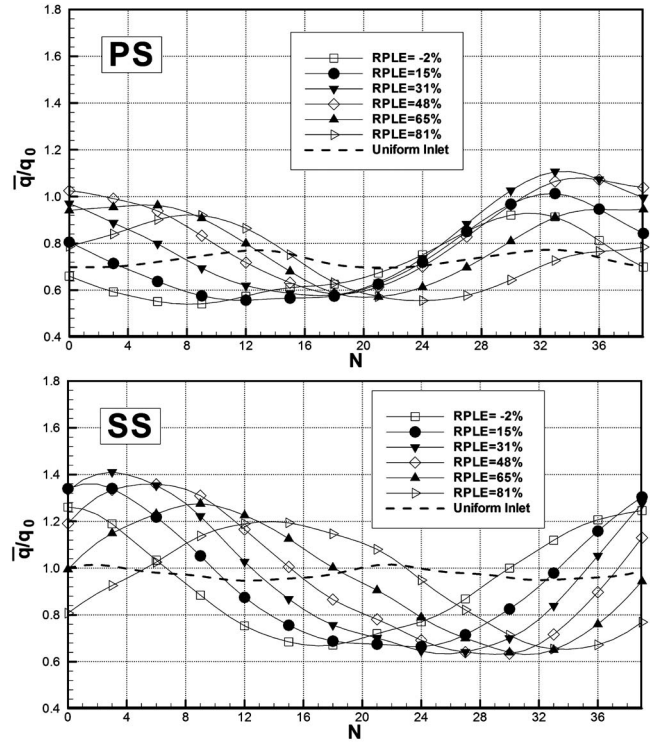


Fig. 25 Transient variation of the averaged q/q_0 on the blade surface

Acknowledgment

The authors wish to acknowledge the financial support from the National 973 Research Program of China through Grant No. 2007CB210108.

Nomenclature

- C = axial blade chord (m)
- H = blade height (m)
- h = wall heat transfer coefficient ($W/m^2 K$)
- h_0 = reference wall heat transfer coefficient ($W/m^2 K$)
- k = turbulent kinetic energy (m^2/s^2)
- Ma = Mach number
- N = time step number
- p = pressure (Pa)
- q = wall heat flux (W/m^2)
- q_0 = reference wall heat flux (W/m^2)
- TE1 = trailing edge of Vane 1
- TE2 = trailing edge of Vane 2
- t = pitch (m)
- T = temperature (K)
- Tu = turbulence intensity (%)
- x = axial distance (m)
- y^+ = nondimensional distance from wall

Greek Symbols

- α = exit flow angle (deg)
- ω = dissipation rate of turbulent kinetic energy (m^2/s^3)

Subscripts

- 0 = inlet plane

Superscripts

- * = stagnation condition
- = averaged value or relative value

References

- [1] Jenkins, S., Varadarajan, K., and Bogard, D. G., 2004, "The Effects of High Mainstream Turbulence and Turbine Vane Film Cooling on the Dispersion of a Simulated Hot Streak," *ASME J. Turbomach.*, **126**(1), pp. 203–211.
- [2] Jenkins, S., and Bogard, D. G., 2004, "The Effects of the Vane and Mainstream Turbulence Level on Hot Streak Attenuation," ASME Paper No. GT2004-54022.
- [3] Zhao, Q. J., Wang, H. S., Zhao, X. L., and Xu, J. Z., 2007, "Numerical Investigation on the Influence of Hot Streak Temperature Ratio in a High-Pressure Stage of Vaneless Counter-Rotating Turbine," *Int. J. Rotating Mach.*, **2007**, pp. 56097.
- [4] Ji, L. C., Xu, J. Z., and Chen, J., 2001, "Study of Hot Streak Effects in a Counter-Rotating Turbine," ASME Paper No. 2001-GT-0173.
- [5] Dorney, D. J., and Gundy-Burlet, K. L., 1996, "Hot-Streak Clocking Effects in a 1-1/2 Stage Turbine," *J. Propul. Power*, **12**(3), pp. 619–620.
- [6] He, L., Menshikova, V., and Haller, B. R., 2004, "Influence of Hot Streak Circumferential Length-Scale in Transonic Turbine Stage," ASME Paper No. GT2004-53370.
- [7] Dorney, D. J., Davis, R. L., Edwards, D. E., and Madavan, N. K., 1992, "Unsteady Analysis of Hot Streak Migration in a Turbine Stage," *J. Propul. Power*, **8**(2), pp. 520–529.
- [8] Gundy-Burlet, K. L., and Dorney, D. J., 2000, "Effects of Radial Location on the Migration of Hot Streaks in a Turbine," *J. Propul. Power*, **16**(3), pp. 377–387.
- [9] Shang, T., and Epstein, A. H., 1997, "Analysis of Hot Streak Effects on Turbine Rotor Heat Load," *ASME J. Turbomach.*, **119**(3), pp. 544–553.
- [10] Zilli, A., Pachidis, V., Jackson, A., and Piliadis, P., 2005, "CFD Investigation of the Performance of a Military HP Axial Turbine Subjected to Inlet Temperature Distortion," ASME Paper No. GT2005-68503.
- [11] Hylton, L. D., Mihelc, M. S., Turner, E. R., Nealy, D. A., and York, R. E., 1983, "Analytical and Experimental Evaluation of the Heat Transfer Distribution Over the Surfaces of Turbine Vanes," NASA Report No. NASA-CR-168015.

Extended Models for Transitional Rough Wall Boundary Layers With Heat Transfer—Part I: Model Formulations

M. Stripf
A. Schulz
H.-J. Bauer
S. Wittig

Lehrstuhl und Institut für Thermische
Strömungsmaschinen,
Universität Karlsruhe (TH),
Kaiserstraße 12,
Karlsruhe 76128, Germany

Two extended models for the calculation of rough wall transitional boundary layers with heat transfer are presented. Both models comprise a new transition onset correlation, which accounts for the effects of roughness height and density, turbulence intensity, and wall curvature. In the transition region, an intermittency equation suitable for rough wall boundary layers is used to blend between the laminar and fully turbulent states. Finally, two different submodels for the fully turbulent boundary layer complete the two models. In the first model, termed KS-TLK-T in this paper, a sand roughness approach from Durbin et al. (2001, "Rough Wall Modification of Two Layer $k-\epsilon$," ASME J. Fluids Eng., 123, pp. 16–21), which builds upon a two-layer $k-\epsilon$ -turbulence model, is used for this purpose. The second model, the so-called DEM-TLV-T model, makes use of the discrete-element roughness approach, which was recently combined with a two-layer $k-\epsilon$ -turbulence model by the present authors. The discrete-element model will be formulated in a new way, suitable for randomly rough topographies. Part I of the paper will provide detailed model formulations as well as a description of the database used for developing the new transition onset correlation. Part II contains a comprehensive validation of the two models, using a variety of test cases with transitional and fully turbulent boundary layers. The validation focuses on heat transfer calculations on both the suction and the pressure side of modern turbine airfoils. Test cases include extensive experimental investigations on a high-pressure turbine vane with varying surface roughness and turbulence intensity, recently published by the current authors as well as new experimental data from a low-pressure turbine vane. In the majority of cases, the predictions from both models are in good agreement with the experimental data.

[DOI: 10.1115/1.2992511]

1 Introduction

The optimization of cooling technologies continues to be a major task in achieving a further increase in efficiency and thereby CO₂ reduction. A key requisite for such an optimization is the exact knowledge of the heat transfer distribution around the airfoil's surface. While today's computational models permit a satisfactory calculation of the smooth wall heat transfer distribution (e.g., Refs. [1–3]), it is still a challenge to simulate a rough surface transitional boundary layer. This is a major restriction and requires the designers to use large safety factors, as the increasing surface roughness during a turbine's service life is expected to have a certain effect on the boundary layer. Indeed, several recent experimental studies have shown that the roughness found on used turbine components may lead to a considerable increase in heat load [4–14]. This is especially true for aft loaded airfoils where boundary layer transition on the suction side usually occurs far downstream on smooth surfaces but is moved upstream by the increased roughness. In such cases, heat transfer can easily increase by a factor of 10 in regions where the boundary layer becomes turbulent due to the roughness. It thus becomes apparent that it is crucial to correctly predict the rough wall transitional boundary layer.

It was recently shown by the present authors [15] that this task could be fulfilled by the combination of a rough wall turbulence

model and a suitable intermittency transition model. The current paper will extend the method previously presented through the inclusion of additional experimental data and the consideration of roughness density and wall curvature effects. In addition, a second roughness model for turbulent boundary layers will be introduced and compared with the discrete-element model used in Ref. [15].

2 Model Formulations

The Favre- and mass-averaged conservation equations for mass, momentum, and energy form the starting point of the following model development. For the sake of clarity, we will concentrate, in this paper, on two-dimensional compressible boundary layers using the boundary layer approximations of Cebeci and Smith [16] together with the Boussinesq eddy viscosity assumption. In order to provide a general formulation suitable for different kinds of roughness models, the effect of roughness elements penetrating the boundary layer is taken into account by considering the roughness blockage through the porosity β . In addition, the momentum and heat transfer to the roughness elements can be described by two additional sink terms S_{FR} and S_{QR} in the momentum and energy equations, respectively. Taylor et al. [17] gave a rigorous derivation of the following set of equations.

For continuity,

$$\frac{\partial}{\partial x}(\rho\beta U) + \frac{\partial}{\partial y}(\rho\beta\tilde{V}) = 0 \quad (1)$$

For momentum,

Contributed by the International Gas Turbine Institute of ASME for publication in the JOURNAL OF TURBOMACHINERY. Manuscript received June 20, 2008; final manuscript received August 5, 2008; published online April 20, 2009. Review conducted by David Wisler. Paper presented at the ASME Turbo Expo 2008: Land, Sea and Air (GT2008) Berlin, Germany, June 9–13, 2008.

$$\rho\beta U \frac{\partial U}{\partial x} + \rho\beta \tilde{V} \frac{\partial U}{\partial y} = -\frac{d}{dx}(\beta P) + \frac{\partial}{\partial y} \left[\beta(\mu + \mu_t) \frac{\partial U}{\partial y} \right] - S_{FR} \quad (2)$$

For energy,

$$\rho\beta U \frac{\partial H}{\partial x} + \rho\beta \tilde{V} \frac{\partial H}{\partial y} = \frac{\partial}{\partial y} \left[\beta \left(\frac{\mu}{Pr} + \frac{\mu_t}{Pr_t} \right) \frac{\partial H}{\partial y} \right] + \frac{\partial}{\partial y} \left[\beta \left(\mu + \mu_t \right) - \left(\frac{\mu}{Pr} + \frac{\mu_t}{Pr_t} \right) \right] U \frac{\partial U}{\partial y} + S_{QR} \quad (3)$$

with the boundary conditions at the wall ($y=0$):

$$U_w = \tilde{V}_w = 0 \quad (4)$$

The total enthalpy at the wall may either be specified through the wall temperature distribution (Dirichlet condition),

$$H_w(x) = c_{p,w} T_w(x) \quad (5a)$$

or the heat flux (Neumann condition),

$$\frac{\partial H}{\partial y}(x) \Big|_w = -q_w(x) \frac{Pr_w}{\mu_w} \quad (5b)$$

At the boundary layer edge ($y=\delta_{99}$), the time averaged velocity distribution for $U_\infty(x)$ has to be specified as well as the total enthalpy H_∞ , which is assumed to be constant.

Using the turbulent Prandtl number of $Pr_t=0.86$ for wall bounded flows, the model closure is achieved by determining the eddy viscosity μ_t , the porosity β , and the two additional sink terms S_{FR} and S_{QR} .

In the laminar boundary layer, μ_t equals zero, and because the roughness effect on heat transfer and friction in the laminar region is negligible [12], the porosity β will be set to 1 and $S_{FR}=S_{QR}=0$.

In the transitional and turbulent boundary layers, however, suitable transition, turbulence, and roughness submodels have to be used to close Eqs. (1)–(3). In the following paragraphs, two such models for rough wall fully turbulent boundary layers will be presented. A method to determine the start of transition and to blend between the laminar and fully turbulent regions will be given thereafter.

2.1 Two Roughness Models for Turbulent Boundary Layers. There are usually two approaches to describe the influence of roughness on a turbulent boundary layer. The first method, widely used in commercial computational fluid dynamics (CFD) codes, does not resolve the individual effects of the roughness such as fluid blockage and momentum and heat transfer to the roughness elements. Rather, the effect of roughness on the velocity profile is solely captured by an extended turbulence model used to calculate μ_t . Mostly, the only parameter describing the roughness topography in this case is the so-called equivalent sand roughness k_s . A modern representative of such a model is the one developed by Durbin et al. [18], whose formulation is given below. It will be combined with a new transition model later in this paper.

Another approach, called the discrete-element method (DEM), does account for the roughness element blockage and the momentum and heat exchanged with the elements. In addition, the turbulence model used to calculate μ_t is modified to reflect the additional turbulence produced in the wakes of the roughness elements. The formulation of this model, which was presented in our last paper [15], is given again below in a different way to facilitate its usage with randomly rough surfaces. It will also be combined with the new transition model developed later in this paper.

2.1.1 The KS-TLK Model of Durbin et al. Durbin et al. [18] extended the two-layer k - ε -model from Chen and Patel [19] in order to calculate rough wall turbulent boundary layers. The effect

of roughness is included by solely modifying the calculation of the eddy viscosity μ_t , i.e., $\beta=1$ and $S_{FR}=S_{QR}=0$ in Eqs. (1)–(3). Their model will be summarized briefly here to facilitate comparison with the discrete-element model. It will be denoted by KS-TLK as it is based on the sand roughness k_s and a two-layer turbulence model using $k^{(1/2)}$ as the turbulent velocity scale.

Like in most eddy viscosity models, μ_t is expressed as the product of a turbulent velocity scale (here $k^{(1/2)}$) and an appropriate length scale (here l_μ).

$$\mu_t = \gamma \rho c_\mu \sqrt{k} \cdot l_\mu \quad (6)$$

with the constant $c_\mu=0.09$. We will use the so-called intermittency factor γ later in this paper to account for transitional boundary layers. For now, as only fully turbulent boundary layers are considered, $\gamma=1$. In the outer layer, the turbulent kinetic energy k and the length scale l_μ can be readily calculated with the standard- k - ε model of Launder and Spalding [20].

For turbulent kinetic energy,

$$\rho U \frac{\partial k}{\partial x} + \rho \tilde{V} \frac{\partial k}{\partial y} = \frac{\partial}{\partial y} \left[\left(\mu + \frac{\mu_t}{\sigma_k} \right) \frac{\partial k}{\partial y} \right] + \mu_t \left(\frac{\partial U}{\partial y} \right)^2 - \rho \varepsilon \quad (7)$$

For dissipation,

$$\rho U \frac{\partial \varepsilon}{\partial x} + \rho \tilde{V} \frac{\partial \varepsilon}{\partial y} = \frac{\partial}{\partial y} \left[\left(\mu + \frac{\mu_t}{\sigma_\varepsilon} \right) \frac{\partial \varepsilon}{\partial y} \right] + \left[c_1 \mu_t \left(\frac{\partial U}{\partial y} \right)^2 - \rho c_2 \varepsilon \right] \frac{\varepsilon}{k} \quad (8)$$

with the usual values for the coefficients $\sigma_k=1.0$, $\sigma_\varepsilon=1.3$, $c_1=1.44$, and $c_2=1.92$. The length scale l_μ in the outer layer then becomes

$$l_{\mu,outer} = \frac{k^{3/2}}{\varepsilon} \quad (9)$$

Note that until now the model does not contain any modification to consider roughness. Also, the transport equation for dissipation (Eq. (8)) is only valid for high Reynolds numbers and is, therefore, not valid very close to the wall. Chen and Patel [19] solved this problem by using the one equation model of Wolfshtein [21] in the immediate vicinity of the wall. Durbin et al. [18] introduced several changes to this model, which allow the inclusion of roughness effects. The length scale l_μ in the inner layer can then be calculated with the simple algebraic expression

$$l_{\mu,inner} = 2.5 y_{eff} f_\mu \quad (10)$$

For smooth surfaces, y_{eff} reflects the actual wall distance, whereas for a rough surface $y_{eff}=y+y_0$. The shift in wall distance y_0 takes into account that the turbulent fluctuations on a rough surface do not go to zero where the time averaged velocity is zero.

The damping function f_μ is needed on smooth walls, where the length scale $l_{\mu,inner}$ has to decrease much slower than linearly to reflect its real behavior very close to the wall. On fully rough surfaces, the logarithmic layer reaches down to $y_{eff}=0$, the length scale decreases linearly, and f_μ should be one. Durbin et al. [18] provided the following expression for f_μ , which blends between smooth and fully rough behaviors.

$$f_\mu = 1 - \exp\left(-\frac{Re_y}{A_\mu}\right) \quad (11)$$

with

$$Re_y = \frac{\sqrt{ky}}{\nu} \quad (12)$$

and

$$A_\mu = \max \left[1, 62.5 \left(1 - \frac{k_s^+}{90} \right) \right] \quad (13)$$

Equation (13) implies that the boundary layer obeys fully rough behavior as soon as $k_s^+ = k_s u_\tau^+ / \nu \geq 90$. This is strictly true only for sand roughness but will probably serve for the majority of randomly rough surfaces as well.

Even though the dissipation ε is not needed to calculate l_μ in the inner layer, it is needed in Eq. (7) to calculate k in the inner layer. With the following algebraic expression, ε may be determined in the inner region, where Eq. (8) is not valid.

$$\varepsilon_{\text{inner}} = \frac{k^{3/2}}{l_\varepsilon} \quad (14)$$

with

$$l_\varepsilon = 2.5 y_{\text{eff}} f_\varepsilon \quad (15)$$

The damping function f_ε is the same for smooth and rough surfaces.

$$f_\varepsilon = 1 - \exp\left(\frac{\text{Re}_y}{2 \times 2.5}\right) \quad (16)$$

The coupling between the outer and inner layer models is conducted, where $f_\mu = 0.95$. That is, for $f_\mu < 0.95$, the length scale l_μ is calculated with Eq. (10) and, ε is determined by Eq. (14), whereas for $f_\mu \geq 0.95$, Eqs. (9) and (8) are used.

To complete the model, a rule to calculate the shift in wall distance y_0 has to be specified. In Fig. 2 of their paper, Durbin et al. [18] provided a relationship between $y_0^+ = y_0 u_\tau^+ / \nu$ and k_s^+ . An expression reflecting their calibration curve is

$$y_0^+ = \begin{cases} \frac{-1.16 + 0.85\sqrt{k_s^+} - 0.071k_s^+}{1 - 0.16\sqrt{k_s^+} + 0.01k_s^+}, & k_s^+ \leq 90 \\ 0.035k_s^+ - 1.548, & k_s^+ > 90 \end{cases} \quad (17)$$

Expression (17) was developed for sand roughness and should be adjusted if applied to other roughness geometries. Because this normally requires additional boundary layer measurements, the approach followed in this paper is to use Eq. (17) for other roughness types as well. To account for the effects of different geometries, the concept of an equivalent sand roughness will be used instead.

Due to the introduction of two additional transport equations (Eqs. (7) and (8)), the boundary conditions for k and ε have to be specified. For smooth walls $k_w = 0$, but for fully rough boundary layers $k_w = u_\tau^2 / \sqrt{c_\mu}$. Durbin et al. [18] used the following equation to blend between the smooth and fully rough conditions.

$$k_w = \frac{u_\tau^2}{\sqrt{c_\mu}} \min\left[1; \left(\frac{k_s^+}{90}\right)^2\right] \quad (18)$$

The dissipation at the wall ε_w is then calculated with Eq. (14). At the boundary layer edge, $k_\infty(x)$ and $\varepsilon_\infty(x)$ are known from the transport equations (Eqs. (7) and (8)), which can be integrated due to the vanishing gradients in wall normal direction, given the starting values k_1 and ε_1 (or Tu_1 and $L_{\varepsilon,1}$) in the inlet plane.

This completes the KS-TLK submodel to determine μ_t for fully turbulent boundary layers with rough walls. In order to calculate transitional boundary layers, the model has to be extended by specifying γ in Eq. (6). The required transition model is presented later in this paper, after an alternative roughness model—the DEM-TLV model—has been introduced.

2.1.2 The DEM-TLV Model. The DEM, which is based on a suggestion by Schlichting [22], uses additional terms in the transport equations to describe the effects of roughness. To account for the flow blockage due to the roughness elements, a porosity factor β is introduced in Eqs. (1)–(3). Note, that elsewhere (e.g., Ref. [17]), $1 - \beta$ is often called blockage factor. In general, β can be expressed as follows:

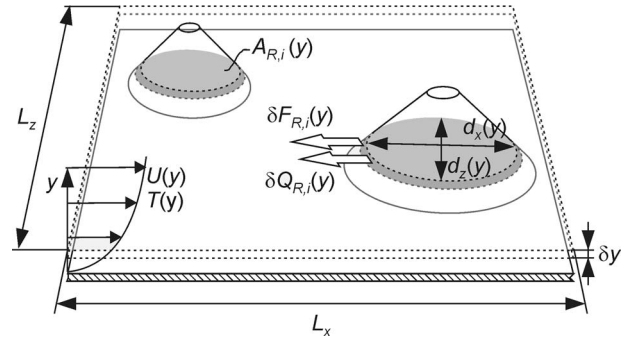


Fig. 1 The discrete-element approach

$$\beta(y) = 1 - \frac{\sum_{i=1}^{N_R} A_{R,i}(y)}{L_x L_z} \quad (19)$$

where $L_x L_z$ is the reference surface area, N_R is the number of elements inside this area, and $A_{R,i}$ is the cross-sectional area of an individual roughness element in the x - z -plane (see Fig. 1). In order to provide a formulation suitable for random roughness, Eq. (19) is simplified by introducing an average element cross section \bar{A}_R and an element density $\zeta(y) = N_R(y) / (L_x L_z)$.

$$\beta(y) = 1 - \zeta(y) \cdot \bar{A}_R(y) \quad (20)$$

The protruding roughness elements exert a drag force on the fluid, which must be considered in the momentum equation. The drag force per unit volume, which is equal to the sink term in Eq. (2), is as follows:

$$S_{FR}(y) = \frac{\sum \delta F_{R,i}}{L_x L_z \delta y} = \frac{1}{L_x L_z} \frac{1}{2} \rho U^2 \sum_{i=1}^{N_R} C_{d_{z,i}} d_{z,i} \quad (21)$$

Equation (21) is not practical when considering randomly rough surfaces, as the drag coefficients and diameters of each individual roughness element have to be known for all y positions. As the drag coefficient is a function of the element diameter, this means that a two-dimensional diameter distribution is needed to describe a surface. To simplify the above expression, a suitable correlation for the drag coefficient has to be found. In previous studies, the simple correlation provided by Taylor et al. [17] and extended by McClain [23] for elliptical roughness elements has proven to give the best results, even though it does not take into account the effect of neighboring elements such as the more complex correlation from Ref. [24]. An overview of other correlations is given in Ref. [15]. With the eccentricity $e = d_z / d_x$, the drag coefficient becomes

$$C_{d_{z,i}} = \left(\frac{\text{Re}_{d_z}}{1000}\right)^{-1/8} e^{0.735} = \left(\frac{U \cdot d_z}{1000 \cdot \nu}\right)^{-1/8} e^{0.735} \quad (22)$$

After some arithmetic, Eq. (21) can be simplified to

$$S_{FR}(y) = \frac{1}{2} \rho U^2 \zeta C_d d_F \quad (23)$$

with the characteristic diameter distribution for momentum transfer,

$$d_F(y) = \left(\frac{1}{N_R} \sum_{i=1}^{N_R} d_{z,i}^{7/8} e^{0.735}\right)^{8/7} \quad (24)$$

The drag coefficient used in Eq. (23) simply is as follows:

$$C_d = \left(\frac{\text{Re}_{d_F}}{1000} \right)^{-1/8} = \left(\frac{U \cdot d_F}{1000 \cdot \nu} \right)^{-1/8} \quad (25)$$

as the eccentricity is already included in the characteristic diameter d_F . With Eq. (23) we have now reduced the required surface description from a two-dimensional diameter distribution to a simple distribution $d_F(y)$, which can be directly deduced from surface map measurements.

Similar to momentum transfer, the heat transfer to the individual roughness elements is accounted for by an additional source term in the energy equation. Thus the heat flux exchanged with an element per unit volume is (see Fig. 1) as follows:

$$S_{QR}(y) = \frac{\sum \delta Q_{R,i}}{L_x L_z \delta y} = \frac{1}{L_x L_z} k_f (T_R - T) \sum_{i=1}^{N_R} \frac{\text{Nu}_{d,i}}{d_{z,i}} c_{R,i} \quad (26)$$

Assuming elliptical elements, the circumference c_R can be approximated with

$$c_R = \pi d_z \frac{3}{4} \left(1 + \frac{1}{e} - \frac{2}{3\sqrt{e}} \right) = \pi d_z K_e \quad (27)$$

Again, Eq. (26) requires a two-dimensional diameter distribution, and it can be simplified if a correlation for Nu_d is known. A comparison between different correlations (see Ref. [15]) gave the best results for the one provided by Hosni et al. [25] and used by McClain [23] for elliptic elements as well.

$$\text{Nu}_d = 1.7 \text{Pr}^{0.4} \text{Re}_d^{0.49} \quad (28)$$

With Eqs. (27) and (28), Eq. (26) can be simplified to

$$S_{QR}(y) = \pi k_f \zeta \text{Nu}_{dQ} (T_R - T) \quad (29)$$

where the Nusselt number Nu_{dQ} is calculated with Eq. (28) using the characteristic diameter distribution for heat transfer.

$$d_Q(y) = \left(\frac{1}{N_R} \sum_{i=1}^{N_R} K_{e,i} d_{z,i}^{0.49} \right)^{1/0.49} \quad (30)$$

It is important to note that the roughness element temperature $T_R(y)$ in Eq. (29) is not necessarily constant and equal to the wall temperature. Especially for roughness elements with low thermal conductivity, the temperature distribution of an element has to be calculated because it may considerably affect the overall heat transfer. The following differential equation (sometimes called the *fin equation*) can be iteratively solved for this purpose.

$$\frac{d}{dy} \left(\frac{1 - \beta d T_R}{\zeta} \frac{dT_R}{dy} \right) - \frac{\pi k_f}{2 k_R} \text{Nu}_{dQ} \frac{d(d_Q)}{dy} (T_R - T) = 0 \quad (31)$$

With Eqs. (20), (23), and (29), the porosity β and the additional terms S_{FR} and S_{QR} required in the transport equations (Eqs. (1)–(3)) are defined. Still missing is a turbulence model to calculate the eddy viscosity μ_t . As was shown in our last paper [15], the two-layer model presented by Sieger et al. [1], which combines the standard k - ε model and the k - l model of Rodi et al. [26], is well suited for this purpose. In order to consider the additional turbulence produced in the wakes of the roughness elements, the model is extended with an additional source term following Finson and Wu [27] and Tarada [24]. The transport equations for k and ε used with the discrete-element method become the following.

For turbulent kinetic energy,

$$\rho \beta U \frac{\partial k}{\partial x} + \rho \beta \bar{V} \frac{\partial k}{\partial y} = \frac{\partial}{\partial y} \left[\beta \left(\mu + \frac{\mu_t}{\sigma_k} \right) \frac{\partial k}{\partial y} \right] + \beta \mu_t \left(\frac{\partial U}{\partial y} \right)^2 - \rho \beta \varepsilon + \rho c_k U^3 d_F \zeta \quad (32)$$

For dissipation,

$$\rho \beta U \frac{\partial \varepsilon}{\partial x} + \rho \beta \bar{V} \frac{\partial \varepsilon}{\partial y} = \frac{\partial}{\partial y} \left[\beta \left(\mu + \frac{\mu_t}{\sigma_\varepsilon} \right) \frac{\partial \varepsilon}{\partial y} \right] + \left[\beta c_1 \mu_t \left(\frac{\partial U}{\partial y} \right)^2 - \rho \beta c_2 \varepsilon \right] \frac{\varepsilon}{k} \quad (33)$$

Note that the difference between these two equations and Eqs. (7) and (8) are the additional blockage factors and the additional source term in the k -equation. In preliminary calculations, using a variety of test cases, best results could be achieved using a value of 0.05 for the constant c_k , which is slightly bigger than the value we found previously in Ref. [15]. With Eqs. (32) and (33), it is now possible to calculate the eddy viscosity in the outer layer.

$$\mu_{t,outer} = \gamma \rho c_\mu \frac{k^2}{\varepsilon} \quad (34)$$

Similar to Eq. (6), the intermittency factor γ is set equal to one in the fully turbulent boundary layer and will be modified later in this paper to account for laminar-turbulent transition. In the inner layer, where $\mu_t/\mu \leq 16$, Eq. (33) is not valid and the one equation model of Rodi et al. [26] is used to calculate μ_t .

$$\mu_{t,inner} = \gamma \rho \sqrt{v'^2} l_{\mu,v} \quad (35)$$

with the new velocity scale $\sqrt{v'^2}$ and the length scale,

$$l_{\mu,v} = c_{l,\mu} y = 0.30 y \quad (36)$$

An advantage of using $\sqrt{v'^2}$ as the velocity scale instead of $k^{(1/2)}$ such as in the one equation model of Wolfshtein [21] is that no damping function is needed. A relation between v'^2 and k has been deduced by Rodi et al. [26] from direct numerical simulation (DNS) data:

$$\frac{v'^2}{k} = 4.65 \cdot 10^{-5} \left(\frac{\sqrt{ky}}{\nu} \right)^2 + 4 \cdot 10^{-4} \frac{\sqrt{ky}}{\nu} \quad (37)$$

To calculate the dissipation ε in the inner layer, the following equation is used instead of Eq. (33):

$$\varepsilon_{inner} = \frac{\sqrt{v'^2} k}{l_{\varepsilon,v}} \quad (38)$$

with the length scale,

$$l_{\varepsilon,v} = \frac{1.3y}{1 + 2.12\nu/(\sqrt{v'^2}y)} \quad (39)$$

In contrast to the KS-TLK model, the wall boundary condition for k and ε is zero, because the position $y=0$ reflects a location at the bottom of the roughness elements, where the turbulent fluctuations disappear. The conditions at the boundary layer edge are determined, like in the KS-TLK model, from integrating Eqs. (7) and (8). This concludes the submodel to calculate fully turbulent boundary layers on smooth and rough walls. It will be denoted by DEM-TLV as it is based on a discrete-element method and a two-layer turbulence model using v' as turbulent velocity scale.

After solving the transport equations with an implicit and forward marching finite-volume boundary layer code based on the method of Patankar and Spalding [28], the skin friction coefficient is calculated from

$$C_f = \frac{\beta_w \mu \left. \frac{\partial U}{\partial y} \right|_{y=0} + \frac{1}{2} \zeta \int_0^\infty \rho U^2 C_d d_F dy}{0.5 \rho_\infty U_\infty^2} \quad (40)$$

and the Stanton number $\text{St} = h/(\rho c_p U_\infty)$ is determined using

$$\text{St} = \frac{-\beta_w k_f \left. \frac{\partial T}{\partial y} \right|_{y=0} + \pi \zeta \int_0^\infty k_f \text{Nu}_{dQ} (T_R - T) dy}{\rho_\infty U_\infty c_p (T_w - T_\infty)} \quad (41)$$

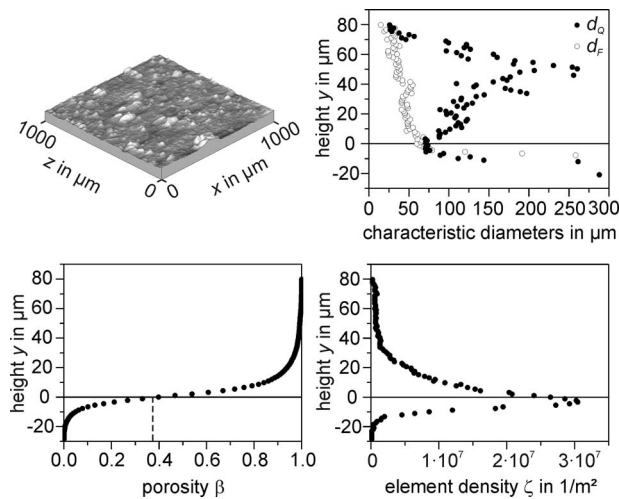


Fig. 2 Rough surface description for the DEM-TLV model

At this point some remarks on the specification of rough surfaces for the DEM-TLV model are in order. Figure 2 shows typical distributions for the porosity β , the element density ζ , and the two characteristic diameters for momentum and heat transfer d_F and d_Q , which completely define a realistic rough surface. An alternative method to reduce the surface description for the discrete-element method was recently presented by McClain and Brown [29]. By assuming certain universal distributions for the porosity and element diameters, the authors presented an even more compressed surface parametrization. At least for certain roughness types, where the underlying distributions are valid, their method is an elegant way to describe a rough surface with only a few parameters.

A certain difficulty generally arises when defining the point of origin ($y=0$) for a randomly rough or very dense roughness geometry, because in those cases it is not possible to distinguish individual roughness elements or their diameter distribution very close to the wall. In the current work, this problem is overcome by setting the point of origin at the location where the porosity β is equal to 0.37 (Fig. 2). This means, that the distributions below $y=0$, where most of the flow is blocked and the roughness elements are grown together, are disregarded. Consequently, the area between the roughness elements at $y=0$ is considered to be smooth.

A similar criterion is used by McClain and co-workers [23,30], who use the mean elevation or “melt down” height as the reference location. The authors demonstrated that this criterion works very well with random and closely packed roughness. It should be stated that for most closely packed and random roughness geometries, the melt down height and $\beta=0.37$ give about the same y location. The reason why the β criterion is favored in this paper is that it does not affect the y -location of sparse roughness configurations, where the roughness elements are distinguishable all the way down to the wall, and there is no necessity to change the point of origin.

Some artificial roughness geometries, such as truncated cones, require special consideration, as the forces and heat fluxes at the top of the flat roughness elements are not contained in the source terms of the discrete-element model. Preceding attempts to include these forces and heat fluxes via correlations similar to Eqs. (21) and (26) were not successful. The approach finally followed in this work is rather pragmatic but gives very good results on a variety of surfaces with truncated cones. Figure 3 illustrates how elements with flat tops are geometrically expanded by adding a dome at the top of the element. This way the fluxes at the top are approximated with fluxes at the lateral surface.

2.2 Modeling Transition. With the KS-TLK and the DEM-

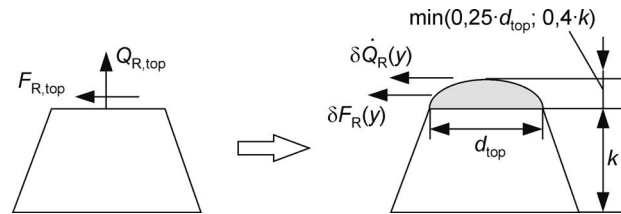


Fig. 3 Roughness elements with flat tops

TLV model, two different methods to calculate fully turbulent boundary layers are available. On the majority of turbine airfoils however, substantial regions of the boundary layer are transitional. Therefore, the remaining task of this paper is to provide a new model to include the laminar-turbulent transition.

In general, three modes of transition can be distinguished: natural transition, bypass-transition, and separated flow transition. Because it is the one encountered in the front stages of a turbine, we will concentrate on the bypass type of transition, where the Tollmien-Schlichting instability is completely bypassed and transition is triggered by large disturbances in the external flow and/or surface roughness.

The approach followed is to apply the intermittency concept based on the turbulent spot theory of Emmons [31] and to use a new correlation to determine the onset of transition.

2.2.1 Intermittency Model for the Transition Zone. Figure 4 illustrates the bypass-transition process, which starts with the formation of streaks of high intensity streamwise fluctuations inside the laminar boundary layer. Depending on turbulence, surface roughness, pressure gradient, curvature, and other factors, the turbulent streaks break down into small turbulent spots having the shape of an arrowhead. The spots are then transported downstream while they grow in size until a fully turbulent boundary layer is formed by the coalescing spots. With the formation of turbulent spots, the distributions of heat transfer and surface shear stress begin to depart remarkably from their laminar values. Even though the turbulent streaks also have a certain influence on heat transfer and surface shear stress, it is secondary compared with the effect of turbulent spots. The following model will therefore concentrate on the evolution of spots downstream of the position x_t (see Fig. 4).

To describe the behavior in the transitional region, Emmons [31] introduced the intermittency factor γ , which characterizes the fraction of time during which the flow at one point on the surface is turbulent. Thus for a laminar boundary layer $\gamma=0$, whereas for

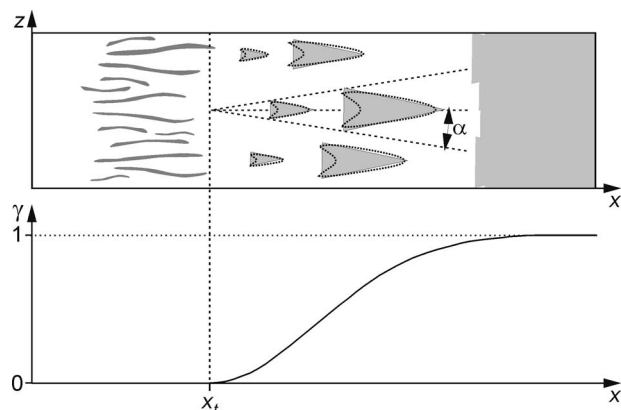


Fig. 4 Modeling bypass-transition with an intermittency factor describing the transition progress

a fully turbulent boundary layer $\gamma=1$ (Fig. 4). Once γ is known inside the transitional region, it can be used in Eqs. (6), (34), and (35) to calculate an effective eddy viscosity μ_t . In addition it is used to switch off the discrete-element model in the laminar boundary layer by the use of a simple blending function for the element density ζ .

$$\zeta_{\text{eff}} = \min(\zeta, 3\gamma\zeta) \quad (42)$$

With assumption of Narasimha [32] that the production of turbulent spots occurs randomly along a single line at the onset of transition x_t , Solomon et al. [33] gave the following expression for γ for positions downstream of the transition onset location, i.e., $x > x_t$.

$$N_t = \begin{cases} 0.86 \times 10^{-3} \exp(-0.564 \ln Tu_t + 2.134\lambda_{\theta,t} \ln Tu_t - 59.23\lambda_{\theta,t}), & \lambda_{\theta,t} \leq 0 \\ 0.86 \times 10^{-3} \exp(-0.564 \ln Tu_t - 10\sqrt{\lambda_{\theta,t}}), & \lambda_{\theta,t} > 0 \end{cases} \quad (45)$$

The spot spreading half angle α is around 11 deg for nonaccelerated flow, but may vary considerably with pressure gradient. The following correlation was found by Gostelow et al. [36], who conducted excessive measurements with artificially generated turbulent spots.

$$\alpha = 4 + \frac{22.14}{0.79 + 2.72 \exp(47.63\lambda_\theta)} \quad (46)$$

D'Ovidio et al. [37] confirmed Eq. (46) and slightly updated the original correlation of Gostelow et al. [36] for the spot propagation.

$$\sigma = 0.024 + \frac{0.604}{1 + 5 \exp(66\lambda_\theta)} \quad (47)$$

Even though recent investigations (e.g., Ref. [38]) have shown that turbulent spots artificially triggered by pressure pulses differ considerably from spots generated through the natural breakdown of turbulent streaks, their propagation and spreading behaviors given in Eqs. (46) and (47) seem comparable. The excellent performance of transition models based on these two equations is otherwise not explicable.

Equations (42)–(46) give good results on smooth and rough turbine airfoils. On very rough surfaces ($k/\delta_1 > 1$) and on aft loaded airfoils, the model behavior may be improved as was shown in our last paper [15] by simply limiting the Pohlhausen parameter used in Eqs. (45)–(47).

$$\lambda_{\theta,\text{eff}} = \max(\lambda_\theta - 0.01) \quad k/\delta_1 < 1.0$$

$$\lambda_{\theta,\text{eff}} = \min(\max(\lambda_\theta - 0.01), 0.06) \quad k/\delta_1 \geq 1.0 \quad (48)$$

At least at high turbulence levels and accelerated boundary layers, no further adjustment in the spot production or spreading and propagation rates is needed to account for roughness (see Ref. [15]). However, the roughness may have an enormous effect on the onset of transition x_t , which is needed in Eq. (43). The next section will provide a new transition onset correlation that accounts for roughness height and density, turbulence intensity, and wall curvature.

2.2.2 A New Transition Onset Correlation. The development of the new correlation for rough surfaces begins with finding a suitable correlation for smooth surfaces, which is optimized to work with the transition model presented above. Because the tur-

$$\gamma(x) = 1 - \exp \left[-n_t \int_{x_t}^x \frac{\sigma}{U_\infty \tan \alpha} dx \int_{x_t}^x \tan \alpha dx \right] \quad (43)$$

where n is the spot formation rate, α is the spot spreading half angle (Fig. 4) and σ is the spot propagation parameter. The spot formation rate n_t , which reflects the frequency of spot formation per unit length, is usually correlated in terms of the nondimensional breakdown parameter N_t .

$$N_t = n_t \sigma_t \theta_t^3 / \nu = n_t \sigma_t \frac{\text{Re}_{\theta,t}^3 \nu^2}{U_\infty^3} \quad (44)$$

Combining the work of Gostelow et al. [34] and Fraser et al. [35], Solomon et al. [33] gave the following correlation for N_t , which considers the influence of turbulence intensity Tu_t and freestream acceleration through the Pohlhausen parameter λ_θ .

turbulence intensity is the major parameter influencing the onset of transition on a smooth wall, it is usually correlated with the momentum thickness Reynolds number $\text{Re}_{\theta,t}$ at the transition onset location. Schiele [39] showed that it is advantageous to define an effective turbulence intensity Tu_{eff} , which differs for flat plates and airfoils. In addition, following Dris and Johnson [40], we include a parameter f_C to account for the effect of wall curvature.

$$Tu_{\text{eff}} = \begin{cases} Tu_t + f_C, & \text{airfoils} \\ 0.5(Tu_t + Tu_1) + f_C, & \text{flat plates} \end{cases} \quad (49)$$

The reason for the distinction between airfoils and flat plates is the difference in leading edge flow acceleration, which is far larger on airfoils than on flat plates with or without pressure gradient. Therefore it is assumed that the freestream turbulence acting on the boundary layer close to an airfoil's leading edge, where the acceleration parameter K is greater than 3×10^{-6} , is of lower importance than the local turbulence intensity Tu_t . On flat plates, however, an average between the turbulence intensity of the approaching flow Tu_1 and the local value Tu_t considers the boundary layer history and gives a good estimate of Tu_{eff} .

The parameter f_C is zero on convex surfaces (suction sides) and takes a value greater than zero on concave surfaces (pressure sides). Its determination will be discussed later in this paper.

Figure 5 shows the transition onset data obtained from postdiction of the measured heat transfer or shear stress distributions using the intermittency transition model presented before and manually adjusting x_t in Eq. (43). The data include several very different turbine cascades (Refs. [12,14,39,41–44]) and flat plates with pressure gradient (Refs. [45–48]). In addition, three commonly used correlations are shown (Refs. [3,39,49]). The one provided by Menter et al. [3] also included the effect of flow acceleration but is shown here for zero pressure gradients only ($\lambda_{\theta,t} = 0$).

While all the curves in Fig. 5 show a similar behavior, the following new correlation is optimized to be used with the intermittency model and gives a best fit to the data.

$$\text{Re}_{\theta,t,\text{smooth}} = 500 \cdot Tu_{\text{eff}}^{-0.75} \quad (50)$$

The concave surface at the pressure side of an airfoil has a destabilizing effect on the boundary layer through several mechanisms (e.g., Taylor–Görtler vortices). Dris and Johnson [40] accounted for this effect by correlating the parameter f_C with a

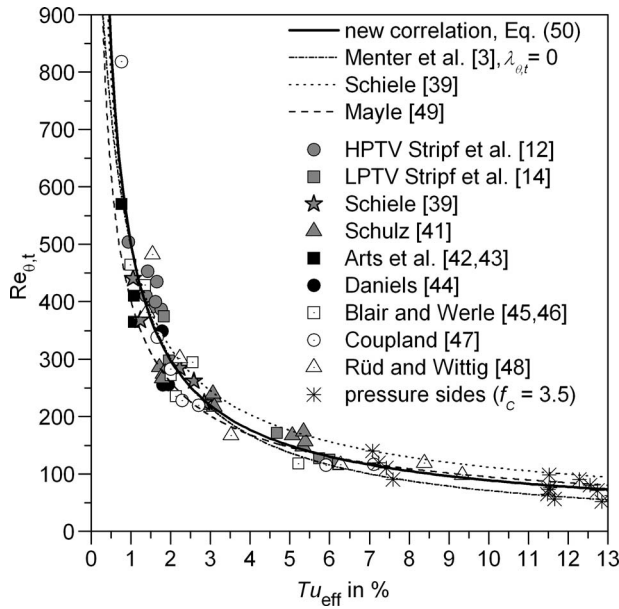


Fig. 5 Smooth wall transition onset correlations

Reynolds number based on the local radius of curvature and the local turbulence intensity, using data from different sources. Another major parameter influencing f_C , not accounted for in Ref. [40], is the strong flow acceleration on the pressure side boundary layer. Even though several researchers have shown the damping effect of a favorable pressure gradient on the Taylor-Görtler vortex structure and evolution (Refs. [50–52]), it is difficult to develop a transition onset correlation from those results. In preliminary studies using the correlation from Ref. [40] together with Eq. (50) the effect of curvature on the pressure sides of all the turbine cascade test cases was consistently overestimated. The reason for this is probably the damping effect of flow acceleration, which has not been accounted for.

A better result was achieved by using a constant value of $f_C = 3.5$ on the pressure side of an airfoil and $f_C = 0$ on the suction side and on flat plates. Figure 5 shows the pressure side transition data using $f_C = 3.5$, which is in good accordance with Eq. (50). The approach taken is admittedly debatable but has shown to work well on a lot of different pressure side boundary layers with and without surface roughness. It has to be noted that $f_C = 3.5$ can only be used for concave surfaces with strong favorable pressure gradient as observed on the pressure side of turbine airfoils. With more data being available, future correlations should certainly take into account the nonlinear combined effect of curvature, turbulence, and pressure gradient.

In order to include the effect of roughness height and density in Eq. (50), the experimental data obtained in the authors' previous investigations [12,14] on a high and low-pressure turbine vane are used. Again the measured heat transfer distributions were postdicted to determine the onset of transition. The investigations contain more than 30 different rough surfaces with the majority consisting of regular arrangements of truncated cones with varying heights and densities but also random roughness configurations. In addition, for each type of roughness, measurements are available at several freestream turbulence levels and Reynolds numbers.

To characterize the effect of roughness density on the onset of transition, the following roughness spacing parameter has proven successful (see Ref. [14]):

$$\Lambda_R = \frac{k}{h_m} \quad (51)$$

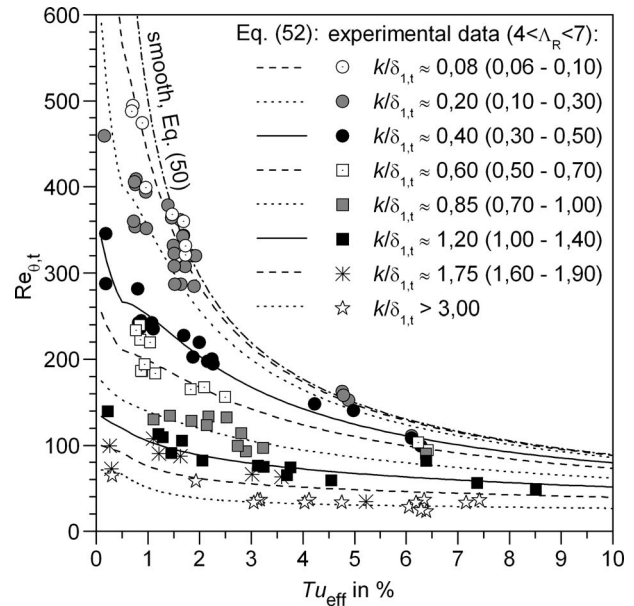


Fig. 6 Transition onset on rough surfaces with roughness densities $4 < \Lambda_R < 7$ (Tu_{eff} - $Re_{\theta,t}$ plane)

It was shown in Ref. [14] that the roughness has a maximum effect on transition when Λ_R takes a value of around 6. For this reason, only test cases with rough surfaces having a roughness density with a spacing parameter $4 < \Lambda_R < 7$ are selected at first. Figures 6 and 7 show two different views on the same data set. In Fig. 6 test cases are grouped by similar relative roughness height k/δ_1 , where δ_1 is the displacement thickness, while in Fig. 7 grouping is based on similar turbulence intensity at transition onset. From both figures it can be seen, that increasing relative roughness causes transition to move upstream to smaller momentum thickness Reynolds numbers.

The higher the turbulence intensity is, the smaller is the additional effect of the roughness. Conversely, at large roughness heights, the additional effect of increasing turbulence intensity is

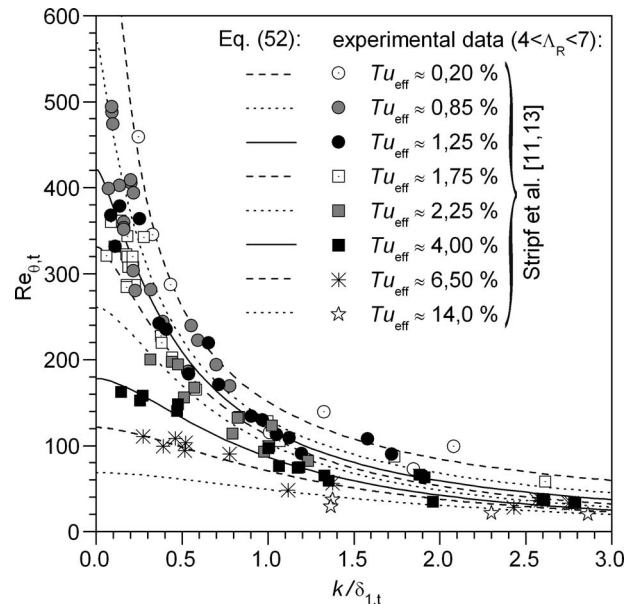


Fig. 7 Transition onset on rough surfaces with roughness densities $4 < \Lambda_R < 7$ (k/δ_1 - $Re_{\theta,t}$ plane)

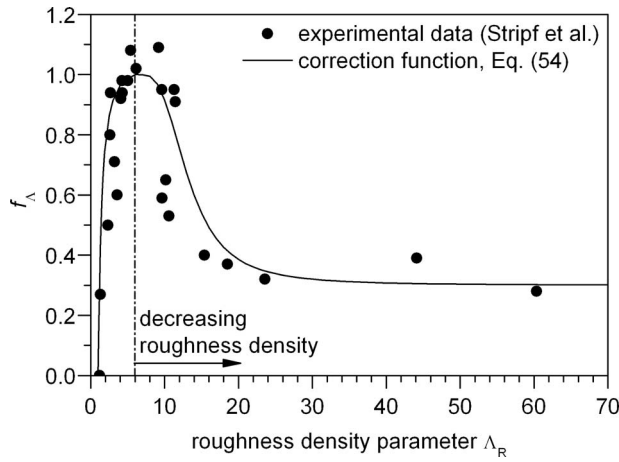


Fig. 8 Correction function f_Λ to account for different roughness densities

small. The observed behavior is well captured by the following correlation, which supersedes the one provided in Ref. [15].

$$Re_{\theta,t,rough} = \begin{cases} Re_{\theta,t,smooth}, & \frac{k}{\delta_1} \leq 0.01 \\ \left[\frac{1}{Re_{\theta,t,smooth}} + 0.0061 \cdot f_\Lambda \cdot \left(\frac{k}{\delta_1} - 0.01 \right)^{f_{Tu}} \right]^{-1}, & \frac{k}{\delta_1} > 0.01 \end{cases} \quad (52)$$

with f_{Tu} as function of the effective turbulence intensity in percent,

$$f_{Tu} = \max[0.9, 1.61 - 1.15 \exp(-Tu_{eff})] \quad (53)$$

The function f_Λ serves to account for roughness topographies whose roughness density is outside the range $4 < \Lambda_R < 7$. Using $f_\Lambda = 1$, the maximum effect of a given roughness height on transition can be estimated. This is important, as the type of roughness encountered on real turbine airfoils is expected to vary significantly depending on operational area and type of operation. In this case, the maximum roughness height might be the only parameter known a priori to the turbine designer.

If more information on the roughness topography is available, the effect of roughness density can be accounted for by applying the following correction function:

$$f_\Lambda = \begin{cases} 1.028(1 - \Lambda_R^{-2}), & \Lambda_R < 6 \\ 1, & 6 \leq \Lambda_R \leq 7 \\ 0.3 + [1.43 + 0.01(\Lambda_R - 7)^{2.7}]^{-1}, & \Lambda_R > 7 \end{cases} \quad (54)$$

Figure 8 shows the curve representing Eq. (54). Each of the data points in this figure reflects a different roughness geometry and its corresponding optimal value for f_Λ leading to a minimum error. For roughness densities close to one, f_Λ must take a value of zero because the surface is smooth in this case. The data points at $\Lambda_R = 1.2$ and $\Lambda_R = 1.3$ are from roughness topographies exhibiting small holes (pits) within an otherwise smooth surface (see Ref. [14]). All other data are from rough surfaces with regular arrays of truncated cones. In principle the transition onset correlation is thus applicable to surfaces with pits. However, the uncertainty is expected to be higher than for surfaces with protrusions, as only two test cases with pits have been available. It should also be mentioned that the DEM-TLV model in its formulation presented is not readily applicable to surfaces with pits, as no discrete roughness elements can be found for such a surface. The KS-TLK model may be used if the equivalent sand roughness is known

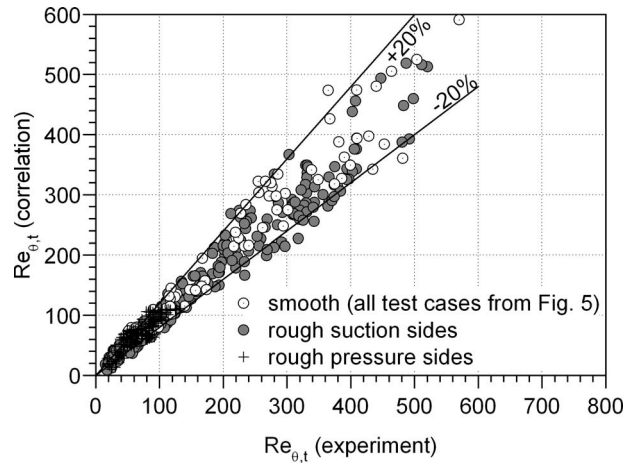


Fig. 9 Comparison of predicted and measured momentum thickness Reynolds numbers at transition onset

from measurements or correlations.

Care should be taken if rough surfaces with a step change in roughness height are considered. Measurements of Pinson and Wang [53,54] have shown that in this case, the step height can become the dominating length scale. In this case, it should be checked if using the step height together with $f_\Lambda = 1$ at the step location triggers transition prior to the case where the roughness height is used with the corresponding f_Λ value. Part II of this paper [55] contains an evaluation of the models using two test cases with locally varying surface roughness.

Figure 9 gives an overview of the performance of the new transition onset correlation (Eqs. (50)–(54)). The diagram includes all smooth wall test cases shown in Fig. 5 and all rough wall test cases from Refs. [12,13], which exhibit a bypass-transition on the suction and/or pressure sides. It can be seen that the onset of transition is well predicted in most cases. The average deviation is 12.4% for all smooth surface test cases, 13.3% for rough wall suction sides, and 16.7% for rough wall pressure sides.

The new correlation may now be combined with the intermittency transition model and the two roughness models DEM-TLV or KS-TLK. Hereafter, the overall models with transition prediction capability will be denoted DEM-TLV-T and KS-TLK-T, depending on the underlying roughness and turbulence model.

A final conclusion about the performance of both models will be given in Part II of the paper [55], where a variety of turbulent and transitional boundary layers on rough surfaces are calculated and compared with measurements.

3 Summary and Conclusion

Two new models of different complexity were presented to calculate transitional boundary layers with heat transfer on rough surfaces. The KS-TLK-T model can easily be implemented in existing CFD codes without considerable performance penalty. The drawbacks of the model are its dependence on the correct determination of an equivalent sand roughness and the assumption of an analogy between heat and momentum transfers, which is incorrect on a rough surface. It will be shown in Part II of the paper that despite of these limitations, the model gives a good estimate of the heat transfer on rough surfaces. The DEM-TLV-T model, which makes use of the more complex discrete-element approach and the same transition model, is more computationally intensive but avoids the limitations of the KS-TLK-T model. With its new formulation provided in this paper, a measured surface topography can readily be used as boundary condition without the need to determine an equivalent sand roughness. In addition, the model does not rely on an analogy between momentum and heat transfer and also allows the consideration of roughness elements

with low thermal conductivity. The comparative evaluation in Part II of this paper will provide further insight into the performance of both models.

The new common transition model considers most of the parameters that are important in the hot gas path of a turbine. It is optimized for the calculation of transitional boundary layers on turbine airfoils but may be used in a variety of different technical applications as long as the turbulence intensity, the roughness, and the wall curvature are within the limits covered in the transition onset correlation.

Acknowledgment

Financial support from the research initiative "Power Plant Technology of the 21st Century," which is partially funded by the State of Baden-Württemberg, Germany, is gratefully acknowledged.

Nomenclature

A_μ	= damping parameter in the KS-TLK model
A_R	= element cross-sectional area in x - z -plane (m^2)
C_d	= drag coefficient
C_f	= friction coefficient
c_k	= coefficient in the DEM-TLV model
c_p	= specific heat at constant pressure ($\text{J}/(\text{kg K})$)
c_μ, c_1, c_2	= coefficients in the k - ε model
d_F	= characteristic diameter for momentum transfer (m)
d_Q	= characteristic diameter for heat transfer (m)
d_z	= element diameter in z direction (m)
e	= eccentricity
f_C, f_Λ, f_{Ti}	= functions in the transition onset correlation
f_ε, f_μ	= damping functions in the KS-TLK model
H	= total enthalpy (J/kg)
h	= heat transfer coefficient ($\text{W}/(\text{m}^2 \text{K})$)
h_m	= mean elevation of roughness topography (m)
k	= turbulent kinetic energy (m^2/s^2)
k	= roughness height (m)
K	= acceleration parameter, $K=(\nu/U_\infty^2) \cdot (dU_\infty/dx)$
K_e	= eccentricity factor
k_f	= thermal conductivity of fluid ($\text{W}/(\text{m K})$)
k_R	= thermal conductivity of roughness element ($\text{W}/(\text{m K})$)
k_s	= sand roughness or equivalent sand roughness (m)
k_s^+	= roughness Reynolds number, $k_s^+=k_s u_\tau / \nu$
$l_e, l_{e,v}$	= turbulent length scales (m)
$l_\mu, l_{\mu,v}$	= turbulent length scales (m)
L_x, L_z	= reference lengths (m)
L_ε	= turbulence length scale, $L_\varepsilon=k^{3/2}/\varepsilon$ (m)
n	= spot production rate ($\text{m}^{-1} \text{s}^{-1}$)
N	= dimensionless spot production rate
N_R	= number of roughness elements
P	= static pressure (Pa)
Pr, Pr_t	= Prandtl number, turbulent Prandtl number
q	= heat flux (W/m^2)
Re	= Reynolds number
Re_θ	= momentum thickness Reynolds number, $Re_\theta=U_\infty \theta / \nu$
S_{FR}	= source term in the momentum equation (N/m^3)
S_{QR}	= source term in the energy equation (W/m^3)
St	= Stanton number, $St=h/(\rho c_p U_\infty)$
T	= temperature (K)
T_R	= roughness element temperature (K)
Tu	= turbulence intensity, $Tu=(3/2k)^{1/2}/U_\infty$ (%)
U	= mean streamwise velocity (m/s)

u_τ	= shear stress velocity, $u_\tau=(\tau_w/\rho)^{1/2}$ (m/s)
\tilde{V}	= Favre-averaged wall normal velocity (m/s)
v'	= wall normal velocity fluctuations (m/s)
x, y, z	= coordinates (m)
y_0	= shift in wall distance (m)

Greek

α	= spot spreading half angle (deg)
β	= porosity or openage factor
δ_{99}	= boundary layer thickness (m)
δ_1	= displacement thickness (m)
ε	= turbulent dissipation (m^2/s^3)
γ	= intermittency factor
λ_θ	= Pohlhausen parameter, $\lambda_\theta=\theta^2/\nu \cdot dU_\infty/dx$
Λ_R	= roughness spacing parameter
μ	= dynamic viscosity ($\text{N s}/\text{m}^2$)
μ_t	= eddy viscosity ($\text{N s}/\text{m}^2$)
ν	= kinematic viscosity (m^2/s)
θ	= boundary layer momentum thickness (m)
ρ	= density (kg/m^3)
σ	= spot propagation parameter
$\sigma_k, \sigma_\varepsilon$	= coefficients in the k - ε model
ζ	= roughness element density ($1/\text{m}^2$)

Subscripts

i	= incident flow
eff	= effective
$inner$	= inner layer
$outer$	= outer layer
t	= transition onset
w	= wall
∞	= boundary layer edge

References

- [1] Sieger, K., Schiele, R., Kaufmann, F., Wittig, S., and Rodi, W., 1995, "A Two-Layer Turbulence Model for the Calculation of Transitional Boundary-Layers," ERCOFTAC Bulletin, **24**, pp. 21–25.
- [2] Schiele, R., Kaufmann, F., Schulz, A., and Wittig, S., 1999, "Calculating Turbulent and Transitional Boundary-Layers With Two-Layer Models of Turbulence," Engineering Turbulence Modelling and Experiments, **4**, pp. 543–554.
- [3] Menter, F. R., Langtry, R. B., Likki, S. R., Suzen, Y. B., Huang, P. G., and Völker, S., 2006, "A Correlation-Based Transition Model Using Local Variables: Part I—Model Formulation," ASME J. Turbomach., **128**, pp. 413–422.
- [4] Turner, A. B., Tarada, F. H. A., and Bayley, F. J., 1985, "Effects of Surface Roughness on Heat Transfer to Gas Turbine Blades," AGARD Paper No. CP-390.
- [5] Hoffs, A., Drost, U., and Böls, A., 1996, "Heat Transfer Measurements on a Turbine Airfoil at Various Reynolds Numbers and Turbulence Intensities Including Effects of Surface Roughness," ASME Paper No. 96-GT-169.
- [6] Abuaf, N., Bunker, R. S., and Lee, C. P., 1997, "Effects of Surface Roughness on Heat Transfer and Aerodynamic Performance of Turbine Airfoils," ASME J. Turbomach., **120**, pp. 522–529.
- [7] Bunker, R. S., 1997, "Separate and Combined Effects of Surface Roughness and Turbulence Intensity on Vane Heat Transfer," ASME Paper No. 97-GT-135.
- [8] Boyle, R. J., Spuckler, C. M., Lucci, B. L., and Camperchioli, W. P., 2001, "Infrared Low Temperature Turbine Vane Rough Surface Heat Transfer Measurements," ASME J. Turbomach., **123**, pp. 168–177.
- [9] Boyle, R. J. and Senyitko, R. G., 2003, "Measurements and Predictions of Surface Roughness Effects on Turbine Vane Aerodynamics," ASME Paper No. GT2003-38580.
- [10] Boyle, R. J. and Senyitko, R. G., 2005, "Effects of Surface Roughness on Turbine Vane Heat Transfer," ASME Paper No. GT2005-68133.
- [11] Blair, M., 1994, "An Experimental Study of Heat Transfer in a Large-Scale Turbine Rotor Passage," ASME J. Turbomach., **116**, pp. 1–13.
- [12] Stripf, M., Schulz, A., and Wittig, S., 2005, "Surface Roughness Effects on External Heat Transfer of a HP Turbine Vane," ASME J. Turbomach., **127**, pp. 200–208.
- [13] Stripf, M., Schulz, A., and Bauer, H.-J., 2007, "Roughness and Secondary Flow Effects on Turbine Vane External Heat Transfer," J. Propul. Power, **23**(2), pp. 283–291.
- [14] Stripf, M., 2007, "Einfluss der Oberflächenrauigkeit auf die transitionale Grenzschicht an Gasturbinenschaukeln," doctoral, thesis, Institut für Thermische Strömungsmaschinen, Universität Karlsruhe, Germany.
- [15] Stripf, M., Schulz, A., and Bauer, H.-J., 2008, "Modeling of Rough Wall Boundary Layer Transition and Heat Transfer on Turbine Airfoils," ASME J.

- Turbomach., **130**, p. 021003.
- [16] Cebeci, T., and Smith, A. M. O., 1974, *Analysis of Turbulent Boundary Layers*, Academic, New York.
- [17] Taylor, R. P., Coleman, H. W., and Hodge, B. K., 1984, "A Discrete Element Prediction Approach for Turbulent Flow Over Rough Surfaces, Mississippi State University, Report No. TFD-84-1.
- [18] Durbin, P. A., Medic, G., Seo, J., Eaton, J. K., and Song, J., 2001, "Rough Wall Modification of Two-Layer $k-\epsilon$," ASME J. Fluids Eng., **123**, pp. 16–21.
- [19] Chen, H. C., and Patel, V. C., 1988, "Near-Wall Turbulence Models for Complex Flows Including Separation," AIAA J., **26**, pp. 641–648.
- [20] Launder, B. E., and Spalding, D. B., 1974, "The Numerical Computation of Turbulent Flows," Comput. Methods Appl. Mech. Eng., **3**, pp. 269–289.
- [21] Wolfshtein, M., 1969, "The Velocity and Temperature Distribution in One-Dimensional Flow With Turbulence Augmentation and Pressure Gradient," Int. J. Heat Mass Transfer, **12**, pp. 301–318.
- [22] Schlichting, H., 1936, "Experimentelle Untersuchungen zum Rauigkeitsproblem," Ing.-Arch., **7**, pp. 1–34.
- [23] McClain, S. T., 2002, "A Discrete-Element Model for Turbulent Flow Over Randomly-Rough Surfaces," Ph.D. thesis, Mississippi State University, Starkville.
- [24] Tarada, F., 1990, "Prediction of Rough-Wall Boundary Layers Using a Low Reynolds Number Boundary Layers Using a Low Reynolds Number $k-\epsilon$ Model," Int. J. Heat Fluid Flow, **11**, pp. 331–345.
- [25] Hosni, M. H., 1989, "Measurement and Calculation of Surface Roughness Effects on Turbulent Flow and Heat Transfer," Ph.D. thesis, Mississippi State University, Starkville.
- [26] Rodi, W., Mansour, N. N., and Michelassi, V., 1993, "One-Equation Near-Wall Turbulence Modeling With the Aid of Direct Simulation Data," ASME J. Fluids Eng., **115**, pp. 196–205.
- [27] Finson, M. L., and Wu, P. K. S., 1979, "Analysis of Rough Wall Turbulent Heating With Application to Blunted Flight Vehicles," AIAA Paper No. 79-0008.
- [28] Patankar, S. V., and Spalding, D. B., 1970, *Heat and Mass Transfer in Boundary Layers*, 2nd ed., International Textbook, London.
- [29] McClain, S. T., and Brown, J. M., 2007, "Reduced Rough-Surface Parameterization for Use With the Discrete-Element Model," ASME Paper No. GT2007-27588.
- [30] McClain, S. T., Collins, S. P., Hodge, B. K., and Bons, J. P., 2006, "The Importance of the Mean Elevation in Predicting Skin Friction for Flow Over Closely Packed Surface Roughness," ASME J. Fluids Eng., **128**, pp. 579–586.
- [31] Emmons, H., 1951, "The Laminar-Turbulent Transition in a Boundary Layer: Part I," J. Aeronaut. Sci., **18**, pp. 490–498.
- [32] Narasimha, R., 1957, "On the Distribution of Intermittency in the Transitional Region of a Boundary Layer," J. Aeronaut. Sci., **24**, pp. 711–712.
- [33] Solomon, W. J., Walker, G. J., and Gostelow, J. P., 1996, "Transition Length Prediction for Flows With Rapidly Changing Pressure Gradients," ASME J. Turbomach., **118**, pp. 744–751.
- [34] Gostelow, J., Blunden, A., and Walker, G., 1994, "Effects of Free-Stream Turbulence and Adverse Pressure Gradients on Boundary Layer Transition," ASME J. Turbomach., **116**, pp. 392–404.
- [35] Fraser, C. J., Higazy, M. G., and Milne, J. S., 1994, "End-Stage Boundary Layer Transition Models for Engineering Calculations," Proc. Inst. Mech. Eng., Part C: J. Mech. Eng. Sci., **208**, pp. 47–58.
- [36] Gostelow, J. P., Melwani, N., and Walker, G. J., 1996, "Effects of Streamwise Pressure Gradient on Turbulent Spot Development," ASME J. Turbomach., **118**, pp. 737–743.
- [37] D'Ovidio, A., Harkins, J. A., and Gostelow, J. P., 2001, "Turbulent Spots in Strong Adverse Pressure Gradients—Part II: Spot Propagation and Spreading Rates," ASME Paper No. 2001-GT-0406.
- [38] Anthony, R., Jones, T., and LaGraff, J., 2005, "High Frequency Surface Heat Flux Imaging of Bypass Transition," ASME J. Turbomach., **127**, pp. 241–250.
- [39] Schiele, R., 1999, "Die transitionale Grenzschicht an Gasturbinenschaufeln," doctoral thesis, Institut für Thermische Strömungsmaschinen, Universität Karlsruhe, Germany.
- [40] Dris, A., and Johnson, M. W., 2005, "Transition on Concave Surfaces," ASME J. Turbomach., **127**, pp. 507–511.
- [41] Schulz, A., 1986, "Zum Einfluß hoher Freistromturbulenz, intensiver Kühlung und einer Nachlaufströmung auf den äußeren Wärmeübergang einer konvektiv gekühlten Gasturbinenschaufel," doctoral thesis, Institut für Thermische Strömungsmaschinen, Universität Karlsruhe, Karlsruhe.
- [42] Arts, T., and De Rouvoit, M. L., 1990, "Aero-Thermal Investigation of a Highly Loaded Transonic Linear Turbine Guide Vane Cascade," Von Kármán Institute for Fluid Dynamics, Technical Report No. 174.
- [43] Arts, T., and De Rouvoit, M. L., 1992, "Aero-Thermal Performance of a Two-Dimensional Highly Loaded Transonic Turbine Nozzle Guide Vane," ASME J. Turbomach., **114**, pp. 147–154.
- [44] Daniels, L., 1978, "Film-Cooling of Gas Turbine Blades," Ph.D. thesis, Department of Engineering Science, University of Oxford, Oxford.
- [45] Blair, M. F., and Werle, M. J., 1980, "The Influence of Freestream Turbulence on the Zero Pressure Gradient Fully Turbulent Boundary Layer," United Technologies Research Center, Report No. R80-914388-12.
- [46] Blair, M. F., and Werle, M. J., 1980, "Combined Influence of Freestream Turbulence and Favourable Pressure Gradients on Boundary Layer Transition and Heat Transfer," United Technologies Research Center, Report No. R81-914388-17.
- [47] Coupland, J., 1993, "ERCOFTAC Special Interest Group Test Cases," personal communication.
- [48] Rüd, K., and Wittig, S., 1986, "Laminar and Transitional Boundary Layer Structures in Accelerating Flow With Heat Transfer," ASME J. Turbomach., **108**, pp. 116–123.
- [49] Mayle, R. E., 1991, "The Role of Laminar-Turbulent Transition in Gas Turbine Engines," ASME J. Turbomach., **113**, pp. 509–537.
- [50] Crane, R. I., and Umur, H., 1990, "Concave-Wall Laminar Heat Transfer and Görtler Vortex Structure: Effects of Pre-Curvature Boundary Layer and Favourable Pressure Gradients," ASME Paper No. 90-GT-94.
- [51] Finnis, M. V., and Brown, A., 1996, "The Streamwise Development of Görtler Vortices in a Favorable Pressure Gradient," ASME J. Turbomach., **118**, pp. 162–171.
- [52] Floryan, J. M., 1991, "On the Görtler Instability of Boundary Layers," Prog. Aerosp. Sci., **28**, pp. 235–271.
- [53] Pinson, M. W., and Wang, T., 2000, "Effect of Two-Scale Roughness on Heat Transfer in Transitional Boundary Layers, Part I: Surface Heat Transfer," ASME J. Turbomach., **122**, pp. 301–307.
- [54] Pinson, M. W., and Wang, T., 2000, "Effect of Two-Scale Roughness on Heat Transfer in Transitional Boundary Layers, Part II: Analysis of Boundary Layer," ASME J. Turbomach., **122**, pp. 308–316.
- [55] Stripf, M., Schulz, A., Bauer, H.-J., and Wittig, S., 2009, "Extended Models for Transitional Rough Wall Boundary Layers With Heat Transfer—Part II: Model Validation and Benchmarking," ASME J. Turbomach., **131**, p. 031017.

Extended Models for Transitional Rough Wall Boundary Layers With Heat Transfer—Part II: Model Validation and Benchmarking

M. Stripf

A. Schulz

H.-J. Bauer

S. Wittig

Lehrstuhl und Institut für Thermische
Strömungsmaschinen,
Universität Karlsruhe (TH),
Kaiserstraße 12,
Karlsruhe 76128, Germany

*Two extended models for the calculation of rough wall transitional boundary layers with heat transfer are presented. Both models comprise a new transition onset correlation, which accounts for the effects of roughness height and density, turbulence intensity, and wall curvature. In the transition region, an intermittency equation suitable for rough wall boundary layers is used to blend between the laminar and fully turbulent states. Finally, two different submodels for the fully turbulent boundary layer complete the two models. In the first model, termed KS-TLK-T in this paper, a sand roughness approach from (Durbin, et al., 2001, "Rough Wall Modification of Two-Layer $k-\epsilon$," ASME J. Fluids Eng., **123**, pp. 16–21), which builds on a two-layer $k-\epsilon$ -turbulence model, is used for this purpose. The second model, the so-called DEM-TLV-T model, makes use of the discrete-element roughness approach, which was recently combined with a two-layer $k-\epsilon$ -turbulence model by the present authors. The discrete-element model will be formulated in a new way suitable for randomly rough topographies. Part I of this paper will provide detailed model formulations as well as a description of the database used for developing the new transition onset correlation. Part II contains a comprehensive validation of the two models, using a variety of test cases with transitional and fully turbulent boundary layers. The validation focuses on heat transfer calculations on both the suction and the pressure side of modern turbine airfoils. Test cases include extensive experimental investigations on a high pressure turbine vane with varying surface roughness and turbulence intensity, recently published by the current authors, as well as new experimental data from a low pressure turbine vane. In the majority of cases, the predictions from both models are in good agreement with the experimental data.*

[DOI: 10.1115/1.2992512]

1 Introduction

In Part I of this paper [1] two models for the calculation of rough wall transitional boundary layers with heat transfer were formulated. The first model was termed KS-TLK-T and consisted of an extended two-layer turbulence model from Durbin et al. [2] and a newly developed transition model for rough surfaces. The second model, called DEM-TLV-T, is based on a discrete-element approach and formulated in a new way suitable for random roughness. It was combined with a two-layer turbulence model and the new transition model for rough surfaces.

The two models follow very different approaches to describe the effect of roughness on the turbulent boundary layer. The DEM-TLV-T model avoids two shortcomings of the KS-TLK-T model, as it does not rely on an equivalent sand roughness or an analogy between momentum and heat transfer on rough surfaces. It is, however, computationally more expensive and takes a bigger effort to be implemented in existing computational fluid dynamics (CFD) codes.

It is the intention of this part of the paper to provide a thorough and comparative assessment of the two models regarding their predictive quality. In Sec. 2, fully turbulent boundary layers on

flat plates with and without pressure gradient are calculated and compared with measurements. In Sec. 3, the interplay of the two roughness models and the newly developed transition model is tested by calculating the transitional boundary layers on turbine airfoils with different rough surfaces.

2 Turbulent Boundary Layers on Rough Walls

While quite a number of measurements of rough wall turbulent boundary layers are available in the open literature, not all of them are suitable for the comparative evaluation of the KS-TLK and DEM-TLV models.¹ Apart from the required documentation of all fluid dynamic and thermal boundary conditions, the definition of the rough surface used in the experiment has to be detailed enough to deduce all information needed by the two models. The experimental program conducted at Mississippi State University on surfaces with hemispherical roughness elements and the investigations at Stanford University on most dense arrays of spheres do contain all necessary information and will be used in the following study. In addition, experiments conducted on realistic rough surfaces at the Air Force Research Laboratory Dayton will be used to show the capability of the DEM-TLV model to calculate stochastic roughness configurations.

All calculations are performed with the forward marching boundary layer code ALFA, which is based on the method of Pa-

¹Contributed by the International Gas Turbine Institute of ASME for publication in the JOURNAL OF TURBOMACHINERY. Manuscript received June 20, 2008; final manuscript received August 5, 2008; published online April 20, 2009. Review conducted by David Wisler. Paper presented at the ASME Turbo Expo 2008: Land, Sea and Air (GT2008), Berlin, Germany, June 9–13, 2008.

¹As only the roughness models without the transition model are validated in this section, the model names do not include the affix "-T" (see Ref. [1]).

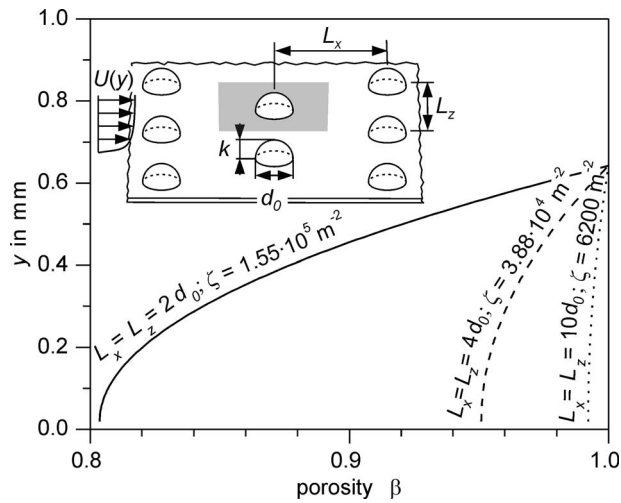


Fig. 1 Roughness geometry for the test cases of Hosni [4] and Chakroun [6]

tankar and Spalding [3]. In order to assure grid independent solutions in all cases, the forward step is limited to 5% of the momentum thickness. In addition, the dimensionless wall distance y^+ of the grid point nearest to the wall is set to smaller than 0.3, and the aspect ratio of the cell closest to the wall is limited to 10. For calculations using the discrete-element approach, at least 30 cells are within the roughness sublayer. These high requirements on the computational grid guarantee comparability among the different models. For practical calculations, near grid independent solutions can be achieved on much coarser grids.

2.1 Flat Plates With Hemispherical Roughness Elements.

Hosni and co-workers [4,5] and Chakroun and co-worker [6,7] conducted measurements in the closed loop wind tunnel of the Mississippi State University on a 2.4 m long flat plate consisting of 24 individually heated aluminum modules, which are equipped with the desired roughness. Three rough surfaces composed of regular arrays of hemispherical elements with diameter $d_0 = 1.27$ mm and different element distances were investigated. Figure 1 illustrates the roughness geometry and the three resulting porosity distributions needed for the DEM-TLV model (see Ref. [1]). Due to the uniform roughness, the characteristic diameter distributions are identical, i.e., $d_F(y) = d_Q(y) = d(y)$ and the element densities ζ are independent of wall distance (see Fig. 1). The equivalent sand roughness heights needed for the KS-TLK model are calculated using the correlation of Waigh and Kind [8]. For the most dense roughness ($L_x = L_z = 2d_0$) their correlation gives a sand roughness $k_s = 1.354$ mm, for the intermediate density $k_s = 0.328$ mm, and for the lowest density $k_s = 0.05$ mm.

Hosni and co-workers [4,5] measured the distributions of heat transfer and friction coefficients using a constant freestream velocity U_∞ between 12 m/s and 58 m/s. Depending on U_∞ the resulting roughness Reynolds numbers k^+ range from 1 to 400, covering the transitionally and fully rough regimes. The air temperature was set to 299.5 K and the individual modules were heated to 317 K. Because the thermal conductivity of the roughness elements is high ($k = 211$ W/(m K)), the element temperature is constant and equal to the wall temperature. The static pressure inside the wind tunnel was around 1.01×10^5 Pa, and the turbulence intensity Tu_1 was less than 0.3%. At the beginning of the flat plate, a trip wire was used to assure fully turbulent boundary layers at all conditions. The authors quote a relative measuring error in the Stanton number of between $\pm 1.6\%$ and $\pm 6\%$ and an error of about $\pm 12\%$ in the friction coefficient c_f .

Figure 2 shows the measured Stanton number distributions for the three rough surfaces and two different freestream velocities.

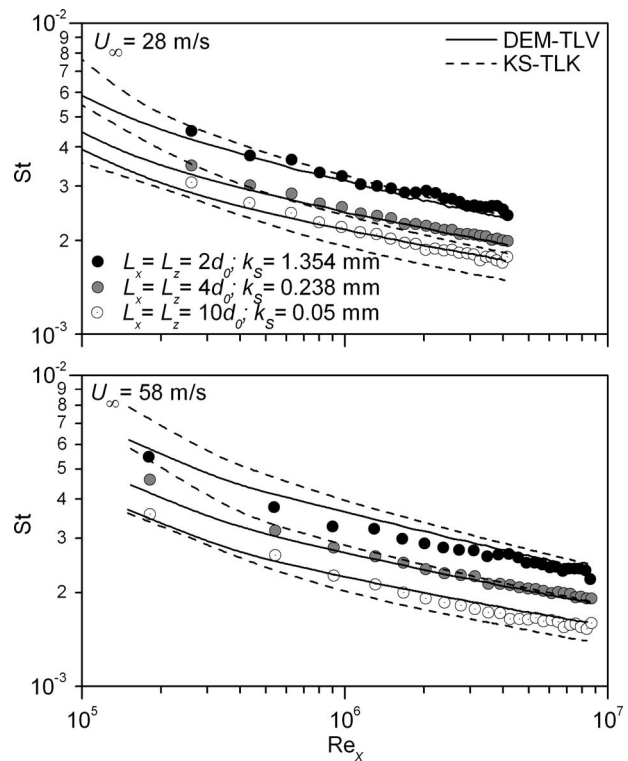


Fig. 2 Test cases of Hosni and co-workers [4,5]: calculated and measured heat transfer distributions

Calculated distributions are shown in solid lines for the DEM-TLV model and in dashed lines for the KS-TLK model. Both models give a good prediction of the increase in heat transfer with increasing roughness density. The KS-TLK model underestimates the Stanton numbers most notably at the smallest roughness density. Altogether, the DEM-TLV model shows a slightly better agreement with the experiment, and its predictions are within the measurement error in all cases.

With complementary hot wire measurements Hosni and co-workers [4,5] determined the friction coefficients along the unheated surface for selected test cases. Figure 3 shows the measured distributions, which are available for two freestream velocities and different roughness densities (no data are available for the $L_x = L_z = 10d_0$ surface and a freestream velocity of 58 m/s). Again, the calculated distributions are shown in solid and dashed lines for the DEM-TLV and KS-TLK models, respectively. At a low freestream velocity, both models agree quite well with the measurements. For the higher freestream velocity, the DEM-TLV model's predicted friction coefficients are slightly too high.

Chakroun and co-worker [6,7] modified the experimental setup of Hosni [4] using a flexible wall opposite to the 2.4 m long instrumented plate, in order to investigate the effect of flow acceleration. The authors used the same roughness geometries as Hosni; however, the roughness with the smallest density was replaced by a smooth wall. The static pressure, the fluid and wall temperatures, as well as the turbulence intensity are about the same as in the experiments of Hosni. The freestream velocity distribution realized through the flexible wall is shown in Fig. 4. The velocity increases over a distance of around 400 mm from 28 m/s to 36 m/s, which results in an acceleration parameter $K = \nu / U_\infty^2 (dU_\infty / dx)$ of about 0.3×10^{-6} .

A comparison of the measured and calculated Stanton number distributions is given in Fig. 5. It can be seen that both models give a good prediction of the measured values even though some differences exist. The KS-TLK model slightly overestimates heat transfer in the accelerated regions, while the DEM-TLV model

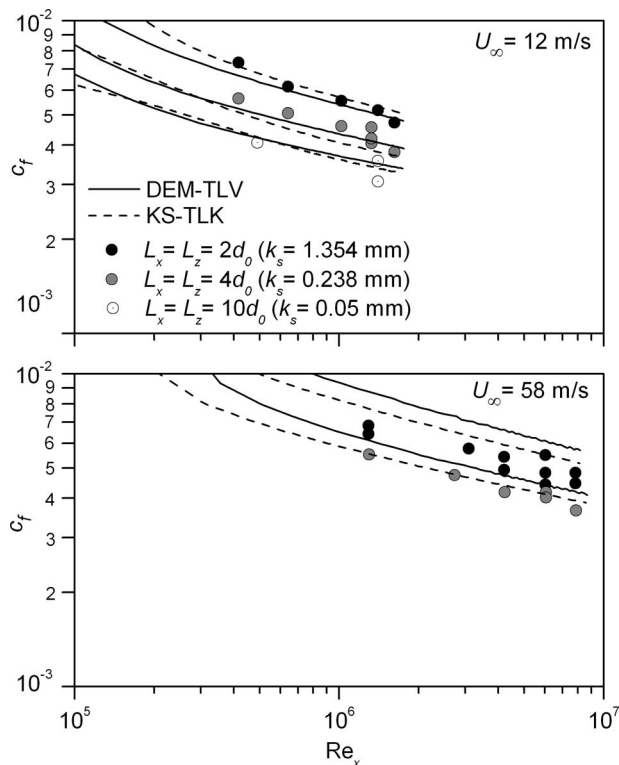


Fig. 3 Test cases of Hosni and co-workers [4,5]: calculated and measured friction coefficients

calculates the exact values. Both models predict Stanton numbers that are somewhat too small in the relaxation region downstream of the freestream acceleration. On the smooth wall, the calculated heat transfer distributions from both models deviate from the measured values in the accelerated region. This is not surprising, as the underlying two-layer models of turbulence are unable to predict the heavy damping of turbulent fluctuations due to the strong freestream acceleration.

With additional hot wire measurements, Chakroun [6] measured the velocity profiles and determined the displacement thickness δ_1 at several positions along the flat plate. Figure 5 shows the evolution of δ_1 and the corresponding calculated values. Both models predict the right trend of δ_1 but consistently underestimate the displacement thickness by almost 15%. In both, experiment and calculation, the same incompressible formulation to determine the

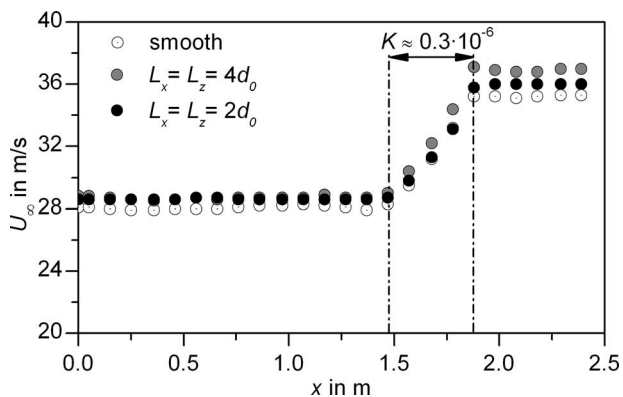


Fig. 4 Test cases of Chakroun and co-workers [6,7]: freestream velocity distribution

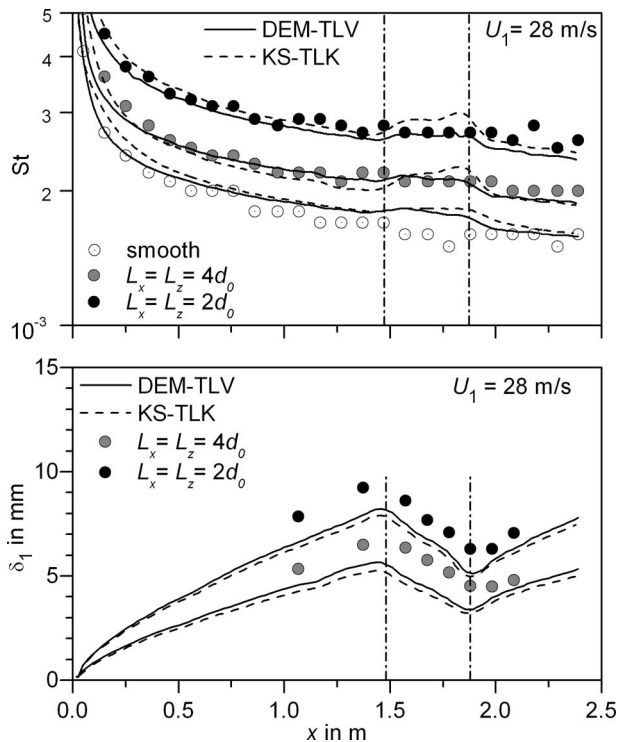


Fig. 5 Test cases of Chakroun and co-workers [6,7]: calculated and measured Stanton numbers and displacement thicknesses

displacement thickness was used. However, an uncertainty exists, as it is not clear, where the origin of the velocity profiles was set in the experiment.

2.2 Flat Plates With Spherical Roughness Elements in a Most Dense Array. An extensive and thoroughly documented experimental program was conducted at Stanford University on a rough flat surface. The experimental setup with 24 individually heated modules is similar to the one described above and used at Mississippi State University, as the latter one is based on the Stanford setup. The porous surface used consists of copper balls with a diameter of $d_0 = 1.27$ mm brazed together in a most dense configuration. Although the experimental program also included measurements with uniform blowing through the porous plate, only the test cases without blowing are considered in the current paper. Figure 6 illustrates the roughness geometry and shows the distributions of porosity factor β and diameter d . As discussed in Part I of this paper [1] the origin is set at the y -location where $\beta = 0.37$, i.e., the roughness below this point, is not considered. Because of the roughness element shape and the uniform arrangement, the characteristic diameters for heat and momentum transfer are identical to the real element diameter, i.e., $d_F(y) = d_Q(y) = d(y)$. For the same reason the element density is constant $\zeta = 7.159 \times 10^5 \text{ m}^{-2}$. This concludes the surface description for the DEM-TLV model. However, for the KS-TLK model, the equivalent sand roughness is needed. Instead of using the correlation of Waigh and Kind [8], the exact value obtained by Healzer [9] from hot wire measurements will be used: $k_s = 0.62d_0 = 0.79$ mm.

Coleman et al. [10–12] conducted heat transfer and hot wire measurements on the before mentioned configuration using several variable freestream velocity distributions along the flat plate. Three of the distributions used are shown in Fig. 7. In the accelerated cases, the velocity distributions are designed to give equilibrium rough wall boundary layers, i.e., the friction coefficients are constant in the accelerated regions. Because in a fully rough boundary layer, the roughness length scale is the important param-

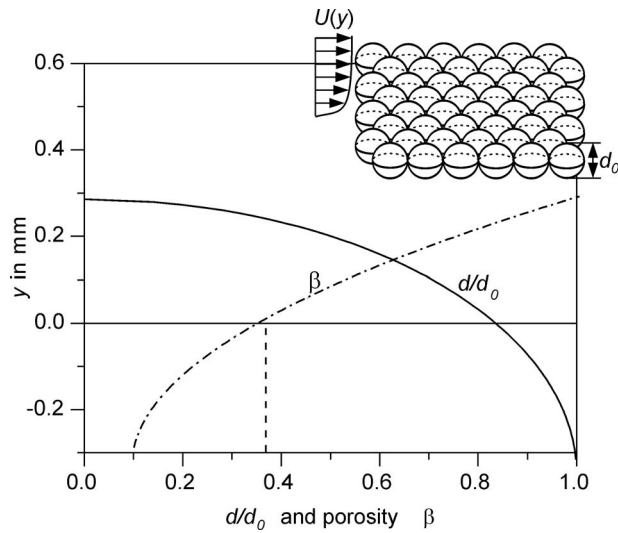


Fig. 6 Roughness geometry for the test cases of Coleman et al. [10–12]

eter instead of the viscous length scale ν/U_∞ , Coleman et al. [10–12] defined a new acceleration parameter K_r for the fully rough flow using the diameter d_0 of a spherical element as the new length scale

$$K_r = \frac{d_0 dU_\infty}{U_\infty dx} \quad (1)$$

With this new parameter, the velocity distributions shown in Fig. 7 can be characterized. In the regions where K_r is constant and greater than zero, the friction coefficients are expected to be constant.

Figure 8 shows the measured distributions of friction coefficients and Stanton numbers. It can be seen that in the regions with acceleration the friction coefficients are indeed constant. The predictions of friction coefficients from both models are shown as solid and dashed lines and are seen to be in excellent agreement with the measurements. The calculated Stanton numbers correspond well to the measured values. Especially in the accelerated cases, the KS-TLK model gives a slightly better prediction of heat transfer. However, both models calculate a somewhat too steep decrease of Stanton numbers in the accelerated regions.

Altogether, the performance of both models calculating rough wall turbulent boundary layers is seen to be good in all cases. In the remainder we shall address the model quality with regard to calculating stochastic surface roughness.

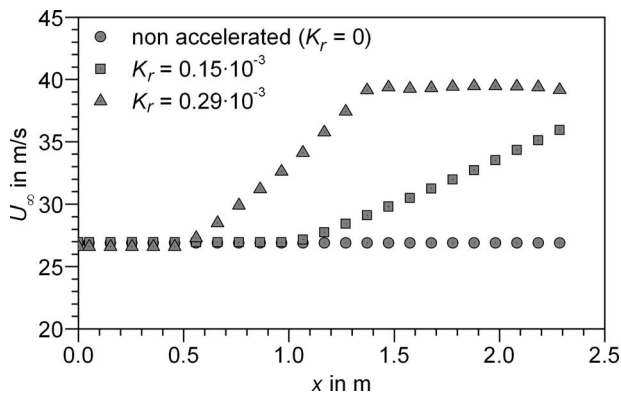


Fig. 7 Test cases of Coleman et al. [10–12]: freestream velocity distributions

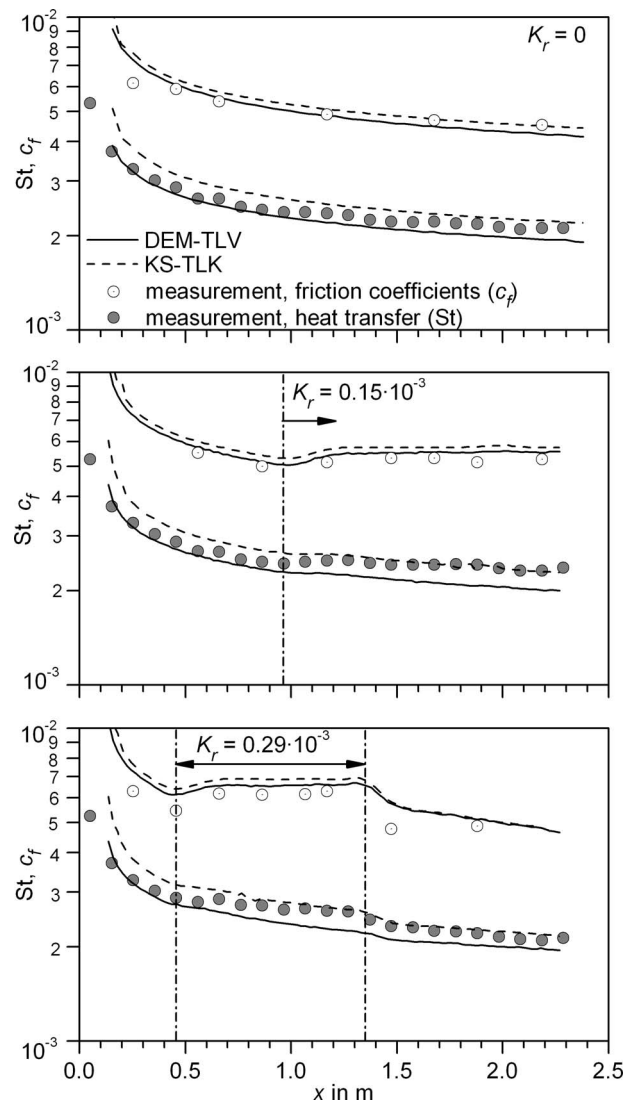


Fig. 8 Test cases of Coleman et al. [10–12]: calculated and measured Stanton numbers and friction coefficients

2.3 Flat Plate With Stochastic (Realistic) Surface Roughness.

In Part I of this paper, a new surface description method for the DEM-TLV model, using two characteristic diameter distributions for heat and momentum transfer, was introduced. In order to test this surface description method, experimental data on surfaces with eccentric roughness elements and a stochastic diameter distribution are needed. The measurements conducted at the Air Force Research Laboratory Dayton in collaboration with the Mississippi State University are well suited for this purpose as they provide enough information about the surface topology. The four surfaces tested are based on the extensive surface roughness measurements of Bons et al. [13] on almost 100 used turbine airfoils and components of land based gas turbines. From the plentitude of surfaces, McClain and co-workers [14,15] selected a characteristic surface with deposits and one with erosion from which they produced scaled-up polyester models using a 3D-printer (see Ref. [16]). Two additional surfaces investigated in Ref. [15] were constructed to have the same spacings and heights of the roughness elements, but use idealized elements with an elliptic cross section that have the same area as the original elements. Those idealized surfaces are named with the suffix “layered” in Ref. [15] and in the following discussion. The experimental setup consists of a 1.5 m long flat plate, where the first 1.05 m is equipped with a smooth surface. The adjacent 0.26 m long

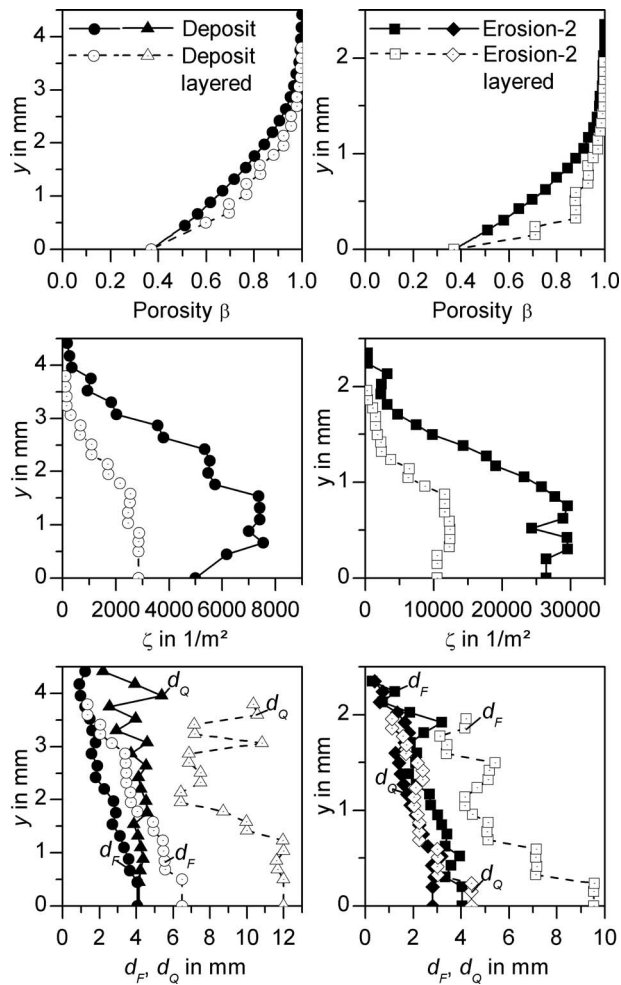


Fig. 9 Roughness parameters for the surfaces of McClain et al. [14]

floating test panel with surface roughness is then used to determine the average friction coefficient of the rough surface. A detailed description of the experimental setup can be found in Refs. [15,16].

Figure 9 shows the distributions of porosity $\beta(y)$, roughness element density $\zeta(y)$, and characteristic diameters for heat and momentum transfer $d_Q(y)$ and $d_F(y)$ as determined from the rough surface descriptions given in Ref. [14]. The distributions for d_Q and d_F are afflicted with some uncertainty, as only the distributions of average element diameter and of average eccentricity are given in Ref. [15]. In addition, the distributions were not available below the average (meltdown) height, which corresponds roughly to $\beta=0.5$. For the DEM-TLV model, values are required down to $\beta=0.37$ (see Ref. [1]), meaning that the first value of each distribution at $y=0$ had to be found from extrapolation.

McClain and co-workers [14,15] measured the average friction coefficients at two different freestream velocities (7 m/s and 12.5 m/s) at constant fluid properties for each rough surface. The results are shown in Fig. 10. The lower c_f values for each rough surface correspond to the lower freestream velocity. Comparison with the calculated values using the DEM-TLV model shows a good agreement with a maximum error of $\pm 8\%$ occurring with the Erosion-2 surface. This indicates that the DEM-TLV model using the rough surface description method introduced in Ref. [1] is suitable for stochastic roughness as well. Further validation

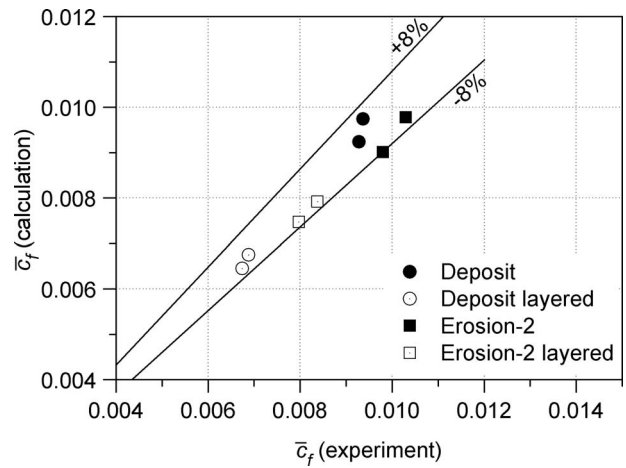


Fig. 10 Test cases of McClain et al. [14]: measured friction coefficients and calculated values using the DEM-TLV model

using additional test cases with realistic surfaces is required, however, in order to give a better conclusion of the model quality under those circumstances. In addition, the model has to be tested against heat transfer measurements on stochastic rough surfaces. Later in this paper (Fig. 18), the model's capability in predicting the heat transfer distribution around an airfoil with a transitional boundary layer and a surface roughness with random distribution of roughness elements will be demonstrated.

3 Transitional Boundary Layers on Rough and Smooth Walls

After the successful validation of the DEM-TLV and KS-TLK models for fully turbulent boundary layers, this section will provide an evaluation of the overall models (DEM-TLV-T and KS-TLK-T) containing the new transition model introduced in Ref. [1]. Again, only those test cases available in the open literature will be selected, which document all necessary boundary conditions and provide enough information about the rough surfaces. The experimental program conducted by the present authors (see Refs. [17–19]) on two different turbine cascades is predestined for this purpose as a wide range of exactly defined rough surfaces was investigated. Test cases include deterministic roughness with arrays of truncated cones of different heights and distances as well as random and locally varying roughness. To shed light on the combined effect of roughness and turbulence, inlet turbulence intensities were varied within a wide range between $Tu_1=0.4\%$ and $Tu_1=10\%$.

Figure 11 shows the two turbine cascades used in the investigations. In each case, the central airfoil was equipped with an exchangeable rough surface and the instrumentation to determine the heat transfer distribution. The lower and upper airfoils were used together with adjustable tailboards to generate periodic flow conditions. The turbulence intensity in the inflow was varied using turbulence grids at two different positions upstream of the cascade. Details about the experimental setup can be found in Refs. [17,19].

3.1 High Pressure Turbine Vane. From the 14 surfaces investigated on the high pressure turbine vane (HPTV), three rough surfaces with roughness heights k of $20 \mu\text{m}$, $37 \mu\text{m}$, and $70 \mu\text{m}$ and the smooth reference surface are selected for the following evaluation. The measurements and calculations are presented at two different inflow Reynolds numbers ($Re_1=1.4 \times 10^5$ and

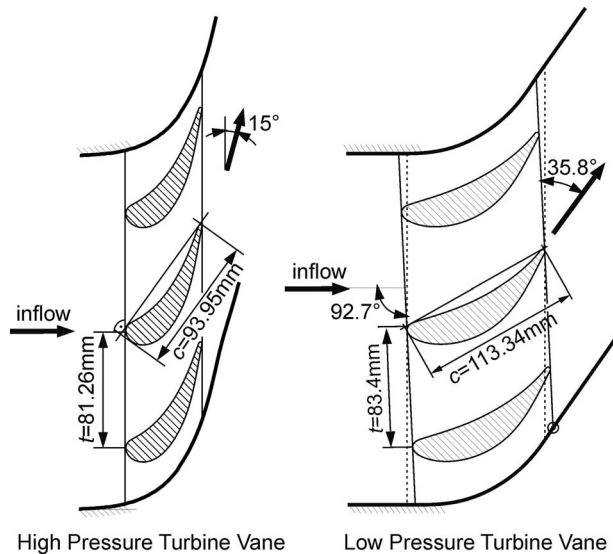


Fig. 11 Geometry of the high and low pressure turbine cascades

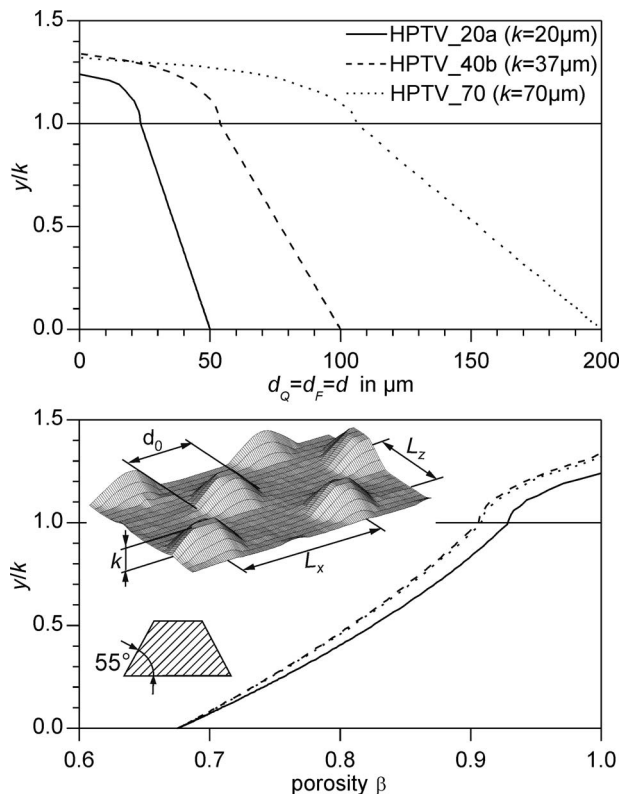


Fig. 12 Surface roughness and corresponding diameter and porosity distributions for the HPTV test cases

$Re_1=2.5 \times 10^5$) and two turbulence intensities² ($Tu_1=3.5\%$ and $Tu_1=8\%$). Figure 12 shows the actual topography of the rough surfaces as well as the diameter and porosity distributions. The distributions for $y/k > 1$ are due to the virtual expansion of the

²The turbulence intensities quoted in Refs. [17,18] are around 10% higher than the ones given in this paper and in Ref. [19]. The authors apologize for this inconsistency and recommend using the new values provided here and in Ref. [19] as they are based on additional extensive measurements of the spectral distributions of turbulence.

roughness elements with flat tops, which is needed by the DEM-TLV-T model (see Ref. [1]). The element density ζ in all three cases is constant and equal to $1.653 \times 10^8 \text{ m}^{-2}$, $4.132 \times 10^7 \text{ m}^{-2}$, and $1.033 \times 10^7 \text{ m}^{-2}$ for the HPTV_20a (r20-m), HPTV_40b (r40-m), and HPTV_70 (r80-m) surfaces, respectively. Note that the surfaces were renamed in Ref. [19] to obtain a more consistent naming convention. In addition, the roughness heights of the two latter surfaces were slightly updated after additional surface roughness measurements. The terms in brackets correspond to the old names used in Refs. [17,18]. The equivalent sand roughness needed by the KS-TLK-T model is calculated using the correlation of Waigh and Kind [8]; the corresponding values are given in Fig. 13.

Before discussing any results, it should be pointed out that, due to the parabolic nature of the boundary layer equations presented in Ref. [1], it is not possible to calculate separating boundary layers. Hence, any calculation is aborted as soon as the wall shear stress becomes zero. This is not a limitation of the roughness models but a consequence of the simplified transport equations we use for the sake of clarity and to reduce computational effort. In addition, as the parabolic boundary layer equations are solved, the calculation starts slightly downstream of the stagnation point, where the distributions of velocity and turbulence quantities have to be specified (see Ref. [1]). Therefore, no computed values are given in the stagnation region.

Figure 13 shows the measured Nusselt numbers at midspan around the high pressure turbine vane at varying surface roughness and flow conditions. Calculated distributions are shown in solid and dashed lines for the DEM-TLV-T and KS-TLK-T models, respectively.

The DEM-TLV-T model gives a good prediction of the observed distributions. Particularly, the turbulent heat transfer level is satisfactorily calculated by the model, although the decreasing Nusselt numbers in the accelerated turbulent region on the suction side are not well reproduced. The dissimilar transition behavior on the pressure and the suction side, which is due to the different velocity distributions and wall curvature effects, is well captured by the simple transition model.

The largest errors are encountered at the smallest Reynolds number and at the smallest turbulence intensity ($Re_1=1.4 \times 10^5$ and $Tu_1=3.5\%$), due to an inaccurate determination of the transition onset location. At the smallest roughness (HPTV_20a) no bypass transition is predicted but misleadingly separation is calculated at $s/c \approx 0.99$. For the reason mentioned above, the calculation is aborted at the separation location. The calculated heat transfer distribution of the smooth surface is identical to that of the HPTV_20a surface; however, in the smooth case the separation is correctly predicted.

Another inaccuracy in the calculation occurs at the highest Reynolds number and turbulence intensity, where on the pressure side the transition is falsely predicted for the smooth and HPTV_20a surfaces. This behavior of the transition onset correlation is very probably due to the simple treatment of the curvature effect in Eq. (49) of Part I of this paper [1]. Nevertheless, a satisfactory determination of the onset of transition is achieved in the vast majority of test cases on the pressure side as well.

The KS-TLK-T model shows the same characteristics predicting the onset and progress of transition as it is using the same transition model. However, in all cases with rough surface, turbulent heat transfer is heavily overestimated on the suction side. Rightfully, it should be said that the three rough surfaces feature roughness densities, which lead to a maximum equivalent sand roughness k_s for a given roughness height k . For small deviations in roughness density, k_s drops rapidly. It is therefore not surprising that the correlation of Waigh and Kind [8] bears the highest error around this roughness density. For example, increasing the element distance of surface HPTV_70 by 10% leads to a decrease in equivalent sand roughness height from $238 \text{ } \mu\text{m}$ to $40 \text{ } \mu\text{m}$. This in turn would result in the correct turbulent heat transfer predic-

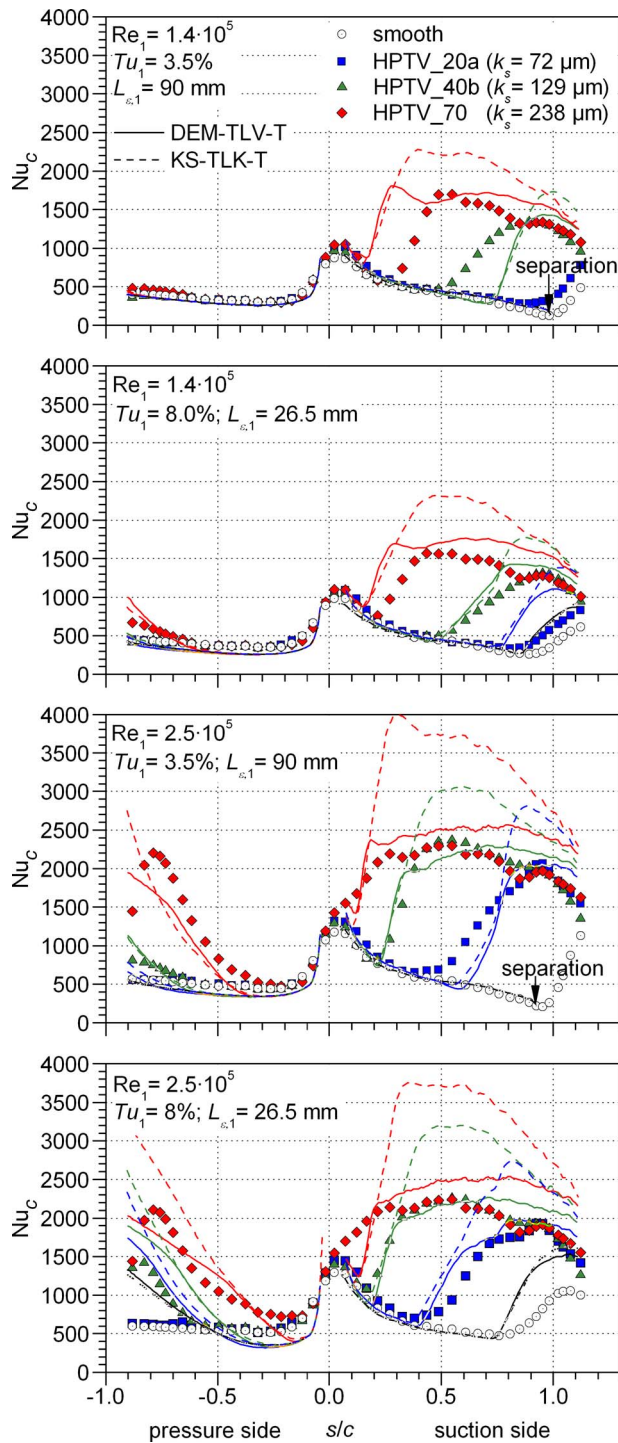


Fig. 13 High pressure turbine vane test cases of Stripf and co-workers [17,19]: calculated and measured heat transfer distributions

tion with the KS-TLK model.

The laminar heat transfer in the highly accelerated boundary layer on the pressure side is underestimated especially at the high Reynolds number and turbulence intensity. This is due to the neglect of turbulence effects on the accelerated laminar boundary layer and cannot be attributed to the roughness or transition models. First approaches to include this effect through the calculation of an effective viscosity can be found in the work of Smith and Kueth [20] and Byvaltsev and Nagashima [21].

An overall assessment of all 269 high pressure turbine vane test

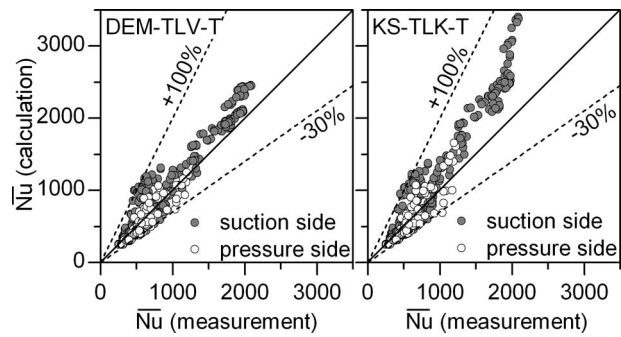


Fig. 14 Comparison of the calculated and measured average heat transfer for all high pressure turbine vane test cases

cases can be drawn from Fig. 14, where the average calculated Nusselt numbers are shown versus the measured values. Note that the area around the stagnation point ($|s/c| < 0.1$) was omitted when calculating the average values on the suction and pressure side. Especially at large roughness heights (large average Nusselt numbers), the DEM-TLV-T predictions are closer to the measurement than the KS-TLK-T model. The relatively strong deviations of both models in the Nusselt number range of between 500 and 1000 can be attributed to small inaccuracies determining the onset of transition, which cause a large change in the average heat transfer. The onset of transition, however, tends to be predicted somewhat too far upstream, which is for the purpose of a secure dimensioning. However, the designer has to keep in mind that the transition location might vary during a turbine's lifetime and with it the temperature and thermal stress distribution in the airfoil.

An impression of the maximum deviation between calculated and measured heat transfer coefficients can be obtained from Fig. 13, which shows a representative selection of all test cases. The maximum error in peak heat transfer coefficients using the DEM-TLV-T model is from -15% to $+38\%$. With the KS-TLK-T model, maximum errors are within -10% to $+82\%$.

3.2 Low Pressure Turbine Vane. The experimental investigation conducted on the low pressure turbine vane (LPTV) shown in Fig. 11 is an important supplement to the HPTV measurements. Apart from the effect of different roughness heights, the influence of varying roughness density, random roughness, and locally varying roughness is examined in more detail. A complete overview of the experimental setup and results is given in Ref. [19]. Out of 20 different surfaces investigated, 10 are selected for a closer comparison with the calculations carried out in this paper. Table 1 contains an overview of the roughness geometries used. With the exception of LPTV_40rnd, the rough surfaces consist of regular arrays of truncated cones with an angle of approximately 55° , as illustrated in Fig. 12. With the information given in Table 1, the diameter and porosity distributions needed by the DEM-TLV-T model are readily calculated using the equations from Part I of this paper [1].

The measured and calculated heat transfer distributions for three selected rough surfaces and the smooth reference surface are shown in Fig. 15. The diagrams are grouped by the inlet Reynolds number and the turbulence intensity. For the sake of clarity, the two diagrams for a Reynolds number of $Re_1 = 4.5 \times 10^5$ do not contain the curves for the LPTV_50a roughness. As explained earlier in this paper, no calculated values are shown in the leading edge region of the airfoil, due to the numerical method used (see Ref. [1]).

An inspection of the measured and calculated distributions shows that, except for a few cases, the onset and progress of transition are well predicted. The DEM-TLV-T model realistically calculates the heat transfer level on the suction side but underestimates the Nusselt numbers on the pressure side with rough surfaces. A possible explanation for this behavior is the effect of

Table 1 Roughness definition for the LPTV test cases

Surface	k (μm)	d (μm)	ζ (m^{-2})	k_s (μm)	Λ_R
Smooth			Hydraulically smooth		
LPTV_27a	27	80	8.33×10^7	56	4.0
LPTV_30a	30	180	2.08×10^7	36	2.4
LPTV_30b	30	140	2.08×10^7	94	4.3
LPTV_30c	30	100	2.08×10^7	45	9.6
LPTV_30le	30	80	3.70×10^7	53	9.5
LPTV_40rnd	40		See Fig. 17	n/a	8.6
LPTV_40te	40	80	3.70×10^7	71	11.6
LPTV_50a	50	200	7.41×10^6	103	6.2
LPTV_90	90	200	1.03×10^7	282	6.1

curvature on the turbulent rough wall boundary layer, which is not taken into account by the current model. The inclusion of curvature effects in the turbulence model, and not just in the transition model, will probably improve heat transfer predictions in the regions with a streamwise concave curvature.

The KS-TLK-T model yields similar results. However, heat transfer is heavily overestimated on the suction side for the largest roughness (LPTV_90). The reason for this is the same as mentioned above for the high pressure turbine vane, namely, the uncertainty in the correlation of Waigh and Kind [8] at roughness densities leading to a maximum equivalent sand roughness.

Additional test cases with varying roughness density are shown in Fig. 16 together with the distribution for a smooth surface. The calculated onsets of transition agree reasonably well with the measurements. Just the suction side start of transition for the LPTV_30b surface is predicted somewhat too far downstream. Overall, the simple roughness spacing parameter $\Lambda_R = k/h_m$ used in the transition onset correlation (cf. Part I of this paper [1]) is seen to be well suited to consider the effect of roughness density. On the suction side, Nusselt numbers calculated by the DEM-TLV-T model are in good accordance with the measurements, while the KS-TLK-T model overestimates heat transfer for the LPTV_30b surface with the largest sand roughness height. Again, this can be attributed to the uncertainty of Waigh and Kind's correlation.

On the pressure side the neglect of curvature effects in the turbulence model is most probably the reason for the low calculated values observed from both models (DEM-TLV-T and KS-TLK-T). Only for the LPTV_30b rough surface, the KS-TLK-T model gives the correct level of heat transfer, which, however, has to be attributed to the inaccurate determination of the equivalent sand roughness height.

Until now, the quality of both models was demonstrated by calculating rough wall boundary layers with a homogeneous and deterministic distribution of roughness elements. We still owe an evaluation of the models with a random and locally varying roughness. Figure 17 gives a representation of the surface LPTV_40rnd, which consists of a stochastic arrangement of random roughness elements. The square cutout shown in the picture is periodically repeated to build up the complete surface and therefore provides a complete description. The element density ζ is now a discontinuous function of the wall distance, as shown in Fig. 17. This is due to the unequal heights and the merging of roughness elements close to the wall. Because the application of Waigh and Kind's correlation on this random roughness is not possible without creating huge uncertainties, the equivalent sand roughness is unknown. Only the DEM-TLV-T model will therefore be used to calculate the boundary layer on this surface.

Figure 18 shows the measured and calculated heat transfer distributions for a turbulence intensity of $Tu_1 = 10\%$ and three different inlet Reynolds numbers. At the lowest Reynolds number the onset and progress of transition, as well as the turbulent heat transfer level on the suction and pressure side, are well predicted.

At higher Reynolds numbers, the calculated suction side onset of transition is slightly too far downstream. Predicted turbulent heat transfer distributions, however, agree well with the measurements. On the pressure side, transition is correctly captured, but heat transfer for the two highest Reynolds numbers is heavily underestimated.

A last important test of the models is conducted using a locally varying roughness along the airfoils' surface. The test case LPTV_30le is equipped with a rough leading edge only. The interface between the rough and smooth surfaces is such that the smooth surface is at the level of the roughness valleys. Another test case, termed LPTV_40te, has a rough trailing edge, while the remaining surface is smooth. Here, the smooth surface is at the level of the peak roughness height. Figure 19 shows the measured and calculated heat transfer distributions. The corresponding areas with a rough surface are marked for each of the two test cases.

The results show a similar quality of the KS-TLK-T and DEM-TLV-T models. The calculated onset of transition agrees well with the measurements, except for the LPTV_30le suction side at a low Reynolds number. Here, the model predicts an onset of transition at the end of the area with roughness, which in reality does not occur. On the LPTV_40te pressure side, the calculated turbulent heat transfer increases rapidly at the beginning of the rough area and then drops below the measured level. In reality, the increase is more gradual, which is not correctly described by either of the models.

As before for the high pressure turbine vane test cases, a final assessment of both models is given by the comparison of the calculated and measured average heat transfer of all 270 low pressure turbine vane test cases. Because the transition model developed in Part I of this paper [1] is for bypass transition only, it is not suited for the calculation of boundary layers with a very low freestream turbulence intensity. Nevertheless, the low turbulence test cases ($Tu_1 = 0.4\%$) from the LPTV investigation were calculated for curiosity. The resulting average Nusselt numbers are shown in Fig. 20 together with the measured values. It becomes apparent that heat transfer is overestimated for the $Tu_1 = 0.4\%$ test cases, which is due to the failure of the transition onset correlation at such low turbulence intensities.

A comparison of the model qualities at higher turbulence levels reveals a better overall agreement with the data for the DEM-TLV-T model than for the KS-TLK-T model. A weakness of both models is the underestimation of heat transfer on the pressure side, which again becomes apparent in Fig. 20. The inclusion of curvature effects in the turbulence model should be taken into account in a next step, to improve the quality in such flow configurations.

Comparing average Nusselt numbers gives an overall impression of the model, including the transitional and turbulent heat transfer as well as the transition onset position. It is clear that this comparison cannot deliver insight into local deviations in heat transfer. For this purpose, observation of the heat transfer distri-

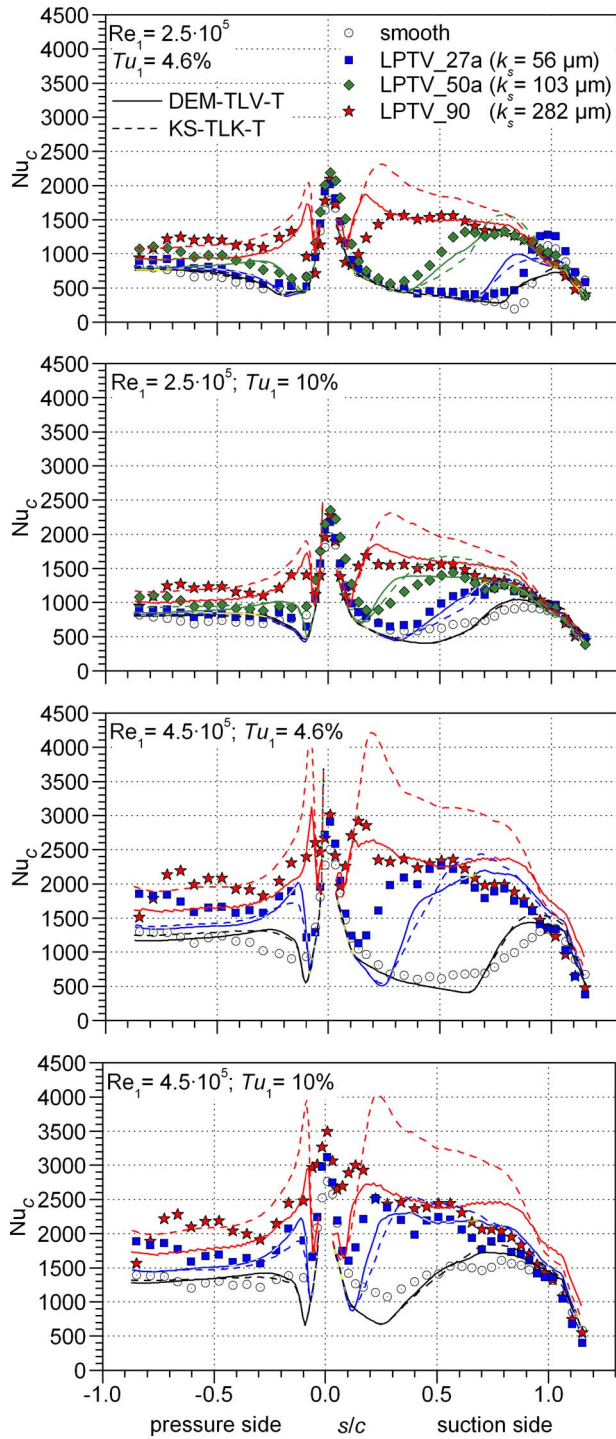


Fig. 15 Low pressure turbine vane test cases of Stripf [19]: calculated and measured heat transfer distributions at varying roughness heights

butions shown in Figs. 13–19 will provide a representative thought of such maximum deviations and the locations where they can be expected to occur.

The maximum error in peak heat transfer coefficients using the DEM-TLV-T model is from -30% to $+6\%$, where the large underprediction of heat transfer occurs on the pressure side, as discussed before. With the KS-TLK-T model, maximum errors are within -30% to $+30\%$.

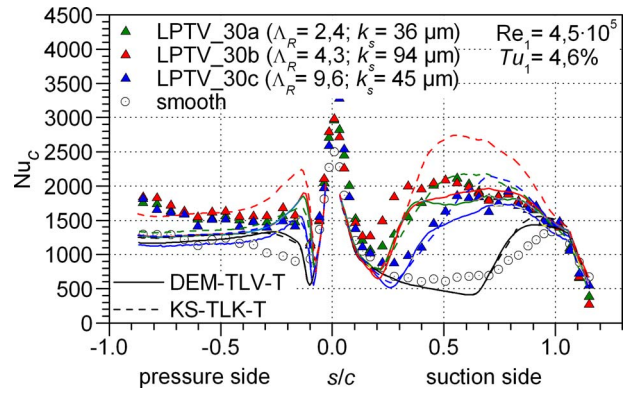


Fig. 16 Low pressure turbine vane test cases of Stripf [19]: calculated and measured heat transfer distributions at varying roughness densities

4 Summary and Conclusion

In Part I of this paper we presented the formulation of two extended models capable of calculating transitional boundary layers on rough surfaces. With Part II a comprehensive and comparative evaluation of both models has now followed. Test cases included flat plate turbulent boundary layers on rough walls with and without a pressure gradient as well as a great number of heat transfer measurements on two different turbine cascades. It turns

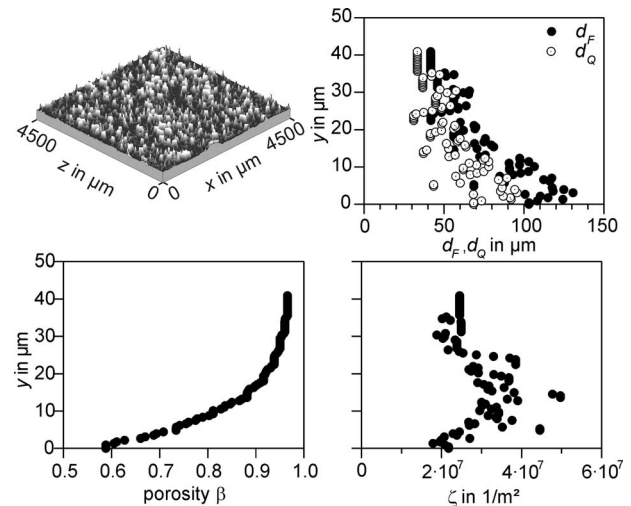


Fig. 17 Surface parameters for the LPTV_40rnd test case

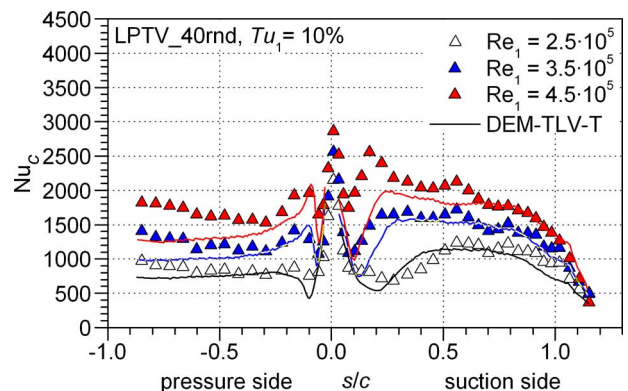


Fig. 18 LPTV_40rnd test case: calculated and measured heat transfer distributions at varying Reynolds numbers

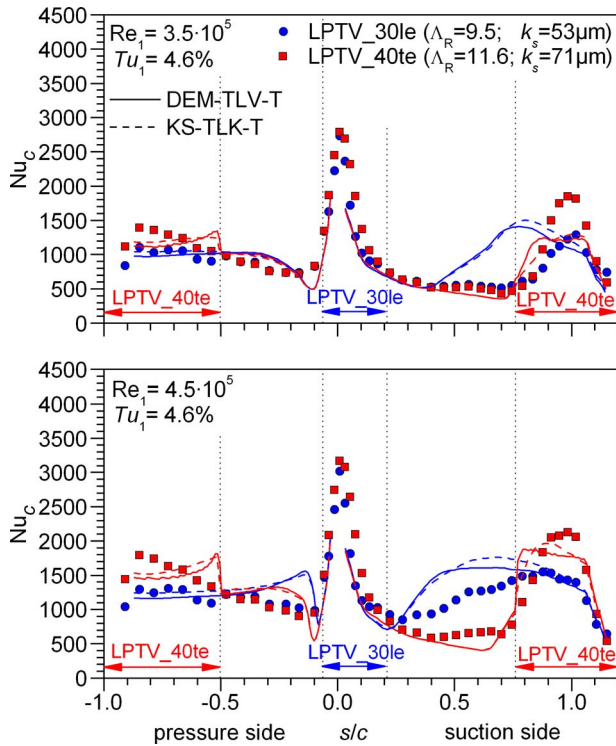


Fig. 19 Low pressure turbine vane test cases with locally varying surface roughness: calculated and measured heat transfer distributions

out that both models are well suited for the intended purpose and that in most of the test cases, the heat transfer predictions are in good accordance with the measurements. The computationally more expensive DEM-TLV-T model gives slightly better predictions than the KS-TLK-T model in the majority of test cases. The KS-TLK-T model, however, allows reasonable predictions as well and is less complicated to implement in existing CFD codes. It depends however on a correlation to determine the equivalent sand roughness height. In addition, it has to be pointed out that the DEM-TLV-T model currently is the only one capable of considering the effect of roughness elements with a low thermal conductivity. Unfortunately, all test cases investigated have rough surfaces made of a high thermal conductivity material so that this effect could not be addressed in the model evaluation. New heat transfer experiments with identical rough surfaces made from different materials with varying thermal conductivity could serve for this purpose.

If the maximum in-service roughness is known, the new models can readily be applied with sufficient confidence, keeping in mind

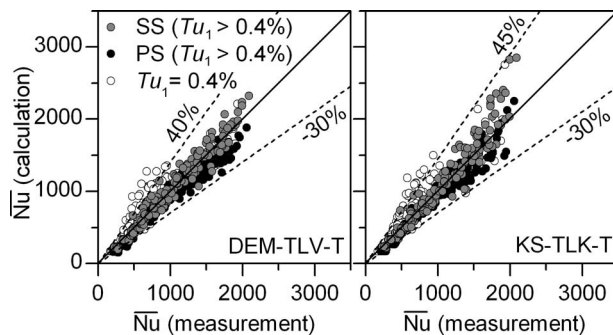


Fig. 20 LPTV: comparison of the calculated and measured average heat transfer for all test cases

that heat transfer is underestimated on rough surfaces with concave curvature (pressure sides). In addition, the designer has to take care of the effect of a moving transition onset position during the turbine's lifetime because the surface roughness might vary considerably due to particle deposits and/or erosion.

Acknowledgment

Financial support from the State of Baden-Württemberg, Germany provided within the research initiative "Power Plant Technology of the 21st Century" is gratefully acknowledged.

Nomenclature

- c = chord length (m)
- c_f = friction coefficient (see Eq. (40) in Ref. [1])
- d = diameter of a circular roughness element (m)
- d_0 = base diameter of a circular roughness element (m)
- d_F = characteristic diameter for momentum transfer (m)
- d_Q = characteristic diameter for heat transfer (m)
- h = heat transfer coefficient ($W/(m^2 K)$)
- h_m = mean elevation of roughness topography (m)
- k = roughness height (m)
- k_s = equivalent sand roughness (m)
- K = acceleration parameter, $K = \nu / U_\infty^2 (dU_\infty / dx)$
- K_r = acceleration parameter for rough surfaces
- L_x, L_z = reference lengths (m)
- L_ε = turbulent length scale (m)
- Nu = Nusselt number
- s = surface length (m)
- St = Stanton number
- Tu = turbulence intensity, $Tu = \sqrt{u'^2} / U$ (%)
- U = mean streamwise velocity (m/s)
- x, y, z = coordinates (m)

Greek

- β = porosity or openness factor (see Eq. (19) in Ref. [1])
- δ_1 = displacement thickness (m)
- Λ_R = roughness spacing parameter, $\Lambda_R = k / h_m$
- ζ = roughness element density ($1/m^2$)

Subscripts

- l = incident flow
- c = based on the chord length
- w = wall
- ∞ = boundary layer edge

References

- [1] Stripf, M., Schulz, A., Bauer, H.-J., and Wittig, S., 2009, "Extended Models for Transitional Rough Wall Boundary Layers With Heat Transfer—Part I: Model Formulations," *ASME J. Turbomach.*, **131**, p. 031016.
- [2] Durbin, P. A., Medic, G., Seo, J., Eaton, J. K., and Song, J., 2001, "Rough Wall Modification of Two-Layer $k-\varepsilon$," *ASME J. Fluids Eng.*, **123**, pp. 16–21.
- [3] Patankar, S. V., and Spalding, D. B., 1970, *Heat and Mass Transfer in Boundary Layers*, 2nd ed., International Textbook, London.
- [4] Hosni, M. H., 1989, "Measurement and Calculation of Surface Roughness Effects on Turbulent Flow and Heat Transfer," Ph.D. thesis, Mississippi State University, Starkville, MS.
- [5] Hosni, M. H., Coleman, H. W., and Taylor, R. P., 1991, "Heat Transfer Measurements and Calculations in Transitionally Rough Flow," *ASME J. Turbomach.*, **113**, pp. 404–411.
- [6] Chakroun, W., 1992, "Experimental Investigation of the Effects of Acceleration on Flow and Heat Transfer in the Turbulent Rough-Wall Boundary Layer," Ph.D. thesis, Mississippi State University, Starkville, MS.
- [7] Chakroun, W., and Taylor, R. P., 1993, "The Effects of Moderately Strong Acceleration on Heat Transfer in the Turbulent Rough-Wall Boundary Layer," *ASME J. Heat Transfer*, **115**, pp. 782–785.
- [8] Waigh, D. R., and Kind, R. J., 1998, "Improved Aerodynamic Characterization of Regular Three-Dimensional Roughness," *AIAA J.*, **36**, pp. 1117–1119.
- [9] Healzer, J. M., 1974, "The Turbulent Boundary Layer on a Rough, Porous

Plate: Experimental Heat Transfer With Uniform Blowing," Ph.D. thesis, Stanford University, Palo Alto, CA.

- [10] Coleman, H. W., Moffat, R. J., and Kays, W. M., 1976, "Momentum and Energy Transport in the Accelerated Fully Rough Turbulent Boundary Layer," Stanford University, Report No. HMT-24.
- [11] Coleman, H. W., Moffat, R. J., and Kays, W. M., 1977, "The Accelerated Fully Rough Turbulent Boundary Layer," *J. Fluid Mech.*, **82**, pp. 507–528.
- [12] Coleman, H. W., Moffat, R. J., and Kays, W. M., 1981, "Heat Transfer in the Accelerated Fully Rough Turbulent Boundary Layer," *ASME J. Heat Transfer*, **103**, pp. 153–158.
- [13] Bons, J. P., Taylor, R. T., McClain, S. T., and Rivir, R. B., 2001, "The Many Faces of Turbine Surface Roughness," *ASME J. Turbomach.*, **123**, pp. 739–748.
- [14] McClain, S. T., Hodge, B. K., and Bons, J. P., 2003, "Predicting Skin Friction for Turbulent Flow Over Randomly-Rough Surfaces Using the Discrete-Element Method," *Proceedings of the FEDSM 03*, Paper No. FEDSM2003-45411.
- [15] McClain, S. T., 2002, "A Discrete-Element Model for Turbulent Flow Over Randomly-Rough Surfaces," Ph.D. thesis, Mississippi State University, Starkville, MS.
- [16] Bons, J. P., 2002, "Study of Augmentation for Real Turbine Roughness With Elevated Freestream Turbulence," *ASME J. Turbomach.*, **124**, pp. 632–644.
- [17] Stripf, M., Schulz, A., and Wittig, S., 2005, "Surface Roughness Effects on External Heat Transfer of a HP Turbine Vane," *ASME J. Turbomach.*, **127**, pp. 200–208.
- [18] Stripf, M., Schulz, A., and Bauer, H.-J., 2007, "Roughness and Secondary Flow Effects on Turbine Vane External Heat Transfer," *J. Propul. Power*, **23**(2), pp. 283–291.
- [19] Stripf, M., 2007, "Einfluss der Oberflächenrauigkeit auf die Transitionale Grenzschicht an Gasturbinenschaufeln," doctoral thesis, Universität Karlsruhe, Germany.
- [20] Smith, M. C., and Kuethé, A. M., 1966, "Effects of Turbulence on Laminar Skin Friction and Heat Transfer," *Phys. Fluids*, **9**, pp. 2337–2344.
- [21] Byvaltsev, P. M., and Nagashima, T., 1998, "Correlation of Numerical and Experimental Heat Transfer Data at the Turbine Blade Surface," *JSME Int. J., Ser. B*, **41**, pp. 191–199.

On the Coupling of Designer Experience and Modularity in the Aerothermal Design of Turbomachinery

Jerome P. Jarrett
Tiziano Ghisu
Geoffrey T. Parks

Department of Engineering,
University of Cambridge,
Trumpington Street,
Cambridge CB2 1PZ, UK

The turbomachinery aerodynamic design process is characterized both by its complexity and the reliance on designer experience for success. Complexity has led to the design being decomposed into modules; the specification of their interfaces is a key outcome of preliminary design and locks-in much of the final performance of the machine. Yet preliminary design is often heavily influenced by previous experience. While modularity makes the design tractable, it complicates the appropriate specification of the module interfaces to maximize whole-system performance: coupling of modularity and designer experience may reduce performance. This paper sets out to examine how such a deficit might occur and to quantify its cost in terms of efficiency. Two disincentives for challenging decomposition decisions are discussed. The first is where tried-and-tested engineering “rules of thumb” accord between modules: the rational engineer will find alluring a situation where each module can be specified in a way that maximizes its efficiency in isolation. The second is where there is discontinuity in modeling fidelity, and hence difficulty in accurately assessing performance exchange rates between modules. In order to both quantify and reduce the potential cost of this coupling, we have recast the design problem in such a way that what were previously module interface constraints become key system design variables. An example application of our method to the design of a generic turbofan core compression system is introduced. It is shown that nearly one percentage point of the equivalent compressor adiabatic efficiency can be saved.
[DOI: 10.1115/1.2992513]

1 Introduction

The design of gas turbines is dominated by their complexity. Strategies to cope with this complexity introduce a number of potential limitations to the design. The resulting designs are characterized both by their modularity and in that, historically, as was noted by Cumpsty and Greitzer [1], the performance of the machines has often exceeded the capabilities of the analysis tools used in their design.

Design decomposition [2] and modular layouts have much to commend them: they facilitate the creation of engine families offering a wide thrust range by permitting a degree of interchangeability of engine modules and subsystems such as offering a re-designed fan on an existing core. However, modularity comes at a cost: module interchangeability requires fixed module interfaces, including aerothermal and mechanical considerations, thus these interfaces become design constraints. These design constraints are not “real,” in the sense of the second law of thermodynamics or a material rupture strength, but “design-process-intrinsic,” i.e., artifacts of the design process alone.

Throughout the development of the gas turbine, the performance of such machines has consistently exceeded the performance of the analysis tools used to design them [1]: designer experience and understanding are fundamental to successful turbomachinery design. This experience need not be acquired by the individual engineer: much is contained in proprietary models (based on correlation and empiricism), which are used in the preliminary design to make key architectural decisions about the lay-

out of the design, for example, the number of stages, number of shafts, and so on. Such decisions lock-in much of the final performance of the machine [3].

Where the needs of a modular layout accord with designer experience there results a strong incentive for the design process to follow a particular path; the *opportunity cost* of which it may be hard to determine.

Throughout the development of the gas turbine much effort has gone into improving the performance of modules. This has been highly successful: component efficiencies in excess of 90% are now commonplace. However, this also implies that any future improvements are likely to be small and hard-won [4]. In this paper, we therefore seek to examine the potential costs resulting from the coupling of designer experience and engine modularity and thus to explore methods by which performance gains may be attained by recasting component interfaces without losing the flexibility afforded by modularity.

2 An Example Design

We shall use a generic core engine compression system to explore the coupling between modularity and designer experience. High bypass ratio turbofans, as offered by the three main manufacturers, all exhibit some form of modularity in their compression system designs whether it be a fan/booster/HPC or a fan/LPC/HPC depending on whether a two- or three-shaft layout is used. In all cases an interduct is required to link the HPC to the upstream turbomachinery while accommodating the radial offset required due to differing shaft speeds. A generic LPC/booster-interduct-HPC core compression system is sketched in Fig. 1.

The “classical” way of viewing this geometry would be to consider it as three modules: the LPC/booster, the HPC, and the interduct that links them together. Designer experience, often in the form of correlation or empirical methods in preliminary design

Contributed by the International Gas Turbine Institute of ASME for publication in the JOURNAL OF TURBOMACHINERY. Manuscript received June 27, 2008; final manuscript received July 25, 2008; published online April 20, 2009. Review conducted by David Wisler. Paper presented at the ASME Turbo Expo 2008: Land, Sea and Air (GT2008) Berlin, Germany, June 9–13, 2008.

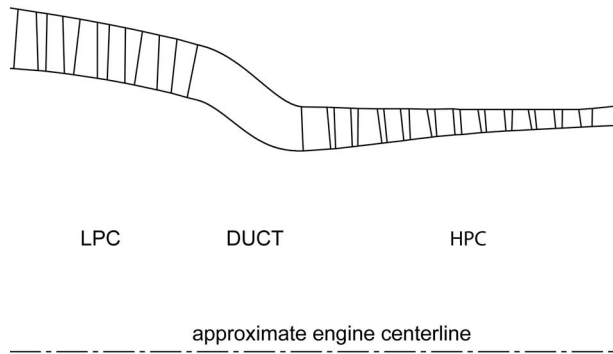


Fig. 1 Schematic of a LPC/duct/HPC system

tools, lays down a number of engineering rules of thumb regarding appropriate ranges of values of key module inlet and outlet design variables. While, naturally, many of these rules are proprietary, some are in the open literature. We shall use those from Walsh and Fletcher [5], especially focusing on those aspects that control flow velocities along the main gas path, in our analysis.

Let us first consider the axial compressors. Walsh and Fletcher [5] stated that, while it is desirable to have high inlet Mach numbers in order to minimize the frontal area, this leads to high relative velocities at the first stage blade tip and hence inefficiency. Mean inlet Mach numbers in the range 0.4–0.6 are common, with the highest level being for aeroengines in supersonic applications. Higher compressor inlet Mach numbers are also desirable in subsonic turbofans in order to minimize the core engine size. When considering exit conditions for the compressor, the primary aim is to prevent excessive downstream stagnation pressure losses. Thus the meanline exit Mach number should be no greater than 0.35 and should ideally be 0.25. The exit swirl should ideally be zero but certainly less than 10 deg [5].

Turning now to the intercompressor duct, its primary aerodynamic role is to transfer the flow from the exit of the low pressure compressor to the inlet of the high pressure compressor with maximum efficiency and minimum distortion. For our purposes, the principal mechanism of generating distortion is flow separation from either the hub or outer casing of the duct. For this reason, as Walsh and Fletcher [5] note, intercompressor ducts normally combine accelerating flow with the required reduction in meanline radius. This also benefits losses: whether accelerating or diffusing the duct will suffer wall friction losses, yet diffusing ducts generally have higher loss coefficients due to the flow being more prone to separate as a result of the adverse static pressure gradient. While acceleration is thus clearly desirable, its use is limited by the associated reduction in the static pressure rise of the core compression system.

2.1 Structural Struts. For practical purposes, intercompressor ducts commonly contain structural struts. These may be required for a range of reasons: often to provide structural support for thrust bearings and to permit access for various services, such as electrical, cabin bleed air, fuel, or auxiliary component drive-shafts. It is therefore necessary to gauge the impact of the presence of struts on the efficiency of the duct and distortion levels and to judge whether this effect may be included in the preliminary compression system design by reasonable estimate or whether direct calculation will be required.

The flow in the intercompressor duct that we are considering in this paper is accelerating. The duct is likely to contain perhaps eight nonlifting struts, uniformly distributed around its circumference, with a typical thickness-to-chord ratio of around 12%. In practice, the increased blockage levels caused by the presence of the struts would be allowed for, and the “clean-duct” area distribution with length restored, by the appropriate contouring of the

Table 1 Outline compression system designs using values from Ref. [5]

	LPC exit Mach	Duct area ratio	HPC inlet Mach
Rule of thumb	0.25–0.35		0.40–0.60
Case 1	0.25	~0.4	0.60
Case 2	0.35	~0.6	0.60
Case 3	0.30	~0.6	0.50

endwalls.

Several authors have studied the effect of struts in intercompressor ducts. Norris et al. [6] studied interturbine ducts. Compared with the mildly accelerating intercompressor duct, such ducts in the turbine tend to be diffusing, with Norris et al. [6] studying ducts with an area ratio of 1.5. Adding 26 struts to their clean data design increased both distortion levels and losses, the latter by a factor of 1.9. Unfortunately for comparative purposes, the authors found that their original “clean” (i.e., unstruted) duct was characterized by a separation bubble on the first bend, resulting from locally high diffusion levels. The introduction of the leading edge of the duct in this vicinity therefore exacerbated an existing source of distortion and increased already highly demanded diffusion levels.

Wallin and Eriksson [7] considered an intercompressor duct with an area ratio of one into which they added eight struts. They reported that the addition of the struts almost doubled the total pressure loss coefficient of the clean duct.

Bailey et al. [8] also tested an intercompressor duct with an area ratio of 1. They introduced a single strut of a typical 12% thickness ratio and observed the attached flow over its entire surface. While some thickening of the casing boundary layer upstream of the leading edge of the strut and a well-defined wake at its trailing edge were noted, no significant regions of flow separation were observed. Furthermore, by the careful positioning of the trailing edge of the strut it was possible to use the favorable pressure gradient in the duct to assist in the mixing out of the wake and boundary layer in the more critical inner wall region. With respect to losses they concluded that, if it could be assumed that the duct geometry was varied to account for the blockage introduced by the struts and the flow field associated with each strut was independent of its nearest neighbor, then (with compressor-generated inlet conditions) eight struts would increase the duct total pressure loss coefficient from 0.035 to approximately 0.058, i.e., a factor of around 1.7.

Given that we are considering separation to be the key driver of increased distortion, and that while the duct that we are considering will be accelerating, nonaccelerating ducts of similar radial offset ratios were reported to be free of separation, we proceed without directly evaluating struts but will account for their presence by conservatively doubling our total pressure loss coefficients (once they have been calculated) for a clean axisymmetric duct.

Preferred values for the duct therefore are to have an inlet Mach number in the range 0.3–0.4 with zero swirl in order to limit friction losses and be compatible with simple symmetrical-section nonlifting struts, and to combine this with a reasonable degree of acceleration in order to prevent the flow distortion and increased losses associated with separation. In practice, despite the bulk acceleration, care must still be taken to avoid the separation of the annulus boundary layers arising from local diffusion due to the endwall curvature.

2.2 Development of an Outline Compatible System. Table 1 shows a range of possible outline designs decomposed into the three modules. By applying the above rules of thumb to the duct and both compressors, a number of *compatible systems* can be designed. For example, Case 1 adopts the “ideal” LPC exit Mach

number of 0.25 and combines this with the highest HPC inlet Mach number of 0.6 in order to minimize the size of the latter. However, as can be seen from Table 1, the approximate area ratio (with average Mach numbers in the duct of around 0.4 it is assumed that compressibility effects are small), and hence the acceleration, of the duct is quite severe and suggests a significant reduction in the static pressure rise of the whole compression system. Case 2 therefore increases the LPC exit Mach number while maintaining the HPC inlet and this gives a significant improvement in the duct static pressure reduction. However, the flow velocities (and thus friction losses) through the duct are increased by this approach hence Case 3 is produced, which strikes a balance between the compressor demands and those of the duct (by selecting the midrange values for the compressor inlet and outlet conditions), such that a system can be designed where the correlation-based rules of thumb for all three modules are satisfied.

3 Experience/Modularity Coupling

To the rational engineer, the ability to produce an outline design of a complex system, decomposed into modules, with each module specified such that its performance *in isolation* remains not only within the “safe” region of trust of the correlation/experience base but, better still, at points known to give high-efficiency is alluring: a disincentive to challenge the outline design that results.

A second disincentive to challenging the specification of the modules arises from the nonuniformity of modeling and analysis tools available to the designer. This nonuniformity may be inter-module, for example, while myriad meanline analysis tools exist in the open literature for the compressor turbomachinery aerodynamics (see, for example, Ref. [9]) the same could not be said of the duct and thus the designer may well have to rely on rig test data or 3D computational fluid dynamics (CFD).

While this is not necessarily a problem in itself, it clouds the engineer’s view of the intermodule design space since discontinuities in the modeling level along the main gas path complicate the calculation of meaningful and accurate performance exchange rates. This reinforces the engineer’s reluctance to deviate from the decomposition strategy based on tried-and-tested correlations and experience, which indicate that each module can be specified in a way that maximizes its efficiency in isolation.

4 Assessing the Opportunity Cost

Our aim in this work is to assess the degree to which modular decomposition decisions based on experience, while optimal at the module level, are similarly optimal at the system level. If they are not, the lost system performance is a quantifiable opportunity cost of the reliance on designer experience in making preliminary design decisions.

In order to make this assessment as realistic as possible we shall conduct a *partial* redesign of a generic modular core compression system. As might be the situation in practice, we shall assume that sufficient time and/or resources are not available to permit a complete redesign of the whole system. Rather, the principal benefit conferred by a modular layout will be exploited: a new LPC will be designed to be mated to an existing HPC.

We assume that the existing HPC was designed for an inlet Mach number of 0.5, in accordance with the engineering rules of thumb. Therefore, from this point onward in our study, the inlet conditions to both the LPC and HPC are held fixed.

We proceed by *recasting* the design problem: instead of viewing the core compression system as three modules (LPC/duct/HPC) we reduce it to two: a combined LPC/duct module and a fixed HPC. Thus the LPC exit Mach number, having previously been a *design constraint* on both the separate LPC and duct, now becomes a *user variable* in the design of the combined LPC/duct module without necessarily affecting the HPC.

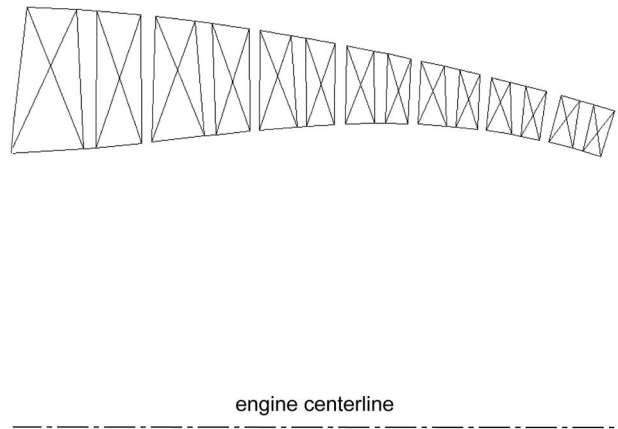


Fig. 2 Donor LPC geometry [10]

We begin by evaluating the effects on the separate components of the combined module of the design freedom afforded by recasting the design problem in this way.

5 Recasting the LPC Design

In order to more closely represent common industrial practice, we deliberately do not begin with a completely clean sheet of paper: rather, we shall modify an existing candidate design. The design we shall use for this purpose was introduced in a previous paper [10]. This is a moderately loaded seven-stage design with a polytropic efficiency in excess of 90%, as shown in Fig. 2.

We begin the redesign by removing the constraint on the design of the LPC module of an exit Mach number below 0.35 and ideally of 0.25. We will assess the potential gain in compressor adiabatic efficiency resulting from this design freedom without, at this point, concerning ourselves with the effects on downstream components.

We then use our previously reported [10] design tool to modify the candidate design. This tool incorporates a number of proprietary compressor aerothermal performance analysis codes, together with a hierarchical data store, design process management software, simple gradient-based optimizer, and user interface.

The constraints placed on the redesign are that the design-point pressure rise, surge margin, disk locations, and shaft speed with respect to the donor LPC must be maintained, with the latter two constraints to minimize effects on other components (such as the associated turbine) and cross-disciplinary effects (such as vibration), which are beyond the scope of this study.

Critically, the exit Mach number from the LPC is *not* constrained: the design tool is given the task of designing a series of low pressure compressors for maximum adiabatic efficiency, given the constraints listed above, in 0.01 increments over a user-defined range of target exit Mach numbers. In this way an *exchange rate curve* of efficiency versus the exit Mach number (all other things being equal) may be produced.

Such an exchange rate curve for the donor LPC is shown in Fig. 3. The plotted data are derived from proprietary analysis codes; the principal physical mechanism influencing the shape of the curve is the reduced demands, with increasing exit Mach numbers, for static diffusion in the rear-stage stators, which at the upper end of the Mach range is offset by increasing shock losses.

While the proprietary nature of these analysis tools does not permit direct comment concerning their absolute accuracy in predicting compressor efficiency, it should be noted that this paper is fundamentally concerned with the *design process* rather than the machine that results from it. What is therefore of primary importance is the ability of these tools to predict *relative* changes between designs more than correct absolute values of efficiency. As has previously been noted [3], preliminary design tools tend to be

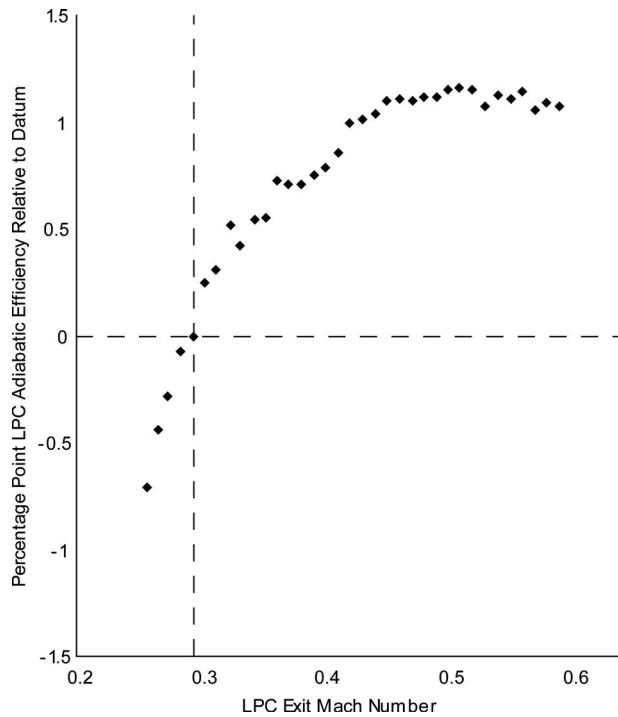


Fig. 3 Exchange rate curve of the design exit Mach number versus the LPC adiabatic efficiency

better at the former rather than the latter. However, in respect of absolute performance prediction levels, despite the relative decline of establishments like NASA and the British National Gas Turbine Establishment (NGTE) compared with gas turbine manufacturers over the past 30 years (and the resulting reduction in the proportion of knowledge about the subject in the open literature [9]), by the late 1970s such methods were reported to be able to predict stage efficiencies to within 1% [11] and by the early 1990s to have reached a similar level of accuracy for multistage compressors [12,13].

The selection from Table 1 of an exit Mach number of 0.30 results in an LPC whose adiabatic efficiency is of the order of 1.2 percentage points below the peak value, which occurs at an exit Mach number of approximately 0.51.

6 Recasting the Duct Design

Not only is the peak efficiency LPC exit Mach number well above the maximum permitted by the rule of thumb, it is also above the maximum “permitted” inlet Mach number of the duct. The principal aim of limiting the LPC exit Mach number was to minimize stagnation pressure losses in downstream components. We now therefore assess the impact of such a high inlet Mach number on the duct performance.

It will be necessary to overcome the second disincentive introduced above, i.e., we must ensure uniformity in the modeling fidelity between the codes used to analyze the performance of both the compressors and the duct. Though the capture of radial distortion development through the duct is desirable, since we have used correlation-based meanline methods in assessing the LPC performance, it would be inappropriate to use full 3D CFD modeling for the duct. However, as noted above, there is, to the knowledge of the authors, little in the open literature by way of similar models for duct performance. We have therefore proceeded by producing our own meanline design charts from a specially written Navier–Stokes solver, which we have benchmarked against published duct rig test data and commercial CFD.

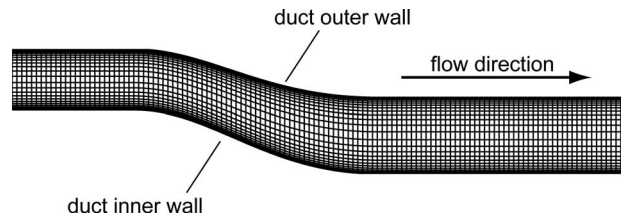


Fig. 4 2D CFD computational grid

7 Duct Design Charts

We have written a finite-volume fully-viscous 2D axisymmetric CFD solver with the aim of producing physics-based meanline design charts for unstrutted intercompressor ducts.

7.1 Description of the Flow Solver. The Gauss–Seidel method is used in a time-marching scheme [14] to solve the familiar governing Reynolds-averaged Navier–Stokes equations. In order to avoid the problem of pressure-velocity decoupling typical of collocated variable arrangements, a velocity-staggered quasi-orthogonal body-fitted mesh has been used (following the work of Harlow and Welsh [15] and Patankar [16]) with a hybrid discretization of convective fluxes and a second order discretization of diffusive fluxes.

An algebraic two-layer Prandtl mixing length model [17] was used for turbulence closure because of the reliability of the method in the analysis of bounded attached turbulent flows and of its computational efficiency. Given that one of the principal aims of the CFD code was to identify separation, due to its effect not only on loss but also distortion levels, a safety margin of 2 was applied to the maximum boundary layer shape factor with separation indicated by any reverse flow in the x -wise direction.

The calculations were performed on a 200 axial by 60 spanwise node grid with near-wall refinement, as shown in Fig. 4. This grid was used throughout the experiment. A value of y^+ of approximately 10 was found to give a grid-independent solution (in the presence of a wall function). Locally variable time-step, residual smoothing, and matrix preconditioning were used to accelerate the convergence to the steady-state solution.

Each simulation took approximately 20 min (8000 iterations) on an AMD Opteron 2.4 GHz machine. The use of an in-house code guaranteed the possibility of scheduling the required simulations in a parallel environment without restrictions, with important reductions in computational times. All mean output variables were determined by mass averaging.

7.2 Validation of the Flow Solver. A fundamental requirement for a design system is the reliability of the modeling used. We have therefore validated our 2D axisymmetric CFD code against both published rig test data and commercial CFD.

In their experimental study of the effect of length on the performance of intercompressor ducts, Ortiz-Duenas et al. [18] compared measured static pressure distributions (on both the inner and outer endwalls of the duct) and the duct-exit spanwise stagnation pressure distribution with commercial CFD that permitted the testing of two turbulence models against the rig test data.

The commercial CFD package used was FLUENT v6.1.22. As with our grid, shown in Fig. 4, long parallel sections were provided both upstream and downstream of the duct to permit the development of the boundary layers and to minimize interference between the static pressure field in the duct and the boundary conditions: The CFD inlet plane was 3.65 times the inlet duct height upstream of the duct inlet plane. Grid independent solutions of the 2D calculations were obtained using a 520 axial by 120 spanwise node grid, with fully resolved boundary layers [18].

Ortiz-Duenas et al. [18] used both the one-equation Spalart–Allmaras (Sp-A1) model and the two-equation k - ω model. Figure

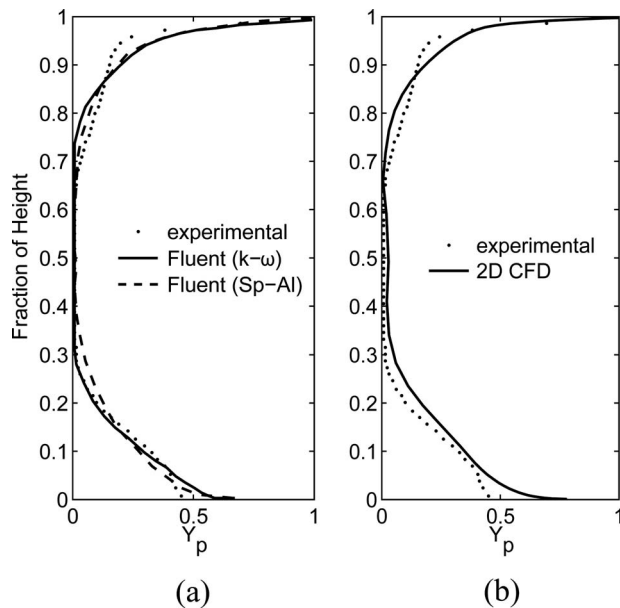


Fig. 5 Duct exit stagnation pressure: 2D CFD comparison with experiment and commercial CFD (partially reproduced from Ref. [18])

5(a) shows the duct-exit stagnation pressure coefficient plotted against the fraction of duct height at a Reynolds number of 260,000 and was reproduced from Ortiz-Duenas et al. [18].

Figure 5(b) shows the results of our 2D axisymmetric CFD code plotted against the same experimental data. While there are differences between the measured and predicted distributions (particularly near the outer wall) it can be seen that our 2D CFD simulation is close to that predicted by FLUENT, especially when using the two-equation $k-\omega$ model, with the exception that our code predicts a slightly greater loss toward the lower wall, and thus may give a more pessimistic prediction of the total loss of the duct (though it should be noted that Ortiz-Duenas et al. [18] reported that the $k-\omega$ turbulence model *underpredicted* the net end-wall loss by 0.004).

In addition to the total loss introduced by the duct, the other key duct feature that must be considered is the introduction of distortion, which, for our purposes, is considered to primarily result from flow separation. We have therefore also examined the performance of our 2D axisymmetric CFD code in predicting the static pressure profiles on the duct endwalls.

Figure 6 shows good general agreement between the inner and outer wall static pressure plots predicted by our 2D CFD and those measured by Ortiz-Duenas et al. [18].

7.3 Duct Design Endwall Separation Boundaries. Using the above described CFD model, we have simulated the flow through 121 different duct geometries on an 11×11 matrix of differing area and radial offset ratios (the latter being $\Delta R/L$: the radius change nondimensionalized by the duct length). The resulting data are then reduced and plotted as a meanline design chart. Closer examination of the data has permitted the estimation of the hub and casing separation boundaries for the axisymmetric duct, which are superimposed on these data presented in Fig. 7.

8 Re-evaluating the System Decomposition

The identification of the duct endwall separation boundaries now permits the decomposition of the compression system into its constituent parts to be re-evaluated.

Examination of meridional engine slices in the open literature

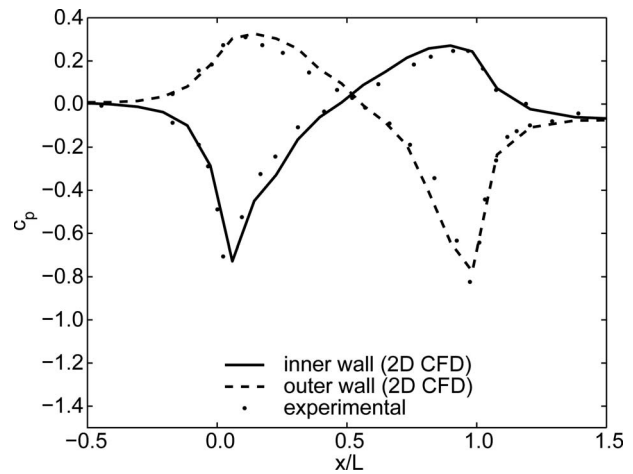


Fig. 6 Inner and outer duct wall static pressures: 2D CFD comparison with the experiment (partially reproduced from Ref. [18])

(see, for example, Ref. [19]) suggests typical intercompressor duct $\Delta R/L$ geometric values of around 0.6, and this is the value that we shall therefore use in our evaluation.

If the primary design intent of the duct is the transfer of the working fluid between compressors without separation, then the data indicate that the designer cannot specify the exit Mach number from the LPC at the value that will maximize the adiabatic efficiency of the LPC module, in this case 0.51. Figure 7 indicates that, at a $\Delta R/L$ ratio of 0.6, the maximum area ratio that can be tolerated is approximately 0.8. Therefore, neglecting the small compressibility effect, the fixed HPC inlet Mach number of 0.5 reduces the allowable exit LPC Mach number to 0.4. As can be seen from Fig. 3, this reduces the LPC redesign adiabatic efficiency potential gain by a third to 0.8 percentage points.

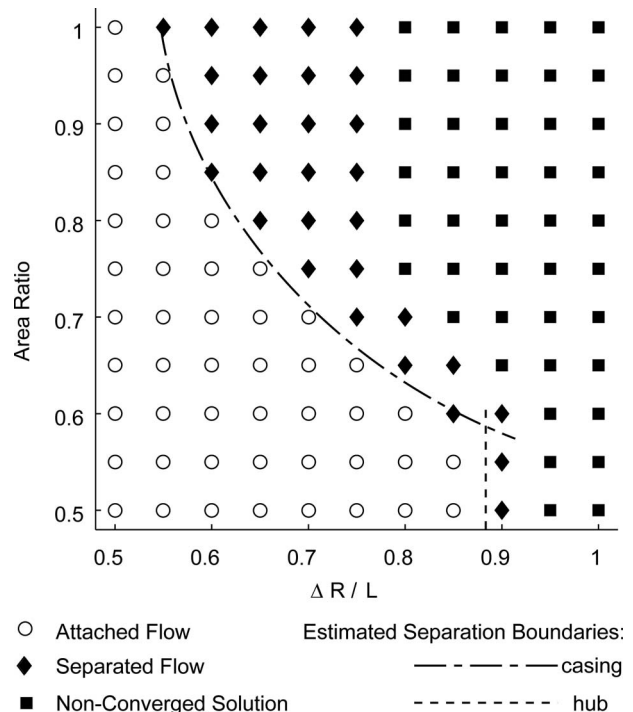


Fig. 7 Duct separation boundaries

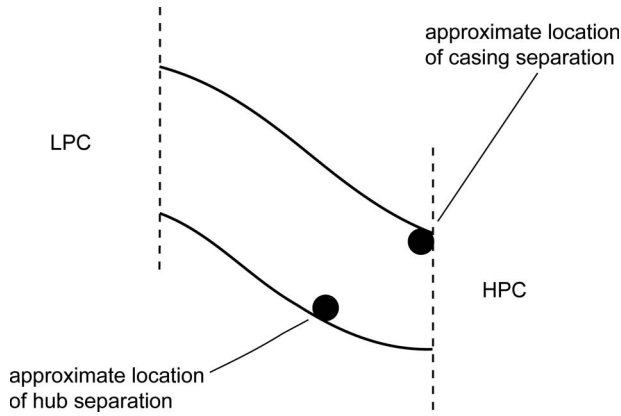


Fig. 8 Locations of duct endwall separations

One way for the designer to proceed at this point, which may be compelling, is to return to the safety of the trusted engineering rules of thumb. Another might be to improve the general separation performance of the duct.

9 Duct Endwall Profiling

As Fig. 7 indicates, the behavior of the duct is dominated by two separation mechanisms: separation from the hub and separation from the casing. The locations of the separation points, as sketched in Fig. 8, are determined by the relative surface curvature of the duct walls and by how it affects the local pressure gradient to which the boundary layer is subjected.

Our analysis of the duct to this point has assumed a constant variation of the duct cross-sectional area with the axial position. Yet, as Ghisu et al. [20] have shown, optimization by the redistribution of the area variation to give early diffusion and consequent stronger acceleration in the region where separation is more likely (due to the duct wall curvature) can significantly reduce pressure losses and the likelihood of separation, as shown in Fig. 9.

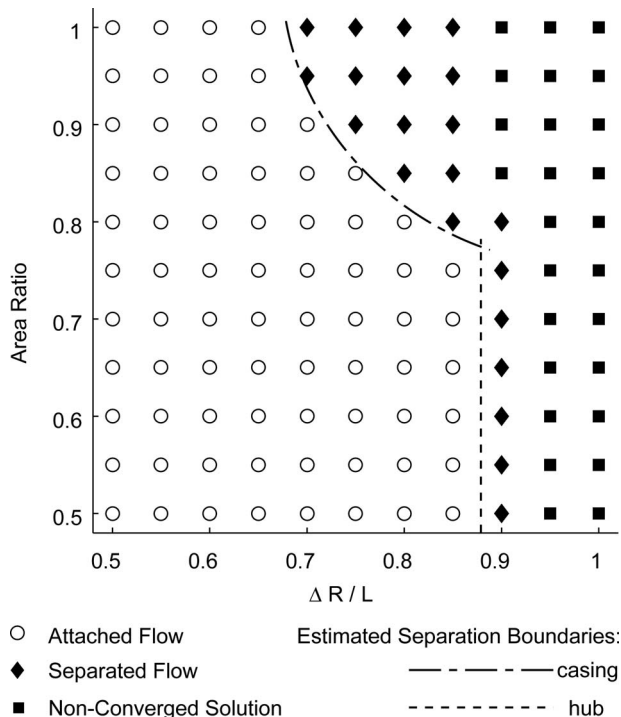


Fig. 9 Redesigned duct separation boundaries

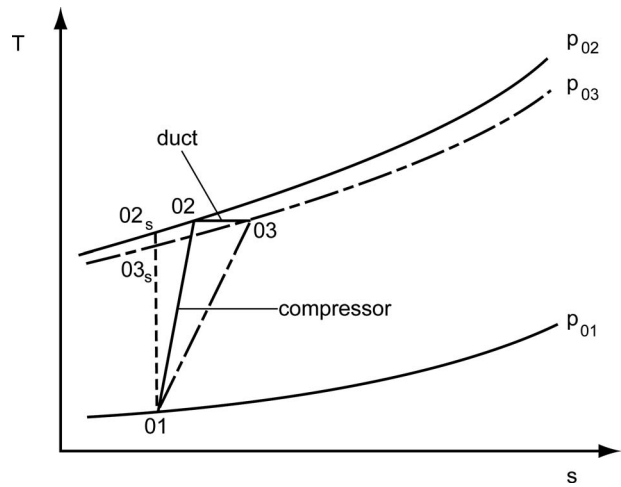


Fig. 10 T - s Diagram of the LPC/duct system

It is now possible for the designer to specify an area ratio of unity for the duct with $\Delta R/L=0.6$, and thus place the LPC at its efficiency-maximizing exit Mach number.

We recall, at this point, that the rule of thumb restriction to the duct inlet Mach number was partially intended to reduce frictional losses in the duct. We can now quantify these losses with our meanline tool.

9.1 Establishing a Unified Measurement System. One of the disincentives for the engineer challenging established rules of thumb was the lack of analysis uniformity through the main gas path. Our modeling has sought to overcome this disincentive, but even with the same modeling level to be truly effective it is necessary to quantify key performance metrics using the same measurement system. Thus, we must form a “common language” to compare directly the adiabatic efficiency of the LPC with duct stagnation pressure losses.

The T - s diagram for the LPC/duct combination is sketched in Fig. 10. The LPC raises the pressure and temperature from State 01 to State 02, with State 02s being the latter’s isentropic equivalent.

Since no work is done in the duct, it is represented by the horizontal line from State 02 to State 03 (the difference between p_{02} and p_{03} is exaggerated in the interests of clarity). The adiabatic efficiency of the LPC alone can be defined in conventional terms by considering the stagnation temperature changes, which can then be simplified by substituting the stagnation pressure ratio of the LPC, R as follows:

$$\eta_{LPC} = \frac{T_{02s} - T_{01}}{T_{02} - T_{01}} = \frac{R^{(\gamma-1)/\gamma} - 1}{T_{02}/T_{01} - 1}$$

The adiabatic efficiency of the LPC/duct combination can be defined in similar terms, into which can be substituted the above expression for the LPC adiabatic efficiency alone

$$\eta_{system} = \frac{T_{03s} - T_{01}}{T_{03} - T_{01}} = \eta_{LPC} \frac{T_{03s}/T_{01} - 1}{R^{(\gamma-1)/\gamma} - 1}$$

Noting that

$$\frac{T_{03s}}{T_{01}} = \left(\frac{p_{03}}{p_{02}} \cdot R \right)^{(\gamma-1)/\gamma}$$

and defining the duct stagnation pressure loss coefficient, ω , as the reduction in stagnation pressure from State 02 to State 03, the nondimensionalized by the exit stagnation pressure from the LPC

$$\omega = \frac{p_{02} - p_{03}}{p_{02}} \rightarrow \frac{p_{03}}{p_{02}} = 1 - \omega$$

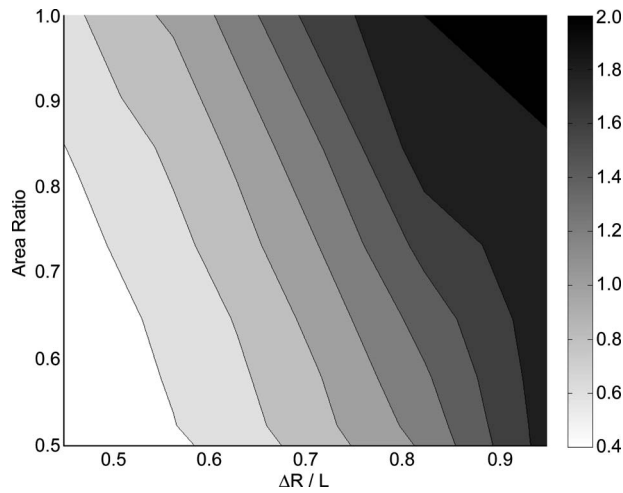


Fig. 11 Duct stagnation pressure loss (%)

We can reduce the expression for the system adiabatic efficiency to

$$\eta_{\text{system}} = \eta_{\text{LPC}} \frac{\{(1 - \omega) \cdot R\}^{(\gamma-1)/\gamma} - 1}{R^{(\gamma-1)/\gamma} - 1}$$

Inclusion of the duct loss therefore reduces the potential gain (by recasting the design process and moving from an LPC exit Mach number of 0.3 to 0.51) to 0.9 percentage point LPC adiabatic efficiency.

10 Including the Effect of Struts on Loss

As we noted above, the literature suggests that we can reasonably assume that the inclusion of eight typically slender struts will not significantly increase distortion levels in a well-designed accelerating duct. This will be particularly true in practice with a combination of good strut design and the imposition of a sufficient “safety margin” from the relevant separation boundaries. We must, however, allow for the increased loss and, as we indicated above, we will (possibly pessimistically given the acceleration level) double the losses calculated for our clean duct.

Inclusion of this doubled loss term further reduces the potential gain (by recasting the design process and moving from an LPC exit Mach number of 0.3 to 0.51) to 0.6 percentage point LPC adiabatic efficiency, i.e., half that suggested by Fig. 3.

However, to gain more insight into the *system* behavior we now plot the duct stagnation pressure loss against area ratio and $\Delta R/L$, as shown in Fig. 11.

Thus, as $\Delta R/L$ is held constant at 0.6, the stagnation pressure loss varies as a function of area ratio: the implication being a modified exchange rate curve for the LPC/duct combined module. Hence Fig. 3 can be redrawn with a new plot of the LPC/duct system adiabatic efficiency versus LPC exit Mach number, as plotted in Fig. 12.

By plotting the exchange rate curve for the LPC/duct combined module we see that the optimum LPC exit Mach number for efficiency is not that indicated by considering either the LPC or the duct in isolation. If its value of 0.42 is adopted, half of the performance gain lost by considering the strutted duct at a Mach number of 0.51 may be recovered.

The “optimum” LPC exit Mach number of 0.42 is not indicated by the engineering rules of thumb for either the duct or the LPC. The opportunity cost of following the rules of thumb in this case can be quantified by comparing, as shown in Fig. 12, the efficiency of the LPC/“strutted” duct system at a design LPC exit Mach number of 0.3 with that at 0.42: a performance deficit of 0.8 percentage point LPC adiabatic efficiency.

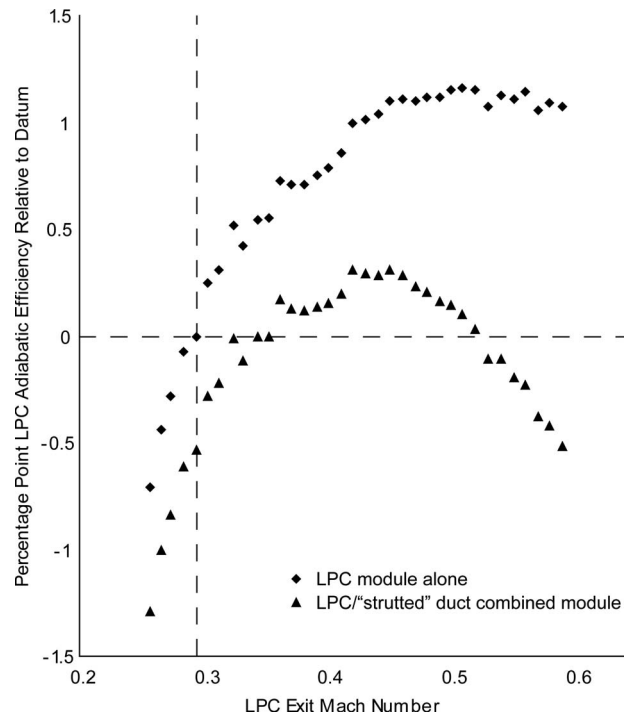


Fig. 12 Exchange rate curve for the LPC/duct combined module

11 Discussion

We have sought in this paper to quantify the potential opportunity cost of reliance on engineering experience (in the form of rules of thumb) caused by its coupling with a modular engine layout.

Our study has been necessarily limited in scope: we have considered a partial redesign of part of the main gas path in a single engineering discipline (aerothermal). Yet coupling of this nature is inherently multidimensional; in striving to set up our experiment to minimize effects on engine modules (such as the turbine) and disciplines (such as aeroelastics), which were beyond the scope of our study, we have inevitably introduced our own design-process-intrinsic constraints and thus clouded the wider system view.

The gain of nearly one percentage point equivalent LPC adiabatic efficiency was achieved without recourse to new technology, materials, flow modeling, or conventional optimization. It was achieved by simply recasting the design process in a way that converts constraints into variables. The possibility exists that there are similar gains to be had by removing comparable artificial constraints that occur in other parts of a typical aeroengine. Some may take the form of physical constraints at the interfaces between other engine modules; others may exist within modules in the form of methodological and analysis constraints at the interfaces between different engineering specialisms.

The disincentives to challenging tried-and-tested engineering rules of thumb are as likely to be seen here as in our own study. A similar strategy may prove useful in identifying and reducing performance lost due to constraints that are not physical, merely artifacts of the design process.

The strategy may be summarized as follows:

- Closely examine the interfaces between modules and disciplines, particularly where there is an “easy fit” with standard engineering rules of thumb.
- Recast the design problem to convert constraints to variables.
- Establish a common frame of reference and system of measurement (of known accuracy) across the interface.

- (d) Thus develop effective performance exchange rate curves for the system.

12 Conclusions

The turbomachinery aerodynamic design process is characterized by its complexity and the continued reliance on designer experience for success. Complexity has encouraged a modular approach to the design, which has undoubted advantages for producing large engine families.

Designer experience, in the form of knowledge, rules of thumb, and correlation-based methods, continues to play a significant role in preliminary design, where the interfaces between these modules are set, and thus much of the eventual performance of the machine is locked-in.

By recasting the core engine compression system design problem with the LPC and duct as one rather than two modules, and redesigning the LPC/duct combination by considering the Mach number at their interface as a designer variable rather than as a constraint, we have shown that nearly one percentage point of the adiabatic efficiency can be gained while preserving the fundamental benefits of a modular layout by leaving the HPC unchanged.

Our hope is that the re-evaluation of the design process in this way encourages the critical examination of standard engineering rules of thumb, which, while continuing to be a vital tool, can place artificial constraints on the design and introduce a measurable performance deficit.

Acknowledgment

We thank Rolls-Royce plc. for their support.

Nomenclature

c_p	= static pressure coefficient
γ	= ratio of specific heats
η_{LPC}	= LPC adiabatic efficiency
η_{system}	= LPC/duct combined module adiabatic efficiency
HPC	= high pressure compressor
L	= length of the intercompressor duct
LPC	= low pressure compressor
ν	= kinematic viscosity
p_0	= stagnation pressure
R	= LPC stagnation pressure rise ratio
ΔR	= radial offset of the intercompressor duct
ρ	= density
T	= temperature
τ_w	= wall friction

$$u^* = (\tau_w / \rho)^{0.5}$$

Y_p = stagnation pressure coefficient

y = distance from the wall

$$y^+ = u^* y / \nu$$

ω = duct stagnation pressure loss coefficient

References

- [1] Cumpsty, N. A., and Greitzer, E. M., 2004, "Ideas and Methods of Turbomachinery Analysis: A Historical View," *J. Propul. Power*, **20**(1), pp. 15–26.
- [2] Sobieszanski-Sobieski, J., 1990, "Sensitivity Analysis and Multidisciplinary Optimization for Aircraft Design: Recent Advances and Results," *J. Aircr.*, **27**(12), pp. 993–1000.
- [3] Gallimore, S., 1998, "Axial Flow Compressor Design," *The Successful Exploitation of CFD in Turbomachinery*, IMechE, London, UK.
- [4] Wisler, D. C., 1998, "The Technical and Economic Relevance of Understanding Blade Row Interaction Effects in Turbomachinery," *Blade Row Interference Effects in Axial Turbomachinery Stages* (Lecture Series 1998-02), von Karman Institute For Fluid Dynamics.
- [5] Walsh, P. P., and Fletcher, P., 2004, *Gas Turbine Performance*, Blackwell Science, Oxford, UK.
- [6] Norris, G., Dominy, R. G., and Smith A. D., 1998, "Strut Influences Within a Diffusing Annular S-Shaped Duct," ASME Paper No. 98-GT-425.
- [7] Wallin, F., and Eriksson L.-E., 2006, "Response Surface-Based Transition Duct Shape Optimization," ASME Paper No. GT2006-90978.
- [8] Bailey, D. W., Britchford, K. M., Carotte, J. F., and Stevens, S. J., 1997, "Performance Assessment of an Annular S-Shaped Duct," *ASME J. Turbomach.*, **119**(1), pp. 149–156.
- [9] Cumpsty, N. A., 1989, *Compressor Aerodynamics*, Longmans, Harlow, UK.
- [10] Jarrett, J. P., Dawes, W. N., and Clarkson, P. J., 2007, "An Approach to Integrated Turbomachinery Design," *ASME J. Turbomach.*, **129**(3), pp. 488–494.
- [11] Howell, A. R., and Calvert, W. J., 1978, "A New Stage Stacking Technique For Axial-Flow Compressor Performance Prediction," *ASME J. Eng. Power*, **100**(4), pp. 698–703.
- [12] Miller, D. C., and Wasdell, D. L., 1987, "Off-Design Prediction of Compressor Blade Losses," *Proceedings of the IMechE: Turbomachinery—Efficiency Prediction and Improvement*, IMechE, London, UK, Paper No. C279/87.
- [13] Wright, P. I., and Miller, D. C., 1991, "An Improved Compressor Performance Prediction Model," *Proceedings of the IMechE: Turbomachinery: Latest Developments in a Changing Scene*, IMechE, Bury St. Edmunds, UK, Paper No. C423/028.
- [14] Lomax, H., Pulliam, T. H., and Zingg, D. W., 2001, *Fundamentals of Computational Fluid Dynamics*, Springer, New York.
- [15] Harlow, F. H., and Welsh, J. E., 1965, "Numerical Calculation of Time Dependent Viscous Incompressible Flow of Fluid With Free Surface," *Phys. Fluids*, **8**, pp. 2182–2197.
- [16] Patankar S. V., 1980, *Numerical Heat Transfer and Fluid Flow*, Taylor & Francis, New York.
- [17] Tannehill, J. C., Anderson, D. A., and Pletcher, R. H., 1997, *Computational Fluid Mechanics and Heat Transfer*, Taylor & Francis, New York.
- [18] Ortiz-Duenas, C., Miller, R. J., Hodson, H. P., and Longley, J. P., 2007, "Effect of Length on Compressor Inter-Stage Duct Performance," ASME Paper No. GT2007-27752.
- [19] Cumpsty, N. A., 1997, *Jet Propulsion*, Cambridge University Press, Cambridge, UK.
- [20] Ghisu, T., Molinari, M., Parks, G. T., Dawes, W. N., Jarrett, J. P., and Clarkson, P. J., 2007, "Axial Compressor Intermediate Duct Design and Optimization," *Proceedings of the Third AIAA MDO Specialist Conference*, Honolulu.

On the Role of the Deterministic and Circumferential Stresses in Throughflow Calculations

J.-F. Simon

Techspace Aero,
Safran Group,
Route de Liers 121,
B-4041 Milmort, Belgium
e-mail: jsimon@techspace-aero.be

J. P. Thomas

FNRS Research Fellow
e-mail: jp.thomas@ulg.ac.be

O. Léonard

e-mail: o.leonard@ulg.ac.be

Turbomachinery Group,
University of Liège,
Chemin des Chevreuils 1,
B-4000 Liège, Belgium

This paper presents a throughflow analysis tool developed in the context of the average-passage flow model elaborated by Adamczyk. The Adamczyk's flow model describes the 3D time-averaged flow field within a blade row passage. The set of equations that governs this flow field is obtained by performing a Reynolds averaging, a time averaging, and a passage-to-passage averaging on the Navier–Stokes equations. The throughflow level of approximation is obtained by performing an additional circumferential averaging on the 3D average-passage flow. The resulting set of equations is similar to the 2D axisymmetric Navier–Stokes equations, but additional terms resulting from the averages show up: blade forces, blade blockage factor, Reynolds stresses, deterministic stresses, passage-to-passage stresses, and circumferential stresses. This set of equations represents the ultimate throughflow model provided that all stresses and blade forces can be modeled. The relative importance of these additional terms is studied in the present contribution. The stresses and the blade forces are determined from 3D steady and unsteady databases (a low-speed compressor stage and a transonic turbine stage) and incorporated in a throughflow model based on the axisymmetric Navier–Stokes equations. A good agreement between the throughflow solution and the averaged 3D results is obtained. These results are also compared to those obtained with a more “classical” throughflow approach based on a Navier–Stokes formulation for the endwall losses, correlations for profile losses, and a simple radial mixing model assuming turbulent diffusion.
[DOI: 10.1115/1.2992514]

Keywords: throughflow model, deterministic stresses, circumferential stresses

Introduction

The throughflow level of approximation still remains an important tool for designing turbomachines [1] even though 3D calculations are used more and more early in the design process. Throughflow codes are mainly used at the preliminary design stage for specifying the target aerodynamic performances to be achieved by the blading. They can be used either in the design mode, where the angular momentum and/or the total conditions are prescribed and the flow angles are sought, or in the analysis mode, where a known machine geometry is analyzed for its performance. The throughflow models are also used to exploit experimental results or to couple single blade row calculations in order to compute the flow field inside a multistage machine [2].

Unfortunately, these models rely heavily on empirical inputs, such as profile loss correlations or endwall loss models. They can accurately predict the flow field inside a turbomachine provided that the design parameters are not too far from those of the reference machines that were used to calibrate the throughflow model. This approach has shown to be efficient but lacks of generality.

The most widespread throughflow method is certainly the streamline curvature (SLC) method, which has been (and still is) very successful. In 1980, Spurr [3] has proposed another approach based on the Euler equations. This approach has only started to retain attention in the 1990. Recent works using this approach can be found in Refs. [4,5]. The methods based on the Euler equations present some interesting features and eliminate some of the draw-

backs of the streamline curvature approach, such as a shock capturing property or a natural unsteady capability with the generally adopted time-marching technique.

However, the treatment of the annulus endwalls is probably the major concern for the throughflow models based on the SLC method as well as the ones based on the Euler equations. A common practice is to introduce an aerodynamic blockage—equivalent to the displacement thickness of the endwall boundary layers—which corrects the mass flow in order to obtain the correct level of velocity in the core flow. The blockage factor is a very sensitive quantity relying on empiricism for which a misprediction can lead to a mismatch of the stages. Another solution is to perform a separate boundary layer calculation. However, it is recognized that the use of the boundary layer theory for computing the endwall flows inside a turbomachine (especially in a compressor) is inappropriate [6,7].

Recently another solution has been proposed by the authors with a throughflow model directly based on the Navier–Stokes equations. It is able to resolve the viscous flow on the annulus endwalls and the corresponding aerodynamic blockage. It can also capture 2D recirculations. The θ -averaged Navier–Stokes equations are solved by a finite volume technique. By including more physics in the model, less empiricism is needed and a more general method can be devised. Details of this model, as well as the numerical techniques used, can be found in Refs. [8,9].

In the present contribution, the authors propose another step toward less empiricism in throughflow calculations with a high-order throughflow method. This model is based on the Adamczyk cascade of averaging procedure [10].

Adamczyk addressed the 3D unsteady and turbulent flow field via several averaging operations. The first one is the well known Reynolds averaging, which eliminates the effects of the turbulence, leaving a deterministic unsteady flow. The second one is a time averaging removing the remaining effects of the unsteadiness

Contributed by the International Gas Turbine Institute of ASME for publication in the JOURNAL OF TURBOMACHINERY. Manuscript received June 30, 2008; final manuscript received July 30, 2008; published online April 20, 2009. Review conducted by David Wisler. Paper presented at the ASME Turbo Expo 2008: Land, Sea, and Air (GT2008), Berlin, Germany, June 9–13, 2008.

due to the movement of the rotor blades with respect to the stator ones. Finally an aperiodic averaging eliminates the aperiodicity of the flow due to the blade indexing. The resulting flow field is steady and periodic but it incorporates the mean effects of the turbulence, the unsteadiness and the aperiodicity. The equations associated with this flow show different unknown terms bringing the aforementioned effects. These terms are the Reynolds stresses, the deterministic stresses, the passage-to-passage stresses, and the blade forces. These equations, which have been rigorously obtained, are the so-called average-passage equations and describe the steady flow field inside a blade row embedded in a multistage environment.

In this contribution a subsequent step is performed by circumferentially averaging the average-passage equations in order to obtain an axisymmetric representation of the flow. These equations are rigorously obtained and contain the effects of the non-axisymmetry of the flow through circumferential stresses and blade forces. This set of equations represents the ultimate throughflow model. The sole assumptions are those prevailing to the establishment of the Navier–Stokes equations. However, these throughflow equations present several unknown terms, which have to be modeled or closed. This tremendous task is far beyond the scope of this paper. In the present contribution, the relative importance of the different terms of such a throughflow calculation is studied as well as the benefit brought by this model compared to more classical throughflow models.

These analyses are performed with the help of 2D and 3D test-cases. The development of a boundary layer over a flat plate and the spreading of a wake allow us to highlight the main properties of the averaged equations and to perform a first attempt to evaluate the relative importance of the different unknowns brought by the averaging process. The high-order throughflow model is also applied to two turbomachine test-cases, a low-speed compressor stage and a transonic turbine stage. These test-cases reside in 3D steady and unsteady numerical simulations from which the different terms needed for the closure of the throughflow equations are extracted. They allow to further study the high-order throughflow model and to show the improvements compared to a classical throughflow.

Circumferential-Averaged Equations

The average-passage set of equations of Adamczyk is obtained by successively averaging the unsteady Navier–Stokes equations on an ensemble of realizations—in the sense of Reynolds—on time and on the passages of a given blade row. This triple averaging procedure brings the mean effects of the turbulence, the unsteadiness and the aperiodicity on the steady flow field inside a blade row embedded in a multistage configuration. These effects appear as additional terms in the conservation equations, namely, Reynolds stresses, deterministic stresses, passage-to-passage stresses, blade blockage factors, and blade forces. For example, for a given stator j embedded in a multistage machine, the resulting axial momentum equation is written as follows:

$$\begin{aligned} & \frac{1}{b_j} \frac{\partial b_j (\bar{\rho} \bar{V}_x \bar{V}_x + \bar{p})}{\partial x} + \frac{1}{rb_j} \frac{\partial b_j (\bar{\rho} \bar{V}_r \bar{V}_x)}{\partial r} + \frac{1}{rb_j} \frac{\partial b_j (\bar{\rho} \bar{V}_\theta \bar{V}_x)}{\partial \theta} \\ & = \frac{1}{b_j} \frac{\partial b_j (\bar{\tau}_{xx} - \bar{\rho} V'_x V'_x - \bar{\rho} V''_x V''_x - \bar{\rho} V'''_x V'''_x)}{\partial x} \\ & + \frac{1}{rb_j} \frac{\partial b_j (\bar{\tau}_{rx} - \bar{\rho} V'_r V'_x - \bar{\rho} V''_r V''_x - \bar{\rho} V'''_r V'''_x)}{\partial r} \\ & + \frac{1}{rb_j} \frac{\partial b_j (\bar{\tau}_{\theta x} - \bar{\rho} V'_\theta V'_x - \bar{\rho} V''_\theta V''_x - \bar{\rho} V'''_\theta V'''_x)}{\partial \theta} \\ & + \bar{f}_{bx}^R + \bar{f}_{vx}^R + \bar{f}_{bx}^{Sj} + \bar{f}_{vx}^{Sj} \end{aligned} \quad (1)$$

where $\bar{\rho} V'_i V'_j$ are the Reynolds stresses (which have been time and passage-to-passage averaged), $\bar{\rho} V''_i V''_j$ are the deterministic stresses

(which have been passage-to-passage averaged), and $\bar{\rho} V'''_i V'''_j$ are the aperiodic stresses. The inviscid and viscous blade forces \bar{f}_{bx}^R and \bar{f}_{vx}^R originate from the rotors while the inviscid and viscous blade forces \bar{f}_{bx}^{Sj} and \bar{f}_{vx}^{Sj} are due to the stators other than the one under consideration. b_j is the blade blockage factor. It is due to the blade thickness of all the blade rows except the one under consideration.

To simplify the notations, only one averaging symbol is used for the averaged quantities, e.g., \bar{p} is used instead of $\overline{\overline{p}}$. For rigorous notations and details on the average-passage set of equations, see [10]. A great introduction to the flow physics linked to the average-passage equations can be found in Ref. [11] together with the results from several simulations performed on both high- and low-speed compressors and turbines.

As it is the throughflow level of approximation that is of interest here, an additional (circumferential) averaging operation is performed on the average-passage system of equations. Here again, this procedure brings additional terms in the set of equations. The circumferential average can be defined with the help of a gate function in the same way as the time average defined by Adamczyk [10].

The circumferential average performed on the average-passage flow field of the j th blade row is defined as follows:

$$\bar{f} = \frac{\frac{1}{\Delta\theta} \int_0^{\Delta\theta} F(x, r, \theta) f(x, r, \theta) d\theta}{\frac{1}{\Delta\theta} \int_0^{\Delta\theta} F(x, r, \theta) d\theta} \quad (2)$$

$\Delta\theta$ is equal to the pitch of the blade row under consideration, i.e., $2\pi/N$ where N is the blade count. F is a gate function. Its value is unity when the point located at (x, r, θ) lies inside the flow field. It is equal to zero when the point lies inside the blade. The integral of the gate function over the pitch is equal to the blade blockage factor b as follows:

$$b = \frac{1}{\Delta\theta} \int_0^{\Delta\theta} F(x, r, \theta) d\theta \quad (3)$$

The flow field is next decomposed in an axisymmetric part and in a circumferential fluctuation part as follows:

$$f(x, r, \theta, t) = \bar{f}(x, r, \theta) + f''''(x, r, \theta, t) \quad (4)$$

The Favre average is used for the velocities and the total flow properties. The rule for averaging the partial derivative is the following:

$$\overline{\frac{\partial f}{\partial x_i}} = \frac{1}{b} \frac{\partial \bar{f}}{\partial x_i} - \frac{N}{2\pi b} \left(f_1 \frac{\partial \theta_1}{\partial x_i} - f_2 \frac{\partial \theta_2}{\partial x_i} \right) \quad (5)$$

with

$$f_1 = f(x, r, \theta = \theta_1) \quad \text{and} \quad f_2 = f(x, r, \theta = \theta_2) \quad (6)$$

where θ_1 and θ_2 are the locations of the blade sides in their order of appearance when rotating in the θ direction. They are measured with respect to the blade mean line. The additional term in the right-hand side of Eq. (5) is only nonzero for quantities that are not equal to zero on the blade walls, i.e., the pressure, the viscous shear stress, or the heat flux. This term is responsible for the inviscid and viscous blade forces.

As an example, the resulting axial momentum equation is given hereafter; all details of the derivation can be found in Ref. [12].

$$\begin{aligned}
& \frac{1}{b} \frac{\partial b(\bar{\rho} \tilde{V}_x \tilde{V}_x + \bar{p})}{\partial x} + \frac{1}{rb} \frac{\partial rb(\bar{\rho} \tilde{V}_r \tilde{V}_r)}{\partial r} \\
&= \frac{1}{b} \frac{\partial b(\overline{\tau_{xx}} - \overline{\rho V'_x V'_x} - \overline{\rho V''_x V''_x} - \overline{\rho V'''_x V'''_x} - \overline{\rho V''''_x V''''_x})}{\partial x} \\
&+ \frac{1}{rb} \frac{\partial rb(\overline{\tau_{rx}} - \overline{\rho V'_r V'_x} - \overline{\rho V''_r V''_x} - \overline{\rho V'''_r V'''_x} - \overline{\rho V''''_r V''''_x})}{\partial r} + \overline{f_{bx}^R} \\
&+ \overline{f_{ux}^R} + \overline{f_{bx}^j} + \overline{f_{vx}^j} + \overline{f_{bx}^j} + \overline{f_{vx}^j} \quad (7)
\end{aligned}$$

Compared to the average-passage equation (1) the θ -derivatives disappear but additional terms appear as follows.

- The term $\overline{\rho V''''_i V''''_j}$ is the circumferential stress. It represents the transport of momentum between the 3D periodic and the axisymmetric flow fields.
- The blockage factor b is due to the geometrical blockage resulting from the blades' thickness.
- The momentum equations contain the blade forces f_b^j and f_v^j . These terms are due to the pressure field and the shear stresses acting on the wall surfaces of the blade row j .

The obtained set of equations has been rigorously established from the 3D instantaneous Navier–Stokes equations and represents the ultimate throughflow model. The equations are expressed in terms of the averaged conservative variables. Additionally to these primary unknowns, a large number of other unknown terms appear, which have to be modeled in order to solve the throughflow problem. For example, for the momentum equations, the additional terms are the averaged viscous (laminar) stresses, the Reynolds stresses, the deterministic stresses, the passage-to-passage stresses, and the circumferential stresses, the inviscid and the viscous blade forces.

If all these terms could be modeled adequately, one would obtain a perfect throughflow model able to predict the mean steady axisymmetric effect of the wake chopping phenomenon, the effect of the radial mixing, or the mean effect of the blade clocking. Establishing a closure for that model is far beyond the scope of this work. In the present contribution, the focus will rather be put on the study of the system of equations, which present certain peculiarities. Answers to the two following questions will also be sought.

1. What are the relative importance of the different terms and, from there, the terms that are worth to be modeled?
2. What is the benefit of such a model compared to a classical throughflow model?

In 1966 Smith [13] addressed the first objective, with an analysis of the relative importance of the different terms present in the radial equilibrium equation. However, due not only to the unavailability of 3D Navier–Stokes simulations at that time but also to the less powerful throughflow model used (radial equilibrium versus 3D Navier–Stokes circumferentially averaged), several assumptions were made in his analysis. Noteworthy are a linear evolution of the quantities with θ between the pressure and suction sides and a basically inviscid formulation (with, however, an addition of a friction force). Smith's conclusion concerning the circumferential stresses was that they were negligible although he recognized they could be important for machines with higher loading. Not only with nowadays' tools, but also with more modern compressors and turbines, it is worthwhile analyzing again this problem.

The two objectives described above will be achieved here with the help of 3D steady and unsteady simulations, from which the different contributions to the momentum and energy equations will be extracted to feed a throughflow model. These studies on real turbomachine test-cases will be presented in a later section, after a preliminary study on simple 2D test-cases modeled by a

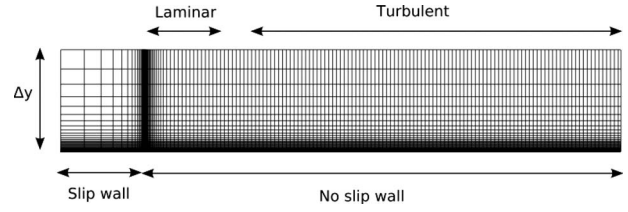


Fig. 1 Flat plate definition and mesh

1D set of averaged equations. In the following, the Reynolds stresses will be modeled by an algebraic turbulence model and the passage-to-passage closure will not be addressed, as single-stage test-cases are considered.

One-Dimensional Studies

The purpose of this section is to present a preliminary study of the different contributions arising from the circumferential averaging process as well as to establish a hierarchy of these contributions. The study will therefore focus on the circumferential closure only; the deterministic stresses or the other terms arising from the time-averaging procedure will not be considered here.

It seems obvious that the inviscid blade force will take a great importance in the momentum and energy balances. However, the relative importance of the circumferential and viscous stresses is less clear. To help evaluating this relative importance, two simple numerical experiments are presented. These experiments consist in averaging a 2D flow and its associated equations, obtaining a 1D set of equations representative of the mean 2D flow.

The 2D Navier–Stokes equations are averaged in the y direction, which is orthogonal to the mean flow. The area-averaging and the Favre-averaging operators of a quantity f are defined as

$$\bar{f} = \frac{1}{\Delta y} \int_0^{\Delta y} f dy, \quad \tilde{f} = \frac{1}{\Delta y \bar{\rho}} \int_0^{\Delta y} \rho f dy \quad (8)$$

where Δy is the height of the computational domain. The fluctuating parts of the quantity f are defined as

$$f = \tilde{f} + f', \quad f = \bar{f} + f'' \quad (9)$$

The rules for averaging the x - and y -derivatives are

$$\frac{\partial f}{\partial x} = \frac{\partial \tilde{f}}{\partial x}, \quad \frac{\partial f}{\partial y} = \frac{1}{\Delta y} (f(\Delta y) - f(0)) = \frac{1}{\Delta y} [f]_0^{\Delta y} \quad (10)$$

Development of a Boundary Layer Over a Flat Plate. The development of a boundary layer over a flat plate is presented. The computational domain is reproduced in Fig. 1. Applying the averaging operator defined above to the 2D equations of conservation and to the flat plate problem gives the following set of equations for mass, momentum, and energy balances:

$$\frac{\partial \bar{\rho} \tilde{V}_x}{\partial x} = 0 \quad (11)$$

$$\frac{\partial (\bar{\rho} \tilde{V}_x \tilde{V}_x + \bar{p})}{\partial x} + \frac{\partial \overline{\rho V'_x V'_x}}{\partial x} = \frac{\partial \overline{\tau_{xx}}}{\partial x} + \frac{1}{\Delta y} \tau_{xy}(0) \quad (12)$$

$$\frac{\partial \bar{\rho} \tilde{V}_x \tilde{V}_y}{\partial x} + \frac{\partial \overline{\rho V'_x V'_y}}{\partial x} = \frac{\partial \overline{\tau_{xy}}}{\partial x} + \frac{1}{\Delta y} \tau_{yy}(0) - \frac{1}{\Delta y} [p]_0^{\Delta y} \quad (13)$$

$$\frac{\partial \bar{\rho} \tilde{V}_x \tilde{H}}{\partial x} + \frac{\partial \overline{\rho V'_x H'}}{\partial x} = \frac{\partial (\overline{\tau_{xx} V_x} + \overline{\tau_{xy} V_y} - \overline{q_x})}{\partial x} \quad (14)$$

where

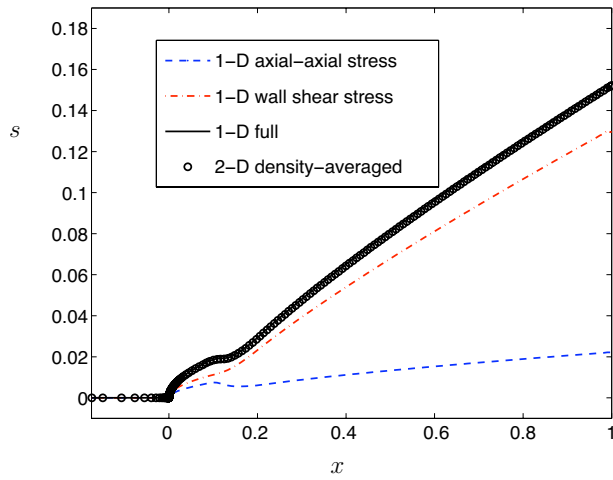


Fig. 2 Impact of the additional terms on entropy along the flat plate

$$\tilde{H} = \tilde{h} + \frac{1}{2}\tilde{V}\tilde{V} + \frac{1}{2}k, \quad k = \frac{1}{\bar{\rho}}(\overline{\rho V'_x V'_x} + \overline{\rho V'_y V'_y}) \quad (15)$$

This system of equations is solved on a 1D mesh. Its unknowns are the averaged conservative variables $\bar{\rho}$, $\bar{\rho}\tilde{V}_x$, $\bar{\rho}\tilde{V}_y$, and $\bar{\rho}\tilde{H}$. Similarly to the circumferentially averaged 3D Navier–Stokes equations, additional terms appear in the momentum and in the energy equations. They can be cast in the following:

- wall stresses: $(1/\Delta y)\tau_{yy}(0)$, $(1/\Delta y)\tau_{xy}(0)$, and $1/\Delta y[p]_0^{\Delta y}$; however, these terms will be reduced to the shear stress at the wall $\tau_{xy}(0)$ since $\tau_{yy}(0)$ is negligible with respect to the shear stress $\tau_{xy}(0)$ and since the static pressure is nearly uniform in the direction perpendicular to the mean flow
- velocity-velocity stresses $\overline{\rho V'_x V'_y}$ and $\overline{\rho V'_x V'_x}$
- velocity-enthalpy stress $\overline{\rho V'_x H'}$

These contributions can be computed from the 2D flow field and included in the 1D solver, as well as the averaged viscous stresses $\overline{\tau_{xy}}$ and $\overline{\tau_{xx}}$ and the viscous contribution to the energy equation $\overline{\tau_{xx}V_x} + \overline{\tau_{xy}V_y} - q_x$.

By switching on or off individually the terms computed from the 2D flow field, their individual impact on the 1D averaged flow field can be evaluated and the predominant terms can be determined. These dominant terms are the axial-axial spatial correlation $\overline{\rho V'_x V'_x}$ and the viscous shear stress at wall $(1/\Delta y)\tau_{xy}(0)$.

The effect of these two terms on the entropy is illustrated in Fig. 2. The wall shear stress takes the greatest importance and it is the sole viscous term that is worth to be modeled in order to close the system of equations. For a separated boundary layer, the conclusion concerning the relative importance of the axial-axial spatial stress and the viscous shear stress at the wall would be inverted as the former would predominate the momentum balance. This will be illustrated on a stator corner stall in the section dedicated to the compressor test-case.

The specific entropy is an intensive quantity that defines a property per unit of mass. Therefore, a meaningful entropy average is the mass-average (\bar{s}^m). However, the set of equations used here, as the one defined by Adamczyk, is based on a density-average. The entropy that is obtained is therefore a density-averaged quantity (\bar{s}). In Ref. [14], a relation between the density time-averaged entropy and the mass time-averaged entropy is given. Applied to the circumferential averaging, it gives the following relation between both average definitions:

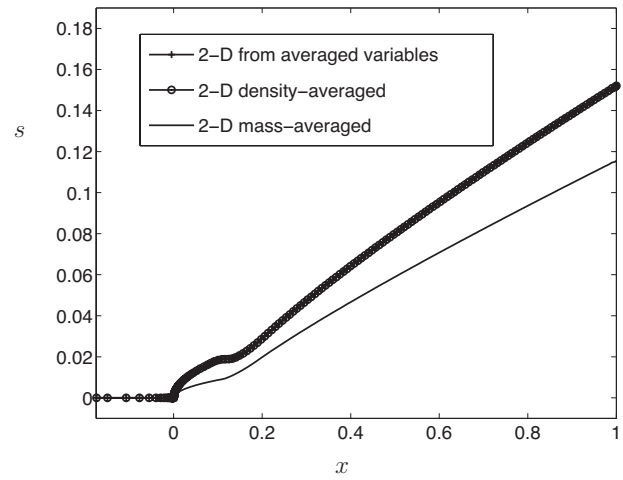


Fig. 3 Mass-averaged versus density-averaged entropy

$$\bar{s}^m = \bar{s} + \frac{\overline{V'_x s'}}{\bar{V}_x} \quad (16)$$

As shown in Fig. 3 the difference between both definitions is far to be negligible.

The density-averaged entropy has been computed with the Gibbs equation directly applied to the averaged variables, although the rigorous and correct way to obtain the entropy is to apply the average operator to the Gibbs equation. It is shown in Ref. [12] that for this test-case, characterized by a low level of the fluctuation, the difference between the two approaches is negligible, as shown in Fig. 3.

Wake Mixing. The second test-case is a wake mixing due to the viscosity. The flow domain is a rectangle. The wake is injected as a deficit of total pressure through the left boundary and travels to the right (Fig. 4). The deficit of the total pressure follows a cosine law and corresponds to a deficit of half of the velocity at the inlet of the domain. Periodic boundary conditions are imposed on the top and on the bottom boundaries. The mesh is uniform in both directions.

Applying the averaging procedure to the 2D Navier–Stokes equations for this periodic wake mixing problem gives the following momentum equations:

$$\frac{\partial(\bar{\rho}\tilde{V}_x\tilde{V}_x + \bar{p})}{\partial x} + \frac{\partial\overline{\rho V'_x V'_x}}{\partial x} = \frac{\partial\overline{\tau_{xx}}}{\partial x} \quad (17)$$

$$\frac{\partial\bar{\rho}\tilde{V}_x\tilde{V}_y}{\partial x} + \frac{\partial\overline{\rho V'_x V'_y}}{\partial x} = \frac{\partial\overline{\tau_{xy}}}{\partial x} \quad (18)$$

The mass and energy balances are identical to Eqs. (11) and (14). Studying the evolution of the entropy is again the main issue. An equation for the entropy evolution is obtained by mul-

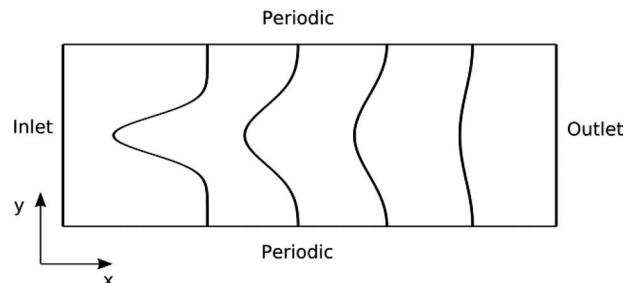


Fig. 4 Wake mixing problem

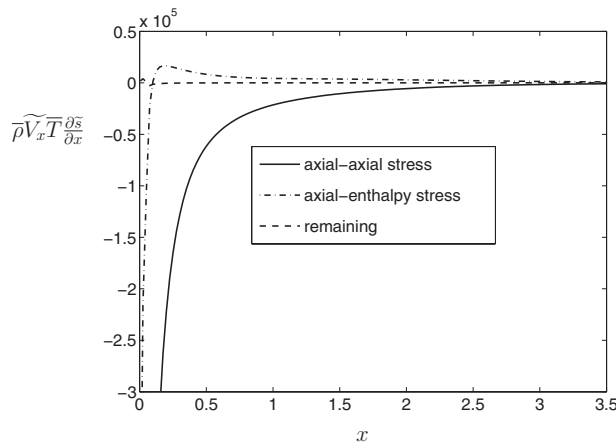


Fig. 5 Contributions to entropy production in the wake

tipling the momentum balance, by the velocity field, subtracting with the energy balance, and introducing the Gibbs equation. The following equation is obtained:

$$\overline{\rho V_x T} \frac{\partial \tilde{s}}{\partial x} = - \frac{\partial \overline{\rho V_x' H'}}{\partial x} - \overline{\rho V_x} \frac{1}{2} \frac{\partial k}{\partial x} + \frac{\partial \overline{\rho V_x' V_x'}}{\partial x} \tilde{V}_x + \frac{\partial \overline{\rho V_x' V_y'}}{\partial x} \tilde{V}_y + \frac{\partial \overline{\tau_{xx} V_x'}}{\partial x} + \frac{\partial \overline{\tau_{xy} V_y'}}{\partial x} + \frac{\partial \overline{V_x}}{\partial x} + \frac{\partial \overline{V_y}}{\partial x} - \frac{\partial \overline{q_x}}{\partial x} \quad (19)$$

Compared to the equation describing the entropy production in a nonaveraged flow, additional terms show up, namely, the spatial stresses. Figure 5 summarizes the different contributions to the entropy production: The major contributions are those of the axial-axial stress due to $\overline{\rho V_x' V_x'}$ and of the axial-enthalpy stress due to $\overline{\rho V_x' H'}$. The remaining terms, including all mean viscous shear stresses, exert no influence on the 1D evolution of entropy in a wake mixing.

The evolution of the entropy is given in Fig. 6. The density-averaged entropy exhibits a very unconventional evolution as it continuously decreases from the inlet to the outlet of the domain. Looking at Eq. (19) and retaining only the main contribution, i.e., $\overline{\rho V_x' V_x'}$, it is clear that the density-averaged entropy can only decrease in the main direction of propagation of a wake, i.e., the x direction. Indeed, due to the homogenization of the wake flow, V_x' decreases in this direction.

For this test-case, the error made by applying the Gibbs relation directly to the averaged variables is also weak as shown in Fig. 6.

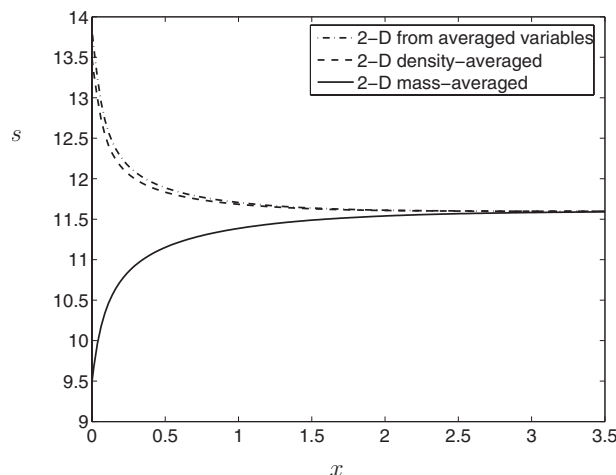


Fig. 6 Entropy evolution in the wake

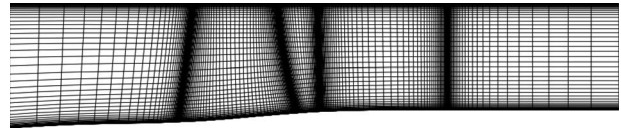


Fig. 7 Meridional mesh of the CME2 compressor

Concluding Remarks on the 1D Test-Cases. From the two test-cases presented above, the following conclusions and remarks can be made.

1. The prioritization of the different contributions to the averaged conservation equations has shown that among all viscous terms, the wall shear stress seems to be the sole viscous contribution to be important. The stresses due to the fluctuations are also important. In the case of a blade passage, some additional circumferential stresses will be generated due to the turning of the flow.
2. The error due to the application of the Gibbs equation directly to the averaged variables instead of the averaged form of the Gibbs equation seems to be weak.
3. The difference observed between the mass-averaged and the density-averaged entropy increases with the nonuniformity of the flow. Extrapolated to the circumferential-average and to a turbomachine configuration, it means that sufficiently far from the inlet and the outlet of a blade row, in the regions where the flow is circumferentially uniform (or close to), the two averages coincide (see Fig. 6). The global performances or radial surveys that would be obtained at the outlet of a machine with a density-average-based computation would thus be correct. Another solution would be to devise a mass-averaged throughflow model. Such an approach has been studied by a few authors (see Ref. [15] for example).
4. Continuing on the subject of the difference between mass and the density-averages, Bardoux [14] has also observed the particular behavior of the density-based average in the frame of 3D steady simulations including the effect of the unsteady deterministic flow, i.e., for the time-average. The effect is, however, expected to be much more important in the circumferential-average problem since the kinetic energy of the circumferential fluctuations can represent a great part of the total kinetic energy. For example, in a recirculation zone, where the averaged velocity reaches zero, the fluctuations represent 30% of the maximum kinetic energy found in the complete flow field. This is in strong contrast with the turbulent kinetic energy or the deterministic kinetic energy and explains why the nature of the averaging is more critical in a throughflow problem.

Low-Speed Compressor Stage

The CME2 is a single-stage low-speed compressor. Its global performances can be summarized as follows: mass flow 11 kg/s, pressure ratio 1.14, efficiency 0.92, and rotational speed 6300 rpm. A meridional view of the flow path and of the mesh used for the throughflow calculations is shown in Fig. 7. A 3D simulation has been performed by Gourdain et al. [16] with the numerical code ELSA developed by ONERA. The turbulent viscosity is computed using the model of Spalart-Allmaras. Wall functions have been used. The 3D mesh is composed of approximately 1×10^6 grid points. The simulation has been run for the nominal conditions. A comparison of the results of the simulation and the experimental measurements is presented in Ref. [16]. The agreement is good.

Throughflow Computation With Additional Terms. In the previous section it was shown for an averaged 2D flow that the sole viscous shear stresses that play a significant role in the momentum and energy balances are the viscous shear stresses at the

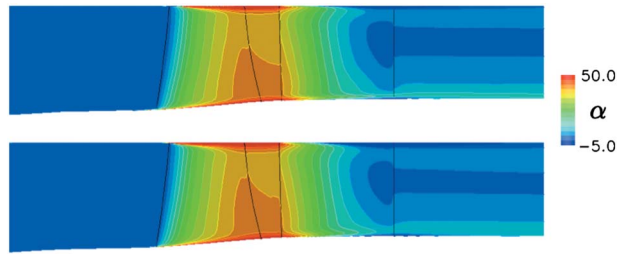


Fig. 8 Absolute flow angle from 3D averaged solution (top) and throughflow solution (bottom)

wall, i.e., the viscous blade forces. Transposed to a circumferentially averaged 3D flow, this means that the mean viscous shear stresses acting in the blade-to-blade surface, $\tau_{x\theta}$ for example, can be neglected. However, contrary to the blade walls, the annulus endwalls are present in the throughflow model. The contribution of the viscous stresses in these regions is expected to be important and is therefore not neglected.

The inviscid and viscous blade forces and the circumferential stresses have been extracted from the 3D simulations and injected in the Navier–Stokes throughflow model. The sole viscous term extracted from the 3D simulation is the viscous blade force. All other viscous terms are neglected or modeled by the 2D axisymmetric Navier–Stokes viscous terms coupled to the Baldwin–Lomax turbulence model. The resulting model is referred to as the high-order throughflow model.

A typical mesh used for such computations is presented in Fig. 7. The mesh is clustered around the leading and trailing edges to capture the strong gradients typical of these regions.

A qualitative overview of the obtained solution is presented in Fig. 8, which compares the absolute flow angle for the throughflow solution and the averaged 3D solution. The agreement is impressive. All the flow features are reproduced, such as the recirculation in the tip gap region or the stator corner stall.

Quantitative investigations can be performed not only by inspecting radial surveys at the inlet and outlet but also inside each blade row as shown in Fig. 9 for the rotor and in Fig. 10 for the stator. The flow field inside the rotor is really well reproduced by the extracted 3D terms and the viscous endwall model. For the stator row, the agreement is still good but some discrepancies occur in the corner stall region.

The discrepancies can be attributed to either numerical or modeling errors. The numerical errors can be due to the interpolation operations needed to compute the forces and the stresses from the 3D flow field, to the discretization of the stresses themselves in the throughflow model (by a Green–Gauss scheme) and/or to the discretization errors in the 3D solution itself.

The modeling errors are related to the assumptions used to build the throughflow model: Only the blade-to-blade viscous blade force contribution is included and the averaged viscous stresses are missing. Secondly, the endwall losses are modeled by the axisymmetric Navier–Stokes equation, which is a simplification compared to the 3D viscous terms circumferentially averaged. Finally, the turbulence model used in the throughflow (the Baldwin–Lomax model) is different from the one used in the 3D computation (the Spalart–Allmaras model coupled to the wall functions).

In the present case, the main discrepancy has been attributed to the 2D Baldwin–Lomax turbulence model. A computation has been run with a fixed turbulent viscosity extracted from the 3D computation circumferentially averaged: The total pressure peaks in the boundary layer have disappeared along both walls. In these regions, the new total pressure distribution fits very well the averaged 3D one. In conclusion, the agreement between the throughflow solution and the 3D averaged solution is considered to be very good. The main improvement lies in introducing a more

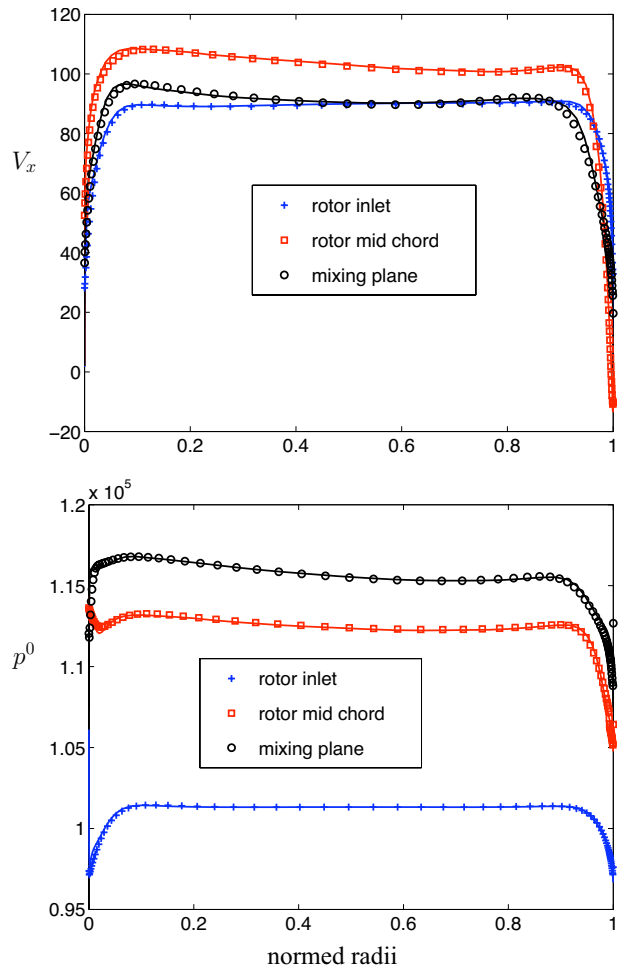


Fig. 9 Comparison between the throughflow solution (plain lines) and the 3D solution circumferentially averaged (symbols) at three locations inside the rotor domain

elaborated turbulence model. A standard 2D model in the hub-to-tip direction as for channel flows should be sufficient.

Hierarchy of the Additional Terms. The relative importance of the different contributions taken from the 3D simulation, i.e., the blade forces and the circumferential stresses, on the momentum and energy equations will be now evaluated. Figure 11 compares the entropy evolution for four computations as follows:

1. a computation with the inviscid blade force only (f_b)
2. a computation with both the inviscid and the viscous blade forces ($f_b + f_v$)
3. a computation with the inviscid blade force and the circumferential stresses (f_b and stresses)
4. a full computation containing all contributions (f_b , f_v , and stresses)

The simulation including only the inviscid blade force shows some entropy generation in the core flow region, where the annulus endwall flows have no influence. This is due to the unbalance of the momentum and energy equations. A similar result would have been obtained with a 3D Euler simulation from which inviscid blade forces and circumferential stresses are extracted and injected in the throughflow model. An isentropic flow would be obtained with the throughflow only if all contributions are introduced in the conservation equations. Removing the stresses leads to an unbalance of the equations and to an unphysical entropy evolution.

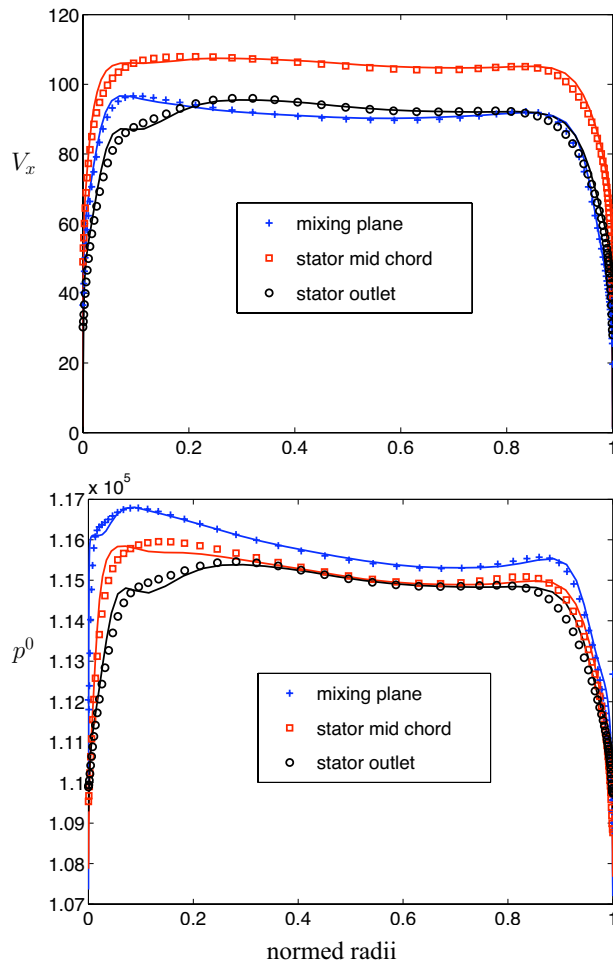


Fig. 10 Comparison between the throughflow solution (plain lines) and the 3D solution circumferentially averaged (symbols) at three locations inside the stator domain

The entropy shows also a strange behavior close to the trailing edge for the computations including the circumferential stresses: An increase-decrease along a streamline in the core flow. The explanation for that phenomenon is the same as the one used for the wake mixing test-case presented above: It is due to the density-based average nature of the solved equations.

Both the viscous blade force and the circumferential stresses participate to the generation of entropy: The viscous blade force is more or less responsible for the level of entropy while the circumferential stresses shape its distribution, such as in the corner stall region. This is confirmed by the inspection of the radial distribution of the entropy at the outlet of the stator (Fig. 12).

It is possible to gain more insight on the role of the different forces and stresses by analyzing individually their effects. These relative contributions are given in Fig. 13 for the axial momentum balance. The complete analysis can be found in Ref. [12] for each balance equation separately.

The inviscid blade force clearly dominates the momentum balance. Next come the circumferential stresses and finally the viscous blade forces. Considering the mean level of the latter, one could conclude that it is not worth to include them in a throughflow simulation. This is misleading as another criterion must be taken into account, i.e., the direction of the force, which is important for the loss generation mechanism. This can be shown by the distributed loss model theory (see Ref. [17] for example). For the present test-case, neglecting the viscous blade force leads to a strong overestimation of the isentropic efficiency: 0.947 to be

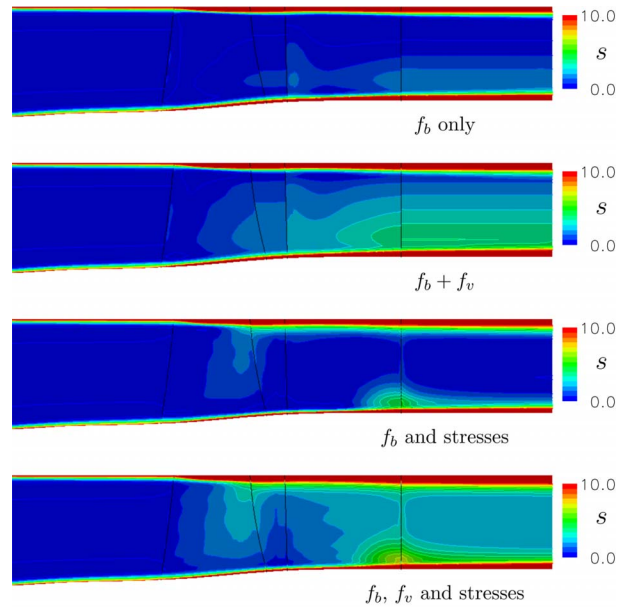


Fig. 11 Impact of the blade forces and of the circumferential stresses on the entropy field

compared to 0.894 for the full throughflow simulation and to 0.891 for the 3D one. This result confirms the conclusion devised from the 1D test-cases.

This conclusion is, however, in contradiction with the results found in literature on the deterministic stresses' closure. One way to address the deterministic stresses' closure is to consider the Adamczyk assumption, i.e., neglecting the purely temporal part of the deterministic stresses and retaining only the spatial part [18]. Some approaches based on this assumption compute explicitly the terms required for the closure and neglect the viscous terms [14,19]. Bardoux [14] has presented some results obtained on the same CME2 compressor that is studied here. He showed a comparison between the 3D flow averaged in the stator and the same flow with the stator modeled by a "ghost row," consisting of an inviscid blade force and the circumferential stresses. He found some differences between the two computations. Following the analysis presented in this work, the discrepancy observed by Bardoux can be attributed to the absence of the viscous blade force in

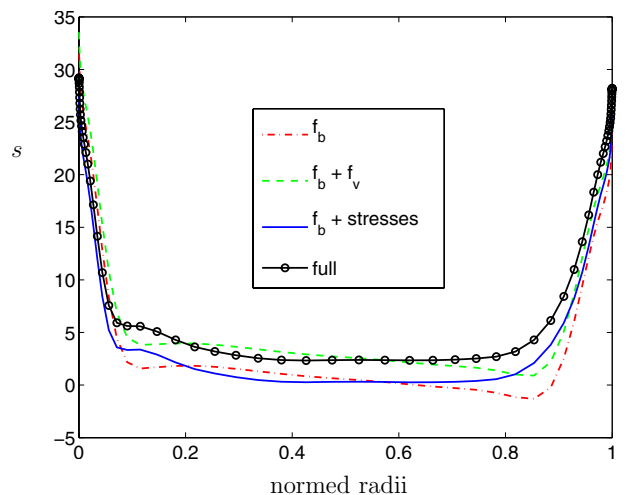


Fig. 12 Impact of the blade forces and of the circumferential stresses on the radial distribution of entropy

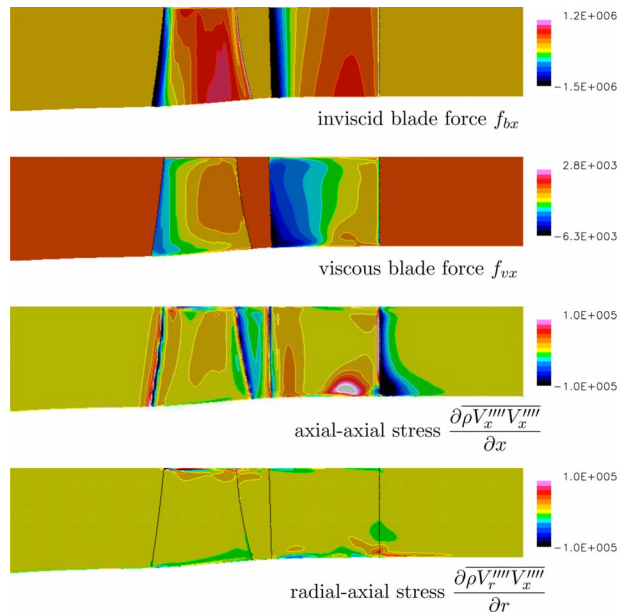


Fig. 13 Contributions to the axial momentum balance

his stator model. Indeed, the discrepancy observed by Bardoux is the same as the one observed between the full simulation and the f_b+ stress one in Fig. 12.

Classical Versus High-Order Throughflow. To end the analysis of the CME2 compressor, a comparison is performed between the high-order throughflow and a more classical throughflow. The latter is based on the axisymmetric Navier–Stokes equations and on the empirical correlations that allow to compute the flow angle (through the deviation) and the losses (through profile loss and 3D loss coefficients). The classical throughflow is based on mass-averaged quantities, while the high-order throughflow is explicitly based on a density-average approach. Therefore the comparison between the throughflow computations has been performed downstream of the stator, not too close to the trailing edge to avoid the difference between the density and the mass averages but not too far, to avoid a completely mixed flow. Two classical throughflow computations are presented: a computation with the Baldwin–Lomax turbulent model for the endwall flows (TF BL) and a computation with a radial mixing model (TF radial mixing). Details on these two models are given in Ref. [8].

Figure 14 shows the axial velocity. The global agreement between the classical throughflow and the 3D results is rather good. In the hub region, the problem arising from the Baldwin–Lomax closure is visible on about 5% of the span for both the high-order throughflow and the classical throughflow without radial mixing model. For the high-order throughflow, the problem is very weak. The classical throughflow with radial mixing model overpredicts the axial velocity close to the hub wall, which results in an overprediction of the total pressure (not shown here) in that region.

From Fig. 15, it is clear that the (weak) radial velocity at the outlet of the compressor can only be predicted by the circumferential stresses. The absolute flow angle is given in Fig. 16. The empirical correlations used here for the classical throughflow computations mispredict the mean level of the deviation angle at the outlet of the compressor stage by 2–3 deg. The 3D loss correlations of Roberts et al. [20] used in the classical throughflow, while providing the correct level of underturning, obviously fail to locate the passage vortex at the hub.

Figure 17, giving the total temperature, highlights the radial mixing phenomenon, which is relatively weak in this machine, but nevertheless present. The Navier–Stokes throughflow computation without radial mixing model overpredicts the temperature at the

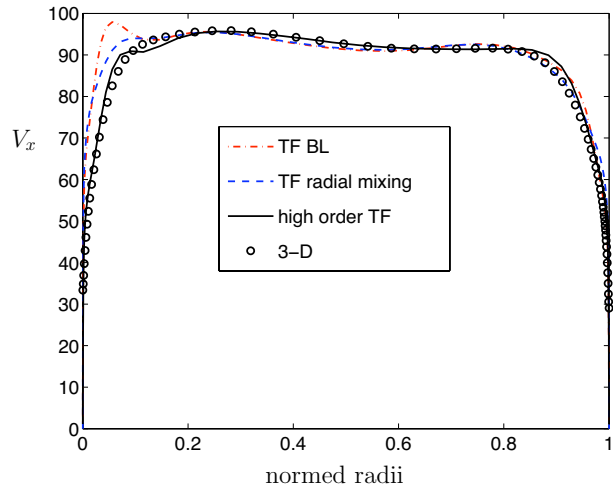


Fig. 14 Classical versus high-order throughflows: axial velocity

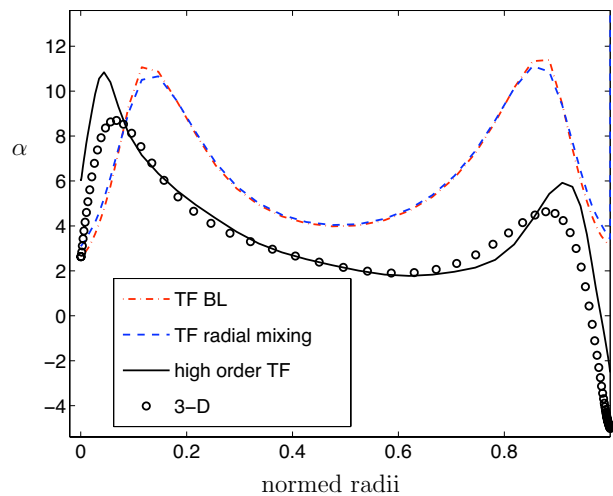


Fig. 15 Classical versus high-order throughflows: radial velocity

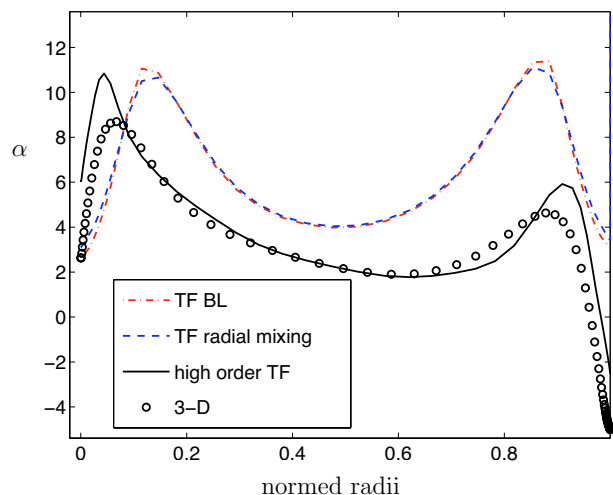


Fig. 16 Classical versus high-order throughflows: flow angle

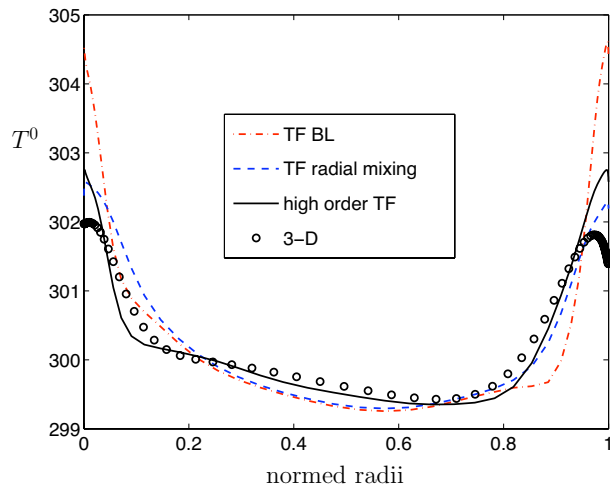


Fig. 17 Classical versus high-order throughflows: total temperature

walls. Both the circumferential stresses and the radial mixing model in the classical throughflow computations succeed in predicting the mixing phenomenon.

Another impressive feature of the high-order throughflow model is its capability to capture the prerotation of the flow approaching a blade row, as illustrated in Fig. 18. Indeed, due to the pure axisymmetric nature of its momentum equations, a classical throughflow is unable to propagate the effect of the blade force upstream of the corresponding blade row. This leads to an unphysical incidence of the incoming flow, whose angle is different from that imposed in the leading edge region by the blade model. This nonadaptation may result in a strong (unphysical) entropy jump. To get rid of this undesirable artifact an adaptation of the leading edge geometry is necessary in order to smooth the transition from the axisymmetric flow direction to the imposed material direction. Fig. 18 clearly shows that, due to the implementation of the circumferential stresses in the high-order throughflow model, the flow is turned upstream of the blade row, following the physics of the (averaged) 3D simulation.

Transonic Turbine Stage

The transonic single-stage turbine VEGA2 is representative of the first stage of a high pressure turbine. Its global performances

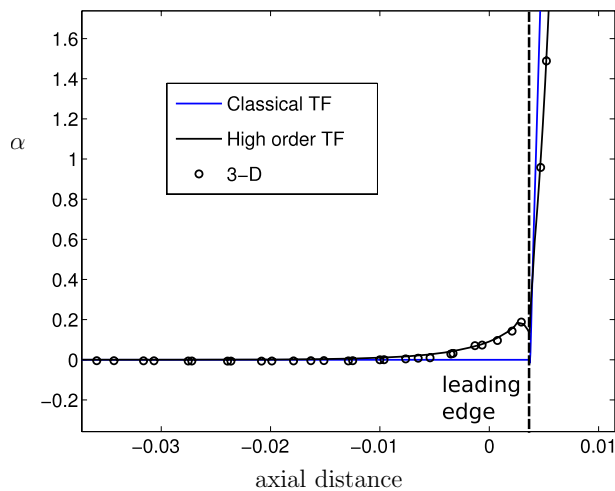


Fig. 18 Prerotation in the leading edge region of the rotor

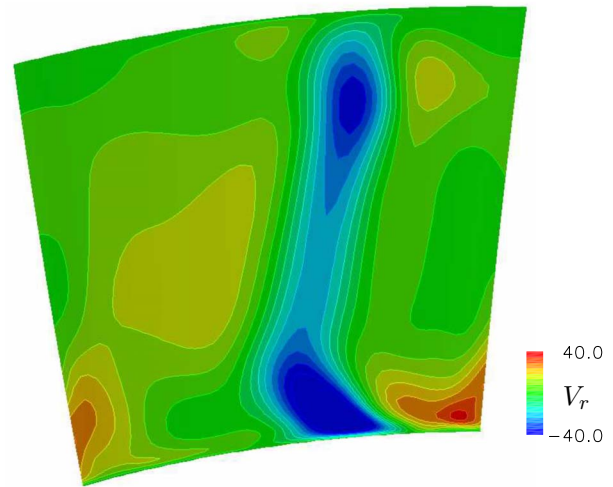


Fig. 19 Time-averaged radial velocity downstream of the stator

can be summarized as follows: mass flow 3.11 kg/s, pressure ratio 0.31, efficiency 0.93, and rotational speed 13,000 rpm.

Both steady and unsteady numerical simulations have been run by Bardoux et al. [21,22] on the same multiblock structured mesh, with the flow solver CANARI-COMET developed by ONERA. The number of grid points is approximately 2×10^6 . The simulations were run without tip clearance and with an algebraic turbulence model. A complete analysis of the simulations is available in Refs. [21,22]. The main particularity of this test-case is recalled hereafter.

This test-case presents an important difference between the unsteady time-averaged solution and the steady one. This difference is mainly due to the radial migration of the stator wake. Indeed the static pressure is approximately constant across the wake for a given spanwise position. The same radial pressure gradient is therefore applied on the core flow and on the wake flow. In the core flow, the centrifugal force generated by the circumferential velocity balances the radial pressure gradient. This is not the case in the wake, resulting in its radial migration toward the hub. This is illustrated in Fig. 19 where the migration of the wake flow is highlighted by the negative radial velocity. The radial migration of the stator wake plus the stator passage vortex is responsible for an accumulation of low energy fluid at the wake foot. This circumferential nonuniformity results in a strong time variation of the inlet condition of the rotor close to the hub. As a consequence, the rotor passage vortex has a pulsating character. The time-averaged representation of the passage vortex therefore appears as spread compared to the passage vortex obtained by the steady simulation obtained with a mixing-plane.

Throughflow Computation With Additional Terms. The deterministic stresses, the circumferential stresses, and the blade forces have been extracted from the unsteady database and injected into the throughflow solver. Figure 20 compares the averaged 3D unsteady simulation and the throughflow solution. The global agreement is not as good as for the CME2 test-case. The zone of high axial velocity at the stator wake foot is more extended in the throughflow calculation than in the 3D one. The developments of the vortex, at the hub and at the shroud of the rotor blade, are also not correctly predicted. The global agreement is, however, thought to be very good.

The main discrepancy occurs close to the stator trailing edge. The losses are underestimated at the outlet of the stator as shown by the radial distributions of entropy in Fig. 21. A throughflow computation with two times more grid points in the axial direction has been performed. No noticeable differences have been ob-

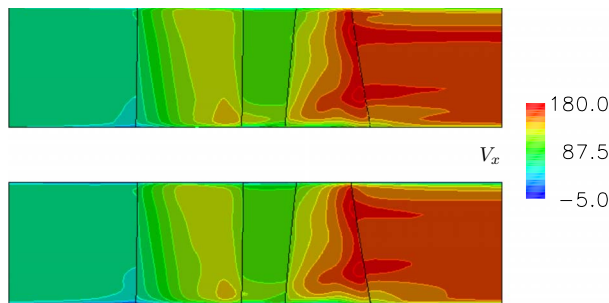


Fig. 20 Axial velocity from 3D averaged solution (top) and throughflow solution (bottom)

served meaning that the discretization errors are low. A possible explanation for this discrepancy is that the blade-to-blade viscous shear stresses have been neglected in the throughflow. The conclusions concerning the impact of these stresses that were elaborated on the flat plate test-case and that have hold for the CME2 test-case could be invalid here, for the aft-part of this high-deflection stator.

The unavailability of the complete 3D viscous stresses does not allow to go further on that subject. However, it should be noted that the discrepancy mainly affects the entropy and the other loss-related quantities; other quantities such as the axial velocity are

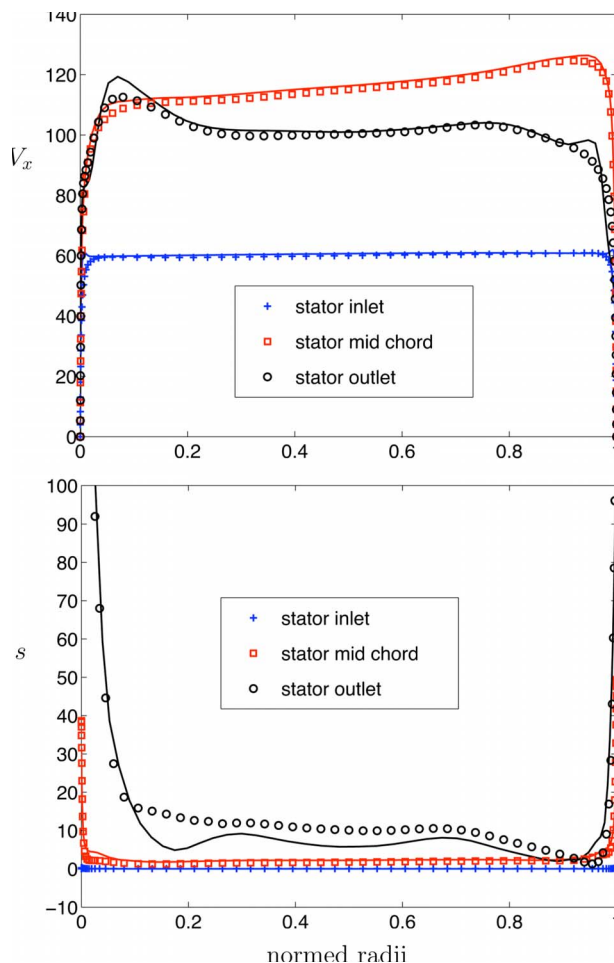


Fig. 21 Comparison between the throughflow solution (plain lines) and the averaged unsteady 3D solution (symbols) at three locations inside the stator domain

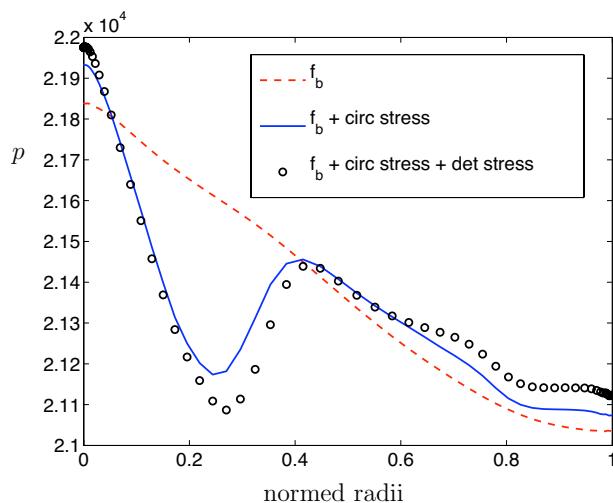


Fig. 22 Comparison of the throughflow simulations with and without deterministic stresses (rotor outlet)

better predicted as shown in Fig. 21.

Finally, the global performances are well predicted. The throughflow computed mass flow is equal to 3.09 kg/s for 3.11 kg/s in the 3D unsteady simulation, the pressure ratio is 0.310 in the throughflow computation for 0.311 in the 3D one, and the efficiency is equal to 0.931 in the throughflow computation for 0.934 in the 3D one.

Relative Importance of the Deterministic and Circumferential Stresses. Bardoux et al. [21,22] showed that including the deterministic stresses in the 3D simulation of the VEGA2 rotor allows to capture the mean effect of the unsteadiness on the mean steady flow. They also showed that the purely temporal part of the deterministic stresses cannot be neglected, contrary to the assumptions of the closure proposed by Adamczyk et al. [18]. The study of Bardoux et al. was focused on 3D simulations and deterministic stresses. The question of the importance of the deterministic stresses must now be addressed at the throughflow level.

As described in the model of Adamczyk, for a single shaft turbomachine, two steady flow fields exist, one per reference frame. The circumferential stresses are relative to a steady flow field in a given reference frame. In other words, the circumferential stresses' field is discontinuous at the stator-rotor interface. This discontinuity is mainly present in the regions of high unsteadiness, and disappears when the deterministic stresses are superimposed to the circumferential stresses. Even though the deterministic stresses are necessary in order to obtain a physically correct averaged solution, it is not clear whether neglecting them would be an important source of error. To this end three throughflow simulations are compared in Fig. 22: One with the blade forces only (f_b), one with the blade forces and the circumferential stresses ($f_b + \text{circ. stress}$), and one including the blade forces and circumferential and deterministic stresses ($f_b + \text{circ. stress} + \text{det. stress}$). The circumferential stresses show a greater influence than the deterministic stresses. They are responsible for the trace of the passage vortex in the pressure distribution. The deterministic stresses do not have a predominant impact on the resulting flow field to the exception of the hub region where the unsteadiness is the strongest.

To further evaluate the error that would be brought by neglecting the deterministic stresses, three results are compared in Fig. 23: Those obtained without the deterministic stresses ($f_b + \text{circ stress}$ (unsteady)), those obtained with the deterministic and the circumferential stresses extracted from the 3D unsteady simulation (full (unsteady)), and those obtained with the circumferential stresses extracted from a 3D steady mixing-plane simulation (full

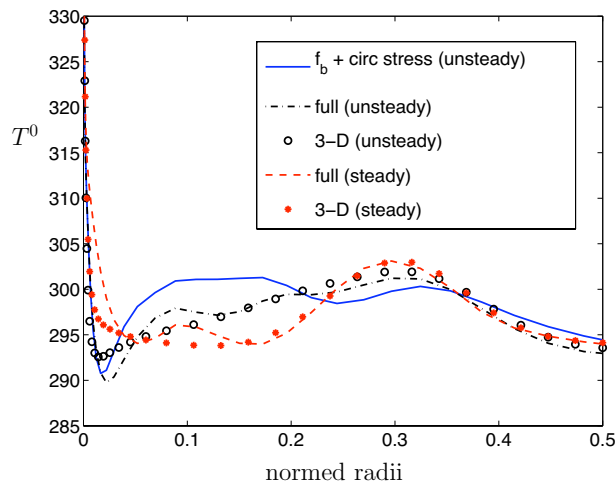


Fig. 23 Comparison of the throughflow simulations with and without deterministic stresses (rotor outlet)

(steady)). The reference 3D unsteady simulation and the 3D steady one are also plotted on the figure with symbols. It is obvious from this comparison that the simulation without the deterministic stresses is not accurate, as it is as far from the reference unsteady solution as the steady one is. Particularly, the radial mixing phenomenon brought by the unsteadiness is mispredicted.

Conclusions

The main motivation of this contribution was to propose a way to reduce the level of empiricism embedded in the throughflow models with the help of the high-order throughflow model.

The potential of this model to capture all flow features has been demonstrated. Concerning the closure of the (steady) problem, it has been shown that the following terms are necessary to correctly reproduce the flow physics: the inviscid blade force, the circumferential stresses, the viscous blade force, and a 2D viscous model for the endwall flows. The most important contribution is obviously the inviscid blade force. The relative importance of the circumferential stresses increases with the loading. When unsteadiness effects are important, the deterministic stresses should also be included even though they are not preponderant compared to the circumferential ones.

The improvement brought by the high-order throughflow model over a more conventional throughflow model has been shown for the CME2 test-case. It consists in a more accurate capture of the boundary layer flow and of the radial velocity field. The loss coefficient and deviation are also accurately captured.

The features of the high-order throughflow system of equations have also been highlighted in this contribution. The main particularity is probably the evolution of the entropy due to the Favre averaging chosen to derive the equations. This behavior will be difficult to modify unless another system of equations is devised, based on mass-averaged properties.

Nothing has been done on the modeling of the different terms needed to close the equations. Some thoughts on how to address this closure are given hereafter.

For the inviscid blade forces, we believe that the following two solutions are available.

- To use fast 3D models to compute the pressure distribution on the blade walls, such as potential methods (singularity methods) or Euler ones.
- To use blade force models found in classical Euler and Navier–Stokes finite volume throughflows [4,8]. This method is valid for both analysis calculation where the geometry is known and design calculation where a blade loading is prescribed. With these models, a physically correct

isentropic flow is obtained for a shock free inviscid computation. However, the addition of the circumferential stresses modify this isentropic result. The blade force model (more specifically the orthogonality condition it imposes between the blade force and the mean flow) should be adapted to account for the presence of the circumferential stresses.

For the circumferential stresses, adapting techniques inspired from the deterministic stresses' closure seems a natural way; among them are transport equations for the circumferential stresses or the nonlinear harmonic modeling. A project studying the feasibility of a circumferential closure by a method inspired from the nonlinear harmonic method is currently undertaken by Thomas et al. [23]. Some modifications of the original method will be necessary concerning the function chosen to represent the fluctuations.

Finally, for the viscous blade force, a simple model giving the skin friction on the blade walls could be obtained from typical relations used for wall function formulations. Considering that the circumferential stresses' closure will be able to bring some information on the evolution of the velocity in the direction orthogonal to the blade walls, it will be possible to compute the viscous blade force [3].

Acknowledgment

The authors would like to express their deep gratitude to Francis Leboeuf (Ecole Centrale de Lyon) for his valuable advises, and to Stéphane Burguburu (ONERA) who provided the 3D test-cases CME2 and VEGA2.

Nomenclature

b	=	blockage factor
f_b	=	inviscid blade force
f_v	=	viscous blade force
h, H	=	enthalpy, total enthalpy
k	=	kinetic energy of the fluctuations
p, p^0	=	pressure, total pressure
q	=	heat flux
s	=	entropy (relative to inlet conditions)
T^0	=	total temperature
V	=	absolute velocity
x, r, θ	=	axial, radial, and circumferential coordinates
α	=	absolute flow angle
ρ	=	density
τ	=	viscous stress

Operators

$-$	=	averaging operator
\sim	=	Favre-averaging operator

Subscripts

x, r, θ	=	axial, radial, and circumferential components
R	=	relative to a rotor
S	=	relative to a stator

Superscripts

'	=	unsteady nondeterministic fluctuation
"	=	unsteady deterministic fluctuation
'''	=	aperiodic fluctuation
''''	=	circumferential fluctuation

References

- [1] Denton, J. D., and Dawes, W. N., 1999, "Computational Fluid Dynamics for Turbomachinery Design," Proc. Inst. Mech. Eng., Part C: J. Mech. Eng. Sci., **213**(2), pp. 107–124.
- [2] Attia, M. S., 2005, "Semiviscous Method for Compressor Performance Prediction," J. Propul. Power **21**(5), pp. 792–796.
- [3] Spurr, A., 1980, "The Prediction of 3-D Transonic Flow in Turbomachinery Using a Combined Throughflow and Blade-to-Blade Time Marching Method," Int. J. Heat Fluid Flow, **2**(4), pp. 189–199.
- [4] Baralon, S., 2000, "On Multistage Analysis of Transonic Compressors: From

- Axisymmetric Throughflow Time Marching to Unsteady Three Dimensional Methods,” Ph.D. thesis, Chalmers University of Technology, Gothenburg, Sweden
- [5] Sturmayer, A., 2004, “Evolution of a 3-D Structured Navier-Stokes Solver Towards Advanced Turbomachinery Applications,” Ph.D. thesis, Vrije Universiteit Brussel, Brussels, Belgium.
- [6] Cumpsty, N. A., 1989, *Compressor Aerodynamics*, Longman Scientific and Technical, Harlow, Essex, England.
- [7] Horlock, J. H., and Denton, J. D., 2005, “A Review of Some Early Design Practice Using Computational Fluid Dynamics and a Current Perspective,” *ASME J. Turbomach.*, **127**, pp. 5–13.
- [8] Simon, J. F., and Léonard, O., 2005, “A Throughflow Analysis Tool Based on the Navier–Stokes Equations,” *Proceedings of the 6th European Turbomachinery Conference*, Lille, France.
- [9] Simon, J. F., and Léonard, O., 2007, “Modeling of 3-D Losses and Deviations in a Throughflow Analysis Tool,” *J. Therm. Sci.*, **16**(3), pp. 208–214.
- [10] Adamczyk, J. J., 1984, “Model Equation for Simulating Flows in Multistage Turbomachinery,” NASA Report No. TM-86869.
- [11] Adamczyk, J. J., 1999, “Aerodynamic Analysis of Multistage Turbomachinery Flows in Support of Aerodynamic Design,” ASME Paper No. 99-GT-80.
- [12] Simon, J. F., 2007, “Contribution to Throughflow Modelling for Axial Flow Turbomachines,” Ph.D. thesis, University of Liège, Liège, Belgium.
- [13] Smith, L. H., Jr., 1966, “The Radial-Equilibrium Equation of Turbomachinery,” *ASME J. Eng. Power*, **88**, pp. 1–12.
- [14] Bardoux, F., 2000, “Modélisation des interactions instationnaires rotor-stator en turbomachine multi-étages,” Ph.D. thesis, Ecole Centrale de Lyon, Lyon, France.
- [15] Hirsch, C., and Dring, R. P., 1987, “Throughflow Models for Mass and Momentum-Averaged Variables,” *ASME J. Turbomach.*, **109**, pp. 362–370.
- [16] Gourdain, N., Burguburu, S., Michon, G. J., Ouayahya, N., Leboeuf, F., and Plot, S., 2006, “About the Numerical Simulation of Rotating Stall Mechanisms in Axial Compressors,” ASME Paper No. GT2006-90223.
- [17] Hirsch, C., 1988, *Numerical Computation of Internal and External Flows*, Wiley, New York.
- [18] Adamczyk, J. J., Mulac, R. A., and Celestina, M. L., 1986, “A Model for Closing the Inviscid Form of the Average-Passage Equation System,” *ASME J. Turbomach.*, **108**, pp. 180–186.
- [19] Rhie, C. M., Gleixner, A. J., Fischberg, C. J., and Zacharias, R. M., 1995, “Development and Application of a Multistage Navier–Stokes Solver—Part I: Multistage Modeling Using Bodyforces and Deterministic Stresses,” ASME Paper No. 95-GT-342.
- [20] Roberts, W. B., Serovy, G. K., and Sandercock, D. M., 1986, “Modeling the 3-D Flow Effects on Deviation Angle for Axial Compressor Middle Stages,” *ASME J. Eng. Gas Turbines Power*, **108**, pp. 131–137.
- [21] Bardoux, F., Leboeuf, F., Dano, C., and Toussaint, C., 1999, “Characterization of Deterministic Correlations for a Turbine Stage. Part 1: Time Averaged Flow Analysis,” ASME Paper No. 99-GT-100.
- [22] Bardoux, F., Leboeuf, F., Dano, C., and Toussaint, C., 1999, “Characterization of Deterministic Correlations for a Turbine Stage. Part 2: Unsteady Flow Analysis,” ASME Paper No. 99-GT-100.
- [23] Thomas, J. P., Simon, J. F., and Léonard, O., 2008, “Investigating Circumferential Non Uniformities in Throughflow Calculations Using a Harmonic Reconstruction,” ASME Paper No. GT2008-50328.

Some Aerodynamic Problems of Aircraft Engines: Fifty Years After -The 2007 IGTI Scholar Lecture-

Edward M. Greitzer
Gas Turbine Laboratory,
Massachusetts Institute of Technology,
Cambridge, MA 02139

Problems of high technological interest, for example the development of gas turbine engines, span disciplinary, and often organizational, boundaries. Although collaboration is critical in advancing the technology, it has been less a factor in gas turbine research. In this paper it is proposed that step changes in gas turbine performance can emerge from collaborative research endeavors that involve the development of integrated teams with the needed range of skills. Such teams are an important aspect in product development, but they are less familiar and less subscribed to in the research community. The case histories of two projects are given to illustrate the point: the development of the concept of "smart jet engines" and the Silent Aircraft Initiative. In addition to providing a capability to attack multidisciplinary problems, the way in which collaboration can enhance the research process within a single discipline is also discussed.

[DOI: 10.1115/1.2992515]

1 Introduction and Theme

A half-century ago, Sir William Hawthorne, a pioneer in our field, presented a masterful survey of gas turbine aerodynamics entitled "Some Aerodynamic Problems of Aircraft Engines" [1]. In that paper (which would have been an excellent IGTI Scholar Lecture), he described a number of issues, which had major impact on the performance of aeroengines and for which there was no first-principles understanding.¹ In fact, if the latter is taken as a metric, some problems he mentioned are not yet resolved.² The title of this lecture is taken from Hawthorne's paper in recognition not only of the time that has passed since then but also the enormous advances in gas turbine technology that have occurred.

Several aspects of this progress are directly relevant to the present discussion. First, while deeper understanding can provide a route to better products and more effective processes, the history of the jet engine is a monument to the ways in which designers have produced an excellent and highly sophisticated product even when such understanding did not exist. This point, which is made in the introduction to Hawthorne's paper, is echoed (with the benefit of 50 additional years of jet engine history) by Koff [2] and by Cumpsty and Greitzer [3]. Second, the deeper understanding referred to has been achieved in a number of areas. In terms of impact on the product, therefore, an argument can be made that achieving additional understanding in the above sense is less important than when Hawthorne wrote his paper.³

Third, the framework of Hawthorne's paper, and the problems he described, were single discipline issues. To avoid any misunderstanding, let me state at the outset that the point of the lecture is *not* that there are no important problems of this sort that need to be addressed. However, as in the two previous IGTI Scholar

Lectures, microengines and active control of combustion,⁴ both of which described activities that cut across disciplines to offer potential for step changes in performance, the thesis here is that the major technology gains now lie in research that requires the integration of disciplines.⁵ Put another way, the highly interactive nature of modern engine design means that the engine needs to be looked at as a system. This type of approach, which almost invariably involves collaboration across disciplines, enables greater reach in attacking such technical challenges and offers opportunities for achieving goals beyond those defined by conventional design constraints.

The above so far are just assertions, but I will endeavor to make them more plausible through the histories of two research collaborations, which (I claim) illustrate the points. The first involved the theoretical description and experimental realization of enhanced turbomachinery range capability through the use of dynamic control, i.e., through alterations of the unsteady compression system behavior. The second was the conceptual design of an aircraft, which would be imperceptible from a noise standpoint outside the perimeter of an urban airport.

It seems helpful to provide some explanation for the choice of examples and the overall perspective taken in this paper. For the former, it is hoped that the topics are of interest to a broad technical community. Further, because the projects achieved the stated goals and the research led to results not foreseen before the project started, there is some justification for viewing them as successful. The narrative of the technical aspects thus provides context, and perhaps some credibility, for the message concerning collaboration. For the latter—and I cannot emphasize this too strongly—it is the intention to highlight some of the difficulties through recounting, from the personal perspective of someone deeply embedded in the technology, the learning about collaboration that took place. The focus of the description is therefore one particular team rather than a broad survey of the field. However, recognizing that many other organizations have had similar (or even more successful) experiences, several other collaborative enterprises, within IGTI and elsewhere, are introduced in the latter part of this paper.

¹The word "understanding" is used here to indicate predictive capability that stems from clear definition of the important mechanisms.

²Operability and stall inception and combustor design are examples of two areas that still rely heavily on empirical information.

³The tendency to strive for additional refinement is portrayed succinctly by Bridgeman [4]: "No analysis is self-terminating, but it can always be pushed indefinitely with continually accumulating refinements."

Contributed by the International Gas Turbine Institute of ASME for publication in the JOURNAL OF TURBOMACHINERY. Manuscript received July 15, 2008; final manuscript received July 25, 2008; published online April 20, 2009. Review conducted by David Wisler. Paper presented at the ASME Turbo Expo 2007: Land, Sea and Air (GT2007), Montreal, QC, Canada, May 14–17, 2007.

⁴IGTI Scholar Lecturers A.H. Epstein in 2003 and B.T. Zinn in 2005, respectively.

⁵Perhaps a clearer way to state this is given by J. A. Armstrong, former VP for research at IBM: "God did not make the natural world according to the departmental structure of research universities" [5].

2 Dynamic Control of Compressor Instability: Smart Jet Engines

The first example concerns control of compressor and compression system aerodynamic instability. We describe the concepts, technical issues, specific achievements, and lessons learned about the overall process.

The idea of a smart jet engine appears to have been initially articulated by Epstein [6] in a National Research Council Workshop, where he posed the challenge of altering the nature of gas turbine engines from open to closed loop operation through the aggressive use of sensors, actuators, and on-board computing. A number of potential applications were identified including active noise control, use of magnetic bearings, and active control of aerodynamic instabilities in compression systems.

Interest in the third of these possibilities was sparked by the visit to MIT of J.E. Ffowcs Williams from Cambridge University, who saw potential for extending concepts from antinoise research [7] to a different and much broader range of flow disturbances.⁶ The preliminary objective was to determine the applications, benefits, and requirements of greatly increased real-time computation and closed-loop control in turbine engines. This evolved through internal and external discussions to a more specific goal of defining one promising technology, demonstrating this in the laboratory, and pursuing transition to practical devices.

We focused on control of the turbomachinery compression system instabilities, surge and rotating stall, because of their importance. These two phenomena put fundamental limits on gas turbine compressor operating range and thus limit the design space. A sizable *stall margin*, or distance between the nominal operating point and instability boundary, must be factored into the compressor design, compromising the ability to utilize the peak pressure rise in the machine as an operating point. Instability limits are difficult to predict and can lead to costly surprises during development. In addition to the technological considerations, rotating stall and surge were topics we knew something about.

The underlying idea was that rotating stall and surge are mature forms of small amplitude disturbances that are the natural modes of oscillation in the compression system. The modal amplitude grows when background (mean flow) conditions cause the damping to become negative. Feedback control operating on these small disturbances, and hence not power or force limited, could change the dynamic behavior of the system, render a given unstable operating point stable, and enhance the operating range [8].

From the beginning, the technology strategy was based on the observation that data are by far the most effective convancers in the gas turbine industry. The plan was to demonstrate often, use these successes to leverage the next steps, and keep close contact with individuals at companies to build support. Furthermore, early in the project, system studies were carried out to identify the impact of the technology that we were proposing. Not all the gains (and costs) were obvious,⁷ and the benefits shown by the system study provided an excellent framework for discussions with customers, both current and potential.

Another important practice was to ensure that focus remained on the overall objective, control of compressor instabilities, rather than on the supporting pieces. Each of the latter has its own interesting scientific and engineering issues, and the challenge is to identify and address those truly necessary for project success.

The project described is inherently multidisciplinary and the development of a team that spanned several disciplines took a year or more. There is sometimes a tendency in academic institutions to regard one's field as challenging whereas the research of others is much more straightforward. A consequence in the beginning was thus questioning whether, for example, compressor ex-

perts really needed the help of controls and structures experts. Positive answers to these questions were initially motivated purely by short-term self-interest: to obtain sponsor support from an interdisciplinary pool, to talk to sponsors in their own discipline, and to obtain the software we saw as necessary. As will be seen, however, this perspective changed markedly as the project progressed.

Initial meetings of the group (the word *team*⁸ does not describe the situation at that point in time) were characterized by a lack of understanding between the various camps and a lack of intellectual and language commonality; the same physical problem was thought about and described differently by different parts of the group. Time was needed for group members to convince themselves that the others brought something to the table and to learn enough of the vocabulary and mindset to be able to communicate effectively. In doing this, we had the enormous advantage of a cadre of energetic, intelligent, and high achieving students who had not yet learned that doing a multidisciplinary project is difficult. The students acted as technical translators for the faculty and accessed expertise wherever appropriate, creating links that strengthened the function of the group. We also co-supervised students so that, in some instances, there would be three faculty (with expertise in control, turbomachinery, and structural dynamics, respectively) that met with a student whose project spanned all three areas. Although this style of supervision carries an increased time commitment, it was useful in team building and in providing insight into the intellectual challenges of the other disciplines involved.

Weekly technical meetings with a presentation on one aspect of the work, ranging through the different disciplines (fluids, structures, and control), were also useful in team building. The presentations started out very much as student talks with questions by faculty, but as the former gained more knowledge (and more confidence), the meetings became dominated by student-student interactions.

3 Control of Surge

3.1 Active Surge Stabilization. The different technical problems addressed during the program had increasing degrees of complexity. The facilities needed also grew in complexity, from laboratory-scale demonstrations using small truck turbochargers to experiments on transonic fans and complete gas turbine engines. The first achievement was active stabilization of compressor surge, a basically one-dimensional phenomenon, in which nonlinear limit cycle oscillations occur in system mass flow and pressure rise. In most instances, the amplitude of the oscillation is large enough so that over a portion of the surge cycle the flow reverses in the compressor.

Surge is important for both centrifugal and axial compressors. In many types of centrifugal machines surge control alone, as opposed to control of rotating stall and surge together, is sufficient to yield a large increase in useable flow range. A centrifugal compressor was thus used as the initial test bed. The focus on surge as an entry point carried several advantages. There was a theoretical framework [10–12] in terms of simple lumped parameter models, which fit well into a control framework. The phenomenon of interest was one-dimensional and control could be achieved with a single sensor and a single actuator. The frequency of the instability was low enough (10–50 Hz) so both sensing and actuating could be achieved with (almost) “off the shelf” devices. This aspect, which will be seen again in the discussion of rotating stall, meant that we could move rapidly to address the proof-of-concept questions that were at the heart of early success demonstration

⁶Specifically to extend the applications from pressure disturbances, the major domain of the acoustician, to the entropy and vorticity disturbances that are inherent in gas turbine operation.

⁷This was true for the silent aircraft project as well.

⁸One definition of a *team* is an enterprise that judges success in terms of a collective work product. This can be contrasted with a *working group* in which the success metric is individual work products [9].

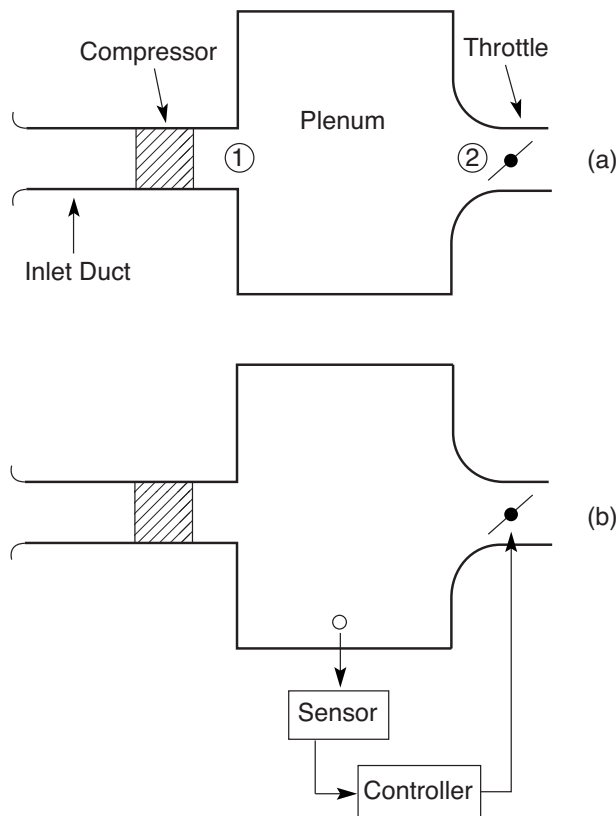


Fig. 1 Lumped parameter compression system: (a) no control, and (b) controlled system with sensor in plenum and throttle actuator

rather than spending a great deal of time on actuator development.

The modeling and control schemes have been described elsewhere [13–16] and will receive only brief mention. A lumped parameter compression system representation is shown in Fig. 1(a), which illustrates a compressor and associated ducting, a plenum (representing the combustor volume in an engine), and a downstream resistance. For feedback stabilization, one measures the system output, compares it with some desired reference level, determines the error, and computes an input signal (command to some actuator) based on this error to drive the error to zero. Figure 1(b) shows a schematic of the controlled compression system. The sensed variable was the plenum pressure, and the controller was a throttle valve at the plenum exit. Surge is a dynamic instability in which the compressor adds energy to small oscillations in the system, increasing their amplitude [17]. A proportional controller, with perturbation in throttle area proportional to plenum pressure, created the necessary dissipation of mechanical energy to offset the perturbation energy put into the system by the unsteady flow through the compressor.

The results from the feedback control are shown in Fig. 2. The abscissa is nondimensional mass flow and the ordinate is nondimensional pressure rise. The symbols represent the performance as measured by steady-state instrumentation. Without control, the surge oscillations were greater than 100% of the prestall value in mass flow and 30% in pressure rise, leading to a time-average pressure rise 20% below the prestall value. With the controller, the amplitudes were reduced by an order of magnitude, the time mean pressure rise was maintained roughly at the prestall value, and the useful flow range was increased by nearly 25%. Switching on the controller when the system had entered surge also enabled the compressor to recover from a limit cycle oscillation back to a stable operating point.

3.2 Stabilization of Surge Using Structural Feedback. To

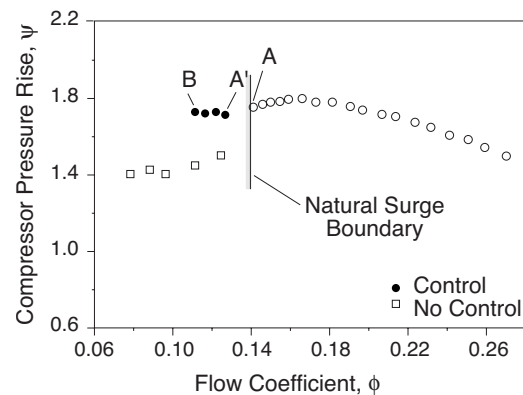


Fig. 2 Compressor pressure increase characteristic indicating time-mean operating points with and without control [13]

achieve stabilization, one must alter the dynamic behavior of the compression system. There are ways to do this, however, which do not necessitate the use of sensors and external actuators and can be easier or more robust to implement than active control. A tailored structure, such as that in Fig. 3, can absorb energy and damp pressure and mass flow oscillations. The figure shows the original compression system (compressor, plenum, and throttle) plus a moveable plenum wall, which is a mass-spring-damper dynamically coupled to the aerodynamic system. The combined device, with non-rigid walls, gives greater damping of aerodynamic perturbations than did the original [18]. Details of the analysis, experiment design, and results are given in Refs. 18 and 19, but Fig. 4 illustrates some main findings. The figure shows an increase in stable flow range of between 20–30% over the range of speeds examined. It also indicates that the lumped parameter model that was used in designing the structural feedback adequately captures the system parametric behavior. Even for this simple configuration, there are five nondimensional parameters, which characterize different aerodynamic, structural dynamic, and aeromechanical effects, and modeling played a critical role in negotiating the path to a useful solution. In summary, both active control and structural feedback enhanced stability by altering the dynamic behavior of the system, with the steady-state performance virtually unaltered.

4 Control of Rotating Stall

4.1 Active Stabilization of Rotating Stall. For axial compressors, one also needs to control rotating stall, a situation in

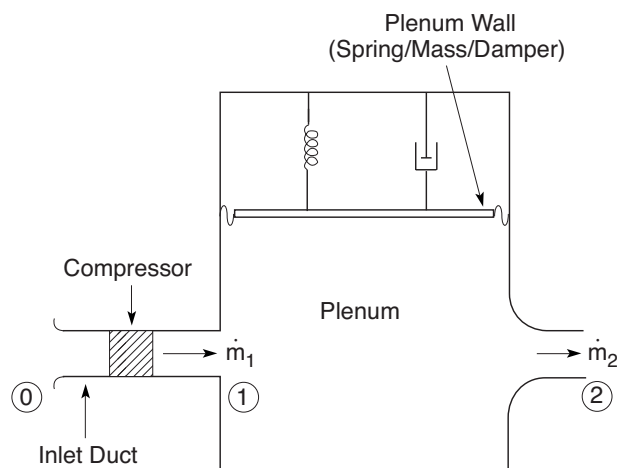


Fig. 3 Schematic of moveable plenum wall compression system [18]

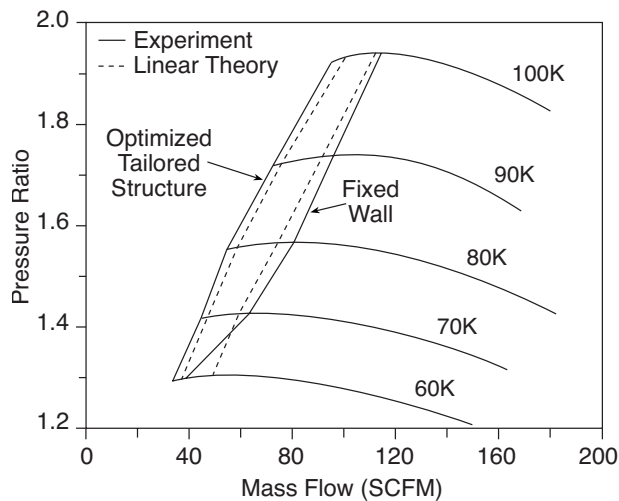


Fig. 4 Predicted and measured compressor stability limits with dynamic structural control; labels denote corrected speed (100 K=100,000 rpm) [18]

which cells of stalled flow propagate round the circumference of the turbomachine at between (roughly) 20–50% of rotor speed, depending on the configuration. Time mean performance in rotating stall causes much decreased efficiency (an order of magnitude in some cases) and pressure rise compared to the prestall value [20]. Further, the decrease in pressure rise during rotating stall development can cause the overall system stability criteria to be violated leading to surge. In this sense, one can say that rotating stall in a multistage axial compressor “triggers” surge, with the consequence that one needs to control both types of instabilities.

For rotating stall, the control problem is multidimensional, implying, at least for linear control schemes, the use of arrays of actuators and sensors. Rotating stall phenomena are less well understood than surge and, at a conceptual level, the approach taken could have been expressed as follows. Theory [21,22] suggested that rotating stall was the mature form of small amplitude circumferential asymmetries (waves), which propagated around the annulus, with the fate of these small amplitude disturbances governed by the mean operating conditions. For operations near design, the disturbances decay. As the flow rate was decreased, however, the disturbance decay rate would decrease until at some flow condition (peak pressure rise or slightly beyond) the disturbances would be neutrally stable, neither damped nor amplified. For further reductions in flow, and consequent operation on the positive sloped part of the pressure rise versus flow compressor pumping curve,⁹ disturbance waves would grow into rotating stall.

The theory implied that damping the waves would inhibit rotating stall. The objective was thus to sense small amplitude traveling waves in the compressor and to use actuators to establish a real-time traveling disturbance that was coupled to these waves. Doing this in an appropriate manner provides an alteration to the dynamic behavior that renders the system stable, enhancing the rotating-stall-free operating range. The elements for realization were wave sensing, wave launching, closing the loop, and the hardware implementation of all three. Demonstration that the waves existed, namely, that the eigenmodes in the compressor annulus were modes in the forms of Fourier harmonics in the circumferential coordinate, was directly tied to the theory for rotating stall control. If so, for a linear system the control could be carried out on a Fourier mode-by-mode basis as separate single input, single output control systems. The overall direction of the experiments was based on this close integration of fluids and con-

⁹In terms of the variables shown in Fig. 2, this means operation in a regime in which $d\psi/d\phi$ is positive.

trols concepts.

Investigations of wave structure were carried out at the Gas Turbine Laboratory, MIT, and at the Whittle Laboratory, Cambridge University [23,24]. There was a strong interaction between these two organizations (electronically and face-to-face), which sometimes included heated discussion of apparently contradictory results, as discussed subsequently.

Stall sensing experiments were carried out on low speed single-stage and three-stage compressors, and a schematic of the latter is given in Fig. 5 [25]. The control scheme was a row of individually controlled inlet guide vanes upstream of the compressor. The required bandwidth (say up to two times the rotor rotation rate) could be achieved using off-the-shelf high bandwidth electric motors. As with surge, the control scheme was chosen to enable focus on demonstration of an actively controlled compressor rather than necessitating extensive development of actuator technology.

The results of stall control experiments on a three-stage compressor are given in Fig. 6, which shows the amplitude of the first Fourier mode of the propagating axial velocity disturbance versus time, expressed in terms of rotor revolutions, the natural time scale of the problem. Wave phase measurements, not shown here, indicate a disturbance phase speed approximately 30% of rotor rotation. Measurements such as this confirmed the existence of the small amplitude propagating perturbations. The figure also shows the theoretical results; in spite of the approximate nature, the theory gives a useful description of the transient behavior. Small amplitude waves are seen for tens of rotor revolutions; the transition from conditions when the perturbations are small to near-final amplitude occurs over a shorter time (several rotor revolutions). At the final amplitude, the nonuniformities in axial velocity are larger than the time-mean value.

Figure 7 shows the open-loop response for a single-stage compressor, i.e., the transfer function from inlet guide vane angle perturbation to compressor inlet axial velocity perturbation for the first spatial harmonic of the disturbance. The upper plot is the amplitude and the lower plot is the phase, plotted against frequency of disturbance normalized by rotor frequency. The resonant peak near 20% of rotor speed corresponds closely to the rotating stall propagation speed. As the compressor is throttled to stall, the peak height increases as the system damping increases in accord with the theoretical concepts. The behavior is well described by a second order fit, also in agreement with the theory. The experiments thus gave confidence that the association of rotating stall with the growth of the eigenmodes in the compressor annulus was well founded and that control approaches based on this idea would be worth pursuing.

Closed-loop control results are given in Fig. 8 for the low speed single-stage compressor. Control of the first mode alone yielded an 11% increase in range, control of the first and second modes yielded a 20% increase, and control of the three modes together gave a 25% percent range increase.

4.2 Stabilization of Rotating Stall With Structural Feedback.

Many of the comments about structural control of surge apply to rotating stall. The main difference is that one now has, as for active control of rotating stall, a distribution rather than a single structural element. The use of structural feedback was demonstrated by Gysling [26,27] with an array of reed valves controlling the injection of high pressure air in front of the compressor. An increase of 10% in stable flow range was obtained. Gysling [26] also provided a unifying view of structural and active control of rotating stall through the examination of the energetics of the wave growth process. He showed that the flexible structure created phase relationships between pressure and flow rate perturbations through the valve similar to those in an active control system in which pressure was sensed and flow was controlled. This work gave a framework in which to view all linear control schemes examined up to then.

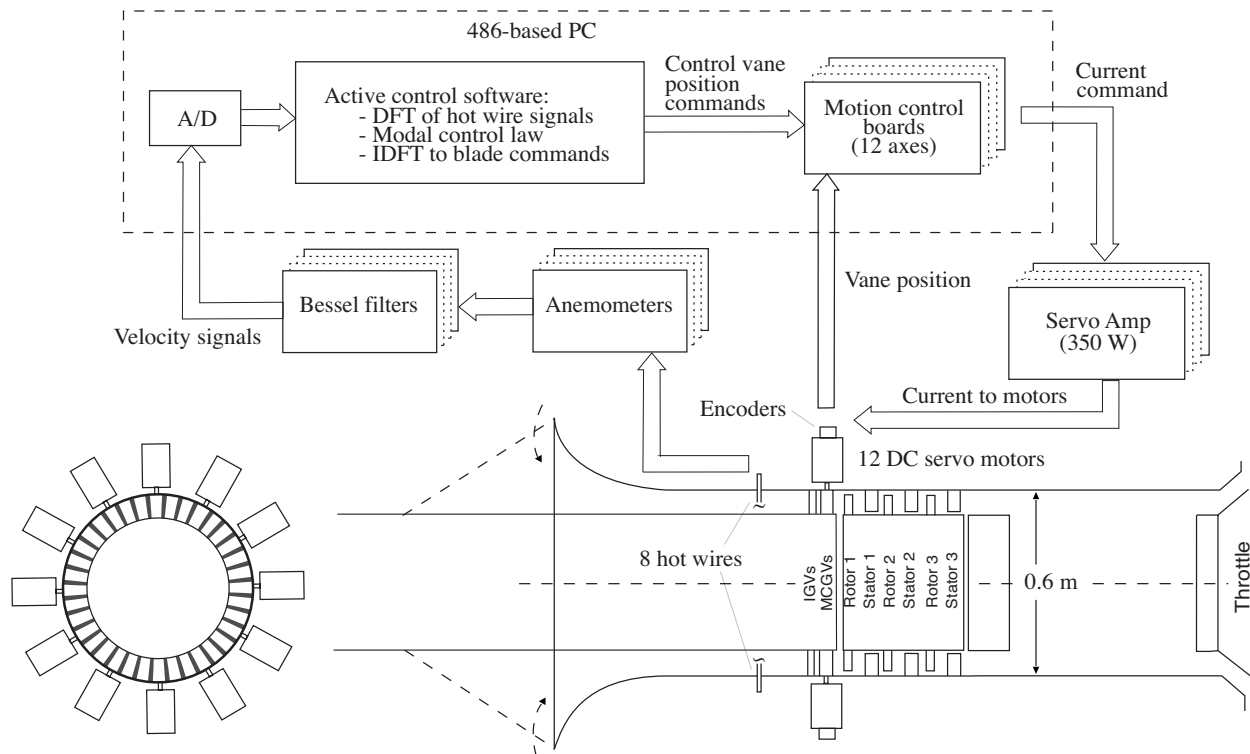


Fig. 5 Closed-loop control feedback path for three-stage compressor [25]

5 A Counterpoint Concerning Collaboration: The Benefits of “Putting Your Theories in Jeopardy”¹⁰

A counterpoint to the main theme provides an illustration of a way in which collaboration can also be a strong enabler for technical progress within a discipline. The control philosophy presented so far has been in terms of a scenario for instability associated with the growth of small disturbances. The results for compressor response, and the mode-by-mode ability of the controller to delay rotating stall, provide clear evidence for the reality of this mechanism. However, the linear theory fails to address the observation that some compressors encounter rotating stall in a

regime where the slope of the compressor pressure rise characteristic is negative, and the theory states that the flow is stable with respect to small disturbances.

Major steps to resolve this dilemma were taken at Cambridge by Day [28] who showed there was a qualitatively different process, with a different physical mechanism than the route described above. The disturbances associated with rotating stall inception in this second process were much shorter in circumferential extent than the modes (the relevant length scale was several blade pitches rather than the annulus circumference, which is the appropriate length scale for the modes). The disturbances were also seen in the tip region of rotors rather than being roughly two-dimensional, and they were large amplitude even when first observed at the measuring stations that were used. The time for

¹⁰Phrase due to Dr. D. C. Wisler.

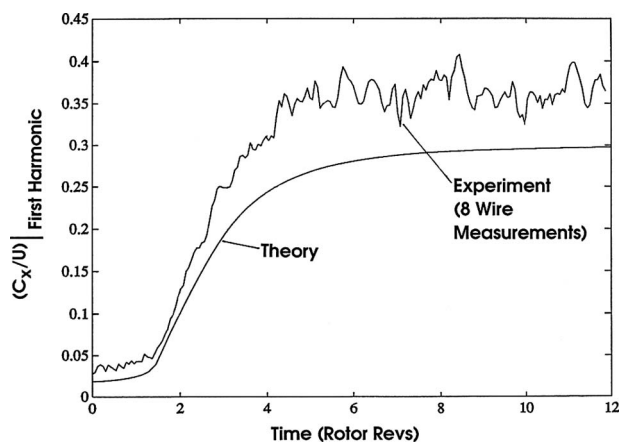


Fig. 6 Time evolution of first harmonic of the axial velocity in a three-stage compressor during rotating stall inception [24]

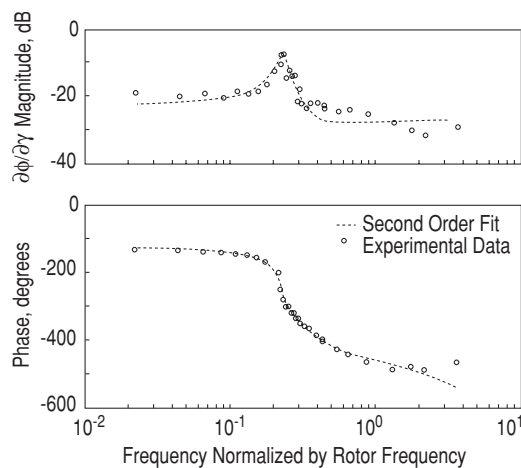


Fig. 7 Bode plot showing single-stage compressor response to a sine wave forcing excitation at $\phi=0.475$ [16]

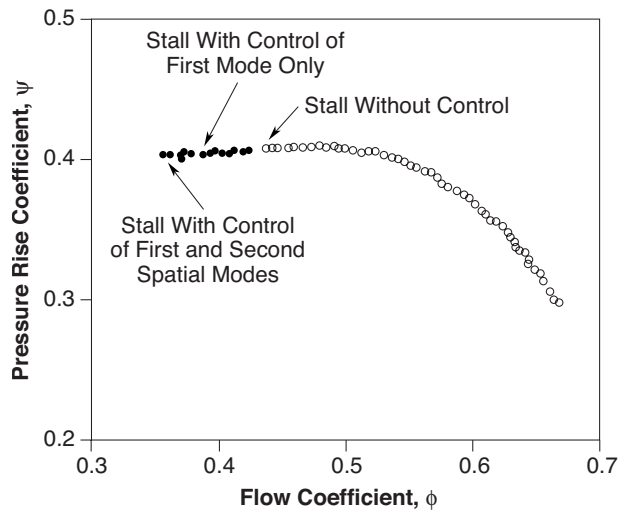


Fig. 8 Single-stage compressor characteristic with active control of first and second spatial modes [14]

growth to the mature form of the disturbance from first sensing of these “spikes”¹¹ was typically only several rotor revolutions. Figure 9 shows this behavior with data from eight hot wires equally spaced around the circumference in front of the compressor; here modal disturbances are not apparent prior to the onset of rotating stall. The spike disturbances were found on the negatively sloped portion of the compressor speed lines, another indication that the mechanism was different than the modal disturbances.

The existence of the two routes is important both for capturing the phenomenon in a rigorous prediction methodology and also with relevance to one’s ability to enhance compressor stability. The criterion for which of the two routes would occur was shown

¹¹The name is at least partly due to the way the disturbances appear in time-resolved data such as Fig. 9, in which the “emerging stall cell” can be characterized as a spikelike form.

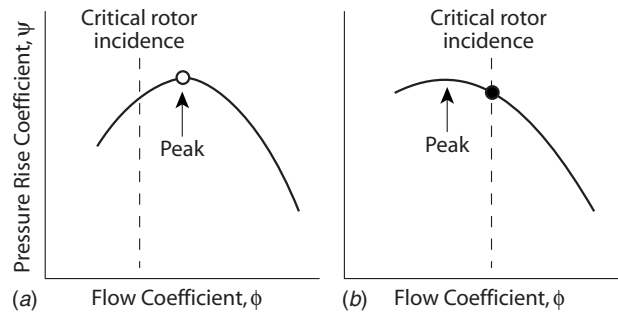


Fig. 10 Hypothesis for spike versus modal behavior as a route to rotating stall [29]; (a) modal stall inception, and (b) spike stall inception

in an incisive experimental investigation to be the incidence at the tip of the stalling rotor [29], and Fig. 10 gives the concept that underpins this result. The figure shows two situations: one in which the compressor characteristic slope becomes zero (or slightly positive) before critical incidence is reached (Fig. 10(a)), the other in which the critical incidence¹² occurs at a higher flow coefficient than the zero slope condition (Fig. 10(b)). In the former, the compressor is unstable to propagating modes; in the latter, modal perturbations decay so that rotating stall onset only occurs as a result of spikes.

Experimental data supporting this hypothesis are given in Fig. 11. The abscissa is the nondimensional slope of the compressor pressure rise curve, and the ordinate is the incidence angle at the tip of the stalling rotor in a three-stage compressor. Spike behavior is found at conditions of negative compressor pressure rise slope where the critical incidence for that compressor is exceeded. A subsequent computational study by Gong et al. [30] examined the evolution of the spikes and found that, as one would expect for a nonlinear system, the structure of a fully-developed single cell

¹²The value of the critical incidence depends on the compressor parameters; it is not the same for all compressors.

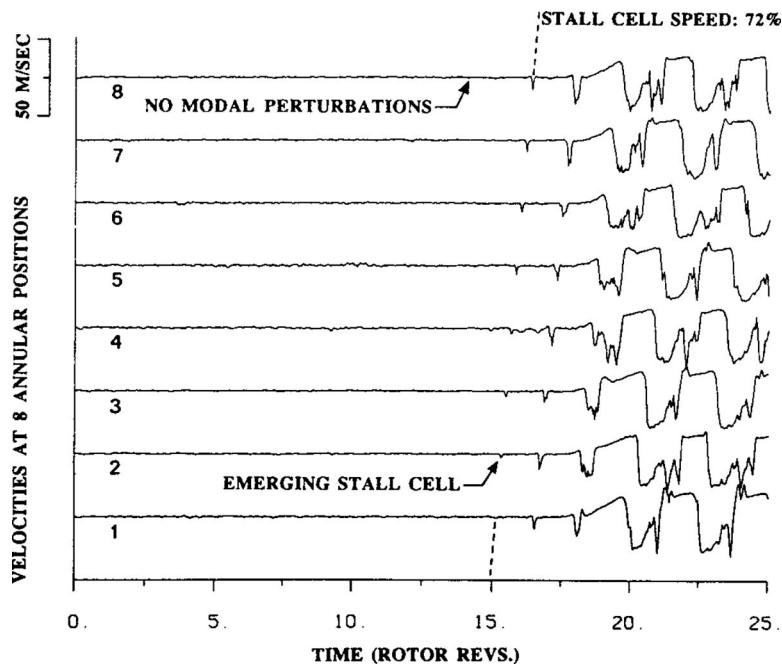


Fig. 9 Rotating stall onset preceded by “spikes;” hot wire measurements at eight circumferential positions upstream of a four-stage compressor [28]

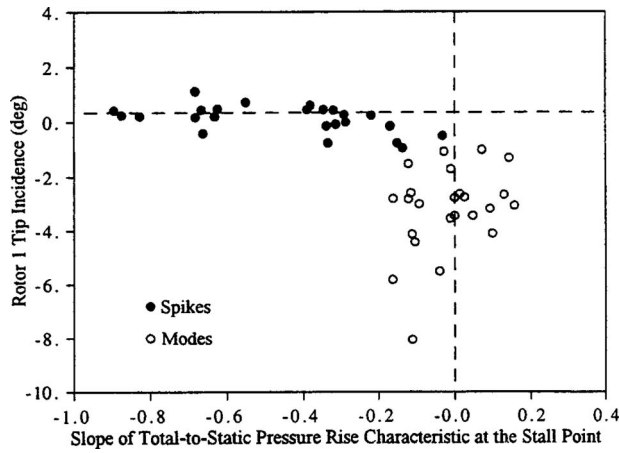


Fig. 11 Compressor stall inception results showing spike and modal behavior [29]

in a multistage compressor is not dependent on the initial route. For additional details of the fluid mechanic origins of this type of disturbance, see Vo et al. [31].

The connection to the theme of collaboration is that close interaction between research groups during the sorting out of two diverging views led to a dialectic “thesis, antithesis, synthesis” scenario. The initial wave description was the thesis, the description in terms of the spikes was the antithesis, and the work by Camp and Day [29] (and the later computations of Gong et al. [30]) was the synthesis unifying the two concepts into a more powerful and general statement about compressor rotating stall inception.

There is no claim here that the results could not have been achieved in isolation by one or the other group, or (perhaps more likely) by someone else. However, the observation is that a number of new statements were made about a complicated process in a period that is short on the academic time scale, and it is useful to look at possible contributing factors. Two of these seem key. First was the willingness to engage in substantive discussions including open sharing of ideas and thoughts (see the phrase in the section heading). Second, and much related, was an explicit respect for the other party’s technical arguments; there was a desire to understand how the two different views could be resolved rather than a “not invented here” attitude.¹³ The perspective was not a zero sum game but rather a recognition that even though someone else’s idea is correct it does not necessarily mean that your idea is not or detracts from any credit. Both these factors led to the rapid uptake of ideas into each group and the ability to use pieces of the concepts in new and different ways.

6 Application of Dynamic Control to More Complex Situations

The applications described to this point are appropriately regarded as a first phase of work on smart engines, with the aim of providing proof-of-concept demonstrations of *both* the theoretical framework and the ability to enhance stable flow range (i.e., both theory and execution). Once achieved, the focus shifted to technical challenges associated with implementation in devices that are closer to the actual product. The collaboration also expanded to organizations (NASA and GE), which had the capabilities to take on the different issues that arose from this shift.

¹³This is a concept whose importance is noted at the CEO level in major corporations: “We did have to kill not-invented-here. We have to make ‘reapplied with pride’ just as important a part of the culture as ‘invented here’” [32].

6.1 Compressor Operation With Inlet Distortion. The experiments introduced in Sec. 4 were conducted with a uniform inlet flow, but many compressor instability problems are associated with *inlet distortion*, commonly circumferential asymmetries in inlet stagnation pressure. With inlet distortion, the modes are no longer pure sinusoids (the analogy is wave propagation through a nonhomogeneous medium). The first mode, for example, will have not only a first Fourier harmonic (a single lobed sinusoidal component) but also a zeroth harmonic, a second harmonic, and so on. The control can no longer be single input, single output, but needs to be multiple input and multiple output. The control problem was examined by van Schalkwyk et al. [33], whose experiments showed the coupling of harmonics, providing additional evidence for the wave theory of rotating stall inception.

In connection with defining compressor response to distortion, a detailed investigation of the fluid mechanics associated with time-dependent inlet distortion was carried out at the GE Aerodynamics Research Laboratory [34]. The specific aspect examined was the severe adverse effect on compressor stability found with a rotating distortion, i.e., a distortion that propagated around the circumference [35]. This is seen when a low pressure compressor in a jet engine goes into rotating stall, imposing this type of distortion on the high pressure compressor.

It was known that for propagation speeds near the rotating stall speed, the stable flow range could decrease markedly. While it is plausible to associate the cause of the decrease as a resonance with the modes (which are the “natural frequencies” of the flow in the compressor annulus) some compressors exhibited another band of propagation speeds at a higher frequency, where there was also a large effect. This additional decrease in stability occurred at rotation near the speed of spike propagation. Detailed time resolved measurements indicated that the compressors, which exhibited modal stall behavior, showed only a single region of stability as a function of distortion rotation speed, while compressors exhibiting spike stall exhibited two regimes of decreased stability. The rotating distortions thus appeared able to excite either or both of the stall onset mechanisms.

6.2 Active Control of Transonic Turbomachinery. A second direction was toward representative engine Mach number regimes, in other words transonic turbomachines. Four distinct aspects of the problem have been addressed. Three of these were identification of wave structure in these machines, development of models for the compressible flow regime, and adaptation of the models to forms suitable for control [36,37]. For compressible flow, in contrast to the situation for incompressible flow, an infinite number of compressible propagating modes exist for *each* Fourier harmonic because there are now additional phenomena that support wave behavior. For a given harmonic (e.g., the first), there is thus more than one lightly damped mode which can exhibit instability. The issues associated with these modes were new and unanticipated, and they needed to be dealt with to achieve control of rotating stall.

The fourth aspect was implementation of the idea on a transonic fan, examined in experiments at NASA Glenn Research Center [38,39]. The rotor speed was high enough so moveable inlet guide vanes were not feasible and the fluid dynamic effectors were injectors fed by high bandwidth (400 Hz) valves. Flow range extensions of approximately 10% at a tip Mach number of unity were achieved. The experiments also showed that the modes of interest can have propagation speeds at or greater than the rotor speed, consistent with the behavior of the newly discovered class of disturbance modes in the compressible theory. It was also found that (with radial distortion) the inclusion of tip blowing could change the instability behavior from spikes to modes, in accord with the findings of Camp and Day [29] introduced in Sec. 5.

6.3 Engine Stability Management. Reference [40] discusses the development and full-scale engine rig demonstration of an active stability management system, yet another step in complex-

ity and scope. In the context of collaboration, the paper provides an illustration of a successful university-industry teaming, carried out as part of a targeted alliance strategy to provide the capability to tackle a product-oriented situation calling on a range of skills. The nine coauthors span different disciplines, in line with the sentiments expressed in the Abstract.

7 Lessons Learned

Several lessons can be taken from the history of the smart engine project. First is that an interdisciplinary (fluids, control, structures, and instrumentation) approach was needed for success because the “systems” aspects are critical. To this end, there was focus on teaming to create the end product, including the development of a viewpoint not as fluids people, controls people, or structures people, but rather smart engines people. Some of the difficulties in team building have already been noted: possible long start-up time, lack of a common language and of an appreciation for cross-disciplinary challenges, and a tension between the need for breadth across and depth within the different disciplines. To aid the process, it was important to have tangible recognition from project leaders for work in other than their home disciplines (in our case, the senior faculty were from the turbine engine aerodynamics community). One measure of the teaming can be seen from the reference list, which contains publications with three or more faculty and with colleagues from the industry and the government.

Second, as known all along by control practitioners, adding feedback control can change the system dynamics. A controlled compressor is thus a different machine with different stability properties. This difference can mitigate or remove design constraints that previously existed. The lesson for device experts is to recognize that some of the tried and true rules of thumb for fluid machinery may have to be reexamined in light of new approaches.

A third lesson relates to knowledge flow and learning. A feature not apparent when we started is that such flow can occur in (at least) two directions. The author’s initial (naive) view was that we would gather information from the various disciplines and meld it together to enable the development of an actively controlled compression system. What was found was quite different. The controlled compressor, in association with system identification techniques, is a new diagnostic tool for exploring compressor fluid dynamics, offering enhanced ways to obtain information. This is an exciting aspect with a benefit that does not need to wait for the development of flight-critical active control systems and that can carry over to other unsteady phenomena.

An illustration of the learning is found in forced response experiments such as those leading to Fig. 7. The original theory treated the unsteady flow in the blade rows as an inviscid channel flow, with the consequence that all modes were calculated to become unstable at the same flow coefficient. The forced response experiments showed this was not correct and that a simple first order rate-process description of the unsteady viscous response would be an appropriate addition, leading to the agreement between experiment and theory seen in Haynes et al. [25]. The use of the controlled compressor as a diagnostic tool thus provided insight into compressor fluid mechanics which was not previously achievable.

A fourth aspect, inherent in projects spanning a range of disciplines, is that there are fields with which some of the participating senior technical experts are not well acquainted. For academia this is a departure from the tradition in which faculty advisors use their expertise to guide the students. For the smart engine project, there were numerous situations in which the students in a given field were much more knowledgeable than most of the faculty. This posed no difficulties (except perhaps for the time needed to explain basic ideas to various faculty), but it can be a potential bar to creating the necessary linkages between technical experts.

Finally, the idea of demonstrating often, of aiming at specific targets rather than trying to formulate the most general (with the

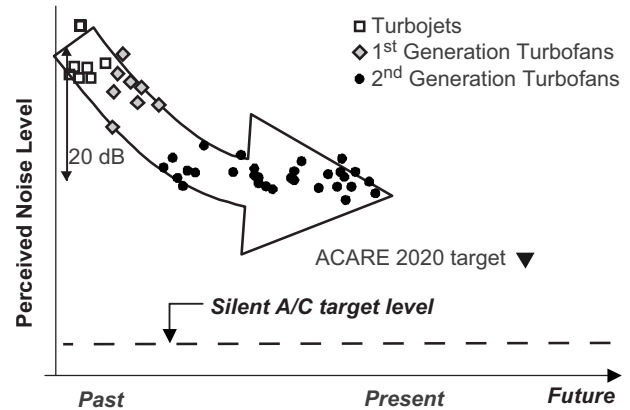


Fig. 12 Progress in noise reduction [45]

implication also of longest to develop) success goal for active control, and of having a clearly defined road map of objectives and barriers which is shared by all participants cannot be overemphasized. This carries over directly into the second case history, the silent aircraft initiative (SAI), where, although the project was very different, we will see many of the same points concerning collaboration.

8 The Silent Aircraft Initiative (SAI)

Aircraft noise is recognized as a major barrier in the expansion of airport operation [41,42]. The evolution of noise reductions shows a progression that had an initially steep downward trend but is now leveling out. As stated in Ref. [43], “the downward trend in noise exposure around airports of past years...has now flattened out at major airports. Virtually all the older aircraft have been phased out and, while the continued fleet renewal will introduce progressively quieter types, the benefit will be appreciably less than has been achieved from phasing out of Chapter 2 aircraft.” Figure 12 is one version of an often-seen chart showing the evolution of aircraft noise reductions.

SAI was created to address this challenge. The approach was to set the objective of a radical reduction in noise as a primary design criterion, taking a “clean sheet of paper” outlook. The specific project goal was to provide the conceptual design of an aircraft quiet enough to be imperceptible to people in the urban environment around airports. A key question is how such an aircraft would compare to existing and next generation aircrafts in terms of fuel burn and emissions, i.e., what would be the penalties for designing for low noise? As seen below, the answer was that, according to the design calculations, one can reduce both the noise and the fuel burn.

A number of noise limitation targets have been set by the aviation industry, but SAI aimed at a major step beyond these. This stretch goal called for highly integrated airframe and engines as well as for operations and design optimized together for low noise, implying that the capabilities of a range of partners in academia, industry, and government would be needed. From the beginning, therefore, the project was viewed as involving collaboration between organizations and between individuals with different skills and interests. The scope of work included airframe and engine research, ways to reduce noise by changing takeoff and approach procedures, and an economic assessment of the scenarios under which the aircraft would present an attractive business case to an airline and of the possible benefits to the UK economy, both nationally and regionally.

SAI was one of the Cambridge-MIT Institute’s (CMI) Knowledge Integration Communities (KICs), research communities exploring new ways for the academia, industry, and government to

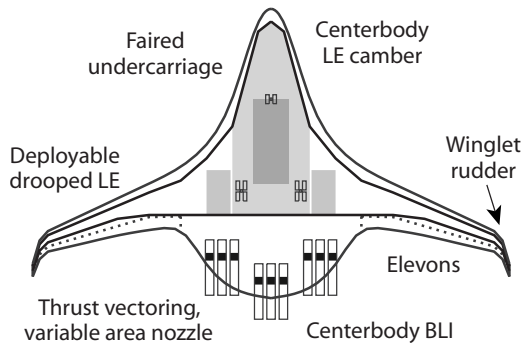


Fig. 13 SAI conceptual design: major features of SAX-40 [44]

work together.¹⁴ The role of the KIC is to foster linkages and two-way flows of information between academic researchers and their colleagues in commerce that enhance the impact of the research. SAI community was comprised of airframers, engine manufacturers, airport and airline operators, air traffic controllers, regulators and measurement specialists at over 30 partners, in addition to the academics.

The discussion of the smart engines research was presented along roughly chronological lines. For SAI, however, which had a compressed time frame (three years) and which was seen from the start as an enterprise with different efforts in parallel, it is more appropriate to describe the overall project from the perspective of the design results and then examine the critical aspects in achieving these. This is done in what follows.

9 Features of the Silent Aircraft Design

The aircraft mission is to carry 215 passengers with a range of 5000 nautical miles at a cruise Mach number of 0.8. The conceptual design, denoted as SAX-40 (SAX=silent aircraft experimental) is depicted in Fig. 13. The aircraft has a cruise ML/D of 20 (for reference the Boeing Phantom Works Blended Wing Body has an ML/D of 17–18 and the Boeing 777 has an ML/D of 17) [44]. The span is 67.5 m including winglet and the maximum take-off weight (MTOW) is 151,000 kg.

The SAX-40 airframe has major differences from civil aircraft either in current use or under current development. There are conventional supercritical wings but the fuselage is a lifting body with no flaps and no tail. The aircraft is propelled by high bypass ratio turbofans (cruise bypass ratio of 12) embedded in the fuselage. There are nine geared fans driven by three gas generators so each inlet feeds one turbofan engine driving the other two fans in that cluster. Figure 14(a) shows a top view of the engines, indicating the gearing for the cluster (of three fans/one engine) that sits in each of the three intakes. Figure 14(b) shows a side view of the engine in the duct, to illustrate the length of duct available for acoustic liners. The overall conceptual design is aimed at the 2030 time frame, but part of the project strategy is that some of the quiet technologies could be incorporated nearer term.

The features of the silent aircraft have been reported in some depth at a public dissemination meeting and in a special session at the 2007 AIAA Aerospace Sciences Meeting [44–50]. Only a summary of the performance and underpinning technology is therefore given.

For the concept aircraft, the community noise levels are estimated not to exceed 63 dBA for typical missions, comparable to the background noise in urban daytime environments. As described by Hileman et al. [44] a reduction in cumulative noise

¹⁴The Cambridge-MIT Institute was a UK government-supported joint venture between Cambridge University and MIT. SAI was one of a number of projects that CMI supported in areas (such as aerospace) in which the UK industry has a demonstrable competitive position.

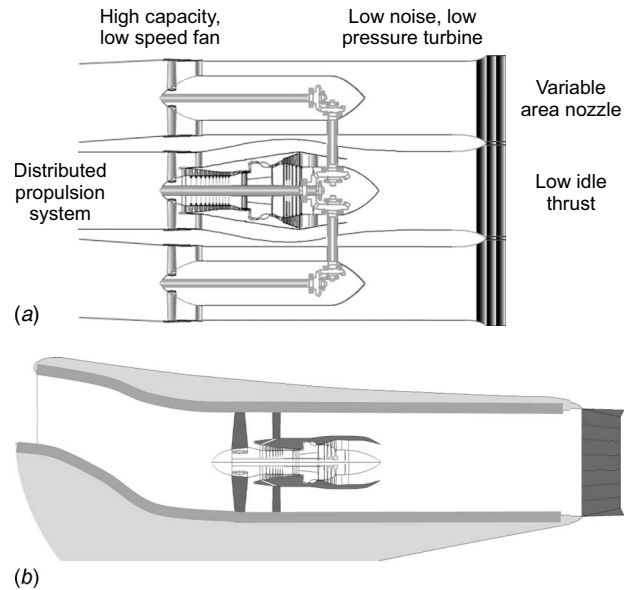


Fig. 14 Propulsion system for the SAX-40 design [47]; (a) top view of gas generator and two gear-driven fans for each inlet cluster, and (b) side view of engines in duct

(sideline, takeoff, and approach) of 75 cumulative EPNdB is estimated relative to the ICAO Chapter 4 requirement. The estimated noise levels of SAX-40, computed according to the FAA procedures documented in Part 36, are compared to the existing fleet in Fig. 15 [44].¹⁵

The estimated fuel burn is shown in Fig. 16 [46], in terms of energy per airline-seat-kilometer. The non-SAX data is from Ref. [51]. The predicted fuel use relative to current civil aircraft is 124 passenger-miles/gal compared to 101 passenger-miles/gal for a 777, a 23% increase.¹⁶ An important point is that further fuel efficiency, even with respect to this saving, would be expected if the aircraft were targeted to minimize fuel consumption rather than noise.

9.1 Enabling Technologies. The low noise is not achieved by a single design feature but results from many disciplines integrated into the design and operation of a noise-minimizing aircraft system. These are portrayed in Fig. 17 [46], which indicates that a

¹⁵Tone corrections were neglected because tonal noise could not be computed for the airframe noise sources.

¹⁶For reference, the Toyota Prius hybrid car carrying two passengers is reported as having a fuel burn of 120 passenger-miles/gal [44].

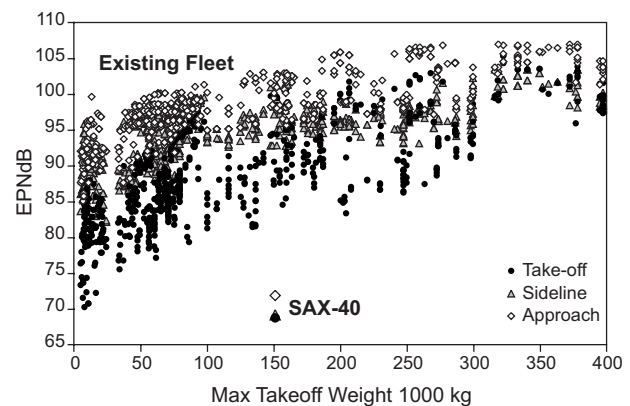


Fig. 15 Effective perceived noise level (EPNL) for existing fleet and (estimated) for SAX-40 [44]

	Passenger Miles per gallon	ML/D
SAX-40	~124	20.1
Toyota Prius hybrid car	~120 w/ 2 people	---
Boeing 777	86 - 101	15.5
Boeing 707	46 - 58	13.5

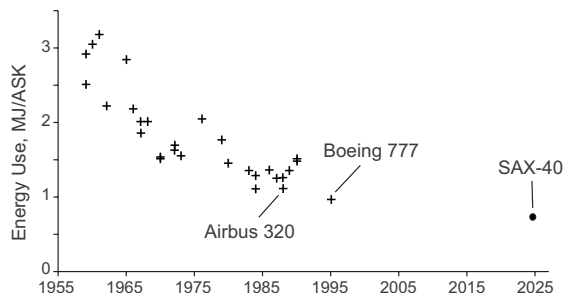


Fig. 16 Estimated fuel burn for SAX-40 [44]

number of aspects of the aircraft must undergo major alteration to give the desired noise reduction. Many of the noise reduction design choices are also beneficial in terms of fuel burn, as implied in Fig. 18, which gives the corresponding technologies for decreased fuel burn.

The rationale for the features of the aircraft and propulsion system can be briefly listed as follows:

- *Efficient airframe centerbody design.* On approach the airframe generates half the noise. To create the desired noise reductions, the aircraft has conventional supercritical wings that blend into a lifting body fuselage. As described by Hileman et al. [44] “the leading edge region of the

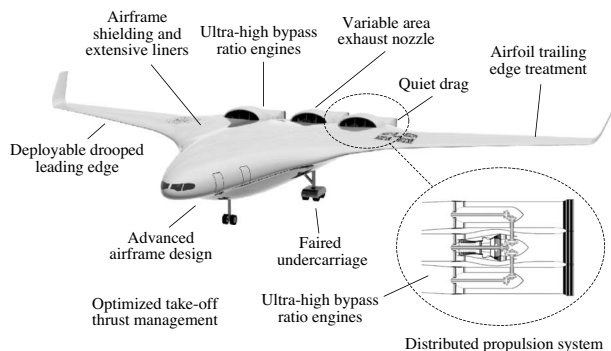


Fig. 17 Enabling technologies for noise reduction [46]

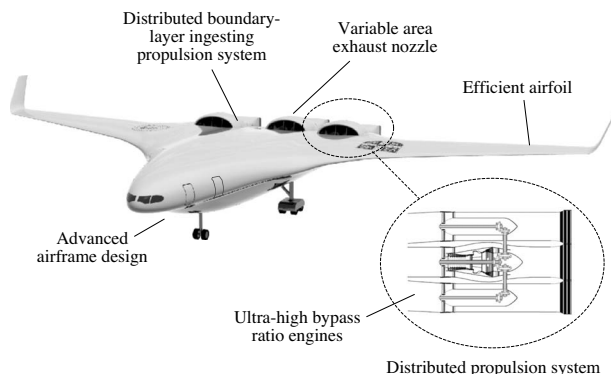


Fig. 18 Enabling technologies for decreased fuel burn [46]

centerbody...achieves an elliptical span load on cruise yielding a 15% improvement in ML/D compared to current blended-wing body aircraft design.”

- *Airfoil trailing edge treatment.* Trailing edge brushes [52] have been found to reduce scattering of turbulence from the trailing edges. The estimated trailing edge noise reduction for SAX-40 is 4 dBA.
- *Faired undercarriage.* The undercarriage noise sources can be mitigated by partially enclosing wheels and axles. The estimated noise reduction from the use of fairings is 6 dBA.
- *Deployable drooped leading edge.* A deployable drooped leading edge can provide the required lift during low speed operations without the use of slats, thus eliminating slat noise. The drooped leading edge is stowed at cruise. Deployment power levels are comparable to a conventional slat. (This configuration is used on the Airbus A380.)
- *Quiet drag (needed on approach) via increased induced drag.* Large wing area and high angle of attack provide the lift at low speed without using flaps, eliminating a major source of airframe noise on takeoff and landing. A combination of elevons and thrust vectoring can increase the induced drag to the required level, while trimming the aircraft.
- *Embedded, aircraft boundary layer ingesting, distributed propulsion system.* Boundary layer ingestion allows a potential reduced fuel burn [48,53]. There is a trade between this gain and the losses due to increased duct length for noise attenuation. Embedding the engines within the airframe implies a need for a high level of airframe-engine integration because the airframe and engine flow is much more strongly coupled than in tube and wing designs. In particular, there are several major challenges associated with the ingestion of the fuselage boundary layer and the creation of a nonuniform flow into the engine (distortion), which must be addressed for a practical aircraft configuration.
- *Variable area exhaust nozzle to permit ultra-high bypass ratio, low fan pressure ratio, engines.* To reduce the engine noise at takeoff, the engine exhaust velocity must be decreased. To ensure fan operability at the low fan pressure ratio needed for low exhaust velocity, the exhaust nozzle is designed to have variable area, with takeoff bypass ratio of 18 and cruise bypass ratio of 12. The low engine rotational speed during approach enabled by the variable nozzle reduces the rearward fan noise and the airframe drag requirements.
- *Airframe shielding of engine noise.* Placing the engines above the airframe prevents engine noise from reaching the observer. Engine forward noise sources are virtually eradicated on the ground.
- *Optimized extensive liners.* The embedded propulsion system allows smaller engine diameter and thus increases non-dimensional (length/diameter) duct length. The long inlet and exit ducts allow additional acoustic liners, compared to conventional nacelles, to absorb engine noise. The use of a multisegment liner design provides an estimated 20 dBA reduction of engine noise.
- *Optimized takeoff thrust management.* Thrust, climb angle, and nozzle area would be continuously varied during takeoff to maintain a set noise level outside the airport boundary, allowing the specified noise level to be met all through departure.
- *Low noise approach operational procedures.* The sound power level (SPL) scales as $SPL \propto ((\text{velocity})^n / (\text{distance})^2)$, with the exponent n between 5 and 6. Achieving low noise involves low speed approach (decreased velocity), displaced threshold for landing (increased distance), and a continuous descent approach (increased distance and lower engine thrust).

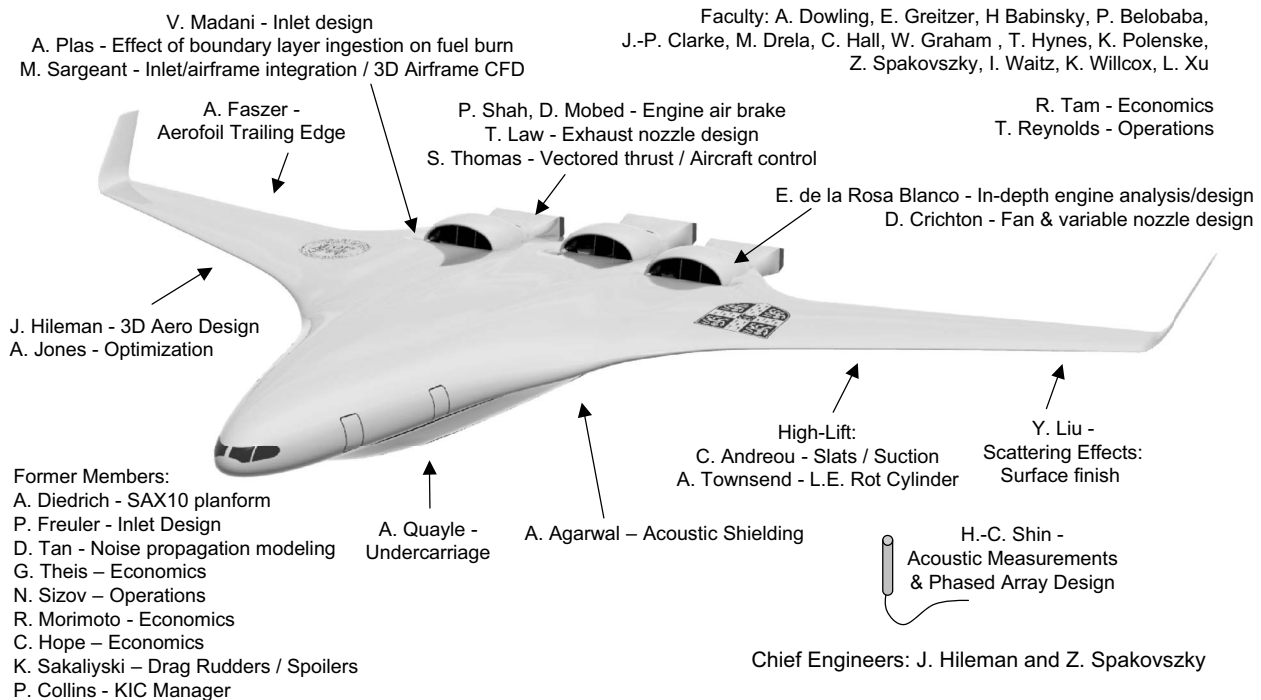


Fig. 19 Cambridge/MIT silent aircraft team

10 The SAI Collaborative Process

10.1 University-Industry-Government Interaction. A range of skills and interests beyond those of the two universities were needed to address the above technologies and the collaboration included regulators, airport operators, airlines, aerospace manufacturers, and representatives of community groups. Our observation in this regard is that SAI has been an instructive and useful experiment in academic-industry interactions on several levels, from strategic planning and decisions (input from the KIC members had a direct impact on the project goals) to detailed working level technical interchange.

There were formal meetings of all the KIC partners at roughly eight-month intervals, but interaction with some organizations was much more frequent and in-depth in terms of access to in-house design codes and consulting help. For example, Boeing made available their multidisciplinary design optimization code, WingMOD, which optimizes the aircraft platform for a given mission, and academic researchers were able to use Rolls-Royce design, performance, and noise evaluation tools to examine concepts for potential engine designs. In addition Boeing, Rolls-Royce, NASA, and ITP conducted reviews and provided feedback on the designs.

As mentioned previously, a team project that is carried out as part of student degree programs contains a set of goals, which has an inherent tension. Each student needs to develop the new ideas that comprise his or her thesis to receive a degree; these need to be visible as a contribution that the particular student has made. However, there is also a need for the research results to be integrated into a workable design concept. To help with this latter issue, Fig. 19, put together early in the project and modified as necessary, shows how the contributions of students, staff, and faculty fit into the overall design. The figure, which appeared in a number of presentations and which was almost an icon for the project, provided a very real framework for discussions of responsibility and deliverables, strengthening the ability to work as an integrated product team.

Weekly videoconferences, and even more regular email and telephone contact, were essential for this design integration. Also essential was a clear, mutual, and explicit understanding of advi-

sor and student as to what the expected intellectual contribution for the thesis would be and how it was consistent with participation in the overall design.

During several stages in the project, there were design decisions to be taken, and ad hoc task forces were formed to address these. Major questions dealt with in this manner were: "What should be the design range?" and "Should the engines be podded or embedded?" The task forces were focused activities of a few weeks duration, drawing on members from all relevant aspects of the research and involving exchanges of personnel, thus (again) building working relationships and diffusing "we-they" perspectives.

Collaboration was integral throughout the project, but it was perhaps most critical in the area of aircraft operations, in which the team in Operations worked to develop an advanced form of continuous descent approach (CDA) for current aircraft to be assessed in trials at Nottingham East Midlands Airport [54]. Putting the new procedures in place was a many-step task that required agreements between air traffic controllers, regulators, suppliers, airport operators, and airlines; it was an example of something that could not have been achieved without this type of partnership.

The silent aircraft project brought industry, academia, and other stakeholders together around a "grand challenge" that captured the enthusiasm and imagination of the participants, who felt they were involved in something special. The KIC included industry, government, and academia and provided an exciting way to address problems with a large reach and a potential for step-change improvements. In addition to the conceptual design for a new type of aircraft, some of the technologies developed could be introduced into more incremental aircraft and engine designs. In short, collaboration and teaming occurred in basically all aspects of the project and because of this SAI was very much an enterprise in which the whole was greater than the sum of the separate parts.

11 Some Additional Perspectives and the Connection With IGTI

The two project histories have been put forward as representatives of a more general application, and it is useful to now place the ideas in a broader context. This will be done along two different lines. One is to give an indication of the extent to which these

ideas have impacted by including perspectives from outside the gas turbine industry that are relevant to the overall theme. Second, recognizing that a primary constituency is IGTI members, we can briefly make the connection with other activities of individuals and organizations within our professional society.

There are many examples that show the strong influence of the collaborative process on engineering. Space permits discussion of a few only, chosen to illustrate different venues: research, technology development, and business practices. While these cannot be claimed to prove the case, what can be said is that there is much other documentation that can be assembled to support the point.

In *research*, the most recent newsletter from my graduate school contains an article about a materials engineering professor recognized for collaborative research, as noted in the description of the committee that chose him as recipient of the ASME Timoshenko Award. This individual comments: "Collaboration is unquestionably effective in research. The synergy of multiple minds working on a problem can be huge, especially when the individuals bring different knowledge and skills to the table."

In *technology*, a recent book by Broers [55] makes a clear case concerning the need for interaction all across the development process of high technology devices. This is the only way to obtain the necessary information to enable focus on the critical issues that stand in the way of product development. (The second of six chapters in the book is, in fact, entitled "Collaboration.")

A historical trend described by Broers [55] is that the large industrial laboratories, which had a major scientific presence when he started his career, have either ceased to exist or have changed their focus to product development. As a consequence, it is now more likely that important new ideas will originate outside of a company's laboratory. Because of this, the aim is to partner with other research entities and draw on "the entire world of science and technology" [55].

The partnering theme and its relation to innovation (defined as "how companies utilize and advance technologies to create new products and services") can also be seen in studies of several corporations [56]. The open innovation paradigm described is one in which there is a strong linkage between the technical personnel within a company and universities and other research centers outside the company.

The third aspect, the way in which collaboration affects the environment for conducting *business*, is described in compelling detail by Friedman in the book *The World is Flat* [57], with one chapter entitled "From Command and Control to Collaborate and Connect," and another with a section "Open Sourcing: Self Organizing Collaborative Communities." Friedman did not just say that collaboration and partnerships are useful, he stated flatly that this is now the way the business world works; not to recognize and act on this decreases one's competitive position.

As the final part of the discussion, I would like to focus on IGTI and the interests of its members. For gas turbine engine manufacturers and suppliers, collaboration in product development is well established. The interactions, which occur to bring an engine to certification, in both civil and military aeroengines, are now often multinational and multicompany. This is a part of the business we are in.

Participants in IGTI conferences have also seen the emphasis on teaming and collaboration in major presentations at the meetings. The topic of the keynote address in the 2006 conference was "The Global Market and Collaborative Ventures." A large part of this is the teaming between companies just referred to, but an important additional trend is that both aeroengine and land-based gas turbine companies are now interested in developing strategic relationships with universities. One of the keynote presentations, in fact, described the background, rationale, and operation of an engine company's university connections, specifically the targeting of strategic needs relating to different technologies and the formation of long-term relationships with universities having expertise in those areas.

A different sort of successful joint project was highlighted in a previous IGTI Scholar Lecture [58] on turbine heat transfer and aerodynamics. That lecture discussed an investigation of turbine vane-blade interaction, with Allison (now Rolls-Royce) as the main industry participant, Ohio State the main academic organization, and other industry and academic collaborators. One result was multiauthor papers with participants from two (competing) engine manufacturers, teaming together to define answers to an important and longstanding problem.

The partnerships mentioned in the different parts of this paper are all offered as illustrations of the way in which gas turbine engine research can benefit from collaboration. There are differences in research questions, specific objectives, organizations, and team members, but an attribute in all was that the resulting enterprise had the capability to address successfully a difficult problem that was of high interest to the technical community. Cutting edge problems in our industry increasingly bridge across disciplines and across the technical skills of individuals; in-depth collaboration to attack them will be more and more a key part of the professional activity of IGTI members.

12 Summary and Conclusions

The content and process of two different multidisciplinary projects have been described, as a way to illustrate features, and benefits, of teaming and collaboration in research. One project was a decade-long investigation on the phenomena of compressor stability enhancement, leading to a number of basic results and first-of-a-kind demonstrations. The other was a three-year development of the conceptual design of an aircraft whose noise would be imperceptible outside an airport in an urban environment. Both projects involved industry and government organizations as members of the collaboration enterprise. A common thread was that a team approach, subscribed to by the participants, was essential to the program success. In this, key aspects were:

- an emphasis on the overall project goal
- a system, rather than component or discipline, or focus
- an appreciation of cross-disciplinary challenges, including a willingness by experts in a given field to address the intellectual, technical, and organizational issues inherent in research, which spans several engineering disciplines outside this field
- a willingness to accept (and perhaps even embrace) ideas from outside one's particular research group, field, or organization
- a realization that although collaboration can have its own overhead there can be a major return on the investment

Acknowledgment

The smart engines work and the SAI research and design information are the results of contributions from a number of individuals, many of whom are listed in the authorship of the cited papers. It has been a pleasure to work with the students on these projects. In addition I would like to mention my gratitude to (in alphabetical order of organization) J. D. Paduano (Aurora Flight Sciences); R. H. Liebeck (Boeing Phantom Works), F. E. Marble (Caltech), I. J. Day, A. P. Dowling (the Cambridge lead for SAI), J. E. Ffowcs Williams, C. A. Hall, T. P. Hynes, and J. P. Longley (Cambridge University), D. L. Gysling (Cidra); D. C. Wisler (GE Aircraft Engines); N. A. Cumpsty (Imperial College); A. H. Epstein, J. I. Hileman, Z. S. Spakovszky, C. S. Tan, I. A. Waitz (MIT); A. J. Strazisar (NASA Glenn Research Center); G. J. Hendricks (Pratt & Whitney). I also thank J. J. Adamczyk and R. J. Shaw (NASA), M. G. Dunn (OSU), and reviewers, for useful comments and D. I. Park for superb help in preparing the manuscript.

Financial support for the smart engines work was from the Air Force Office of Scientific Research, Office of Naval Research, NASA Glenn Research Center, Pratt & Whitney, and U.S. Army Propulsion Directorate, Aviation Systems Command. Financial

support for the silent aircraft project has come from the Cambridge-MIT Institute and from NASA Langley Research Center. All these sources are gratefully acknowledged. I would also like to express my appreciation to Sir William Hawthorne who gave me the initial opportunity, many years ago, to embark on collaborations across the Atlantic. Finally the author is grateful to the IGTI for allowing him the opportunity to present the Scholar Lecture on a topic, which has been an important and enjoyable part of his career.

References

- [1] Hawthorne, W. R., 1957, "Some Aerodynamic Problems of Aircraft Engines," *J. Aeronaut. Sci.*, **24**, pp. 713–730.
- [2] Koff, B. L., 2004, "Gas Turbine Technology Evolution: A Designer's Perspective," *J. Propul. Power*, **20**, pp. 577–595.
- [3] Cumpsty, N. A., and Greitzer, E. M., 2004, "Ideas and Methods of Turbomachinery Aerodynamics: A Historical View," *J. Propul. Power*, **20**, pp. 15–26.
- [4] Bridgeman, P. W., 1961, *The Nature of Thermodynamics*, Harper, New York.
- [5] Armstrong, J. A., 1994, "Is Basic Research a Luxury Our Society Can No Longer Afford," *The Bridge*, **24**(2), pp. 9–16.
- [6] Epstein, A. H., 1986, "Smart Engine Components: A Micro in Every Blade?" *Aerosp. Am.*, **24**(1), pp. 60–64.
- [7] Ffowcs Williams, J. E., 1984, "Review Lecture: Anti-Sound," *Proc. R. Soc. London*, **395**, pp. 63–88.
- [8] Epstein, A. H., Ffowcs Williams, J. E., and Greitzer, E. M., 1989, "Active Suppression of Aerodynamic Instabilities in Turbomachines," *J. Propul. Power*, **5**(2), pp. 204–211.
- [9] Katzenback, J. R., and Smith, D. K., 1993, "The Discipline of Teams," *Harvard Business Review Reprint Collection, Harvard Business Review's Ten Most Requested*, Product No. 49512, pp. 13–25.
- [10] Emmons, H. W., Pearson, C. E., and Grant, H. P., 1955, "Compressor Surge and Stall Propagation," *Trans. ASME*, **77**, pp. 455–469.
- [11] Greitzer, E. M., 1981, "The Stability of Pumping Systems—The 1980 Freeman Scholar Lecture," *ASME J. Fluids Eng.*, **103**, pp. 193–242.
- [12] Hansen, K. E., Jorgensen, P., and Larsen, P. S., 1981, "Experimental and Theoretical Study of Surge in a Small Centrifugal Compressor," *ASME J. Fluids Eng.*, **103**, pp. 391–395.
- [13] Pinsley, J. E., Guenette, G. R., Epstein, A. H., and Greitzer, E. M., 1991, "Active Stabilization of Centrifugal Compressor Surge," *ASME J. Turbomach.*, **113**, pp. 723–732.
- [14] Paduano, J. D., Epstein, A. H., Valavani, L., Longley, J. P., Greitzer, E. M., and Guenette, G. R., 1993, "Active Control of Rotating Stall in a Low-Speed Axial Compressor," *ASME J. Turbomach.*, **115**, pp. 48–56.
- [15] Greitzer, E. M., 1998, "Smart Jet Engines: Case History of a Multidisciplinary Research Program," *JSME Int. J.*, Ser. B, **41**(1), pp. 90–102.
- [16] Paduano, J. D., Greitzer, E. M., and Epstein, A. H., 2001, "Compression System Stability and Active Control," *Annu. Rev. Fluid Mech.*, **33**, pp. 491–517.
- [17] Greitzer, E. M., Tan, C. S., and Graf, M. B., 2004, *Internal Flows: Concepts and Applications*, Cambridge University Press, Cambridge.
- [18] Gysling, D. L., Dugundji, J., Greitzer, E. M., and Epstein, A. H., 1991, "Dynamic Control of Centrifugal Compressor Surge Using Tailored Structures," *ASME J. Turbomach.*, **113**, pp. 710–722.
- [19] Paduano, J. D., Greitzer, E. M., Epstein, A. H., Guenette, G. R., Gysling, D. L., Haynes, J., Hendricks, G. J., Simon, J. S., and Valavani, L., 1993, "Smart Engines: Concept and Application," *Integr. Comput. Aided Eng.*, **1**, pp. 3–28.
- [20] Cumpsty, N. A., 2004, *Compressor Aerodynamics*, Kreiger Publishers, New York.
- [21] Moore, F. K., and Greitzer, E. M., 1986, "A Theory of Post Stall Transients in Axial Compressors: Part I—Development of the Equations," *ASME J. Eng. Gas Turbines Power*, **108**, pp. 68–76.
- [22] Greitzer, E. M., and Moore, F. K., 1986, "A Theory of Post Stall Transients in Axial Compression Systems: Part II—Application," *ASME J. Eng. Gas Turbines Power*, **108**, pp. 231–239.
- [23] McDougall, N. M., Cumpsty, N. A., and Hynes, T. P., 1990, "Stall Inception in Axial Compressors," *ASME J. Turbomach.*, **112**, pp. 116–125.
- [24] Garnier, V. H., Epstein, A. H., and Greitzer, E. M., 1991, "Rotating Waves as a Stall Inception Indication in Axial Compressors," *ASME J. Turbomach.*, **113**, pp. 290–301.
- [25] Haynes, J. M., Hendricks, G. J., and Epstein, A. H., 1994, "Active Stabilization of Rotating Stall in a Three-State Axial Compressor," *ASME J. Turbomach.*, **116**, pp. 226–239.
- [26] Gysling, D. L., 1993, "Dynamic Control of Rotating Stall in Axial Compressors Using Aeromechanical Feedback," MIT Gas Turbine Laboratory Report No. 219.
- [27] Gysling, D. L., and Greitzer, E. M., 1995, "Dynamic Control of Rotating Stall in Axial Flow Compressors Using Aeromechanical Feedback," *ASME J. Turbomach.*, **117**, pp. 307–319.
- [28] Day, I. J., 1993, "Stall Inception in Axial Flow Compressors," *ASME J. Turbomach.*, **115**, pp. 1–9.
- [29] Camp, T., and Day, I. J., 1998, "A Study of Spikes and Modal Stall Phenomena in a Low-Speed Axial Compressor," *ASME J. Turbomach.*, **120**, pp. 393–401.
- [30] Gong, Y., Tan, C. S., Gordon, K. A., and Greitzer, E. M., 1999, "A Computational Model for Short Wavelength Stall Inception and Development in Multistage Compressors," *ASME J. Turbomach.*, **121**, pp. 726–734.
- [31] Vo, H. D., Tan, C. S., Greitzer, E. M., 2005, "Criteria for Spike Initiated Rotating Stall," *ASME Paper No. GT2005-68374*.
- [32] Colvin, G., 2006, "An Interview with P&G and GE CEOs Lafley and Immelt," *FORTUNE*, C-Suite Strategies website, November 27.
- [33] van Schalkwyk, C. M., Paduano, J. D., Greitzer, E. M., and Epstein, A. H., 1997, "Active Stabilization of Axial Compressors with Circumferential Inlet Distortion," *ASME J. Turbomach.*, **120**, pp. 431–439.
- [34] Longley, J. P., Shin, H.-W., Plumley, R. E., Silkowski, P. D., Day, I. J., Greitzer, E. M., Tan, C. S., and Wisler, D. C., 1996, "Effects of Rotating Inlet Distortion on Multistage Compressor Stability," *ASME J. Turbomach.*, **118**, pp. 181–188.
- [35] Kozarev, L. A., and Federov, R. M., 1983, "Aspects of the Appearance and Elimination of Breakdown in an Axial-Flow Compressor in the Presence of a Rotating Non-Uniformity at the Inlet," *Izvestiya VUZ Avioatsionnaya Tekhnika (IzAvT)*, **26**(1), pp. 33–37.
- [36] Tryfonidis, M., Etchevers, O., Paduano, J. D., Epstein, A. H., and Hendricks, G. J., 1995, "Pre-Stall Behavior of Several High-Speed Compressors," *ASME J. Turbomach.*, **117**, pp. 62–80.
- [37] Feulner, M. R., Hendricks, G. J., and Paduano, J. D., 1994, "Modeling for Control of Rotating Stall in High Speed Multi-Stage Axial Compressors," *ASME Paper No. 94-GT-200*.
- [38] Weigl, H. J., Paduano, J. D., Frechette, L. G., Epstein, A. H., Greitzer, E. M., Bright, M. M., and Strazisar, T. J., 1998, "Active Stabilization of Rotating Stall and Surge in a Transonic Single Stage Axial Compressor," *ASME J. Turbomach.*, **120**, pp. 625–636.
- [39] Spakovszky, Z. S., Weigl, H. J., Paduano, J. D., van Schalkwyk, C. M., Suder, K. L., and Bright, M. M., 1999, "Rotating Stall Control in a High-Speed Stage With Inlet Distortion I: Radial Distortion, and II: Circumferential Distortion," *ASME J. Turbomach.*, **121**, pp. 510–524.
- [40] Christensen, D., Catlin, P., Gutz, D., Szucs, P. N., Wadia, A. R., Armor, J., Dhingra, M., Neumeier, Y., and Prasad, J. V. R., 2006, "Development and Demonstration of a Stability Management System for Gas Turbine Engines," *ASME Paper No. GT-2006-90324*.
- [41] Green, J. E., 2006, "Civil Aviation and the Environment: The Next Frontier for the Aerodynamicist," *Aeronaut. J.*, **110**, pp. 469–486.
- [42] Walker, R. S., Aldrin, B., Bolen, E. M., Buffenbarger, R. T., Douglass, J. W., Fowler, T. K., Peters, F. W., Hamre, J. J., Schneider, W., Stevens, R. J., Tyson, N. deG., and Wood, H. R., 2002, Final Report of the Commission on the Future of the United States Aerospace Industry.
- [43] Greener by Design Science and Technology Sub-Group, 2005, *Air Travel: Greener by Design, Mitigating the Environmental Impact of Aviation: Opportunities and Priorities*, Royal Aeronautical Society, London.
- [44] Hileman, J., Spakovszky, Z., Drela, M., and Sargeant, M., 2007, "Airframe Design for 'Silent Aircraft'," *AIAA Paper No. AIAA-2007-0453*.
- [45] Crichton, D., and Hileman, J., 2007, "Design and Operation for Ultra Low Noise Take-Off," *AIAA Paper No. AIAA-2007-0456*.
- [46] Dowling, A., and Greitzer, E., 2007, "The Silent Aircraft Initiative—Overview," *AIAA Paper No. AIAA-2007-0452*.
- [47] de la Rosa Blanco, E., and Hall, C., 2007, "Challenges in the Silent Aircraft Engine Design," *AIAA Paper No. AIAA-2007-0454*.
- [48] Plas, A., Madani, V., Sargeant, M., Crichton, D., Greitzer, E., Hall, C., and Hynes, T., 2007, "Performance of a Boundary Layer Ingesting (BLI) Propulsion System," *AIAA Paper No. AIAA-2007-0450*.
- [49] Hileman, J., Spakovszky, Z., and Reynolds, T., 2007, "Airframe Design for 'Silent Aircraft'," *AIAA Paper No. AIAA-2007-0451*.
- [50] Tam, R., Belobaba, P., Polenske, K., and Waitz, I., 2007, "Assessment of Silent Aircraft-Enabled Regional Development and Airline Economics in the UK," *AIAA Paper No. AIAA-2007-0455*.
- [51] Lee, J. J., Lukachko, S. P., Waitz, I. A., and Schafer, A., 2001, "Historical and Future Trends in Aircraft Performance, Cost and Emissions," *Annu. Rev. Energy Environ.*, **26**, pp. 167–200.
- [52] Herr, M., and Dobrzynski, W., 2005, "Experimental Investigations in Low-Noise Trailing-Edge Design," *AIAA J.*, **43**, pp. 1167–1175.
- [53] Smith, L. H., 1993, "Wake Ingestion Propulsion Benefit," *J. Propul. Power*, **9**, pp. 74–82.
- [54] Reynolds, T. G., Ren, L., and Clarke, J.-P. B., 2007, "Advanced Noise Abatement Approach Activities at Nottingham East Midlands Airport, UK," Seventh USA/Europe Air Traffic Management R&D Seminar (ATM 2007), Barcelona, Spain.
- [55] Broers, A. N., 2005, *The Triumph of Technology*, Cambridge University Press, Cambridge.
- [56] Chesbrough, H. W., 2003, *Open Innovation*, Harvard Business School Press, Boston.
- [57] Friedman, T. L., 2005, *The World is Flat: A Brief History of the Twenty-First Century*, Farrar, Strauss, and Giroux, New York.
- [58] Dunn, M. G., 2001, "Convective Heat Transfer and Aerodynamics in Axial Flow Turbines," *ASME J. Turbomach.*, **123**, pp. 637–686.